DEVELOPMENT AND TESTING OF THE CBM-IV FOR URBAN AND REGIONAL MODELING

by

M. W. Gery
G. Z. Whitten

Systems Applications, Inc.
101 Lucas Valley Road
San Rafael, California 94903

and

J. P. Killus
433 Michigan Avenue
Berkeley, California 94707

Contract No. 68-02-4136

Project Officer

Dr. Marcia C. Dodge
Atmospheric Chemistry and Physics Division
Atmospheric Sciences Research Laboratory
Research Triangle Park, North Carolina 27711

ATMOSHERIC SCIENCES RESEARCH LABORATORY
OFFICE OF RESEARCH AND DEVELOPMENT
U. S. ENVIRONMENTAL PROTECTION AGENCY
RESEARCH TRIANGLE PARK, NC 27711

REVISIONS TO THE CB4 MECHANISM

The following revisions should be made to the CB4 mechanism listed in TABLE 1-3:

Reaction (46) C2O3 + NO → NO2 + XO2 + FORM + HO2

Change the Reaction Rate Data to the following:

Pre-factor	Temp. Factor	Rate Constant @ 298K
5.15 E+04	EXP(- 180/T)	2.82 E+04

Reaction (47) C2O3 + NO2 → PAN

Change the Reaction Rate Data to the following:

Pre-factor	Temp. Factor	Rate Constant @ 298K
3.84 E+03	EXP(+ 380/T)	1.37 E+04

Reaction (48) PAN → C2O3 + NO2

Change the Reaction Rate Data to the following:

Pre-factor	Temp. Factor	Rate Constant @ 298K
1.20 E+18	EXP(- 13500/T)	2.54 E-02

Reaction (82)

Add the following reaction:

XO2 + HO2 → (No Products)

With the following Reaction Rate Data:

Pre-factor	Temp. Factor	Rate Constant @ 298K
1.134 E+02	EXP(+ 1300/T)	8.90 E+03

****
BiblioFile Catalog
****

Title: Development and Testing of the CBM-IV (Carbon-Bond Mechanism) for Urban and Regional Modeling.
Author: Gery, M. W. Whitten, G. Z. Killus, J. P.
Author: Systems Applications, Inc., San Rafael, CA. Environmental Protection Agency, Research Triangle Park, NC. Atmospheric Sciences Research Lab.
Collation: 431p
Subject: Photochemical reactions Kinetics Simulation Models Methodology Condensing Evaluation Photolysis Tables(Data) Carbon Bond Mechanism(CBM) Air quality
Location: EPA NTIS.....: AVAILABLE MOST LIBRARIES

Leader:

Control #	1	epa00036086
Future Tag	5	891103
Fixed Data	8	000000
Local Ctrl #	35	a814618339
Local Ctrl #	35	zTLC NO CTRL
Stock No.	37	aPB88-180039
Cat. Source	40	aNTIS/MT
LC Call	50	aPB88-180039
Report No.	88	aEPA-68-02-4136 aEPA/600/3-88/012
Future Tag	89	aEPA68024136 aEPA600388012
ME:Pers Name	100	aGery, M. W. aWhitten, G. Z. aKillus, J. P.
ME:Corp Name	110	aSystems Applications, Inc., San Rafael, CA. aEnvironmental Protection Agency Research Triangle Park, NC. Atmospheric Sciences Research Lab.
Title	245	aDevelopment and Testing of the CBM-IV (Carbon-Bond Mechanism) for Urban and Regional Modeling.
Future Tag	248	aFinal rept. Jul 85-Jun 87.
Future Tag	262	aMar 88
Phys Descrpt	300	a431p
Note:Dissert	502	aSponsored by Environmental Protection Agency, Research Triangle Park, NC. Atmospheric Sciences Research Lab.
Subj:Pers	600	aPhotochemical reactions aKinetics aSimulation aModels aMethodology aCondensing aEvaluation aPhotolysis aTables(Data) aCarbon Bond Mechanism(CBM) aAir quality
SE:Pers Name	800	a55A a99F a68A a91A
Future Tag	802	aPC A19/MF A01
Future Tag	806	a600/09
Future Tag	900	bCAT
Future Tag	900	eNT
Future Tag	900	c880904
Future Tag	901	aThe development and testing of an updated Carbon Bond Mechanism (CBM) is described. The new mechanism, called CBM-IV, was designed for use in EPA's OZIPM-EKMA model. The mechanism, however, is also suitable for use in large air quality simulation models such as the Urban Airshed Model and EPA's Regional Oxidant Model. The mechanism differs from earlier versions of the CBM in that the chemistry of aromatic hydrocarbons has been significantly altered to account for the sensitivity of ozone formatieq aThe development and testing of an updated Carbon Bond Mechanism (CBM) is described. The new mechanism, called CBM-IV, was designed for use in EPA's OZIPM-EKMA model. The mechanism, however, is also suitable for use in large air quality simulation models such as the Urban Airshed Model and EPA's Regional Oxidant Model. The mechanism differs from earlier versions of the CBM in that the chemistry of aromatic hydrocarbons has been significantly altered to account for the sensitivity of ozone formatieq bNTIS b1988 aEPXXbAVAILABLE MOST LIBRARIES

DEVELOPMENT AND TESTING OF THE CBM-IV FOR URBAN AND REGIONAL MODELING

by

M. W. Gery
G. Z. Whitten

Systems Applications, Inc.
101 Lucas Valley Road
San Rafael, California 94903

and

J. P. Killus
433 Michigan Avenue
Berkeley, California 94707

Contract No. 68-02-4136

Project Officer

Dr. Marcia C. Dodge
Atmospheric Chemistry and Physics Division
Atmospheric Sciences Research Laboratory
Research Triangle Park, North Carolina 27711

ATMOSHERIC SCIENCES RESEARCH LABORATORY
OFFICE OF RESEARCH AND DEVELOPMENT
U. S. ENVIRONMENTAL PROTECTION AGENCY
RESEARCH TRIANGLE PARK, NC 27711

DISCLAIMER

This report has been reviewed by the Atmospheric Sciences Research Laboratory, U. S. Environmental Protection Agency, and approved for publication. Approval does not signify that the contents necessarily reflect the view and policies of the U. S. Environmental Protection Agency, nor does mention of trade names or commercial products constitute endorsement or recommendation for use.

ABSTRACT

A new chemical kinetics mechanism for simulating urban and regional photochemistry based on the carbon-bond method of hydrocarbon condensation was developed and evaluated in this project. The Carbon-Bond Mechanism-IV (CBM-IV) is a condensed version of an expanded mechanism (CBM-X) that was initially developed using currently available laboratory and smog chamber data. In addition to a general updating of the mechanism to include the most recent kinetic, mechanistic, and photolytic information, the CBM-IV comprises extensive improvements to the chemical representations of aromatic species, biogenic hydrocarbons and PAN. CBM-IV performance in predicting ozone, formaldehyde, and PAN concentrations was evaluated against the results of approximately 160 experiments from four different smog chambers. Both the maximum predicted concentrations and the time to the maximum were compared. Other parameters such as hydrocarbon and NO_x decay rates were also addressed. The results of these evaluations indicate substantial improvement in the ability of the CBM-IV to simulate aromatic and isoprene systems. Formaldehyde predictions for the isoprene experiments were also very good. The CBM-IV overpredicted maximum ozone concentrations by 2% and underpredicted formaldehyde by 9% for 68 different hydrocarbon/NO_x mixture experiments from three different smog chambers.

CONTENTS

List of Illustrations..... vii

List of Tables..... xx

1 INTRODUCTION..... 1

Chronological Development of the CBM..... 1
Surrogate Hydrocarbon Approximations..... 5
Description of the Carbon Bond Mechanism(s)..... 7
Specific Improvements to the Mechanisms..... 22

2 MECHANISM DEVELOPMENT METHODOLOGY..... 25

Formulation of the Mechanism..... 25
Mechanism Evaluation and Adjustment..... 26
Mechanism Condensation..... 29
Atmospheric Applications..... 30

3 THE INORGANIC AND CARBONYL REACTION SET..... 33

Inorganic Chemistry..... 33
Formaldehyde Reactions..... 46
Acetaldehyde and PAN Reactions..... 49
Photolysis Reactions..... 70
Condensation of Inorganic and Carbonyl Reactions..... 95

4 REACTIVE HYDROCARBON CHEMISTRY..... 99

Alkyl Group (Paraffin) Chemistry..... 99
Development of Alkyl Chemistry for the CBM-X..... 116
Olefin and Ethene Chemistry..... 130

Aromatic Chemistry..... 139
Isoprene..... 156

5 REPRESENTATION OF SMOG CHAMBER PROCESSES AND CHARACTERISTICS..... 159

Photolytic Processes..... 159
Wall-Related Processes..... 175

6 EVALUATION AND DEMONSTRATION OF THE CBM-IV..... 206

Aldehydes and PAN..... 207
Ethene and Olefins..... 210
Aromatics..... 212
Biogenic Hydrocarbons..... 215
Mixtures..... 215
Summary of Simulation Results..... 220

7 SUMMARY AND CONCLUSIONS..... 395

References..... 400

FIGURES

1-1 Schematic of Carbon-Bond Mechanism development..... 3

1-2 Schematic description of the hierarchy of species for the Carbon Bond Mechanism-IV..... 9

2-1 Schematic representation of the development, condensation, evaluation and application of a photochemical kinetics mechanism..... 27

3-1 Simulation results and experimental data for the UNC biacetyl-NO_x experiment of 8 August 1980..... 54

3-2 Simulation results and experimental data for the UNC acetaldehyde-NO_x experiment of 8 August 1980..... 55

3-3 Simulation results and experimental data for the UNC acetaldehyde-NO_x experiment of 26 December 1977..... 56

3-4 Simulation results and experimental data for the UNC acetaldehyde-NO_x experiment of 19 November 1977..... 57

3-5 Simulation results and experimental data for the UNC acetaldehyde-NO_x experiment of 20 November 1977..... 59

3-6 Simulation results and experimental data for the UCR acetaldehyde-NO_x experiment EC-254..... 60

3-7 Simulation results and experimental data for the UCR acetaldehyde-NO_x experiment EC-253..... 61

3-8 Temperature dependence functions for the peroxyacetyl radical reactions with NO and NO_2..... 63

3-9 m-Xylene concentration traces for UCR EC-345 comparing the effects of including radical disproportionation products in the HO2 plus RO2 reactions..... 67

3-10 Actinic flux for 20 and 60 degree solar zenith angles in bin sizes of 1 and 5 nm..... 72

3-11 Photoaction spectra for NO_2 using 1 and 5 nm bins..... 76

3-12 Comparison of absorption cross sections for formaldehyde from Moortgat (top) and Bass (bottom)..... 86

3-13 Photoaction spectra for formaldehyde to stable products (top) and formaldehyde to radicals (bottom) using the 10 nm bins of NASA (1855) and the 1 nm bins from Bass (1980)..... 87

3-14 Photoaction spectra for acetaldehyde using 1 and 5 nm bins.... 89

3-15 Comparison of relative j-value curve shapes with respect to solar zenith angle for five major photolytic species..... 90

3-16 Comparison of photoaction spectra for j_{NO2} and j_{O1D} at 20 and 60 degrees solar zenith angles..... 91

4-1 Schematic representation of the PAR reaction scheme..... 121

4-2 Rate constants for OH plus aromatics..... 143

4-3 Experimental results for JN2784B..... 146

4-4 Experimental resuls for JN2784R..... 147

5-1 Comparison of experimental data for EC-232 and EC-246..... 164

5-2 Data points are daily average atmospheric turbidity in North Carolina..... 168

5-3 Specific photolysis rate of nitrogen dioxide and incidental total solar radiation and ultraviolet radiation as a function of time for 13 October 1976..... 170

5-4 Data points from Zafonte..... 173

5-5 Data points from Stedman..... 174

5-6 Simulation results for UNCR 72179..... 181

5-7 Estimated hydroxyl radical concentrations for UCR EC-238 using two different radical estimation techniques..... 186

5-8 Estimated radical concentrations for a set of UCR EC experiments..... 187

5-9 Estimated radical concentrations for two UCR ITC experiments..... 188

5-10 Ozone and PAN traces for ITC-627, an acetaldehyde-only experiment..... 191

5-11 Experimental data from the two-day, ITC-631 experiment with the dark period removed and the two light periods merged..... 196

5-12 Estimated radical source strengths for five UNC smog chamber experiments using two different estimation techniques..... 198

5-13 Comparison of estimated radical input rates and k_1 (j_{NO2}) for chamber characterization experiments in the UNC chamber... 201

5-14 Histogram used to estimate the relationship of radical input rate to k_1 (j_{NO2})..... 203

6-1 Simulation results for UNC experiment OC0984B (symbols are experimental measurements)..... 222

6-2 Simulation results for UNC experiment OC0984R (symbols are experimental measurements)..... 223

6-3 Simulation results for UNC experiment AU0179B (symbols are experimental measurements)..... 224

6-4 Simulation results for UNC experiment AU0279B (symbols are experimental measurements)..... 225

6-5 Simulation results for UNC experiment AU0479B (symbols are experimental measurements)..... 226

6-6 Simulation results for UNC experiment AU0579B (symbols are experimental measurements)..... 227

6-7 Simulation results for UNC experiment AU1280R (symbols are experimental measurements)..... 228

6-8 Simulation results for UNC experiment JN1482R (symbols are experimental measurements)..... 229

6-9 Simulation results for UNC experiment AU2482B (symbols are experimental measurements)..... 230

6-10 Simulation results for UNC experiment JN1482B (symbols are experimental measurements)..... 231

6-11 Simulation results for UNC experiment AU2482R (symbols are experimental measurements)..... 232

6-12 Simulation results for UNC experiment AU0479R (symbols are experimental measurements)..... 233

6-13 Simulation results for UNC experiment OC0584B (symbols are experimental measurements)..... 234

6-14 Simulation results for UNC experiment OC0584R (symbols are experimental measurements)..... 235

6-15 Simulation results for UNC experiment AU1078B (symbols are experimental measurements)..... 236

6-16 Simulation results for UNC experiment AU1078R (symbols are experimental measurements)..... 237

6-17 Simulation results for UNC experiment AU2378B (symbols are experimental measurements)..... 238

6-18 Simulation results for UNC experiment AU2378R (symbols are experimental measurements)..... 239

6-19 Simulation results for UNC experiment JL0880R (symbols are experimental measurements)..... 240

6-20 Simulation results for UNC experiment JL0986B (symbols are experimental measurements)..... 241

6-21 Simulation results for UNC experiment JL0986R (symbols are experimental measurements)..... 242

6-22 Simulation results for UNC experiment JL1386B (symbols are experimental measurements)..... 243

6-23 Simulation results for UNC experiment JL1386R (symbols are experimental measurements)..... 244

6-24 Simulation results for UNC experiment OC1184B (symbols are experimental measurements)..... 245

6-25 Simulation results for UNC experiment OC1284B (symbols are experimental measurements)..... 246

6-26 Simulation results for UNC experiment AU1679R (symbols are experimental measurements)..... 247

6-27 Simulation results for UNC experiment OC1278B (symbols are experimental measurements)..... 248

6-28 Simulation results for UNC experiment OC2578B (symbols are experimental measurements)..... 249

6-29 Simulation results for UNC experiment SE2383B, and SE2383R (symbols are experimental measurements)..... 250

6-30 Simulation results for UNC experiment SE2583B, and SE2583R (symbols are experimental measurements)..... 251

6-31 Simulation results for UNC experiment SE2783B, and SE2783R (symbols are experimental measurements)..... 252

6-32 Simulation results for UCR experiment EC-177 (symbols are experimental measurements)..... 253

6-33 Simulation results for UCR experiment EC-121 (symbols are experimental measurements)..... 254

6-34 Simulation results for UCR experiment EC-278 (symbols are experimental measurements)..... 255

6-35 Simulation results for UCR experiment EC-123 (symbols are experimental measurements)..... 256

6-36 Simulation results for UCR experiment EC-124 (symbols are experimental measurements)..... 257

6-37 Simulation results for UNC experiment JN2779B (symbols are experimental measurements)..... 258

6-38 Simulation results for UNC experiment JL3080R (symbols are experimental measurements)..... 259

6-39 Simulation results for UNC experiment JN2784B (symbols are experimental measurements)..... 260

6-40 Simulation results for UNC experiment AU1579B (symbols are experimental measurements)..... 261

6-41 Simulation results for UNC experiment AU0183R (symbols are experimental measurements)..... 262

6-42 Simulation results for UNC experiment OC2782R (symbols are experimental measurements)..... 263

6-43 Simulation results for UNC experiment AU2782B (symbols are experimental measurements)..... 264

6-44 Simulation results for UCR experiment EC-266 (symbols are experimental measurements)..... 265

6-45 Simulation results for UCR experiment EC-271 (symbols are experimental measurements)..... 266

6-46 Simulation results for UCR experiment EC-327 (symbols are experimental measurements)..... 267

6-47 Simulation results for UCR experiment EC-340 (symbols are experimental measurements)..... 268

6-48 Simulation results for UCR experiments EC-264,EC-265, EC-269, and EC-273 (symbols are experimental measurements).... 269

6-49 Simulation results for UNC experiment JN2784R (symbols are experimental measurements)..... 270

6-50 Simulation results for UCR experiment EC-346 (symbols are experimental measurements)..... 271

6-51 Simulation results for UCR experiment EC-345 (symbols are experimental measurements)..... 272

6-52 Simulation results for UCR experiment EC-344 (symbols are experimental measurements)..... 273

6-53 Simulation results for UNC experiments JL3080B, AU2782R, AU0183B, and OC2782B (symbols are experimental measurements)..... 274

6-54 Simulation results from the CALL (Carter et al., 1986) and earlier CBMX (Whitten et al., 1985) mechanisms from UNC JL3080R..... 275

6-55 Simulation results for UNC experiment JL1480B (symbols are experimental measurements)..... 276

6-56 Simulation results for UNC experiment JL1480R (symbols are experimental measurements)..... 277

6-57 Simulation results for UNC experiment JL1680B (symbols are experimental measurements)..... 278

6-58 Simulation results for UNC experiment JL1680R (symbols are experimental measurements)..... 279

6-59 Simulation results for UNC experiment JL1780B (symbols are experimental measurements)..... 280

6-60 Simulation results for UNC experiment JL1780R (symbols are experimental measurements)..... 281

6-61 Simulation results for UNC experiment JN1780B (symbols are experimental measurements)..... 282

6-62 Simulation results for UNC experiment JN1780R (symbols are experimental measurements)..... 283

6-63 Simulation results for UNC experiment JN2080R (symbols are experimental measurements)..... 284

6-64 Simulation results for UNC experiment JN2280B (symbols are experimental measurements)..... 285

6-65 Simulation results for UNC experiment JN2280R (symbols are experimental measurements)..... 286

6-66 Simulation results for UNC experiment JN2380B (symbols are experimental measurements)..... 287

6-67 Simulation results for UNC experiment JL2580B (symbols are experimental measurements)..... 288

6-68 Simulation results for UNC experiment JL258OR (symbols are experimental measurements)..... 289

6-69 Simulation results for UNC experiment JN158OB (symbols are experimental measurements)..... 290

6-70 Simulation results for UNC experiment JN158OR (symbols are experimental measurements)..... 291

6-71 Simulation results for UNC experiment JL158OB (symbols are experimental measurements)..... 292

6-72 Simulation results for UNC experiment JL158OR (symbols are experimental measurements)..... 293

6-73 Simulation results for UNC experiment JN148OB (symbols are experimental measurements)..... 294

6-74 Simulation results for UNC experiment JN148OR (symbols are experimental measurements)..... 295

6-75 Simulation results for UNC experiment JN218OR (symbols are experimental measurements)..... 296

6-76 Simulation results for UNC experiment AU2284R (symbols are experimental measurements)..... 297

6-77 Simulation results for UNC experiment AU2584B (symbols are experimental measurements)..... 298

6-78 Simulation results for UNC experiment STO184B (symbols are experimental measurements)..... 299

6-79 Simulation results for UNC experiment STO284B (symbols are experimental measurements)..... 300

6-80 Simulation results for UNC experiment STO284R (symbols are experimental measurements)..... 301

6-81 Simulation results for UNC experiment STO384R (symbols are experimental measurements)..... 302

6-82 Simulation results for UNC experiment AUO484R (symbols are experimental measurements)..... 303

6-83 Simulation results for UNC experiment AU0584B (symbols are experimental measurements)..... 304

6-84 Simulation results for UNC experiment AU0584R (symbols are experimental measurements)..... 305

6-85 Simulation results for UNC experiment AU0684B (symbols are experimental measurements)..... 306

6-86 Simulation results for UNC experiment AU0684R (symbols are experimental measurements)..... 307

6-87 Simulation results for UNC experiment AU0784R (symbols are experimental measurements)..... 308

6-88 Simulation results for UNC experiment AU0884B (symbols are experimental measurements)..... 309

6-89 Simulation results for UNC experiment AU0984R (symbols are experimental measurements)..... 310

6-90 Simulation results for UNC experiment ST0884B (symbols are experimental measurements)..... 311

6-91 Simulation results for UNC experiment ST0884R (symbols are experimental measurements)..... 312

6-92 Simulation results for UNC experiment ST1784R (symbols are experimental measurements)..... 313

6-93 Simulation results for UNC experiment ST2184B (symbols are experimental measurements)..... 314

6-94 Simulation results for UNC experiment ST2184R (symbols are experimental measurements)..... 315

6-95 Simulation results for UCR experiment EC-231 (symbols are experimental measurements)..... 316

6-96 Simulation results for UCR experiment EC-232 (symbols are experimental measurements)..... 317

6-97 Simulation results for UCR experiment EC-233 (symbols are experimental measurements)..... 318

6-98 Simulation results for UCR experiment EC-237 (symbols are experimental measurements)..... 319

6-99 Simulation results for UCR experiment EC-238 (symbols are experimental measurements)..... 320

6-100 Simulation results for UCR experiment EC-241 (symbols are experimental measurements)..... 321

6-101 Simulation results for UCR experiment EC-242 (symbols are experimental measurements)..... 322

6-102 Simulation results for UCR experiment EC-243 (symbols are experimental measurements)..... 323

6-103 Simulation results for UCR experiment EC-245 (symbols are experimental measurements)..... 324

6-104 Simulation results for UCR experiment EC-246 (symbols are experimental measurements)..... 325

6-105 Simulation results for UCR experiment EC-247 (symbols are experimental measurements)..... 326

6-106 Simulation results for UCR experiment ITC-630 (symbols are experimental measurements)..... 327

6-107 Simulation results for UCR experiment ITC-631 (symbols are experimental measurements)..... 328

6-108 Simulation results for UCR experiment ITC-633 (symbols are experimental measurements)..... 329

6-109 Simulation results for UCR experiment ITC-635 (symbols are experimental measurements)..... 330

6-110 Simulation results for UCR experiment ITC-637 (symbols are experimental measurements)..... 331

6-111 Simulation results for UNC experiment OC0382B (symbols are experimental measurements)..... 332

6-112 Simulation results for UNC experiment OC0382R (symbols are experimental measurements)..... 333

6-113 Simulation results for UNC experiment AU3181B (symbols are experimental measurements)..... 334

6-114 Simulation results for UNC experiment AU3181R (symbols are experimental measurements)..... 335

6-115 Simulation results for UNC experiment JL2281B (symbols are experimental measurements)..... 336

6-116 Simulation results for UNC experiment JL2281R (symbols are experimental measurements)..... 337

6-117 Simulation results for UNC experiment JN2581B (symbols are experimental measurements)..... 338

6-118 Simulation results for UNC experiment JN2581R (symbols are experimental measurements)..... 339

6-119 Simulation results for UNC experiment DE0782B (symbols are experimental measurements)..... 340

6-120 Simulation results for UNC experiment DE0782R (symbols are experimental measurements)..... 341

6-121 Simulation results for UNC experiment SE1682B (symbols are experimental measurements)..... 342

6-122 Simulation results for UNC experiment SE1682R (symbols are experimental measurements)..... 343

6-123 Simulation results for UNC experiment NV1182B (symbols are experimental measurements)..... 344

6-124 Simulation results for UNC experiment NV1182R (symbols are experimental measurements)..... 345

6-125 Simulation results for UNC experiment SE1882B (symbols are experimental measurements)..... 346

6-126 Simulation results for UNC experiment SE1882R (symbols are experimental measurements)..... 347

6-127 Simulation results for both sides of UNC experiments SE1481, SE2081, and SE2981 (symbols are experimental measurements)..... 348

6-128 Simulation results for both sides of UNC experiments SE0381 and SE1081 (symbols are experimental measurements)..... 349

6-129 Simulation results for UNC experiment AU2681B (symbols are experimental measurements)..... 350

6-130 Simulation results for UNC experiment AU2681R (symbols are experimental measurements)..... 351

6-131 Simulation results for UNC experiment SE1984B (symbols are experimental measurements)..... 352

6-132 Simulation results for UNC experiment SE1984R (symbols are experimental measurements)..... 353

6-133 Simulation results for UNC experiment OC0483B (symbols are experimental measurements)..... 354

6-134 Simulation results for UNC experiment OC0783B (symbols are experimental measurements)..... 355

6-135 Simulation results for UNC experiment OC0783R (symbols are experimental measurements)..... 356

6-136 Scatter diagrams comparing predicted maximum ozone concentration versus measured values for aldehyde (top) and alkene (bottom) smog chamber experiments..... 357

6-137 Scatter diagrams comparing predicted maximum ozone concentration versus measured values for aromatic (top) and biogenic hydrocarbon (bottom) smog chamber experiments..... 358

6-138 Scatter diagrams comparing predicted maximum ozone concentration versus measured values for reactive hydrocarbon mixture experiments (top) and all simulated experiments (bottom)..... 359

6-139 Scatter diagrams comparing predicted formaldehyde concentration versus measured values for aldehyde (top) and alkene (bottom) smog chamber experiments..... 360

6-140 Scatter diagrams comparing predicted maximum formaldehyde concentration versus measured values for aromatic (top) and biogenic hydrocarbon (bottom) smog chamber experiments..... 361

6-141 Scatter diagrams comparing predicted maximum formaldehyde concentration versus measured values for reactive hydrocarbon mixture experiments (top) and all simulated experiments (bottom)..... 362

TABLES

1-1 The Carbon-Bond Mechanism series..... 2

1-2 The Carbon Bond Mechanism-X..... 10

1-3 The Carbon Bone Mechanism-IV..... 17

3-1 Absorption cross sections and quantum yields for NO_2 photolysis..... 73

3-2 Results of j_{NO2} calculations..... 75

3-3 Absorption cross sections and quantum yields for formaldehyde photolysis to radical products..... 78

3-4 Absorption cross sections and quantum yields for formaldehyde photolysis to stable products..... 79

3-5 Absorption cross sections and quantum yields for ozone photolysis to $O(^1D)$..... 80

3-6 Absorption cross sections and quantum yields for acetaldehyde photolysis to radical products..... 81

3-7 Absorption cross sections and quantum yields for nitrous acid photolysis..... 82

3-8 Absorption cross sections and quantum yields for hydrogen peroxide photolysis..... 83

3-9 Results of j-value calculations..... 85

4-1 Average concentration (ppb) of each hydrocarbon species identified in ambient air by the ERT and WSU methods for 23 common analyses..... 100

4-2 Calculated nitrate yields compared to measured yields for various alkanes..... 115

4-3 Explicit alkyl group chemistry..... 117

4-4 Carbon and bond types..... 122

4-5 Alkyl group chemistry of the Carbon Bond Mechanism-X..... 125

4-6 Species involved in the oxidation of paraffin..... 126

5-1 Relative spectral distribution for the blacklights in the SAPRC 6400-liter Indoor Teflon Chamber (ITC)..... 161

5-2 Summary of average relative spectral distributions used in modeling the SAPRC Evacuable Chamber (EC) experiments by Carter et al. (1986)..... 163

5-3 Comparison of total NO_x with measured HONO in the UCR-EC..... 179

5-4 Estimated radical levels using two different methodologies for the UCR-ITC..... 190

5-5 Chamber background radical sources as a fraction of total radical inputs for the UCR-EC..... 193

5-6 Chamber background radical sources as a fraction of total radical inputs for smog chambers other than the UCR-EC..... 194

5-7 Radical inputs for CO/NO_x experiments in the UNC smog chamber..... 200

6-1 Initial conditions for UNC formaldehyde smog chamber simulations..... 363

6-2 Results of UNC formaldehyde simulations..... 364

6-3 Initial conditions for acetaldehyde and propionaldehyde smog chamber simulations..... 365

6-4 Results of acetaldehyde and propionaldehyde simulations..... 366

6-5 Initial conditions for UNC ethene smog chamber simulations..... 368

6-6 Results of UNC ethene simulations..... 369

6-7 Initial conditions for olefin smog chamber simulations..... 370

6-8 Results of olefin simulations..... 371

6-9 Initial conditions for toluene smog chamber simulations..... 373

6-10 Results of toluene simulations..... 374

6-11 Initial conditions for xylene smog chamber simulations..... 376

6-12 Results of xylene simulations..... 377

6-13 Initial conditions for UNC isoprene and α-pinene smog chamber simulations..... 379

6-14 Results of UNC isoprene and α-pinene simulations..... 380

6-15 Initial conditions for UNC SynUrban and SynAuto mixture simulations..... 382

6-16 Results of UNC SynUrban and SynAuto mixture simulations..... 383

6-17 Initial conditions for UCR-EC seven component hydrocarbon mixture simulations..... 385

6-18 Results of UCR-EC seven component hydrocarbon mixture simulations..... 386

6-19 Initial conditions for UCR-ITC multi-day simulations..... 387

6-20 Results of UCR ITC multi-day experiment simulations..... 388

6-21 Initial conditions for UNC hydrocarbon reactivity experiment simulations..... 390

6-22 Results of UNC hydrocarbon reactivity experiment simulations..... 393

1 INTRODUCTION

For over a decade, the United States Environmental Protection Agency (EPA) has supported the development and testing of photochemical kinetics mechanisms used in urban and regional air quality simulation models (AQSMs). This report describes the development and evaluation of the most recent version of the Carbon-Bond Mechanism (CBM), known as the CBM-IV. As a technical basis for this condensed version, a full (expanded) version, the CBM-X, was first developed. The CBM-X is suitable for use in less complex and computationally demanding AQSMs or chemical kinetic models, but serves primarily as the basis for the CBM-IV, which was developed for use in larger models such as the Urban Airshed Model (UAM), the EPA Regional Oxidant Model (ROM), the EPA OZIPM/EKMA model, and various Systems Applications models [i.e., Regional Transport Model (RTM)].

The remainder of this section contains an overview of the CBM. We briefly consider the chronology of its development and discuss the fundamental difference between the CBM approach and those of mechanisms that use other hydrocarbon surrogate approximations. Section 2 describes the methodology of formulation, condensation, and evaluation used in the CBM. Sections 3 and 4 document the chemical characteristics of the individual components of the chemical mechanisms, including photolysis rate calculations and descriptions and specific examples of condensation techniques used to formulate the CBM-IV. Section 5 discusses smog chamber characteristics and artifacts. Section 6 summarizes model evaluation results.

CHRONOLOGICAL DEVELOPMENT OF THE CBM

Since 1976, Systems Applications has been developing the CBM for use in urban and regional AQSMs. The series of mechanisms developed to date is given in Table 1-1; a flow chart depicting the logical succession of mechanisms is shown in Figure 1-1. The first version of the CBM was formulated in 1977 (Whitten and Hogo, 1977) and was highly parameterized due to the limited state of knowledge at the time. Since then, our knowledge of photochemical processes has expanded considerably, primarily as a result of the efforts of the EPA and other organizations to gather experimental data, particularly chemical kinetic and smog chamber data. This increased knowledge was first reflected in CBM-II and CBM-III. All three

TABLE 1-1. The Carbon-Bond Mechanism series.

Mechanism	Description	Number of Reactions/Species	Reference
CBM-I	Original CBM	35/20	Whitten and Hogo (1977) Whitten et al. (1980a)
CBM-II	Update/Expansion of CBM-I	65/27	Whitten et al. (1980b)
CBM-III	Update of CBM-II with improved aromatics chemistry	75/36	Killus and Whitten (1982a)
CBM-X	Expanded version of CBM suitable for use in EKMA	146/67	Whitten et al. (1985a)
CBM-XR	CBM-X with isoprene chemistry for regional scale modeling	170/78	Whitten et al. (1985b)
CBM-RR	Condensed version of CBM-XR	113/47	Whitten et al. (1985b)
CBM-IV	Original, highly condensed version of CBM-RR	70/28	Whitten and Gery (1986)
CBM-X	Update of 1985 CBM-X	164/71	This work
CBM-IV	Latest version of condensed CBM	81/33	This work

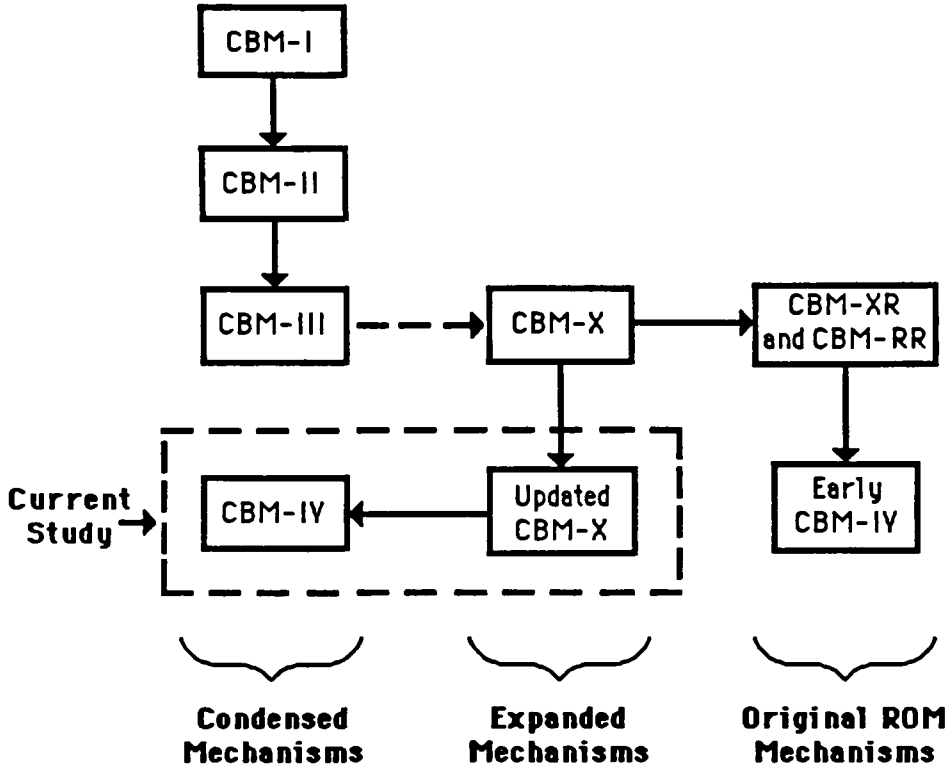

FIGURE 1-1. Schematic of Carbon-Bond Mechanism development.

of these early CBM mechanisms were developed for use in sophisticated AQSMs and are, therefore, highly condensed.

In 1985, Whitten et al. (1985a) presented an expanded version of the CBM known as the CBM-X for use in the OZIPM-3/EKMA model. The CBM-X contained a more complete kinetic description than was previously employed with that version of OZIPM, but its use was feasible because the computational demands of OZIPM were much less than those of larger AQSMs. The CBM-X provided the basis on which previous versions had been developed; it was validated by comparing the chemistry of species common to almost all organic systems (e.g., formaldehyde, acetaldehyde, PAN, and CO) with the results of numerous smog chamber experiments containing those compounds. In addition, the first formulations of ethene (ETH), 1-olefins (OLE), mono-alkylbenzenes (TOL), multi-alkylbenzenes (XYL), and paraffins (PAR) were developed and tested and the complete mechanism was evaluated with smog chamber data from the University of North Carolina (UNC) facility (Jeffries et al., 1985a) for a series of authentic and synthetic automobile exhaust/NO_x experiments; and for a series of aromatic/NO_x experiments in the Battelle chamber.

The CBM-X was then further expanded for regional use by the inclusion of isoprene (ISOP) chemistry (Whitten et al., 1985b). Following this addition, the complete mechanism was again evaluated with a set of smog chamber data from the University of California at Riverside (UCR) (Carter et al., 1985). These experiments provided a multi-day testing environment in which nighttime reactions could be investigated for their accuracy and importance to condensation procedures. The use of a large data set from this second outdoor chamber also provided a clearer description of significant smog chamber characteristics. The mechanism was then condensed for use in the first version of the EPA/ROM. As shown in Table 1-1, the resulting mechanism (CBM-RR) contained 113 reactions and 47 species. Although the CBM-RR was appropriate for use in the ROM, it was still a very large and complex mechanism. As a result of changes in the ROM mechanism input requirements, we developed a more condensed version of the CBM-RR nominally identified as CBM-IV (Whitten and Gery, 1986).

Through the development process just described and shown in Figure 1-1, it can be seen that the initial version of the CBM-IV was based on the original CBM-X and the ensuing evaluations with smog chamber data. Throughout this lengthy evaluation process, certain aspects of the original CBM-X became better understood. As a result, the work reported here was undertaken to update the technical basis of the CBM-X and to transfer this new representation to the condensed CBM-IV. We have also evaluated CBM-IV performance against smog chamber data and provided information and alterations needed to implement the CBM-IV in the ROM and the newly revised OZIPM-4/EKMA.

SURROGATE HYDROCARBON APPROXIMATIONS

The CBM-IV developed in this project uses a combination of inorganic chemistry and explicit and surrogate organic reaction schemes. The Inorganic and Carbonyl Reaction Set (ICRS) explicitly treats inorganic chemistry and the reactions of some product species (e.g., formaldehyde, acetaldehyde, and PAN) common to several hydrocarbon mechanisms. Reactive hydrocarbons are usually treated within a surrogate approximation; however, some specific hydrocarbons that (1) cannot easily be included into surrogate schemes and (2) are common constituents of polluted atmospheres (i.e., ethene, isoprene, and to a lesser degree, toluene, xylene, and acetaldehyde) warrant individual treatment. The determination of species to be treated in either surrogate or explicit reaction schemes was performed by Whitten et al., (1985a) for a large number of species reportedly measured in the atmosphere. To test the significance of individual hydrocarbon species, Whitten et al. used three ranking schemes: the OH reaction rate, relative concentration, and fraction of reacted hydrocarbon after 12 hours. This work established the importance of ethene, toluene, and the xylenes (and possibly isoprene). The reader is referred to that work (Whitten et al., 1985a) for further details.

The large number of hydrocarbons involved in tropospheric photochemistry precludes a fully explicit chemical treatment of each individual compound, causing problems of generalization and categorization in kinetic mechanism development for organic species. Surrogate approaches, in which individual entities are used to represent a variety of similarly reacting compounds, offer sets of natural categories for hydrocarbon classification; however, each surrogate approximation inevitably involves departures from the true chemistry of individual compounds. If the classification error becomes too great, then another category must be added to the mechanism, and the simulation process becomes less compact and analytically tractable and more expensive.

Several techniques have been devised to generalize and classify reactive hydrocarbons and their chemistry. Molecular lumping is outwardly the simplest (e.g., Atkinson et al., 1982; Carter et al., 1986; NCAR, 1987). In this methodology, a general hydrocarbon category is developed from the average behavior of a number of different compounds. The principal requirement for a molecular lumping scheme is that the behavior of the individual compounds not depart too greatly from the average behavior of the category. Rate constants for each generalized hydrocarbon class

should, in theory, be some appropriate average rate of the individual compounds contained in each class.*

Noninteger stoichiometric parameters are also required to describe reaction pathways for the lumped molecular species and the lumped intermediates generated by the chemistry. The choice of the proper values for the stoichiometric parameters poses an additional problem similar to the averaging of rate constants. In practice, these mechanisms usually specify some default value that may or may not approximate the ensemble average. If the hydrocarbon mixture to be modeled is sufficiently dissimilar to the mixture used to create the default values, an erroneous prediction of chemical dynamics could result. The proper conversion of such dissimilar mixtures into lumped molecular concentrations is often a complicated problem that may not have a unique solution. The stoichiometric parameters that describe the average molecular size and product distribution of the lumped species can also affect both reactivity and carbon balance. The specification of these parameters to simultaneously satisfy all of these constraints can be difficult, and some lumped mechanisms have been shown to violate the reactive-carbon-conservation requirement (Whitten, 1983).

Another technique that has been used to reduce the difficulty of the generalization problem is lumped structural reactivity classification. In this technique categorization is based on the similarity of unique structural groups common to many different molecules. The source of this approach is the explicit decoupling of submolecular reactivity components from the method of carbon conservation. The physical basis of such an

---

* The averaging of rate constants can be a difficult and potentially serious problem. The range of values over which such averaging is performed must be minimized so that the effects of highly reactive compounds will not be underpredicted at the beginning of simulations and the effects of the less reactive compounds remaining at the end of the simulations will not be exagerated. Most smog chamber experiments involve initial concentrations of precursors with no additional precursors added during the course of the experiment; the most reactive compounds strongly affect the chemistry in the early parts of these experiments. A generalized mechanism using average rate constants based on a wide range of initial reactivities might test well against smog chamber data, but still not have appropriate averages for accurate atmospheric simulations. A generalized mechanism using average rate constants based on narrow ranges of reactivities will be reliable over a wide spectrum of conditions.

empirical finding appears to be that the forces between atoms in the same or different molecules are very "short range"; that is, they are appreciable only over distances of the order of 0.1 to 0.3 nm (Benson, 1976; Benson and Bass, 1958). Benson and Bass have shown that it is possible to describe many molecular properties using a hierarchical system of additivity laws in which the simplest- or "zeroth-order" law would be the law of additivity of atom properties. In an atom-additivity scheme, one assigns partial values for the property in question to each atom in the molecule. The molecular property is thereby the sum of all the atom contributions. Thus, in the lumped structure approach, the carbon atom structures within the hydrocarbon molecules are the lumping category. For example, one lumped species might be used to represent all the single-bonded carbon atoms that occur not only in alkanes, but also in other organics such as olefins and substituted aromatics. Another lumped species might be used to represent pi-bonded carbon in the double-bond groups that are found in olefins.

The lumped structure approach offers several advantages over the lumped molecular approach. Because similar structures have similar reaction rate constants, the averaging problem is minimized. Carbon conservation can be expressly maintained, and carbon balance during the simulation can be monitored. Because the number of structural carbon bonding groups is relatively small, a large number of compounds can be uniquely assigned to carbon-bond concentrations. Some problems will occur in attempting to assign structures not expressly accounted for (e.g., esters, ethers, alcohols, amines, mercaptans, etc.) in the CBM. The principal disadvantage is that intramolecular processes such as decomposition can be difficult to treat. Also, because the lumped structure approach is less intuitive than the lumped molecule approach, extensive documentation is required to enable others to use mechanisms based on this approach. The structural reactivity generalization method has been the basis for our mechanism design philosophy because it eliminates many of the troublesome features inherent in the molecular lumping method.

DESCRIPTION OF THE CARBON BOND MECHANISM(S)

CBM-IV and CBM-X were developed and evaluated on the basis of relationships among hierarchical species in the overall chemical mechanism. The core of this hierarchy includes both a set of inorganic reactions and the reactions of carbonyl species common to most tropospheric photooxidation systems, the ICRS. The remaining reactions are made up of various organic reaction subsets that describe either specific hydrocarbons or condensed forms of the chemistry of other hydrocarbons (or hydrocarbon structures). The hierarchical approach to mechanism development was first outlined in Whitten et al. (1979); a more recent description of mechanism

development and evaluation based on the independent development and evaluation of individual components of a chemical mechanism in a hierarchical manner is contained in Gery (1987). The most important objective of this approach is the minimization of compensating errors in the final, overall chemical mechanism. We now focus on the hierarchical relationship between general reactivity groups of the CBM as illustrated in Figure 1-2. The specific reaction mechanisms of CBM-X and CBM-IV are given in Tables 1-2 and 1-3. The subgroups of these mechanisms that appear in the hierarchical structrue are briefly described next.

Inorganic Chemistry

Reactions 1 through 36 describe the atmospheric chemistry of species that contain only oxygen, nitrogen, and hydrogen atoms and one reaction involving CO.

Common Carbonyl and Methane Chemistry

Reactions 37 through 73 in the CBM-X (Table 1-2) describe the detailed chemistry of the common carbonyl compounds formaldehyde, acetaldehyde, and acetone. Other carbonyls such as methylglyoxal and benzaldehyde, are considered along with their respective parent hydrocarbons. The common carbonyl chemistry has been condensed to reactions 37 through 50 in the CBM-IV (Table 1-3). CBM-X reaction 74 (reaction 51 in the CBM-IV) describes the chemistry of methane. Since methane in the atmosphere does not decay from an assumed constant level of 1.85 ppm, the concentration of methane has been lumped into the rate constant. The reactions to this point provide enough overall chemistry to generate photochemical ozone and PAN; therefore, this set can be independently tested against smog chamber experiments. Section 3 describes the development of this reaction set and describes some of these tests.

Paraffinic or Single-Bonded Carbon Chemistry

CBM-X reactions 75 through 92 are designed to describe the chemistry of a typical atmospheric mixture of paraffins. The single-bonded constituents of other types of molecules, such as olefins and aromatics, are also treated as the one-carbon PAR species. This reaction scheme has been condensed to reactions 52 through 55 in the CBM-IV.

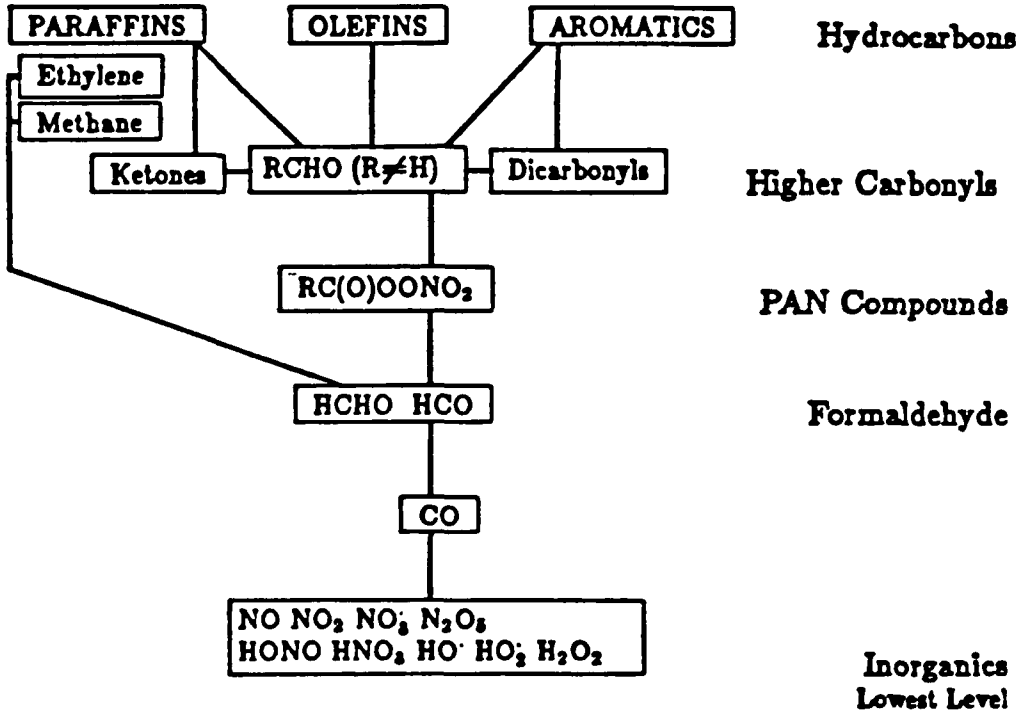

FIGURE 1-2. Schematic Description of the Hierarchy of Species for the Carbon Bond Mechanism-IV.

TABLE 1-2. The Carbon Bond Mechanism-X.

Number	Reaction[1]			Reaction Rate Data: Pre-factor ($ppm^{-n}min^{-1}$)	Temp. Factor exp((-E/R)/T)	Rate Constant @ 298K k_{298} ($ppm^{-n}min^{-1}$)
1)	NO2	-hv1->	NO + O			see notes
2)	O	----->	O3	8.383 E+04	*EXP(1175/T)	4.323 E+06
3)	O3 + NO	----->	NO2	2.643 E+03	*EXP(- 1370/T)	2.664 E+01
4)	O + NO2	----->	NO	1.375 E+04		1.375 E+04
5)	O + NO2	----->	NO3	2.303 E+02	*EXP(687/T)	2.309 E+03
6)	O + NO	----->	NO2	3.233 E+02	*EXP(602/T)	2.438 E+03
7)	O3 + NO2	----->	NO3	1.760 E+02	*EXP(- 2450/T)	4.731 E-02
8)	O3	-hv1->	O	5.300 E-02		5.300 E-02*k_1
9)	O3	-hv4->	O1D			see notes
10)	O1D	----->	O	1.147 E+05	*EXP(390/T)	4.246 E+05
11)	O1D + H2O	----->	2.00OH	3.260		3.260
12)	O3 + OH	----->	HO2	2.344 E+03	*EXP(- 940/T)	1.000 E+02
13)	O3 + HO2	----->	OH	2.100 E+01	*EXP(- 580/T)	2.999
14)	NO3	-hv1->	0.89NO2 + 0.89O + 0.11NO	3.390 E+01		3.390 E+01*k_1
15)	NO3 + NO	----->	2.00NO2	1.909 E+04	*EXP(250/T)	4.416 E+04
16)	NO3 + NO2	----->	NO + NO2	3.660 E+01	*EXP(- 1230/T)	5.901 E-01
17)	NO3 + NO2	----->	N2O5	7.849 E+02	*EXP(256/T)	1.853 E+03
18)	N2O5 + H2O	----->	2.00HNO3	1.900 E-06		1.900 E-06
19)	N2O5	----->	NO3 + NO2	2.110 E+16	*EXP(-10897/T)	2.776
20)	NO + NO	----->	2.00NO2	2.600 E-05	*EXP(530/T)	1.539 E-04
21)	NO + NO2 + H2O	----->	2.00HONO	1.600 E-11		1.600 E-11
22)	OH + NO	----->	HONO	6.554 E+02	*EXP(806/T)	9.799 E+03
23)	HONO	-hv1->	OH + NO	1.975 E-01		1.975 E-01*k_1
24)	OH + HONO	----->	NO2	9.770 E+03		9.770 E+03
25)	HONO + HONO	----->	NO + NO2	1.500 E-05		1.500 E-05
26)	OH + NO2	----->	HNO3	1.537 E+03	*EXP(713/T)	1.682 E+04
27)	OH + HNO3	----->	NO3	7.600	*EXP(1000/T)	2.179 E+02
28)	HO2 + NO	----->	OH + NO2	5.482 E+03	*EXP(240/T)	1.227 E+04
29)	HO2 + NO2	----->	PNA	1.640 E+02	*EXP(749/T)	2.025 E+03
30)	PNA	----->	HO2 + NO2	2.876 E+15	*EXP(-10121/T)	5.115
31)	OH + PNA	----->	NO2	1.909 E+03	*EXP(380/T)	6.833 E+03
32)	HO2 + HO2	----->	H2O2	8.739 E+01	*EXP(1150/T)	4.144 E+03
33)	HO2 + HO2 + H2O	----->	H2O2	7.690 E-10	*EXP(5800/T)	2.180 E-01
34)	H2O2	-hv3->	2.00OH	2.550 E-01		2.550 E-01*k_{39}
35)	OH + H2O2	----->	HO2	4.720 E+03	*EXP(- 187/T)	2.520 E+03
36)	OH + CO	----->	HO2	3.220 E+02		3.220 E+02
37)	FORM + OH	----->	HO2 + CO	1.500 E+04		1.500 E+04
38)	FORM	-hv2->	2.00HO2 + CO			see notes
39)	FORM	-hv3->	CO			see notes
40)	FORM + O	----->	OH + HO2 + CO	4.302 E+04	*EXP(- 1550/T)	2.370 E+02
41)	FORM + NO3	----->	HNO3 + HO2 + CO	9.300 E-01		9.300 E-01
42)	FORM + HO2	----->	FROX	1.480 E+01		1.480 E+01
43)	FROX	----->	HO2 + FORM	9.000 E+01		9.000 E+01
44)	FROX + HO2	----->	PROX	9.600 E+03		9.600 E+03
45)	FROX + NO	----->	NO2 + HO2 + FACD	1.040 E+04		1.040 E+04
46)	ALD2 + O	----->	C2O3 + OH	1.739 E+04	*EXP(- 986/T)	6.360 E+02
47)	ALD2 + OH	----->	C2O3	1.037 E+04	*EXP(250/T)	2.400 E+04
48)	ALD2 + NO3	----->	C2O3 + HNO3	3.700		3.700
49)	ALD2	-hv5->	MEO2 + HO2 + CO			see notes

(Continued)

TABLE 1-2. (Continued).

Number	Reaction[1]	Reaction Rate Data: Pre-factor ($ppm^{-n}min^{-1}$)	Temp. Factor exp((-E/R)/T)	Rate Constant @ 298K k_{298} ($ppm^{-n}min^{-1}$)
50)	C2O3 + NO -----> NO2 + MEO2	7.915 E+03	*EXP(250/T)	1.831 E+04
51)	C2O3 + NO2 -----> PAN	1.180 E-04	*EXP(5500/T)	1.223 E+04
52)	PAN -----> C2O3 + NO2	5.616 E+18	*EXP(-14000/T)	2.220 E-02
53)	MEO2 + NO2 -----> MPNA	3.810 E+02	*EXP(821/T)	5.990 E+03
54)	MPNA -----> MEO2 + NO2	1.190 E+17	*EXP(-10371/T)	9.145 E+02
55)	MEO2 + NO -----> MEO + NO2	6.140 E+03	*EXP(180/T)	1.123 E+04
56)	MEO + NO -----> MNIT	2.296 E+04	*EXP(200/T)	4.443 E+04
57)	MEO + NO -----> FORM + HO2 + NO	1.920 E+03		1.920 E+03
58)	MEO + NO2 -----> MEN3	2.217 E+04		2.217 E+04
59)	MEO -----> FORM + HO2	2.605 E+07	*EXP(- 1200/T)	4.645 E+05
60)	MEN3 + OH -----> FORM + NO2	4.000 E+02		4.000 E+02
61)	MNIT + OH -----> FORM + NO	3.000 E+02		3.000 E+02
62)	MNIT -hvl-> MEO + NO	3.000 E-01		3.000 E-01×k_1
63)	MEO2 + MEO2 -----> 2.00MEO	1.910 E+02		1.910 E+02
64)	MEO2 + MEO2 -----> FORM + MEOH	3.560 E+02		3.560 E+02
65)	MEO2 + C2O3 -----> MEO2 + MEO	4.400 E+03		4.400 E+03
66)	C2O3 + C2O3 -----> 2.00MEO2	3.700 E+03		3.700 E+03
67)	MEO2 + HO2 -----> PROX	2.550 E+01	*EXP(1300/T)	2.000 E+03
68)	MEO2 + HO2 -----> MEO + OH	8.541 E+01	*EXP(1300/T)	6.700 E+03
69)	C2O3 + HO2 -----> PROX	2.000 E+03		2.000 E+03
70)	C2O3 + HO2 -----> MEO2 + OH	7.600 E+03		7.600 E+03
71)	AONE -hvl-> MEO2 + C2O3	4.000 E-05		4.000 E-05×k_1
72)	AONE + OH -----> ANO2	5.800 E+02		5.800 E+02
73)	ANO2 + NO -----> C2O3 + FORM + NO2	1.200 E+04		1.200 E+04
74)	OH -----> MEO2	6.521 E+03	*EXP(- 1710/T)	2.100 E+01
75)	PAR + OH -----> RO2	1.360 E+02		1.360 E+02
76)	PAR + OH -----> RO2R	1.067 E+03		1.067 E+03
77)	RO2 + NO -----> NO2 + HO2 + ALD2 + X	1.140 E+04		1.140 E+04
78)	RO2 + NO -----> NTR	6.584 E+04	*EXP(- 1400/T)	6.000 E+02
79)	RO2R + NO -----> NO2 + ROR	1.033 E+04		1.033 E+04
80)	RO2R + NO -----> NTR	1.836 E+05	*EXP(- 1400/T)	1.673 E+03
81)	ROR + NO2 -----> NTR	2.200 E+04		2.200 E+04
82)	ROR -----> KET + HO2	9.546 E+04		9.546 E+04
83)	ROR -----> KET + D	1.236 E+16	*EXP(- 8000/T)	2.706 E+04
84)	ROR -----> ALD2 + D + X	2.394 E+16	*EXP(- 8000/T)	5.250 E+04
85)	ROR -----> AONE + D + 2.0OX	2.621 E+16	*EXP(- 8000/T)	5.749 E+04
86)	X + PAR ----->	1.000 E+04		1.000 E+04
87)	D + PAR -----> RO2	7.500 E+03		7.500 E+03
88)	D + PAR -----> AO2 + 2.0OX	2.250 E+03		2.250 E+03
89)	D + PAR -----> RO2R	2.500 E+02		2.500 E+02
90)	D + KET -----> C2O3 + X	1.000 E+04		1.000 E+04
91)	AO2 + NO -----> NO2 + AONE + HO2	1.200 E+04		1.200 E+04
92)	KET -hvl-> C2O3 + RO2 + 2.0OX	3.000 E-04		3.000 E-04×k_1
93)	O + OLE -----> 2 PAR	6.146 E+03	*EXP(- 324/T)	2.072 E+03
94)	O + OLE -----> ALD2	6.146 E+03	*EXP(- 324/T)	2.072 E+03
95)	O + OLE -----> HO2 + CO + RO2	1.756 E+03	*EXP(- 324/T)	5.920 E+02
96)	O + OLE -----> RO2 + X + CO + FORM + OH	3.512 E+03	*EXP(- 324/T)	1.184 E+03
97)	OH + OLE -----> MEO2 + ALD2 + X	7.740 E+03	*EXP(504/T)	4.200 E+04

(Continued)

TABLE 1-2. (Continued).

Number	Reaction[1]				Reaction Rate Data: Pre-factor ($ppm^{-n}min^{-1}$)	Temp. Factor exp((-E/R)/T)	Rate Constant @ 298K k_{298} ($ppm^{-n}min^{-1}$)
98)	O3	+ OLE	----->	ALD2 + CRIG + X	4.208	*EXP(- 2105/T)	3.600 E-03
99)	O3	+ OLE	----->	FORM + MCRG + X	4.208	*EXP(- 2105/T)	3.600 E-03
100)	O3	+ OLE	----->	ALD2 + HOTA + X	6.312	*EXP(- 2105/T)	5.400 E-03
101)	O3	+ OLE	----->	FORM + HTMA + X	6.312	*EXP(- 2105/T)	5.400 E-03
102)	NO3	+ OLE	----->	PNO2	1.135 E+01		1.135 E+01
103)	PNO2	+ NO	----->	DNIT	1.000 E+03		1.000 E+03
104)	PNO2	+ NO	----->	FORM + ALD2 + X + 2.00NO2	1.000 E+04		1.000 E+04
105)	O	+ ETH	----->	MEO2 + HO2 + CO	1.078 E+04	*EXP(- 792/T)	7.560 E+02
106)	O	+ ETH	----->	FORM + HO2 + CO + OH	4.620 E+03	*EXP(- 792/T)	3.240 E+02
107)	OH	+ ETH	----->	ETO2	3.000 E+03	*EXP(411/T)	1.192 E+04
108)	ETO2	+ NO	----->	NO2 + 2.00FORM + HO2	9.360 E+03		9.360 E+03
109)	ETO2	+ NO	----->	NO2 + ALD2 + HO2	2.640 E+03		2.640 E+03
110)	O3	+ ETH	----->	HCHO + CRIG	7.424	*EXP(- 2633/T)	1.080 E-03
111)	O3	+ ETH	----->	HCHO + HOTA	1.114 E+01	*EXP(- 2633/T)	1.620 E-03
112)		HOTA	----->		2.000 E+01		2.000 E+01
113)		HOTA	----->	CO	7.000 E+01		7.000 E+01
114)		HOTA	----->	2.00HO2	1.000 E+01		1.000 E+01
115)		HTMA	----->		2.000 E+01		2.000 E+01
116)		HTMA	----->	MEO2 + CO + OH	3.200 E+01		3.200 E+01
117)		HTMA	----->	MEO2 + HO2	3.200 E+01		3.200 E+01
118)		HTMA	----->	FORM + CO + 2.00HO2	8.000		8.000
119)		HTMA	----->	MEO2 + HO2	8.000		8.000
120)	CRIG	+ NO	----->	NO2 + FORM	1.035 E+04		1.035 E+04
121)	CRIG	+ H2O	----->	FACD + H2O	5.900 E-01		5.900 E-01
122)	CRIG	+ FORM	----->	OZD	2.950 E+03		2.950 E+03
123)	CRIG	+ ALD2	----->	OZD	2.950 E+03		2.950 E+03
124)	MCRG	+ NO	----->	NO2 + ALD2	1.035 E+04		1.035 E+04
125)	MCRG	+ H2O	----->	ACAC + H2O	5.900 E-01		5.900 E-01
126)	MCRG	+ FORM	----->	OZD	2.950 E+03		2.950 E+03
127)	MCRG	+ ALD2	----->	OZD	2.950 E+03		2.950 E+03
128)	OH	+ TOL	----->	BO2	2.393 E+02	*EXP(322/T)	7.050 E+02
129)	OH	+ TOL	----->	CRES + HO2	1.115 E+03	*EXP(322/T)	3.285 E+03
130)	OH	+ TOL	----->	TO2	1.751 E+03	*EXP(322/T)	5.160 E+03
131)	BO2	+ NO	----->	NO2 + BZA + HO2	1.200 E+04		1.200 E+04
132)		BZA	-hvl->		4.000 E-03		4.000 E-03*k_1
133)	OH	+ BZA	----->	BZO2	2.000 E+04		2.000 E+04
134)	BZO2	+ NO	----->	NO2 + PHO2 + CO	3.700 E+03		3.700 E+03
135)	BZO2	+ NO2	----->	PBZN	2.500 E+03		2.500 E+03
136)		PBZN	----->	BZO2 + NO2	5.566 E+18	*EXP(-14000/T)	2.200 E-02
137)	PHO2	+ NO	----->	NO2 + PHO	1.200 E+04		1.200 E+04
138)	PHO	+ NO2	----->	NPHN	2.000 E+04		2.000 E+04
139)	OH	+ CRES	----->	CRO	2.440 E+04		2.440 E+04
140)	OH	+ CRES	----->	CRO2	3.660 E+04		3.660 E+04
141)	NO3	+ CRES	----->	CRO + HNO3	3.250 E+04		3.250 E+04
142)	CRO	+ NO2	----->	NCRE	2.000 E+04		2.000 E+04
143)	CRO2	+ NO	----->	NO2 + OPEN + HO2	6.000 E+03		6.000 E+03
144)	CRO2	+ NO	----->	NO2 + ACID + HO2	6.000 E+03		6.000 E+03
145)	TO2	+ NO	----->	NO2 + OPEN + HO2	1.080 E+04		1.080 E+04
146)	TO2	+ NO	----->	NTR	1.200 E+03		1.200 E+03
147)		TO2	----->	HO2 + CRES	2.500 E+02		2.500 E+02

(Continued)

TABLE 1-2. (Continued).

Number	Reaction[1]	Reaction Rate Data: Pre-factor ($ppm^{-n}min^{-1}$)	Temp. Factor exp((-E/R)/T)	Rate Constant @ 298K k_{298} ($ppm^{-n}min^{-1}$)
148)	OH + XYL -----> XLO2	2.453 E+03	*EXP(116/T)	3.620 E+03
149)	OH + XYL -----> CRES + PAR + HO2	4.906 E+03	*EXP(116/T)	7.240 E+03
150)	OH + XYL -----> TO2	7.358 E+03	*EXP(116/T)	1.086 E+04
151)	OH + XYL -----> XINT	9.810 E+03	*EXP(116/T)	1.448 E+04
152)	XLO2 + NO -----> NO2 + HO2 + BZA + PAR	1.200 E+04		1.200 E+04
153)	XINT + NO -----> NO2 + HO2 + 2 MGLY + 2 PAR	1.200 E+04		1.200 E+04
154)	OH + MGLY -----> MGPX	2.600 E+04		2.600 E+04
155)	MGPX + NO -----> NO2 + C2O3	1.200 E+04		1.200 E+04
156)	MGLY -hv2-> C2O3 + CO + HO2	9.640		9.640 $*k_{38}$
157)	OH + OPEN -----> OPPX + C2O3 + HO2 + CO	4.400 E+04		4.400 E+04
158)	OPPX + NO -----> NO2 + FORM + HO2 + CO	1.200 E+04		1.200 E+04
159)	OPEN -hv2-> C2O3 + CO + HO2	9.040		9.040 $*k_{38}$
160)	OPEN + O3 -----> ALD2 + MGPX + FORM + CO	2.409 E-03	*EXP(- 500/T)	4.500 E-04
161)	OPEN + O3 -----> FORM + CO + OH + 2 HO2	6.424 E-03	*EXP(- 500/T)	1.200 E-03
162)	OPEN + O3 -----> MGLY	1.606 E-02	*EXP(- 500/T)	3.000 E-03
163)	OPEN + O3 -----> C2O3 + FORM + HO2 + CO	4.738 E-02	*EXP(- 500/T)	8.850 E-03
164)	OPEN + O3 ----->	8.030 E-03	*EXP(- 500/T)	1.500 E-03

(Continued)

TABLE 1-2 (continued).

Notes:

1. Pressure dependent values for M, O_2 and CH_4 are included in the rate constant data (see text).

   $[M] = 1 \times 10^6$ ppm, $[O_2] = 2.095 \times 10^5$ ppm, and $[CH_4] = 1.85$ ppm.

   The symbols hν1 through hν5 in the reaction listing indicate photolysis reactions with rates dependent on solar irradiation. The basis for these rates is discussed in Section 3; the symbols represent:

   $h\nu 1 = j_{NO2}$, $h\nu 2 = j_{HCHO}$ (to radicals). $h\nu 3 = j_{HCHO}$ (to H_2 + CO),

   $h\nu 4 = j_{O3}$ (to $O_2 + O(^1D)$), $h\nu 5 = j_{CH3CHO}$.

   Other photolysis reactions are ratioed to these functions and noted in the K_{298} column of the mechanism listing.

2. Chemical species in the CBM-X are:

Species Name	Representation
Nitric Oxide	NO
Nitrogen Dioxide	NO2
Nitrogen Trioxide (nitrate radical)	NO3
Dinitrogen Pentoxide	N2O5
Nitrous Acid	HONO
Nitric Acid	HNO3
Peroxynitric acid (HO_2NO_2)	PNA
Oxygen Atom (singlet)	O1D
Oxygen Atom (triplet)	O
Hydroxyl Radical	OH
Water	H2O
Ozone	O3
Hydroperoxy Radical	HO2
Hydrogen Peroxide	H2O2
Carbon Monoxide	CO
Formaldehyde (CH_2=O)	FORM
Hydroxymethylperoxy Radical ($HOCH_2OO^{\cdot}$)	FROX
Organic Peroxide (ROOH)	PROX
Formic Acid (HCOOH)	FACD

TABLE 1-2 (continued).

Species Name	Representation
High Molecular Weight Aldehydes (RCHO, R>H)	ALD2
Peroxyacyl Radical ($CH_3C(O)OO^{\bullet}$)	C2O3
Peroxyacyl Nitrate ($CH_3C(O)OONO_2$)	PAN
Methylperoxy Radical ($CH_3OO^{\bullet}$)	MEO2
Methylperoxy Nitric Acid ($CH_3O_2NO_2$)	MPNA
Methoxy Radical ($CH_3O^{\bullet}$)	MEO
Methyl Nitrite (CH_3ONO)	MNIT
Methyl Nitrate (CH_3ONO_2)	MEN3
Methanol (CH_3OH)	MEOH
Acetone ($CH_3C(O)CH_3$)	AONE
Acetylmethylperoxy Radical ($CH_3C(O)CH_2OO^{\bullet}$)	ANO2
Paraffin Carbon Bond (C-C)	PAR
Primary Organic Peroxy Radical	RO2
Secondary Organic Peroxy Radical	RO2R
Organic Nitrate	NTR
Secondary Organic Oxy Radical	ROR
Ketone Carbonyl Group (-C(O)-)	KET
Dimethyl Secondary Organic Peroxide Radical	AO2
Olefinic Carbon Bond (C=C)	OLE
Cregiee Biradical ($H_2\dot{C}OO^{\bullet}$)	CRIG
Methyl Cregiee Biradical ($CH_3(H)\dot{C}OO^{\bullet}$)	MCRG
"Excited" Formic Acid	HOTA
"Excited" Acetic Acid	HTMA
Nitrated Organic Peroxy Radical ($-CH(ONO_2)-CH(OO^{\bullet})-$)	PNO2
C_2 Dinitrate Group	DNIT
Ethene ($CH_2=CH_2$)	ETH
Ethanol Peroxide Radical ($CH_2OH-CH_2OO^{\bullet}$)	ETO2
Ozonide and further products	OZD
Acetic Acid (CH_3COOH)	ACAC
Toluene ($C_6H_5-CH_3$)	TOL
Benzylperoxy Radical	BO2
Cresol and higher molecular weight Phenols	CRES
Toluene-Hydroxyl Radical Adduct	TO2
Benzaldehyde	BZA
Peroxybenzoyl Radical	BZO2
Peroxybenzoyl Nitrate	PBZN
Phenylperoxy Radical	PHO2
Phenoxy Radical	PHO
Nitrophenol	NPHN
Methylphenylperoxy Radical	CRO2

TABLE 1-2 (concluded).

Species Name	Representation
Methylphenoxy Radical	CRO
Nitrocresol	NCRE
High Molecular Weight Aromatic Oxidation Ring Fragment	OPEN
Aromatic Ring Fragment Acid	ACID
Xylene (C_6H_4-$(CH_3)_2$)	XYL
Methylbenzylperoxy Radical	XLO2
Xylene-Hydroxyl Radical Adduct	XINT
Methylglyoxal ($CH_3C(O)C(O)H$)	MGLY
Peroxide Radical of MGLY ($CH_3C(O)C(O)OO^{\cdot}$)	MGPX
Peroxide Radical of OPEN	OPPX
Paraffin Loss Operator (-PAR)	X
Paraffin-to-Peroxy Radical Operator	D
TOTAL =	71

TABLE 1-3. The Carbon Bond Mechanism-IV.

Number	Reaction[1]	Reaction Rate Data: Pre-factor ($ppm^{-n}min^{-1}$)	Temp. Factor exp((-E/R)/T)	Rate Constant @ 298K k_{298} ($ppm^{-n}min^{-1}$)
1)	NO2 -hv1-> NO + O			see notes
2)	O -----> O3	8.383 E+04	*EXP(1175/T)	4.323 E+06
3)	O3 + NO -----> NO2	2.643 E+03	*EXP(- 1370/T)	2.664 E+01
4)	O + NO2 -----> NO	1.375 E+04		1.375 E+04
5)	O + NO2 -----> NO3	2.303 E+02	*EXP(687/T)	2.309 E+03
6)	O + NO -----> NO2	3.233 E+02	*EXP(602/T)	2.438 E+03
7)	O3 + NO2 -----> NO3	1.760 E+02	*EXP(- 2450/T)	4.731 E-02
8)	O3 -hv1-> O	5.300 E-02		5.300 E-02*k_1
9)	O3 -hv4-> O1D			see notes
10)	O1D -----> O	1.147 E+05	*EXP(390/T)	4.246 E+05
11)	O1D + H2O -----> 2.00OH	3.260		3.260
12)	O3 + OH -----> HO2	2.344 E+03	*EXP(- 940/T)	1.000 E+02
13)	O3 + HO2 -----> OH	2.100 E+01	*EXP(- 580/T)	2.999
14)	NO3 -hv1-> 0.89NO2 + 0.89O + 0.11NO	3.390 E+01		3.390 E+01*k_1
15)	NO3 + NO -----> 2.00NO2	1.909 E+04	*EXP(250/T)	4.416 E+04
16)	NO3 + NO2 -----> NO + NO2	3.660 E+01	*EXP(- 1230/T)	5.901 E-01
17)	NO3 + NO2 -----> N2O5	7.849 E+02	*EXP(256/T)	1.853 E+03
18)	N2O5 + H2O -----> 2.00HNO3	1.900 E-06		1.900 E-06
19)	N2O5 -----> NO3 + NO2	2.110 E+16	*EXP(-10897/T)	2.776
20)	NO + NO -----> 2.00NO2	2.600 E-05	*EXP(530/T)	1.539 E-04
21)	NO + NO2 + H2O -----> 2.00HONO	1.600 E-11		1.600 E-11
22)	OH + NO -----> HONO	6.554 E+02	*EXP(806/T)	9.799 E+03
23)	HONO -hv1-> OH + NO	1.975 E-01		1.975 E-01*k_1
24)	OH + HONO -----> NO2	9.770 E+03		9.770 E+03
25)	HONO + HONO -----> NO + NO2	1.500 E-05		1.500 E-05
26)	OH + NO2 -----> HNO3	1.537 E+03	*EXP(713/T)	1.682 E+04
27)	OH + HNO3 -----> NO3	7.600	*EXP(1000/T)	2.179 E+02
28)	HO2 + NO -----> OH + NO2	5.482 E+03	*EXP(240/T)	1.227 E+04
29)	HO2 + NO2 -----> PNA	1.640 E+02	*EXP(749/T)	2.025 E+03
30)	PNA -----> HO2 + NO2	2.876 E+15	*EXP(-10121/T)	5.115
31)	OH + PNA -----> NO2	1.909 E+03	*EXP(380/T)	6.833 E+03
32)	HO2 + HO2 -----> H2O2	8.739 E+01	*EXP(1150/T)	4.144 E+03
33)	HO2 + HO2 + H2O -----> H2O2	7.690 E-10	*EXP(5800/T)	2.181 E-01
34)	H2O2 -hv3-> 2.00OH	2.550 E-01		2.550 E-01*k_{39}
35)	OH + H2O2 -----> HO2	4.720 E+03	*EXP(- 187/T)	2.520 E+03
36)	OH + CO -----> HO2	3.220 E+02		3.220 E+02
37)	FORM + OH -----> HO2 + CO	1.500 E+04		1.500 E+04
38)	FORM -hv2-> CO + 2.00HO2			see notes
39)	FORM -hv3-> CO			see notes
40)	FORM + O -----> OH + HO2 + CO	4.302 E+04	*EXP(- 1550/T)	2.370 E+02
41)	FORM + NO3 -----> HNO3 + HO2 + CO	9.300 E-01		9.300 E-01
42)	ALD2 + O -----> C2O3 + OH	1.739 E+04	*EXP(- 986/T)	6.360 E+02
43)	ALD2 + OH -----> C2O3	1.037 E+04	*EXP(250/T)	2.400 E+04
44)	ALD2 + NO3 -----> C2O3 + HNO3	3.700		3.700
45)	ALD2 -hv5-> FORM + XO2 + CO + 2.00HO2			see notes
46)	C2O3 + NO -----> NO2 + XO2 + FORM + HO2	7.915 E+03	*EXP(250/T)	1.831 E+04
47)	C2O3 + NO2 -----> PAN	1.180 E-04	*EXP(5500/T)	1.223 E+04
48)	PAN -----> C2O3 + NO2	5.616 E+18	*EXP(-14000/T)	2.220 E-02
49)	C2O3 + C2O3 -----> 2.00FORM + 2.00XO2 + 2.00HO2	3.700 E+03		3.700 E+03
50)	C2O3 + HO2 -----> 0.79FORM + 0.79XO2 + 0.79HO2 + 0.79OH	9.600 E+03		9.600 E+03
51)	OH -----> XO2 + FORM + HO2	6.521 E+03	*EXP(- 1710/T)	2.100 E+01

(Continued)

TABLE 1-3. (Continued)

Number	Reaction[1]			Reaction Rate Data: Pre-factor ($ppm^{-n}min^{-1}$)	Temp. Factor exp((-E/R)/T)	Rate Constant @ 298K k_{298} ($ppm^{-n}min^{-1}$)
52)	PAR + OH	----->	0.87XO2 + 0.13XO2N + 0.11HO2 + 0.11ALD2 + 0.76ROR - 0.11PAR	1.203 E+03		1.203 E+03
53)	ROR	----->	1.10ALD2 + 0.96XO2 + 0.94HO2 + 0.04XO2N + 0.02ROR - 2.10PAR	6.250 E+16	*EXP(- 8000/T)	1.371 E+05
54)	ROR	----->	HO2	9.545 E+04		9.545 E+04
55)	ROR + NO2	----->		2.200 E+04		2.200 E+04
56)	O + OLE	----->	0.63ALD2 + 0.38HO2 + 0.28XO2 + 0.30CO + 0.20FORM + 0.02XO2N + 0.22PAR + 0.20OH	1.756 E+04	*EXP(- 324/T)	5.920 E+03
57)	OH + OLE	----->	FORM + ALD2 + XO2 + HO2 - PAR	7.740 E+03	*EXP(504/T)	4.200 E+04
58)	O3 + OLE	----->	0.50ALD2 + 0.74FORM + 0.33CO + 0.44HO2 + 0.22XO2 + 0.10OH - PAR	2.104 E+01	*EXP(- 2105/T)	1.800 E-02
59)	NO3 + OLE	----->	0.91XO2 + FORM + ALD2 + 0.09XO2N + NO2 - PAR	1.135 E+01		1.135 E+01
60)	O + ETH	----->	FORM + 0.70XO2 + CO + 1.70HO2 + 0.30OH	1.540 E+04	*EXP(- 792/T)	1.080 E+03
61)	OH + ETH	----->	XO2 + 1.56FORM + HO2 + 0.22ALD2	3.000 E+03	*EXP(411/T)	1.192 E+04
62)	O3 + ETH	----->	FORM + 0.42CO + 0.12HO2	1.856 E+01	*EXP(- 2633/T)	2.700 E-03
63)	OH + TOL	----->	0.08XO2 + 0.36CRES + 0.44HO2 + 0.56TO2	3.106 E+03	*EXP(322/T)	9.150 E+03
64)	TO2 + NO	----->	0.90NO2 + 0.90HO2 + 0.90OPEN	1.200 E+04		1.200 E+04
65)	TO2	----->	CRES + HO2	2.500 E+02		2.500 E+02
66)	OH + CRES	----->	0.40CRO + 0.60XO2 + 0.60HO2 + 0.30OPEN	6.100 E+04		6.100 E+04
67)	CRES + NO3	----->	CRO + HNO3	3.250 E+04		3.250 E+04
68)	CRO + NO2	----->		2.000 E+04		2.000 E+04
69)	OPEN	-hv2->	C2O3 + HO2 + CO	9.040		9.040 $*k_{38}$
70)	OPEN + OH	----->	XO2 + 2.00CO + 2.00HO2 + C2O3 + FORM	4.400 E+04		4.400 E+04
71)	OPEN + O3	----->	0.03ALD2 + 0.62C2O3 + 0.70FORM + 0.03XO2 + 0.69CO + 0.08OH + 0.76HO2 + 0.20MGLY	8.030 E-02	*EXP(- 500/T)	1.500 E-02
72)	OH + XYL	----->	0.70HO2 + 0.50XO2 + 0.20CRES + 0.80MGLY + 1.10PAR + 0.30TO2	2.453 E+04	*EXP(116/T)	3.620 E+04
73)	OH + MGLY	----->	XO2 + C2O3	2.600 E+04		2.600 E+04
74)	MGLY	-hv2->	C2O3 + HO2 + CO	9.640		9.640 $*k_{38}$
75)	O + ISOP	----->	0.60HO2 + 0.80ALD2 + 0.55OLE + 0.50XO2 + 0.50CO + 0.45ETH + 0.90PAR	2.700 E+04		2.700 E+04
76)	OH + ISOP	----->	XO2 + FORM + 0.67HO2 + 0.40MGLY + 0.20C2O3 + 1.00ETH + 0.20ALD2 + 0.13XO2N	1.420 E+05		1.420 E+05
77)	O3 + ISOP	----->	FORM + 0.40ALD2 + 0.55ETH + 0.20MGLY + 0.10PAR + 0.06CO + 0.44HO2 + 0.10OH	1.800 E-02		1.800 E-02
78)	NO3 + ISOP	----->	XO2N	4.700 E+02		4.700 E+02
79)	XO2 + NO	----->	NO2	1.200 E+04		1.200 E+04
80)	XO2 + XO2	----->		2.550 E+01	*EXP(1300/T)	2.000 E+03
81)	XO2N + NO	----->		1.000 E+03		1.000 E+03

(Continued)

TABLE 1-3 (continued).

Notes:

1. Pressure dependent values for M, O_2 and CH_4 are included in the rate constant data (see text).

   $[M] = 1 \times 10^6$ ppm, $[O_2] = 2.095 \times 10^5$ ppm, and $[CH_4] = 1.85$ ppm.

   The symbols hν1 through hν5 in the reaction listing indicate photolysis reactions with rates dependent on solar irradiation. The basis for these rates is discussed in Section 3; the symbols represent:

   $h\nu 1 = j_{NO2}$, $h\nu 2 = j_{HCHO}$ (to radicals), $h\nu 3 = j_{HCHO}$ (to H_2 + CO),

   $h\nu 4 = j_{O3}$ (to $O_2 + O(^1D)$), $h\nu 5 = j_{CH3CHO}$.

   Other photolysis reactions are ratioed to these functions and noted in the K_{298} column of the mechanism listing.

2. Chemical species in the CBM-IV are:

Species Name	Representation
Nitric Oxide	NO
Nitrogen Dioxide	NO2
Nitrogen Trioxide (nitrate radical)	NO3
Dinitrogen Pentoxide	N2O5
Nitrous Acid	HONO
Nitric Acid	HNO3
Peroxynitric acid (HO_2NO_2)	PNA
Oxygen Atom (singlet)	O1D
Oxygen Atom (triplet)	O
Hydroxyl Radical	OH
Water	H2O
Ozone	O3
Hydroperoxy Radical	HO2
Hydrogen Peroxide	H2O2
Carbon Monoxide	CO
Formaldehyde (CH_2=O)	FORM
High Molecular Weight Aldehydes (RCHO, R>H)	ALD2
Peroxyacyl Radical ($CH_3C(O)OO^{\cdot}$)	C2O3

TALBE 1-3 (concluded).

Species Name	Representation
Peroxyacyl Nitrate ($CH_3C(O)OONO_2$)	PAN
Paraffin Carbon Bond (C-C)	PAR
Secondary Organic Oxy Radical	ROR
Olefinic Carbon Bond (C=C)	OLE
Ethene ($CH_2=CH_2$)	ETH
Toluene ($C_6H_5-CH_3$)	TOL
Cresol and higher molecular weight Phenols	CRES
Toluene-Hydroxyl Radical Adduct	TO2
Methylphenoxy Radical	CRO
High Molecular Weight Aromatic Oxidation Ring Fragment	OPEN
Xylene ($C_6H_4-(CH_3)_2$)	XYL
Methylglyoxal ($CH_3C(O)C(O)H$)	MGLY
Isoprene	ISOP
NO-to-NO_2 Operation	XO2
NO-to-Nitrate Operation	XO2N
TOTAL =	33

Olefin and Ethene Chemistry

Reactions 93 through 127 in the CBM-X and reactions 56-62 in the CBM-IV constitute the subset of reactions specific to molecules containing double bonds. Since such molecules can have a wide range of reactivity, the atmospheric mix of olefins in the CBM-X is treated in three different ways:

(1) Terminal olefins such as propene and 1-butene are handled in condensed form via the species OLE. OLE is a two-carbon lumped-structure species that represents the carbon bond found in 1-olefins. These reactions are condensed to reactions 56 through 59 in the CBM-IV.

(2) Ethene, which is the least reactive of the olefins, is treated explicitly. The ethene mechanism has little significant condensation, and is described by reactions 60 through 62 of the CBM-IV.

(3) Highly reactive olefins such as those with internal double bonds (e.g., cis-2-butene) are treated by assuming that they have already reacted in the atmosphere to form two higher aldehydes (i.e., 2 ALD2). This condensation has been successfully demonstrated in Whitten et al. (1979) and was recommended for use in earlier versions of the CBM (Whitten et al., 1980a; Whitten et al., 1980b).

Aromatic Chemistry

The chemistry of all aromatic structures is separated into monofunctional and multifunctional rings. The aromatic structure chemistry of molecules with only one functional group is represented by the reactions of the toluene molecule (TOL), whereas the m-xylene (XYL) reactions are used for multifunctional aromatic rings. Reactions 128 through 164 in the CBM-X (63 through 74 in the CBM-IV) represent the reactions of these species and their products which include two highly reactive dicarbonyls, methylglyoxal (MGLY) and a lumped, higher molecular weight dicarbonyl (OPEN).

Isoprene Chemistry

Isoprene (ISOP) chemical reactions are included in the CBM-IV as a surrogate for biogenic, terpenoid hydrocarbon species. The chemistry of isoprene is represented by reactions 75 through 78 in the CBM-IV.

SPECIFIC IMPROVEMENTS TO THE MECHANISMS

The following major improvements have been implemented in the CBM:

(1) New chemical kinetics and stoichiometric information have been included in both versions to update both inorganic and organic components.

(2) Water is now explicitly represented in the CBM-IV mechanism (it is no longer "hidden" from the user by embedding its concentration in the kinetic expression).

(3) The chemistry of $O(^1D)$ is explicitly represented in the CBM-IV. Again, the "hidden" kinetics are now visible.

(4) The species ROR is now explicitly represented in the PAR-plus-OH reaction sequence of the CBM-IV. This alteration, along with alterations 2 and 3, was performed to eliminate the complicated empirical stoichiometric and kinetic representations that were necessarily included in the previous version of the CBM-IV. Provided that the earlier algorithms were correctly implemented by users, no functional differences should result from these changes.

(5) The temperature-dependence of acetylperoxy radical reactions with NO and NO_2 has been improved in both mechanisms.

(6) The product distribution and kinetics of the acetylperoxy radical reactions with RO_2 radicals have been improved to better simulate experimental evidence from environmental chambers.

(7) The sensitivity of XO_2 chemistry has been further tested, and the reactions of that species have been updated in the CBM-IV.

(8) The chemistry of ETH was altered to account for glycolaldehyde formation in both mechanisms.

(9) The reaction of ALD2 with HO_2 was removed from both mechanisms because there is no substantial proof of its occurrence.

(10) The chemical equilibrium between HO_2, NO_2 of peroxynitric acid (PNA) is listed in both the mechanisms. In our earlier work, this reaction was considered optional for warm-temperature conditions, which enhance the PNA decomposition reaction; however, we feel its inclusion will prevent it from being ignored under conditions for which it is needed.

(11) The use of FORM as surrogate for GLY has been eliminated in the CBM-IV, making the species FORM an explicit representation of formaldehyde and allowing the CBM-IV to be used for formaldehyde-specific simulations.

(12) The chemistry of aromatic species (TOL and XYL) has been significantly altered in both mechanisms to account for the sensitivity of ozone formation to NMHC/NO_x (particularly for TOL).

(13) A new condensed isoprene (ISOP) mechanism has been developed and evaluated for the CBM-IV.

(14) A new carbon fractionation scheme for α-pinene was developed and evaluated.

2 MECHANISM DEVELOPMENT METHODOLOGY

In this section we briefly describe our mechanism development methodology in order to clearly define relevant sources of uncertainty. In addition, because the photochemical kinetics mechanisms used to simulate atmospheric chemistry are (1) developed and evaluated using data of different types and quality, (2) condensed on the basis of differing philosophies, and (3) implemented in different ways, a general description will provide the reader with a better understanding of the components of mechanism development not evident from a description of only the final mechanism.

FORMULATION OF THE MECHANISM

Photochemical kinetics mechanisms such as the CBM are formulated by review and evaluation of fundemental kinetic data. In the development of the CBM, we have drawn heavily on such published review articles as the work of NASA (DeMore et al., 1985), CODATA (Baulch et al., 1984), and Atkinson and Lloyd (1984). Such review is a time-consuming process and portions of these works are somewhat dated; therefore, we have supplemented this information with a review of more current information available in chemical journals. Since we will continue to add the results of future experimental studies and mechanism development efforts to this basic data pool, it is necessary to clearly document the methodology used so that new information can be easily integrated. In our mechanism formulation (which is documented in the following sections), we have attempted to (1) base all condensations or approximations on elementary reactions and experimentally or thermodynamically determined rate constants, (2) reference all sources of basic kinetic and mechanistic data, and (3) describe all relevant decisions concerning our choices and uses of these data. In this way, the basic data available for model development at this time have been formally selected and are no longer considered to be adjustable parameters. As our discussion will illustrate, however, the assumptions used to combine these fundamental data into a working mechanism will evolve as additional information becomes available.

MECHANISM EVALUATION AND ADJUSTMENT

The evaluation of chemical mechanisms against smog chamber data using a simple stepwise hierarchy of simulations was first suggested by Demerjian, Kerr, and Calvert (1974), who noted that smog chamber data were most effectively analyzed by starting with simple systems and increasing the complexity of the hydrocarbon components in a stepwise fashion. Whitten (1979) later put forth the principles of the hierarchy of species approach, a method of model development and testing intended to identify sources of simulation uncertainty. Figure 1-2 shows the hierarchy of species for the CBM-X. The basic concept of this hierarchy is that mechanisms should be validated starting from the lowest level. In the case of smog chamber data, this level includes chamber background and dilution experiments. Once acceptable agreement between simulation results and measurements is obtained, no changes in rate constants and reaction stoichiometry can be made for the part of the mechanism that has been tested. Simulations then increase to higher hierarchical levels. Thus, if disagreement between simulation results and measurements occurs at a higher hierarchical level and all lower species data have already been simulated successfully, it is most likely that the new chemistry for the higher level species is in error. This methodology minimizes the possibility of fortuitous agreement between simulations and measurements caused by compensating errors that can occur in a mechanism created from only basic kinetic data. Jeffries and Arnold (1987) point out that the hierarchical approach narrows the macroscopic nature of data from smog chamber experiments so that it more clearly confronts individual portions of the theory. The opposite method, direct creation of a mechanism to simulate a mixture of hydrocarbons and NO_x in the atmosphere without simulating the products of the hydrocarbon mixture, is less certain because of the possibility of compensating errors.

Smog chamber experiments provide one source of additional information. While our understanding of fundamental atmospheric processes provides the basic descriptions of chemical variability used in initial mechanism development, evaluation of the mechanism through comparison with smog chamber data allows refinement derived from a real, controlled test environment. That is, whereas fundamental chemical data may lack information on unstudied reactions, data obtained from smog chamber experiments inherently contain much of this information because these experiments are designed to reproduce many of the chemical processes in the atmosphere. Therefore, the iterative adjustment of mechanism assumptions through simulation of smog chamber experiments combines the strengths of both types of data so that uncertainties in each become more apparent and can be eliminated. This iterative type of approach is shown in Figure 2-1, which is an idealized representation of the mechanism development process, as the

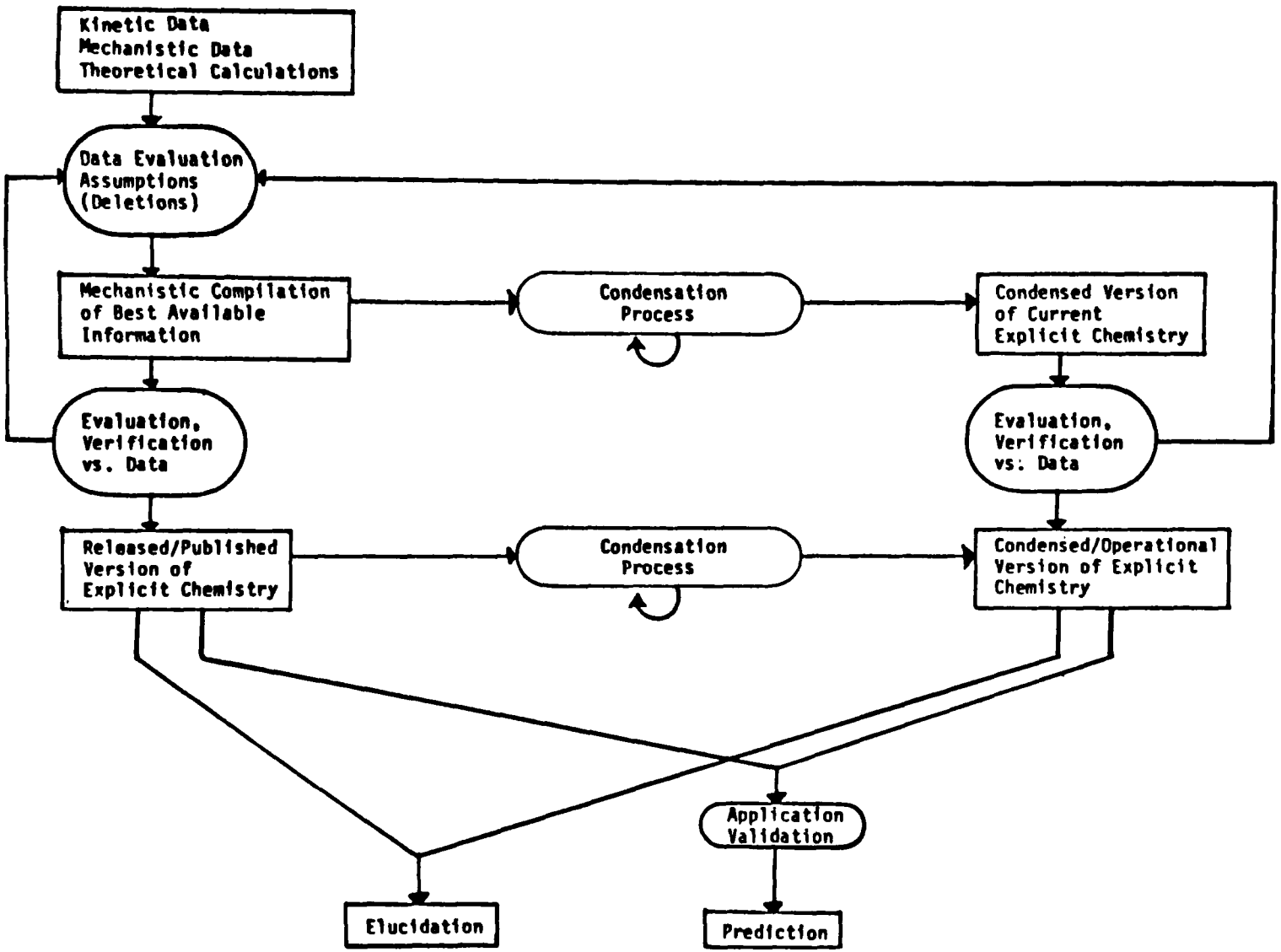

FIGURE 2-1. Schematic representation of the development, condensation, evaluation and application of a photochemical kinetics mechanism.

first loop in the top left portion of the drawing. The boxes in the figure represent real (though sometimes changing) data, compilations, and mechanism development points; in short, they are starting, nodal, and stopping points. Listings of data, results, and mechanisms can be obtained at any of these points to represent the current development status. The ovals represent processes that often require a certain level of ingenuity, test data, and validation. These processes are the sources of uncertainty that must be clearly described in formulating a predictive chemical kinetics mechanism from basic data, and clearly documented in each application.

The evaluation and adjustment of current explicit mechanisms, as shown in Figure 2-1, is the primary objective of projects such as the one reported here. Since the smog chamber experiments performed at different facilities (and even at the same facility) are extremely variable, this portion of the mechanism development effort can accumulate significant uncertainty. Therefore, it is essential to establish a robust data set prior to any mechanism evaluation and adjustment. In the work reported here, we have utilized data from smog chambers at the University of North Carolina (UNC), the University of California at Riverside (UCR), and Battelle Columbus Research Laboratories for a variety of single hydrocarbon species and mixtures, and different initial conditions (especially HC/NO_x ratios) and times of year (for outdoor chambers). For the UNC dual outdoor chambers data, we have also attempted to always simulate both sides of an experiment at the same time, using identical chamber artifact and light conditions for each side so that the objective of each specific experiment could be studied through comparison of the results for each side.

It is also critical to estimate or define the basic characteristics and conditions of each chamber. Although these features will be discussed in a later section, we note here that they are still very uncertain, and that no meaningful comparison of individual mechanism characteristics can be conducted if those mechanisms were developed using different artifact assumptions. This is because artificial inorganic chamber chemistry may be included as part of the mechanism's organic reactivity, or too much or too little artificial chemistry might be assumed, resulting in an organic chemistry section that contains inaccurate treatment of reactivity. At the level of atmospheric modeling, where these assumptions are supposedly eliminated from the mechanisms, two mechanisms using different artifact or light assumptions that match chamber data equally well will give different atmospheric predictions because one will have excluded or included more chamber artifacts than the other.

MECHANISM CONDENSATION

A photochemical kinetics mechanism used to predict the chemical behavior of a complex mixture of hydrocarbons under atmospheric conditions must be condensed enough to be implemented in an AQSM. The process by which a condensed mechanism is formulated and verified is a stepwise loop similar to the smog chamber evaluation of explicit mechanisms. We show the condensation process in Figure 2-1 as a set of parallel loops leading to a verified, condensed mechanism. The solid lines describe the condensation of an explicit mechanism that has first been tested with smog chamber data, while the dashed lines imply production of an explicit mechanism from fundamental kinetic data, followed by evaluation of a condensed mechanism with experimental data. In both cases, the evaluation with smog chamber data is an essential test against real atmospheric data in order to establish the completeness of the explicit compilation. It is our preference to proceed along the path that provides a validated explicit mechanism (solid lines) prior to condensation since (1) compensating errors in the mechanism will not be as easily masked by condensation prior to evaluation with smog chamber, and (2) a complete explicit mechanism that has been verified against all available data can be used to produce a number of different levels of condensation for different applications. The alternate pathway requires a new condensation for every iterative step in the smog chamber evaluation loop, resulting in a more complicated task to produce the same results.

The objective of the condensation process leads to a more clearly defined methodology than that of the smog chamber evaluation process. This is because the object of condensation is not to simulate smog chamber experiments correctly, or to improve the theory, but to duplicate the ability of the explicit mechanism in a more widely applicable form. The condensed mechanism should not simulate the smog chamber results more accurately since it is based only on the explicit mechanism. Therefore, because the object of a condensation evaluation test is to duplicate the results of a more explicit set of reactions, it is not always necessary to use real test conditions since the reference standard is not the smog chamber data, but the results of the explicit mechanism simulation. Thus, we usually attempt both to verify that the condensed mechanism is an accurate map of the explicit formulation within the range of physical and chemical conditions available in smog chamber data, and to test the condensation results in more extreme conditions than will be used in the intended application. Therefore, it is often necessary to fabricate these conditions to achieve such a comparison.

In Sections 3 and 4 of this report we present the theoretical basis for our development of explicit mechanisms, followed by a discussion of the development of the CBM-X and the condensation of that mechanism to the

CBM-IV. The CBM-X is primarily an explicit mechanism, though it does employ hydrocarbon surrogate assumptions, whereas the CBM-IV is highly condensed. (The reader is referred to Sections 3 and 4 for discussion of specific techniques and results.) In both mechanisms, the inorganic portion of the chemistry is maintained in the explicit form. Our primary strategy for development of a CBM-IV mechanism is shown by the solid line in Figure 2-1. After evaluation of the fundemental kinetic and mechanistic data, an initial formulation of the CBM-X was attempted. We then optimized the agreement of the CBM-X with smog chamber data by improving our mechanistic assumptions. We proceeded to condense the CBM-X to the CBM-IV in the stepwise manner documented in Sections 3 and 4. This overall process was revisited at various points throughout the project before the final versions of these mechanisms were decided upon. In both the development of the CBM-X and the condensation to the CBM-IV. the hierarchy of species within the photochemical systems to be modeled allowed compensating errors in these steps to be minimized.

ATMOSPHERIC APPLICATIONS

Although this report is devoted mainly to a discussion of the condensation of the CBM-X into the CBM-IV, we note one final area of uncertainty in mechanism development and application. Even though a condensed mechanism with "minimal" uncertainty has been developed using fundamental and smog chamber data and a well-devised condensation scheme, it is not necessarily valid for all intended applications. For instance, one might say that even with an ideal fit to all smog chamber tests and a very good condensation technique, the chemical mechanism has only been validated for the chemical and physical conditions exhibited in those data. Different ranges of concentrations and meteorological conditions are applicable in the atmosphere; there are also other applications for photochemical kinetics mechanisms than the prediction of ozone formation.

To address the issue of uncertainty in mechanism application for specific AQSMs and ambient conditions, we must consider a few facts. First, the description of conditional variation in the chemical mechanisms is not based solely on ozone-related smog chamber data. Although the smog chamber simulations are used to test the completeness of the mechanism, the inherent conditional variations are usually based on kinetic studies with much wider physical ranges than the smog chamber experiments. Therefore, though the explicit mechanism is only verified against real measurements within the range of conditions available in a smog chamber, there is no reason to expect a rapid deterioration of the chemical description for conditions somewhat beyond those of a smog chamber. As noted, however, it is necessary to confirm that the condensed mechanism sucessfully duplicates the explicit mechanism over the entire range of application.

Although smog chamber and ambient concentration ranges can be vastly different, we must rely on our development effort to make the mechanism reasonably complete so that it can handle chemical situations that are untested in smog chambers. We know the concentration characteristics of such conditions from ambient measurements. For instance, the effects of background species such as methane and CO, which are generally of little importance in high concentration smog chamber experiments, must be included in atmospheric models. Reactions expected to be significant for conditions of extremely low NO_x and VOC, must also be included to account for such conditions in rural applications. We have attempted to include the chemistry for these conditions in the CBM.

3 THE INORGANIC AND CARBONYL REACTION SET

This section describes the Inorganic and Carbonyl Reaction Set (ICRS). The ICRS is the portion of the CBM that contains (1) the basic inorganic chemistry of oxygen, nitrogen, and hydrogen species plus one reaction of CO and (2) the chemistry of simple oxygenated organic species. These chemical reactions are common to virtually all tropospheric chemistry and are the foundation of the CBM. In the current reevaluation of the mechanism, the basic kinetic and mechanistic information contained in the ICRS was reviewed and updated. Our description of the ICRS is divided into a discussion of (1) inorganic chemistry, (2) formaldehyde reactions, (3) acetaldehyde and PAN reactions, (4) photolysis reactions, and (5) condensation of the ICRS. The carbonyl reactions of higher molecular weight species (such as acetone and dicarbonyls) are considered in later discussions of the hydrocarbon classes from which they are formed.

INORGANIC CHEMISTRY

The inorganic portion of the ICRS is composed of the first 36 reactions listed in Tables 1-2 and 1-3.* The ICRS contained in these versions of the CBM includes recently published information; therefore, a brief discussion of the individual chemical reactions is in order here. The ICRS includes both photolytic and thermal reactions. Calculation of photolytic reaction rates will be discussed in detail later in this section. The current discussion is limited to a description of photolytic mechanisms. The reaction rates of thermal reactions and their temperature dependencies in the range of tropospheric interest are discussed first. Reaction rates are presented for 298 K; temperature-dependent expressions are presented in Arrhenius form:

$$k = A \exp((-E/R)(1/T)).$$

---

* Reaction numbers given in the text refer to the CBM-IV unless they are preceeded with an X; an X indicates that a particular reaction is from the CBM-X (Table 1-2).

Rate constants for reactions of the type

$$A + B \longleftrightarrow [AB]^* \xrightarrow{M} AB,$$

which are in the fall-off regime between bimolecular and termolecular reactions, were initially determined from the following formula (DeMore et al., 1985):

$$k(M,T) = \left(\frac{k_0(T)[M]}{1 + (k_0(T)[M]/k_\infty(T))}\right) 0.6^{\{1 + [\log_{10}(k_0(T)[M]/k_\infty(T))]^2\}^{-1}}$$

The third order expression is given by

$$k_0(T) = k_0^{300}(T/300)^{-n}\ cm^6s^{-1},$$

where the value is suitable for air as a third body. The high-pressure rate constant is given by:

$$k_\infty(T) = k_\infty^{300}(T/300)^{-m}\ cm^3s^{-1}.$$

The values used in this discussion are taken primarily from the NASA review (DeMore et al., 1985) (the reader is referred to that document for further description of the foregoing expressions). The curves resulting from these expressions were then fit with the Arrhenius formula for the temperature range of interest in the atmosphere and smog chambers (260 K to 320 K). In addition, the CBM-IV reported here is designed for simulation of photochemistry near the earth's surface. It should not be used for high altitude (low pressure) calculations without implementation of the appropriate pressure-dependent rate expressions.

The photolysis of NO_2 leads to the production of $O(^3P)$:

$$NO_2 \xrightarrow{h\nu} NO + O(^3P). \qquad (1)$$

$O(^3P)$ will subsequently be referred to as O. The rate of this photolysis reaction is usually used to gauge the magnitude of light intensity in experimental facilities and in the atmosphere. However, it is really a measure of the actinic flux only in the region of NO_2 absorption; therefore, the photolysis rates of all other species are not uniquely determined by the rate of reaction 1. Calculation of k(1) and its relationship to other photolytic rates will be discussed later in this section.

O atoms react with oxygen molecules through the three-body process:

$$O + O_2 + M \text{ ------> } O_3 + M.$$

This is the only significant source of ozone in the earth's atmosphere. We used the low pressure limit of NASA (DeMore et al., 1985) and the high-pressure value from CODATA (Baulch et al., 1984):

$$k_o = 6.0 \times 10^{-34} \ (T/300)^{-2.3} \ \ cm^6 molecule^{-2} s^{-1},$$

and

$$k_\infty = 2.8 \times 10^{-12} \ \ cm^3 molecule^{-1} s^{-1}.$$

For temperature-dependent values of M and O_2 (at 1 atmosphere), the reaction can be simplified to

$$O \ (+ O_2 + M) \text{ ------> } O_3 \ (+ M), \qquad (2)$$

resulting in an Arrhenius expression of

$$k(2) = 8.383 \times 10^4 \exp(1175/T) \ min^{-1},$$

and

$$k(2)_{298} = 4.32 \times 10^6 \ min^{-1}.$$

In the subsequent discussion and the listing given in Tables 1-2 and 1-3, we have simplified our descriptions by including the temperature-dependent values of M and O_2 in the rate expression, noting the simplifications given next by the use of parentheses in the equation. In a similar way, products included in parentheses are not tracked in the mechanism (generally, because they are species with nearly constant concentrations, e.g., M, O_2, and CO_2, or because their subsequent reactions are not further treated in the CBM, e.g., nitrates, nitrocresols, and organic acids).

The third reaction in the ICRS, which along with the first two forms the basis of the photostationary state relationship, is

$$O_3 + NO \text{ ------> } NO_2 \ (+O_2). \qquad (3)$$

The NASA review (DeMore et al., 1985) places the rate expression at

$$k(3) = 2.643 \times 10^3 \exp(-1370/T) \ ppm^{-1} min^{-1},$$

and

$$k(3)_{298} = 26.6 \ ppm^{-1} min^{-1} \ ,$$

with an uncertainty of about 20 percent.

O atoms react with NO_2 in two ways:

$$O + NO_2 \text{ ------> } NO\ (+O_2), \tag{4}$$

and

$$O + NO_2\ (+M) \text{ ------> } NO_3\ (+M). \tag{5}$$

For reaction 4, NASA (DeMore et al., 1985) recommends

$$k(4)_{298} = 1.375 \times 10^4\ ppm^{-1}min^{-1},$$

with an uncertainty of about 10 percent. The fall-off values for reaction 5 are also from NASA (DeMore et al., 1985):

$$k_o = 9.0 \times 10^{-32}\ (T/300)^{-2.0}\ \ cm^6molecule^{-2}s^{-1},$$

and

$$k_\infty = 2.2 \times 10^{-11}\ \ cm^3molecule^{-1}s^{-1},$$

which lead to an effective Arrhenius expression of

$$k(5) = 2.303 \times 10^2\ exp(687/T)\ ppm^{-1}min^{-1},$$

and

$$k(5)_{298} = 2.31 \times 10^3\ ppm^{-1}min^{-1}.$$

The similar three-body reaction for NO is

$$O + NO\ (+M) \text{ ------> } NO_2\ (+M). \tag{6}$$

The NASA (DeMore et al., 1985) low- and high-pressure limit values for reaction 6 are

$$k_o = 9.0 \times 10^{-32}\ (T/300)^{-1.5}\ \ cm^6molecule^{-2}s^{-1},$$

and

$$k_\infty = 3.0 \times 10^{-11}\ \ cm^3molecule^{-1}s^{-1},$$

which lead to an effective Arrhenius expression of

$$k(6) = 3.233 \times 10^2\ exp(602/T)\ ppm^{-1}min^{-1},$$

and

$$k(6)_{298} = 2.44 \times 10^3\ ppm^{-1}min^{-1}.$$

The reaction of O_3 and NO_2 can be significant when most of the NO has been converted to NO_2. This is an important scenario downwind of an urban area late in the day or at night, since this reaction represents a nonphotolytic source of radicals:

$$NO_2 + O_3 \text{ ------> } NO_3\ (+O_2). \tag{7}$$

NASA (DeMore et al., 1985) and Atkinson and Lloyd (1984) use an Arrhenius expression of

$$k(7) = 1.760 \times 10^{2} \exp(-2450/T)\ ppm^{-1}min^{-1},$$

and

$$k(7)_{298} = 4.73 \times 10^{-2}\ ppm^{-1}min^{-1},$$

assuming an uncertainty of approximately 15 percent.

Ozone photolysis occurs in two channels with photoaction spectra in significantly different spectral locations (see the discussion of photolysis rate later in this section). The higher energy (short wavelength) process results in the formation of $O(^1D)$, while the process that occurs at longer wavelengths forms $O(^3P)$ (referred to as O):

$$O_3 \text{ --hv--> } O \quad (+ O_2) \tag{8}$$

$$O_3 \text{ --hv--> } O(^1D) \ (+ O_2) \tag{9}$$

In the ICRS, the photolytic rate of reaction 8 is implemented as a ratio to k(1) (since NO_2 absorbs at long wavelengths), while photolytic rate 9 must be explicitly input with respect to zenith angle because its short wavelength energy source does not vary uniquely with j_{NO_2}.

The $O(^1D)$ formed in reaction 9 can be converted to the lower electronic energy state of O via energy transfer to oxygen and nitrogen molecules:

$$O(^1D) \ (+ O_2) \text{ ------> } O \ (+ O_2),$$

and

$$O(^1D) \ (+ N_2) \text{ ------> } O \ (+ N_2).$$

Following the recommendations of NASA (DeMore et al., 1985), we combine these reactions to yield

$$O(^1D) \ (+ \ M) \text{ ------> } O \ (+ M). \tag{10}$$

The combined kinetic expression for reaction 10 is

$$k(10) = 1.147 \times 10^{10} \exp(390/T)\ min^{-1},$$

and

$$k(10)_{298} = 4.25 \times 10^{10}\ min^{-1},$$

with an uncertainty of about 20 percent.

Atmospheric water vapor can compete with M for $O(^1D)$ through reaction 11:

$$O(^1D) + H_2O \text{ ------> } 2\ OH. \qquad (11)$$

Although an insignificant reaction loop results from the combination of reactions 8 through 10, reaction 11 is an important hydroxyl-radical-forming process. One way of thinking of this is that the presence of ozone in daylight can convert water vapor to hydroxyl radicals. This process is important near the period of ozone buildup, when radical concentrations are increasing. At that point, reaction 11 tends to provide a "bootstrap" function, in which the formation of new ozone promotes the formation of new hydroxyl radicals. The rate of reaction 11 is temperature-independent and NASA (DeMore et al., 1985) recommends

$$k(11)_{298} = 3.26 \times 10^5\ ppm^{-1}min^{-1}.$$

This reaction rate is also uncertain to about 20 percent. Because (1) reactions 10 and 11 are the only important reactions of $O(^1D)$, (2) are strongly dependent on the $O(^1D)$ formation rate, and (3) deplete any $O(^1D)$ extremely rapidly, a steady-state concentration is easily established for $O(^1D)$ under all daylight conditions. This steady state can be represented equally as well in the ICRS if we lower k(10) and k(11) by an identical factor, thus minimizing some stiffness in the solution. In the ICRS, therefore, both rates have been divided by 10^5. The time constant for decay via reactions 10 and 11 is of the order of 10^{-11} minutes. Thus, a significant change in $O(^1D)$ in even 1 minute is still accurately simulated to about 6 significant figures with this stiffness reducing factor of 10^5.

The temperature dependence of the reactions of ozone with OH and HO_2,

$$O_3 + OH \text{ ------> } HO_2\ (+\ O_2), \qquad (12)$$

and

$$O_3 + HO_2 \text{ ------> } OH\ \ (+\ 2O_2), \qquad (13)$$

are taken from the NASA review (DeMore et al., 1985). For reaction 12,

$$k(12) = 2.344 \times 10^3 \exp(-940/T)\ ppm^{-1}min^{-1},$$

and

$$k(12)_{298} = 1.00 \times 10^2\ ppm^{-1}min^{-1},$$

with an uncertainty of approximately 30 percent.

For reaction 13,

$$k(13) = 2.100 \times 10^{1} \exp(-580/T)\ ppm^{-1}min^{-1},$$

and

$$k(13)_{298} = 3.00\ ppm^{-1}min^{-1},$$

with an uncertainty of approximately 50 percent at 298 K.

The NO_3 radical undergoes photolysis in the visible region of the surface solar spectrum; therefore, its j-value is determined through a ratio to j_{NO_2} (see the discussion of this rate at the end of this section). Two possible channels occur:

$$NO_3 \text{ --hv--> } NO_2 + O,$$

and

$$NO_3 \text{ --hv--> } NO + O_2.$$

These have been combined into reaction 14:

$$NO_3 \text{ --hv--> } 0.89\ NO_2 + 0.89\ O + 0.11\ NO\ (+\ 0.11\ O_2). \qquad (14)$$

The reaction of NO_3 with NO,

$$NO_3 + NO \text{ ------> } 2NO_2, \qquad (15)$$

has been recently studied by two separate research groups and the accepted rate constant has been increased. We have used the NASA rate (DeMore et al., 1985), which yields

$$k(15) = 1.909 \times 10^{4} \exp(250/T)\ ppm^{-1}min^{-1},$$

and

$$k(15)_{298} = 4.42 \times 10^{4}\ ppm^{-1}min^{-1}.$$

In light of the values recently determined by Sander and Kircher (1986; $k(15)_{298} = 3.54 \times 10^{4}\ ppm^{-1}min^{-1}$) and Hammer et al. (1986; $k(15)_{300} = 4.36 \times 10^{4}\ ppm^{-1}min^{-1}$), we assume an uncertainty of 25 percent at 298 K.

The next four reactions (16 through 19) in the ICRS represent a set of NO_x reactions that often prove to be an important source of nitric acid through the reaction of the equilibrium species dinitrogen pentoxide. First, NO_2 and NO_3 can react in two ways:

$$NO_3 + NO_2 \text{ ------> } NO + NO_2\ (+\ O_2), \qquad (16)$$

and

$$NO_3 + NO_2\ (+\ M) \text{ ------> } N_2O_5\ (+\ M). \qquad (17)$$

The rate expressions are

$$k(16) = 3.66 \times 10^{1} \exp(-1230/T)\ ppm^{-1}min^{-1},$$

with,

$$k(16)_{298} = 0.590\ ppm^{-1}min^{-1}\ \text{(Atkinson and Lloyd, 1984)},$$

and

$$k(17) = 7.849 \times 10^{2} \exp(256/T)\ ppm^{-1}min^{-1},$$

with,

$$k(17)_{298} = 1.853 \times 10^{3}\ ppm^{-1}min^{-1}\ \text{(DeMore et al., 1985)}.$$

Reaction 17 obviously appears to be more important. However, reaction 16 cannot be ruled out because of its somewhat unique reduction of NO_3 to NO. For conditions of low NO, such as at night when O_3 titrates all of the NO to NO_2 and NO_3, reaction 16 is the only source of NO in the ICRS.

N_2O_5 chemistry consists of reactions 18 and 19:

$$N_2O_5 + H_2O \text{ ------> } 2\ HNO_3, \tag{18}$$

and

$$N_2O_5\ (+\ M) \text{ ------> } NO_2 + NO_3\ (+\ M). \tag{19}$$

Reaction 19 is the reverse of reaction 17; the combination of these reactions represents the N_2O_5 equilibrium. The K_{eq} value and its temperature dependence are highly uncertain and the subject of much recent research. The rate for reaction 19 is based on the K_{eq} value of NASA (DeMore et al., 1985) and the k(17) expression:

$$k(19) = k(17)/K_{eq},$$

where

$$k(17) = 5.346 \times 10^{-13} \exp(256/T)\ cm^{3}molec^{-1}s^{-1}\ ,$$

and

$$K_{eq} = 1.52 \times 10^{-27} \exp(11153/T)\ cm^{3}molec^{-1}.$$

Then,

$$k(19) = 3.52 \times 10^{14} \exp(-10897/T)\ s^{-1},$$

or

$$= 2.11 \times 10^{16} \exp(-10897/T)\ min^{-1},$$

with

$$k(19)_{298} = 2.78\ min^{-1}.$$

This value is more closely related to the Graham and Johnston (1978) determination suggested by Perner et al. (1985).

The value for k(18) is highly uncertain and the process may be heterogenous. The value selected was recommended for atmospheric use by Atkinson and Lloyd (1984):

$$k(18)_{298} = 1.9 \times 10^{-6}\ ppm^{-1}min^{-1}.$$

The termolecular self reaction of NO in the presence of oxygen,

$$NO + NO\ (+\ O_2) \text{------>}\ 2\ NO_2, \qquad (20)$$

is generally insignificant in the atmosphere, but is included in the ICRS to correctly model conditions of high NO. The rate constant is that of Atkinson and Lloyd (1984):

$$k(20) = 2.60 \times 10^{-5}\ \exp(530/T)\ ppm^{-1}min^{-1},$$

and

$$k(20)_{298} = 1.539 \times 10^{-4}\ ppm^{-1}min^{-1},$$

with an uncertainty of about 25 percent.

The chemical cycle of nitrous acid is included in the ICRS as reactions 21 through 25:

$$NO + NO_2 + H_2O \text{------>}\ 2\ HONO, \qquad (21)$$

$$OH + NO\ (+\ M\ ) \text{------>}\ HONO\ (+\ M), \qquad (22)$$

$$HONO \text{--hv-->}\ OH + NO, \qquad (23)$$

$$OH + HONO \text{------>}\ NO_2\ (+\ H_2O), \qquad (24)$$

$$HONO + HONO \text{------>}\ NO + NO_2\ (+\ H_2O). \qquad (25)$$

The gas-phase equilibrium of HONO, NO_2, NO, and H_2O is represented by reactions 21 and 25; the values of k_{21} and k_{25} are taken from the study by Kaiser and Wu (1977):

$$k(21) = 1.60 \times 10^{-11}\ ppm^{-2}min^{-1},$$

and

$$k(25) = 1.50 \times 10^{-5}\ ppm^{-1}min^{-1},$$

with an unknown temperature dependence. The predominant formation route for nitrous acid is through the reaction of OH, NO, and a third body (reaction 22). The high- and low-pressure fall-off parameters for this reaction are from Atkinson and Lloyd (1984):

$$k_o = 6.7 \times 10^{-31}\ (T/300)^{-3.3}\ cm^6molecule^{-2}s^{-1},$$

and

$$k_\infty = 3.0 \times 10^{-11}\ (T/300)^{-1.0}\ cm^3molecule^{-1}s^{-1},$$

which lead to an effective Arrhenius expression of

$$k(22) = 6.554 \times 10^2 \exp(806/T) \text{ ppm}^{-1}\text{min}^{-1},$$

and

$$k(22)_{298} = 9.80 \times 10^3 \text{ ppm}^{-1}\text{min}^{-1}.$$

The photolysis rate of HONO (reaction 23) is represented as a ratio to the j-value of NO_2. This reaction generally dominates as the loss mechanism for HONO, though the reaction of OH and HONO (reaction 24) cannot be discounted because of its possible role as a sink for OH. The temperature-independent rate of that reaction (Atkinson and Lloyd, 1984) is estimated at

$$k(24)_{298} = 9.77 \times 10^3 \text{ ppm}^{-1}\text{min}^{-1},$$

with an uncertainty factor of 2.

Nitric acid formation and destruction through OH reactions are represented in reactions 26 and 27:

$$OH + NO_2 \ (+ M) \text{ ------> } HNO_3 \ (+ M), \tag{26}$$

and

$$OH + HNO_3 \ (+ M) \text{ ------> } NO_3 \ (+ H_2O + M). \tag{27}$$

The high- and low-pressure fall-off parameters for reaction 26 are those of NASA (DeMore et al., 1985):

$$k_0 = 2.6 \times 10^{-30} \ (T/300)^{-3.2} \ \text{cm}^6\text{molecule}^{-2}\text{s}^{-1},$$

and

$$k_\infty = 2.4 \times 10^{-11} \ (T/300)^{-1.3} \ \text{cm}^3\text{molecule}^{-1}\text{s}^{-1},$$

which lead to an effective Arrhenius expression of

$$k(26) = 1.537 \times 10^3 \exp(713/T) \text{ ppm}^{-1}\text{min}^{-1},$$

and

$$k(26)_{298} = 1.68 \times 10^4 \text{ ppm}^{-1}\text{min}^{-1}.$$

For reaction 27, the pressure and temperature dependence were fit by combining a low-pressure (bimolecular) limit with a Lindemann-Hinshelwood expression for pressure dependence (DeMore et al., 1985):

$$k(M,T) = k_0 + \frac{k_3[M]}{1 + \frac{k_3[M]}{k_2}}$$

where

$$k_0 = 7.2 \times 10^{-15} \exp(785/T).$$
$$k_2 = 4.1 \times 10^{-16} \exp(1440/T),$$
$$k_3 = 1.9 \times 10^{-33} \exp(725/T).$$

The Arrhenius expression fit to these data is

$$k(27) = 7.600 \exp(1000/T) \text{ ppm}^{-1}\text{min}^{-1},$$

with

$$k(27)_{298} = 2.18 \times 10^2 \text{ ppm}^{-1}\text{min}^{-1}.$$

The bimolecular reaction of HO_2 and NO (reaction 28) is

$$HO_2 + NO \text{ ------> } NO_2 + OH. \qquad (28)$$

The Arrhenius expression used is from NASA (DeMore et al., 1985):

$$k(28) = 5.482 \times 10^3 \exp(240/T) \text{ ppm}^{-1}\text{min}^{-1},$$

and

$$k(28)_{298} = 1.23 \times 10^4 \text{ ppm}^{-1}\text{min}^{-1},$$

with an uncertainty at 298 K of approximately 20 percent.

Reactions 29 through 31 represent peroxynitric acid (PNA) chemistry in the ICRS:

$$HO_2 + NO_2 \ (+ M) \text{ ------> } PNA \ (+ M), \qquad (29)$$
$$PNA \ (+ M) \text{ ------> } HO_2 + NO_2 \ (+ M), \qquad (30)$$
$$OH + PNA \text{ ------> } NO_2 \ (+ H_2O + O_2). \qquad (31)$$

The forward rate of the PNA gas-phase equilibrium (reaction 29) is taken from the fall-off parameters given in Atkinson and Lloyd (1984):

$$k_0 = 2.3 \times 10^{-31} \ (T/300)^{-4.6} \ \text{cm}^6\text{molecule}^{-2}\text{s}^{-1},$$

and

$$k_\infty = 4.2 \times 10^{-12} \ (T/300)^{+0.2} \ \text{cm}^3\text{molecule}^{-1}\text{s}^{-1},$$

which lead to an effective Arrhenius expression of

$$k(29) = 1.64 \times 10^2 \exp(749/T)\ ppm^{-1}min^{-1},$$

and

$$k(29)_{298} = 2.03 \times 10^3\ ppm^{-1}min^{-1}.$$

Two alternate pathways have been suggested for these reactants:

$$HO_2 + NO_2 + H_2O \text{ ------> } PNA + H_2O,$$

and

$$HO_2 + NO_2 \text{ ------> } HONO + O_2.$$

The former pathway was studied by Sander and Peterson (1984), but it is highly uncertain; the latter, if it occurs at all, apparently occurs at a rate that is insignificant under all conditions of interest (Atkinson and Lloyd, 1984). Therefore, neither reaction is included in the ICRS.

The rate for PNA decomposition (reaction 30) is based on the K_{eq} value of NASA (DeMore et al., 1985) and the k_{29} expression:

$$k(30) = k(29)/K_{eq},$$

where

$$k(29) = 1.117 \times 10^{-13} \exp(749/T)\ cm^3molecule^{-1}s^{-1},$$

and

$$K_{eq} = 2.33 \times 10^{-27} \exp(10870/T)\ cm^3molecule^{-1}.$$

Then,

$$k(30) = 4.79 \times 10^{13} \exp(-10121/T)\ s^{-1},$$

or

$$= 2.88 \times 10^{15} \exp(-10121/T)\ min^{-1},$$

with

$$k(30)_{298} = 5.11\ min^{-1}.$$

Reaction 31, the OH-plus-PNA reaction, is generally unimportant compared to PNA decomposition, but is included for low-temperature simulations. The product distribution is not clear, but the one used here is often given the highest possibility. Reaction rate information is taken from NASA (DeMore et al., 1985), though both the rate and activation energy values are highly uncertain:

$$k(31) = 1.909 \times 10^3 \exp(380/T)\ ppm^{-1}min^{-1},$$

and

$$k(31)_{298} = 6.83 \times 10^3\ ppm^{-1}min^{-1}.$$

Hydrogen peroxide chemistry is shown in reactions 32 through 35.

$$HO_2 + HO_2 \text{ ------> } H_2O_2 \ (+ O_2), \tag{32}$$

$$HO_2 + HO_2 + H_2O \text{ ------> } H_2O_2 \ (+ O_2 + H_2O), \tag{33}$$

$$H_2O_2 \text{ --hv--> } 2\ OH, \tag{34}$$

$$OH + H_2O_2 \text{ ------> } HO_2 \ (+ H_2O). \tag{35}$$

The HO_2 self reaction is enhanced by the presence of water vapor; thus, two reactions (32 and 33) are used to represent this process. ICRS rate constants are from Atkinson and Lloyd (1984). At surface atmospheric pressure,

$$k(32) = 8.739 \times 10^1 \exp(1150/T)\ ppm^{-1}min^{-1},$$

and

$$k(32)_{298} = 4.14 \times 10^3\ ppm^{-1}min^{-1}.$$

For the reaction with water,

$$k(33) = 7.690 \times 10^{-10} \exp(5800/T)\ ppm^{-2}min^{-1},$$

and

$$k(33)_{298} = 2.18 \times 10^{-1}\ ppm^{-2}min^{-1}.$$

The photoaction spectrum of H_2O_2 photolysis is near that of formaldehyde photolysis (to stable products); therefore, the photolysis rate, k(34), is determined by ratioing to j_{HCHOs} at varying zenith angles (as opposed to j_{NO_2}).

The reaction of OH can be an important loss mechanism for H_2O_2 during some daylight conditions. The reaction rate used in the ICRS is from NASA (DeMore et al., 1985), which recommends

$$k(35) = 4.720 \times 10^3 \exp(-187/T)\ ppm^{-1}min^{-1},$$

and

$$k(35)_{298} = 2.52 \times 10^3\ ppm^{-1}min^{-1}.$$

The last reaction in the ICRS is the oxidation of CO by OH:

$$OH + CO \text{ ------> } HO_2 \ (+ CO_2). \tag{36}$$

NASA (DeMore et al., 1985) recommends the formula:

$$k(36) = 1.5 \times 10^{-13}\ (1+0.6P_{atm})\ cm^3molecule^{-1}s^{-1},$$

or

$$k(36) = 2.217 \times 10^2\ (1+0.6P_{atm})\ ppm^{-1}min^{-1}.$$

At 640 m, the temperature-independent rate is approximately

$$k(36) = 3.22 \times 10^2 \text{ ppm}^{-1}\text{min}^{-1}.$$

FORMALDEHYDE REACTIONS

Formaldehyde (CH2=O) is the simplest carbonyl species in polluted atmospheres and is also a key organic oxidation product of almost all larger organic species. Since it is capable of being both oxidized and photolyzed and is therefore an important source of radicals in photochemical systems, careful consideration must be given to the representation and uncertainties of these chemical processes. In addition, because formaldehyde is considered a toxic species, we have chosen to explicitly represent its chemical reactions. As will be apparent in later discussions of hydrocarbon representations, this choice entailed the removal of FORM as a surrogate for some carbonyl species, in particular, glyoxal formed from aromatics.

In the reaction with formaldehyde (designated FORM in the CBM), the hydroxyl radical abstracts one of the hydrogens to form water, leaving the formyl radical ($O{=}\dot{C}H$):

$$\text{FORM} + {}^{\bullet}OH \text{ ------> } O{=}\dot{C}H + H_2O$$

In the troposphere (at surface concentrations of O_2) it is a good approximation to assume that the only reaction of formyl radical is:

$$O{=}\dot{C}H + O_2 \text{ ------> } CO + HO_2^{\bullet}$$

These reactions are combined to yield

$$\text{FORM} + OH\ (+\ O_2) \text{ ------> } CO + HO2\ (+\ H_2O), \qquad (37)$$

with a rate constant of

$$k(37)_{298} = 15000 \text{ ppm}^{-1}\text{min}^{-1},$$

and an uncertainty of about 25 percent (DeMore et al., 1985).

Two formaldehyde photolysis reactions occur in the middle ultraviolet region of the surface spectrum. Assuming that all product $H^{\bullet}$ radicals react exclusively with tropospheric O_2, these are

$$\text{FORM} \xrightarrow{h\nu} 2\ \text{HO2} + \text{CO}, \tag{38}$$

and

$$\text{FORM} \xrightarrow{h\nu} \text{CO}\ (+\ H_2). \tag{39}$$

The ratio of photolysis rates between j_{38} and j_{39} varies with the spectral distribution of surface light (which changes with the zenith angle of the sun). The calculation of these photolysis rates is discussed later in this report. At present, we note that the rate of reaction 39 is always greater than that of reaction 38 for solar irradiation. However, at low zenith angles near solar noon, the relative importance of the radical-producing reaction becomes greater than it is at higher zenith angles.

The reaction of $O(^3P)$ with formaldehyde is usually unimportant, but we include it because we already treat $O(^3P)$ in the mechanism; thus, the inclusion of this reaction is not a computational burden. In addition, it is an organic source of $^{\bullet}OH$, since the O atom extracts a formaldehyde hydrogen atom. Again, assuming all $H^{\bullet}$ produced reacts exclusively with O_2, the reaction is

$$\text{FORM} + \text{O} \longrightarrow \text{OH} + \text{HO2} + \text{CO}. \tag{40}$$

The reaction rate used in the ICRS is that of NASA (DeMore et al., 1985):

$$k(40) = 4.302 \times 10^4 \exp(-1550/T)\ \text{ppm}^{-1}\text{min}^{-1},$$

and

$$k(40)_{298} = 2.37 \times 10^2\ \text{ppm}^{-1}\text{min}^{-1}.$$

The NO_3 radical also reacts with formaldehyde through the abstraction of a hydrogen atom to produce nitric acid. Assuming all of the $H^{\bullet}$ intermediate reacts with atmospheric O_2, the reaction is

$$\text{FORM} + \text{NO3} \longrightarrow \text{HNO3} + \text{HO2} + \text{CO}, \tag{41}$$

with a rate constant used by Cantrell et al. (1985) for 298 K:

$$k(41)_{298} = 0.93\ \text{ppm}^{-1}\text{min}^{-1}.$$

Although this rate is closely supported in the review by NASA [DeMore et al. (1985) use a rate of 0.88 $\text{ppm}^{-1}\text{min}^{-1}$], both groups suggest high uncertainty limits. Those of NASA are 50 percent.

A final reaction scheme for formaldehyde that may be important under some limited conditions is the addition (and later regeneration) of the $HO_2^{\bullet}$ radical. This reaction, and postulated subsequent reactions, were originally presented by Su et al. (1979a; 1979b). The overall scheme is

$$HCHO + HO_2^{\cdot} \longleftrightarrow HOOCH_2O^{\cdot}$$
$$HOOCH_2O^{\cdot} \longleftrightarrow HOCH_2OO^{\cdot}$$
$$HOCH_2OO^{\cdot} + HO_2^{\cdot} \longrightarrow HO_2CH_2OOH + O_2$$
$$HOCH_2OO^{\cdot} + NO \longrightarrow NO_2 + HOCH_2O^{\cdot}$$
$$HOCH_2O^{\cdot} \ (+ O_2) \longrightarrow HO_2^{\cdot} + HCOOH$$

The initial equilibrium shows the presence of a transition intermediate that appears capable of rearrangement to a more stable peroxy radical (Su et al., 1979b) through a subsequent equilibrium. We have followed the example of Veyret et al. (1982) and represent these two equilibria by

$$HCHO + HO_2^{\cdot} \longrightarrow HOCH_2OO^{\cdot},$$
$$HOCH_2OO^{\cdot} \longrightarrow HCHO + HO_2^{\cdot},$$

where the peroxy radical results from the combined equilibria. We also assume that the last reaction is rapid and is the only loss mechanism for the $HOCH_2O^{\cdot}$ radical. Hence,

$$HOCH_2OO^{\cdot} + NO \ (+ O_2) \longrightarrow NO_2 + HO_2^{\cdot} + HCOOH.$$

In our listing of the CBM-X, we use FROX to represent the peroxy radical and PROX to represent total non-H_2O_2 peroxides. The overall scheme is

FORM + HO2 ------> FROX,		(X-42)
FROX ------> FORM + HO2,		(X-43)
FROX + HO2 ------> PROX,		(X-44)
FROX + NO ------> NO2 + HO2 + FACD.		(X-45)

The rate of the initial reaction has been reported by a number of researchers as 14.8 $ppm^{-1}min^{-1}$ (Su et al, 1979a; 1979b), 110.9 $ppm^{-1}min^{-1}$ (Veyret et al., 1982), and 162.6 $ppm^{-1}min^{-1}$ (Barnes et al., 1985). The back reaction to the original products was determined to be 90 min^{-1} (Su et al, 1979a; 1979b), and 1800 min^{-1} (Veyret et al., 1982). These are relatively rapid reverse rates, and appear to force the equilibria to the original products under all conditions. This is especially true if one notes that the reaction of HO_2 and NO (reaction 28) is fast, resulting in little HO_2 for high-NO conditions and a relatively ineffectual reaction of NO with FROX for low-NO conditions. We use the reaction rates of Su et al. (1979b) for the equilibrium reactions in the CBM-X; the remaining two rates are

$$k(X\text{-}44) = 9.60 \times 10^{3} \text{ (Vayret et al., 1982)},$$

and

$$k(X\text{-}45) = 1.04 \times 10^{4} \text{ (Su et al, 1979b)}.$$

Even for the more conservative rates of Su et al., reaction X-43 is rapid, causing reactions X-42 through X-45 to be unimportant under most conditions. Therefore, they have not been included in the CBM-IV.

ACETALDEHYDE AND PAN REACTIONS

Acetaldehyde is the next highest molecular weight aldehyde after formaldehyde, and it is also capable of both photolysis and oxidation by most of the radical species that oxidize formaldehyde. The key reactive product of the acetaldehyde reactions is the peroxyacetyl radical ($CH_3C(O)OO\cdot$; also denoted by C2O3 in the CBM), which is capable of a number of important reactions including reaction with NO_2 to form peroxyacetylnitrate ($CH_3C(O)OONO_2$), commonly known as PAN. PAN decomposes to its original formation products in a temperature-dependent manner that allows those NO_2 and C2O3 radicals formed earlier in a photochemically reactive air mass to be stored and released at later or warmer periods. The accurate representation of PAN chemistry is a critical aspect in the correct simulation of oxidant chemistry, and we have sought to enhance our representation of important PAN-related processes in our current revision of the CBM. We begin, however, with acetaldehyde reactions.

Acetaldehyde reactions are listed in the CBM-X (Table 1-2) as reactions X-46 through X-49 (reactions 42 through 45 of the CBM-IV in Table 1-3). The reaction with O results in the abstraction of the carbonyl hydrogen to form hydroxyl and acetyl radicals:

$$CH_3\overset{\overset{\displaystyle O}{\|}}{C}H + O \text{ ------> } CH_3\overset{\overset{\displaystyle O\cdot}{\|}}{C}\cdot + \cdot OH.$$

In the CBM, we assume that the peroxyacetyl radical forms rapidly (exclusively) under tropospheric conditions through reaction with O_2:

$$CH_3\overset{\overset{\displaystyle O}{\|}}{C}\cdot + O_2 \text{ ------> } CH_3\overset{\overset{\displaystyle O}{\|}}{C}OO\cdot$$

Combining these reactions results in

$$CH_3\overset{\overset{\displaystyle O}{\|}}{C}H + O\ (+O_2) \text{--> } CH_3\overset{\overset{\displaystyle O}{\|}}{C}OO\cdot + \cdot OH. \qquad (42)$$

The reaction rate used in the ICRS is derived from Atkinson and Lloyd (1984):

$$k(42) = 1.739 \times 10^4 \exp(-986/T)\ ppm^{-1}min^{-1},$$

and

$$k(42)_{298} = 6.36 \times 10^2 ppm^{-1}min^{-1}.$$

The reaction of the hydroxyl radical with acetaldehyde is also expected to proceed by abstraction of the carbonyl hydrogen atom to form water. Again, by assuming that only C2O3 is formed from the acetyl radical, the CBM representation of the reaction is

$$CH_3\overset{\overset{\displaystyle O}{\|}}{C}H + OH \text{ ------> } CH_3\overset{\overset{\displaystyle O}{\|}}{C}OO\cdot\ (+\ H_2O). \qquad (43)$$

The kinetic expression we have used in the past is very similar to that recommended by Atkinson (1985). We therefore use

$$k(43) = 1.037 \times 10^4 \exp(250/T)\ ppm^{-1}min^{-1},$$

and

$$k(43)_{298} = 2.40 \times 10^4 \text{ ppm-1 min-1}.$$

As we note in our discussion of the CBM-IV condensation steps, the reaction with OH is a key oxidation reaction for higher molecular weight aldehydes, and acetaldehyde (designated ALD2) is used to describe the chemistry of the aldehyde functional group for higher molecular weight aldehydes.

Acetaldehyde reaction with NO_3 radical is expected to proceed in a manner analogous to these reactions, following the scheme

$$CH_3\overset{\overset{\displaystyle O}{\|}}{C}H + NO_3 \text{ ------> } CH_3\overset{\overset{\displaystyle O}{\|}}{C}OO\cdot + HNO_3. \qquad (44)$$

We derive our rate constant for this reaction on an estimate by Kerr and Calvert (1985) of

$$k(44)_{298} = 3.70\ ppm^{-1}min^{-1}.$$

This reaction is often unimportant in the daytime, when NO_3 concentrations are usually low. However, in nighttime situations of high ozone and NO_x, reaction 44 can result in the elimination of acetaldehyde and the production of PAN.

The photolysis of acetaldehyde occurs at wavelengths near the surface cut-off of ultraviolet light in a region similar to ozone photolysis to $O(^1D)$. The three primary processes under tropospheric conditions (after reaction of initial products with O_2) are

$$CH_3\overset{\overset{\displaystyle O}{\|}}{C}H \text{--}h\nu\text{-->} \quad CH_3OO^{\cdot} + HO_2 + CO, \qquad \text{(I)}$$

$$\text{--}h\nu\text{-->} \quad CH_4 + CO, \qquad \text{(II)}$$

$$\text{--}h\nu\text{-->} \quad CH_3\overset{\overset{\displaystyle O}{\|}}{C}OO^{\cdot} + HO_2. \qquad \text{(III)}$$

On the basis of the quantum yields reported by Horowitz and Calvert (1982), we assume that only photodissociation channel I is important for conditions common in the lower troposphere. Therefore, we use

$$\text{ALD2} \ \text{--}h\nu\text{-->} \ \text{MEO2} + \text{HO2} + \text{CO}, \qquad \text{(X-49)}$$

where $CH_3OO^{\cdot}$ is designated MEO2. The photolysis of acetaldehyde is also included in the CBM-IV, but as we explain later in this section, a universal peroxy operator (XO2), FORM and HO_2 are used to represent MEO2 in the condensed mechanism.

The calculation of the acetaldehyde photolysis rate is discussed later in this section. We note here, however, that though the hydroxyl radical reaction rate constant is larger for acetaldehyde (and higher molecular weight aldehydes) than for formaldehyde, the opposite is true for photolysis rates. Hence, the hydroxyl radical reaction, which forms C2O3 products, is relatively more important than photolysis (not yielding C2O3) for higher molecular weight aldehydes than it is for formaldehyde.

As noted, the chemistry of PAN (and higher molecular weight, PAN-like compounds) must be accurately described to ensure realistic simulation of radical dynamics when NO_x and C2O3 or PAN are present. We know from experience that good representations of the PAN chemistry almost always lead to better simulation of the relationships among ozone, organics, and NO_x, both temporally and with respect to measured concentrations. Therefore, one of the goals of this CBM evaluation was to examine and, if possible, enhance the PAN reaction set. The following discussion describes the formulation of our new reaction scheme. As a starting point, we

examined the scientific literature for sources of basic kinetic information and to determine the degree of uncertainty associated with that information. We were also aware that the smog chamber data from both UNC and UCR comprised key information thus far not integrated with the basic data in any systematic way. Therefore, we also discuss an evaluation of that smog chamber data in combination with the published information to provide a more complete description of the PAN and C2O3 reaction scheme.

As noted, the decomposition of PAN,

$$\text{PAN} \longrightarrow \text{C2O3} + \text{NO2}, \tag{48}$$

is strongly temperature-dependent. We utilize the kinetic information reported by Atkinson and Lloyd (1984) to derive

$$k(48) = 5.616 \times 10^{18} \exp(-14000/T)\ \text{min}^{-1},$$

or

$$k(48)_{298} = 2.22 \times 10^{-2}\ \text{min}^{-1}.$$

Another critical aspect of the association between PAN and ozone chemistry, however, is the strong dependence upon the ratio of the C2O3 reactions with NO and NO_2:

$$\text{C2O3} + \text{NO} \longrightarrow NO_2 + \text{MEO2}, \tag{X-50}$$

and

$$\text{C2O3} + NO_2 \longrightarrow \text{PAN}. \tag{X-51}$$

Examination of the UNC data set revealed three acetaldehyde-NO_x experiments conducted during the fall and winter of 1977 that showed good evidence of the temperature-dependent relationship between competing peroxyacetyl reactions X-50 and X-51. Previous attempts to simulate these experimental data (see, for example, Whitten et al., 1980b) resulted in either greatly overpredicted ozone, overpredicted PAN, or both. Whitten et al. (1983) attempted to improve these simulations by reducing acetaldehyde photolysis at low temperatures; this procedure improved the fits for ozone, but yielded poor results for PAN.

For the experimental conditions of these experiments (low temperature and a high ratio of acetaldehyde to NO_x), PAN formation is the major radical termination process in the photochemically reactive system. This is because the PAN decay rate is small, while the availabilty of OH for the key OH-plus-NO_2 reaction is suppressed by the presence of excess acetaldehyde. Thus, PAN production at low temperatures is strongly sensitive to total radical input from any source (chamber radical production should be less significant at low temperatures, but even where chamber sources are significant, their existence would not alter such a sink phenomenon).

For the three low-temperature acetaldehyde-NO_x experiments in the UNC chamber, we found that the production of ozone, and the total conversion of NO to NO_2, was strongly related to the ratio of C2O3 reaction with NO and NO_2. In addition, the ratio of C2O3 reaction with NO and NO_2 over the temperature range of 266 to 290 K seemed to be significantly higher than that for experiments at 300 to 315 K. A probable cause of a variation in this ratio is a negative activation energy for the reaction of C2O3 plus NO_2 (reaction X-51), since this reaction is known to be pressure-dependent (Basco and Parmar, 1987). (In the following discussion and in Tables 1-2 and 1-3, note that a negative activation energy is listed as a positive exponent since the exponent is the value of -E/R.) In the following analysis, we describe the changes in the ratio of k(X-50)/k(X-51) with temperature in terms of negative activation energy for reaction X-51. However, for negative activation energies, the Arrhenius formulation must break down at some point of temperature reduction because it will predict an infinitely increasing rate constant.

The best simultaneous fits of PAN and ozone for the high-temperature (298 to 312 K) acetaldehyde-NO_x and biacetyl-NO_x experiments of 8 August 1980 and the two low-temperature acetaldehyde-NO_x experiments (UNCB-122677 and UNCB-111978) and were achieved using

$$k(X\text{-}50) = 7.915 \times 10^3 \exp(250/T)\ ppm^{-1}min^{-1},$$

and

$$k(X\text{-}50)_{298} = 1.83 \times 10^4\ ppm^{-1}min^{-1},$$

for the reaction of C2O3 with NO (reaction X-50). The corresponding best-fit Arrhenius expression for the reaction of C2O3 with NO_2 (reaction X-51) is

$$k(X\text{-}51) = 1.180 \times 10^{-4} \exp(5500/T)\ ppm^{-1}min^{-1},$$

and

$$k(X\text{-}51)_{298} = 1.22 \times 10^4\ ppm^{-1}min^{-1}.$$

The results of these simulations are shown in Figures 3-1 through 3-4.

For the high-temperature experiments (Figures 3-1 and 3-2), the PAN predictions are somewhat higher than reported concentrations, but the decay rates are correctly simulated. The measured PAN sometimes exceeds the measured NO_x (generally assumed to be NO_2 plus PAN) and we suggest that the PAN calibration factors may have been high on that date. Since the modeled NO_2 plus PAN for both experiments is nearly exact, we consider this simulation to be as close as the data allow. We also note that for the acetaldehyde-NO_x experiment of 8 August 1980, it was necessary to use 20 ppb of HONO as an initial condition to initiate the early morning

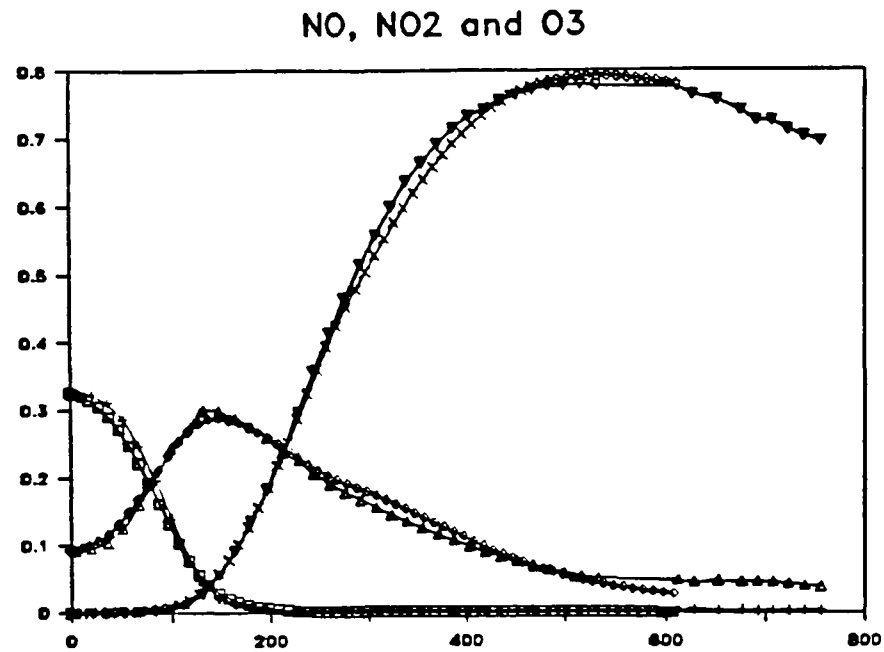

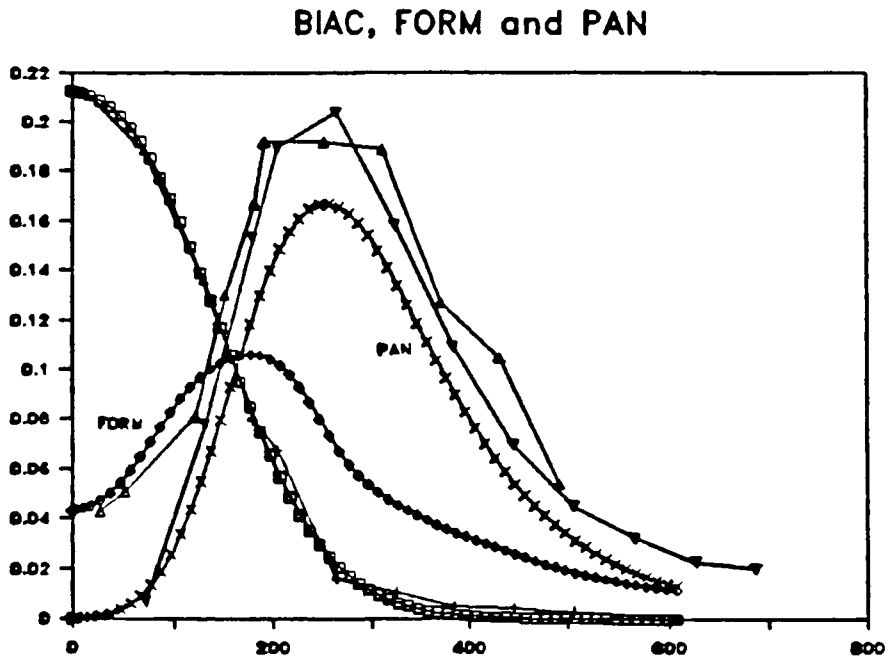

FIGURE 3-1. Simulation results and experimental data for the UNC biacetyl-NOx experiment of 8 August 1980 (lines with many symbols are simulation results).

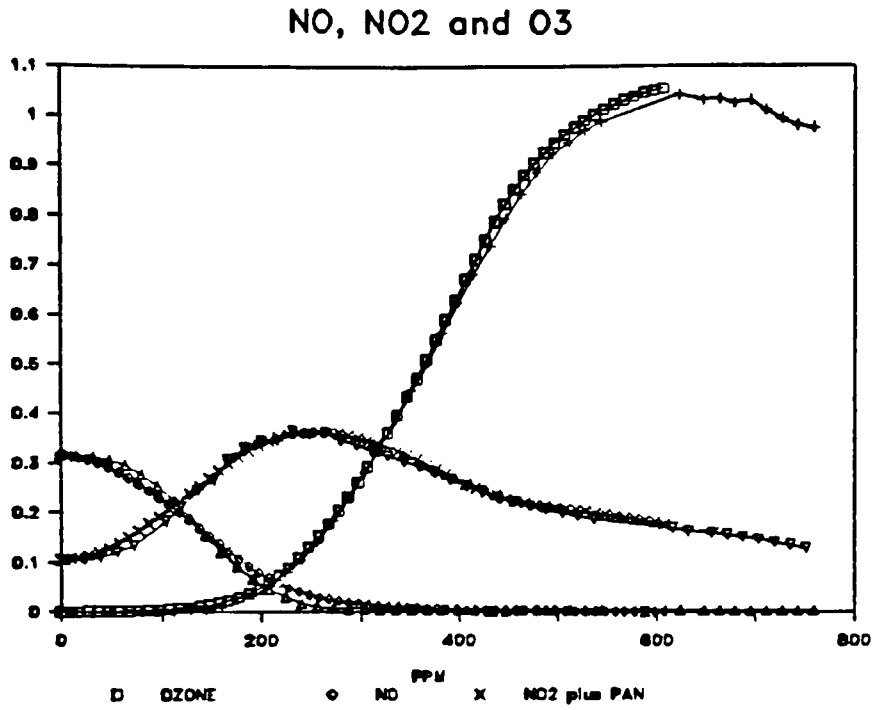

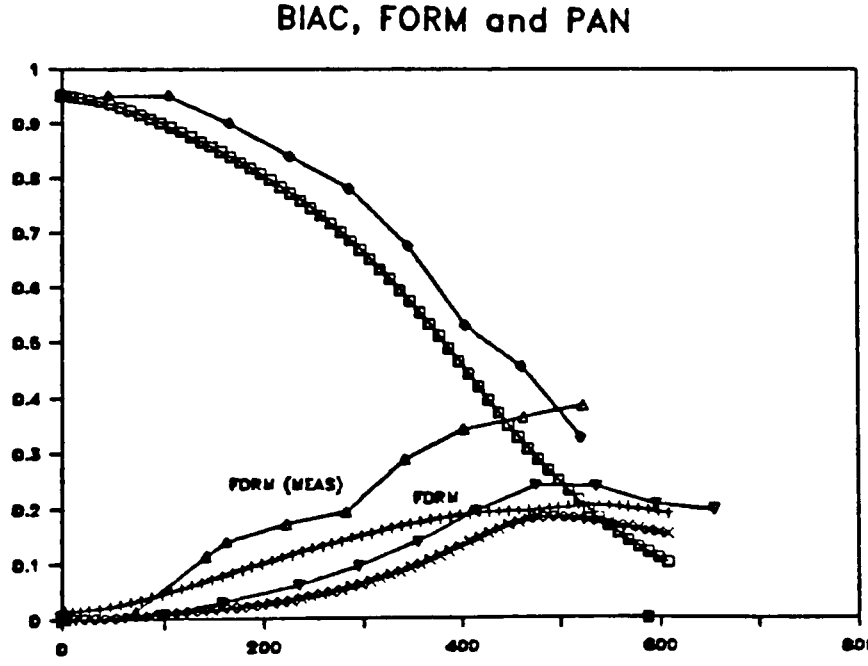

FIGURE 3-2. Simulation results and experimental data for the UNC acetaldehyde-NOx experiment of 8 August 1980 (lines with many symbols are simulation results).

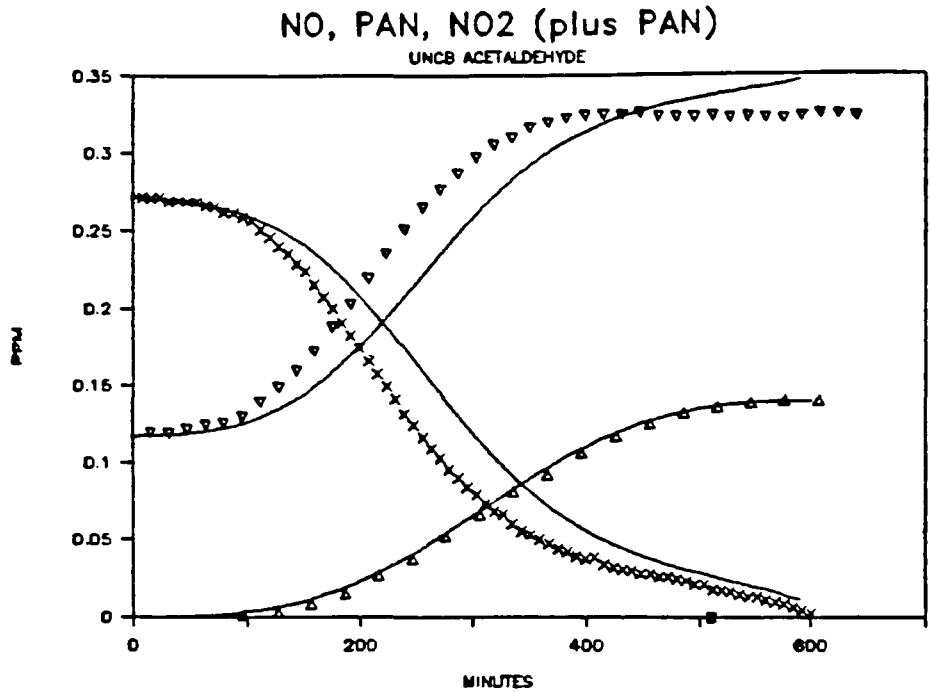

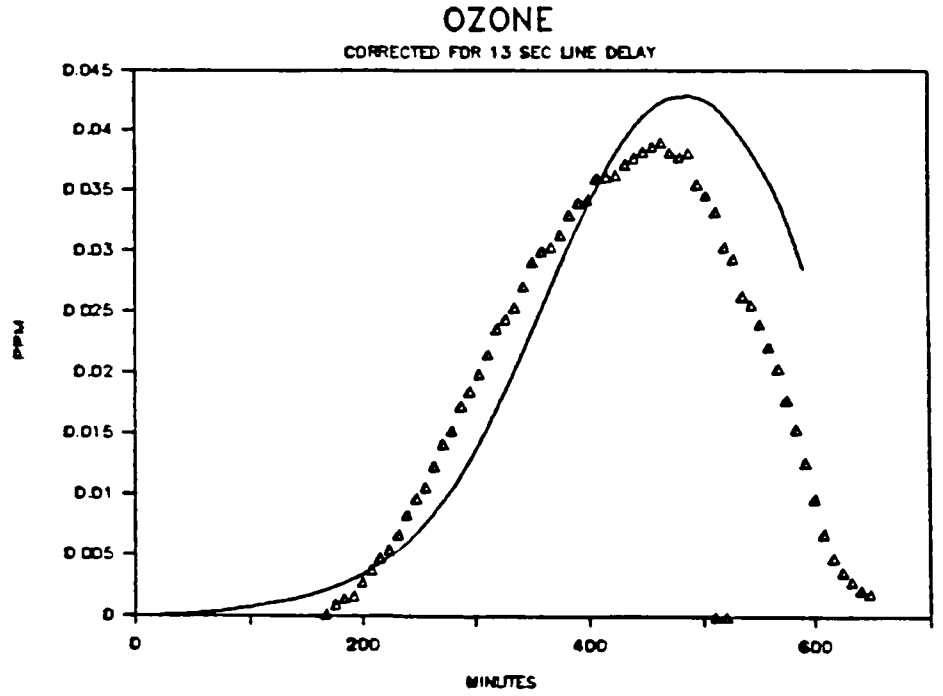

FIGURE 3-3. Simulation results and experimental data for the UNC acetaldehyde-NOx experiment of 26 December 1977 (symbols are data).

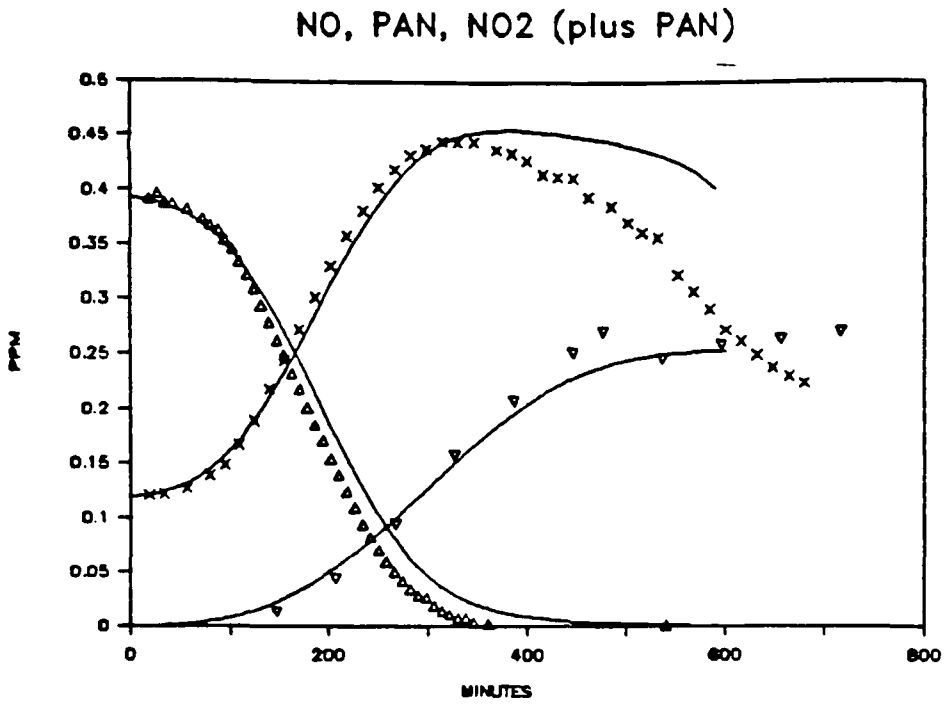

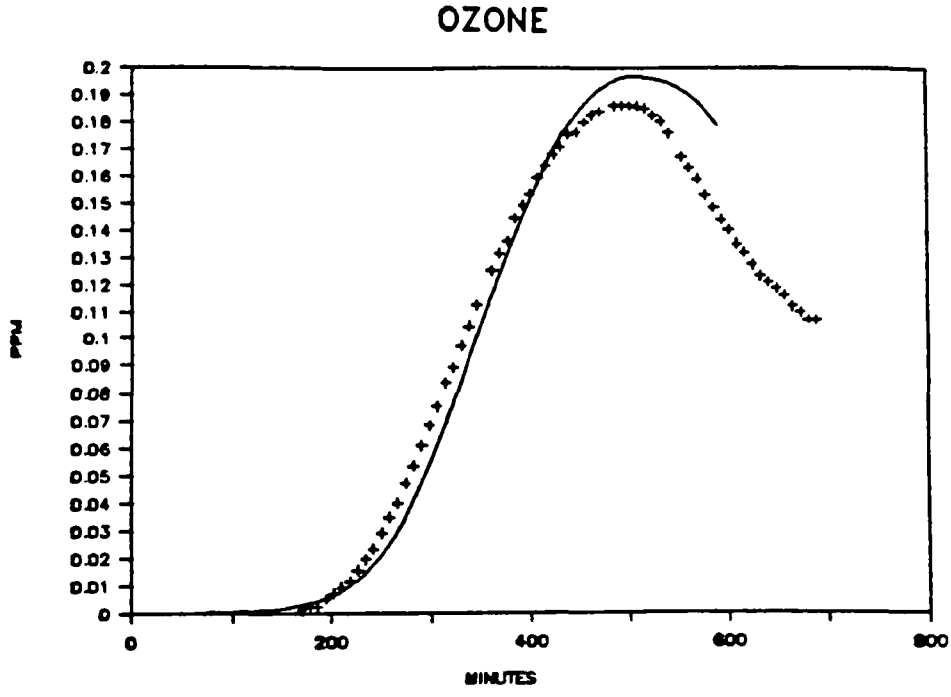

FIGURE 3-4. Simulation results and experimental data for the UNC acetaldehyde-NOx experiment of 19 November 1977 (symbols are data).

reactivity. This may indicate that the current estimates of in-chamber acetaldehyde photolysis rate variation with zenith angle results in too low a radical production rate at high zenith angles (reactivity for high-zenith-angle fall and winter experiments is often underpredicted with the current photolysis functions); however, we lack sufficient information about early morning chamber characteristics to make a judgement at this time. In any case, this does not affect the overall evaluation of simulations, nor the implications for the k(X-50)/k(X-51) variation.

The low-temperature experiments (Figures 3-3 and 3-4) also fit well with these rate expressions. Experimental and simulation results from a third low-temperature experiment of 20 November 1977 (Figure 3-5) were somewhat underpredicted by the mechanism (Figure 3-5a), while a better fit can be obtained with the same k(X-51) activation energy and an Arrhenius prefactor that is 32 percent lower (Figure 3-5b). We take this as one indication of the uncertainty of these results. We also note that the NO decay in all three low-temperature simulations tends to lag behind the observed values, which might indicate an underestimation of k(X-50)/k(X-51). Fitting the NO decay rate invariably results in overestimation of ozone, however. Therefore, there appears to be either an inconsistency in the simulation input or experimental data or another process at work that we have not yet considered. [The low ozone simulations of 26 December and 20 November 1977 have been corrected for a 13-second sample line delay in the UNC ozone monitoring system (Jeffries, 1987); the magnitude of this correction is noted in Figure 3-5.]

There have been few previous estimates of the ratio of C2O3 reaction with NO and NO_2. Atkinson and Lloyd (1984) based their recommendation of 1.5 on the 1979 modeling study of Carter et al., which derived the ratio from a single smog chamber experiment (UCR EC-164). During the course of this experiment, temperature control was apparently lost and the temperature increased to 312 K, with a relative humidity of about 75 percent (nearly 40000 ppm of H_2O). Under conditions of elevated temperature and humidity, the UCR evacuable chamber has been shown to desorb large amounts of contaminants (Carter et al., 1982), so any conclusions drawn from modeling this experiment might be suspect. Moreover, the ratio of k(X-50)/k(X-51) derived from this experiment is directly contradicted by other experiments in the same chamber that suggest a ratio of 2.06 (see Figures 3-6 and 3-7 for EC-254 and EC-253). Chamber contamination is also important in these experiments, especially for EC-253, since no NO_x was added in this experiment and thus the only source of NO_x for PAN formation was chamber desorption and initial NO_x bypassing the clean air system. The amount of NO_x necessary to explain the PAN formation in EC-253 is about 20 percent greater than the radical source derived from the study of Carter et al. (1982). Thus the "unknown chamber radical source" may primarily be HONO. For these UCR EC simulations we used the following chamber reactions:

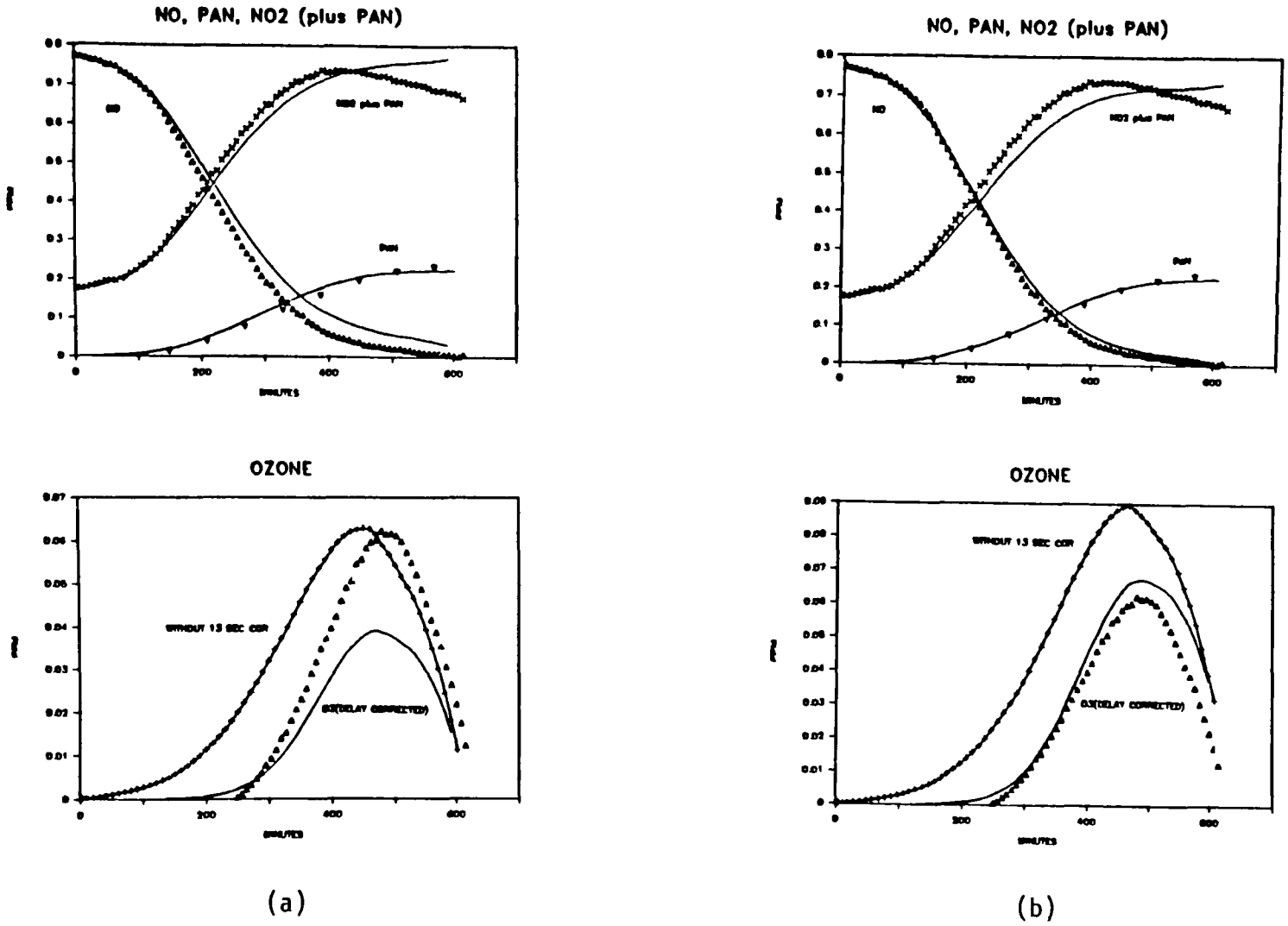

FIGURE 3-5. Simulation results and experimental data for the UNC acetaldehyde-NO_x experiment of 20 November 1977 (symbols are data). (a). Simulation based on rates in Table 1-2. (b) Best fit simulation using a k(X-51) Arrhenius pre-factor reduced by 32 percent.

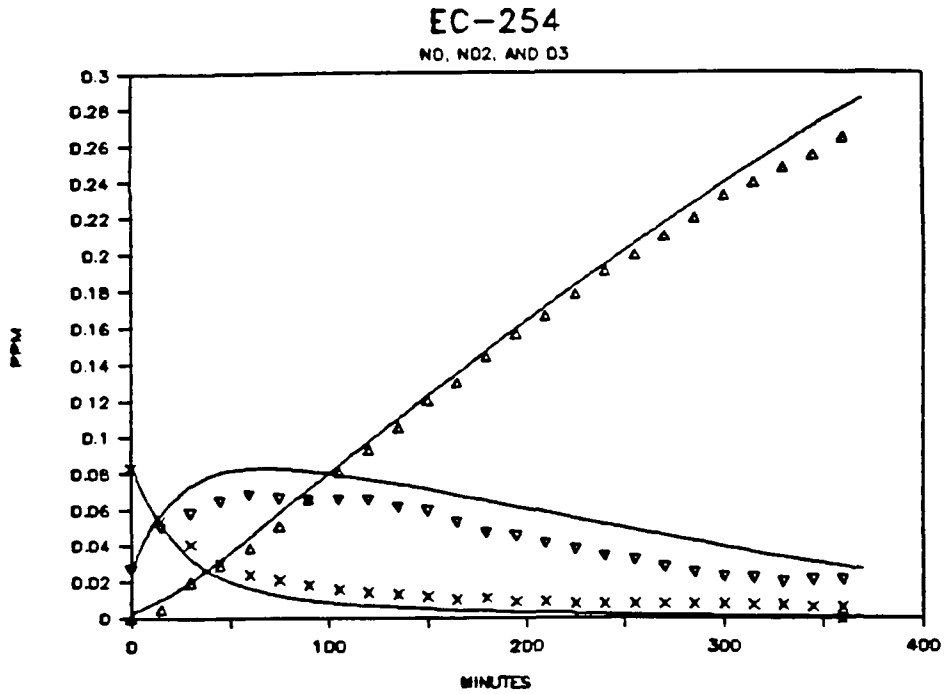

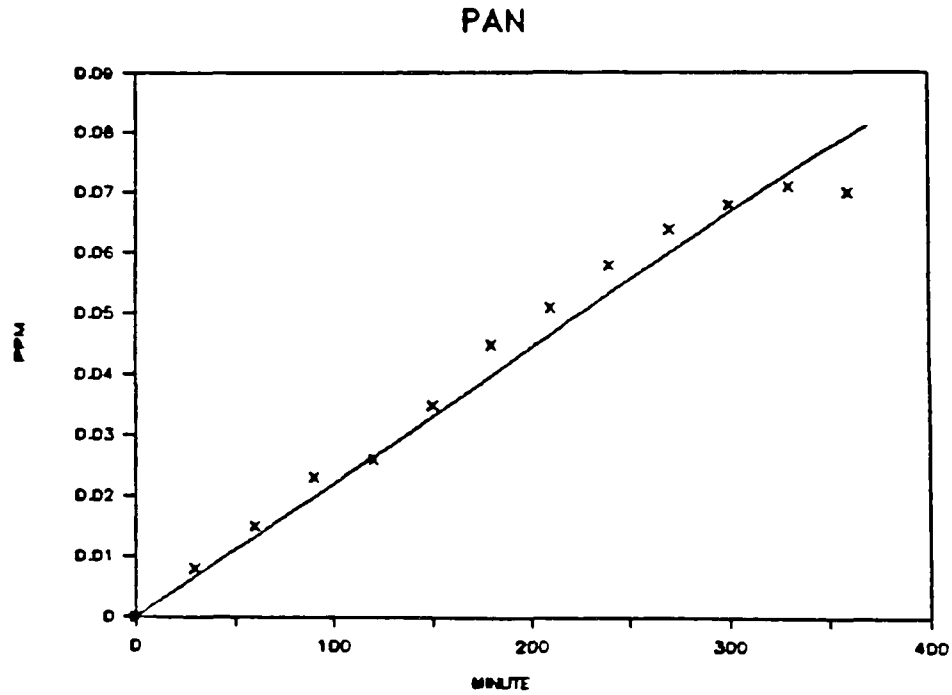

FIGURE 3-6. Simulation results and experimental data for the UCR acetaldehyde-NO_x experiment EC-254 (symbols are data).

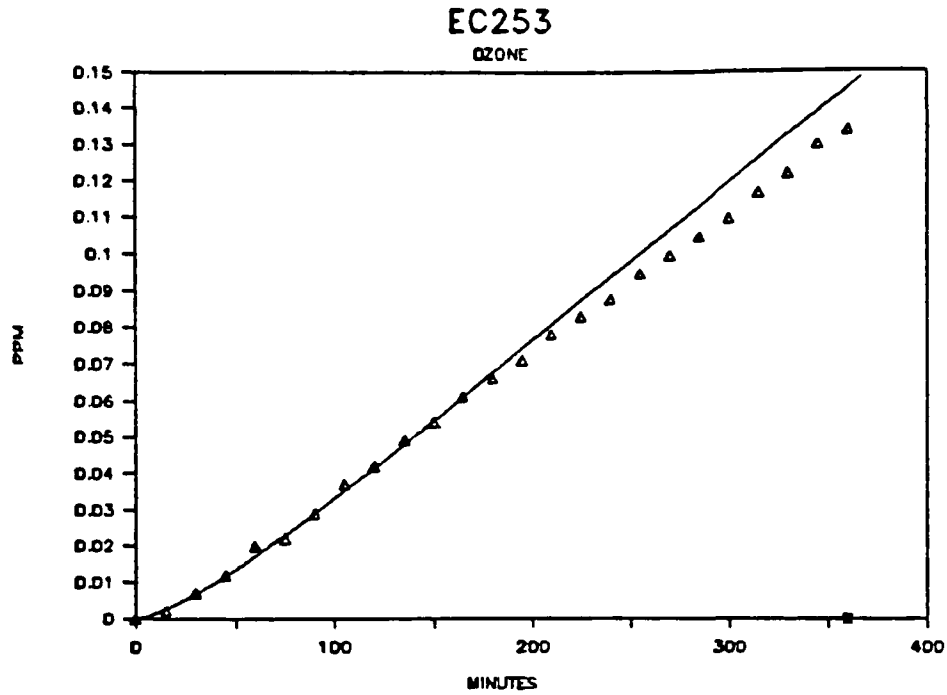

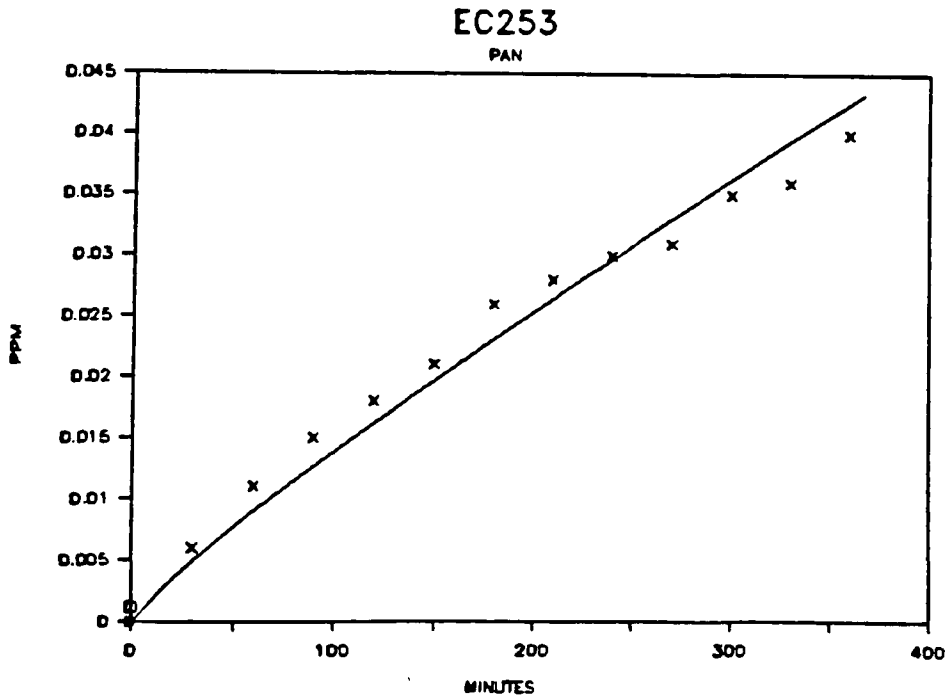

FIGURE 3-7. Simulation results and experimental data for the UCR acetaldehyde-NOx experiment EC-253 (symbols are data).

(wall) ------> HONO		k = 0.00039 x k(1),
(wall) ------> NO		k = 0.00008 x k(1),
NO_2 ------> HONO		k = 0.00137 x k(1).
NO_2 ------> NO		k = 0.00040 x k(1),
NO_2 ------> wall		k = 0.00230 x k(1),
O_3 ------>		k = 0.00180.

There is an observed decrease in the PAN production rate after 200 minutes in both of these experiments, which suggests that both the NO_x and radical source from the chamber walls is finite and diminishes after this time. Since the data reported in Carter et al. (1982) were all taken from periods shorter than 200 minutes, the finite nature of the wall source might not have been observed. This phenomenon may have important implications in chamber experiments involving longer reaction times.

The other available estimates for kX-50/kX-51 are from Cox and Roffey (1977) and Cox et al. (1975). Although Cox and Roffey judged that their data indicated no obvious temperature dependence, we can see from Figure 3-8 that this is due to data scatter as much as to any other factor. Two regression lines are plotted in Figure 3-8a. The line with the smaller slope (indicitave of an activation energy (E/R) of about -1500 K) is associated with a very poor correlation coefficient (r^2 = 0.21). However, the highest temperature point (T = 328 K) is an outlier; removal of this point gives the second line a correlation coefficient of 0.56 and indicates an activation energy of -3000 K. Since the data of Cox and Roffey were obtained by adding NO to higher concentrations of PAN, it is possible that features of PAN decay other than NO and NO_2 competition for C2O3, especially radical-radical reactions, resulted in a loss of oxidizing potential (i.e., PAN decay can occur without the oxidation of NO), especially at high temperatures. This oxidation loss would then produce a falloff of the NO conversion rate at increasing temperatures which is consistent with the data of Cox and Roffey.

Figure 3-8b shows the full data set available to us including our estimates of k(X-50)/k(X-51) for the beginning and ending temperatures of the UNC low-temperature acetaldehyde experiments. The lower slope line is the least squares estimate based on the entire data set, excluding the highest temperature point for Cox and Roffey. The slope indicates an activation energy of -4000 K. The higher slope line uses our best estimate of the temperature dependence of reaction X-51. Given the probability of high temperature rolloff in the Cox and Roffey data, we plan to use this estimate until more data become available.

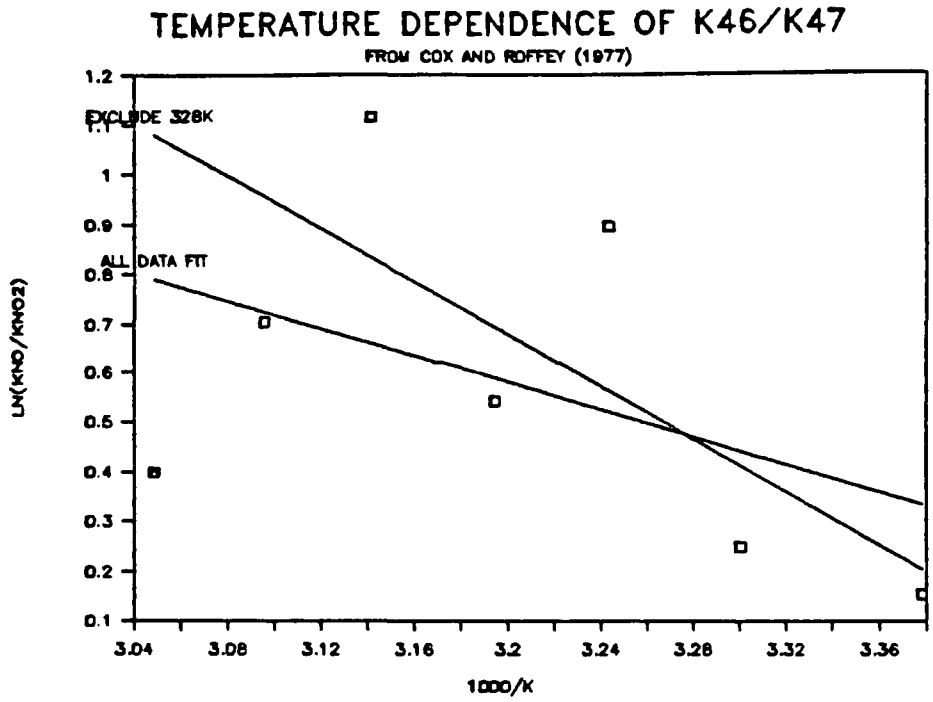

(a) using the data from Cox and Roffey (1977)

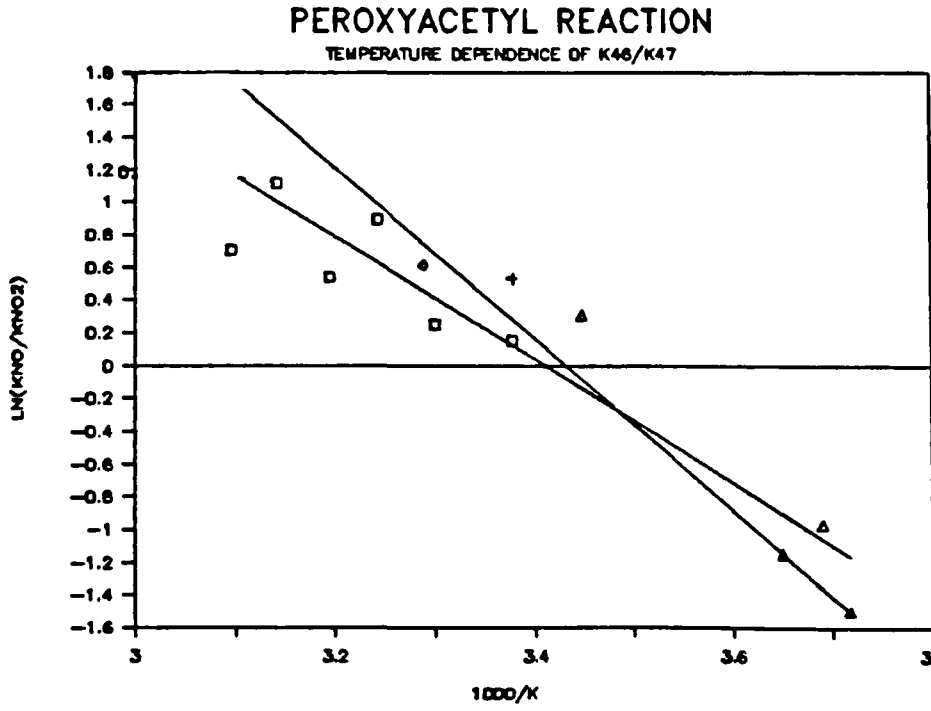

(b) using all available data as described in the text.

FIGURE 3-8. Temperature dependent functions for the peroxyacetyl radical reactions with NO and NO_2: (a) using the data from Cox and Roffey (1977); (b) using all available data [□ Cox and Roffey (1977), + Cox et al. (1981), ◇ EC-253 and EC-254, Δ UNC low-temperature experiments]

At this point, we must also describe our evaluation of the radical-radical reactions important in the C2O3 reaction scheme. In this and earlier studies (Whitten et al., 1983; Killus and Whitten, 1984) we noted the importance of radical-radical reactions in the complete description of PAN decay. As shown in Figures 3-1 through 3-5, changing PAN decay rates are frequently observed in the UNC chamber as the temperature increases during the day. The accurate simulation of PAN decay through the changing conditions of a smog chamber experiment requires careful consideration of radical recombination rates. In the CBM-X, C2O3 plus radical reactions are represented by

C2O3 + MEO2 ------> MEO2 + MEO, (X-65)

C2O3 + C2O3 ------> 2 MEO2, (X-66)

C2O3 + HO2 ------> PROX, (X-69)

C2O3 + HO2 ------> MEO2 + OH. (X-70)

The rates for the first two reactions are based on the results of Addison et al. (1980):

$$k(X\text{-}65) = 4.40 \times 10^3 \text{ ppm}^{-1}\text{min}^{-1},$$

and

$$k(X\text{-}66) = 3.70 \times 10^3 \text{ ppm}^{-1}\text{min}^{-1},$$

independent of temperature.

The methylperoxy (MEO2) plus HO2 reactions analogous to these HO_2 reactions with C2O3 are

MEO2 + HO2 ------> PROX, (X-67)

and

MEO2 + HO2 ------> MEO + OH. (X-68)

These four HO2 reactions are very important in the simulation of oxidant chemistry during the afternoon because HO_2 generally occurs at concentrations higher than those of any individual organic radicals. For several years, we have used rate constants for the C2O3 reactions based on the results of Addison et al. (1980):

$$k(X\text{-}69) = 2.00 \times 10^3 \text{ ppm}^{-1}\text{min}^{-1},$$

and

$$k(X\text{-}70) = 7.60 \times 10^3 \text{ ppm}^{-1}\text{min}^{-1}.$$

We also use the rates determined by Cox and Tyndall (1980) for the MEO2 reactions with HO_2:

$$k(X\text{-}67) = 2.550 \times 10^1 \exp(1300/T)\ ppm^{-1}min^{-1},$$

with

$$k(X\text{-}67)_{298} = 2.00 \times 10^3\ ppm^{-1}min^{-1},$$

and

$$k(X\text{-}68) = 8.541 \times 10^1 \exp(1300/T)\ ppm^{-1}min^{-1},$$

with

$$k(X\text{-}68)_{298} = 6.70 \times 10^3\ ppm^{-1}min^{-1}.$$

We now consider the combined rates of the radical loss reactions (k(X-67) + K(X-68) and k(X-69) + k(X-70). These values are larger than some other estimates (e.g., Kan et al., 1980; Niki et al., 1982) by up to a factor of five. However, the C2O3 plus HO2 study of Addison et al., and the MEO2 plus HO2 study of Cox and Tyndall were the only investigations that directly measured the actual rates of peroxyacetyl and methylperoxy radical decay. All other studies reviewed inferred the radical-radical reaction rates from observed products such as organic peroxides. Thus, those studies could have suffered from underprediction of the reaction rate if the observed products were not representative of the entire product yield.

Additional direct measurements have recently become available for methylperoxy (MEO2) and analogous ethylperoxy radical reactions with HO_2 (McAdam et al., 1987 and Cattell et al., 1986). These data also support the higher rates based on earlier radical decay studies, and indicate that the discrepancies between the values obtained from observation of the radical decays and observation of product (peroxide) yields could indicate the existence of alternate product pathways for these reactions. We suggest that the observed peroxide products could form at the lower rates determined from observation of those products, whereas the differences between the direct and product rates could be due to undetected disproportionation reactions:

C2O3 + HO2 ------> MEO2 + OH (+ O2 + CO2),

MEO2 + HO2 ------> MEO + OH (+ O2),

ETO2 + HO2 ------> ETO + OH (+ O2).

Our simulations suggest that the failure to represent such reactions in the PAN reaction mechanism is responsible for the general failure of many current kinetic mechanisms to adequately account for hydrocarbon decay subsequent to the ozone peak, as NO concentrations become very low (see for example, Leone and Seinfeld, 1984, Figure 8; or Atkinson et al., 1982). Under such conditions, the production of OH by

$$NO + HO2 \text{ ------> } NO2 + OH \quad (28)$$

is limited, and the other major source of OH at the time is the reaction

$$O3 + HO2 \text{ ------> } OH\ (+2\ O2). \quad (13)$$

The rate constant for this reaction has been recently remeasured and is apparently more than a factor of four too low to account for the observed, post-ozone-maximum hydrocarbon losses. Other possible sources of OH would include ozone photolysis to $O(^1D)$ and chamber wall emissions of HONO. In smog chamber simulations, both of these sources are an order of magnitude too low to be responsible for the "missing OH source" and would, moreover, have a major effect upon the simulations prior to the ozone peak.

If we include the postulated disproportionation reactions in the mechanism, we obtain excellent fits to post ozone peak hydrocarbon decays for a number of different hydrocarbon types. An example of this improvement is shown in Figure 3-9 for a typical UCR-EC m-xylene trace. This example and others using the CBM-IV condensed mechanism can be found throughout the plots given in Section 6. The effect on post-ozone hydrocarbon decay is usually most visible for aromatic hydrocarbons. However, the "missing OH source" is not a special feature of aromatic oxidation, but is more clearly shown in that system because (1) aromatics have high rates of reaction with OH and (2) they have low rates with competing oxidizers such as ozone (the former being necessary to distinguish OH loss from chamber dilution and the latter being a confounding effect). The effect appears directly related to PAN levels and decay and applies across a variety of hydrocarbon mixes and reactivity levels.

We briefly discuss the additional MEO2 and MEO reactions in the CBM-X next. The methylperoxynitric acid (MPNA) equilibrium reactions are expected to be analogous to those of PNA (reactions 29 and 30):

$$MEO_2 + NO_2\ (+ M) \text{ ------> } MPNA\ (+ M), \quad (X\text{-}53)$$

and

$$MPNA\ (+ M) \text{ ------> } MEO_2 + NO_2\ (+ M). \quad (X\text{-}54)$$

The rate of MPNA formation is taken from the falloff parameters given by NASA (DeMore et al., 1985):

$$k_0 = 1.5 \times 10^{-30}\ (T/300)^{-4.0}\ cm^6 molecule^{-2} s^{-1},$$

and

$$k_\infty = 6.5 \times 10^{-12}\ (T/300)^{-2.0}\ cm^3 molecule^{-1} s^{-1},$$

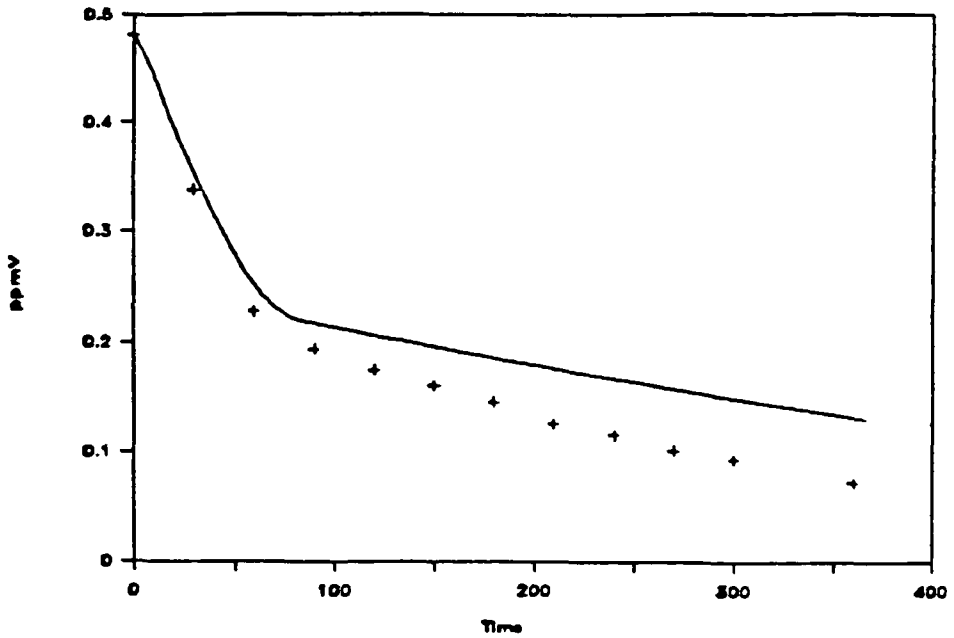

(a) without radical disproportionation products.

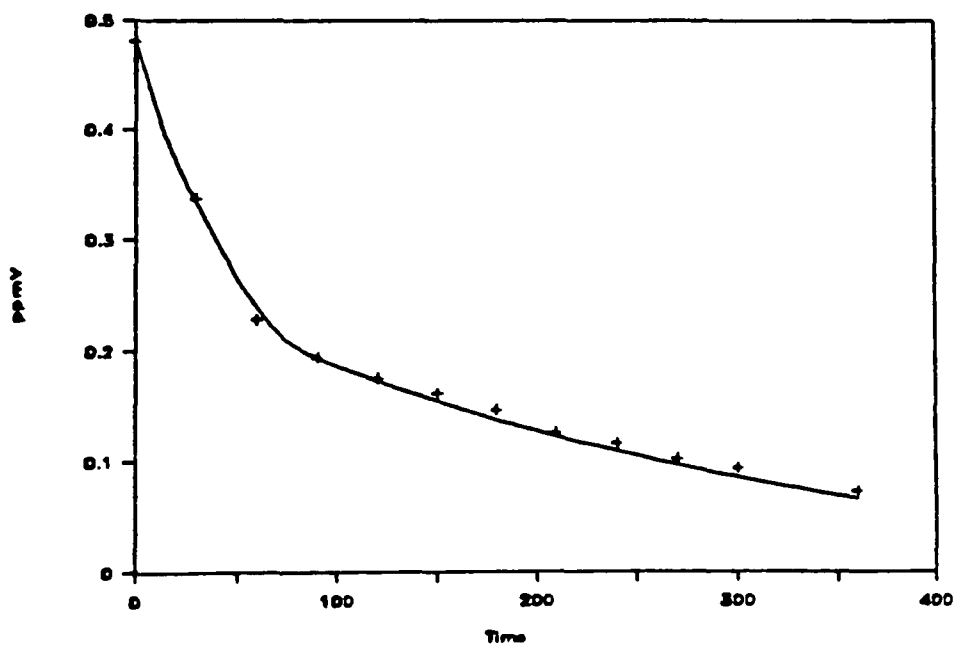

(b) with radical disproportination products.

FIGURE 3-9. m-Xylene concentration traces for UCR EC-345 comparing the effects of including radical disproportionation products in the HO2 plus RO2 reactions.

which lead to an Arrhenius expression of

$$k(X\text{-}53) = 3.810 \times 10^{2} \exp(821/T)\ ppm^{-1}min^{-1},$$

and

$$k(X\text{-}53)_{298} = 5.99 \times 10^{3}\ ppm^{-1}min^{-1}.$$

The rate of decomposition of MPNA is also based on the equilibrium constant data of NASA (DeMore et al., 1985):

$$k(X\text{-}54) = k(X\text{-}53)/k_{eq},$$

where

$$k(X\text{-}53) = 2.583 \times 10^{-13} \exp(821/T)\ cm^{3}molecule^{-1}s^{-1},$$

and

$$k_{eq} = 1.30 \times 10^{-28} \exp(11192/T)\ cm^{3}molecule^{-1},$$

then

$$k(X\text{-}54) = 1.99 \times 10^{15} \exp(-10371/T)\ s^{-1},$$

or

$$k(X\text{-}54) = 1.19 \times 10^{17} \exp(-10371/T)\ min^{-1},$$

with

$$k(X\text{-}54)_{298} = 9.15 \times 10^{2}\ min^{-1}.$$

The additional reactions of MEO2 and MEO (reactions X-55 through X-64) are generally noncompetitive channels that ultimately yield a distribution of stable products and NO-to-NO_2 conversions. These reactions are briefly described next. The reader is referred to the review of Atkinson and Lloyd (1984) and the kinetic compilations of NASA (DeMore et al., 1985) and CODATA (DeMore et al., 1985) for a more complete description of the formulation and kinetics of these reactions.

The remaining reactions of MEO2 (recall that the MEO2 plus HO2 reactions were discussed previously) are

MEO2 + NO ------> MEO + NO2, (X-55)

MEO2 + MEO2 ------> 2 MEO, (X-63)

MEO2 + MEO2 ------> FORM + MEOH, (X-64)

where MEOH is methanol and MEO is the methoxy radical ($CH_3^{\cdot}$). The kinetic expression for reaction X-55 is from NASA (DeMore et al. 1985):

$$k(X\text{-}55) = 6.140 \times 10^{3} \exp(180/T)\ ppm^{-1}min^{-1},$$

and

$$k(X\text{-}55)_{298} = 1.12 \times 10^{4}\ ppm^{-1}min^{-1}.$$

The rate for the self reaction of MEO2 was taken from CODATA (Baulch et al., 1984); the ratio between the two product pathways [k(X-63) and k(X-64)] is also taken from that review. Thus,

$$k(X\text{-}63) = 1.91 \times 10^2 \text{ ppm}^{-1}\text{min}^{-1},$$

and

$$k(X\text{-}64) = 3.56 \times 10^2 \text{ ppm}^{-1}\text{min}^{-1}.$$

The reactions of MEO are

$$\text{MEO} + \text{NO} \text{ ------> } \text{MNIT}, \quad (X\text{-}56)$$

$$\text{MEO} + \text{NO} \text{ ------> } \text{FORM} + \text{HO2} + \text{NO}, \quad (X\text{-}57)$$

$$\text{MEO} + \text{NO2} \text{ ------> } \text{MEN3}, \quad (X\text{-}58)$$

$$\text{MEO} (+ O_2) \text{ ------> } \text{FORM} + \text{HO2}. \quad (X\text{-}59)$$

The initial three kinetic expressions are taken from Atkinson and Lloyd (1984); their rate for methylnitrite (MNIT) formation is

$$k(X\text{-}56) = 2.296 \times 10^4 \exp(200/T) \text{ ppm}^{-1}\text{min}^{-1},$$

and

$$k(X\text{-}56)_{298} = 4.44 \times 10^4 \text{ ppm}^{-1}\text{min}^{-1}.$$

The rate for the alternate reaction products (reaction X-57) is

$$k(X\text{-}57) = 1.92 \times 10^3 \text{ ppm}^{-1}\text{min}^{-1}.$$

The reaction rate constant for reaction with NO_2 is

$$k(X\text{-}58) = 2.22 \times 10^4 \text{ ppm}^{-1}\text{min}^{-1}.$$

The recent NASA evaluation (DeMore et al., 1985) uses the temperature-dependent kinetic expression for reaction X-59 of

$$k(X\text{-}59) = 2.605 \times 10^7 \exp(-1200/T) \text{ min}^{-1} \quad ,$$

and

$$k(X\text{-}59)_{298} = 4.64 \times 10^5 \text{ min}^{-1}.$$

Finally, methyl nitrate and nitrite losses are given in reactions X-60 through X-62:

$$\text{MEN3} + \text{OH} \text{ ------> } \text{FORM} + \text{NO2}, \quad (X\text{-}60)$$

$$\text{MNIT} + \text{OH} \text{ ------> } \text{FORM} + \text{NO}, \quad (X\text{-}61)$$

$$\text{MNIT} \text{ --h}\nu\text{--> } \text{MEO} + \text{NO}. \quad (X\text{-}62)$$

The reaction of methyl nitrate with the hydroxyl radical is relatively slow for a hydroxyl radical rate constant, as are the per-carbon reaction rate constants of higher molecular weight alkyl nitrates (Atkinson et al., 1982). For k(X-60), we use (Atkinson and Lloyd, 1984)

$$k(X\text{-}60) = 4.00 \times 10^2 \text{ ppm}^{-1}\text{min}^{-1}.$$

The reaction of methyl nitrite with OH (X-61) is relatively unimportant compared with photolysis (X-62). As recommended by Atkinson and Lloyd, we use

$$k(X\text{-}61) = 3.00 \times 10^2 \text{ ppm}^{-1}\text{min}^{-1},$$

and

$$j_{MNIT} = j_{NO2} \times 3.00 \times 10^{-1} \text{ min}^{-1}.$$

PHOTOLYSIS REACTIONS

Calculations of specific photolysis rates (j-values) are required because the photolysis of key photoreceptor species provides radical products that must be accurately described to correctly simulate both smog chamber data sets and atmospheric conditions. Photolysis of stable molecules is the major source of new radicals in the gas phase. The accurate determination of the photolysis rates, especially early in the day when the "radical pool" is limited, is critical in achieving the proper representation of the balance with radical termination reactions. In this subsection we describe the data and calculation methods used to determine in-chamber photolysis rates. In addition, we compare atmospheric photolysis rates calculated with our data and procedures with those recently determined by Jeffries and Sexton (1987) at UNC. The UNC rates have been recommended for use with the CBM-IV during atmospheric simulation with OZIPM-4 (Hogo and Gery, 1988). We felt that comparison of these recently reported values with data and methods used at Systems Applications would be useful in understanding the ranges of uncertainty of different calculation methods and data.

The j-value of a specific molecular process is defined at any given time by the integral of the triple product, $I\sigma\Phi$, over the wavelength interval of interest,

$$j_n = \int_{\lambda_{min}}^{\lambda_{max}} I(\lambda)\sigma(\lambda)\Phi(\lambda)d\lambda \quad .$$

where I is the actinic flux, σ is the molecular absorption cross section, and Φ is the quantum yield for a specific photolysis process (n). From

this simple formulation, it is apparent that uncertainties in j-value calculations result from two sources: (1) the measure of "in-chamber" actinic flux and its spectral distribution and variation with time and conditions, and (2) the uncertainties associated with the experimental determination of the absorption cross section and quantum yields. The actinic flux calculations have been a source of controversy and uncertainty because of the many variables that must be included in site-specific descriptions. Although the UNC facility has the best characterization of any outdoor chamber, certain aspects have yet to be determined. The most important of these are the changes in spectral distribution due to attenuation and reflection by the Teflon film at different solar zenith angles and the differences in cloud attenuation caused by different cloud types. These remaining uncertainties are the object of experimental studies at UNC and must currently be estimated for modeling purposes. The values and assumptions we have used to determine the actinic flux within the UNC chambers are described in Section 5.

The experimentally determined photolysis rate of NO_2 (j_{NO2} or k_1) is often used in photochemical kinetics models as the indicator of the amount of light energy available at the given time of day being simulated. It must be kept in mind, however, that NO_2 absorbs light and photolyzes in a specific (rather long wavelength) region compared to other key photoreceptors. As the zenith angle of the sun changes (and therefore, the spectral distribution of the solar irradiation), the photolysis rates of the other species will not directly follow the j_{NO2} value. This is because the effects of different atmospheric processes (e.g., molecular absorption and scattering; albedo and aerosol scattering) vary with spectral distribution. Therefore, though the j_{NO2} value can be used to track the relative amount of energy available for photolysis throughout the day. another factor related to the changing spectral distribution must be considered so that the absolute amount of energy available to species that absorb in other spectral regions (such as ozone and formaldehyde) can be determined. For this, we use the zenith angle of the solar disk as an indicator of the spectral distribution. This results in a set of nonlinear ratios that can be multipled by the experimental j_{NO2} value for a given time of day to determine the specific j-values at that time of day (and zenith angle). If time-varying and wavelength-resolved actinic flux measurements become available, it will be beneficial to directly calculate the j-values of all important species. At present, however, these data are not available and the ratio of the clear-sky relationships to experimental j_{NO2} data is required.

The ratios of j-values to j_{NO2} can be determined by calculating absolute photolysis rate constants for each photolysis process using a standard set of actinic flux distributions for a range of zenith angles. In this case the clear-sky, ground-level values calculated with the model of Demerjian

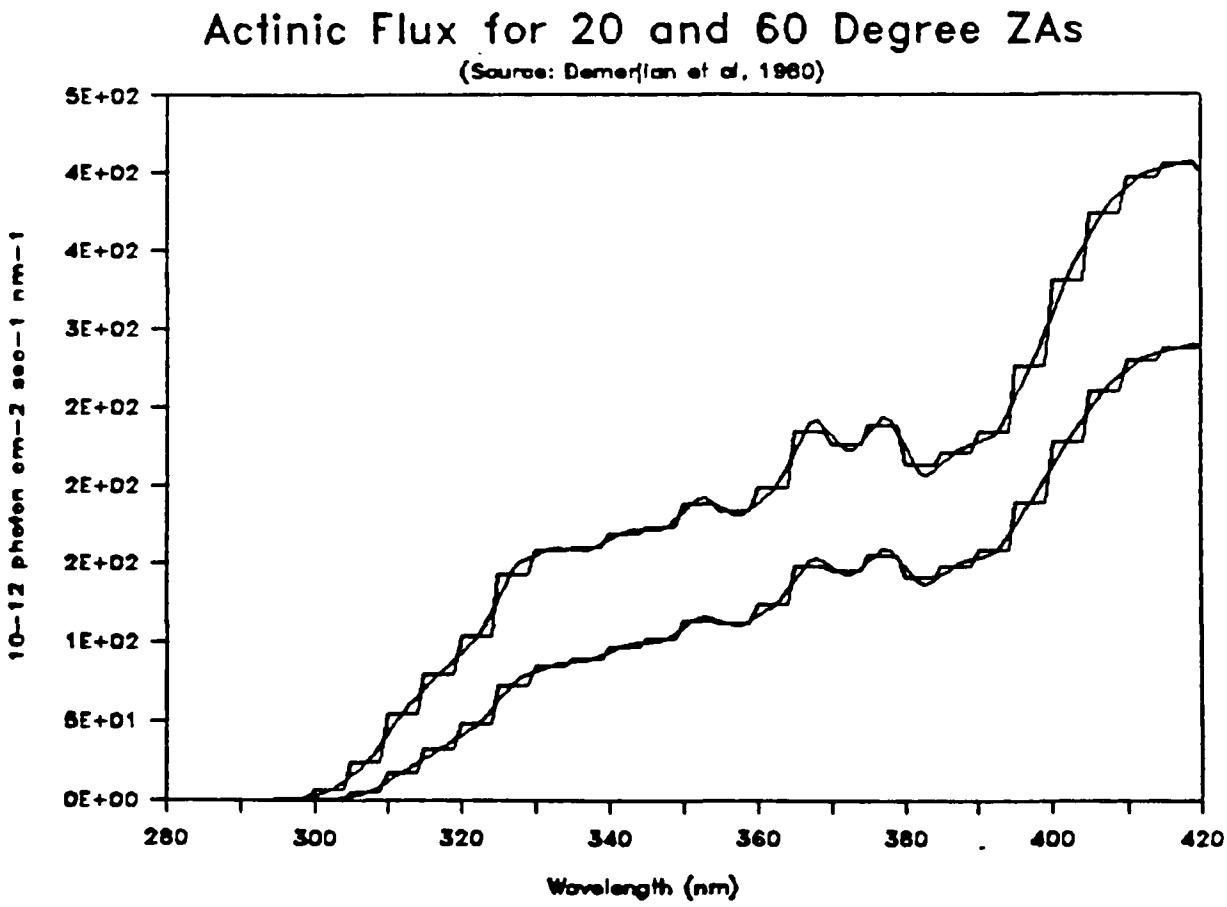

FIGURE 3-10. Actinic flux for 20 and 60 degree solar zenith angles in bin sizes of 1 and 5 nm. Areas under curves are equal. Source: Demerjian et al., 1980.

TABLE 3-1. Absorption cross sections and quantum yields for NO_2 photolysis:

$$NO_2 \xrightarrow{h\nu} NO + O \quad .$$

Wavelength (nm)	Cross Section (cm2/molec.) (x 1.E+20)	Quantum Yield	Wavelength (nm)	Cross Section (cm2/molec.) (x 1.E+20)	Quantum Yield
280	5.54	0.984	315	22.50	0.968
281	5.58	0.984	316	21.31	0.967
282	5.36	0.984	317	23.29	0.966
283	5.36	0.984	318	24.81	0.966
284	6.25	0.984	319	23.14	0.965
285	6.99	0.984	320	25.37	0.964
286	7.29	0.984	321	26.53	0.963
287	7.37	0.984	322	26.49	0.962
288	7.66	0.984	323	27.68	0.962
289	7.89	0.984	324	26.75	0.961
290	8.18	0.984	325	27.86	0.960
291	9.90	0.984	326	28.79	0.959
292	9.37	0.984	327	29.09	0.958
293	9.75	0.984	328	30.77	0.958
294	9.48	0.984	329	29.98	0.957
295	9.68	0.984	330	29.87	0.956
296	9.30	0.983	331	30.50	0.955
297	12.17	0.982	332	30.05	0.954
298	11.72	0.982	333	37.27	0.954
299	12.57	0.981	334	29.80	0.953
300	11.72	0.980	335	34.52	0.952
301	12.28	0.980	336	35.08	0.951
302	13.87	0.978	337	34.63	0.950
303	15.92	0.978	338	34.78	0.950
304	15.96	0.977	339	39.88	0.949
305	16.56	0.976	340	38.80	0.948
306	15.81	0.975	341	41.66	0.947
307	16.33	0.974	342	38.32	0.946
308	16.18	0.973	343	35.45	0.946
309	18.38	0.973	344	40.21	0.945
310	17.56	0.972	345	40.70	0.944
311	18.78	0.971	346	42.93	0.943
312	19.61	0.970	347	42.78	0.942
313	20.35	0.970	348	48.21	0.942
314	19.42	0.969	349	46.12	0.941

(Continued)

TABLE 3-1 (Concluded)

$$NO_2 \xrightarrow{h\nu} NO + O \quad .$$

Wavelength (nm)	Cross Section (cm2/molec.) (x 1.E+20)	Quantum Yield	Wavelength (nm)	Cross Section (cm2/molec.) (x 1.E+20)	Quantum Yield
350	40.99	0.940	385	59.41	0.770
351	45.20	0.939	386	53.20	0.840
352	44.38	0.938	387	56.02	0.750
353	39.88	0.938	388	59.78	0.810
354	50.40	0.937	389	60.23	0.780
355	51.30	0.936	390	60.01	0.800
356	46.05	0.935	391	58.29	0.880
357	55.80	0.934	392	60.49	0.840
358	50.37	0.934	393	54.54	0.900
359	45.53	0.933	394	55.42	0.900
360	45.13	0.932	395	58.89	0.840
361	53.87	0.931	396	61.45	0.830
362	50.40	0.930	397	56.65	0.820
363	51.23	0.930	398	64.06	0.770
364	48.74	0.929	399	56.03	0.780
365	57.81	0.928	400	67.59	0.680
366	53.98	0.912	401	65.25	0.650
367	51.86	0.896	402	57.10	0.620
368	53.42	0.881	403	51.04	0.570
369	51.82	0.865	404	60.67	0.420
370	54.20	0.849	405	63.17	0.320
371	52.12	0.833	406	53.90	0.330
372	59.81	0.817	407	47.28	0.250
373	55.02	0.802	408	62.61	0.200
374	52.12	0.786	409	59.00	0.190
375	53.53	0.770	410	57.73	0.150
376	62.35	0.780	411	58.78	0.100
377	56.69	0.920	412	53.65	0.090
378	51.74	0.820	413	70.04	0.080
379	54.68	0.870	414	59.41	0.080
380	59.86	0.900	415	60.41	0.070
381	56.62	0.810	416	48.47	0.060
382	56.36	0.700	417	53.12	0.050
383	53.72	0.680	418	55.17	0.040
384	59.67	0.700	419	52.79	0.030
			420	57.72	0.020

TABLE 3-2. Results of j_{NO2} calculations. (Albedo = 0.05)

Zenith Angle (deg)	j_{NO2} (min^{-1})	
	SAI	UNC
0	0.485	0.503
10	0.481	0.499
20	0.469	0.487
30	0.448	0.464
40	0.415	0.430
50	0.366	0.379
60	0.295	0.306
70	0.194	0.202
78	0.095	0.099
86	0.020	0.019

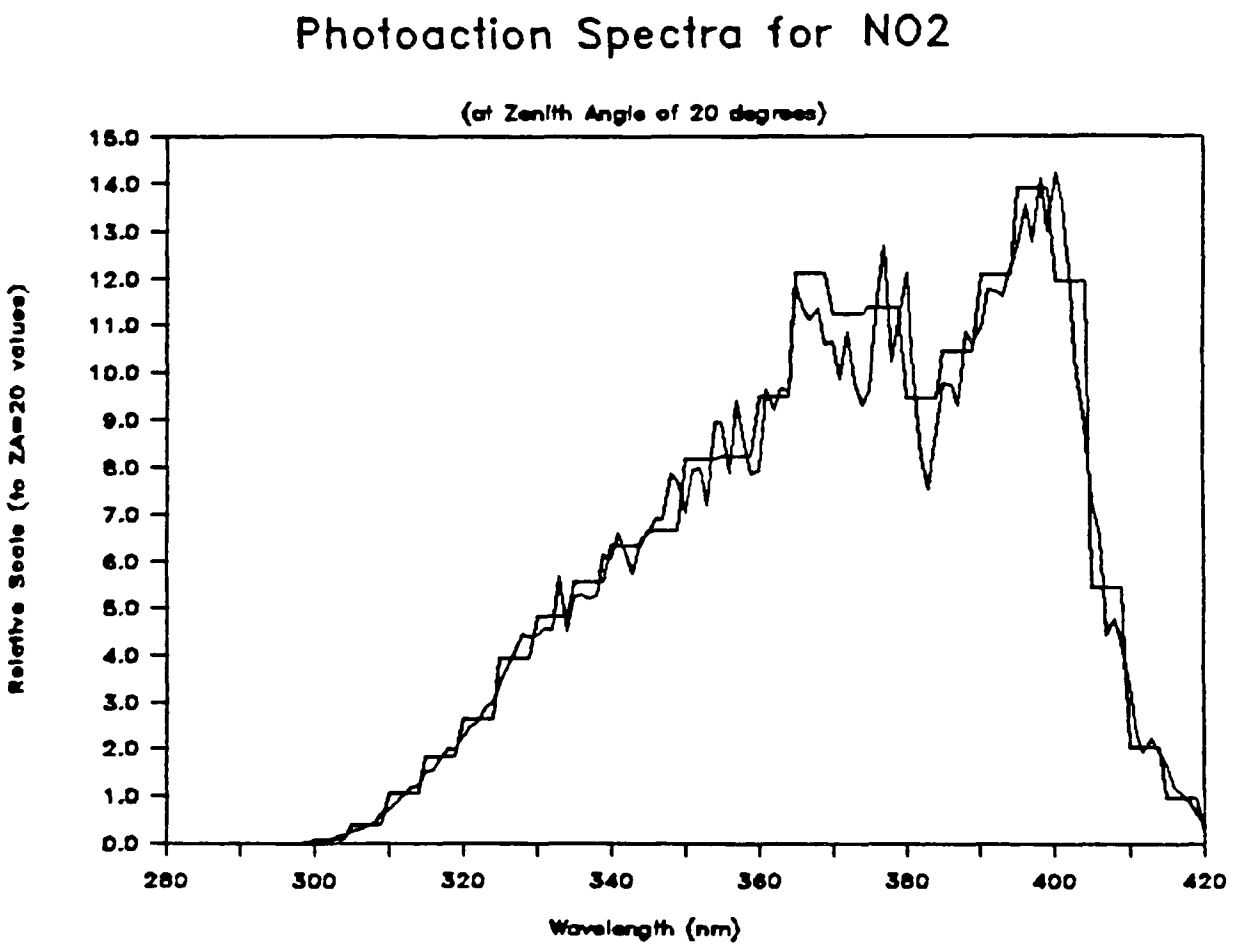

FIGURE 3-11. Photoaction spectra for NO_2 using 1 nm bins (this report) and 5 nm bins (Jeffries and Sexton, 1987).

et al. (1980) were used. These data provide the number of photons cm^{-2} sec^{-1} in wavelength bins of 5 nm for ten zenith angles from 0 to 86 degrees. The calculations that produced these data assumed one specific aerosol distribution, surface albedo (0.05), and ozone column density (0.292 cm-atm). Because we perform our numerical integration of j-values in 1 nm bins, we have interpolated the larger bins of Demerjian and co-workers to 1 nm values, verifying at all times that the sum of the energy within five 1 nm bins is equal to the energy in the original 5 nm bin. The spectral distributions at two zenith angles (20 and 60 degrees) for 1 nm and 5 nm bins are shown in Figure 3-10.

The photolysis rates for the process:

$$NO_2 \xrightarrow{h\upsilon} NO + O \qquad (1)$$

were calculated using the actinic fluxes of Demerjian et al. (1980) and the absorption cross sections and quantum yields listed in Table 3-1. These results are given in Table 3-2 and compared to values recently determined by UNC (Jeffries and Sexton, 1987). The rates determined by Systems Applications are between 2 and 4 percent lower than those of UNC. In both cases, the data were taken from the NASA (DeMore et al., 1985) review; however, the UNC calculations are based on 5 nm bin averages of quantum yield and cross section, whereas our calculations were performed at 1 nm. The resulting photoaction spectra (the product $I\sigma\Phi$ versus wavelength) are shown in Figure 3-11 for a 20° zenith angle. Our calculations using 1 nm and 5 nm bins show that the variation in methodologies results in the minor j_{NO2} differences. Such a difference in j_{NO2} is not a significant deviation and is certainly bounded by the uncertainty of the experimentally derived data.

The absorption cross sections and quantum yields used for formaldehyde, ozone, acetaldehyde (ALD2), nitrous acid, and hydrogen peroxide are presented in Tables 3-3 through 3-8. In the following discussion, the processes we refer to are

j_{HCHOr}:

$$HCHO \xrightarrow{h\upsilon} 2H\cdot + CO \qquad (38)$$

j_{HCHOs}:

$$HCHO \xrightarrow{h\upsilon} H_2 + CO \qquad (39)$$

j_{ALD2r}:

$$CH_3CHO \xrightarrow{h\upsilon} H\cdot + CO + CH_3OO\cdot \qquad (45)$$

TABLE 3-3. Absorption cross sections and quantum yields for formaldehyde photolysis to radical products:

$$HCHO \xrightarrow{h\nu} 2H\cdot + CO \quad .$$

Wavelength (nm)	Cross Section (cm2/molec.) (x 1.E+20)	Quantum Yield	Wavelength (nm)	Cross Section (cm2/molec.) (x 1.E+20)	Quantum Yield
280	2.34	0.560	310	1.03	0.760
281	1.65	0.580	311	0.81	0.750
282	0.76	0.600	312	1.49	0.740
283	0.46	0.620	313	1.55	0.730
284	3.93	0.630	314	3.99	0.720
285	3.46	0.650	315	2.88	0.700
286	2.32	0.670	316	2.79	0.690
287	0.95	0.680	317	3.59	0.670
288	2.32	0.700	318	1.65	0.650
289	2.50	0.710	319	0.73	0.630
290	1.43	0.720	320	1.71	0.610
291	1.32	0.730	321	1.32	0.590
292	0.66	0.750	322	0.43	0.570
293	5.22	0.760	323	0.60	0.540
294	4.30	0.760	324	0.75	0.510
295	3.21	0.770	325	2.19	0.490
296	1.59	0.780	326	3.44	0.460
297	1.96	0.790	327	1.75	0.430
298	3.66	0.790	328	1.01	0.390
299	1.55	0.790	329	3.03	0.360
300	0.72	0.800	330	1.96	0.330
301	1.51	0.800	331	0.79	0.290
302	0.74	0.800	332	0.32	0.250
303	4.35	0.800	333	0.15	0.210
304	4.79	0.800	334	0.17	0.170
305	4.94	0.790	335	0.02	0.130
306	3.02	0.790	336	0.17	0.083
307	1.16	0.790	337	0.32	0.038
308	2.18	0.780	338	1.93	0.000
309	2.25	0.770	339	2.15	0.000
			340	1.07	0.000

TABLE 3-4. Absorption cross sections and quantum yields for formaldehyde photolysis to stable products:

$$HCHO \xrightarrow{h\nu} CO + H_2 \quad .$$

Wavelength (nm)	Cross Section (cm2/molec.) (x 1.E+20)	Quantum Yield	Wavelength (nm)	Cross Section (cm2/molec.) (x 1.E+20)	Quantum Yield
280	2.34	0.440	320	1.71	0.390
281	1.65	0.420	321	1.32	0.410
282	0.76	0.400	322	0.43	0.430
283	0.46	0.380	323	0.60	0.460
284	3.93	0.370	324	0.75	0.490
285	3.46	0.350	325	2.19	0.510
286	2.32	0.330	326	3.44	0.540
287	0.95	0.320	327	1.75	0.550
288	2.32	0.300	328	1.01	0.570
289	2.50	0.290	329	3.03	0.580
290	1.43	0.280	330	1.96	0.590
291	1.32	0.270	331	0.79	0.600
292	0.66	0.250	332	0.32	0.610
293	5.22	0.240	333	0.15	0.620
294	4.30	0.240	334	0.17	0.620
295	3.21	0.230	335	0.02	0.620
296	1.59	0.220	336	0.17	0.620
297	1.96	0.210	337	0.32	0.620
298	3.66	0.210	338	1.93	0.610
299	1.55	0.210	339	2.15	0.610
300	0.72	0.200	340	1.07	0.600
301	1.51	0.200	341	0.31	0.590
302	0.74	0.200	342	0.94	0.570
303	4.35	0.200	343	1.37	0.560
304	4.79	0.200	344	0.57	0.540
305	4.94	0.210	345	0.12	0.520
306	3.02	0.210	346	0.04	0.500
307	1.16	0.210	347	0.04	0.470
308	2.18	0.220	348	0.07	0.450
309	2.25	0.230	349	0.03	0.420
310	1.03	0.240	350	0.03	0.390
311	0.81	0.250	351	0.09	0.360
312	1.49	0.260	352	0.90	0.330
313	1.55	0.270	353	1.17	0.300
314	3.99	0.280	354	0.72	0.260
315	2.88	0.300	355	0.26	0.230
316	2.79	0.310	356	0.05	0.200
317	3.59	0.330	357	0.03	0.160
318	1.65	0.350	358	0.04	0.130
319	0.73	0.370	359	0.03	0.100

TABLE 3-5. Absorption cross sections and quantum yields for ozone photolysis to $O(^1D)$:

$$O_3 \xrightarrow{h\nu} O(^1D) + O_2 \quad .$$

Wavelength (nm)	Cross Section (cm2/molec.) (x 1.E+20)	Quantum Yield	Wavelength (nm)	Cross Section (cm2/molec.) (x 1.E+20)	Quantum Yield
280	397.00	0.900	300	39.20	0.900
281	360.00	0.900	301	34.40	0.900
282	324.00	0.900	302	30.30	0.900
283	301.00	0.900	303	26.30	0.900
284	273.00	0.900	304	23.50	0.900
285	244.00	0.900	305	20.20	0.884
286	221.00	0.900	306	18.00	0.848
287	201.00	0.900	307	15.60	0.800
288	176.00	0.900	308	13.60	0.740
289	158.00	0.900	309	12.30	0.660
290	141.00	0.900	310	10.30	0.560
291	126.00	0.900	311	9.27	0.450
292	110.00	0.900	312	8.00	0.340
293	98.90	0.900	313	6.92	0.250
294	86.20	0.900	314	6.29	0.180
295	76.70	0.900	315	5.22	0.120
296	66.40	0.900	316	4.78	0.080
297	58.80	0.900	317	4.04	0.050
298	51.00	0.900	318	3.72	0.020
299	45.20	0.900	319	2.91	0.000

TABLE 3-6. Absorption cross sections and quantum yields for acetaldehyde photolysis to radical products:

$$ALD_2 \xrightarrow{h\nu} H\cdot + CO + CH_3 \quad .$$

Wavelength (nm)	Cross Section (cm2/molec.) (x 1.E+20)	Quantum Yield	Wavelength (nm)	Cross Section (cm2/molec.) (x 1.E+20)	Quantum Yield
280	4.50	0.580	305	3.40	0.370
281	4.54	0.575	306	3.27	0.350
282	4.58	0.570	307	3.14	0.330
283	4.62	0.565	308	3.01	0.310
284	4.66	0.560	309	2.88	0.290
285	4.70	0.555	310	2.75	0.270
286	4.74	0.550	311	2.62	0.250
287	4.78	0.545	312	2.49	0.230
288	4.82	0.540	313	2.36	0.210
289	4.86	0.535	314	2.23	0.190
290	4.90	0.530	315	2.10	0.170
291	4.82	0.520	316	2.04	0.156
292	4.74	0.510	317	1.98	0.142
293	4.66	0.500	318	1.92	0.128
294	4.58	0.490	319	1.86	0.114
295	4.50	0.480	320	1.80	0.100
296	4.46	0.470	321	1.66	0.088
297	4.42	0.460	322	1.52	0.076
298	4.38	0.450	323	1.38	0.064
299	4.34	0.440	324	1.24	0.052
300	4.30	0.430	325	1.10	0.040
301	4.12	0.418	326	1.18	0.032
302	3.94	0.406	327	0.94	0.024
303	3.76	0.394	328	0.85	0.016
304	3.58	0.382	329	0.77	0.008
			330	0.69	0.000

TABLE 3-7. Absorption cross sections and quantum yields for nitrous acid photolysis:

$$HONO \xrightarrow{h\nu} OH + NO \quad .$$

Wavelength (nm)	Cross Section (cm2/molec.) (x 1.E+20)	Quantum Yield	Wavelength (nm)	Cross Section (cm2/molec.) (x 1.E+20)	Quantum Yield
280	2.09	1.000	315	0.32	1.000
281	2.00	1.000	316	0.30	1.000
282	1.90	1.000	317	0.29	1.000
283	1.81	1.000	318	0.27	1.000
284	1.71	1.000	319	0.26	1.000
285	1.62	1.000	320	0.25	1.000
286	1.54	1.000	321	0.23	1.000
287	1.46	1.000	322	0.22	1.000
288	1.39	1.000	323	0.21	1.000
289	1.31	1.000	324	0.20	1.000
290	1.23	1.000	325	0.19	1.000
291	1.17	1.000	326	0.18	1.000
292	1.11	1.000	327	0.17	1.000
293	1.05	1.000	328	0.16	1.000
294	0.99	1.000	329	0.15	1.000
295	0.93	1.000	330	0.14	1.000
296	0.89	1.000	331	0.14	1.000
297	0.84	1.000	332	0.13	1.000
298	0.80	1.000	333	0.12	1.000
299	0.75	1.000	334	0.12	1.000
300	0.71	1.000	335	0.11	1.000
301	0.67	1.000	336	0.11	1.000
302	0.64	1.000	337	0.10	1.000
303	0.61	1.000	338	0.09	1.000
304	0.57	1.000	339	0.09	1.000
305	0.54	1.000	340	0.08	1.000
306	0.51	1.000	341	0.08	1.000
307	0.49	1.000	342	0.08	1.000
308	0.47	1.000	343	0.07	1.000
309	0.44	1.000	344	0.07	1.000
310	0.42	1.000	345	0.06	1.000
311	0.40	1.000	346	0.06	1.000
312	0.38	1.000	347	0.06	1.000
313	0.36	1.000	348	0.05	1.000
314	0.34	1.000	349	0.05	1.000
			350	0.05	1.000

TABLE 3-8. Absorption cross sections and quantum yields for hydrogen peroxide photolyis:

$$H_2O_2 \xrightarrow{h\nu} 2\ OH \quad .$$

Wavelength (nm)	Cross Section (cm2/molec.) (x 1.E+20)	Quantum Yield	Wavelength (nm)	Cross Section (cm2/molec.) (x 1.E+20)	Quantum Yield
310	0.00	1.000	351	17.40	1.000
311	0.00	1.000	352	11.40	1.000
312	0.20	1.000	353	37.10	1.000
313	0.42	1.000	354	49.60	1.000
314	0.46	1.000	355	24.60	1.000
315	0.42	1.000	356	11.90	1.000
316	0.30	1.000	357	9.35	1.000
317	0.46	1.000	358	7.78	1.000
318	3.60	1.000	359	7.29	1.000
319	6.10	1.000	360	6.83	1.000
320	2.10	1.000	361	6.90	1.000
321	4.27	1.000	362	7.32	1.000
322	4.01	1.000	363	9.00	1.000
323	3.93	1.000	364	12.10	1.000
324	4.01	1.000	365	13.30	1.000
325	4.04	1.000	366	21.30	1.000
326	3.13	1.000	367	35.20	1.000
327	4.12	1.000	368	45.00	1.000
328	7.55	1.000	369	29.30	1.000
329	6.64	1.000	370	11.90	1.000
330	7.29	1.000	371	9.46	1.000
331	8.70	1.000	372	8.85	1.000
332	13.80	1.000	373	7.44	1.000
333	5.91	1.000	374	4.77	1.000
334	5.91	1.000	375	2.70	1.000
335	6.45	1.000	376	1.90	1.000
336	5.91	1.000	377	1.50	1.000
337	4.58	1.000	378	1.90	1.000
338	19.10	1.000	379	5.80	1.000
339	16.30	1.000	380	7.78	1.000
340	10.50	1.000	381	11.40	1.000
341	8.70	1.000	382	14.00	1.000
342	33.50	1.000	383	17.20	1.000
343	20.10	1.000	384	19.90	1.000
344	10.20	1.000	385	19.00	1.000
345	8.54	1.000	386	11.90	1.000
346	8.32	1.000	387	5.65	1.000
347	8.20	1.000	388	3.20	1.000
348	7.49	1.000	389	1.90	1.000
349	7.13	1.000	390	1.20	1.000
350	6.83	1.000	391	0.50	1.000

j_{O1D}:

$$O_3 \xrightarrow{h\upsilon} O(^1D) + O_2 \qquad (9)$$

Both the absolute photolysis rates (calculated with the actinic flux of Demerjian et al., 1980) and the zenith-angle-dependent ratios for these j-values to j_{NO2} are given in Table 3-9 to facilitate comparison of these rates for different types of photochemical kinetics simulation models. For instance, the Photochemical Kinetics Simulation System (PKSS) developed by Jeffries (1986) allows input of absolute photolysis rates, while the CHEMK program, which is used at Systems Applications and is the basis of the OZIPP computer code, utilizes zenith-angle-dependent ratios to j_{NO2} to internally determine absolute rates. At present, this is primarily a format difference. That is, even though absolute rates can be input in PKSS, they are currently derived by the ratio-to-j_{NO2} process since there are no spectrally resolved experimental actinic flux measurements that would allow direct calculation of the other j-values.

The formaldehyde photolysis rates and ratios in Table 3-9 are considerably lower than the values recommended by Jeffries and Sexton (1987). Our j_{HCHOr} and j_{HCHOs} rates are approximately 90 and 70 percent of the UNC-determined values, and the differences are due almost completely to the choices of quantum yield and absorption cross section data. Our quantum yield data for both formaldehyde photolysis channels are 1 nm values that were fit by Calvert (1980) through his data and that of Moortgat and co-workers (1978, 1979). Ten nm averages of these data are approximately zero to ten percent lower than the 10 nm values used by UNC. The two major sources of absorption cross section data for formaldehyde are from Bass (1980) and Moortgat (1986). We have communicated with both researchers and obtained their data. As shown in Figure 3-12, the results differ by more than thirty percent, especially at the longer wavelength end. After considering both data sets for the UNC chamber simulations, we found that use of the 0.05 nm resolved data of Bass to derive 1 nm bin averages provided the in-chamber absolute rates needed to model measured formaldehyde decay. This does not imply that the Bass data are more correct, but only that when combined with other chamber-dependent factors these data allowed good simulation of simple formaldehyde systems. Compared to our 1 nm data from Bass (1980) UNC utilized 10 nm bin values given by NASA (DeMore et al., 1985), which were determined by averaging the two sets of absorption cross section data. Figure 3-13 shows the photoaction spectra for both formaldehyde photolysis channels using our 1 nm values, the UNC 10 nm bins, and a 5 nm light source (the amount of light was equal for both photoaction spectra). The noted differences in j-values above result almost completely from the differences in quantum yield and absorption cross section data; the significant differences

TABLE 3-9. Results of j-value calculations.

Absolute Photolysis Rates (j-values)

Zenith Angle (deg)	(x1000, min^{-1}, no chamber corrections) HCHOr	HCHOs	O1D	ALD2	H2O2	(min^{-1}) HONO	O3P	NO3
0	1.575	1.898	2.370	0.346	0.532	0.097	0.024	14.11
10	1.552	1.875	2.300	0.339	0.525	0.096	0.024	14.11
20	1.470	1.803	2.068	0.315	0.500	0.094	0.023	13.88
30	1.330	1.677	1.710	0.275	0.458	0.090	0.022	13.54
40	1.135	1.491	1.277	0.222	0.398	0.082	0.021	12.98
50	0.885	1.235	0.815	0.160	0.320	0.072	0.019	12.10
60	0.592	0.905	0.402	0.096	0.225	0.057	0.017	10.73
70	0.295	0.515	0.126	0.040	0.121	0.037	0.012	8.29
78	0.111	0.224	0.029	0.013	0.050	0.018	0.007	5.11
86	0.017	0.045	0.003	0.002	0.010	0.004	0.001	0.74

Ratios to j_{NO2}

Zenith Angle (deg)	(x1000) HCHOr	HCHOs	O1D	ALD2	H2O2	(x1) HONO	O3P	NO3
0	3.247	3.913	4.887	0.713	1.097	0.201	0.049	29.09
10	3.227	3.898	4.782	0.705	1.091	0.201	0.049	29.33
20	3.134	3.844	4.409	0.672	1.066	0.200	0.049	29.59
30	2.969	3.743	3.817	0.614	1.022	0.200	0.049	30.22
40	2.735	3.593	3.077	0.535	0.959	0.199	0.050	31.28
50	2.418	3.374	2.227	0.437	0.874	0.197	0.052	33.06
60	2.007	3.068	1.363	0.325	0.763	0.194	0.056	36.37
70	1.521	2.655	0.649	0.206	0.624	0.189	0.064	42.71
78	1.168	2.358	0.305	0.137	0.526	0.186	0.078	53.74
86	0.850	2.250	0.150	0.100	0.500	0.197	0.055	37.00

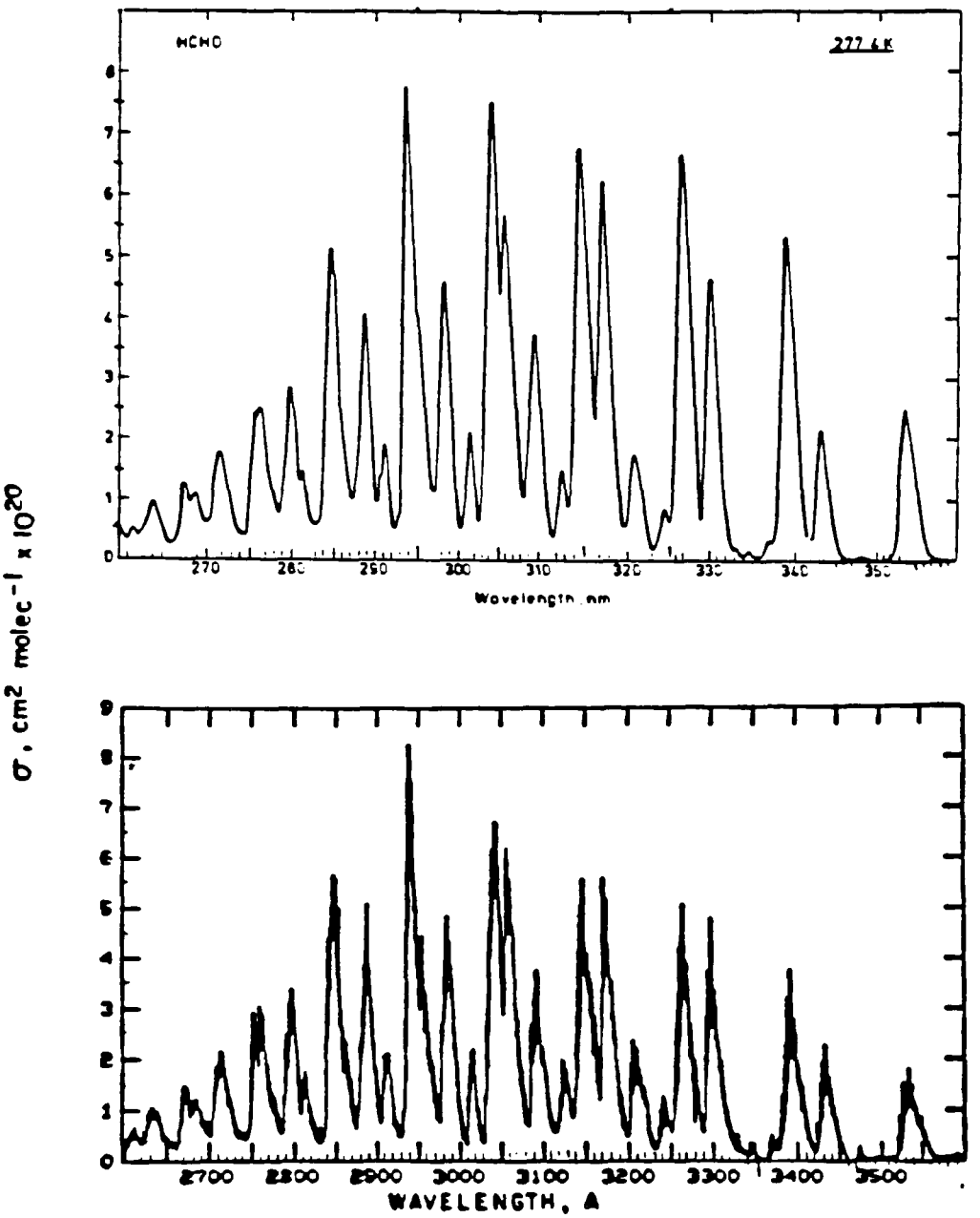

FIGURE 3-12. Comparison of absorption cross sections for formaldehyde from Moortgat (top) and Bass (bottom).

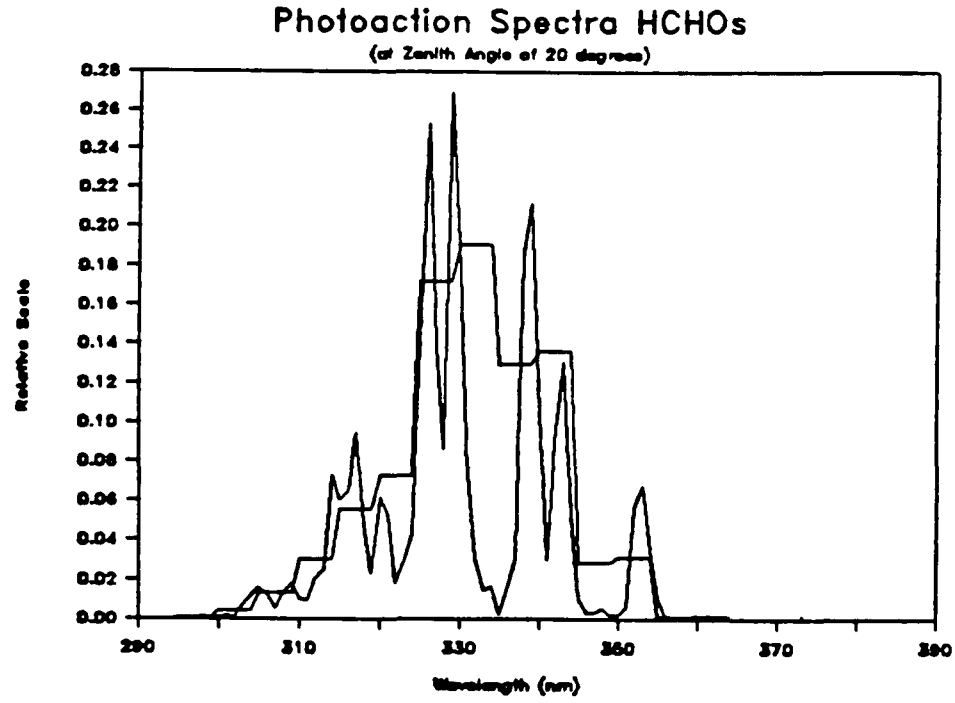

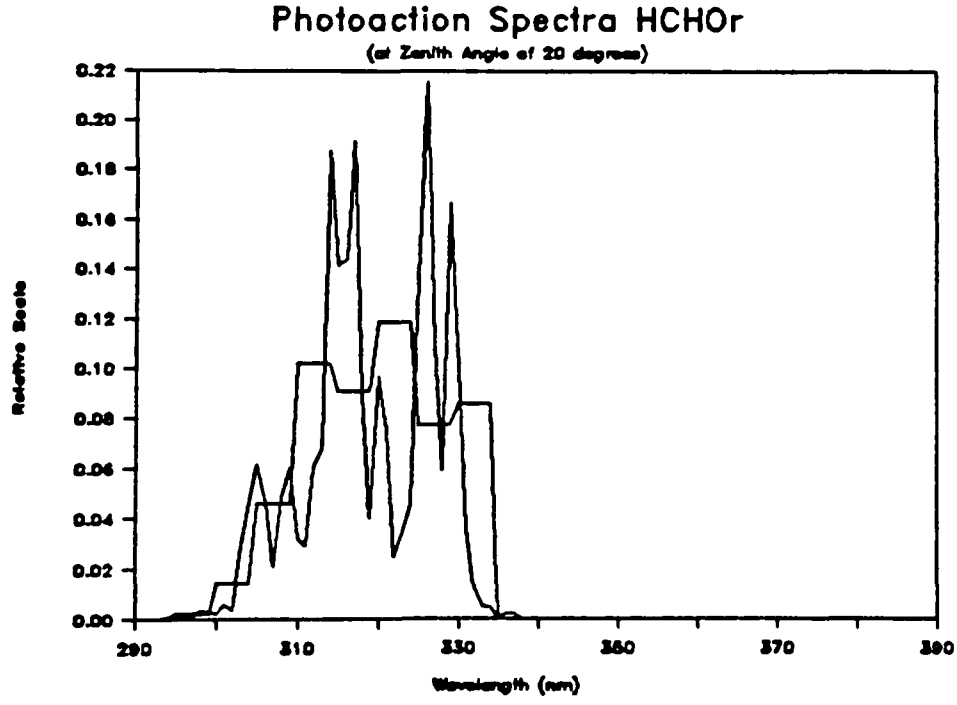

FIGURE 3-13. Photoaction spectra for formaldehyde to stable products (top) and formaldehyde to radicals (bottom) using the 10 nm bins of NASA (1985) and the 1 nm bins from Bass (1980).

between the Bass (1980) and Moortgat (1986) cross section data lead to the larger variation for j_{HCHOs}, since the discrepancy between these data is mainly towards the longer wavelength region.

Our determination of j_{O1D} is approximately 10 percent higher than that recommended by UNC, again resulting from the use of slightly different data sources. Our absorption cross section data were calculated by obtaining 1 nm averages of high-resolution data provided by Dr. Arnold Bass of the National Bureau of Standards (1985). Quantum yield data were obtained from Atkinson and Lloyd (1984). Our acetaldehyde j-values differ significantly from those recommended by UNC (our values are approximately 20 percent larger). Again, this indicates the range of variability in data sets. Our j_{ALD2r} values were derived from the quantum yields and absorption cross sections reported in the latest CODATA review (Baulch et al., 1984). UNC used values from Carter et al. (1986), who utilized the quantum yields listed in Atkinson and Lloyd (1984) and absorption cross sections from Calvert and Pitts (1966). Figure 3-14 shows the differences in photoaction spectra resulting from these different values.

These j-values, namely j_{NO2}, j_{HCHOr}, j_{HCHOs}, j_{O1D} and j_{ALD2}, represent important, short wavelength tropospheric photolysis reactions. Each process responds somewhat differently to diurnal changes in solar spectra (as represented by changes in zenith angle), depending on the proximity of their absorption cross section to the more highly attenuated blue side of the solar spectrum. Figure 3-15 shows the differences in j-value curve shapes, and the need for model input of either direct j-values or zenith-angle-dependent ratios to J_{NO2}. To illustrate the resulting differences, Figure 3-16 shows photoaction spectra, j_{O1D} and j_{NO2}, at solar zenith angles of 20° and 60° (solar spectra shown in Figure 3-10). While j_{NO2} diminishes by only 37 percent, j_{O1D} decreases by over 80 percent because a large fraction of the light energy needed for $O(^1D)$ production (below 300 nm) is not avaliable at zenith angles of 60 degrees.

As noted earlier, our in-chamber calculations of j-values were performed at a high wavelength resolution (1 nm bins) using the best absorption cross section and quantum yield data available. However, since the j-values previously calculated by Jeffries and Sexton (1987) are recommended for use with the CBM-IV in OZIPM-4 atmospheric simulations, we have compared the two sets of calculated j-values to show the differences in atmospheric values that can occur as a result of the technique and data used. This was done by eliminating the chamber-dependent factors (such as Teflon reflection and absorption) from our in-chamber rates and comparing the results with the rates of Jeffries and Sexton (1987). Those differences have already been noted.

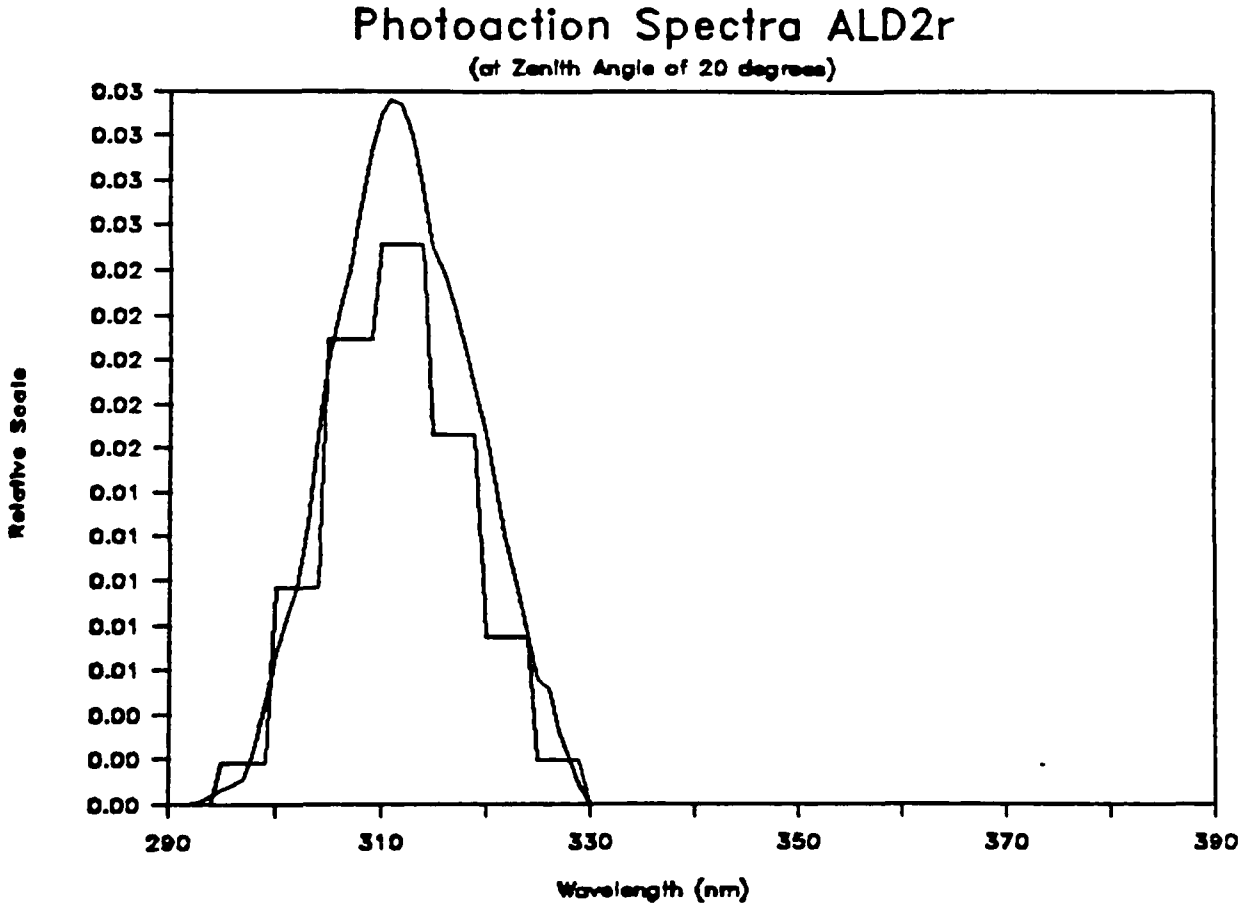

FIGURE 3-14. Photoaction spectra for acetaldehyde using 1 nm bins (this report) and 5 nm bins (Jeffries and Sexton, 1987).

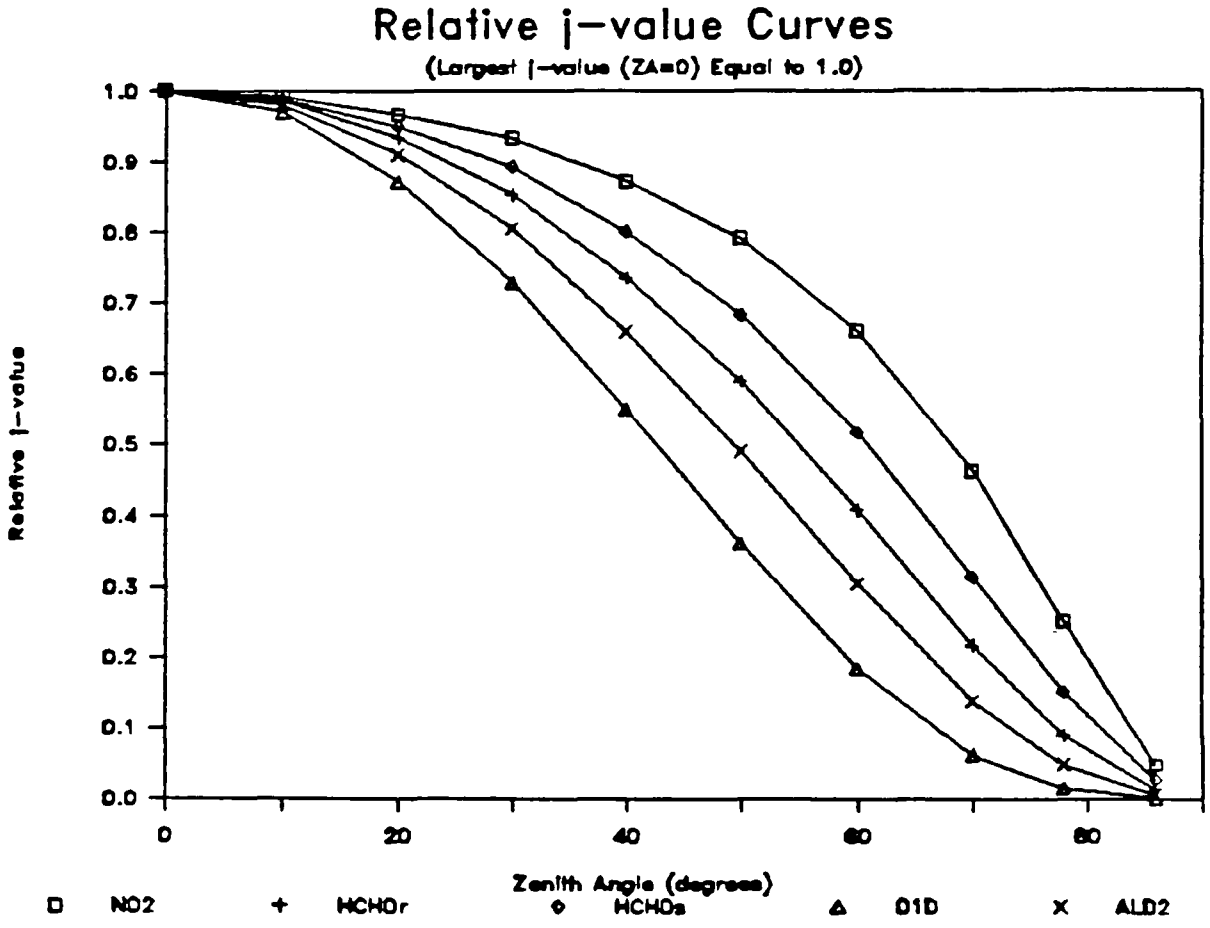

FIGURE 3-15. Comparison of relative j-value curve shapes with respect to solar zenith angle for five major photolytic species.

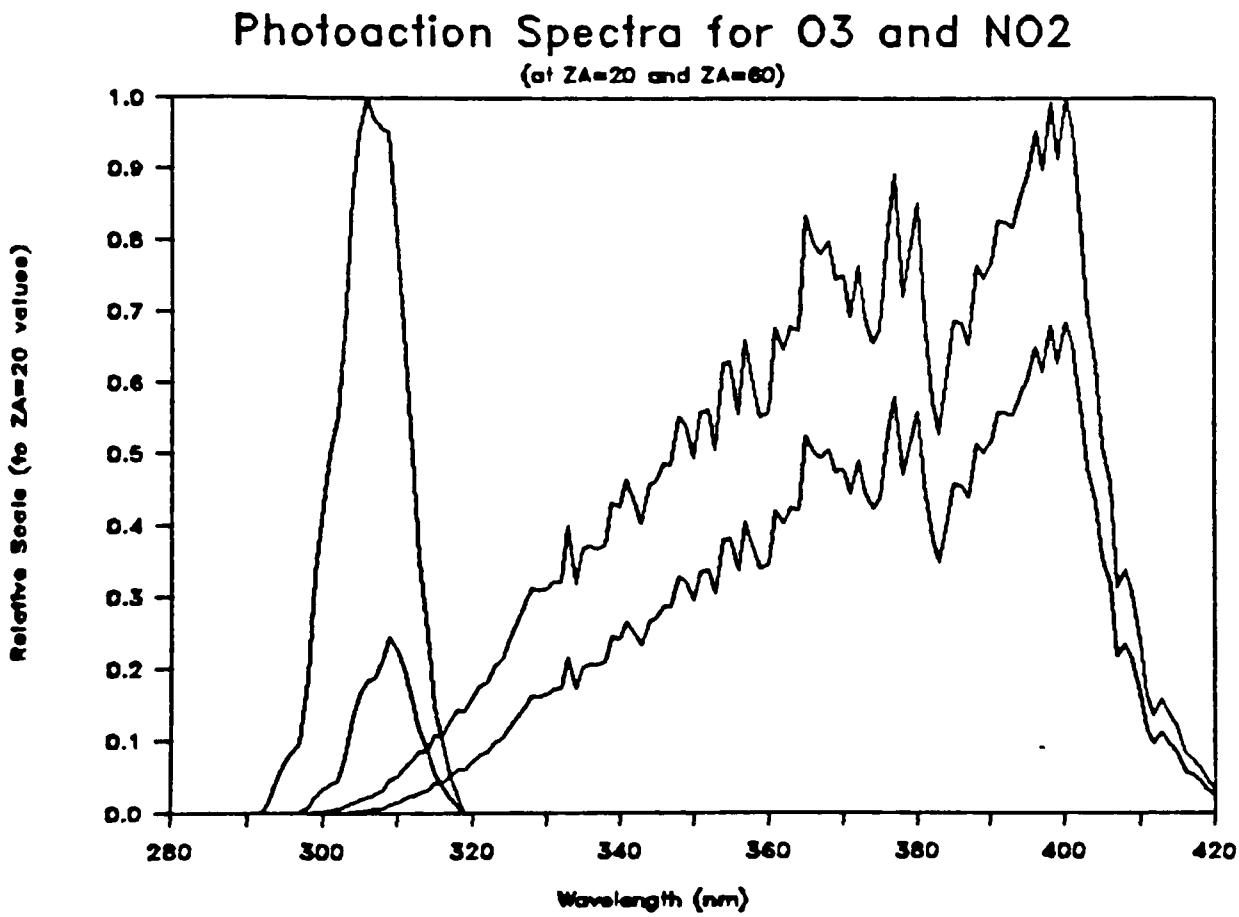

FIGURE 3-16. Comparison of photoaction spectra for j_{NO2} and j_{O1D} at 20 and 60 degrees solar zenith angles.

However, the recommended atmospheric rates and our in-chamber j-values used for mechanism development are mutually exclusive because of the existence of poorly defined chamber factors; thus neither data set can be used to support the use of the other for the opposing application. For example, though the Bass formaldehyde absorption cross section data combined with our current understanding of chamber-dependent radiation factors provides good agreement with formaldehyde rates obtained in the smog chamber, this fact alone is not sufficient to justify use of the Bass data in atmospheric simulations because the chamber factors are highly uncertain. It does, however, indicate that we have a good representation of the absolute in-chamber formaldehyde photolysis rate so that we can proceed with a hierarchical mechanism development process. If current efforts to better define chamber radiation factors are fruitful, it will be both instructive and necessary to utilize one set of quantum yield and cross section data for both in-chamber and atmospheric j-value calculations. Such calculations would also benefit from an expanded effort to minimize uncertainties in the molecular and solar distribution data used. At present, however, we see no problem in using two slightly different data sets for mechanism development and atmospheric simulation provided that (1) the calculated in-chamber absolute rates allow accurate simulation of simple experimental photolytic systems, and (2) the uncertainty associated with the quantum yield and cross section data is considered in atmospheric and smog chamber j-value calculations.

In addition to the photolysis processes just described, we represent four other processes,

j_{HONO}:

$$HONO \xrightarrow{h\upsilon} HO\cdot + NO \tag{23}$$

j_{O3P}:

$$O_3 \xrightarrow{h\upsilon} O(^3P) + O_2 \tag{8}$$

j_{NO3}:

$$\begin{aligned} NO_3 &\xrightarrow{h\upsilon} NO_2 + O \\ &\longrightarrow NO + O_2 \end{aligned} \tag{14}$$

by fixed ratios to j_{NO2}. Quantum yields and absorption cross sections for NO_3 were taken from the review of Atkinson and Lloyd (1984). The NASA review (DeMore, 1985) was the source of the ozone quantum yields and HONO cross sections. Finally, HONO quantum yields were taken from Baulch et al. (1984) and a high resolution ozone cross section was obtained from the National Bureau of Standards (Bass, 1985).

The absolute j-values and ratios to j_{NO2} are shown in Table 3-9. j_{HONO} tracks the shape of the upper curve in Figure 3-15 (j_{NO2}) quite well, as is apparent in Table 3-9 from the generally constant ratios to j_{NO2}. Taking the mean of the ratios to j_{NO2} for the values between 20° and 70° zenith angles, we find

$$j_{HONO} = 0.197\ (\pm\ 0.009) \times j_{NO2},$$

where the associated error is two standard deviations. For both j_{O3P} and j_{NO3}, the values are

$$j_{O3P} = 0.053\ (\pm\ 0.012) \times j_{NO2},$$

and,

$$j_{NO3} = 33.9\ (\pm\ 9.9) \times j_{NO2},$$

where j_{NO3} represents the combined NO_3 photolysis channels, since the ratios between them are independent of zenith angle, resulting in

$$NO_3 \xrightarrow{h\upsilon} 0.89\ (NO_2 + O) + 0.11\ (NO + O_2). \qquad (14)$$

The good correspondence of j_{HONO}, j_{O3P}, and j_{NO3} with j_{NO2} (seen in Table 3-9) is not surprising since these species absorb light at wavelengths longer than most of the molecules discussed, and are, therefore, near to the spectral region of NO_2 absorption. The correlation of j_{O3P} and j_{NO3} to j_{NO2} is not as good as that of j_{HONO}; however, these species will respond to changes in spectral distribution (zenith angle) much as NO_2 does.

Hydrogen peroxide photolyzes at a comparatively slow rate through the process j_{H2O2}:

$$H_2O_2 \xrightarrow{h\upsilon} 2OH.$$

The absorption cross section is given by CODATA (Baulch et al., 1984) and the quantum yield is assumed equal to unity over the spectral region of interest. Unlike HONO and NO_3, hydrogen peroxide absorbs light at shorter wavelengths and has a zenith angle response similar to that of the photolysis of formaldehyde to stable products (CBM-IV reaction 39). It is therefore possible to formulate a fixed ratio factor for determining j_{H2O2} from either j_{NO2} or our j_{HCHOs}. These are calculated to be

$$j_{H2O2} = 0.255\ (\pm\ 0.040) \times j_{HCHOs},$$

and

$$j_{H2O2} = 8.33\ (\pm\ 4.09) \times 10^{-4} \times j_{NO2}.$$

Care must be exercised in using ratios such as these because the reference j-values (j_{NO2} and j_{HCHOs}) may vary for different applications. For example, the ratio of 0.255 is based on j_{HCHOs} calculations used to model smog chamber experiments. As noted, our j_{HCHOs} values differ from the results of Jeffries and Sexton (1987) by approximately 30 percent. Hence, if their calculated formaldehyde rates are used (as in atmospheric modeling with OZIPM-4), the appropriate relationship is

$$j_{H2O2} = 0.189 \times j_{HCHOs} \quad .$$

For cases in which it is difficult to determine the relationship to j_{HCHOs}, the ratio to j_{NO2} should be used since that value is somewhat more certain. The values given in Tables 1-2 and 1-3 show H_2O_2 photolysis ratioed to our HCHOs rates.

Two other photolysis reactions occur in the CBM-IV:

j_{OPEN}:

$$\text{OPEN} \text{ -----> } C_2O_3 + HO_2 + CO \qquad (69)$$

j_{MGLY}:

$$\text{MGLY} \text{ -----> } C_2O_3 + HO_2 + CO \qquad (74)$$

Little is known about the photolysis of these species (particularly that of OPEN, since it is composed of highly reactive aromatic ring decomposition products). The absorption cross section of MGLY has been reported (Carter et al., 1986), but since a wavelength-resolved quantum yield function has not yet been determined, it is difficult to apply this information to solar spectra. Instead, these rates have been estimated through smog simulations that will be described in a later section. For our applictions, we have used

$$j_{OPEN} = 9.04 \times j_{HCHOr}$$

$$j_{MGLY} = 9.64 \times j_{HCHOr}$$

When these rates are used with the j_{HCHOr} values from Jeffries and Sexton (1987) in OZIPM-4, the following ratios should be applied:

$$j_{OPEN} = 8.40 \times j_{HCHOr}$$

$$j_{MGLY} = 8.96 \times j_{HCHOr}$$

Tables 1-2 and 1-3 contain rate constant ratios to our j_{HCHOr} values.

CONDENSATION OF INORGANIC AND CARBONYL REACTIONS

In previous versions of the CBM-X, the third-body effect of molecular nitrogen and oxygen was explicitly represented in the mechanism as a reactant. In the current version, we have calculated the temperature-dependent concentrations of M and O_2 in molecules per cm^3 prior to determination of temperature-dependent rate constants in $ppm^{-n}min^{-1}$ units. In addition to this minor change in format, we have condensed the two NO_3 photolysis channels into one reaction, since the stoichiometry does not vary with zenith angle to any appreciable degree (both channels absorb light far into the visible range). These reactions would normally be separate in the CBM-X formulation, but because this was the only difference in CBM-X and CBM-IV inorganic reaction sets, this combination in the CBM-X allowed identical inorganic sets to be used in both mechanisms.

The reactions of FORM are explicitly included in both mechanisms with the exception of the FORM plus $HO_2^{\bullet}$ equilibrium and reaction scheme. Using the above noted rates of Su et al. (1979), we found that elimination of this scheme had virtually no effect over a wide range of NO_x concentration simulations. It should also be noted that use of the more recent rates of Vayret et al. (1982) or Barnes et al. (1985) shift the equilibria further toward the original products, making this set of reactions even less significant. Therefore, though the reaction set is still included in the CBM-X, it has been eliminated from the CBM-IV.

As noted, the chemistry and condensation of acetone (AONE), the higher ketones (KET), methylglyoxal (MGLY), and a lumped dicarbonyl species (OPEN) are discussed in the following section. AONE and KET are considered with the alkyl group chemistry and MGLY and OPEN are discussed with aromatics. In the remainder of this subsection, we discuss the condensation of acetaldehyde and higher molecular weight aldehydes (ALD2). More specifically, we present the condensation steps and chemistry operators we have developed to handle generalized alkylperoxy, acylperoxy and alkoxy radical chemistry.

The loss mechanisms of ALD2 and its primary radical product, acetylperoxy radical (C2O3), are represented identically in the CBM-X and the CBM-IV. However, the chemistry of their reaction products, primarily methylperoxy radical (MEO2) and methoxy radical (MEO), has been condensed for the CBM-IV. Because the higher molecular weight aldehydes are intimately linked with alkane chemistry through the hydrocarbon oxidation/radical chain degradation reaction sequence, the condensation steps discussed here also apply directly to the alkane scheme. The reactions to be condensed are 53 to 70 in Table 1-2. The methodology is as follows:

The methoxy radical ($CH_3O^{\cdot}$) is a rapidly reacting intermediate in this radical chain cycle. At tropospheric concentrations of O_2, the dominant reaction of MEO is reaction 59 (of the CBM-X):

MEO (+ O_2) ------> FORM + HO2. (X-59)

In addition, the alternate sinks of MEO form products that either regenerate the initial reactants through other reactions, or yield the products of this reaction. Therefore, we make a steady-state assumption for MEO:

MEO ≡ FORM + HO2

that eliminates species MEO, MNIT, and MEN3 and reactions 56 through 62 in the CBM-X, and transforms the product yields of MEO-forming reactions as in

MEO2 + NO ------> NO2 + MEO, (X-55)

MEO2 + MEO2 ------> 2 MEO, (X-63)

MEO2 + C2O3 ------> MEO2 + MEO, (X-65)

which are now

MEO2 + NO ------> NO2 + FORM + HO2,

MEO2 + MEO2 ------> 2 FORM + 2 HO2,

MEO2 + C2O3 ------> MEO2 + FORM + HO2.

Before we discuss the condensation of the chemistry of MEO2, we describe our general approach to peroxy radical chemistry. The reactions of MEO2 and other peroxy radicals (C2O3, ANO2, RO2, RO2R, AO2, TO2, etc.) are very similar because the peroxy radical structure common to all of these species is the main functional group. In the presence of NO, the predominant fate of these radicals is the oxidation of NO to form NO_2 and a variety of organic products. In the CBM-IV, most of these peroxy radicals (with the exception of those producing C2O3 and TO2) have been eliminated by substituting the specific organic products that they form in an NO-to-NO_2 conversion reaction, and an operator that can convert an NO to an NO_2. For example, the reaction sequence

AONE + OH ------> ANO2 (X-72)

ANO2 + NO ------> NO2 + C2O3 + FORM (X-73)

is represented by

$$AONE + OH \text{ ------> } XO2 + C2O3 + FORM,$$

where the universal peroxy opertor (XO2) is assumed to react with NO via

$$XO2 + NO \text{ ------> } NO2, \tag{79}$$

at a rate of 12000 $ppm^{-1}min^{-1}$. Because the main chemical function of all peroxy radicals occurs with the common peroxy radical group, the reaction rates with NO are fairly similar, and this approximation is a good one.

When NO concentrations are low, other species can compete with NO to reduce peroxy radicals. In most cases, however, the self and cross reactions of peroxy radicals themselves are the most probable peroxy termination reactions. Unfortunately, the chemistry of only a few organic peroxy-peroxy and HO_2-organic peroxy reactions have been studied. We have discussed these reactions and have included them in the CBM when appropriate. Since much of the radical mass is routed through the C2O3 and MEO2 radicals of the CBM-X, many of the peroxy radical termination reactions are accounted for. However, we have also included the termination of the XO2 operator as a necessary reaction under conditions of low NO:

$$XO2 + XO2 \text{ -----> }. \tag{80}$$

Methylperoxy radical chemistry can now be condensed using the general peroxy radical chemistry just discussed. Product MEO2 in the CBM-X is replaced by XO2 + MEO, and, using MEO ≡ FORM + HO2 from above, the reactions

$$ALD2 \text{ --h}\nu\text{--> } MEO2 + HO2 + CO, \tag{X-49}$$

$$C2O3 + NO \text{ ------> } NO2 + MEO2, \tag{X-50}$$

and

$$C2O3 + C2O3 \text{ ------> } 2\ MEO2, \tag{X-66}$$

can now be condensed to

$$ALD2 \text{ --h}\nu\text{--> } XO2 + FORM + 2\ HO2 + CO, \tag{45}$$

$$C2O3 + NO \text{ ------> } NO2 + FORM + HO2 + XO2, \tag{46}$$

and

$$C2O3 + C2O3 \text{ ----> } 2\ FORM + 2HO2 + 2XO2. \tag{49}$$

Finally, we have eliminated the product PROX from the C2O3 + HO2 reaction in the CBM-IV. Because the atmospheric reactivity of organic peroxides is

poorly understood, we felt it was improper to follow the hypothetical chemical reactions of these species and thus possibly mislead potential users of the mechanism. Consequently, the reactions

C2O3 + HO2 ----> PROX $k = 2 \times 10^3\ ppm^{-1}min^{-1}$ (X-69)

C2O3 + HO2 ----> MEO2 + OH $k = 7.6 \times 10^3\ ppm^{-1}min^{-1}$ (X-70)

have been replaced with

C2O3 + HO2 ---> 0.79 (FORM + HO2 + XO2 + OH) $k = 9.6 \times 10^3\ ppm^{-1}min^{-1}$ (50)

In the following section, we utilize much of this chemistry to describe the chemistry of reactive organic species.

4 REACTIVE HYDROCARBON CHEMISTRY

In this section we describe the reactive hydrocarbon chemistry used in the most recent versions of CBM. Our discussion covers alkyl group (paraffin) chemistry, olefin and ethene chemistry, aromatic chemistry, and isoprene and α-pinene. The chemical mechanisms for these groups employ both explicit structures and reactive surrogates as the entities of lumping and reaction; therefore, a single molecule can include several reactive structural groups. For each of these four groups, we examine relevant chemical kinetic and mechanistic data, its treatment in development of the CBM-X, and subsequent condensation to the CBM-IV. Reaction numbers in the text refer to the CBM-IV (Table 1-3) unless preceded by an X, which indicates that they refer to CBM-X (Table 1-2) reactions only. Many of the rates and stoichiometries discussed in this section are dependent to some degree upon the composition of the reacting hydrocarbons. To derive these parameters we used the hydrocarbon profile given in Table 4-1. This profile represents the average of 23 samples taken in Los Angeles as analyzed by Environmental Research and Technology and Washington State University (Grosjean et al., 1981).

ALKYL GROUP (PARAFFIN) CHEMISTRY

Structural reactivity generalization is especially appropriate for alkyl group chemistry because it allows a complex reaction scheme to be reduced to a much smaller set of lumped reactions.

Photooxidation of alkyl carbon in urban smog results almost exclusively from hydrogen abstraction by OH in the general form:

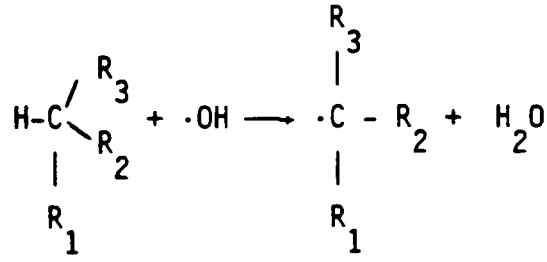

TABLE 4-1. Average concentration (ppb) of each hydrocarbon species identified in ambient air by the ERT and WSU methods for 23 common analyses. (Source: Grosjean et al., 1981.)

ID	Species	Ave. ERT (ppb)	Ave. WSU (ppb)	Ratio[1] ERT/WSU
1	Ethane	76.68	13.82	5.55
2	Ethylene	40.20	31.38	1.28
3	Acetylene	43.89	39.71	1.11
4	Propane	38.53	45.10	.85
5	Propene	10.65	14.69	.72
6	Propyne	.00	.00	-99.00
7	Propadiene	.00	.00	-99.00
8	Isobutane	15.89	23.50	.68
9	Butane	32.66	53.84	.61
10	1-Butene	.00	2.26	-99.00
11	Isobutene	.00	4.06	-99.00
12	Trans-2-Butene	.00	3.80	-99.00
13	Cis-2-Butene	.00	.34	-99.00
14	Isopentane	34.77	28.72	1.21
15	Pentane	15.30	18.94	.81
16	3-Methyl-1-Butene	.00	.85	-99.00
17	1,3-Butadiene	.00	.00	-99.00
18	1-Pentene	1.24	.34	3.67
19	Isoprene	.00	1.50	-99.00
20	Trans-2-Pentene	.00	1.54	-99.00
21	Cis-2-Pentene	.00	1.58	-99.00
22	2-Methyl-2-Butene	.00	.42	-99.00
23	2,2-Dimethylbutane	.00	.12	-99.00
24	Cyclopentene	.00	.76	-99.00
25	Cyclopentane	.00	2.81	-99.00
26	2,3-Dimethylbutane	3.51	3.31	1.06
27	2-Methylpentane	13.82	11.57	1.19
28	Cis-4-Methyl-2-Pentene	.00	.03	-99.00
29	2-Methylpentane	8.27	8.11	1.02
30	2-Methyl-1-Pentene	.20	1.05	.19
31	Hexane	10.39	8.60	1.21
32	Trans-2-Hexene	.00	.51	-99.00
33	2-Methyl-2-Pentene	.00	.49	-99.00
34	Cis-2-Hexene	.00	.28	-99.00
35	Methylcyclopentane	7.48	9.62	.78

(Continued)

TABLE 4-1. (Continued)

ID	Species	Ave. ERT (ppb)	Ave. WSU (ppb)	Ratio ERT/WSU
36	2,2,3-Trimethylbutane	.39	.00	-99.00
37	2,4-Dimethylpentane	2.83	3.98	.71
38	1-Methylcyclopentene	.00	.00	-99.00
39	Benzene	3.13	13.94	.22
40	Cyclohexane	15.43	35.25	.44
41	2-Methylhexane	.00	5.29	-99.00
42	2,3-Dimethylpentane	4.37	5.30	.83
43	3-Methylhexane	6.47	6.94	.93
44	Dimethylcyclopentane	1.90	4.97	.38
45	2,2,4-Trimethylpentane	7.56	7.55	1.00
46	Heptane	4.63	6.02	.77
47	Methylcyclohexane	5.51	6.37	.86
48	Ethylcyclopentane	.00	.97	-99.00
49	2,5-Dimethylhexane	.84	.14	5.90
50	2,4-Dimethylhexane	.00	2.87	-99.00
51	2,3,4-Trimethylpentane	2.09	1.76	1.19
52	Toluene	33.92	40.37	.84
53	2,3-Dimethylhexane	.00	1.28	-99.00
54	2-Methylheptane	.00	4.76	-99.00
55	3-Methylheptane	2.39	2.49	.96
56	2,2,5-Trimethylhexane	1.18	1.87	.63
57	Dimethylcyclohexane	.06	.00	-99.00
58	Octane	1.76	2.67	.66
59	Ethylcyclohexane	.00	.99	-99.00
60	Ethylbenzene	6.37	7.08	.90
61	P- & M-Xylene	18.06	20.40	.89
62	Styrene	.00	1.21	-99.00
63	O-Xylene	6.83	9.36	.73
64	Nonane	1.13	1.54	.73
65	Isopropylbenzene	.08	.64	.12
66	Propylbenzene	1.17	2.56	.46
67	P-Ethyltoluene	5.47	5.98	.92
68	M-Ethyltoluene	.00	2.72	-99.00
69	1,3,5-Trimethylbenzene	2.46	2.06	1.20
70	O-Ethyltoluene	1.52	1.76	.86
71	Tert-Butylbenzene	.00	.00	-99.00
72	1,2,4-Trimethylbenzene	5.63	7.14	.79
73	Sec-Butylbenzene	.24	.65	.37
74	1,2,3-Trimethylbenzene	1.40	1.71	.82

(Continued)

TABLE 4-1. (Concluded)

ID	Species	Ave. ERT (ppb)	Ave. WSU (ppb)	Ratio ERT/WSU
75	Decane	2.93	1.05	2.79
76	Methylstyrene	.00	1.21	-99.00
77	1,3-Diethylbenzene	.00	1.17	-99.00
78	1,4-Diethylbenzene	.00	1.25	-99.00
79	1,2-Diethylbenzene	.00	.00	-99.00
80	Undecane	.00	.00	-99.00
81	Dodecane	.00	.00	-99.00
82	N-Butylbenzene	.20	.00	-99.00
83		.00	.00	-99.00
84		.00	.00	-99.00
85	Unidentified	80.12	52.62	1.52

[1]Ratio of -99.00 indicates ratio cannot be calculated.

When all the variable functional groups (R) are hydrogen, the organic reactant in this reaction is methane. Methane oxidation is of interest mainly due to its involvement with the global carbon cycle, and is essentially unreactive on the time scale of urban smog. We treat the background reactivity of methane in the CBM by assuming a constant methane concentration of 1.85 ppm:

$$OH\ (+\ CH_4) \xrightarrow{O_2} CH_3O_2\cdot + H_2O \quad . \qquad \text{(X-74)}$$

This results in a pseudo-first-order rate constant (DeMore et al., 1985) of

$$k(X\text{-}74) = 6.521 \times 10^3 \exp(-1710/T)\ min^{-1},$$

and

$$k(X\text{-}74)_{298} = 2.10 \times 10^1\ min^{-1}.$$

<u>OH Abstraction of Primary C - H Bonds</u>

When only one of the R groups in the hydrocarbon reactant is an alkyl chain,

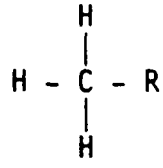

abstraction of one of the three remaining hydrogen atoms by the hydroxyl radical proceeds at a molecular rate of about 260 $ppm^{-1}\ min^{-1}$ (Atkinson, 1986; Atkinson and Lloyd, 1984). In the presence of tropospheric oxygen, the resulting $RCH_2\cdot$ radical rapidly forms a peroxy radical ($RCH_2O_2\cdot$) that can react with NO:

$$RCH_2O_2\cdot + NO \rightarrow NO_2 + RCH_2O\cdot \quad .$$

A minor fractional channel for this reaction results in nitrates:

$$RCH_2O_2^{\cdot} + NO \rightarrow RCH_2ONO_2$$

with a yield that increases with increasing alkyl chain length (maximum yield ≈ 30 percent). We discuss treatment of $RO_2^{\cdot} + NO \rightarrow$ nitrate later in this section.

For R < $CH_3(CH_2)_2$-, or for any molecule in which the maximum carbon chain length is less than 4, the $RCH_2O\cdot$ radical reacts mainly with O_2 to form an aldehyde and a hydroperoxy radical:

$$RCH_2O\cdot + O_2 \rightarrow RCHO + HO_2\cdot \quad .$$

Additional intramolecular reactions can occur for alkoxyl radicals with a carbon chain length of C_4 or greater. Both decomposition and "tailbiting" isomerization reactions are possible (Hendry and Kenley, 1979).

Decomposition reactions follow the general form:

$$RCH_2O\cdot \xrightarrow{+O_2} RO_2\cdot + HCHO$$

in which a carbon-carbon bond is severed to form a stable carbonyl species and a peroxy radical.

The isomerization sequence proceeds as follows:

$$H_3CRCH_2O\cdot \xrightarrow{+O_2} \cdot O_2H_2CRCH_2OH$$

$$\cdot O_2H_2CRCH_2OH + NO \rightarrow NO_2 + \cdot OH_2CRCH_2OH$$

$$\cdot OH_2CRCH_2OH \rightarrow HOH_2CR\dot{C}H(OH) \quad .$$

The α-hydroxy radical could react with O_2 via abstraction of hydrogen from the hydroxy group to yield an aldehyde (Carter et al., 1979):

$$HOH_2CR\dot{C}H(OH) + O_2 \rightarrow HO_2\cdot + HOH_2CRCHO \quad .$$

The overall effect of the isomerization reaction, therefore, is to delay the formation of the RCHO and HO_2 products of the nonisomerization reactions by inserting n alcohol-forming steps and n NO-to-NO_2 conversions:

$$RCH_2O\cdot \xrightarrow{+(n+1)O_2} RCHO + HO_2\cdot + n \text{ (Alcohol groups and NO-to-}NO_2\text{ conversions).}$$

This process can be treated by the following reactions:

$$RCH_2O\cdot \rightarrow HORCH_2O_2\cdot \quad ,$$

$$HORCH_2O_2^{\bullet} + NO \rightarrow NO_2 + \text{(Alcohol group)} + RCH_2O\cdot \quad ,$$

$$RCH_2O\bullet \xrightarrow{+O_2} HO_2^{\bullet} + RCHO \text{ (adlehyde)} \quad .$$

The ratio of the first two reaction rates will determine the number of alcohol groups added to the molecule. A 1:1 ratio, for example, will yield 1 alcohol group per reaction of OH with a primary carbon atom.

The importance of isomerization reactions in alkane chemistry is uncertain since these compounds have not been directly observed and the yield of secondary alcohols in high molecular-weight alkane systems has not been quantified. Treatment of this process would require the introduction of another carbon-bond representation (alcohol groups); however, we note that Whitten et al. (1986) demonstrated that ethanol could be represented as a paraffin in reactivity on a per carbon basis. This is possible because the OH rate constant per carbon atom is nearly twice the paraffinic OH rate constant while the number of NO-to-NO_2 conversions per OH reaction is about half that for paraffins. Such an approximation also depends on the fact that only a fraction of paraffins react per day. If both ethanol and paraffins reacted rapidly, the lower number of NO to NO_2 conversions from the alcohol reaction would produce less overall ozone than the paraffin reaction. If one extends this ethanol for paraffins approximation to alcohol groups in general, then the formation of an alcohol group on a paraffinic carbon atom can be ignored. Until isomerization phenomena are better quantified, we believe that inclusion of alcohol groups in mechanisms is not required. The Carter et al. (1986) mechanism uses an isomerization alcohol yield of about 0.2.

OH Abstraction of Secondary C-H Bonds

The reactivity of OH for secondary C-H hydrogen abstraction is about 1700 $ppm^{-1}min^{-1}$ (Atkinson, 1986). In compounds with an alkyl carbon chain length of 4 carbons or less (butane and methyl substituted butanes), hydroxyl abstraction of a secondary C-H bond yields two main reaction sequences (again, neglecting nitrate formation until later):

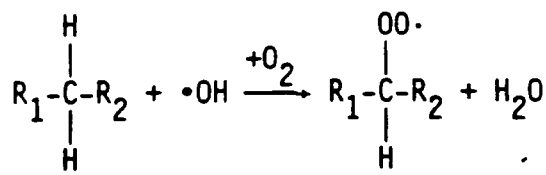

$$R_1\text{-}\overset{\overset{\displaystyle OO\cdot}{|}}{CH}\text{-}R_2 + NO \rightarrow NO_2 + R_1\text{-}\overset{\overset{\displaystyle O\cdot}{|}}{CH}\text{-}R_2$$

$$R_1\text{-}\overset{\overset{\displaystyle O\cdot}{|}}{CH}\text{-}R_2 + O_2 \rightarrow R_1\overset{\overset{\displaystyle O}{\|}}{C}R_2 + HO_2^{\cdot}$$

$$R_1\text{-}\overset{\overset{\displaystyle O\cdot}{|}}{CH}\text{-}R_2 \rightarrow R_1CHO + R_2^{\cdot}$$

Competition between the last two alkoxy reactions (hydrogen abstraction by O_2 and decomposition) is largely governed by variations in the decomposition reaction rate due to molecular size and temperature. For most of the hydrocarbons in the atmospheric mix, the R_1CHO formed in decomposition will be acetaldehyde ($R=CH_3$). Since the average carbon number of alkanes in the atmosphere is about 5.5, the alkyl group (R_2) formed in the reaction will be approximately C_3-C_4.

In the review by Atkinson and Lloyd (1984) the competition between alkoxy radical abstraction by O_2 and decomposition was shown to dramatically change with the number of carbon atoms in the alkoxy radical. For the series sec-propoxyl, sec-butoxyl, sec-pentoxyl and longer sec-radicals the competition can be expected to go from essentially abstraction only to decomposition only.

It is possible that the isomerization reaction occurs in the secondary C-H bond abstraction sequence for alkyl chains equal to or greater than 5:

$$CH_3CH_2CH_2CH_2CH_3 + \bullet OH \xrightarrow{+O_2} H_2O + CH_3CH(O_2^{\cdot})CH_2CH_2CH_3$$

$$CH_3CH(O_2^{\cdot})CH_2CH_2CH_3 + NO \rightarrow NO_2 + CH_3CH(O\cdot)CH_2CH_2CH_3$$

$$CH_3CH(O\cdot)CH_2CH_2CH_3 \xrightarrow{+O_2} CH_3CH(OH)CH_3CH_2CH_2O_2^{\cdot}$$

The importance of this reaction (and the analogous reaction involving the tertiary carbon group) depends on competition from other processes affecting alkoxyl radical decomposition and hydrogen abstraction. The isomerization reaction of rings of greater than 6, i.e., alkyl chains more than 4

carbon atoms in length, has not been studied. Hendry and Kenley (1979) suggest that the 7-member ring is not favored thermodynamically.

The discussion above leads to the following conclusions regarding sec-alkoxyl radicals:

For sec-alkoxyl radicals of 4 or less carbons abstraction is the exclusive or a major pathway;

For sec-alkoxyl radicals of 4 or more carbons decomposition is a major pathway with some isomerization to alcohol groups possible;

Since ambient air contains an average carbon number between 5 and 6, then the first alkoxyl radical formed after reaction with OH will most often decompose. However, the peroxy radical formed from such a decomposition will most often have fewer than 4 carbons and the subsequent alkoxyl radical will therefore undergo abstraction only.

Symbolically, these conclusions lead to the following sequence for secondary attack by OH:

$$OH + \text{paraffin} \xrightarrow{O_2} \text{sec-}RO_2^{\bullet} + H_2O$$

$$\text{sec-}RO_2^{\bullet} + NO \rightarrow NO_2 + \text{sec-}RO\bullet$$

$$\text{sec-}RO\bullet \rightarrow ALD2 + R'O_2^{\bullet}$$

$$R'O_2^{\bullet} + NO \rightarrow NO_2 + R'O\bullet$$

$$R'O\bullet \rightarrow HO_2^{\bullet} + ALD2 \text{ or } KET$$

<u>OH Abstraction of Tertiary C-H Bonds</u>

Hydrogen abstraction by OH from tertiary C-H bonds occurs at a rate of about 3200 $ppm^{-1}min^{-1}$ (Atkinson, 1986). The alkoxyl radical formed in this oxidation sequence is devoid of hydrogen atoms and therefore cannot undergo abstraction (as in the forementioned scheme) by O_2. Hence

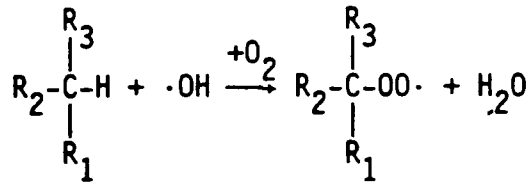

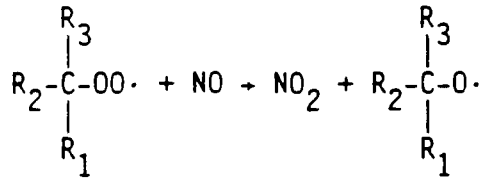

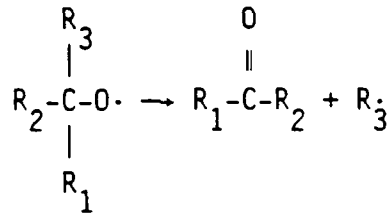

Isomerization reactions might also occur in addition to decomposition for the tertiary alkoxy radical provided the functional groups will support this process. For example, isomerization

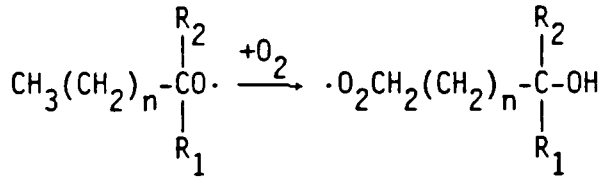

occurs if n is greater than or equal to 2.

A fraction of tertiary alkoxyl decomposition may yield ketones, e.g., 3-methyl pentane could form methylethyl ketone (MEK):

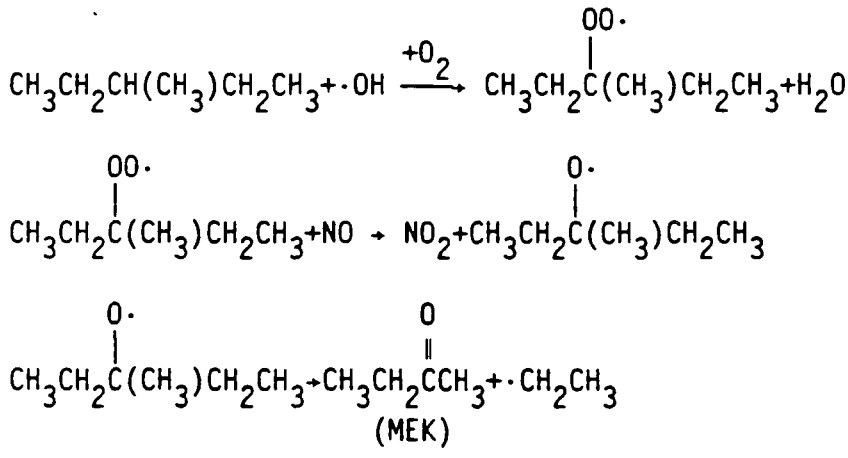

For a specific hydrocarbon, the ketone production ratio from tertiary alkoxyl decomposition can be calculated from its structure, e.g., 2,3,4-trimethylpentane

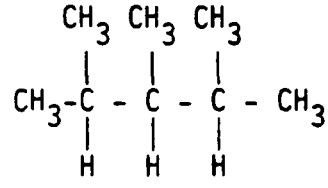

has 3 tertiary carbons. Reaction and decomposition at the 2-carbon site will yield acetone:

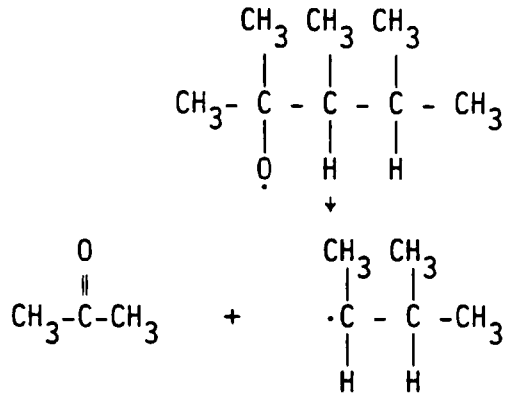

while reaction at the 3-carbon site will yield a higher molecular weight ketone:

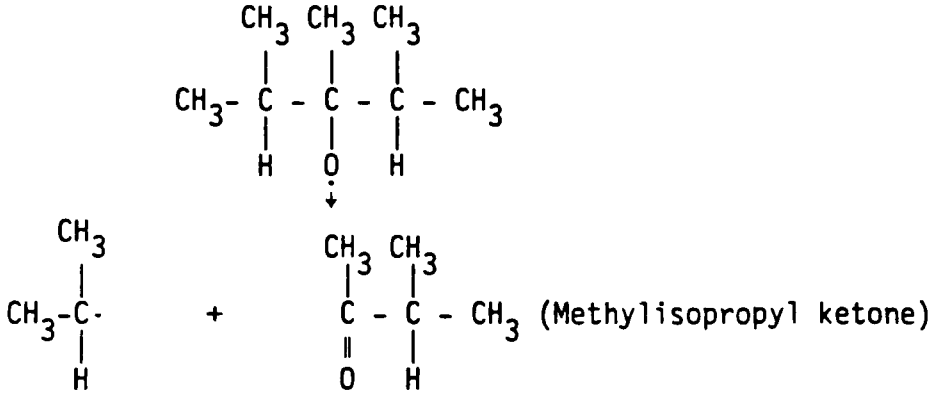

Thus, the overall ketone yield would be 2 acetones to 1 larger ketone if the three sites are equally reactive. From our hydrocarbon profile (Table 4-1), we can estimate the ketone production ratio from tert-alkyl carbons as 2.5 acetone to 1 higher ketone. We also note the existence of three compounds containing quartenary carbons: 2,2,3 trimethylbutane, 2,2,4, trimethylpentane, and 2,2,5 trimethylhexane. All three could be expected to yield acetone if decomposition affects the quartenary carbon.

Quartenary carbon atoms can probably be neglected since compounds containing them appear to be rare in the atmosphere (see Table 4-1). However, it is interesting to note that quartenary carbon atoms cannot be oxidized

directly by OH abstraction since there are no hydrogens available. Oxidation can occur only from the rupture of one of the four carbon-carbon bonds. For example, neopentane might lead to the $(CH_3)_3CCH_2O\cdot$ radical after initial OH attack on a methyl group and reaction of the peroxy radical with NO. Hence, the initial activation possible for the quartenary carbon would be the formation of the $(CH_3)_3\text{-}CO_2^{\cdot}$ radical.

Ketones

The ketone structure,

$$R_1\text{-}\overset{\overset{\displaystyle O}{\|}}{C}\text{-}R_2,$$

appears to be essentially unreactive to hydroxyl chemistry at the carbonyl carbon as might be expected from the lack of labile hydrogens. The primary reaction route involves OH and occurs via decomposition resulting from reactions in the alkyl side chains, e.g., for MEK (Cox et al., 1981):

$$CH_3\text{-}\overset{\overset{\displaystyle O}{\|}}{C}\text{-}\underset{\underset{\displaystyle H}{|}}{\overset{\overset{\displaystyle H}{|}}{C}}\text{-}CH_3 + \cdot OH \xrightarrow{+O_2} H_2O + CH_3\text{-}\overset{\overset{\displaystyle O}{\|}}{C}\text{-}\underset{\underset{\displaystyle OO\cdot}{|}}{\overset{\overset{\displaystyle H}{|}}{C}}\text{-}CH_3$$

$$CH_3\text{-}\overset{\overset{\displaystyle O}{\|}}{C}\text{-}\underset{\underset{\displaystyle OO\cdot}{|}}{\overset{\overset{\displaystyle H}{|}}{C}}\text{-}CH_3 + NO \rightarrow NO_2 + CH_3\text{-}\overset{\overset{\displaystyle O}{\|}}{C}\text{-}\underset{\underset{\displaystyle \dot{O}}{|}}{\overset{\overset{\displaystyle H}{|}}{C}}\text{-}CH_3$$

$$CH_3\text{-}\overset{\overset{\displaystyle O}{\|}}{C}\text{-}\underset{\underset{\displaystyle \dot{O}}{|}}{\overset{\overset{\displaystyle H}{|}}{C}}\text{-}CH_3 \xrightarrow{+O_2} CH_3\text{-}\underset{\underset{\displaystyle OO\cdot}{|}}{\overset{\overset{\displaystyle O}{\|}}{C}} + \underset{\underset{\displaystyle O}{\|}}{\overset{\overset{\displaystyle H}{|}}{C}}\text{-}CH_3$$

Note that the presence of the carbonyl structure creates a peroxyacyl product, whereas an alkyl group would yield an alkylperoxy product.

Acetone is sufficiently dissimilar to higher ketones (like MEK) in its rate of photolysis to warrant explicit treatment. Acetone is formed directly from propane oxidation but the principal formation pathway in the urban atmosphere may be from decomposition of tertiary alkoxy radicals:

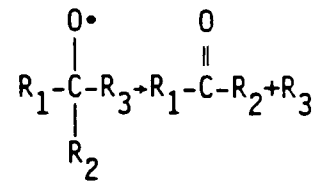

As previously noted, acetone is by far the most significant product of such reactions because methyl side chains are more common than lengthier alkyl branching groups, and also because the C-C bond strength is weaker for carbon chains greater than C_2. Therefore, the decomposition tends to occur preferentially for alkyl side chains over methyl side groups.

Treatment of Decomposition in Carbon-Bond Groups

The alkyl radicals formed from the decomposition reactions of secondary and tertiary alkoxy radicals are similar to, but smaller than, the alkyl radicals formed by the initial hydrogen abstraction reaction of the parent molecules. If an R group is a methyl group, then a methyl radical may be formed. A methyl radical is expected to react with O_2 to form a methyl peroxy radical under tropospheric conditions.

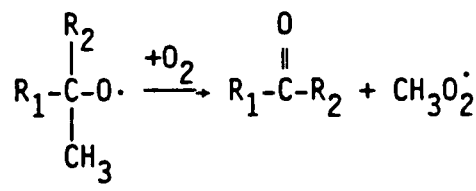

Note that all primary carbons are methyl groups by definition. Therefore, methyl peroxy radicals are formed at a rate relative to the overall number of primary carbon atoms. (The bond strength relative to the secondary and tertiary C-C bonds will also play a role.)

Similarly, if a secondary ($-CH_2R$) group is next to the decomposition site, the alkyl radical formed is equivalent to that formed from the OH abstraction from a primary carbon.

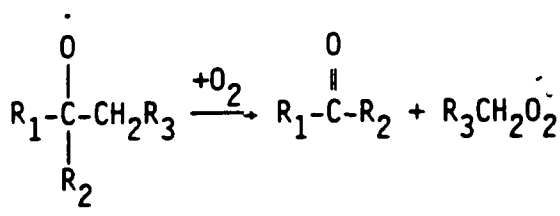

Also, if a branched or tertiary group is involved, then a secondary radical is formed:

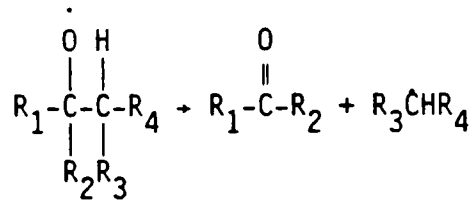

The forementioned reactions can actually be represented by the single reaction:

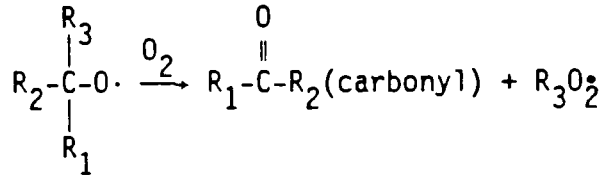

If R_1 is hydrogen the carbonyl product is an aldehyde, otherwise the carbonyl product is a ketone. The nature of the carbon atoms adjacent to the site of decomposition determine the form within the $R_3O_2^{\bullet}$ product. If the general CBM assumption of independently reacting carbon-bonded structures holds, then the distribution of products for $R_3O_2^{\bullet}$ will be related to the distribution of carbon-bonded structures such as primary, secondary, tertiary, and quartenary carbon atoms in the generalized pool of alkyl carbon atoms and other structures such as ketones, etc. Although we will later assume a generalized distribution within a single structure species for alkyl carbon atoms, we can presently assume that four single-bonded carbon atom structure species might be used in some extended form of the CBM.

The generalized decomposition pathway would form a distribution of $R_3O_2^{\bullet}$ radicals at rates related to the relative abundance of the carbon structure groups with perhaps some minor modification by local bonding effects. The minor modifications would also be a function of the distribution of the carbon-bonded structures groups. One way of relating the distribution of products for the generalized peroxy radical product $R_3O_2^{\bullet}$ is the use of a virtual species or operator we will call D. This species D would replace $R_3O_2^{\bullet}$ as a product in the generalized decomposition reaction and then would rapidly "react" with the structure species.

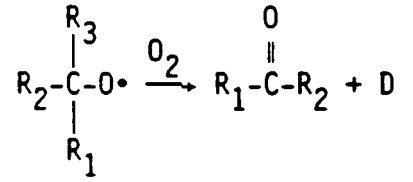

$$\text{Primary Carbon} + D \xrightarrow{+O_2} MeO_2^{\cdot}$$

$$\text{Secondary Carbon} + D \xrightarrow{+O_2} RCH_2O_2^{\cdot}$$

$$\text{Tertiary Carbon} + D \xrightarrow{+O_2} R\,R'CHO_2^{\cdot}$$

$$\text{Quartenary Carbon} + D \xrightarrow{+O_2} R\,R'\,R''CO_2^{\cdot}$$

The relative rate constants would reflect the minor modifications. As noted, quartenary carbon is rare (about 1 percent of typical atmospheric mix, see Table 4-1) and could be neglected. The C-C bond strength of primary carbon is apparently greater than that of secondary or tertiary carbon, so the rate of the first reaction is relatively low.

For ketones, the carbonyl group adjacent to decomposition will result in a peroxyacyl radical, as previously noted. Thus

$$\text{Ketone} + D \xrightarrow{+O_2} RCO_3^{\cdot} \quad .$$

Upon later parameterization of these reactions to stoichiometric yields (parameterization accomplished by assuming that intramolecular reactions take place instantaneously), the "D" species will drop out of the calculations and standard reaction stoichiometrics will result.

Nitrate Formation from Alkanes

Nitrate formation from alkane/NO_x systems has been extensively discussed by Atkinson et al. (1982b, 1983, and 1987). We briefly summarize their observations here. Alkyl nitrate yields in alkane-NO_x photooxidation indicate that

$$RO_2\cdot + NO \rightarrow RONO_2$$

is an important source of alkyl nitrates when R contains three or more carbon atoms (Darnall et al., 1976). In their experimental investigation of these reactions, Atkinson et al. (1982b; 1983) showed that the alkyl nitrate yields from the reaction of NO with the peroxy radical from a specific alkane were the same regardless of (1) the time scale of the

experiment, (2) whether the experiment was conducted in the SAPRC evacuable chamber, large teflon bag chambers, or small (~ 100 liter) teflon bag chambers, and (3) whether the peroxy radicals were generated from NO_x-air, CH_3ONO-NO_x-air, or C_{12}-NO_x-air photolyses. These findings indicate that heterogeneous formation of alkyl nitrates is extremely unlikely. Furthermore, there was no observable induction period for their formation, indicating that they are closely associated with primary products from the initial attack by OH on the alkane.

The alkyl nitrate yields at 740 torr and 300 K have been determined for the n-alkanes (ethane through n-octane), and monotonically increase from less than about 0.014 for ethane to 0.33 for n-octane (Atkinson et al., 1982b). A plot of the yield against carbon number (Atkinson et al., 1982b) indicates a limiting nitrate yield of about 0.35 for the higher alkanes. Assuming that all the n-alkanes have the same limiting high-pressure alkyl nitrate yields, these data, along with temperature and pressure effect data for pentyl and heptyl nitrates (Atkinson et al., 1983), can be fit with an empirical, Troe-type fall-off curve. The best fit to the data results in a maximum nitrate yield of 0.38.

The increase in nitrate yield with increasing carbon number is consistent with increases in nitrate from secondary alkylperoxy reaction with NO. Tertiary alkylperoxy radicals show a low nitrate yield of about 0.04 (Atkinson and Carter, 1987) that does not seem to increase with carbon number. Nitrate from primary radicals is also low and increases more slowly than nitrate from secondary alkylperoxy radicals. The limiting nitrate yields for primary alkyl peroxy radicals may be as low as 5 percent.

The reduction in nitrate formation for primary and tertiary alkyperoxy radicals implies that chain branching has a profound effect on nitrate yields for an alkyl compound. Table 4-2 lists the calculated nitrate yields for alkanes, based on the yields from primary, secondary, and tertiary alkylperoxy yields, weighted by the fraction of hydroxyl reaction at each carbon site. The measured yields for n-alkanes are shown for comparison. It is apparent from the table that variations of as much as a factor of 4 can occur in alkyl nitrate yields for compounds with the same carbon number. A triple branched compound such as 2,3,4-trimethyl pentane might have a nitrate formation yield as low as 0.04, whereas the corresponding n-alkane (n-octane) could have a nitrate yield eight times as great. This phenomenon presents great difficulty for any molecular lumping scheme. To lump alkanes with similar carbon numbers it would be necessary to average greatly dissimilar nitrate yield molecules, whereas to lump compounds with similar nitrate yields it would be necessary to

TABLE 4-2. Calculated nitrate yields compared to measured yields for various alkanes.

	Nitrate Yields			
Carbon Number	Calculated[1]	n-alkanes	single branch alkanes	double branch alkanes
2		0.01	----	----
3		0.036	----	----
4	0.078	0.077	0.042	----
5	0.126	0.128	0.07	0.05
6	0.195	0.22	0.118	0.042
7	0.27	0.31	0.178	0.087
8	0.32	0.33	0.23	0.136

[1]Assuming 0.04 yield from tertiary and 0.05 yield from primary carbons (Carter and Atkinson, 1985); secondary carbon yields vary with carbon number (Atkinson et al., 1987); weighted by OH reactivity taken from Atkinson and Lloyd (1984) and the urban hydrocarbon mixture of Table 4-1.

average a wide range of rate constants. We do not regard the averaging of disparate nitrate yields to be a major problem, as we demonstrate in a subsequent discussion, this can be easily resolved by use of a reactive-structure lumping methodology.

Alkyl nitrate yields also show a temperature dependence that is, within experimental error, the same for all alkoxy radicals yet studied. Using data for six hydrocarbons given in Atkinson et al. (1987) and Atkinson et al. (1983), we calculated an activation energy for the nitrate reaction of 1400 K (a standard deviation of 300 K).

DEVELOPMENT OF ALKANE CHEMISTRY FOR THE CBM-X AND CBM-IV

The reactions given in Table 4-3 are a compilation of the information just presented. When added to standard inorganic, formaldehyde, acetaldehyde, and PAN chemical reactions, this reaction scheme will yield a mechanism for treating the chemistry of paraffinic carbon. Some prior condensation was performed to obtain the reactions given in Table 4-3: quartenary carbon atoms have been ignored, for example, and only one species of secondary carbon is considered, though differences in nitrate formation yields might justify additional class splitting. Nonetheless, considerably more condensation must be implemented before this alkyl carbon mechanism can be used in AQSMs. Even using quasi-steady-state approximations and variable stoichiometries to eliminate the explicit treatment of radical and operator species, the number of species in the alkyl portion of the mechanism is 14, which is large for a class of compounds that probably accounts for less than 25 percent of the atmospheric reactivity (Calvert, 1976). Therefore, we have performed the following simplifications to obtain the explicit mechanism given in Table 4-3.

Higher Molecular Weight Aldehydes

The RCHO species that represent aldehydes with carbon chain length greater than C_3 can be eliminated by using acetaldehyde as a surrogate species. Our analysis of alkoxyl decomposition pathways for the atmospheric mix of hydrocarbons given in Table 4-1 yields a 45/55 split between RCHO aldehydes and acetaldehyde, but also shows that aldehydes from olefins, especially acetaldehyde from propene and 2-olefins, will dominate the paraffin yields. Moreover, our knowledge of the chemistry of higher aldehydes does not justify separate treatment of these species. Similarly, as previously noted, our view is that current knowledge of the isomerization pathway in alkoxy radicals is not sufficient to justify the inclusion in a mechanism of either the pathways or the products.

TABLE 4-3. Explicit alkyl group chemistry.

	Reaction	Reaction Rate (ppm^{-n} min^{-1})	-E/R (K)	Notes
1	PALK + OH --> PAO_2 (+ H_2O)	290		
2	PAO_2 + NO --> PAO + NO_2	11400	250	1
3	PAO_2 + NO --> $PANO_3$	600	250	1
4	PAO --> PCOH + I	0		2, 3
5	PAO --> HO_2 + ALD	693000		4
6	SALK + OH --> SAO_2	1700		
7	SAO_2 + NO --> SAO + NO_2	8820	250	5
8	SAO_2 + NO --> $SANO_3$	3180	250	5
9	SAO --> SCOH + I	0		2, 3
10	SAO --> HO_2 + KET	150000		4
11	SAO --> ALD + D	37000	-8000	6
12	SAO --> ALD_2 + X + D	45000	-8000	6
13	TALK + OH --> TAO_2 + (H_2O)	3110		
14	TAO_2 + NO --> TAO + NO_2	11520	250	1
15	TAO_2 + NO --> $TANO_3$	480	250	1
16	TAO --> TCOH + I	0		2, 3
17	TAO --> AONE + D + X + X	59620	-8000	6
18	TAO --> KET + D	23380	-8000	6
19	D + PALK --> MEO_2	0		7
20	D + SALK --> PAO_2			8
21	D + TALK --> SAO_2			8
22	D + KET --> RCO_3			8
23	I + PALK --> PAO_2			8
24	I + SALK --> SAO_2			8
25	I + TALK --> TAO_2			8
26	X + PALK -->			8
27	C_3H_8 + OH --> PRO_2	2280		9
28	PRO_2 + NO --> NO_2 + HO_2 + AONE	11000		9
29	AONE --> MEO_2 + C_2O_3	(< 0.06 x j_{HCHOr})		9
30	AONE + OH --> ANO_2	500		9
31	ANO_2 + NO --> NO_2 + HCHO + C_2O_3	11000		9
32	RCHO --> HO_2 + CO + D			10
33	RCHO + OH --> RCO_3			10
34	RCO_3 + NO --> NO_2 + CO_2 + D			10
35	RCO_3 + NO --> RPAN			10
36	RPAN --> RCO_3 + NO_2			10
37	QALK + D --> TAO_2	0		11

(Continued)

TABLE 4-3. (Conclude)

Abbreviations

PALK	Primary alkyl carbon
SALK	Secondary alkyl carbon
TALK	Tertiary alkyl carbon
$PANO_3$	Primary alkyl nitrate
$SANO_3$	Secondary alkyl nitrate
$TANO_3$	Tertiary alkyl nitrate
PCOH	Primary alkyl alcohol
SCOH	Secondary alkyl alcohol
TCOH	Teritiary alkyl alcohol
D	Unimolecular decomposition
I	Unimolecular isomerization
X	Negative carbon bookkeeping species
C_2H_8	Propane
PRO_2	$CH_3CH_2(O_2\cdot)CH_3$
AONE	Acetone
ANO_2	$CH_2(O_2\cdot)C(O)CH_3$
RCHO	C_3 + Aldehyde
RCO_3	C_3 + Peroxyacyl
RPAN	C_3 + Peroxyacylnitrate

Notes:

1 Nitrate fraction composition independent for primary and tertiary carbon; varies for secondary alkylperoxy.
2 Recommended yield is zero; for 20 percent yield from isomerization, 0.167 = k4/k5 = k9/k10 = k12/(k13 + k14).
3 Reaction rate constant in min^{-1}.
4 Pseudo first order reaction rate assuming atmospheric concentration of O_2.
5 Nitrate formation from secondary alkylperox radicals varies from 0.04 to 0.35. Average for atmospheric mix is 0.18.
6 Rate dependent on hydrocarbon composition.
7 $C-CH_3$ bond is stable to decomposition relative to C-C bond; k19 = 0.
8 Fast reaction rate: k20 = k21 = k22; k23 = k24 = k25.
9 Explicit chemistry.
10 All rates for RCHO, RCO_3, and RPAN would be similar to those for ALD_2, C_2O_3, and PAN.
11 Quartenary carbon is less than one percent of alkyl carbon; isobutoxy radical is usually formed.

Alkyl Nitrate Products

The amount of carbon lost to alkyl nitrates is apparently fairly small. Although the molecular yields for high-carbon-number n-alkanes can be as high as 38 percent, this yield involves only a single carbon atom per molecule because the alkyl carbons in the nitrate are still available for reaction. Decomposition is apparently the predominate fate of a high-carbon-number alkane subsequent to hydroxyl abstraction, and decomposition rapidly reduces the carbon number of the alkyl group, making further alkyl nitrate formation unlikely. Studies of the kinetics of alkyl nitrates (Atkinson et al., 1982b) suggest that the C-H bond on the same carbon as a nitrate group has a low reactivity to OH abstraction. Thus, nitrated carbon can be treated as an unreactive product.

Lumping of Primary, Secondary, and Tertiary Carbon

The reactivity of OH differs greatly (260 $ppm^{-1}min$, 1700 $ppm^{-1}min^{-1}$, and 3200 $ppm^{-1}min^{-1}$, for primary, secondary, and tertiary carbon respectively; Atkinson, 1986). Usually, such a broad range of rates precludes lumping, and rate-constant averaging. However, if the number of carbons in a paraffin molecule is held constant, the various isomers possible are then related so that the total rate constant is always similar except when quartenary carbons are involved. For example, the difference between a normal alkane and a branched isomer is the loss of two secondary carbons combined with the gain of one primary carbon and one tertiary carbon; twice the secondary rate constant (2 x 1700 = 3400 $ppm^{-1}min^{-1}$) is approximately the sum of the primary and tertiary rate constants (260 + 3200 = 3460 $ppm^{-1}min$). Thus, the overall reactivity of a branched molecule is the same as that of the corresponding n-alkane.

Because the tertiary carbon oxidizes preferentially, one might expect the oxidation process to cause problems in a carbon-structure lumping scheme. However, tertiary alkoxy radicals also preferentially decompose, with acetone as a common product. The formation of acetone removes less reactive primary carbon from the alkyl pool. The formation of acetone removes a total of three carbon atoms from the overall alkyl carbon pool. If the average OH reaction rate constant of the alkyl carbon pool is about 1200 $ppm^{-1}min^{-1}$, then the three carbon loss from acetone formation would remove an equivalent to 3600 $ppm^{-1}min^{-1}$. If the alkyl carbon were divided into primary, secondary, and tertiary groups, the acetone formation would remove one tertiary carbon and two primary carbons. The rate constant total for this combustion is 3200 (for the tertiary carbon) plus 2 x 260 (for the two primary carbons) giving a total of 3740 $ppm^{-1}min$

Hence, the average rate constant of the alkyl carbon pool would not change appreciably if tertiary carbons rapidly were depleted, acetone were the major product of tertiary carbon reaction, and the overall average per alkyl carbon OH rate constant were 1200 $ppm^{-1}min^{-1}$.

To treat acetone explicitly, it is necessary to remove carbon from the alkyl group category by means of a bookkeeping species "X" (used previously in the CBM). In this case, there is simply a transfer of the carbon proportions of primary, secondary, and tertiary alkyl groups in the alkyl group pool (alkyl groups are denoted as PAR and acetone as AONE in the CBM) from one category to another. In alkoxy radical decomposition,

$$ROR \rightarrow AONE + D + 2X \quad , \qquad (X\text{-}85)$$

with X subtracting alkyl carbon from PAR:

$$X + PAR \rightarrow \quad . \qquad (X\text{-}86)$$

For the atmospheric mix of alkanes given in Table 4-1, the relative proportions of primary, secondary, and tertiary carbon are 0.47, 0.39, and 0.13 (Table 4-4). This gives an overall lumped OH reactivity per carbon atom of about 1200 ppm^{-1}.

Figure 4-1 gives a representation of the product ratios and reaction pathways of alkyl carbon subsequent to reaction with hydroxyl. Table 4-5 shows a listing of the resultling alkyl carbon (PAR) mechanism, (this is exerpted from Table 1-2, the CBM-X). The key species are listed in Table 4-6. This reaction sequence lumps secondary and tertiary alkylperoxyl (RO2R) and alkoxyl radicals (ROR) in order to reduce the number of radical species required. The nitrate formation pathway for primary carbon is separated out, since the primary alkoxy (RO2) radical is followed independently. Nitrate formation for RO2R is for lumped radical secondary and tertiary nitrate formation weighted according to the reaction proportions of each. The fraction thus derived, 0.14, can be compared to the 0.16 value computed by weighting on the basis of the fractions of secondary and tertiary carbon only. The lower fraction is preferred because the subsequent reaction of reaction products involves various species that often have lower molecular weights due to decomposition. The average nitrate formation rate of product species will therefore be lower. Thus, the initial nitrate formation rate of 0.14 is, in fact, an upper limit.

The ratios of radical production from unimolecular decomposition of the alkoxy radical ("D + PAR") are derived from the ratio of secondary and tertiary carbon and from the ratio of tertiary carbon expected to yield acetone (reaction 14) and tertiary carbon involving molecular fragments of

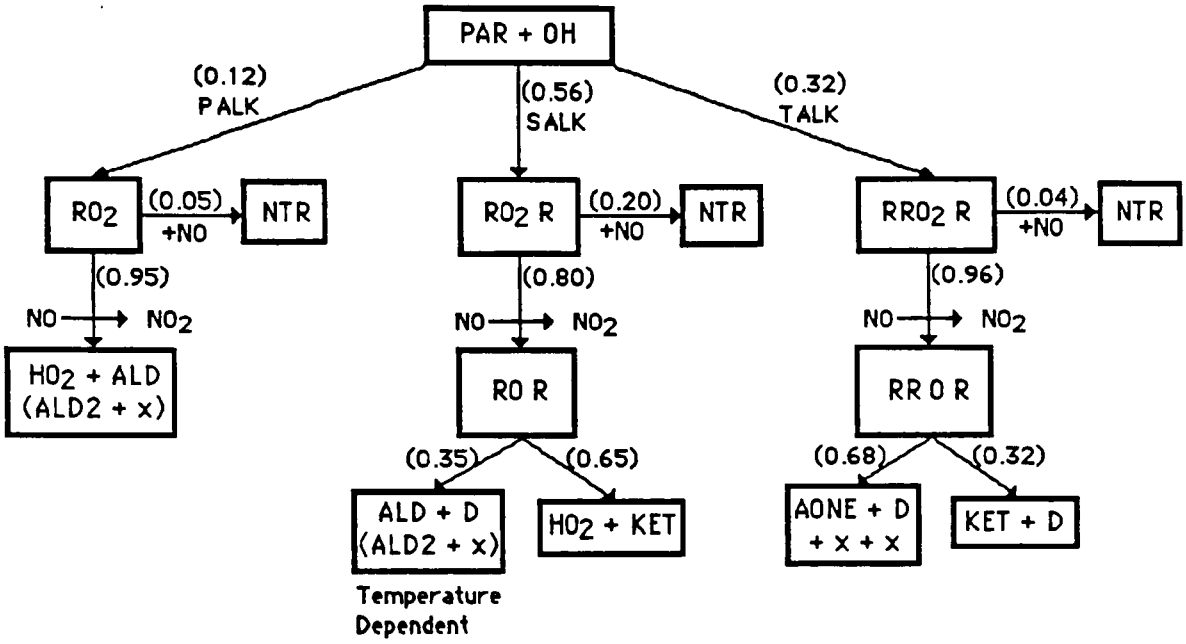

FIGURE 4-1. Schematic representation of the PAR reaction scheme.

TABLE 4-4. Carbon and bond types.

Compound (alkanes)	Concentration ERT (ppbC)	WSU (ppbC)
Isobutane	63.56	94.00
Butane	130.64	215.36
Isopentane	173.85	143.60
Pentane	76.50	94.70
2,2-Dimethybutane	0.00	0.72
Cyclopentane	0.00	14.05
2,3-Dimethlbutane	21.06	19.86
2-Methylpentane	49.62	48.66
Hexane	62.34	51.60
Methylcyclopentane	44.88	57.72
2,2,3-Trimethylbutane	2.73	0.00
2,4-Dimethylpentane	19.81	27.86
2-Methylhexane	0.00	37.03
2,3-Dimethylpentane	30.59	37.10
3-Methylhexane	45.29	48.58
Dimethylcyclopentane	13.30	34.79
2,2,4-Trimethylpentane	60.48	60.40
Heptane	32.41	42.14
Methylcyclohexane	38.57	44.59
Ethylcyclopentane	0.00	6.79
2,5-Dimethylhexane	6.72	1.12
2,4-Dimethylhexane	0.00	22.96
2,3,4-Trimethylpentane	16.72	14.08
2,3-Dimethylhexane	0.00	10.24
2-Methylheptane	0.00	38.08
3-Methylheptane	19.12	19.92
2,2,5-Trimethylhexane	10.62	16.83
Dimethylcyclohexane	0.48	0.00
Octane	14.08	21.36
Ethylcyclohexane	0.00	7.92
Nonane	10.17	13.86
Decane	29.30	10.50
Total carbon (ppbC)	972.84	1256.42
C4-C5	444.55	561.71
C6-C10	528.29	694.71

(Continued)

TABLE 4-4. (Continued)

Compound (alkanes)	Carbon Type Molecule per Hydroxyl Reactivity						
	Primary	Second-ary	Terti-ary	Quarten-ary	Total Carbon	per Molecule	per Carbon
Isobutane	3	0	1		4	3980	995.00
Butane	2	2			4	3980	995.00
Isopentane	3	1	1		5	5680	1136.00
Pentane	2	3			5	5680	1136.00
2,2-Dimethybutane	4	1		1	6	2860	476.67
Cyclopentane		5			5	8500	1700.00
2,3-Dimethlbutane	4	0	2		6	7380	1230.00
2-Methylpentane	3	2	1		6	7380	1230.00
Hexane	2	4			6	7380	1230.00
Methylcyclopentane	1	4	1		6	10200	1700.00
2,2,3-Trimethylbutane	5	0	1	1	7	4560	651.43
2,4-Dimethylpentane	4	1	2		7	9080	1297.14
2-Methylhexane	3	3	1		7	9080	1297.14
2,3-Dimethylpentane	4	1	2		7	9080	1297.14
3-Methylhexane	3	3	1		7	9080	1297.14
Dimethylcyclopentane	2	3	2		7	11900	1700.00
2,2,4-Trimethylpentane	5	1	1	1	8	6260	782.50
Heptane	2	5			7	9080	1297.14
Methylcyclohexane	1	5	1		7	11900	1700.00
Ethylcyclopentane	1	5	1		7	11900	1700.00
2,5-Dimethylhexane	4	2	2		8	10780	1347.50
2,4-Dimethylhexane	4	2	2		8	10780	1347.50
2,3,4-Trimethylpentane	5	0	3		8	10780	1347.50
2,3-Dimethylhexane	4	2	2		8	10780	1347.50
2-Methylheptane	3	4	1		8	10780	1347.50
3-Methylheptane	3	4	1		8	10780	1347.50
2,2,5-Trimethylhexane	5	2	1	1	9	7960	884.44
Dimethylcyclohexane	2	4	2		8	13600	1700.00
Octane	2	6			8	10780	1347.50
Ethylcyclohexane	1	6	1		8	13600	1700.00
Nonane	2	7			9	12480	1386.67
Decane	2	8			10	14180	1418.00

(Continued)

TABLE 4-4. (Concluded)

Compound (alkanes)	Concentration of Carbon Type (ppbC)							
	ERT				WSU			
	Primary	Secondary	Tertiary	Quartenary	Primary	Secondary	Tertiary	Quartenary
Isobutane	47.47	0.00	15.89	0.00	70.50	0.00	23.50	0.00
Butane	65.32	65.32	0.00	0.00	107.68	107.68	0.00	0.00
Isopentane	104.31	34.77	34.77	0.00	86.16	28.72	28.72	0.00
Pentane	30.60	45.90	0.00	0.00	37.88	56.88	0.00	0.00
2,2-Dimethybutane	0.00	0.00	0.00	0.00	0.48	0.12	0.00	0.12
Cyclopentane	0.00	0.00	0.00	0.00	0.00	14.05	0.00	0.00
2,3-Dimethlbutane	14.04	0.00	7.02	0.00	13.24	0.00	6.62	0.00
2-Methylpentane	24.81	16.54	8.27	0.00	24.33	16.22	8.11	0.00
Hexane	20.78	41.56	0.00	0.00	17.20	34.40	0.00	0.00
Methylcyclopentane	7.48	29.92	7.48	0.00	9.62	38.48	9.62	0.00
2,2,3-Trimethylbutane	1.95	0.00	0.39	0.39	0.00	0.00	0.00	0.00
2,4-Dimethylpentane	11.32	2.83	5.66	0.00	15.92	3.98	7.96	0.00
2-Methylhexane	0.00	0.00	0.00	0.00	15.87	15.87	5.29	0.00
2,3-Dimethylpentane	17.48	4.37	8.74	0.00	21.20	5.30	10.60	0.00
3-Methylhexane	19.41	19.41	6.47	0.00	20.82	20.82	6.94	0.00
Dimethylcyclopentane	3.80	5.70	3.80	0.00	9.94	14.91	9.94	0.00
2,2,4-Trimethylpentane	37.80	7.56	7.56	7.56	37.75	7.55	7.55	7.55
Heptane	9.26	23.15	0.00	0.00	12.04	30.10	0.00	0.00
Methylcyclohexane	5.51	27.55	5.51	0.00	6.37	31.85	6.37	0.00
Ethylcyclopentane	0.00	0.00	0.00	0.00	0.97	4.85	0.97	0.00
2,5-Dimethylhexane	3.36	1.68	1.68	0.00	0.56	0.28	0.28	0.00
2,4-Dimethylhexane	0.00	0.00	0.00	0.00	11.48	5.74	5.74	0.00
2,3,4-Trimethylpentane	10.45	0.00	6.27	0.00	8.80	0.00	5.28	0.00
2,3-Dimethylhexane	0.00	0.00	0.00	0.00	5.12	2.56	2.56	0.00
2-Methylheptane	0.00	0.00	0.00	0.00	14.28	19.04	4.76	0.00
3-Methylheptane	7.17	9.56	2.39	0.00	7.47	9.96	2.49	0.00
2,2,5-Trimethylhexane	5.90	2.36	1.18	1.18	9.35	3.74	1.87	1.87
Dimethylcyclohexane	0.12	0.24	0.12	0.00	0.00	0.00	0.00	0.00
Octane	3.52	10.56	0.00	0.00	5.34	16.02	0.00	0.00
Ethylcyclohexane	0.00	0.00	0.00	0.00	0.99	5.94	0.99	0.00
Nonane	2.26	7.91	0.00	0.00	3.08	10.78	0.00	0.00
Decane	5.86	23.44	0.00	0.00	2.10	8.40	0.00	0.00
Carbon Fraction:	0.47	0.39	0.13	0.01	0.46	0.41	0.12	0.01
C4-C5	0.56	0.33	0.11	0.00	0.54	0.37	0.09	0.00
C6-C10	0.40	0.44	0.14	0.02	0.39	0.44	0.15	0.01

TABLE 4-5. Alkyl group chemistry of the Carbon Bond Mechanism-X.

Number	Reaction	A	$e^{((-E/R)/T)}$	k_{298}
1)	PAR + OH -----> RO2	1.360 E+02		1.360 E+02
2)	PAR + OH -----> RO2R	1.067 E+03		1.067 E+03
3)	RO2 + NO -----> NO2 + HO2 + ALD2 + X	1.140 E+04		1.140 E+04
4)	RO2 + NO -----> NTR	6.584 E+04	*EXP(- 1400/T)	6.000 E+02
5)	RO2R + NO -----> NO2 + ROR	1.033 E+04		1.033 E+04
6)	RO2R + NO -----> NTR	1.836 E+05	*EXP(- 1400/T)	1.673 E+03
7)	ROR + NO2 -----> NTR	2.200 E+04		2.200 E+04
8)	ROR -----> KET + HO2	9.546 E+04		9.546 E+04
9)	ROR -----> KET + D	1.236 E+16	*EXP(- 8000/T)	2.706 E+04
10)	ROR -----> ALD2 + D + X	2.394 E+16	*EXP(- 8000/T)	5.250 E+04
11)	ROR -----> AONE + D + 2.00X	2.621 E+16	*EXP(- 8000/T)	5.749 E+04
12)	X + PAR ----->	1.000 E+04		1.000 E+04
13)	D + PAR -----> RO2	7.500 E+03		7.500 E+03
14)	D + PAR -----> AO2 + 2.00X	2.250 E+03		2.250 E+03
15)	D + PAR -----> RO2R	2.500 E+02		2.500 E+02
16)	D + KET -----> C2O3 + X	1.000 E+04		1.000 E+04
17)	AO2 + NO -----> NO2 + AONE + HO2	1.200 E+04		1.200 E+04
18)	KET -hν2-> C2O3 + RO2 + 2.00X	6.000 E-02		6.000 E-02

TABLE 4-6. Species involved in the oxidation of paraffin.

Symbol	Definition
PAR	1-Carbon paraffin group
RO_2	Primary alkyl peroxy radical with C<4
RO_2R	See text--alkyl peroxy and long-chain radicals
ROR	Alkoxyl radicals
KET	Ketones other than acetone
AONE	Acetone
D	Fictitious species to account for alkoxyl radical decomposition and isomerization
AO2	Peroxy isopropyl radical
X	Fictitious steady-state species to maintain carbon balance
NTR	Organic nitrate

C_4 or greater in our assumed atmospheric mix. The sum of paraffinic decomposition involvement is the same as the ketone rate since the alkyl carbon represents several combined pathways.

Condensation of the CBM-X Alkyl Chemistry for CBM-IV

The CBM-X alkyl reaction sequence presented in Table 4-5 is still too large for inclusion in a condensed mechanism such as the CBM-IV. We have therefore performed a number of condensation steps ranging from simple bookkeeping to formulations requiring rather extensive conditional testing to verify their impacts:

(1) Elimination of species X through the use of negative stoichiometry. Since X was a mass balance counter that rapidly removed PAR to conserve carbon, the production of X, as in

$$\text{ROR} \longrightarrow \text{AONE} + \text{D} + 2\text{X} \quad ,$$

can be changed to

$$\text{ROR} \longrightarrow \text{AONE} + \text{D} - 2\text{PAR} \quad .$$

(2) The mechanism can be abbreviated through the use of fixed stoichiometry reaction combinations; e.g., the temperature-dependent ROR reactions can be condensed to

$$\text{ROR} \longrightarrow \text{D} + 0.198\ \text{KET} + 0.383\ \text{ALD2} + 0.419\ \text{AONE} - 1.222\ \text{PAR} \quad ,$$

with a combined decomposition rate at a temperature dependence (-E/R) of -8000K.

(3) We created a second operator (XO2N) similar to XO2 (see the ICRS condensation discussion) to account for the formation of a nitrate from the reaction of NO with a peroxy radical. For example, the reaction set of

$$\text{PAR} + \text{OH} \longrightarrow \text{RO2R} \qquad \text{(X-76)}$$

$$\text{RO2R} + \text{NO} \longrightarrow \text{NO2} + \text{ROR} \qquad k_{298} = 10330\ \text{ppm}^{-1}\text{min}^{-1} \qquad \text{(X-79)}$$

$$\text{RO2R} + \text{NO} \longrightarrow \text{NTR} \qquad k_{298} = 1673\ \text{ppm}^{-1}\text{min}^{-1} \qquad \text{(X-80)}$$

can be written using the earlier XO2 ≡ NO→NO_2 operator or as

PAR + OH ------> 0.86 XO2 + 0.86 ROR + 0.14 XO2N ,

where XO2N is defined through the reaction

XO2N + NO ------> (NTR) . (80)

Thus, using some previous condensations (X ≡ -PAR, XO2 ≡ NO→NO_2, and XO2N ≡ NO→NTR), and an assumption that the alkyl nitrate yields are approximated by the 298 K ratios, we can reduce the initial six reactions of Table 4-5 to one:

PAR + OH ------> 0.871 XO2 + 0.107 HO2 + 0.107 ALD2
+ 0.129 XO2N + 0.764 ROR - 0.107 PAR ,

with a combined k_{OH} of 1203 $ppm^{-1}min^{-1}$.

(4) Acetone (AONE) and ketone (KET) are slowly formed products of alkane chemistry. In addition, the photolytic and reaction losses (with OH) are relatively slow (Atkinson and Lloyd, 1984). For acetone, the central carbon is unable to enter into hydroxyl reaction; therefore, we find the representation of the molecule as 2 PAR to be satisfactory. This results in alteration of product representations; for instance, the ROR reaction just discussed as an example of X elimination

ROR ------> AONE + D - 2PAR ,

is now

ROR ------> D ,

and

AO2 + NO ------> NO2 + HO2 + AONE

is now

AO2 + NO ------> NO2 + HO2 + 2PAR .

The production of AO2 in the reaction

D + PAR ------> AO2 + 2X

can be changed (using the X ≡ -PAR and XO2 ≡ NO→NO2 plus products condensations) to

D + PAR ------> XO2 + HO2 .

For ketones, recall that KET represents the carbonyl carbon that forms when a secondary or tertiary alkoxy radical stabilizes through loss of a radical. The forementioned treatment of acetone assumes no reactivity for this carbon. Simulation results indicate that the mass throughput rates for the two KET reactions are small; i.e., always at least two orders of magnitude less than the D + PAR reactions. Therefore, we eliminate the product KET and eliminate KET photolysis and OH reactions from the CBM-IV.

(5) We can now eliminate D since the elimination of KET allows D to be an operator on PAR only through three non-temperature-dependent reactions:

$$\text{D + PAR} \longrightarrow \text{RO2} \quad ,$$
$$\text{D + PAR} \longrightarrow \text{XO2 + HO2} \quad ,$$
$$\text{D + PAR} \longrightarrow \text{RO2R} \quad .$$

We have already used the XO2 and XO2N condensations for RO2 and RO2R in condensing the initial PAR reactions, and we can use similar product splits to combine these reactions into

$$\text{D + PAR} \longrightarrow 0.959\ \text{XO2} + 0.938\ \text{HO2} + 0.713\ \text{ALD2} + 0.041\ \text{XO2N} + 0.022\ \text{ROR} - 0.713\ \text{PAR} \quad .$$

Since D is an operator with an instantaneous reaction rate, the formation of D removes a PAR and instantly forms the D + PAR products. Hence, the "product" D can be replaced by the D + PAR products minus an additional PAR.

$$\text{D} \equiv 0.959\ \text{XO2} + 0.938\ \text{HO2} + 0.713\ \text{ALD2} + 0.041\ \text{XO2N} + 0.022\ \text{ROR} - 1.713\ \text{PAR} \quad .$$

When substituted into the CBM-X reaction scheme, these condensations result in the CBM-IV alkane machanism:

$$\text{PAR + OH} \longrightarrow 0.87\ \text{XO2} + 0.13\ \text{XO2N} + 0.11\ \text{HO2} + 0.11\ \text{ALD2} + 0.76\ \text{ROR} - 0.11\ \text{PAR} \qquad (52)$$

$$ROR \text{ ------> } 1.10\ ALD2 + 0.96\ XO2 + 0.94\ HO2 + 0.04\ XO2N + 0.02\ ROR - 2.10\ PAR \quad (53)$$

$$ROR \text{ ------> } HO2 \quad (54)$$

$$ROR + NO2 \text{ ------> } \quad (55)$$

The temperature-dependent reaction rates are given in Table 1-3.

OLEFIN AND ETHENE CHEMISTRY

As noted previously, ethene is treated explicitly in the CBM-X and very reactive olefins with alkyl substitutions of 2 or more are treated as surrogate aldehyde and ketones. We treat the remaining class of olefins, monoalkylates (1-olefins), on a reactive structure basis, often using propene chemistry as a model. From a theoretical standpoint, the advantage of the reactive structure approach for olefins is mass conservation. In the CBM-X, as in earlier versions of the CBM, the additional alkyl groups of three carbons and greater are accounted for. We first discuss the treatment of 1-olefins, followed by a discussion of the explicit ethene chemistry.

Olefins are a rather reactive class of hydrocarbons found in the atmosphere. These species are generally involved in atmospheric chemistry during all periods of the day since their structure allows attack by at least four important oxidizing species (O_3, OH, O, and NO_3). These reactions are all treated in the CBM for terminal olefins (1-olefins, designated OLE).

$O(^3P)$-OLE Chemistry

The gas-phase reactions of O and olefins have been studied for over 30 years, yet their chemistry under atmospheric conditions is still somewhat uncertain. On the basis of their review of earlier data, Atkinson and Lloyd (1984) suggest the following scheme for propene:

$$O + CH_3CH{=}CH_2 \text{ ---> } CH_3\overset{O}{\overset{/\ \backslash}{CH}}{-}CH_2 \quad \text{(30 percent)}$$

$$\text{---> } CH_3CH_2CHO \quad \text{(30 percent)}$$

$$\text{---> } (H\dot{C}O + CH_3CH_2{\cdot}) \quad \text{(20 percent)}$$

$$\text{--->} \quad (CH_2{=}CHO^{\cdot} + CH_3^{\cdot}) \qquad \text{(20 percent)}$$

As a point of comparison, the 1-butene yields were found to be 44, 39, 0, and 17 percent, with an uncertainty of up to about 20 percent. In our formulation of the OLE plus O reaction scheme, we use the following splits:

OLE + O ------> 2 PAR	35%	(X-93)
OLE + O ------> ALD2	35%	(X-94)
OLE + O ------> HO2 + CO + RO2	10%	(X-95)
OLE + O ------> RO2 + X + CO + FORM + OH	20%	(X-96)

The epoxide product is represented by the reactivity of 2PAR (based on the k_{OH} calculations of Winer et al. (1978) cited in Atkinson and Lloyd, 1984). ALD2 is used to represent higher aldehydes, and the products of the third reaction are simply represented in the CBM by assuming exclusive reaction of the formyl radical with O_2. We assume that the vinoxy radical ($CH_2{=}CHO^{\cdot}$) reacts exclusively with O_2 to yield the products shown, with RO2 + X representing the formation of a peroxy radical from the remaining carbon in the chain. In their review of kinetic data, Atkinson and Lloyd (1984) recommend

$$k(56) = 1.756 \times 10^4 \exp(-324/T) \text{ ppm}^{-1}\text{min}^{-1}$$

and

$$k(56)_{298} = 5.92 \times 10^3 \text{ ppm}^{-1}\text{min}^{-1} \quad .$$

For the CBM-X, these rates have been partitioned into the reactions just given.

OH-OLE Chemistry

The general reaction scheme for the OH radical addition to the OLE group has been fairly well understood since the FTIR work of Niki et al. (1978). Briefly, OH is assumed to add to either carbon in the OLE group. Abstraction of non-OLE hydrogens (as described by Atkinson and Lloyd, 1984) is handeled in the PAR chemistry. Since terminal olefins are a special subset of the alkenes, two parallel reaction sets can be followed, depending on the initial addition site:

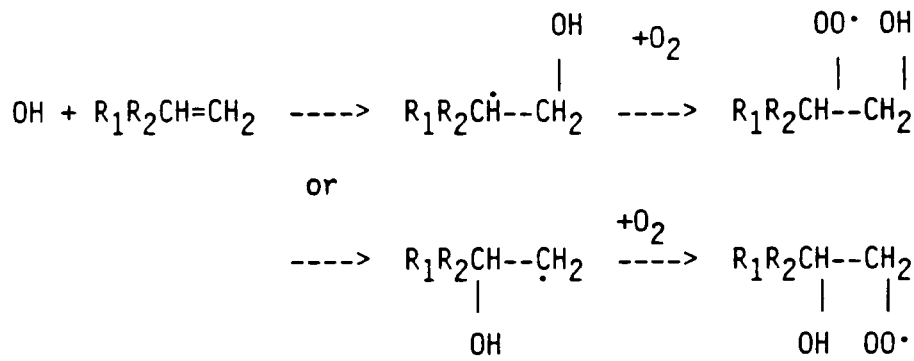

Both peroxy radicals are expected to react with atmospheric NO to form NO_2 and an oxy radical. Decomposition of both radicals through the loss of the hydroxyl hydrogen to atmospheric oxygen (forming $HO_2\cdot$) and the severing of the original olefin sigma bond forms two aldehyde groups at the point of cleavage. For these molecules, the products resulting after $NO \rightarrow NO_2$ conversion, regardless of the initial OH addition site, are

$$R_1R_2CHO + HCHO + HO_2\cdot \quad .$$

Therefore, the CBM-X formulation for OH reaction with a terminal olefin group is

$$OH + OLE \text{ ------> } MEO2 + ALD2 + X \quad , \qquad (X\text{-}97)$$

ALD2 + X describes the -CHO end of a longer chain hydrocarbon whose chemistry is represented by other carbon bond groups, and MEO2 oxidizes NO to NO_2 to form HO2 and FORM.

The kinetic expressions used in the CBM-X are

$$k(57) = 7.740 \times 10^3 \exp(504/T) \text{ ppm}^{-1}\text{min}^{-1} \quad ,$$

and

$$k(57)_{298} = 4.20 \times 10^4 \text{ ppm}^{-1}\text{min}^{-1} \quad .$$

The temperature dependence used is from the review of Atkinson (1986). We use a slightly higher k_{298} value than is suggested therin (38870 $\text{ppm}^{-1}\text{min}^{-1}$), which is easily within the stated uncertainty of 15 percent.

Ozone-Olefin Chemistry

Olefins are unique in their atmospheric reactivity to ozone since other common organics do not react with ozone at significant rates. The chemistry of the ozone-olefin system has been extensively investigated over

the past decade, but has yet to be clearly delineated. Although the secondary reactions are not as uncertain as those of aromatic hydrocarbons, there is much speculation about the tropospheric chemistry of Criegee (biradical) species formed during intermediate reactions. For a more complete discussion, the reader is advised to consult the reviews of Atkinson and Lloyd (1984), Atkinson and Carter (1984), and Kerr and Calvert (1985), keeping in mind that the OLE species represents terminal olefinic groups.

The reaction rate data used for O3 plus OLE in the CBM are

$$k(58) = 2.104 \times 10^{1} \exp(-2105/T)\ ppm^{-1}min^{-1} \quad ,$$

and

$$k(58)_{298} = 1.80 \times 10^{-2}\ ppm^{-1}min^{-1} \quad .$$

The temperature dependence is from the review of Atkinson and Carter (1984) and the k_{298} value is well within their stated uncertainty.

Ozone adds to terminal olefins at the pi bond of the olefin, initially forming a 3-oxygen bridge known as a molozonide which rapidly rearranges to an ozonide and decomposes. Ozonide decomposition apparently results in formation of an aldehyde and a biradical product. Following the recommendations of Atkinson and Lloyd, we assume an equal split of ozonide cleavage channels:

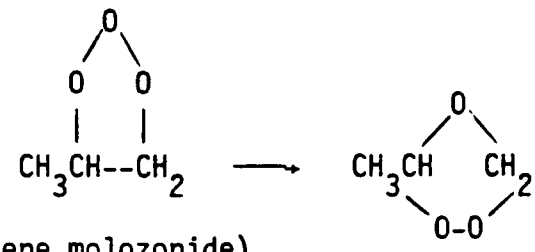

(propene molozonide) (propylene ozonide)

$$\longrightarrow HCHO + [CH_3\dot{C}OO\cdot] \qquad 50\%$$

$$+ [H_2\dot{C}OO\cdot] + CH_3CHO \qquad 50\%$$

in which the biradical species are initially formed with excess energy. Following the work of Herron and Huie (1978), Niki et al., (1977), Su et al. (1980), and Kan et al. (1981), we assume that approximately 40 percent of the biradical products are thermalized in the atmosphere while the remaining 60 percent may rearrange and decompose to smaller products. In the CBM-X, we describe these pathways with

O3 + OLE ------> ALD2 + CRIG + X	20%	(X-98)
O3 + OLE ------> FORM + MCRG + X	20%	(X-99)
O3 + OLE ------> ALD2 + HOTA + X	30%	(X-100)
O3 + OLE ------> FORM + HTMA + X	30%	(X-101)

where half of the O3 + OLE mass passes through reactions 98 plus 100 and 99 plus 101. A 40:60 ratio exists between reactions 98 plus 99 and 100 plus 101: The first set forms the stabilized biradicals (CRIG ≡ $CH_3\dot{C}OO^{\cdot}$ and MCRG ≡ $CH_3\dot{C}OO^{\cdot}$) and the lower two reactions represent the formation of intermediate "hot" formic and acetic acids, which rapidly decompose via (using fractions from Dodge and Arnts, 1979):

HOTA ------> (CO2 + H2)	20%	(X-112)
HOTA ------> CO (+H2O)	70%	(X-113)
HOTA ------> 2 HO2 (+ CO2)	10%	(X-114)

and

HTMA ------> (CH4 + CO2)	20%	(X-115)
HTMA ------> MEO2 + CO + OH	32%	(X-116)
HTMA ------> MEO2 + HO2 (+ CO2)	32%	(X-117)
HTMA ------> 2 HO2 + CO + FORM	8%	(X-118)
HTMA ------> MEO2 + HO2 (+ CO2)	8%	(X-119)

We used the review by Kerr and Calvert (1985) to obtain a compilation of the most likely reactions of the stabilized biradicals. Ignoring the possible reaction with NO_2 (k_{298} = 150 $ppm^{-1}min^{-1}$) the reaction sets are:

CRIG + NO ------> NO2 + FORM	k_{298} = 10350	(X-120)
CRIG + H2O ------> FACD + H2O	k_{298} = 0.59	(X-121)
CRIG + FORM ------> OZD	k_{298} = 2950	(X-122)
CRIG + ALD2 ------> OZD	k_{298} = 2950	(X-123)

and

MCRG + NO ------> NO2 + ALD2	k_{298} = 10350	(X-124)
MCRG + H2O ------> ACAC + H2O	k_{298} = 0.59	(X-125)
MCRG + FORM ------> OZD	k_{298} = 2950	(X-126)
MCRG + ALD2 ------> OZD	k_{298} = 2950	(X-127)

NO_3-OLE Chemistry

The kinetic data for the reaction of NO_3 plus the OLE group are given in Atkinson and Lloyd (1984), but were calculated using the N_2O_5 equilibrium constant of Malko and Troe (1982). We now believe the use of this value, when compared to the data presented in the ICRS section, leads to an undercalculation of k_{298} by a factor of 1.83. Therefore, we have converted the rate suggested by Atkinson and Lloyd by that factor to yield the temperature-independent rate of

$$k(59) = 1.135 \times 10^{1}\ ppm^{-1}min^{-1} \quad .$$

Experimental evidence indicates the addition of NO_3 to the OLE bond, primarily at the 1-position. Following that channel for discussion purposes, oxygen should add to the initial adduct to form a peroxy racical:

$$NO_3 + R_1R_2C{=}CH_2 \text{ ----> } R_1R_2\dot{C}\text{-}CH_2ONO_2 \xrightarrow{+O_2} R_1R_2C(OO^{\bullet})\text{-}CH_2ONO_2 \quad .$$

Reaction with NO to form NO2 or disproportionation with HO_2 should lead to formation of an oxy radical structure under atmospheric conditions, though formation of a dinitrate species can also occur:

$$R_1R_2C(OO^{\bullet})\text{-}CH_2ONO_2 + NO \text{ ----> } NO_2 + R_1R_2C(O^{\bullet})\text{-}CH_2ONO_2$$

$$\text{----> } R_1R_2C(ONO_2)\text{-}CH_2ONO_2 \qquad \text{(minor pathway)}$$

Decomposition of the oxy radical could lead to the lower molecular weight products observed by Bandow and coworkers (as referenced in Atkinson and Lloyd, 1984) in their propene study ($R_1 = CH_3$ and $R_2 = H$):

$$CH_3C(O^{\bullet})H\text{-}CH_2ONO_2 \text{ ----> } CH_3CHO + HCHO + NO_2 \quad .$$

It can be shown that NO_3 addition to the 2-position would yield the same products; therefore, in the CBM-X these reactions are represented by

NO3 + OLE ------> PNO2		(X-102)
PNO2 + NO ------> DNIT		(X-103)
PNO2 + NO ------> FORM + ALD2 + X + 2 NO_2		(X-104)

Ethene (ETH) chemistry is explicitly represented in the CBM because ethene is generally the most abundant olefin, and its chemistry is sufficiently unlike generalized OLE chemistry to warrent individual consideration. The main differences are that its initial oxidation reactions are much slower

than higher molecular weight olefins, and because of its C_2 structure, it will not form PAN as an oxidation product. The specific chemistry of ethene is presented in reactions 105 through 111 of the CBM-X (Table 1-2).

$O(^3P)$-ETH Chemistry

The kinetic data for this reaction (60) are taken from Atkinson and Lloyd (1984) and represent the sum of X-105 and X-106:

$$k(60) = 1.540 \times 10^4 \exp(-792/T) \text{ ppm}^{-1}\text{min}^{-1}$$

and

$$k(60)_{298} = 1080 \text{ ppm}^{-1}\text{min}^{-1} \quad .$$

Unlike the higher molecular weight olefins, ethene does not appear to form stable epoxide products. The assumed product distribution used in the CBM-X is based on the review by Atkinson and Lloyd (1984) and the recent data of Smalley et al. (1986). We use

$$O + C_2H_4 \quad \text{--->} \quad (H\dot{C}O + CH_3\cdot) \qquad 70 \text{ percent}$$

$$\text{--->} \quad (CH_2{=}CHO\cdot + H\cdot) \qquad 30 \text{ percent}$$

Assuming rapid reaction of H· with molecular oxygen and the product chemistry discussed in the O plus OLE section, we represent this chemistry in the CBM-X by

O + ETH ------> MEO2 + CO + HO2 (X-105)

O + ETH ------> HO2 + OH + FORM + CO (X-106)

OH-ETH Chemistry

The kinetic expression for the hydroxyl radical-ethene reaction (61) has been updated to one given by Atkinson (1986):

$$k(61) = 3.000 \times 10^3 \exp(411/T) \text{ ppm}^{-1}\text{min}^{-1}$$

and

$$k(61)_{298} = 1.19 \times 10^4 \text{ ppm}^{-1}\text{min}^{-1} \quad .$$

These values are very close to those of earlier CBM expressions.

The detection of glyocaldehyde as a product of the OH-ethene reaction (Niki et al., 1981) has led to a redevelopment of the reaction mechanism to include that species. Initially, hydroxyl radical is expected to add to ETH, forming a peroxy radical in the atmosphere in a mechanism analogous to that described for OLE:

$$OH + H_2C{=}CH_2 \;\text{---->}\; \begin{array}{c} HO \\ | \\ H_2C\text{--}\dot{C}H_2 \end{array} \xrightarrow{+O_2} \begin{array}{c} HO\;\;OO^{\bullet} \\ |\;\;\;\;| \\ H_2C\text{--}CH_2 \end{array} .$$

In the case of ethene, however, the oxy radical formed from oxidation of NO to NO_2 (for example) can decompose to form two sets of products:

$$\begin{array}{c} HO\;\;OO^{\bullet} \\ |\;\;\;\;| \\ H_2C\text{--}CH_2 \end{array} + NO \;\text{---->}\; NO_2 + \begin{array}{c} HO\;\;O^{\bullet} \\ |\;\;\;\;| \\ H_2C\text{--}CH_2 \end{array}$$

and

$$\begin{array}{c} HO\;\;O^{\bullet} \\ |\;\;\;\;| \\ H_2C\text{--}CH_2 \end{array} \xrightarrow{+O_2} 2\ HCHO + HO_2^{\bullet} \qquad 78 \text{ percent}$$

$$\xrightarrow{+O_2} \begin{array}{c} HO\;\;O \\ |\;\;\;\;| \\ H_2C\text{--}CH \end{array} + HO_2^{\bullet} \qquad 22 \text{ percent}$$

This set of reactions is represented in the CBM-X by

OH + ETH ------> ETO2		(X-107)
ETO2 + NO ------> NO2 + 2 FORM + HO2		(X-108)
ETO2 + NO ------> NO2 + ALD2 + HO2		(X-109)

Ozone-ETH Chemistry

The rate expression used in the CBM-X for the ozone plus ethene reaction (62) is the sum of reactions X-110 plus X-111:

$$k(62) = 1.856 \times 10^{1} \exp(-2633/T)\ ppm^{-1}min^{-1}$$

and

$$k(62)_{298} = 2.70 \times 10^{-3}\ ppm^{-1}min^{-1} \quad .$$

The temperature dependence used is from Atkinson and Carter (1984); the $k(60)_{298}$ value is within the experimental error determination of that review.

The reaction mechanism has received much experimental attention in recent years. These data are summarized by Atkinson and Lloyd (1984). The overall CBM mechanism follows the reaction scheme given for O_3 plus OLE,

except that the symmetry of ethene simplifies the secondary reaction pathways. Therefore, we have

$$O_3 + H_2C{=}CH_2 \text{ ----> } HCHO + [\dot{C}H_2OO\cdot] \quad ,$$

where we again assume a 40:60 split between the thermalized biradical and the decomposing species. In terms of the CBM-X, this is given by

O3 + ETH ------> HCHO + CRIG (X-110)

and

O3 + ETH ------> HCHO + HOTA (X-111)

The reactions of the CRIG and HOTA species have been given previously.

Condensation of the CBM-X OLE and ETH Mechanisms to CBM-IV

The condensation of these CBM-X reactions to a CBM-IV scheme primarily involves a simple algebraic combination of reactions to obtain fewer reactions with fractional stoichiometries. Some steady-state assumptions, such as use of the XO2 and XO2N operators, are employed.

The O plus OLE reactions are easily combined using X ≡ -PAR to yield

O + OLE ------> 0.35ALD2 + 0.50PAR + 0.30CO
+ 0.20FORM + 0.20OH + 0.10HO2
+ 0.30RO2

Assuming the steady-state RO2 assumption used for PAR condensation,

O + OLE ------> 0.63ALD2 + 0.22PAR + 0.30CO
+ 0.20FORM + 0.20OH + 0.38HO2
+ 0.28XO2 + 0.02XO2N (56)

The OH plus OLE reaction is condensed using the MEO2 steady-state assumption (MEO2 ≡ XO2 + FORM + HO2) and -PAR for X:

OH + OLE ------> ALD2 - PAR + FORM + XO2 + HO2 (57)

The O_3 plus OLE reactions can initially be combined using X ≡ -PAR to:

O3 + OLE ------> 0.50ALD2 + 0.50FORM - PAR
+ 0.20CRIG + 0.20MCRG
+ 0.30HOTA + 0.30HTMA

Under most atmospheric conditions, the transformation of thermalized biradicals (CRIG and MCRG) to organic acids in the presence of water vapor should be the dominant reaction. The rate constants given in Table 1-2 are very uncertain, however, and better measurements are needed to add certainty to such an assumption. Since this set of reactions appears to be dominant, the biradical products can be replaced by their respective acids; and because these acids are rather stable in the atmosphere, we do not treat their chemistry in the CBM-IV. The "hot" rearranged biradicals are assumed to decompose in the proportions given in reactions 112 through 119 of Table 1-2. These assumptions lead to

$$\begin{aligned} O3 + OLE \text{ ------> } & 0.50ALD2 + 0.74FORM - PAR \\ & + 0.44HO2 + 0.33CO + 0.22XO2 \\ & + 0.10OH \end{aligned} \tag{58}$$

The NO_3 plus OLE reaction is condensed using the XO2 and XO2N operators to eliminate PNO2. Also, -PAR is substituted for X and DNIT is assumed to be stable and thus is not followed in the CBM-IV. The reaction is

$$\begin{aligned} NO3 + OLE \text{ ------> } & 0.91XO2 + 0.09XO2N + FORM + ALD2 \\ & + NO2 - PAR \quad . \end{aligned} \tag{59}$$

If the assumption that MEO2 ≡ FORM + HO2 + XO2 is made, the O plus ETH reaction can be condensed to the sum of reactions 105 and 106 of the CBM-X:

$$\begin{aligned} O + ETH \text{ ------> } & 1.70HO2 + CO + FORM + 0.70XO2 \\ & + 0.30OH \quad . \end{aligned} \tag{60}$$

ETO2 can be eliminated from the OH plus ETH reaction using the XO2 assumption:

$$OH + ETH \text{ ------> } XO2 + 1.56FORM + 0.22\ ALD2 + HO2 \quad . \tag{61}$$

Finally, the O_3 plus ETH reaction can be condensed using the same assumptions as in the O_3 plus OLE condensation:

$$O3 + ETH \text{ ------> } FORM + 0.42CO + 0.12HO2 \quad . \tag{62}$$

AROMATIC CHEMISTRY

The OH-plus-aromatic reaction mechanisms have been the focus of experiments and modeling investigations for over a decade (Atkinson et al., 1980; Killus and Whitten, 1982b; Leone and Seinfeld, 1984). Because of recent advances in analytical equipment, considerable effort has been

directed toward identification of aromatic ring fragmentation species, especially the larger, conjugated α- and γ-dicarbonyl products (Dumdei and O'Brien, 1984; Shepson et al., 1984). However, experimental studies that attempt to track all of the reacted aromatic carbon have been unable to account for more than a fraction of the reacted carbon atoms in dicarbonyl products. This is especially true for toluene. Hence, a large portion of the secondary product mass has yet to be confidently identified, probably because of the many branching and isomeric pathways involved in the complex photooxidation of aromatics and secondary products. Representation of this missing mass has caused a dilema for atmospheric chemists, who have generally proposed greater yields of the detected dicarbonyl products in place of the unidentified products. Judging from the relatively poor agreement of simulation results with smog chamber data, however, use of the highly reactive dicarbonyl species to account for all of the carbon known to have reacted appears to provide overly reactive mechanisms. Such an inconsistency is especially obvious if the undetected species have significantly different structures, reactivity, or chemical functions than do the surrogate α- and γ-dicarbonyl species in the models (as appears to be the case for toluene).

The development of aromatic reaction schemes is a formidable task in that available smog chamber data is useful, but severely limited. Existing data must be carefully analyzed so that consideration of only a few marginal experiments does not yield misleading conclusions. A large number of individual experiments for toluene have been performed in the UNC dual outdoor smog chambers and the UCR evacuable chambers (EC); however, most UNC experiments were performed on days with non-ideal light conditions, while the EC chamber requires a large (and uncertain) radical source combined with the varying spectral distribution of the EC light source. As discussed next, our development methodology for aromatics chemistry was to use the UNC data with its diurnally varying sunlight in the initial mechanism description efforts, followed by analysis of different chemical conditions, such as HC/NO_x ratio, overall mass loading and initial NO/NO_2 ratio, to identify (1) specific conditions under which the mechanism failed to operate successfully and (2) possible secondary reactions of importance. The UCR-EC experiments were designed in sets to provide data for such tests; although data collection did not usually continue much past the time of the maximum ozone concentration, conditional trends can still be identified from these experiments.

Data for individual higher molecular weight aromatics are sparse. There are four individual o-xylene and one m-xylene data sets available from UNC. There are four m-xylene experiments (one with uncertain light), but no o-xylene experiment, available from the UCR EC. Except for a few UNC experiments, the occurence of higher molecular weight aromatic species in smog chamber experiments is restricted to mixtures, resulting in a less

than clear picture of individual reactivities and chemical characteristics. A third data set (from Battelle Columbus Laboratories) includes NO_x plus toluene, o- and m-xylene, ethylbenzene, and trimethylbenzene. Unfortunately, the light sources in these experiments are not well defined (and simulations are therefore uncertain), though intercomparison of the experimental results using the same light source does permit some chemical sensitivity analysis.

Smog chamber data are used to evaluate the effectiveness of mechanism approximations (such as the secondary product chemistry just described) because these systems provide conditions far more similar to those encountered in the atmosphere than the conditions of fundamental laboratory chemical kinetics studies. On the other hand, the smog chamber can rarely yield specific data on chemical kinetics or mechanism development; this type of information is most often obtained in a laboratory. One connection between the more complex smog chamber system and the individual chemical kinetics experiment has been the ability of the former (given enough well-conceived experiments) to indicate functional trends related to possible atmospheric reactions of secondary species not yet studied individually in the laboratory. That is, though the chamber results cannot point out the exact structure or chemistry of the missing aromatic product species, the chemical nature of potentially missing products is inherent in the smog chamber data. Therefore, our overall mechanism development included both available laboratory kinetic and mechanistic information and systematic or conditional trends ascertained from smog chamber data. As just described, we used the smog chamber data as an indicator of conditional chemical reactions that may have been overlooked in past reaction schemes because they had not been analyzed at the fundemental kinetic level.

CBM-IV mechanism development also involved a number of application-based requirements. For instance, the current generation of photochemical kinetic mechanisms may be used to study formaldehyde chemistry; therefore, the formaldehyde mechanism should be explicit. Formaldehyde was previously used as a surrogate for glyoxal (an aromatic ring fragment). However, since formaldehyde is not a significant primary product of aromatic oxidation by OH (Bandow et al., 1985; Bandow and Washida, 1985a, 1985b; Gery et al., 1985, 1987), that association has now been removed and formaldehyde is explicitly described in the CBM-IV. Other constraints, such as the limitation of the number of species in a condensed mechanism, have led us to develop a secondary reaction scheme for toluene and xylenes that is less oriented toward the chemistry of explicit species and is more functionally based. This shift is mandatory for all aromatic mechanisms to some extent because of the large number of possible reaction branch points and isomers.

Choice of Aromatic Surrogate Species

Two aromatic surrogate species and their respective chemistries are now utilized in Carbon-Bond Mechanisms to represent the chemistry of all aromatics. These surrogate species are TOL for toluene (mono-alkylbenzenes) and XYL for xylene (multi-alkylbenzenes). These surrogate species were selected because the differentiation between surrogate chemistries must represent the widest possible range of aromatic reactivities if they are to provide the most appropriate representation of specific compounds. The most important chemical features to differentiate in the surrogate chemistries are the OH reaction rate and the secondary reaction scheme. Of these two, appropriate representation of the secondary reaction scheme is the most difficult to achieve because this chemistry is complex and varies among aromatic species.

OH is the primary oxidizer of simple aromatic hydrocarbons under atmospheric conditions. Ohta and Ohyama (1985) have shown that the OH-plus-aromatics reaction rates correlate well with aromatic structural configurations of the aromatic species (see Figure 4-2). Therefore, we currently use the OH-plus-toluene rate constant for the OH-plus-monoalkylbenzene reaction. The XYL rate constant is set to that of m-xylene. The sources of these data are discussed next. We do not feel that the present uncertainty in secondary products and their chemistry for higher molecular weight alklbenzenes warrants a third aromatic surrogate. If more data become available, however, and the requirement of a limited number of species is lifted for future photochemical kinetics mechanisms, a good argument for expansion of this scheme to a third (high molecular weight) surrogate could be made on the basis of the high OH reaction rate for that group.

An important issue that is less obvious than the OH reaction rate groupings involves the secondary reaction scheme for different aromatic species. Two different levels of product formation are involved here. First, we assume from limited evidence that aromatic ring reactions are strongly dependent on the number and location of functional groups, but only weakly affected by variations in types of alkyl groups. This assumption allows the use of data for simple alkylbenzenes to describe the initial oxidation reactions and ring cleavage schemes for higher molecular weight species. Second, the yields of the very reactive (and photolytically reactive) α- and conjugated γ-dicarbonyl products demand scrutiny. As noted by many researchers (Shepson et al., 1984; Bandow et al., 1985; Bandow and Washida, 1985a, 1985b; Gery et al., 1985, 1987; Tuazon et al., 1986), the yield of dicarbonyl species from the OH-plus-toluene reaction is relatively low compared to yields from the xylénes and trimethylbenzenes. For whatever reason, the prompt formation of dicarbonyl species

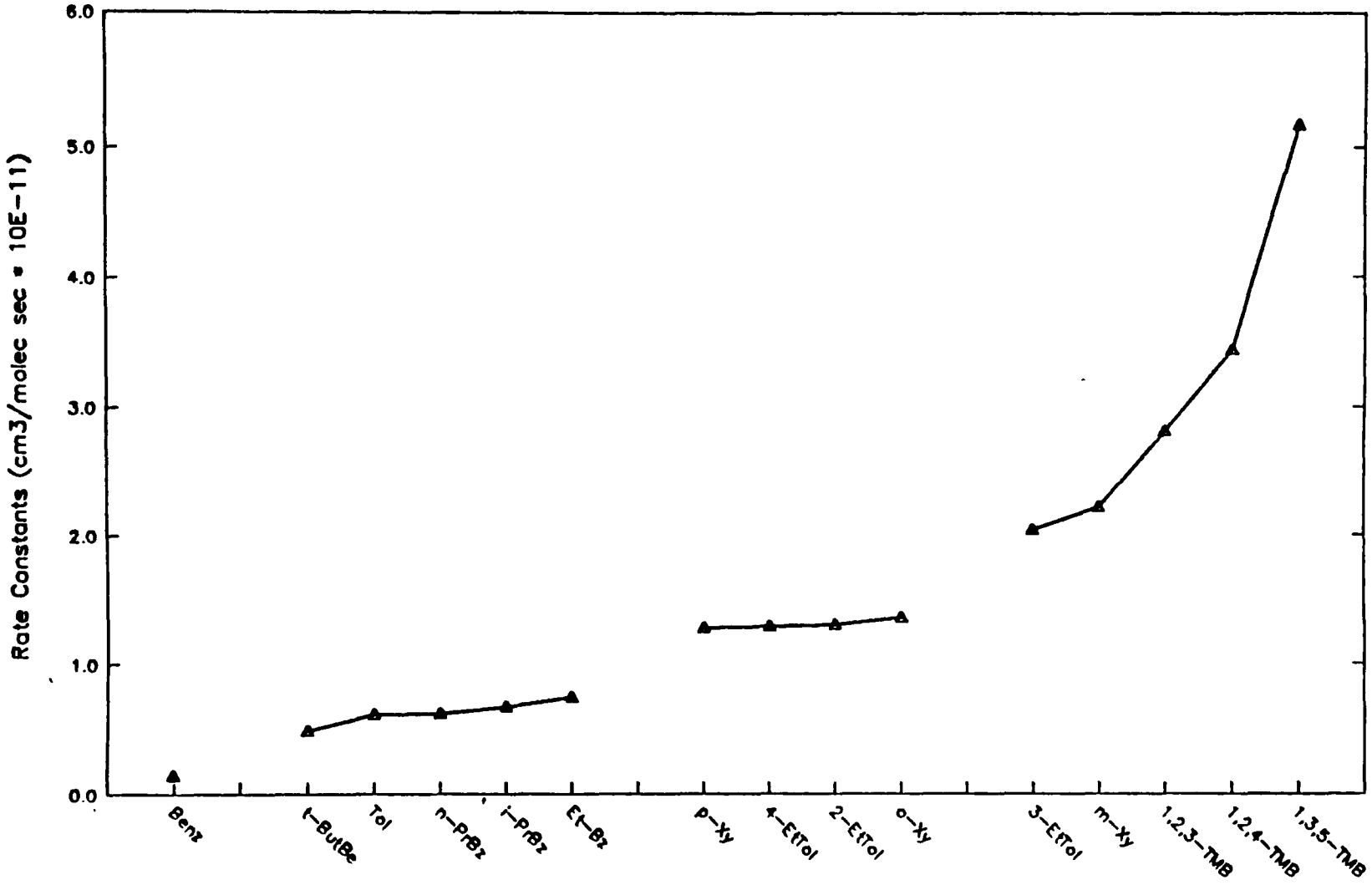

FIGURE 4-2. Rate constants for OH plus aromatics (Source: Ohta and Ohyama; 1985).

after OH-aromatic reaction appears to be a definite feature of multi-alkylbenzene/NO_x smog chamber experiments, but is far less evident in toluene systems. It is not clear whether there is lower energy for the xylene transition states, or whether a different type of reaction intermediate, leading directly to prompt radical formation, could be the result of additional functional ring groups. It is clear that this difference in chemical reactivity between mono-alkyl (toluene-type) and multi-alkylbene (xylene-type) systems can be very important for control strategies; therefore, these different chemistries must be addressed in the chemical mechanism. In this context we particularly include control strategies which might affect the toluene-type emissions differently than the xylene-type emissions.

TOL and XYL Chemical Mechanisms:

As noted, one critical difference between the product yields of toluene and those of higher molecular weight aromatic species is the inability of toluene to form high yields of reactive products (as indicated by α- and γ-dicarbonyl species) promptly after OH reaction. Such products are stable but extremely thermally and photolytically reactive. Therefore, their presence perpetuates the reactive nature of the system even after the initial hydrocarbon is exhausted. Available smog chamber data indicate that toluene systems rapidly consume NO, but limited toluene oxidation is observed to occur well after the period in which reactive product formation via this ring decomposition route would be severely limited by the diminished NO concentration. Radical flux and ozone formation in these toluene experiments initially appear to be very reactive, but then rapidly terminate this stage, and often actually consume ozone throughout the second part of an experiment.

This dichotomous behavior is somewhat unique for a "reactive" hydrocarbon and may indicate that, unlike other aromatics and olefins, the product mixture formed through the initial (relatively reactive) portion of these experiments may develop into less reactive species as experimental conditions (availibility of NO) change. Said another way, it appears that aromatics yield very reactive oxidation products during the initial portion of an experiment, when NO is available, but that the overall system becomes less reactive after that period because the resulting organic product distribution eventually changes to less reactive species.

The extent to which this phenomenon occurs is species-specific, and is at least dependent on the speed of product formation (OH reaction rate) and the types of products formed during the different stages of reaction. Toluene appears to be very sensitive to these reactivity parameters, which results in the dichotomous nature of these smog chamber experiments.

Xylenes and higher molecular weight aromatics react much faster with OH and produce higher yields of reactive products. This faster reaction rate decreases their sensitivity to NO concentrations and results in rapid production of reactive species that can be more correctly approximated by the assumption of prompt dicarbonyl (reactive product) formation.

Figure 4-3 illustrates results obtained from one side of the UNC chamber for a relatively clear day near the summer solstice from a toluene/NO_x experiment with HC/NO_x=14.7. Figure 4-4 illustrates results for the opposite side of the chamber for a similar m-xylene/NO_x experiment with an HC/NO_x value of 5.8. The different reactivities in these experimental systems (which are representative of a number of similar toluene and xylene experiments) are apparent in comparisons of the ozone and hydrocarbon curves. In many toluene experiments in the UNC chambers, the loss of reactivity, which appears to occur just prior to ozone rollover, is related to the system's limited ability to produce NO at that point. In this example, the loss occurs shortly before noon, when NO_2, the primary source of NO on a clear day, is sufficiently depleted and most gas-phase NO_x appears as nitrates (PAN).* Note from the toluene trace in Figure 4-3 that there is more toluene available to react, but that the radical flux becomes abruptly limited. On the m-xylene side, the reactivity of the system as measured by ozone production continues well past the depletion of NO_2, and is not quenched until the system consumes all of the initial hydrocarbon (it becomes m-xylene-limited) and is affected by the decreasing actinic flux at the approach of sunset.

The reaction mechanisms of toluene and o- and m-xylene were specifically studied because of the availability of smog chamber data and the relative abundance of these species in urban atmospheric samples and automobile exhaust. The initial product distributions for toluene and xylene oxidation by OH are taken from the limited set of data available in the literature. OH reacts with toluene in the following manner:

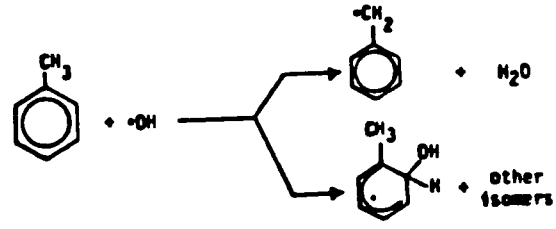

* Because the chemiluminescent NO_x analyzer responds to some nitrates, including PAN, this phenomenon is not evident from the trace shown. However, we know from wet chemical techniques and from subtracting PAN data from NO_2 that the NO_2 curve follows a generally Gaussian curve, which can be approximated by the shape of the NO_2 buildup side, applied to the second side, but extended to zero.

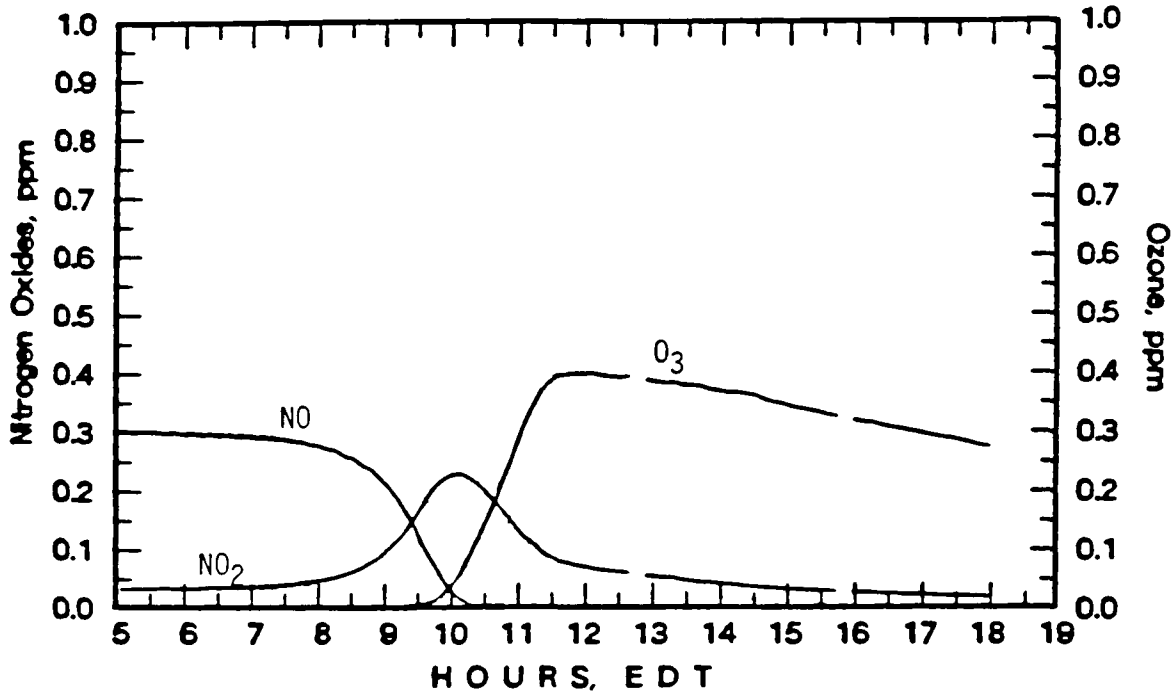

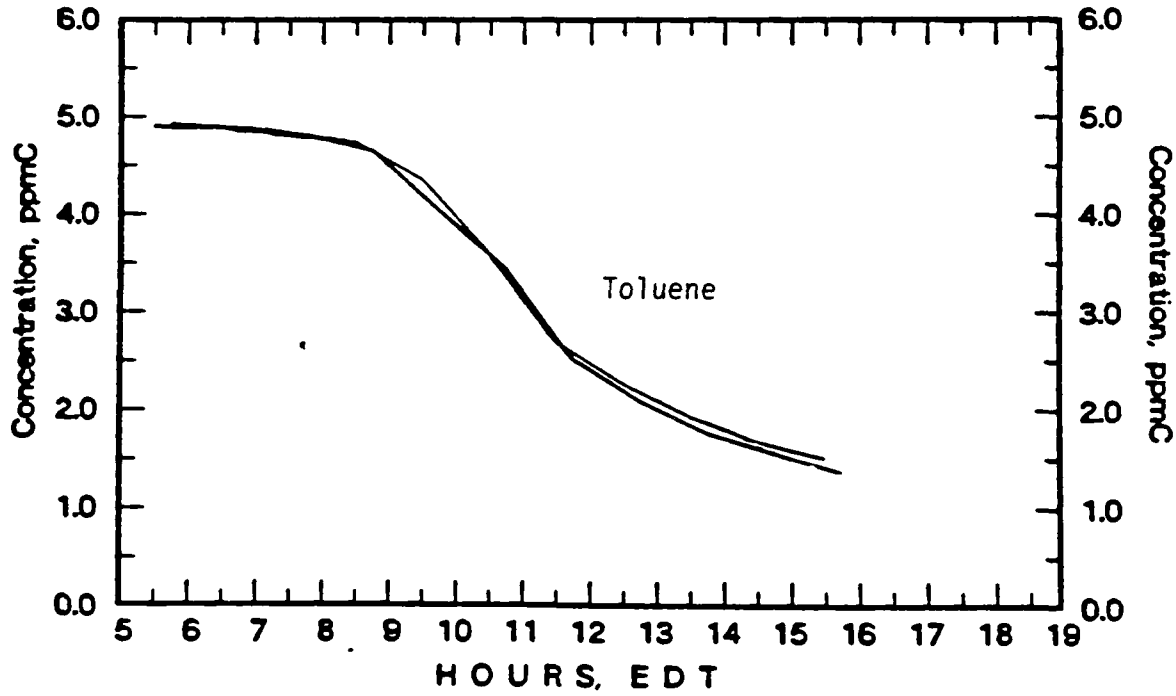

FIGURE 4-3. Experimental results for JN2784B. Top: NO, NO_2, and ozone traces. Bottom: Toluene traces from two different gas chromatographs.

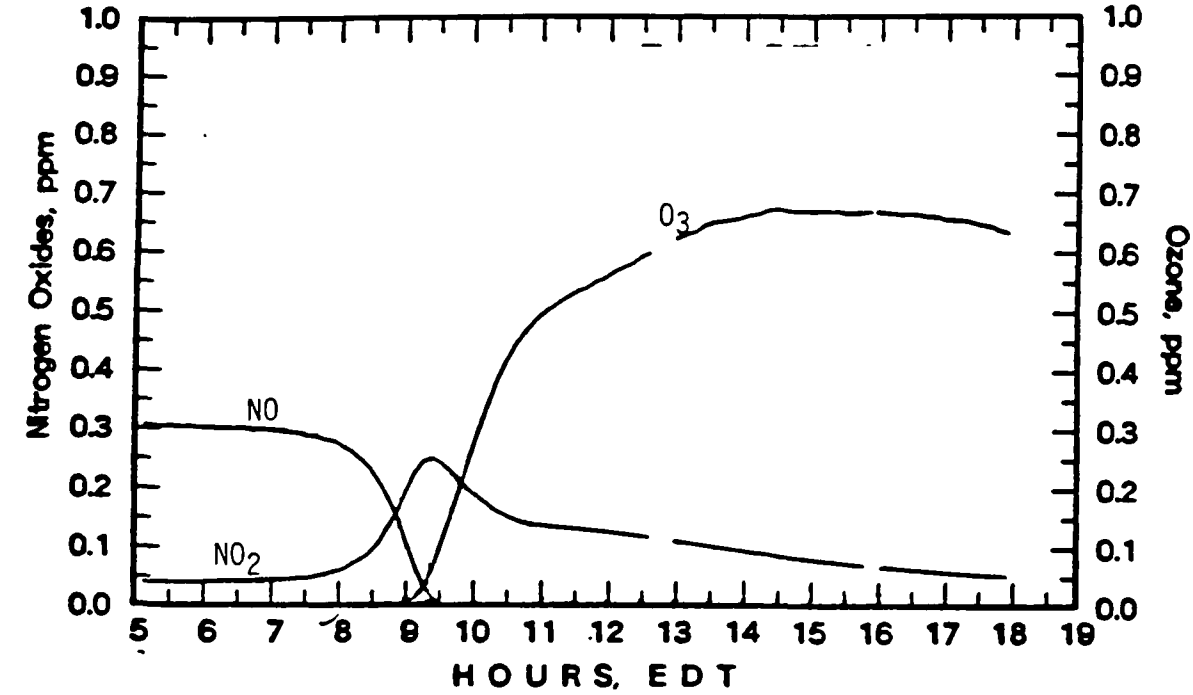

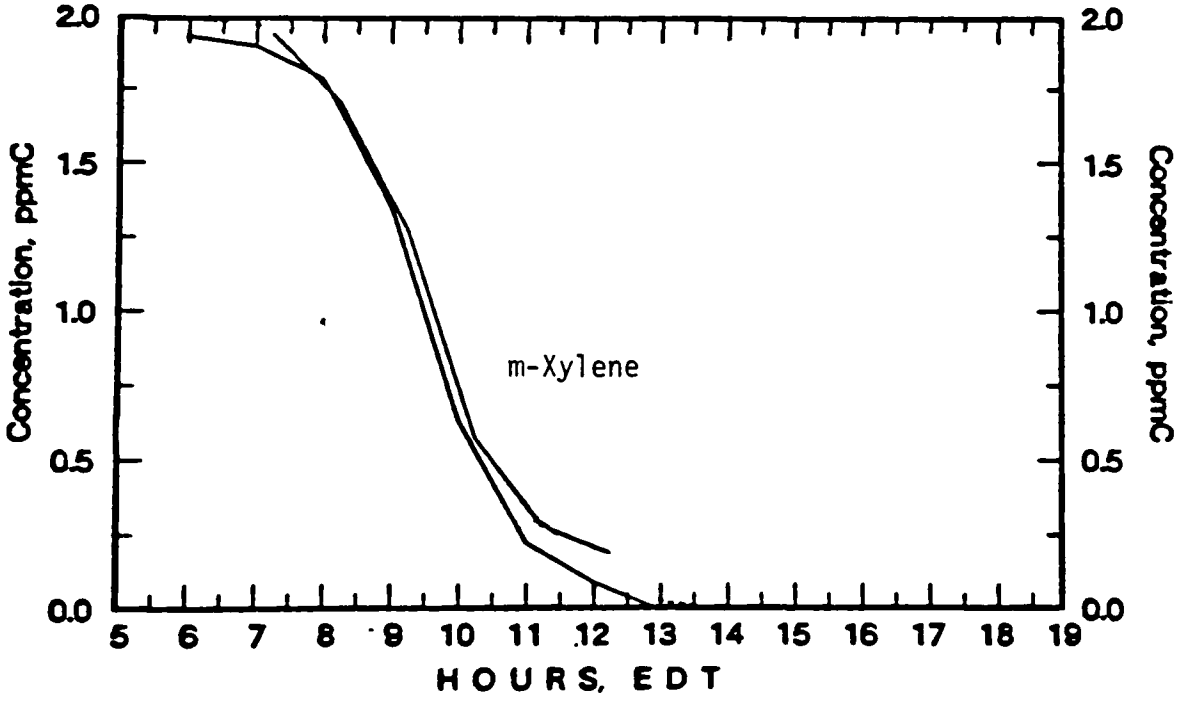

FIGURE 4-4. Experimental results for JN2784R. Top: NO, NO_2, and ozone traces. Bottom: m-xylene traces from two different gas chromatographs.

Reactions for the xylenes are analogous. We assume approximately 8 percent hydrogen abstraction for toluene and 10 percent for m-xylene based on the experimental results of Gery et al. (1985, 1987). The abstraction pathway is minor and is not discussed here. Reactions of the alkylbenzylperoxy radicals (BO2, the methylbenzylperoxy radical; and XLO2, the xylene analogue) and subsequent species are included in the CBM-X (Table 1-2) as X-131 through X-138 and X-152. A discussion of the abstraction pathway and specific sources of reaction rate constants is found in Gery et al. (1985) for toluene and Gery et al. (1987) for xylenes.

Most products are formed by the addition of OH to the aromatic ring structure. This OH adduct can either reversibly add an oxygen molecule or loose a hydrogen atom to form an alkylphenol (CRES for cresol) and $HO_2^{\bullet}$.

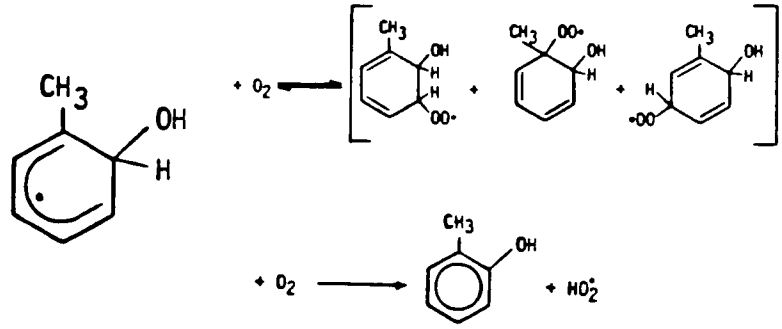

The approximate fractions of phenolic yields (f_{OH}) were again taken from Gery and coworkers. For toluene, $f_{OH} \approx 0.36$; and for m-xylene; $f_{OH} \approx 0.20$.

In the CBM-X, the overall OH-plus-aromatic fractions (including the hydrogen abstraction pathway) are given for toluene (X-128 through X-130) and xylene (X-148 through X-151) as

OH + TOL ------> BO2	8%	(X-128)
OH + TOL ------> CRES + HO2	36%	(X-129)
OH + TOL ------> TO2	56%	(X-130)

and

OH + XYL ------> XLO2	10%	(X-148)
OH + XYL ------> CRES + PAR + HO2	20%	(X-149)
OH + XYL ------> TO2	30%	(X-150)
OH + XYL ------> XINT	40%	(X-151)

where XINT represents the mechanism intermediate from which dicarbonyls (MGLY) may form as a result of ring decomposition. Also, because TO2 is an intermediate of one less carbon than the parent xylene, a nonreactive carbon is formed (a carbon atom is lost). This carbon atom is nonreactive because the formation of 1 PAR would be incorrect in this case.

The reaction rate constant for the overall toluene-plus-OH reaction is (Atkinson, 1986):

$$k(63) = 3.106 \times 10^3 \exp(322/T)\ ppm^{-1}min^{-1}$$

or

$$k(63)_{298} = 9.15 \times 10^3\ ppm^{-1}min^{-1}\ .$$

For the xylene-plus-OH reaction, Atkinson recommends (for m-xylene)

$$k(72) = 2.453 \times 10^4 \exp(116/T)\ ppm^{-1}min^{-1}$$

or

$$k(72)_{298} = 3.62 \times 10^4\ ppm^{-1}min^{-1}\ .$$

Beyond this point, the description of continuing oxidation, especially of the chemistry of the OH-O_2 radical adducts, becomes very speculative. Atkinson and coworkers (1980) proposed a rapid bridging of the O_2 group and relocation of the electron density, followed by a second, reversible addition of O_2:

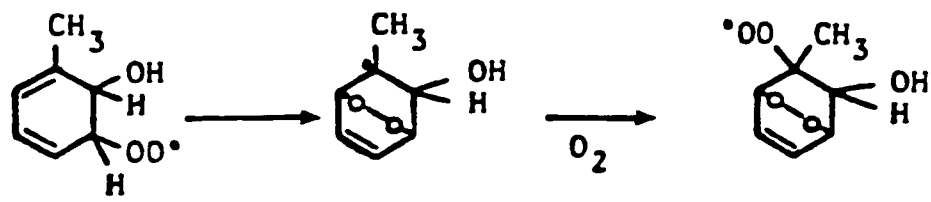

Some experimental evidence for such a structure was found by Gery and coworkers (1985, 1987) in the form of p-alkylbenzoquinone products. In either case, however, all schemes to date show either the initial OH-O_2 radical adduct (I) or the bridged OH-O_2 adduct (II) reacting with NO to form NO_2 and products (generally, reactive ring fragments). (The functional description of most mechanisms is similar up to this point.) In terms of species, these reactions are in the CBM-X:

TO_2 + NO	------> NO_2 + OPEN + HO_2		(X-145)
TO_2 + NO	------> TNTR		(X-146)
XINR + NO	------> NO_2 + 2MGLY + 2PAR + HO_2		(X-153)

For the first two reactions, we use an overall reaction rate constant of 1.20×10^{-4} ppm^{-1} min^{-1}, with a 10 percent nitrate yield to give

$$k(X\text{-}145) = 1.08 \times 10^{-4}\ ppm^{-1}min^{-1}$$

and

$$k(X\text{-}146) = 1.20 \times 10^{-3}\ ppm^{-1}min^{-1}\ .$$

The rate of the XINT plus NO reaction is also $k(X\text{-}153) = 1.20 \times 10^{4}$ $ppm^{-1}min^{-1}$. This reaction represents the fraction of XYL molecules that promptly form dicarbonyl products. We describe the chemistry of CRES, a general phenolic product, and MGLY and OPEN, which are dicarbonyl species, later in this section. However, we note here that our approach to the formation and chemistry of dicarbonyls is to lump all of the dicarbonyl reactions into one general surrogate species (OPEN) and one other explicit species, methylglyoxal (MGLY). We believe this is an appropriate approach because (1) the uncertainty of products and their chemistry subsequent to dicarbonyl formation via ring decomposition is large, and (2) the timing of variations between data and model results appears to result from poor descriptions of mechanistic branching points prior to dicarbonyl formation. Therefore, these dicarbonyl-lumped species contain the essential experimentally determined features of all the known dicarbonyl products and serve to confine the uncertainty to only two species (limiting extensive speculation about a number of unstudied secondary products). This allows some investigation of the pre-fragmentation reaction products and their reactions.

The greatest area of uncertainty in aromatic mechanisms lies in the radical reactions following ring fragmentation. One assumption currently used in many photochemical models of aromatic oxidation is the idea of "prompt" product formation. In models such as the CBM-IV, this idea can be specifically instituted when the (generalized) reaction set,

$$\begin{aligned} RH + OH &\text{-----}> R^{\bullet}(+ H_2O) \\ R^{\bullet} + O_2 &\text{-----}> RO_2^{\bullet} \\ RO_2^{\bullet} + NO &\text{-----}> NO_2 + \text{products}, \end{aligned}$$

is simplified to

$$RH + OH \text{-----}> XO_2 + \text{products} \qquad (O_2 \text{ constant}),$$

with the XO_2 operator defined as

$$XO_2 + NO \text{-----}> NO_2. \tag{79}$$

This concept was formally introduced by Whitten et al. (1985b) to minimize the number of species and reactions in a chemical mechanism by grouping

the common NO-to-NO_2 conversion function of all $RO_2^{\bullet}$ species into the XO_2 operator, thereby eliminating explicit description of specific $RO_2^{\bullet}$ species in favor of their "promptly" formed products. A similar method has since been employed by Carter et al. (1986).

This approximation drifts from the explicit scheme in situations where (1) low NO concentrations are combined with a highly reactive $RO_2^{\bullet}$ or (2) another $RO_2^{\bullet}$ reaction competes with the NO reaction (even at relatively high NO concentrations). The first situation (low NO) is typically handled by the addition of the XO_2 self-reaction, which is also assumed to yield the same products as the NO-to-NO_2 conversion reaction:

$$XO_2 + XO_2 \text{ ------> } . \qquad (80)$$

In the second case, however, where there is competition with NO for $RO_2^{\bullet}$ through another reaction pathway that produces different products, the XO_2 operator must be eliminated and the $RO_2^{\bullet}$ reactions explicitly represented in all other mechanisms that do not use a XO_2-type approximation; a similar effect is found for toluene since there are no species that compete with NO for the toluene-$O_2^{\bullet}$ adduct radical.

On the basis of the smog chamber data and the product yield data for toluene, we believe that this prompt formation of products, especially highly reactive α- and conjugated γ-dicarbonyls, incorrectly describes the secondary chemical reactions of the OH-toluene reaction when NO concentration and production have become limited. One possible pathway that has not been considered is alternate reactions of the OH-O_2 adduct radicals (TO_2). These species probably do not have long reactive half-lives, and if they cannot react with NO, must be lost by an alternate reaction pathway. Our methodology in developing this most recent mechanism has been, in part, to estimate the mechanism, products, and kinetics of an alternate reaction of the TO_2 radical. Such a reaction probably becomes important only at low NO concentrations, and produces less reactive products than the NO-to-NO_2 conversion process. Through an extensive set of simulations and sensitivity tests, we have estimated a TO_2 decomposition of the form

$$TO_2 \text{ ------> } HO_2 + \text{CRES } (+ O_2). \qquad (65)$$

The unimolecular rate of this reaction was estimated to be:

$$k(65) = 2.5 \times 10^2 \text{ min}^{-1}$$

As we will show in the next section, inclusion of this reaction significantly improves the simulation of ozone. We note that though the earlier OH-O_2 adduct radical (I) could conceivably loose oxygen and form cresol and HO_2, we use cresol here only because it is already available in the

CBM and describes a secondary aromatic product that is less reactive than dicarbonyls and that removes nitrogen from the system.

Aromatic Product Species

The species, CRES, represents alkylphenolic products formed after OH addition to the aromatic ring. In the case of toluene, the CRES species formed is cresol, typically o-cresol (o-methylphenol). The CRES chemical reactions in the CBM are formulated for that compound because the chemistry of higher molecular weight alkylphenol homologues and other cresol isomers has been far less studied. For the other cresol isomers, we assume the same chamistry as o-cresol, and for the higher molecular weight homologues, we include alkane surrogates (PAR) groups upon formation. Thus, the dimethylphenol compounds formed from xylene oxidation by OH are represented by CRES plus PAR.

The chemical reactions of cresol and larger alkylphenols are summarized in Atkinson and Lloyd (1984); additional information is found in Gery et al. (1987 and 1985) and Kerr and Calvert (1985). The reader is referred to these works for a complete description of the current state of knowledge with respect to alkylphenol chemistry. We represent this chemistry in the CBM-X with

OH + CRES ------> CRO		(X-139)
OH + CRES ------> CRO2		(X-140)
NO3 + CRES ------> CRO + HNO3		(67)
CRO + NO2 ------> NCRE		(68)
CRO2 + NO ------> NO2 + OPEN + HO2		(X-143)
CRO2 + NO ------> NO2 + ACID + HO2		(X-144)

It should be noted that a discrepancy in NO_3 oxidation rates appears in the abovenoted texts. The rate constant of Atkinson and Lloyd (1984) was based on a dinitrogen pentoxide equilibrium constant that has since been revised. Based on the new equilibrium constant, Kerr and Calvert (1985) recommended a rate constant of

$$k(67) = 3.25 \times 10^4 \text{ ppm}^{-1}\text{min}^{-1} \quad .$$

Our overall rate of hydroxyl reaction with CRES is from Atkinson and Lloyd (1984):

$$k(66) = 6.1 \times 10^4 \text{ ppm}^{-1}\text{min}^{-1} \quad ,$$

with an assumed OH addition fraction of 60 percent and a 40 percent abstraction of the phenol hydrogen by OH to yield CRO, a methylphenoxy radical. The remaining reactions are very speculative, and are based on the review by Atkinson and Lloyd (1984). The ACID species represents organic acids formed from aromatic ring decomposition of the alkylphenol peroxy radical (the O_2 adduct formed after OH addition to CRES).

Methylglyoxal ($CH_3C(O)CHO$) is a dicarbonyl ring fragment found in aromatic systems containing ring methyl groups. It is very reactive with the hydroxyl radical and also photolyzes to radical products. These reactions are represented in the CBM-X by

$$\text{OH} + \text{MGLY} \ (+\ \text{O2}) \ \text{------>} \ \text{MGPX} \ (+\ \text{H2O}) \qquad \text{(X-154)}$$

$$\text{MGPX} + \text{NO} \ \text{------>} \ \text{NO2} + \text{C2O3} \ (+\text{CO2}) \qquad \text{(X-155)}$$

$$\text{MGLY} \ \text{--h}\nu\text{-->} \ \text{C2O3} + \text{CO} + \text{HO2} \qquad \text{(X-156)}$$

where MGPX represents a peroxy radical formed after hydroxyl abstraction of the aldehydic hydrogen.

The kinetic information used in the CBM-X for the OH reaction is from Atkinson and Lloyd (1984):

$$k(\text{X-154}) = 2.60 \times 10^4 \ \text{ppm}^{-1}\text{min}^{-1} \ .$$

The MGPX is assumed to react with NO at

$$k(\text{X-155}) = 1.20 \times 10^4 \ \text{ppm}^{-1}\text{min}^{-1} \ .$$

Photolysis of MGLY has been studied (Plum et al., 1983), though the uncertainty of the quantum yield data causes calculated j-values to be very uncertain in the lower wavelength region of the surface solar spectrum. On the basis of smog chamber data, we use the following rate expression in the CBM-X:

$$j_{MGLY} = 9.64 \times j_{HCHOr} \ \text{min}^{-1} \ ,$$

where j_{HCHOr} is the j-value for formaldehyde photolysis to radicals (reaction 38).

The species OPEN represents a conglomerate of possible dicarbonyl species with up to seven carbons. We felt that, given the limited information concerning dicarbonly chemistry, speculation about the specific structure and reactions of individual compounds was pointless. Instead, we combined the expected kinetics of the anticipated dicarbonyl product structures into one general species that could represent the mass of all products.

Hence, the final rates used for these species are based on the goodness-of-fit for a large set of smog chamber simulations. In addition, since photochemical kinetics mechanisms used in large air quality simulation models require small numbers of species, we felt it was best to implement the improvements to the TO2 chemistry instead of using additional dicarbonyl species (all of which are very reactive). The photolysis of OPEN and the OH reaction in the CBM-X are

$$\text{OPEN} \xrightarrow{h\nu} \text{C2O3} + \text{HO2} + \text{CO} \qquad \text{(X-159)}$$

$$\text{OH} + \text{OPEN} \longrightarrow \text{OPPX} + \text{C2O3} + \text{HO2} + \text{CO} \qquad \text{(X-157)}$$

$$\text{NO} + \text{OPPX} \longrightarrow \text{NO2} + \text{FORM} + \text{HO2} + \text{CO} \qquad \text{(X-158)}$$

The kinetic expression used for OPEN photolysis is similar to that of MGLY:

$$j_{OPEN} = 9.04 \times j_{HCHOr} \ \text{min}^{-1} \ .$$

We assumed the rate for k_{X-157} to be

$$k(X\text{-}157) = 4.40 \times 10^4 \ \text{ppm}^{-1}\text{min}^{-1} \ ,$$

and that of k_{X-158} to be

$$k(X\text{-}158) = 1.20 \times 10^4 \ \text{ppm}^{-1}\text{min}^{-1} \ .$$

The product distributions are very uncertain. Many of the larger assumed products were 5 or 6 carbon α- and γ-dicarbonyls with conjugated alkene groups. We assumed photolysis of only α-dicarbonyl products. Hydroxyl reaction was even more speculative because of the ability of OH to react rapidly with both the olefinic and the aldehydic carbons of α-dicarbonyls.

Ozone reaction with the alkene bonds of larger OPEN species was assumed to proceed along the lines pointed out by Dodge and Arnts (1979) for simpler olefins. We used a hypothetical product distribution to derive product stoichiometries for these reactions. These empirical results are shown in the CBM-X as reactions X-160 through X-164 (Table 1-2). A more explicit version of the same reactions is given in the following condensation discussion and in the CBM-IV (Table 1-3). For the reaction of ozone with OPEN, we use the overall rate expression

$$k(71) = 8.03 \times 10^{-2} \exp(-500/T) \ \text{ppm}^{-1}\text{min}^{-1} \ ,$$

with

$$k(71)_{298} = 1.50 \times 10^{-2} \ \text{ppm}^{-1}\text{min}^{-1} \ .$$

As discussed in the next section, the chemical reactions now used to describe the photooxidation of aromatic hydrocarbons provide simulation results for smog chamber data that are much improved over those of earlier models. On the other hand, because fundamental information on aromatic systems is limited, this mechanism does not rest on as strong a basis as other sections of the CBM. Rather, it is a combination of the available fundamental information and an empirical description of additional information available from more complex smog chamber experiments.

Condensation of the Reaction Schemes:

As noted, the reaction scheme for xylenes just given should ideally include the reactions of xylene carbon product species. Because that chemistry is extremely uncertain, however, we assume the chemistry of BO_2, TO_2 and CRES as a logical approximation. Condensation of the extended chemistry proceeds as follows: For the initial reactions of OH with toluene and xylene, all species except the abstraction products are accounted for by direct combination of reaction stoichiometry and rate constants (see Table 1-3). The abstraction products are represented by

$$BO_2 \equiv XO_2 + HO_2$$

and

$$XLO_2 \equiv XO_2 + HO_2 + PAR \quad ,$$

where XO_2 is generally the NO-to-NO_2 conversion function (as previously described). Hence, the reaction of BO_2 with NO to form NO_2, HO_2, and benzaldehyde is represented by the XO_2 operator and product HO_2, with the BZA product omitted. A similar representation is made for xylenes, except that PAR is used to represent the additional carbon produced from the reaction of XLO_2 with NO. After combination of these reactions, the resulting reactions are

$$OH + TOL \text{ ------> } 0.08\ XO_2 + 0.36\ CRES + 0.44\ HO_2 + 0.56\ TO_2 \qquad (63)$$

$$OH + XYL \text{ ------> } 0.50\ XO_2 + 0.20\ CRES + 0.70\ HO_2 + 0.30\ TO_2 + 0.80\ MGLY + 1.10\ PAR \qquad (72)$$

where XINT is eliminated with an XO2 operator but TO_2 chemistry is explicit, as noted:

$$TO_2 + NO \text{ ------> } 0.90\ NO_2 + 0.90\ HO_2 + 0.90\ OPEN \qquad (64)$$

$$TO_2 \text{ ------> } HO_2 + CRES \ . \qquad (65)$$

The reactions of cresol are combined to

$$OH + CRES \longrightarrow 0.40\ CRO + 0.60\ XO_2 + 0.60\ HO_2 + 0.30\ OPEN \quad (66)$$

$$NO_3 + CRES \longrightarrow CRO + HNO_3 \quad (67)$$

$$CRO + NO_2 \longrightarrow \quad (68)$$

The OH and ozone oxidation reactions of MGLY and OPEN are condensed algebraically and through the elimination of MGPX and OPPX via the XO2 operator, to yield:

$$OH + MGLY \longrightarrow XO2 + C2O3 \quad (73)$$

$$OH + OPEN \longrightarrow XO2 + 2.0CO + 2.0HO2 + C2O3 + FORM \quad (70)$$

$$O3 + OPEN \longrightarrow 0.03ALD2 + 0.62C2O3 + 0.70FORM + 0.03XO2 + 0.69CO + 0.08OH + 0.76HO2 + 0.20MGLY \quad (71)$$

ISOPRENE

Our objective in developing this portion of the CBM-IV was to provide a chemical representation for biogenic hydrocarbons by deriving a condensed mechanism for isoprene and estimating valid carbon bond splits for α-pinene. In the former task, we wished to limit the product species considered in the condensed isoprene mechanism to those already included in the CBM-IV.

The first step in implementing this explicit isoprene mechanism was the development of a good kinetic representation of the initial isoprene oxidation reactions. These oxidation reactions occur with O, NO_3, OH and O_3; the last two are usually most important in daytime atmospheric chemistry. We have reviewed the reaction rate constants published in recent studies, and revised our earlier explicit mechanism rates (Killus and Whitten, 1984), when appropriate.

Since a rate constant for the O atom reaction with isoprene has not been well studied, it was assumed to be the sum of O atom additions to each of the alkene bonds in the isoprene molecule. The dialkylated bond characteristics were estimated to be similar to those of isobutene (Atkinson and Pitts, 1977), and the monoalkylated bond was estimated to be equal to the general 1-alkene (OLE) bond in the CBM (e.g., propene). The resulting rate constant is

$$k(75) = 2.70 \times 10^4\ ppm^{-1}min^{-1}.$$

The OH rate constant for reaction with isoprene was estimated by averaging the rates of Atkinson and Aschmann (1984) and Kleindienst et al. (1982):

$$k(76) = 1.52 \times 10^5 \text{ ppm}^{-1}\text{min}^{-1}.$$

The reaction rate with O_3 is taken as

$$k(77) = 1.80 \times 10^{-2} \text{ ppm}^{-1}\text{min}^{-1},$$

the same as the rate constant for 1-alkenes (OLE) in the CBM and within the error bands of the studies reviewed by Atkinson and Carter (1984). As noted in Killus and Whitten (1984), the reaction of O_3 with isoprene shows evidence of being a complex process, dissimilar in the nature of secondary reactions to both monoalkenes and other dialkenes (e.g., butadiene). This is reflected in our product surrogate choices.

Finally, the rate of reaction with NO_3 is derived from the rate constant presented by Atkinson et al. (1984):

$$k(78) = 4.70 \times 10^2 \text{ ppm}^{-1}\text{min}^{-1}.$$

Our explicit isoprene mechanism was initially developed by Killus and Whitten (1984). In the development of that mechanism we found the following significant phenomena to be associated with isoprene oxidation:

Highly reactive products, including methacrolein and methyl vinyl ketone. Some product reaction with ozone was also indicated, as would be expected from the olefinic character of these two products;

A high rate of radical production, presumably from photolysis of isoprene products;

A high yield of PAN as well as a PAN-like compound, probably from methacrolein; and

A high yield of formaldehyde.

Because the complex secondary chemistry of isoprene and its oxidation products (methacrolein, methylvinyl ketone, and possibly methylglyoxal) precludes a direct condensation to a few representative species, these reactions were represented in condensed CBM-IV format by the use of existing carbon-bond species. Our intent was not to algebraically reduce the explicit reaction scheme, but to simulate the major chemical features (i.e., ozone production, formaldehyde yields, and the temporal characteristics of radical and PAN-type compounds). This was done by simulating

the UNC data set of isoprene/NO_x experiments (some of which are shown and discussed in Section 6).

Our general methodology for the formulation of the condensed isoprene mechanism was based on the following rationale: The olefinic nature of isoprene products would best be simulated by ethene, since the alkene bonds of methacrolein and methylvinyl ketone are partly deactivated and resemble ethene in their reactivity to OH and O_3. This representation also gives a high yield of formaldehyde from the secondary oxidation of ethene, which resembles the formaldehyde yield of isoprene. The formation of PAN and PAN-like compounds from isoprene was simulated with a primary yield of both acetaldehyde and acetylperoxy radical. Inevitably, this can result in an overprediction of measured PAN, since simulated PAN includes the PAN analogues as well. The radical yield for products was simulated by the formation (and photolysis) of methylglyoxal. These separate product yields were adjusted to give the best fits to the mid-range of hydrocarbon-to-NO_x-ratio isoprene experiments, in which notable double ozone peaks become evident. The double ozone peaks in isoprene NO_x experiments are caused by NO_x limitation of PAN formation, ozone reaction with isoprene and isoprene products, and continued ozone formation by PAN decomposition at elevated temperatures. Simulation of the double peak effect gives some indication that a reasonable balance has been achieved for the multiple processes occurring in isoprene oxidation. The condensed isoprene mechanism resulting from simulations of the UNC isoprene/NO_x data set is shown as reactions 75 through 78 in Table 1-3.

In addition to improving the isoprene mechanism in the CBM-IV, we utilized the UNC α-pinene/NO_x data set to test our carbon-bond parameterization of that species. In these simulations we found that a better carbon-bond parameterization for α-pinene would be 0.5 OLE, 1.5 ALD2, and 8.0 PAR. This is a slight alteration from earlier compilations. These results, along with results of the UNC smog chamber simulations are discussed in Section 6.

5 REPRESENTATION OF SMOG CHAMBER PROCESSES AND CHARACTERISTICS

This section discusses the information and assumptions used to represent smog chamber-dependent processes (e.g., heterogenous reactions and dilution) and reactor characteristics (e.g., in-chamber photolysis rates and temperature profiles) that are not included in the homogenous gas-phase chemical reactions of the CBM. Section 6 utilizes the information developed here to compare CBM-IV simulation results and experimental data from various smog chamber facilities. In any mechanism evaluation using smog chamber data, it is first necessary to clearly delineate the mechanistic techniques used to characterize artificial processes that occur in the experimental system (the smog chamber). In this way, the artificial processes represented in smog chamber simulations can be included in the mechanism for testing and then removed prior to simulation of the atmosphere. Therefore, before presenting the experimental data and simulation results we first describe our methodology for handling chamber-specific processes (photolysis, wall radicals and water).

PHOTOLYLTIC PROCESSES

Almost all of the experimental data used to develop and test the CBM-IV performance was generated in smog chamber facilities at

(1) The University of North Carolina (UNC);

(2) The University of California at Riverside (UCR) evacuable chamber (EC);

(3) Indoor Teflon chamber (ITC); and

(4) The Battelle Columbus Laboratories chamber (designated AVOC).

To achieve accurate simulation of photochemical smog chamber data photolysis rates (j-values) must be determined throughout each simulation. We have already discussed the method and data used to calculate j-values for the relevant species in the CBM in Section 3; however, we have not yet discussed our calculation of the actinic flux inside individual smog chambers.

The radiant energy of indoor chambers is generally assumed to be constant over the period of an experiment (therefore, j-values are also assumed to be constant). These chambers use artificial illumination, which can differ from natural sunlight (Pitts et al., 1979; Whitten et al., 1979; Carter et al., 1986). The spectral distribution is usually reported for each experiment, though some facilities report at longer time intervals. Over the longer term, variability in these chambers is higher than in outdoor chambers, because of lamp changes in the irradiation sources. In the UCR-EC, there have also been changes in transmission characteristics of the Pyrex windows used to admit light (Whitten et al., 1979; Carter et al., 1986), resulting from the prolonged exposure of those windows to the intense radiation of the solar simulator light source.

On the basis of the reported light spectrum for the blacklight source used in the UCR Indoor Teflon Chamber (see Table 5-1), we have calculated the photolysis rates for a number of important species. For the series of multiday validation experiments (ITC-625 to ITC-637), having a reported j_{NO2} of 0.3 min^{-1}, we obtain the following j-values:

$$j_{HCHOr} = 5.5 \times 10^{-4}\ min^{-1}$$
$$j_{HCHOs} = 5.8 \times 10^{-4}\ min^{-1}$$
$$j_{ALD2} = 7.2 \times 10^{-5}\ min^{-1}$$
$$j_{O1D} = 3.2 \times 10^{-4}\ min^{-1}$$

The estimates of photolysis rates calculated here differ significantly from those of Carter et al. (1986). We have traced the differences in j_{HCHOr} to two factors: (1) Our use of the absorbtion cross section data of Bass et al. (1980), rather than the averaged values found in the NASA review (DeMore et al., 1985); and (2) The NO_2 photolysis estimates of Carter et al. appear to be based upon earlier NASA recomendations (DeMore et al., 1983) rather than the later, 1985 compilation (DeMore et al., 1985). The combination of these two factors accounts for about a 14 percent difference in the j_{HCHOr} values calculated. The estimate used by Carter et al. for this rate in the ITC is about 6.5 x 10^{-4} min^{-1} (Carter, 1987). It is our belief that this is a significant overestimation of j_{HCHOr} in the ITC and could cause the overly reactive simulations for the ITC experiments in Carter et al. (1986).

The spectral measurements in the UCR Evacuable Chamber (EC) are marginal at best and often inadequate for calculating photolysis rates in the shorter wavelength bins. The most prominant higher uncertainty of these data is the fact that the poorest precision in the EC spectral data always occurs in the region between 280 and 310 nm, where many key photoreceptors absorb light. In addition, information about the run-to-run light source consistency and spectrum determination accuracy is difficult to obtain.

TABLE 5-1. Relative spectral distribution for the blacklights in the SAPRC 6400-liter Indoor Teflon Chamber (ITC)[a] (Source: Carter et al., 1986).

Wavelength (nm)	Intensity[b]	Wavelength (nm)	Intensity[b]	Wavelength (nm)	Intensity[b]
295.7	0.0	347.8	0.952	405.0	0.258
296.7	0.0019	350.0	0.972	406.0	0.264
298.0	0.0024	351.7	0.990	406.7	0.251
300.7	0.0018	353.7	1.00	408.7	0.0596
302.1	0.0043	356.7	0.982	412.0	0.0387
304.3	0.0058	360.0	0.925	416.7	0.0348
306.3	0.0057	363.3	0.829	423.3	0.0298
310.0	0.0140	364.3	0.859	430.0	0.0227
313.0	0.0728	364.7	0.869	434.3	0.0217
313.7	0.0846	365.5	0.870	436.1	0.641
315.0	0.0879	366.9	0.835	436.7	0.709
315.3	0.0856	368.5	0.685	437.3	0.712
316.7	0.0581	370.0	0.639	438.1	0.651
317.3	0.0564	376.7	0.442	439.7	0.0169
318.7	0.0858	383.3	0.261	443.3	0.0140
323.3	0.1495	390.0	0.1423	450.0	0.0081
330.0	0.331	396.7	0.0885	460.0	0.0
336.7	0.563	393.0	0.0535		
343.3	0.851	404.3	0.223		

[a]As measured on June 30, 1983
[b]Intensity in terms of photons per unit area per unit time, normalized so the maximum intensity = 1.0 units.

For instance, the recommended spectral distributions (see Table 5-2) show a significant break between EC-233 and EC-237 such that calculated j_{HCHOr} values for these two spectral distributions differ by 20 percent (6.1×10^{-4} min^{-1} to 5.1×10^{-4} min^{-1}). However, the concentration data reported for EC-232 and EC-246, a pair of replicate experiments, differ only by the initial NO/NO_2 ratio and the length of the experiments (see Figure 5-1). All available tests of radical input levels (hydrocarbon and NO_x decay rates) indicate no appreciable difference between the reactivity of the two experiments. Were the formaldehyde photolysis rate to differ by the amount suggested in Table 5-2, this would not be the case.

Our best estimate of j_{HCHOr} on the basis of observed reactivity for the seven component experiments (see Section 6) is 7.7×10^{-4} min^{-1}. This value appears to be close to the value that would be calculated using the formaldehyde absorption cross sections and quantum yields in Carter et al. (1986) for the EC-237 to EC-257 spectral set.

The UNC facility uses a pair of outdoor, side-by-side Teflon reactors that are illuminated only by the daily transit of the sun. Daily variations in light-source can have a strong effect on these outdoor chamber studies since some atmospheric conditions serve to attenuate light. On the other hand, "clear sky" experiments held a year apart at the UNC chamber show little variability, and replicate experiments on both sides of the two-sided chamber typically show essentially identical results (Jeffries et al., 1976). This is because, unlike indoor chambers, there has been no substantial long-term variation in the energy output of the sun. Thus these outdoor experimental conditions are more akin to those of the ambient atmosphere, and a better test of the mechanism's performance for real conditions. On the other hand, the indoor chambers are far better controlled and do not suffer from the intervention of clouds or haze between the light source and reactor. Hence, we utilized both indoor and outdoor data in the development of the CBM, but use a larger percentage of UNC data in the following evaluation because of their more realistic experimental characteristics. It is therefore necessary to describe our method of calculating the in-chamber actinic flux as it varies through the day at the UNC outdoor facility.

The UNC data sets provide data from an Eppley Ultraviolet (UV) instrument, which is located outside the chamber on an elevated tower. These data are usually accompanied by total solar radiation (TSR) and temperature measurements. It was originally envisioned that these measurements alone would be sufficient to provide an accurate description of radiation within the chamber. However, as additional experiments have been performed and the data set has become more comprehensive, new information concerning the measurement method, the effect of chamber structure, and the variation in

TABLE 5-2. Summary of average relative[a] spectral distributions used in modeling the SAPRC Evacuable Chamber (EC) experiments by Carter et al., (1986).

Run Nos.	Wavelength (nm)												
	290	300	310	320	330	340	350	360	370	380	403	430	500
106	0.001	0.039	0.146	0.357	0.572	0.789	1.000	1.119	1.239	1.316	1.425	1.557	1.618
113-116	0.002	0.034	0.128	0.318	0.533	0.758	1.000	1.172	1.338	1.467	1.682	1.921	2.154
120-125	0.000	0.047	0.121	0.292	0.532	0.767	1.000	1.165	1.291	1.406	1.551	1.736	1.788
142-160	0.000	0.018	0.082	0.238	0.464	0.706	1.000	1.214	1.417	1.605	1.892	2.092	2.419
161-172	0.000	0.016	0.077	0.222	0.449	0.705	1.000	1.189	1.451	1.715	2.107	2.334	2.874
177-178	0.001	0.031	0.167	0.379	0.627	0.837	1.000	1.093	1.241	1.371	1.598	1.771	2.134
216-217	0.000	0.023	0.137	0.347	0.608	0.828	1.000	1.089	1.228	1.344	1.534	1.633	1.587
230-233	0.000	0.024	0.131	0.327	0.593	0.810	1.000	1.168	1.316	1.459	1.753	1.939	2.152
237-257	0.001	0.016	0.110	0.289	0.528	0.773	1.000	1.170	1.418	1.634	1.970	2.350	3.147
264-287	0.001	0.018	0.122	0.316	0.565	0.787	1.000	1.117	1.275	1.396	1.502	1.625	1.688
304-309	0.000	0.020	0.125	0.314	0.558	0.798	1.000	1.131	1.309	1.454	1.602	1.756	1.939
314-320	0.001	0.019	0.131	0.369	0.695	0.970	1.000	1.348	1.557	1.691	1.804	1.915	1.861
327-331	0.000	0.003	0.095	0.283	0.517	0.788	1.000	1.142	1.342	1.486	1.691	1.878	2.167
334-340	0.000	0.000	0.093	0.280	0.525	0.783	1.000	1.161	1.382	1.549	1.778	1.998	2.474
343-346	0.000	0.008	0.106	0.284	0.531	0.775	1.000	1.149	1.359	1.530	1.729	1.941	2.277
389-392	0.000	0.004	0.099	0.272	0.529	0.782	1.000	1.173	1.400	1.587	1.817	2.110	2.684
435-465	0.000	0.000	0.083	0.260	0.521	0.773	1.000	1.189	1.366	1.521	1.699	1.898	2.459
596-603	0.000	0.000	0.044	0.208	0.450	0.732	1.000	1.210	1.458	1.734	2.069	2.457	3.187
898-903	0.000	0.000	0.000	0.018	0.122	0.454	1.000	1.520	1.968	2.234	2.766	3.034	3.596

[a]Normalized to give 1.0 at 350 nm.

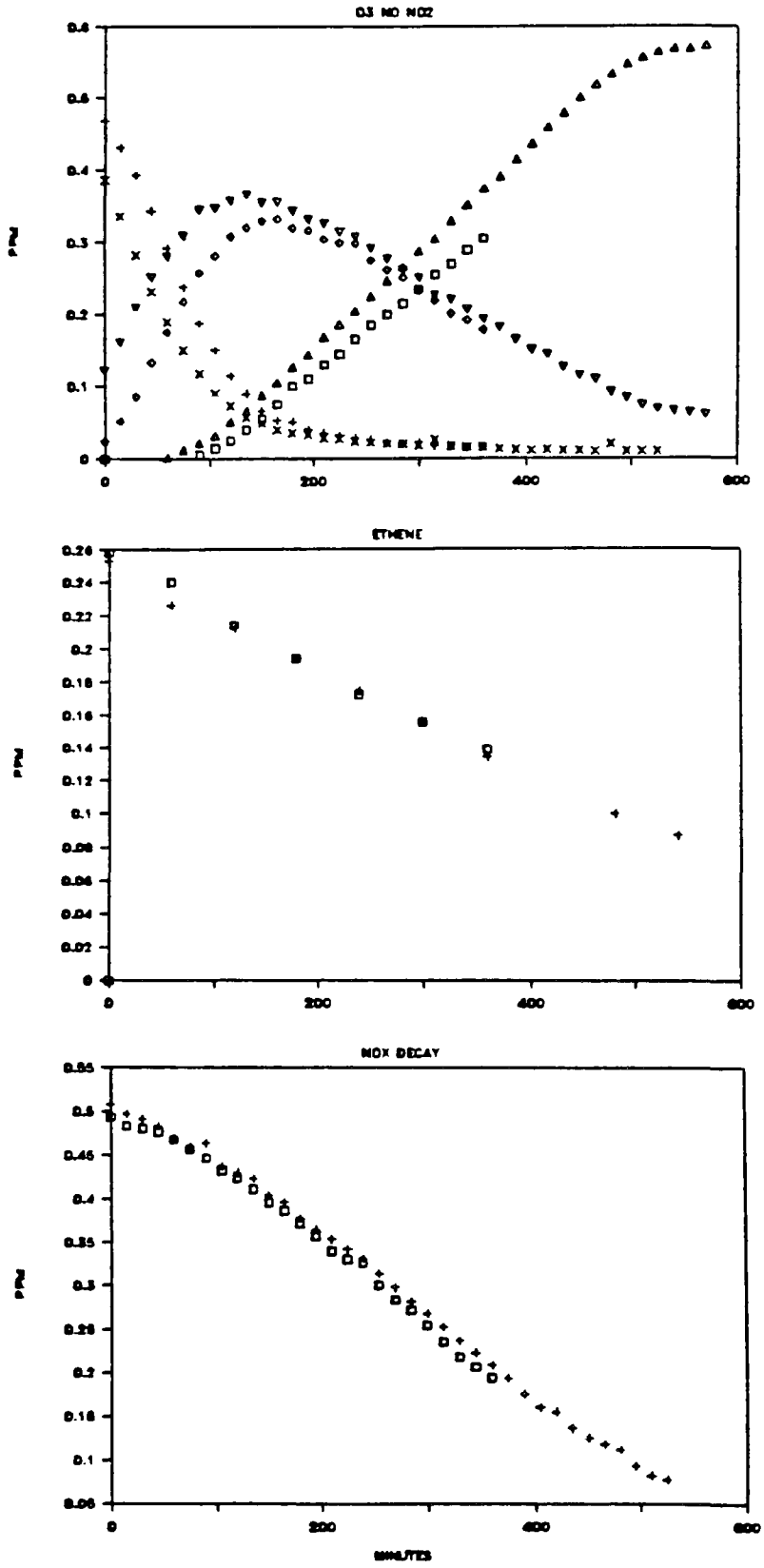

FIGURE 5-1. Comparison of experimental data for EC-232 and EC-246. Top: NO, NO2 and O3; Middle: Ethene decay; Bottom: NO_x decay.

detector(s)' response with time has become available and can now be incorporated into uniform data preparation methods. An investigation into the chamber-specific radiation processes is currently being conducted at UNC to provide greater certainty in these actinic flux calculations. In our mechanism development study, we have used the considerable amount of available data to formulate a clear-sky, in-chamber, radiation algorithm that uses the reported outdoor Eppley UV voltages. A necessary adjunct to this data reduction algorithm is a theoretical solar intensity function, which we use to compare and unify the data, determine true solar time, and fill in gaps in the UNC UV data. We discuss this solar function prior to describing the method for calculating in-chamber light intensity from the outdoor Eppley voltages provided by UNC.

Solar Function

Because the sun is a well-defined light source with an angle of elevation that can be mathematically described at any time, it is possible to derive an expression for clear-sky surface solar radiation with respect to time. Such a solar function is unaffected by chamber and instrument variations. Therefore, it can be used as a standard for both radiation magnitude and timing with any of the UV data sets. It can also be used as a basis for estimation of UV data when there are gaps in the measurements and is beneficial when the laboratory clock data are inaccurate.

The actinic flux inside the chamber is required to determine the in-chamber photolysis rates [$j_{IN}(p)$ for species p]. However, both the values from the solar function and the UNC UV measurements provide values for outside the chamber. Hence, a correction function must be derived so that the outside j-values [$j_{OUT}(p)$] can be used to provide an estimate of the in-chamber photolysis rates. We define a zenith-angle(ω)-dependent correction to $j_{OUT}(p)$ that will yield $j_{IN}(p)$ as

$$j_{IN}(p,\omega) = j_{OUT}(p,\omega) \times f_d(t) \times f_\tau(t) \times f_c(\omega) \times f_a(p),$$

where

$j_{IN}(p,\omega)$ and $j_{OUT}(p,\omega)$ are the zenith-angle(ω)-dependent, in-chamber and outdoor photolysis rate constants for species p,

$f_d(t)$ is a daily correction factor to light intensity for distance between the earth and sun,

$f_\tau(t)$ is a daily correction factor for atmospheric turbidity in North Carolina,

$f_c(\omega)$ is a zenith-angle-dependent correction factor for the effect of chamber structure on the radiation field, and

$f_a(p)$ is the species(p)-dependent fraction of light transmitted through the Teflon film of the chamber.

Solar distance corrections [$f_d(t)$] result primarily from the variation in solar intensity due to changes in the distance to the sun (Becker et al., 1966). The extraterrestrial flux in January is almost 7 percent greater than in July.

The correction for local atmospheric turbidity [$f_\tau(t)$] is based on the work of Peterson et al. (1981). Figure 5-2 shows the curve suggested by Peterson and coworkers. We have flattened this curve during July and August to provide closer agreement with the measured annual variation of NO_2 photolysis found in the UNC solar flux data. Daily turbidity values are determined through linear interpolation between monthly averages of the values from Figure 5-2. The value for $f_\tau(t)$ is then determined by

$$f_\tau(t) = e^{-0.10*T},$$

where T = 2.303 x turbidity (Figure 5-2). The constant, 0.10, was determined to provide a good fit with the observed seasonal variation at UNC.

Because the location of the UV meter is outside and slightly above the smog chamber, an outdoor to in-chamber conversion factor [$f_c(\omega)$] is applied to account for smog chamber structural effects, including reflection by the Teflon film, internal reflection of the aluminum floor, and attenuation by the chamber frame. The calculation of the variable magnitude of these effects provides the greatest uncertainty involved in the determination of in-chamber intensity. This ratio is assumed to be directly proporational to the amount of sky covered by the frame. This is determined geometrically to be between 5 and 8 percent. The primary uncertainty associated with chamber structure results from the poorly documented effect of reflection. The aluminum floor has been shown to enhance NO_2 photolysis inside the chamber (Saeger, 1977), and the external and internal reflections of the Teflon film are only now being addressed by UNC.

The best j-value experiments available at the time of our study were performed in October 1976, near the end of the experimental season. There is no information available for experiments performed near the summer solstice and there have been no actinometric measurements (until the current UNC study) since 1976. On 13 October 1976, several instruments were

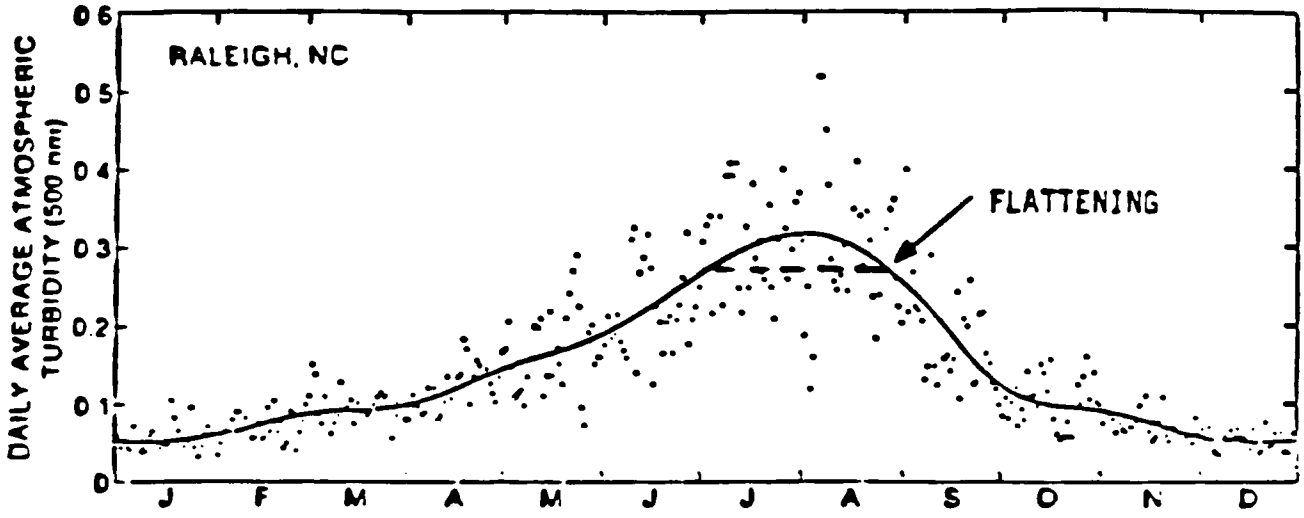

Source: Peterson et al, 1980

FIGURE 5-2. Data Points are daily average atmospheric turbidity in North Carolina (solid line represents the turbidity values used in the calculations).

used to measure j_{NO2} inside and outside of the UNC chamber. Results from this experiment are shown in Figure 5-3. A maximum j_{NO2} enhancement due to chamber effects of 1.15 ± 6 percent was found on that day at minimum solar zenith angle of about 44 degrees (at 0900, ω was about 60 degrees). As expected from consideration of chamber geometry, these results indicate that the enhancement due to reflection increases with decreasing zenith angle. Given the uncertainty associated with the magnitude of the correction, this result is important because the necessary correction appears to be minimal in the hours immediately after sunrise when proper representation of photochemistry is highly critical.

Given the values shown in Figure 5-3 and noted above, it seems likely that a slightly higher enhancement would occur at the calculated annual minimum ω near 11 degrees for Pittsboro, North Carolina. Therefore, we use a factor of 1.20 as our maximum chamber effects enhancement. As noted, the algorithm is dependent on zenith angle (a measure of true solar time) rather than on laboratory time.

For ω greater than 72 degrees: $f_c(\omega) = 1.00$;
for ω between 44 and 72 degrees: $f_c(\omega) = 0.85 + 0.40 \times \cos(\omega)$;
and for ω less than 44 degrees: $f_c(\omega) = 1.20$.

Finally, $f_a(p)$ describes the species (p) related effect of light attenuation by the Teflon film of the chamber. Such a process is probably wavelength-variable and could change as the angle of incidence between the direct solar beam and the Teflon surface varies. Some measurements presently being being performed at UNC may clarify this. At present, approximations involve large uncertainty. Jeffries and Sexton estimated the film transmission factors for j_{HCHOr}, j_{HCHOs}, j_{O1D} and j_{ALD2r} to be 0.50, 0.60, 0.40 and 0.45, on the basis of a preliminary spectrophotometer analysis of the film. It is also possible to utilize computer simulation models to fit specific smog chamber experiments by varying the transmission factors to achieve the best fit. Using the j-values described in Section 3, the film transmission factors for j_{HCHOr}, j_{HCHOs} and j_{ALD2r} were found to be 0.84, 0.84 and 0.88. These ratios are based on the differences between the j-values and the values previously used in the CBM-X (Whitten et al., 1985a), which were determined by the best fit approach. For j_{O1D}, the factor of 0.45 is determined on the basis of the ozone actinometry calculations performed by UNC and analyzed by Systems Applications. These data, though similar to the preliminary UNC measurements, suggest a sharper decline in UV transmission closer to the atmospheric cutoff region.

The variable $j_{OUT}(p,\omega)$ describes the zenith-angle-dependent change in photolysis rate for clear-sky, outdoor actinic flux. The value of

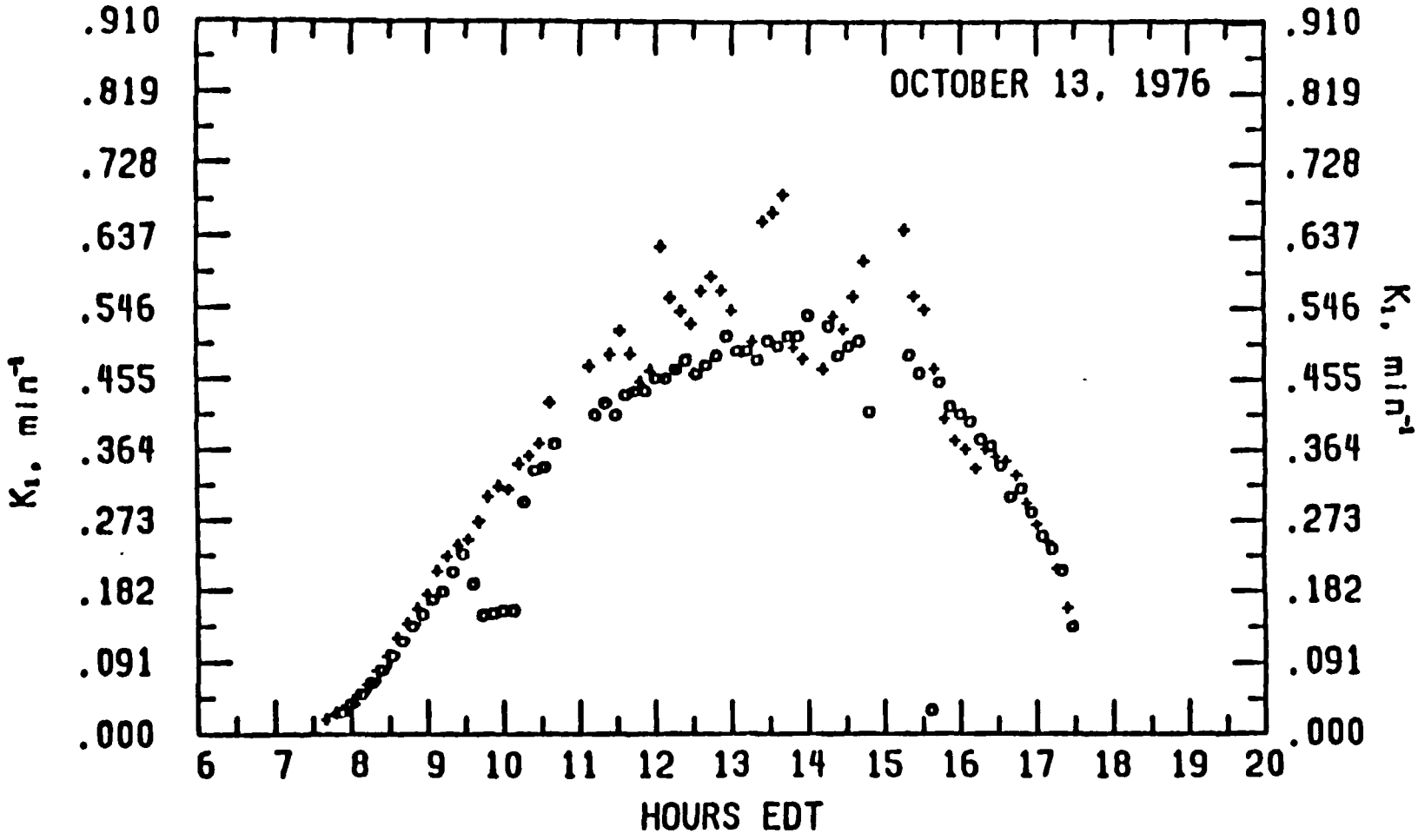

FIGURE 5-3. Specific photolysis rate of nitrogen dioxide and incidental total solar radiation and ultraviolet radiation as a function of time for 13 October 1976.

$j_{OUT}(p,\omega)$ is dependent on the ability of molecules to absorb incident light and photodissociate. Hence, as described in Section 3, this rate can be calculated from the products of clear-sky actinic flux [$UV(\omega,\Delta\lambda)$], absorption cross-section (σ_p), and quantum yield (ϕ_p) summed in the smallest wavelength intervals ($\Delta\lambda$) over the appropriate wavelength region for given zenith angles:

$$j_{OUT}(p,\omega) = \sum_{\Delta\lambda} UV(\omega,\Delta\lambda) \times \sigma_p(\Delta\lambda) \times \phi_p(\Delta\lambda).$$

The values for UV are determined from UNC data or, if necessary, from the actinic flux calculations of Demerjian et al. (1976) as noted by Jeffries and Sexton (1987). The sources for absorption cross-section and quantum yield data are described in Section 3.

UNC Data Reduction

It has been known for several years that the Eppley UV meter sensitivity varies between calibrations. In addition, various artificial processes such as chamber shadowing, floor reflection, and light attenuation within the chamber and meter due to temporary dew or ice formation, have been suggested as causes for inaccurate estimation of in-chamber radiation. Also, since changes in surface spectral distribution result in different rates of photolysis among photoreceptor species, the true time of day must be known because the spectral distribution depends upon solar elevation. Hence, just as errors in radiation magnitude can lead to poor simulation of experimental data, so will uncorrected differences in laboratory time and true solar time.

The j-values used in our simulations are calculated from the UV data supplied by UNC. These calculations are a result of three adjustments made to the initial UV data: (1) application of an annual, long-term correction and calibration factor; (2) conversion of flat-plate Eppley UV data to j_{OUT} values; and (3) application of the outdoor-to-indoor chamber correction function. A fourth adjustment, correction of laboratory time to true solar time, is made in conjunction with the last correction.

Differences in annual correction factors result from variations in the UV instrument sensitivity with time or because instruments have been replaced. UNC has supplied a list of instruments and calibration factors used throughout the experimental period. Consideration of this information, along with comparison of calculated UV data within a given year and over all ten years (see figures), provided the annual factors. We have

found that correction for the years 1982 through 1986 is unnecessary (although we have only a limited number of 1985 and 1986 data sets available), and have used these data as standards for correcting data for earlier years. In some cases (especially 1980 data), the response of the Eppley UV instrument decayed significantly over the experimental season. A linearly increasing correction, beginning at 1.47 on 1 June and ending at 2.06 on 1 September, has been applied for 1980. The correction factors deemed appropriate for 1978, 1979, and 1981 are 1.18, 1.30 and 1.20, respectively.

After the UV data is corrected for annual variations, the flat-plate Eppley UV data to $j_{OUT}(NO_2)$ conversion is applied using the function

$$j_{OUT}(NO_2) = UV_{+}1.533\times10^{-2} - UV^2{}_{+}1.325\times10^{-4} + UV^3{}_{+}3.791\times10^{-7}.$$

This function is shown graphically in Figures 5-4 and 5-5 along with the original data from Stedman et al. (1977) and Zafonte et al. (1976). J-values for other species are calculated from nonlinear zenith-angle-dependent relationships as described in Section 3.

The correction for chamber effects is applied to the derived j_{OUT} data to estimate the in-chamber experimental j-values. Determination of true solar time (laboratory time offsets) is inherent in these calculations. It was necessary to offset (add time to) the laboratory clock by 12 minutes for all experiments for 1978 and 1982. In addition, the experiments for late 1984 (all of October) required an offset of about 40 minutes. The laboratory clock appears to be acceptably correct (within 10 minutes) for all other time periods, but this correction is both critical and elusive. Special care must be taken to account for all clock offsets, but to not "adust" the UV data on a daily basis, since the laboratory clock was adjusted very infrequently.

As noted, UNC is presently assessing the data reduction method and associated uncertainty. We assume an uncertainty in these calculations of up to 20 percent in extreme instances. However, it must be kept in mind that the error associated with the data will not linearly translate into error in the kinetic simulation. For most simulations of UNC experiments, the period between dawn and late morning shows the highest sensitivity to photolysis rates, especially to the photolysis rate of formaldehyde to radical products. Figure 5-3 indicates that there is little difference between indoor and outdoor measurements during this critical time. The outdoor chamber appears to have the same photon flux and spectral distribution as the ambient atmosphere until nearly midday. Hence, the critical errors are those associated with determinations of ambient photolysis

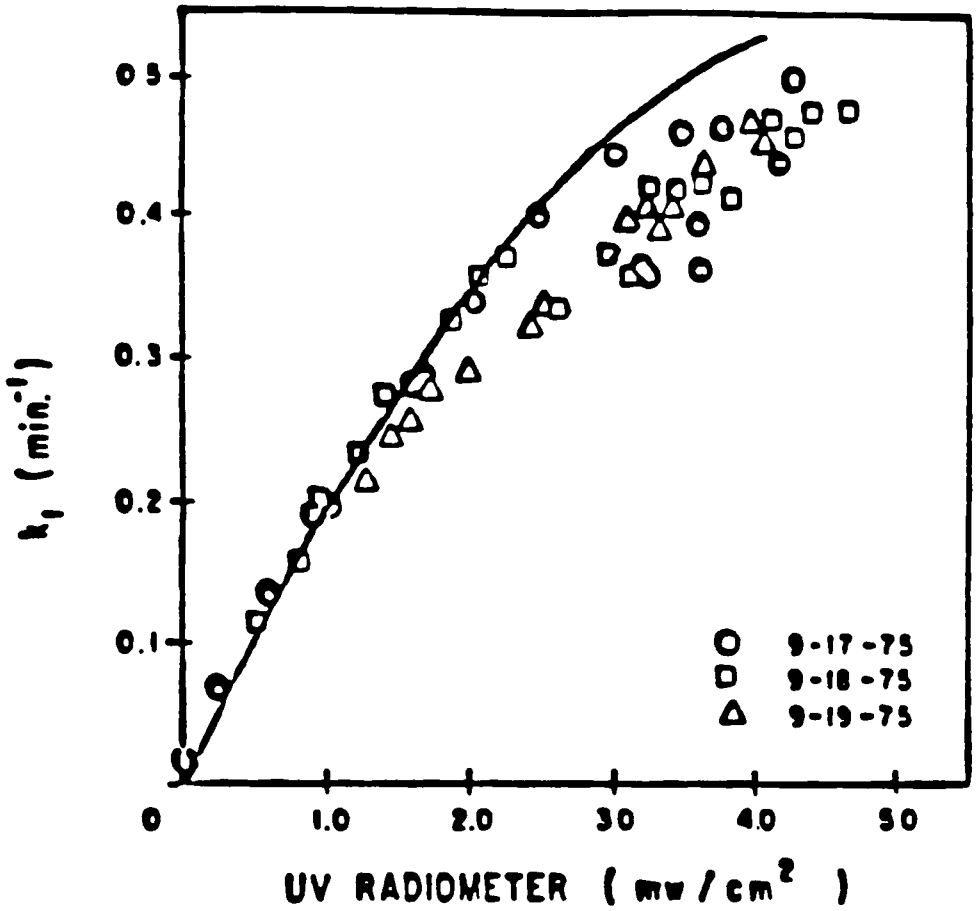

Source: Zafonte et. al, 1976

FIGURE 5-4. Data Points from Zafonte (solid line is Systems Applications' solar function).

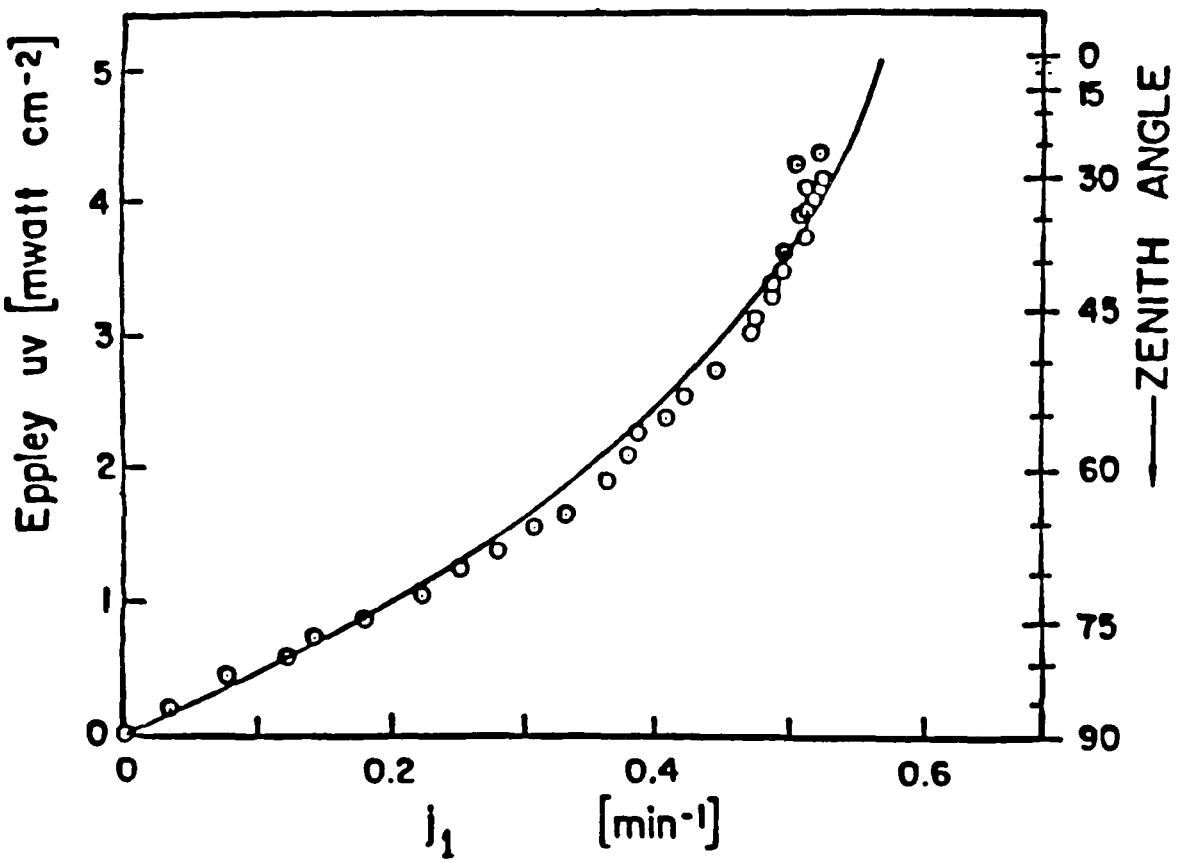

Source: Stedman et al., 1977

FIGURE 5-5. Data points from Stedman (solid line is Systems Applications' solar function).

rates. For clear days, error measurements are not necessary; they are no worse than the errors associated with determining photolysis rates for solar flux as a function of zenith angle. As stated earlier, some errors arise from inaccuracies in the UNC clock time and we have attempted to adjust the timing of these experiments to alleviate such errors. We discuss evidence of these uncertainties later in this section.

WALL-RELATED PROCESSES

The issue of trace contaminants and artificial effects in smog chambers continues to be a major uncertainty in the evaluation of smog chamber results. These effects become important when experimental reproducibility is affected, or when chamber-dependant phenomena mask the homogenous gas-phase photochemistry that an experiment is designed to elucidate. In the latter case, precise characterization of the chamber-dependant processes can extend the range of conditions for which the data can be reliably interpreted. Therefore, we next describe techniques used to characterize chamber processes in an attempt to clarify the nature and magnitude of contaminant effects.

Because smog chambers are batch-type reactors, the entire interior surface is in contact with the reacting medium through all phases of an experiment. Also, since the surface-to-volume ratio of a smog chamber is much greater than that of the atmosphere, the chamber surface effects are greater than those applicable to the atmosphere near the surface of the earth. Although the current practice is to minimize the reactivity of chamber surfaces through the use of nonreactive materials and various cleaning procedures (Pitts et al., 1979; Jeffries et al., 1976; Kelly, 1982), the chamber walls can still be a potential surface for heterogeneous processes, and thus a significant sink and source of some trace species.

Chamber surface effects are manifest in two general ways during smog chamber experiments. First, because smog chambers are usually vented and loaded with reactants prior to illumination (natural or artificial), a period occurs when the trace contaminants produced by dark, heterogenous reactions can accumulate before an experiment begins. During the initial minutes of illumination, these chemical species can then have an initially strong and detectable influence on the chemistry. Second, the reactor walls act as a nonideal surface throughout an experiment. This includes not only heterogenous adsorption and desorption processes, but also leaks and dilution resulting in unintended inclusion of trace contaminants throughout the experiment. In the following discussion, we examine evidence concerning the nature and magnitude of wall-related processes and

their effects on both initial and continuing conditions. We then present our mechanism representations and the values used to model a variety of environmental chambers.

Chemical Description of Artificial Processes

Three different types of chamber trace chemical contaminants can interact with the intended experimental photochemistry:

(1) Free radicals introduced either directly or indirectly, which can initiate or maintain the photooxidation process;

(2) NO_x species, which can allow the formation of O_3, PAN, etc., and serve as a radical sink; and

(3) Organic species that can be photooxidized to provide conversion of OH to RO_2, and NO to NO_2, and allow the formation of O_3, PAN, and other oxidants through smog chemistry.

Although radical sources are probably the most noteworthy "dirty chamber" trace species, NO_x and organic oxidation sources can have a significant effect on low-NO_x or low-reactivity experiments. Also, most trace contaminants have multiple influences. For instance, HONO, when photolyzed, serves as both a radical and an NO_x source. Also, formaldehyde may be eliminated by loss to wet walls early in an experiment, but later released as the chamber is heated up. Proper characterization of the processes affecting these species provides a more rigorous description of their behavior.

Various chamber characterization methodologies have been used to help delineate chamber effects. These include the use of differential tracer decay techniques to assess radical input rates (Carter et al., 1982), high NO_x experiments with and without high concentrations of CO to assess radical levels and oxidation background (Kelly, 1982; Leone et al., 1985; Whitten et al., 1983), acetaldehyde-only simulations to test for trace NO_x by measuring generated PAN (Whitten et al., 1979; Whitten et al., 1983), and blank simulations using only background air to assess unperturbed chamber reactivity and reproducibility (Akimoto et al., 1979; Carter et al., 1986; Whitten et al., 1983). These experiments provide evidence for the type and magnitude of artificial effects due to specific trace species. It is our belief that whenever possible, chamber effects should be described with respect to the actual or likely trace compounds that appear to be involved in these processes. The alternative is to provide a simplified phenomenological description (e.g., sources of pure OH, HO_2,

NO_x, or OH-to-HO_2 reactions) for modeling purposes only. Inevitably, conditions are encountered in the chamber or the atmosphere for which such empirical descriptions are inappropriate. If unrealistic chemical responses have been "built into" a chemical mechanism because of inappropriate chamber artifact descriptions, some description of chamber conditions may be inadvertently included in the mechanism during simulation of the atmosphere. This could result in good chamber simulations, but overly or underly reactive simulations of the atmosphere. We attempt to point out the benefits of a more rigorous chemical description of chamber processes in the following discussion. We begin with consideration of the most commonly used radical source, nitrous acid.

Free Radical and Trace NO_x Sources

Nitrous acid (HONO) is a probable source of both radicals and trace NO_x in smog chambers; it photolyzes rapidly (to OH and NO) and, because it is soluble and can ionize in solution, it is likely to be adsorbed and desorbed by chamber surfaces. Furthermore, a number of processes (mostly heterogeneous) have been proposed for its formation (Besemer and Nieboer, 1985; Pitts et al., 1984; Sakamaki et al., 1983; Lee and Schwartz, 1981). Evidence of trace HONO exists in a variety of experimental circumstances, which seems to indicate that there are different formation pathways. These include:

Non-zero gas-phase concentrations at the beginning of an experiment, which seem to be linked in part to initial chamber NO_x (Leone et al., 1985; Whitten et al., 1979; Whitten et al., 1983; Carter et al., 1982; Pitts et al., 1983);

Continuous emission from nitrated chamber walls (Whitten et al., 1979; Whitten et al., 1983);

Continuous conversion of gas-phase NO_2 to HONO [probably heterogeneous, as studied by Sakamaki et al. (1983) and Pitts et al. (1984); and

Occasional high-input HONO "incidents" involving evaporation of liquid water from (outdoor) chamber walls (Whitten et al., 1983).

It is very difficult to directly measure gas-phase HONO under illuminated conditions because photolysis depresses its concentration to very low levels. Moreover, HONO is also produced under daylight conditions by the reaction of OH with NO. As this formation reaction coincides with the photolysis of HONO under illuminated conditions, these two reactions produce a "do nothing" cycle and a steady-state type of HONO concentration

unrelated to the net source of OH and NO_x derived from other means of producing HONO (i.e., all sources other than the reaction of OH with NO). Hence, the only direct confirmation of HONO involvement in trace "contamination" would come from measurements of HONO under dark conditions. Direct measurements of initial HONO concentrations seem to be related to initial NO_x loading (see Table 5-3).

Continuous conversion of NO_2 to HONO has been studied in several chambers by Sakamaki et al. (1983) and Pitts et al. (1984). Of the two heterogeneous processes for which Sakamaki et al. derived rates, the more important process is

$$NO_2 + H_2O \text{ --(wall)--> } HONO,$$

involving gas-phase water at a rate of 1.01×10^{-8} ppm^{-1} min^{-1}. Dry conversion of NO_2 to HONO,

$$NO_2 \text{ --(wall)--> } HONO,$$

at 3.9×10^{-5} min^{-1} was also estimated. At 20,000 ppm, H_2O (ca. 50 percent relative humidity at 300 K), these two processes give an estimated first-order conversion of NO_2 to HONO of 2.4×10^{-4} min^{-1}. This is twice the conversion rate observed by Pitts et al. for the UCR-EC and four times that of the UCR-ITC. It is worth noting that the NO_2-to-HONO yield in these experiments was observed to be from 0.21 to 0.44 of the first order decay of NO_2. Thus, the magnitude of this process might be crudely estimated from NO_2 dark decay measurements, even in the absence of direct HONO measurements.

Although, as we have previously noted, measurement of continuous HONO emissions in illuminated systems is very difficult due to HONO photolysis, an upper limit may be estimated by measuring total NO_x emissions. This can be done by irradiating pure acetaldehyde and measuring the formation of PAN (Whitten et al., 1979). In the UCR-EC, for example, such an experiment has yielded 40 ppb of PAN (and 190 ppb O_3) after six hours, or a total NO_x-input rate of 0.11 ppb/min. This value for an irradiated experiment is much less than the 0.3 ppb/hr NO_x-input rate reported by Pitts et al. (1981) in the absence of light. The similarity between total NO_x emissions and the magnitude of the chamber radical source (the NO_2-independent term discussed by Carter et al.) for the chambers considered here suggests that NO_x emissions may be primarily in the form of HONO. NO_x offgassing incidents have been shown to occur in the UNC chamber under

TABLE 5-3. Comparison of total NO_x with measured HONO in the UCR-EC (Source: Pitts et al., 1983).

Exp. No. (EC)	NO	NO_2	NO_x	HONO (ppb)	HONO (percent of NO_x)
567	1.450	0.467	1.917	21.	1.1
568	1.032	0.772	1.804	12.	0.7
569-A	1.058	0.100	1.158	> 25.	> 2.2
B	0.668	0.450	1.118	15.	1.4
570-A	1.464	0.370	1.834	29.	1.4
B	1.724	0.840	2.564	17.	0.7
626	0.385	0.103	0.488	5.1	1.0
630-A	2.322	0.824	3.146	21.7	0.7
B	2.163	0.838	3.001	28.6	1.0
631-A	1.936	1.053	2.989	16.6	0.6
B	1.950	0.898	2.848	11.8	0.4
632-A	2.200	0.794	2.994	19.	0.6
B	2.189	0.806	2.995	14.	0.7

special conditions involving the condensation of liquid water on the chamber walls, and additional evidence implies that the NO_x emitted is HONO.

Both evidence of NO_x offgassing in the UNC outdoor chamber and an analysis by Kamens et al. (1980) that is based on ionic and phase equilibria for NO_x species provide examples of HONO acting as a background radical and NO_x source. Nitrate, nitrite, and dissolved NO_x species establish equilibrium concentrations in the liquid phase, and NO_x offgassing may occur as a result of aqueous chemical conversions, ionic equilibrium, and phase equilibrium for various NO_x species. Experimentally, there is also some evidence of heterogeneous conversion of nitric acid to gas-phase NO_x in Teflon chambers (Jeffries, 1979).

For HONO, the aqueous equilibrium concentrations (and offgassing rates) appear to be highly dependent on pH. At low acidity, more HONO ionization is possible, resulting in a larger effective solubility for gas-phase HONO. As acidity increases, however, less ionization of HONO occurs and proportionately more aqueous HONO is available. This should result in the elution of HONO from solution into the gas phase to reestablish phase equilibrium. Different hydrogen ion concentrations will also affect the rates of chemical change in the aqueous phase and shift the overall NO_x balance to different species. Kamens et al. (1981) conjecture that NO_2 becomes the major form of dissolved NO_x at intermediate pH (versus ionic nitrate and nitrite), leading to episodes of chamber NO_2 emissions because NO_2 is at least three orders of magnitude less soluble than HONO (Schwartz, 1984). In addition, as water evaporates off the chamber walls, the aqueous nitrite ion may reform aqueous HONO, which in turn could induce the liberation of HONO to the gas phase.

Figure 5-6 shows experimental concentration data and simulation results for a liquid-water-associated NO_x emission episode in the UNC chamber. Such an experiment measures chamber NO_x emissions by converting the NO_x to PAN, which is easily measured and is not rapidly converted to nitric acid. In this experiment, both sides of the two-sided outdoor chamber were loaded with 1 ppmC of acetaldehyde. As the condensed water on the chamber walls evaporated, 70 and 100 ppb of NO_x were emitted from the two sides, respectively. The rapid buildup of PAN and the lagged formation of O_3 are consistent with a powerful radical source. The ozone formation delay is due to a suppression of NO_2 by radical scavenging processes. In a modeling study (Whitten et al., 1983), attempted to characterize the NO_x emissions as NO or NO_2 caused a rapid increase in O_3 that parallels PAN formation, rather than the experimentally observed 2- to 3-hour delay. However, the use of HONO as the radical source allowed simulation of the delay in ozone formation (Figure 5-6).

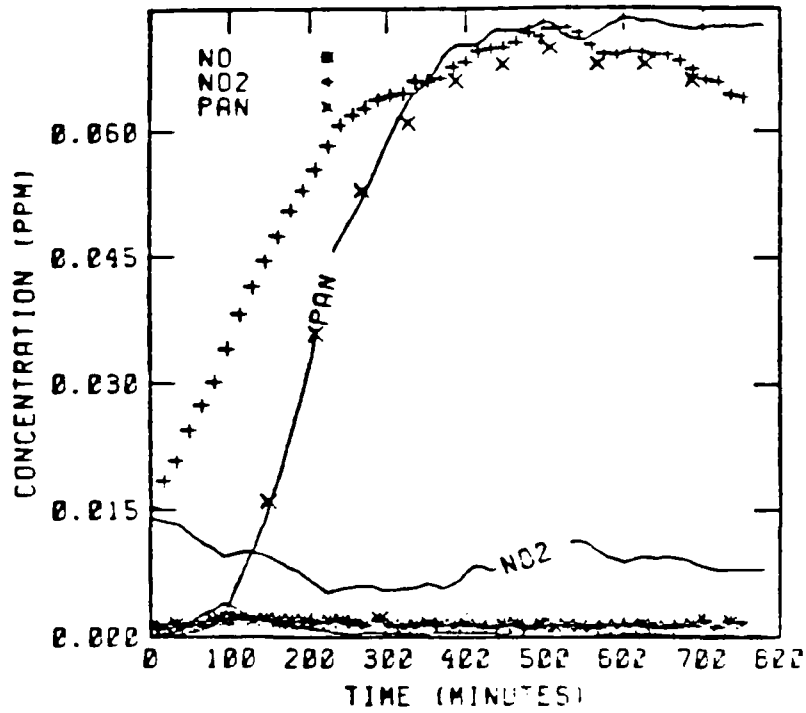

(a) Red Side: NO_x

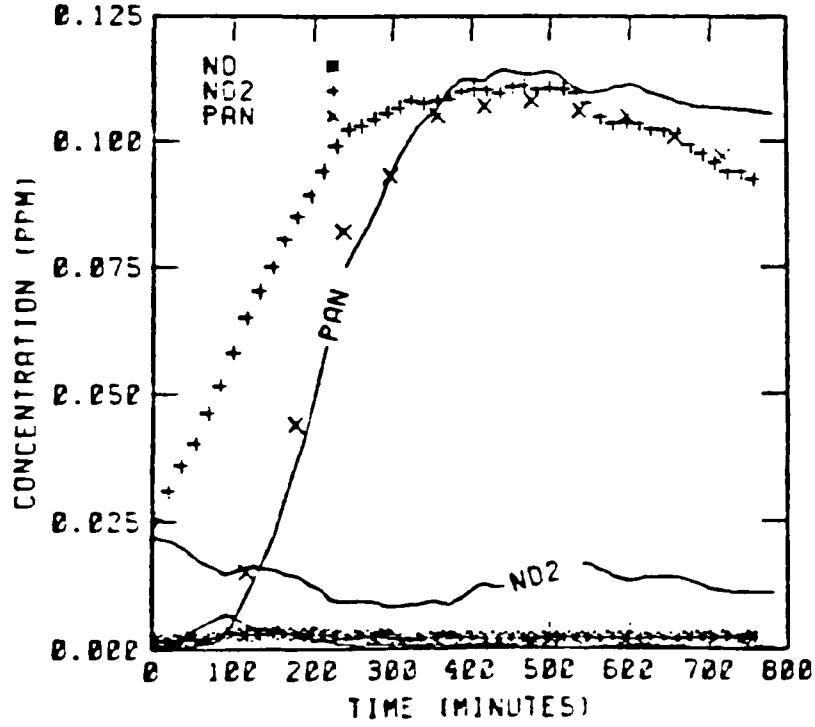

(b) Blue Side: NO_x

FIGURE 5-6. Simulation results for UNCR 72179 (NO_2 data includes PAN).

A large radical and NO_x source such as that caused by HONO emissions in the liquid water incident can render an experiment useless for photochemical analysis and model validation. Additionally, liquid water has been shown to absorb formaldehyde in the gas phase and to re-emit it upon evaporation and warming (Whitten et al., 1983). Such processes further complicate analysis of experimental data. To address this problem, researchers at UNC have developed procedures for predrying the smog chamber (Kamens et al., 1981). Furthermore, since this problem is common in outdoor bag-type experiments, either such drying procedures must be used or data from experiments in which condensation was observed must be carefully considered.

Organic Species

Observed background chamber reactivities are usually significantly greater than the effect of the reactive hydrocarbons measured in the background air would indicate (see below and Whitten et al., 1983). On the other hand, oxygenated hydrocarbons (especially lower molecular weight aldehydes and dicarbonyls) are often not included in the reactive hydrocarbon measurements because they are difficult to measure reliably at low concentrations and they are significantly reactive, even at levels of 10-50 ppbC. Furthermore, since these compounds are soluble and polar, they can be adsorbed on chamber walls or dissolved in any liquid water in the chamber. This causes situations where chamber walls could conceivably collect and later release carbonyl species. As we discuss below, collection could occur prior to illumination during chamber loading or during an experiment, if significant production of one of these species (such as formaldehyde from ethylene oxidation) were to occur rapidly.

The most apparent evidence of aldehyde-type contamination is found in the frequent formation of PAN (~ 10 ppb) in experiments that have no known PAN precursors. Acetaldehyde emissions of 0.05-0.1 ppb/min are generally sufficient to explain measured PAN. It should be noted however that other species may serve as PAN precursors, especially in outdoor chambers where background levels of biogenic hydrocarbons may contribute (Killus and Whitten, 1984).

Although formaldehyde contamination is probably greater than that of other aldehydes because of its higher formation rates and large solubility constant (Ledbury and Blair, 1925), HCHO can be more difficult to measure than higher aldehydes and does not lead to an easily measured product such as PAN. Background concentrations of HCHO have been routinely observed in some chambers (Carter et al., 1982). Unfortunately, the observed concentrations are usually too low (0-50 ppb) to allow precise and accurate measurement by the wet chemical methods that are often the only ones available. Even at concentrations as high as ~ 0.5 ppm, when measured amounts

of HCHO are introduced into the chambers, gas-phase measurements are often scattered and frequently show less than the amounts actually added, perhaps because of adsorption on chamber and instrument surfaces. Even more elusive is the heterogenous nature of dicarbonyl species, which can be formed in high yields in some aromatic oxidation experiments. The more common of these species, glyoxal and methylglyoxal, have solubility constants comparable to that of formandehyde (Betterton and Hoffmann, 1987).

A trace background of HCHO, maintained by continuous desorption from (and adsorption to) the chamber walls, can serve as both a radical source (upon photolysis) and a photooxidant precursor (upon reaction with OH to form HO_2). For example, if the gas-phase concentration of OH is decreased by an increase in NO_2 (an OH sink), proportionately more of the HCHO will photolyze since the competing process is suppressed. Since the increase in NO_2 correlates with an increase in the HCHO radical source, one might conclude that NO_2 is related to a chemical step producing the radical source, but what is actually occurring is that NO_2 is anticorrelated with a radical source suppression, which is not the same as being part of the radical source. Under more reactive conditions (i.e., typical chamber experiments), the trace HCHO background would tend to be oxidized rather than photolyzed and would have little impact on the experiment.

Dilution and Sink Processes

Small quantities of typical ambient hydrocarbons (< C_4 alkanes, ethene, etc.) are often measureable in the initial loading or dilution air of smog chambers (dilution air also includes air entering through small holes in the Teflon walls of a well used chamber). This is especialy true for large outdoor chambers such as the UNC dual chambers or the UCR-OTC. Indoor chambers often use filtered air and have less leaks, thereby negating the consideration of dilution air hydrocarbons. Typically, the total reactive (nonmethane) hydrocarbon loading should be much less than 50 ppb (Killus, 1982). Moreover, these species are usually of low or intermediate reactivity and should have minimal effect on most chamber experiments. We present our estimates of these input fluxes later in this section.

As noted, the chamber walls might serve as a net sink for aldehydes and dicarbonyls during initial phases of smog chamber experiments. Because wall water evaporates, however, a strong source of these species could exist for a few hours in the middle of an experiment. In the experimental results that follow, we repeatedly see no formaldehyde measured in the first few hours of an experiment, followed by an increase that is extremely rapid and cannot be simulated with homogeneous reactions. In some extreme ethylene experiments, we find no formaldehyde formed during

the initial oxidation of ethylene (formaldehyde is the main oxidation product of ethylene), followed later by a period when formaldehyde concentration increases so rapidly that complete conversion of the reacting ethylene could not account for the magnitude of the change in formaldehyde. We will show many instances of such an effect in Section 6. These effects also appear in aromatic experiments where dicarbonyl wall influences could occur. Because the dinitrophenyl-hydrazone/liquid-chromatographic-analysis technique for dicarbonyls is far more cumbersome than measurement with the automated colorimetric (CEA) formaldehyde monitor (at UNC), there is as yet little evidence for the dicarbonyl wall processes.

For other species the sink effects of chamber walls appear to be of little concern except in the case of a few species that accumulate at the end of a 1-day experiment (e.g., HNO_3, H_2O_2, and higher molecular weight peroxides). These species do not normally influence the aspects of the photochemical process under investigation in such experiments. On the other hand, we will present evidence in the following discussion suggesting that the wall losses of these compounds in multi-day experiments could be important and cannot be ignored.

Trace Contaminants in Specific Chambers Simulated in this Study

Indoor Chambers: The UCR EC and ITC

We have suggested that the contaminant species of greatest importance in smog chamber simulation are nitrous acid (HONO) and oxygenated hydrocarbons, especially formaldehyde (HCHO). The analyses reported next further support the hypotheses that HONO is the main radical-and NO_x-source species, while HCHO is responsible for much background oxidation reactivity (conversion of OH to peroxy radicals) and has a lesser effect on radical inputs.

Nitrous acid emissions from smog chamber surfaces differ in one important respect from all other forms of radical inputs to these systems. Because the photolysis of HONO introduces both NO and a hydroxyl radical, no net change of NO_x occurs when the radical terminates as nitric acid or another nitrate species (e.g., PAN). Thus, with the exception of HONO inputs, NO_x decay may provide an easily obtained estimate of intergrated radical inputs, since most radical termination reactions do result in the formation of nitric acid or organic nitrates. This simplified picture of radical input and termination is valid until oxidation has proceeded to the point where nitric oxide (NO) levels are low and radical termination (through radical-radical self-reactions) becomes important. This is approximately the time when NO_3 and N_2O_5 levels become significant relative to total

NO_x, and loss of these species becomes an important NO_x sink. Usually either ozone or PAN, or both, will attain maximum concentrations at this time.

It is possible to obtain an estimate of hydroxyl radical concentrations in a smog chamber experiment by observing the decay behavior of both hydrocarbons and NO_x. The decay rate of many hydrocarbons is primarily due to reaction with hydroxyl radical. In some cases, the hydroxy decay rates are slow enough to require a correction for dilution; in others, (such as olefins) decay due to O_3 and $O(^3P)$ must be taken into account. In order to use NO_x decay to calculate OH levels, a correction for both dilution and for PAN formation must be used. The latter correction must be applied because OH is calculated from the direct loss due to OH:

$$OH + NO_2 \rightarrow HNO_3, \qquad (26)$$

while PAN formation depends upon the production of peroxyacetyl radicals from many sources.

An example of these two methods of OH calculation may be seen in Figure 5-7, which compares estimated OH based on NO_x decay (corrected for dilution and PAN formation) to OH estimated from the decay rates of toluene, xylene, and 2,3,dimethylbutane (corrected for dilution and averaged), for an experiment in the UCR Evacuable Chamber. As may be seen, for most of the experiment the two methods of estimating OH are in good agreement.

In very low reactivity experiments, however, NO_x decay is not consistent with OH calculated from relative hydrocarbon decay. In Figures 5-8 and 5-9 we show results of OH calculated from NO_x decay compared to OH obtained from propene decay, as reported originally by Carter et al. (1982). Over a wide range of chamber operating conditions and NO_x levels, NO_x decays at a much lower rate than one would expect from estimates of OH. There are two possible causes of this phenomenon: (1) the estimates of OH concentration are in error, or (2) some source of NO_x is balancing the radical inputs. The former possibility may be largely discounted, since other techniques of OH radical level estimation corroborate the hydrocarbon decay estimates. Because CO addition and subsequent NO-to-NO_2 conversion in UCR-ITC experiments agree with the hydrocarbon decay estimates of OH (Table 5-4) a counterbalancing NO_x source is very probable.

Given the wide variation in radical levels and input rates estimated from these experiments, it would be an extraordinary coincidence to find a separate NO_x source that so nearly (within about 10 percent) balanced the radical source. It is much more likely that the radical source and the NO_x source are the same species. This suggests photolytic nitrites,

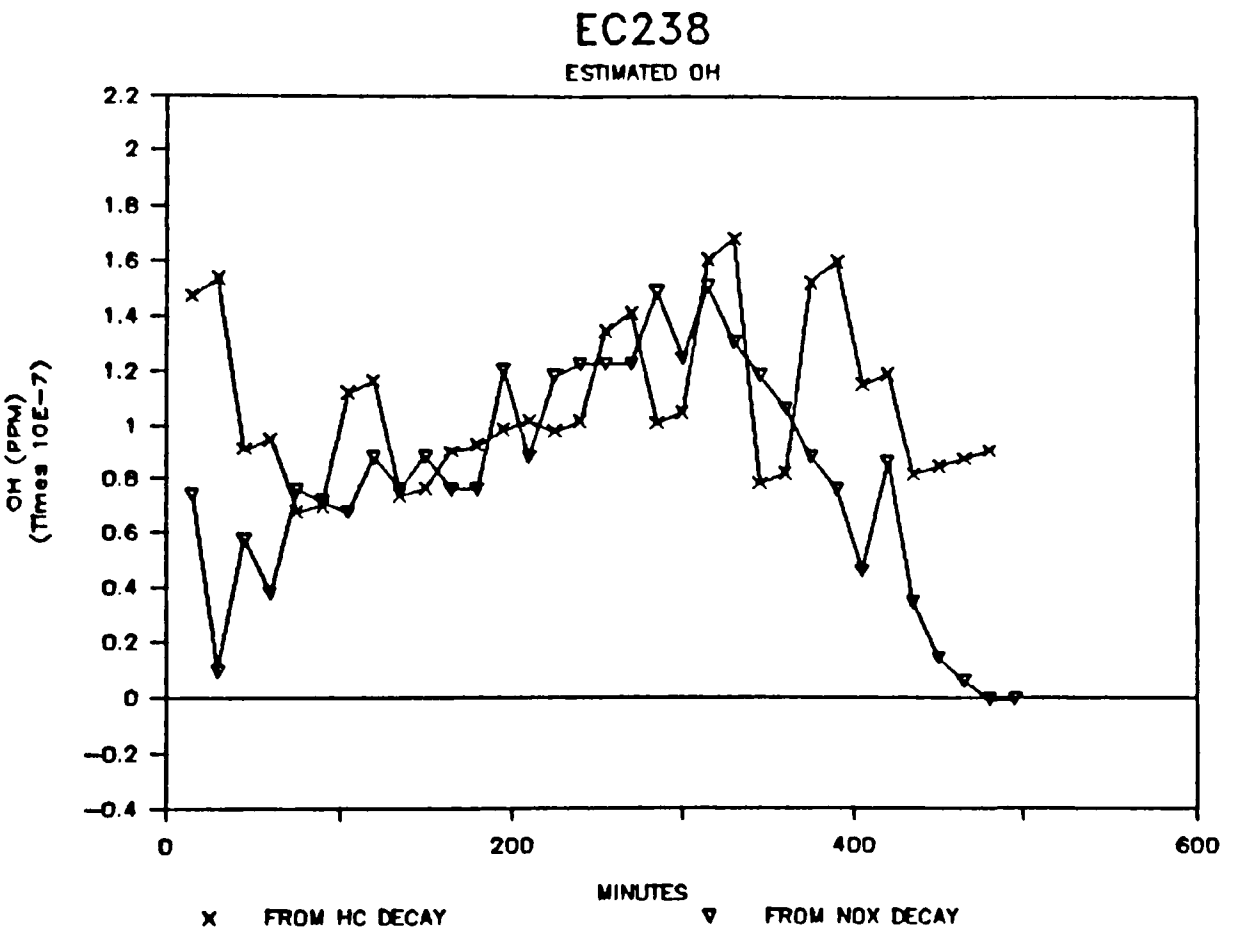

FIGURE 5-7. Estimated hydroxyl radical concentrations for UCR EC-238 using two different radical estimation techniques.

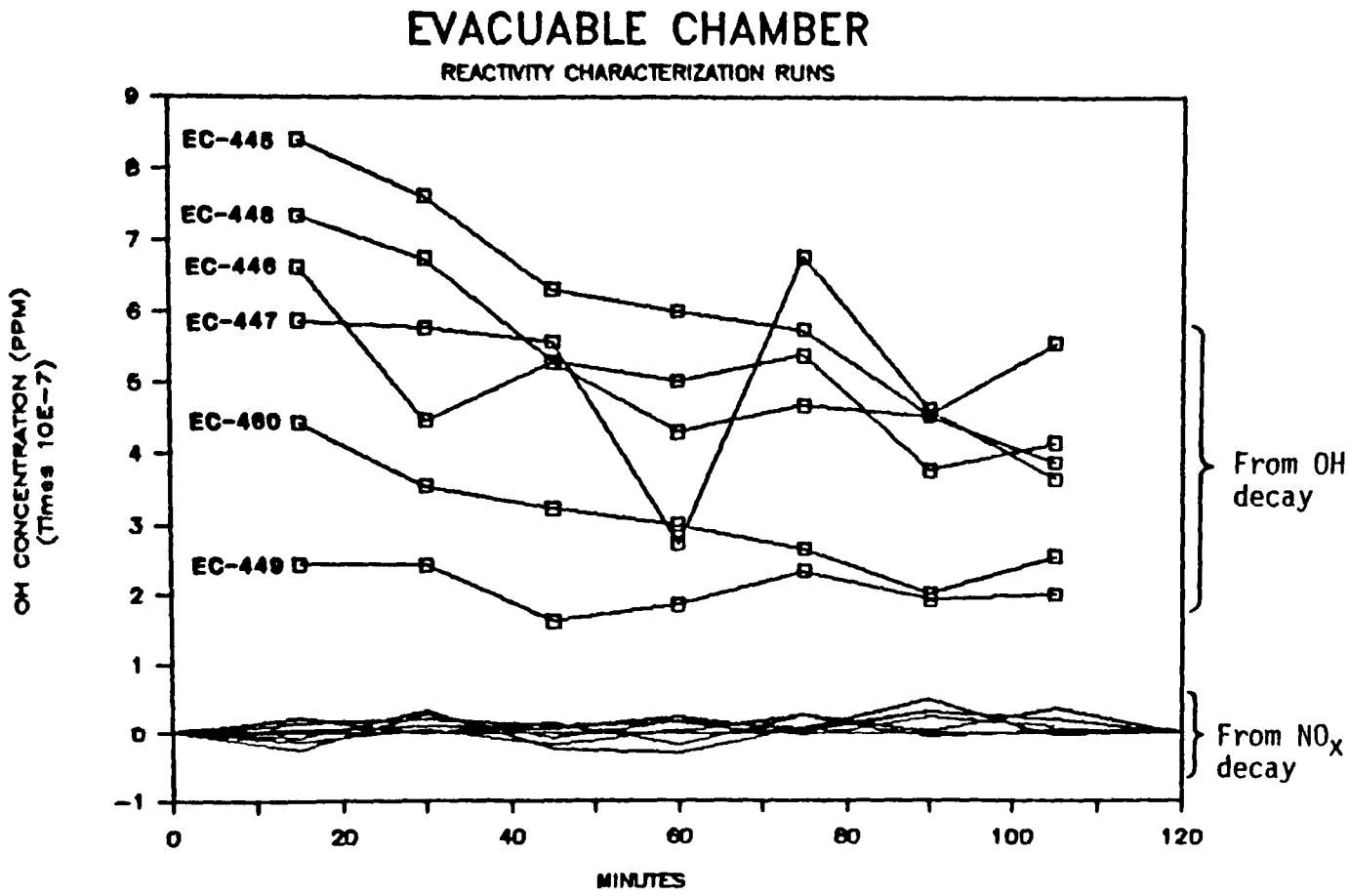

FIGURE 5-8. Estimated radical concentrations for a set of UCR EC experiments.

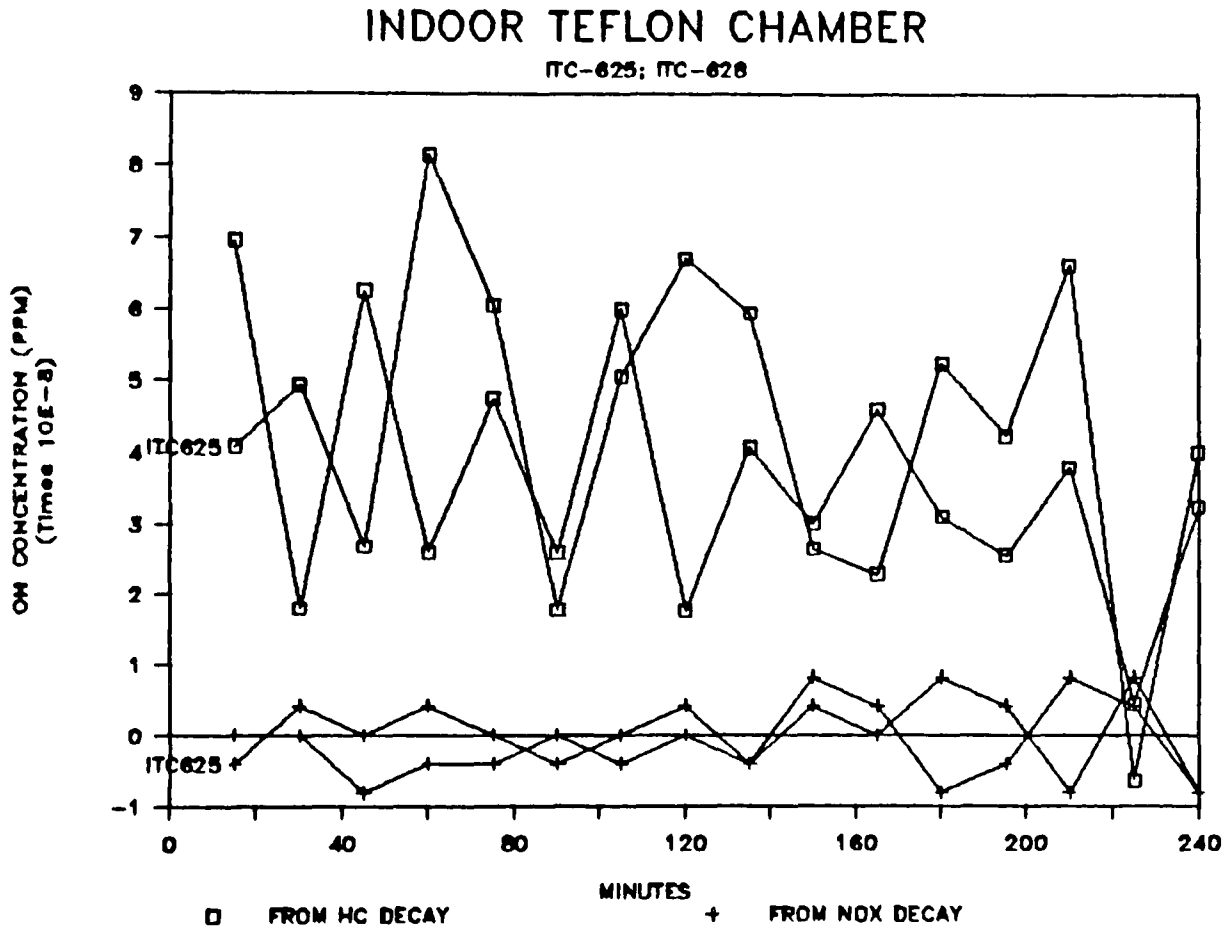

FIGURE 5-9. Estimated radical concentrations for two UCR ITC experiments.

generally, and HONO in particular as the primary radical source species. It is also worth noting that while the radical source seems primarily associated with an NO_x source, the converse is also true; most of the NO_x that is emitted from the chamber walls seems to be associated with radicals. Although NO_x sometimes increases during a low reactivity run, the increase is generally small and may be due to a buildup of compounds that are converted to NO_x during NO_x detection (e.g., nitric acid).

The finding that HONO is the principle NO_x and radical source in the UCR-EC, and possibly other chambers, significantly reduces the problem of chamber radical characterization, since NO_x inputs may be easily monitored as PAN buildup in acetaldehyde-only experiments. We have previously shown and described (Figure 3-7) the simulation results of EC-253, an acetaldehyde-only experiment in the EC using 0.14 ppb/min of NO_x input, 80 percent as HONO (and an initial condition of 5 ppb HONO). These NO_x inputs are consistent with the estimates of radical inputs by Carter et al. (1982) and lead to a good simulation of the experimental system (see Section 3).

Figure 5-10 gives simulation results from ITC-627, an acetaldehyde only experiment. The HONO input required to fit PAN production is 0.035 ppb/min (as in EC-253, a 5 ppb initial condition of HONO fit the initial PAN buildup). The radical input rates indicated by characterization experiments using both the propene tracer technique and the CO NO-to-NO_2 conversion technique are about 0.06 to 0.07 ppb/min. At such low NO_x and radical input levels it is difficult to ascertain the source of the discrepancy between these two values. We note, however, that in ITC-628 the measured NOx did increase during the experiment, perhaps indicating the input of some interfering compound as noted above. The amount of background formaldehyde necessary to supply the "missing" radical inputs of about 0.025 ppb/min is equal to only 25 ppb. This concentration may be maintained with wall emissions of 0.05 ppb/min. However, in our simulations, we use an offgassing rate of 0.1 ppb/min in order to be consistent with our findings for outdoor chambers.

Battelle Chamber

Only three characterization experiments were available for the Battelle chamber. A moderately high NO_x source (0.085 ppb/min) is indicated from an acetaldehyde/PAN formation experiment. A CO/NO_x experiment indicates a radical source similar in magnitude to the NO_x source (~ 0.1 ppb/min). We are again led to speculate that HONO emissions, with some contribution from a small HCHO background (~ 30 ppb assumed), are responsible for the

TABLE 5-4. Estimated radical levels using two different methodologies for the UCR-ITC.

	OH Concentrations ($ppm \times 10^{-8}$)		Radical Source Strength ($ppm/min \times 10^{5}$)		Measured HCHO
	Tracer Method*	$CO + HO_2$ ‡	Tracer Method*	$CO + HO_2$ ‡	(ppm)
ITC-625					
Before added CO					
0 - 60 mins	4.45	--	4.6		--
60 - 120 mins	6.17	--	6.6		--
After added CO					
120 - 180 mins	5.55	4.47	6.8	6.6	--
180 - 240 mins	2.33	3.03	4.6	6.03	--
ITC-628					
Before added CO					
70 - 130 mins	3.82	--	5.8		0.017
130 - 190 mins	3.43	--	4.6		0.069
After added CO					
190 - 250 mins	3.2	3.8	5.8	7.0	
250 - 295 mins	2.3	3.55	5.5	7.5	0.031
ITC-634					
Before added CO					
0 - 60 mins	7.65		16.0		0.002
60 - 120 mins	3.28		7.0		--
After added CO					
120 - 180 mins	3.7	§3.0	8.4	6.9	
180 - 240 mins	1.4	§2.6	3.7	6.8	0.006
ITC-638					
Before added CO					
0 - 60 mins	6.5		8.		0.044
60 - 120 mins	5.4		6.7		0.038
After added CO					
120 - 180 mins	3.1	4.3	4.9	6.8	--
180 - 240 mins	4.2	3.2	8.4	6.7	0.010

* Corrected for O_3 and $O(^3P)$.

‡ Σ NO and NO_2 conversions/min + 50 ppm CO + 320 ppm^{-2} min^{-1}.

§ Corrected for $NO + NO + O_2 \rightarrow NO_2$ and $NO_2 + O \rightarrow 2NO$.

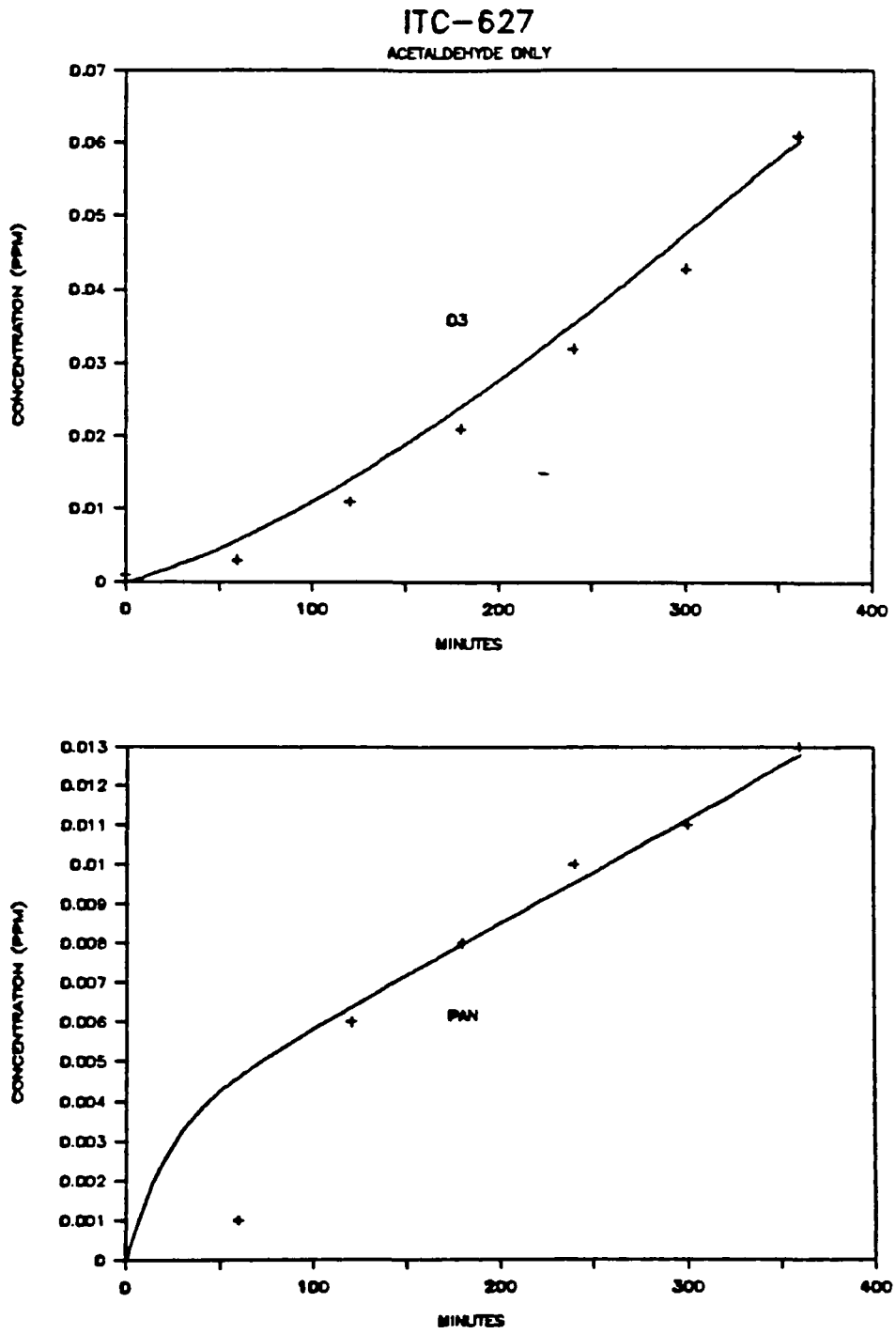

FIGURE 5-10. Ozone and PAN traces for ITC-627, an acetaldehyde-only experiment.

observed radical initiation phenomena. However, the Battelle chamber-characterization data show a significant anomaly; an NO_x clean-air simulation produced an NO oxidation rate that indicates a reactive background (compounds converting OH to RO_2) equivalent to either 12 ppm CO, 0.09 ppm ethene, or 0.03 ppm propene. (These compounds have not been detected at such high levels in the Battelle chamber.) Additional data are required to determine whether this was a temporary effect or a typical characteristic of the chamber; if the latter is the case, the contamination should be identified.

Effects of Chamber Radicals on Experiments

Table 5-5 lists the total calculated chamber radical flux values (using the equation of Carter et al., (1982) for a number of experiments in the UCR-EC that have been published in various studies. The chamber radical source is compared to the NO_x loss for each experiment, and an estimate is presented for the fraction of total radicals that results from chamber sources. As Table 5-5 shows, in the majority of experiments less than 20 percent of total radicals are derived from the chamber. Of the experiments involving high chamber radical fractions, practically all are of low added reactivity (butane-NO_x and acetaldehyde-NO_x). The three urban mix experiments with high chamber radical fractions (EC-232, 233, and 241) all involve mixture A, which is a low-olefin, low-aromatic, high-paraffin mix.

Table 5-6 shows the results of similar calculations for the UCR-ITC and Battelle chambers. Surprisingly, despite a greatly reduced chamber source, the UCR-ITC shows a greater chamber radical fraction than does the UCR-EC, probably because the light source in the ITC and chosen hydrocarbon-NO_x mixtures resulted in low reactivity experiments. Since these experiments were designed as multiday experiments, the long reaction times allowed the small chamber flux to become significant.

Unknown Multi-day Phenomena in the ITC

In the UCR-ITC multi-day experiments, chamber reactivity on the second day appears to be perturbed by the overnight dark period in a way that cannot be explained by any of the previously advanced hypotheses of chamber effects. It is possible that the long dark period between illuminations on successive days of the ITC multi-day experiments provided a means for the oxygenated product species forming at the end of an experiment (e.g., HNO_3 and H_2O_2) to interact with the chamber surface for an extended period. The data from ITC-631 demonstrate the differences in characteristics from one day to another. The first day's reaction ended at the time of NO_2 peak, with ozone and NO almost exactly equal. When the chamber

TABLE 5-5. Chamber background radical sources as a fraction of total radical inputs for the UCR-EC. (Average chamber radical source from Carter et al., 1983.)

Species	EC No.	K_1	Time O_3 Peak (ppm)	Maximum NO_2 (ppm)	Average NO_2 (ppm)	Constant Chamber Radical Source	Average Chamber Radical Source Including NO_2 Dependency	Chamber Radical Flux (ppm)	ΔNO_x (ppm)	Uncorrected Chamber Radical Fraction	Corrected for NO_x Flux
Propene	121	0.3	315	0.341	0.18	0.12	0.19	0.06	0.5	0.17	0.11
Propene	216	0.43	465	0.367	0.16	0.17	0.26	0.12	0.5	0.24	0.21
Propene	314	0.48	330†	0.666	0.2	0.19	0.32	0.11	0.78	0.13	0.12
Toluene	269	0.35	>360	0.26	0.18	0.14	0.22	0.08	0.11	0.20	0.16
Toluene	271	0.36	0.90	0.14	0.08	0.14	0.18	0.016	0.186	0.09	0.08
Toluene	273	0.35	75	0.064	0.038	0.14	0.15	0.12	0.083	0.14	0.12
Toluene	327/340	0.4	>360	0.259	0.16	0.16	0.24	0.088	0.395	0.22	0.19
Ethene	142	0.34	>360	0.3	0.13	0.133	0.2	0.07	0.433	0.16	0.14
Ethene	143	0.33	210	0.375	0.22	0.129	0.238	0.05	0.43	0.12	0.11
n-butane	178	0.33	>495	0.066	0.025	0.13	0.14	0.069	0.093	0.75	0.44
Synthetic urban mixture	231A	0.3	225	0.365	0.16	0.12	0.17	0.038	0.4	0.10	0.09
Synthetic urban mixture	232A	0.3	>360	0.344	0.18	0.12	0.2	0.072	0.282	0.26	0.22
Synthetic urban mixture	233A	0.3	240	0.076	0.04	0.12	0.18	0.0312	0.07	0.44	0.32
Synthetic urban mixture	237A	0.3	240	0.373	0.22	0.12	0.18	0.043	0.4	0.11	0.10
Synthetic urban mixture	238A	0.3	435	0.669	0.25	0.12	0.25	0.174	0.88	0.14	0.12
Synthetic urban mixture	241A	0.3	>360	0.346	0.18	0.12	0.2	0.072	0.311	0.023	0.20
Synthetic urban mixture	242C	0.3	105	0.401	0.22	0.12	0.2	0.021	0.4	0.05	--
Synthetic urban mixture	243	0.3	135	0.394	0.25	0.12	0.22	0.03	0.41	0.07	--
Synthetic urban mixture	245C	0.3	180	0.755	0.46	0.12	0.31	0.056	0.81	0.07	--
Synthetic urban mixture	246C*	0.3	~570	0.374	0.22	0.12	0.17	0.093	0.42	0.22	0.19
Acetaldehyde	254	0.3	330†	0.068	0.04	0.12	0.133	0.044	0.086	0.51	0.35
Butane	305	0.43	345	0.076	0.051	0.17	0.20	0.068	0.066	0.103	0.55
Butane	306	0.44	390	0.146	0.09	0.17	0.23	0.088	0.14	0.63	0.43
Tolulene + Butane	331	0.4	120	0.334	0.2	0.16	0.26	0.032	0.356	0.09	--
m-xylene	344	0.4	180	0.454	0.2	0.16	0.21	0.038	0.671	0.06	--
m-xylene	345	0.39	75	0.192	0.1	0.16	0.18	0.012	0.278	0.04	
Butane	162	0.34	>360	0.279	0.237	0.13	0.24	0.087	0.183	0.48	0.39
Butane + Acetaldehyde (?)	163	0.34	>360	0.299	0.2	0.13	0.23	0.083	0.360	0.23	0.20
Butane + Formaldehyde	168	0.33	690		0.153	0.13	0.2	0.137	0.493	0.28	0.24
Acetaldehyde	164	0.33	>360	0.26	0.22	0.13	0.23	0.085	0.2	0.41	0.34

† PAN peak.

TABLE 5-6. Chamber background radical sources as a fraction of total radical inputs for smog chambers other than the UCR-EC.

Chamber	Species		Time O_3 Peak	Average Radical Source	Radical Flux	ΔNO_x	Chamber Radical Fraction	Corrected for NO_x Flux
ITC								
(k_1 = 0.3 min^{-1})		626	510	0.06	0.03	0.164	0.18	0.15
		637	525	0.06	0.032	0.125	0.26	0.2
		630	>720	0.06	0.043	0.115	0.37	0.29
	Urban mixture	631	>720	0.06	0.043	0.07	0.61	0.4
	Urban mixture	635	>720	0.06	0.043	0.15	0.28	0.23
Batelle								
(k_1 = 0.19 min^{-1})								
	Toluene	AVOC5	200	0.095	0.018	0.43	0.04	
	Toluene	AVOC9	175	0.095	0.017	0.08	0.2	
	Ethylbenzene	AVOC10	405	0.095	0.038	0.38	0.1	

lights were turned off, O_3 and NO titrated to nearly zero concentration and, for the overnight period, only hydrocarbons and NO_2 remained. When the lights were switched on again the next morning, NO and O_3 both reappeared at precisely the same concentrations that existed the previous day when the lights had been switched off. There had been a small decrease in NO_2. As can be seen from Figure 5-11, which shows the data from the two days concatenated and the overnight data deleted, the overall reactivity of the system had noticeably changed from one day to the next.

On the second day the NO_2 decay rate had increased, as had the O_3 production rate and the rate of NO oxidation. If NO_2 had been converted to gas-phase HONO overnight, then the "reactivity boost" should have come as a sharp pulse on the morning of the second day, rather than a continual radical input, as seems to be the case. If an ammount of HONO had been formed on the chamber walls and slowly bled into the system, then, for the reasons noted in the previous section, the increase in reactivity should not have affected the rate of NO_2 loss. The possibility that the HONO inputs somehow "sparked" additional radical inputs from the hydrocarbon species is not persuasive, nor do we think it likely that NO_2 reacted with some hydrocarbon species to yield a radical source with the characteristics seen in Figure 5-11. Both the CBM-IV and the CALL mechanism (Carter et al., 1986) seem to exhibit reactivity discrepancies for multi-day results in the ITC. Unfortunately, consideration of the results for ITC-631 makes it currently impossible to judge whether these discrepancies are due to mechanistic inadequacies or an as yet uncharacterized chamber phenomenon.

Outdoor chambers: The UCR OTC and UNC dual chambers.

Chamber emissions of NO_x in the UNC chamber are highly variable and probably related to the condensation of liquid water on the chamber walls during overnight venting. In four acetaldehyde-only experiments PAN formation was approximately 10 ppb in one single sided experiment; 20, and 40 ppb on both sides in two experiments; and 60 and 100 ppb in the last experiment. In the last experiment (July 21, 1979, described earlier and shown in Figure 5-6) we found that HONO was the only form of NO_x emission that would give accurate results for both ozone and PAN, thus corroborating our finding noted above that HONO is the preponderant form of NO_x emission. Two acetaldehyde-only experiments in the UCR Outdoor Teflon Chamber (UCR-OTC) yielded results of approximately 20 ppb in a six-hour experiment. Both of these experiments showed low dew point measurements (i.e.,less than 15 degrees C).

We have analyzed five additional CO/NO_x experiments conducted at UNC to assess radical inputs: UNCR.62782, UNCB.80282, UNCB.82082, UNCB.82382,

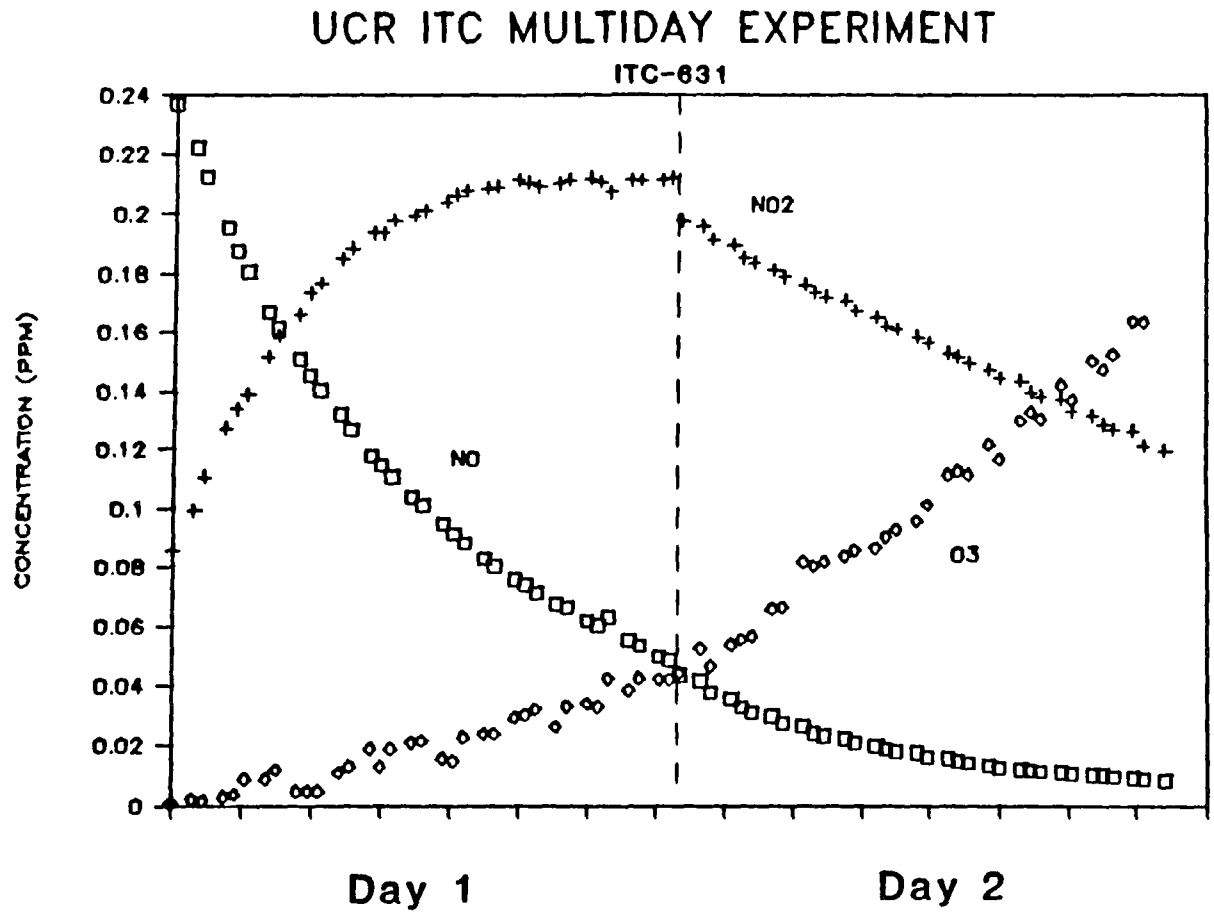

FIGURE 5-11. Experimental data from the two-day, ITC-631 experiment with the dark period removed and the two light periods merged.

and UNCB.90582. Radical inputs were assessed with the above-noted NO_x loss technique, in order to attempt to estimate the significance of non-HONO radical sources, and by assessing NO oxidation by HO_2 formed from the reaction of OH and CO. This latter technique uses the equation

$$OH = \{ \Delta (NO - O3) + (NO2)^2 \times 0.007 \times K1 \} / (CO \times 320).$$

The second term in the equation accounts for the reduction of NO_2 to NO by the reactions

$$NO_2 \text{ ------> } NO + O$$

$$O + NO_2 \text{ ------> } NO + O_2$$

These reactions become significant at about 0.15 ppm NO_2.

Because the NO_x-loss technique involves small changes to large measurements, the scatter for calculated OH is large (see Figure 5-12). The average result for each experiment is quite consistent, however, and indicates that a non-HONO radical source exists in each of these experiments that is approximately equal to the HONO source (Table 5-7). The background of formaldehyde necessary to explain the non-HONO radical source is modest (about 20 ppb) and entirely consistent with UNC measurements of chamber background. Maintenance of this concentration in these experiments would require an offgassing rate of about 0.1 ppb/min.

Although Carter et al. (1982) indicate that the radical sources in the EC and ITC chambers are proportional to light intensity (j_{NO2} or k_1), we find that the correlation between light and radical inputs is fairly weak (see Figure 5-13), explaining only 15-30 percent of the variance of the derived radical inputs (the higher value for r^2 is obtained by eliminating the September 9 experiment, which was very dry). Essentially none of the day-to-day variance may be explained by changes in light, and much of the observed correlation may be due to the formaldehyde radical source, which may be expected to be highly correlated with light. (Note that formaldehyde emissions need not be correlated with light for the radical source to be so correlated, since emissions would be expected to cause only a slow change in formaldehyde background levels). For HONO emissions, photolysis is so fast that light must be diminished to nearly zero before radical inputs are delayed. Only if HONO emissions are directly caused by light would the proportional relationship hold. In the case of outdoor chambers, which have strongly varying temperature and humidity, it is more likely that these phenomena are responsible for variations in HONO emissions rates. It is also worth noting that PAN formation rates in acetaldehyde experiments drop much more rapidly than light intensity in the afternoon; in fact PAN formation in some of the above-noted experiments

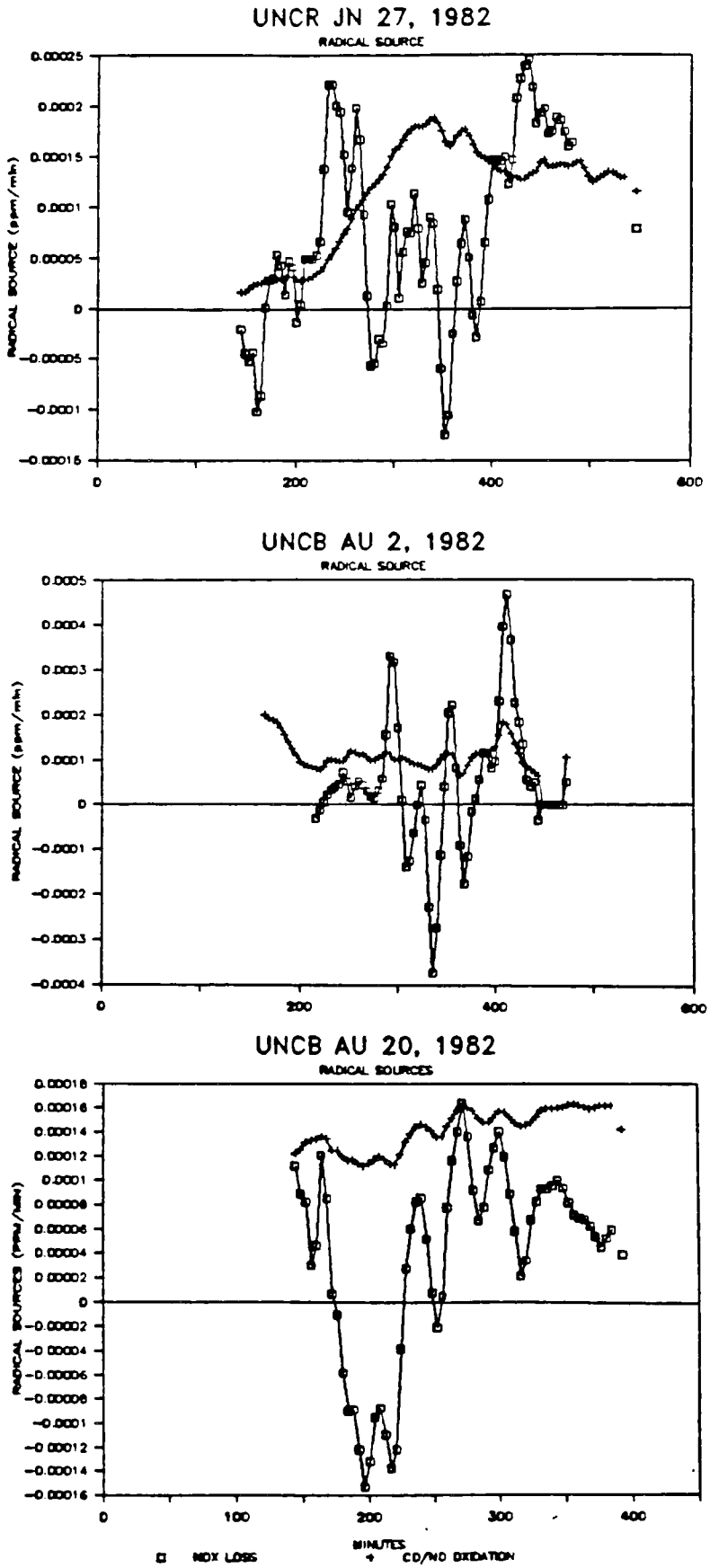

FIGURE 5-12. Estimated radical source strengths for five UNC smog chamber experiments using two different estimation techniques.

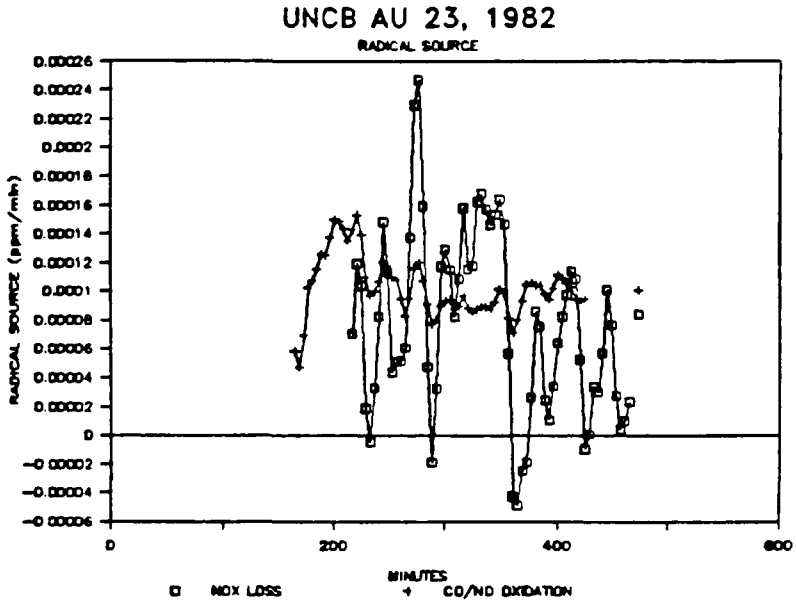

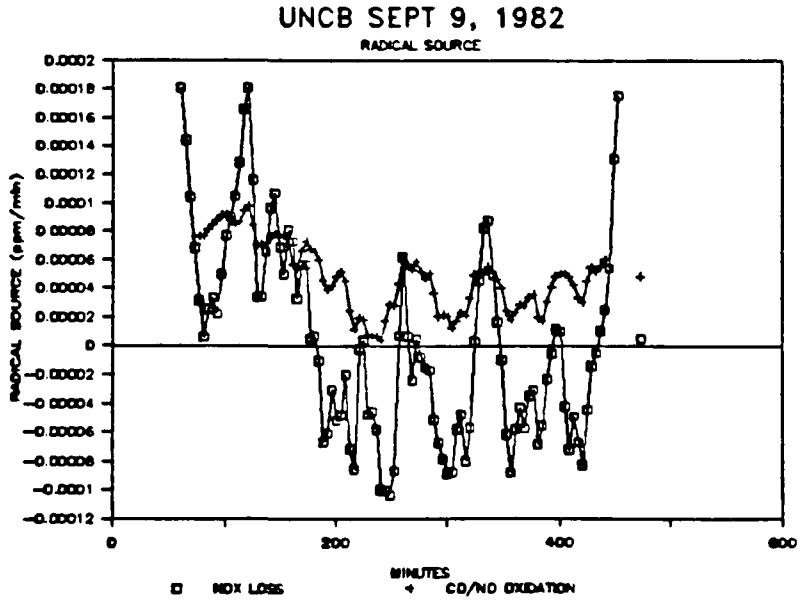

FIGURE 5-12. (concluded).

TABLE 5-7. Radical inputs for CO/NO_x experiments in the UNC smog chamber.

Experiment	Radical Sources (10^{-5} ppm/min)	
	NO_x Decay Method	CO/NO Oxidation Method
JN2782R	3.9	14.1
AU0282B	5.1	10.7
AU2082B	8.4	10.1
AU2382B	7.6	11.3
SE0582B	0.5	4.8

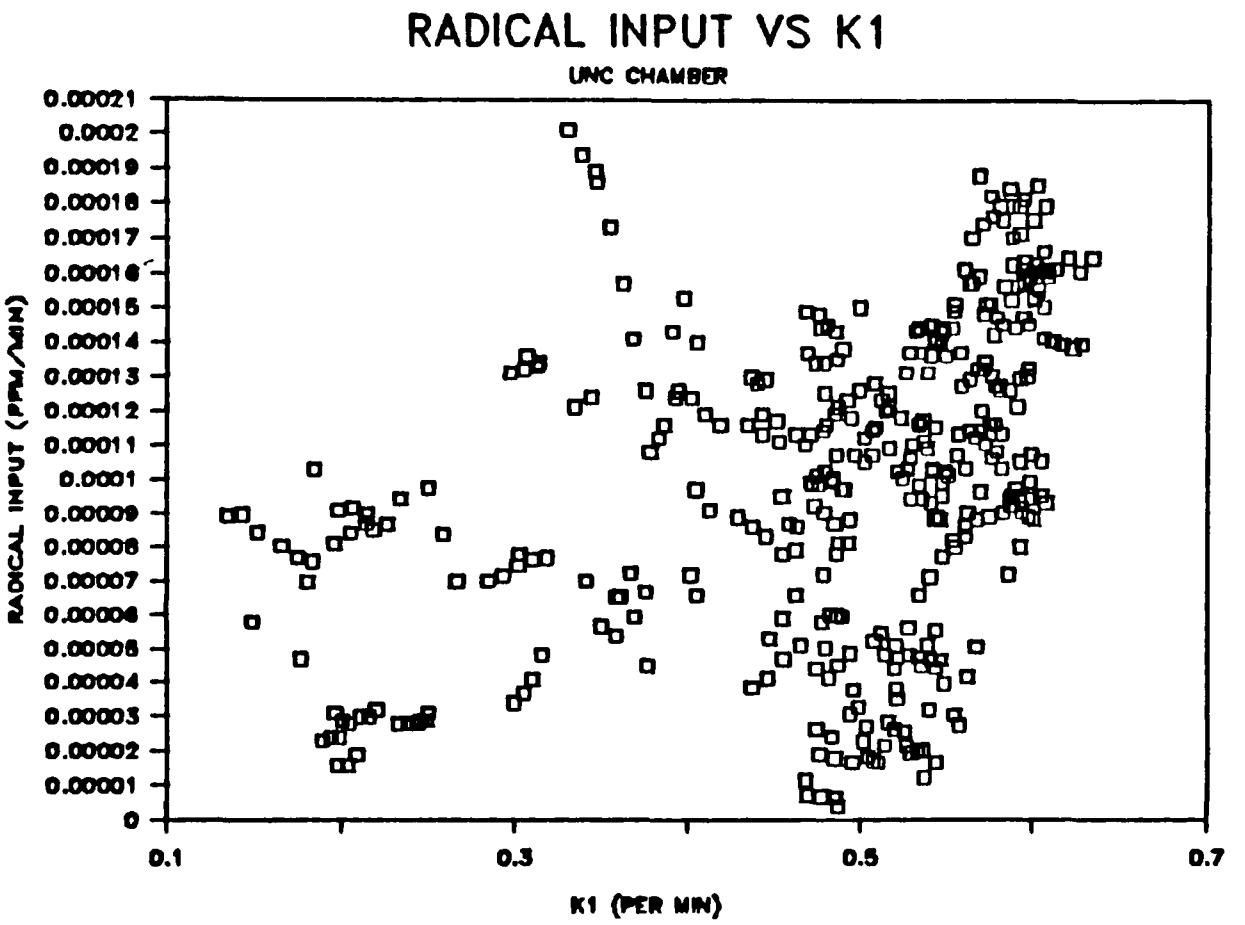

FIGURE 5-13. Comparison of estimated radical input rates and k_1 (j_{NO2}) for chamber characterization experiments in the UNC chamber.

ceases before maximum light intensity, which is indicative that chamber derived HONO is a finite quantity.

In using the light proportionality assumption of Carter et al. for outdoor chamber experiments, we suggest that the following rates should be used: Median chamber radical intensity for these five experiments was 0.22 x k_1 ppb/min (see Figure 5-14); however, since about half of this is provided by a 20 ppb formaldehyde initial condition (and a 0.1 ppb/min offgassing rate--roughly 0.2 x k_1 ppb/min), the HONO emission rate would be 0.11 x k_1 ppb/min, yielding a total emission of 26 ppb of HONO in a typical 10 hour experiment in the UNC chamber.

Carter et al. (1986) also use an oxidation reactivity equation of:

$$OH \longrightarrow HO_2$$

at a rate of 500 min^{-1}. This is equivalent to the effect caused by an additional 33 ppb formaldehyde concentration. The estimate of Carter et al. (1986) for NO_x offgasing (0.2 x k_1 ppb/min) is likewise higher than our estimates. The overall estimate by Carter et al. of the chamber radical source in the UNC and OTC chambers is 0.3 x k_1 ppb/min, although their data for the OTC gives a median value that more closely corroborates our lower figure. Although there are some conditions in the UNC and OTC chambers that will produce chamber contaminants as high or even higher than those used by Carter et al. (1986), typical or average conditions are notably lower.

Kinetic Summary of Heterogenous Chamber Processes

A number of processes have been identified that seem to account for the heterogenous effects occurring in smog chambers. Two such processes mearly account for the mass gained and lost in chamber dilution and sink reactions. Because the decay rates of the many species in smog chamber experiments are unknown, we generally assume they are either low or unimportant. In the case of ozone, however, decay rates are easily measured and we include this loss reaction in the smog chamber mechanisms:

$$O3 \text{ ------>}$$

with k_{loss} = 1.8 x 10^{-4} min^{-1} for UNC and 1.8 x 10^{-3} min^{-1} in the UCR-EC.

Average dilution rates are provided with the data for each experiment in the UCR-EC. Typical dilution rates are between 3.0 x 10^{-4} and 4.0 x 10^{-4}, and it is assumed that clean replacement air concurrently enters the chamber. At UNC, however, dilution is not reported but the concentrations of

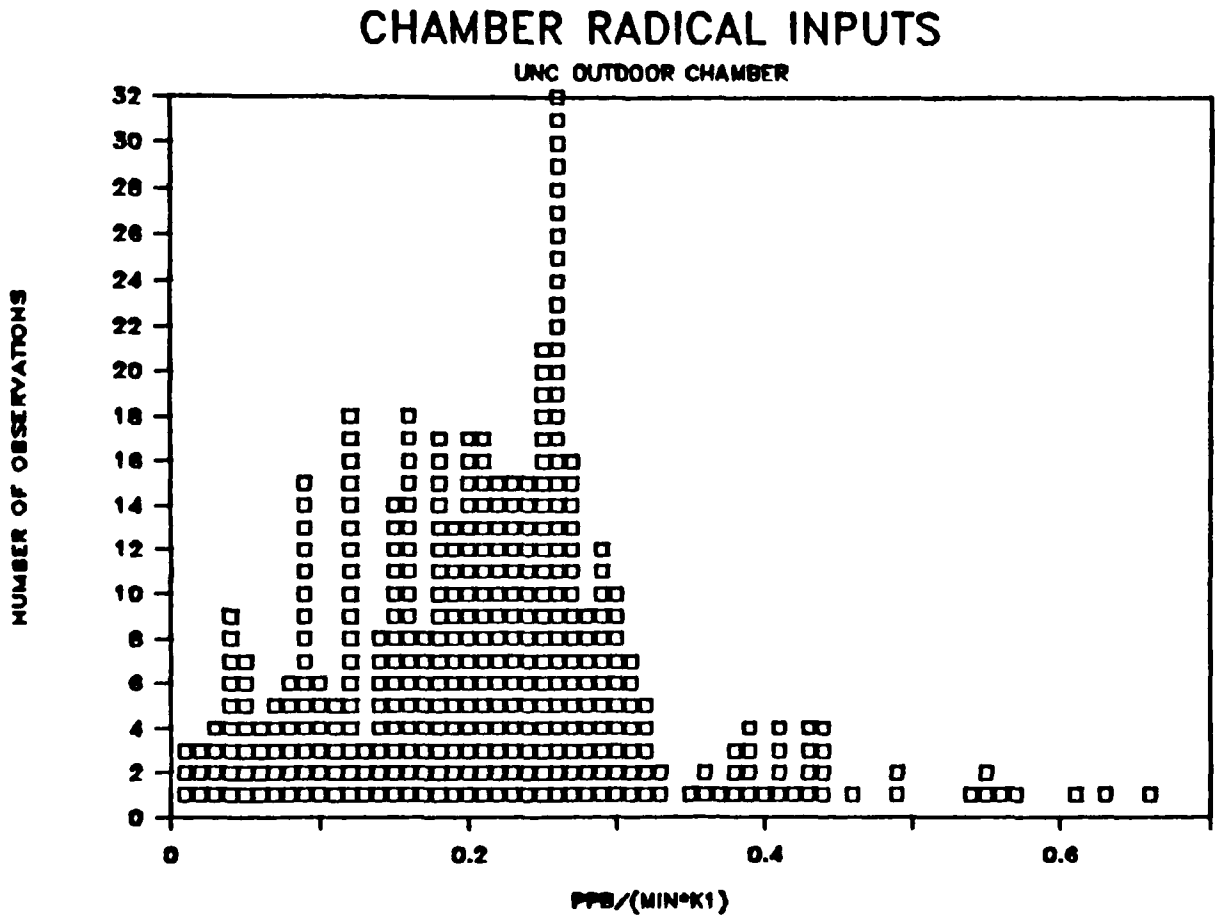

FIGURE 5-14. Histogram used to estimate the relationship of radical input rate to k_1 (j_{NO2}).

dilution tracer species (low concentrations of chlorinated hydrocarbons) often are, which allows the dilution rates to be altered until the tracer curves are fit correctly. We have found that a typical UNC dilution-rate function increases from approximately 5.0×10^{-5} at experiment startup to 2.0×10^{-4} after about 4 hours, to 3.0×10^{-4} after an additional 4 hours. Dilution air entering the chamber is from a relatively clean rural environment. Key among the species entering the chamber at the prescribed dilution rate are ozone (about 0.07 ppm), CO (about 0.3 ppm) and non-methane hydrocarbons (usually less than 0.05 ppm).

Three additional processes are used to account for the background effects of hydroxyl radical initiation in smog chambers. These three represent

(1) Emission of aldehydes (primarily formaldehyde and acetaldehyde) from chamber walls,

(2) Emission of nitrous acid from chamber walls, and,

(3) Heterogenous conversion of gas-phase NO_2 to gas-phase HONO by chamber walls.

The third of these radical initiation processes has been shown to be important only in two structurally similar chambers, both having Pyrex surfaces. Chamber derived radicals in all other chambers that we have studied appear to be caused by a combination of aldehyde and nitrous acid emissions from the chamber surfaces. Although the source(s) of these compounds have not been precisely characterized, absorption and desorption from chamber walls seems most likely for aldehydes, whereas heterogenous reduction of nitric acid could be the main formation route for nitrous acid. It should be noted that phenomena involving nitrous acid (because it contains nitrogen) may have an impact on NO_x chemistry that is comparable to effects on radical chemistry.

As we have already noted, we generally initialize the UNC chambers with less than 20 ppb of formaldehyde and approximately 5 ppb of HONO. In addition, an expendable wall source of formaldehyde is included and usually does not exceed 40 ppb. (Values for individual simulations are presented in the initial conditions tables of Section 6.) The gas-phase formation of these radical-initiating species is simulated with

------> HONO

FORMwall ------> FORM

where

$$k_{HONO} = 2.5 \times 10^{-5} \text{ ppm min}^{-1}$$

and

$$k_{FORM} = 5.81 \times 10^{-4} \exp(-5000/T) \text{ min}^{-1}.$$

These are, no doubt, simplifications of far more complex processes that cannot be more adequately addressed until better data is obtained.

For the UCR-EC, we began with the representation of the EC wall radical source as recommended by Carter et al. (1986), who represented these processes by

$$NO2 \xrightarrow{h\nu} 0.5\ HONO + 0.5\ (\text{wall } NO_x),$$

$$\xrightarrow{h\nu} OH,$$

$$OH \longrightarrow HO2.$$

To be consistent with the above representation, we use

$$NO2 \xrightarrow{h\nu} HONO,$$

$$\xrightarrow{h\nu} HONO,$$

$$FORMwall \longrightarrow HO2.$$

with rates for the first two processes of

$$k_{NO2 \rightarrow HONO} = 1.37 \times 10^{-3} \times j_{NO2} \text{ min}^{-1}$$

and

$$k_{HONO} = 3.90 \times 10^{-4} \times j_{NO2} \text{ ppm min}^{-1}.$$

We utilize the same rate for the formaldehyde reaction as in the UNC chamber.

6 EVALUATION AND DEMONSTRATION OF THE CBM-IV

A large number of data sets from various experimental facilities have been used to develop the CBM-X and CBM-IV. We have selected the best available data (in terms of light, chamber dryness, number of species monitored, data density, and quality) to demonstrate mechanism performance. Since many smog chamber data sets are only marginally useful we do not display all results for each data set available. Rather, we demonstrate the operational characteristics of the CBM-IV, indicating both areas of improved mechanism performance and uncertainty or needed refinement. All simulations discussed in the following section were performed with the CBM-IV.

As in Sections 3 and 4, this section is organized according to hierarchical carbon bond groups. Simulation results and experimental data are compared in tabular form (these tables appear at the end of the section). For a few measurement indicators, we provide group averages and standard deviation values; however, we feel that such indicators may depend on the experiments simulated and thus have the potential to provide misleading impressions of mechanism performance. In addition, a tabular listing of only a few isolated comparison points (such as the maximum concentrations of ozone, PAN and HCHO) in each experiment is not very useful in demonstrating the overall ability of a chemical mechanism to simulate timing and reactivity; for these kinds of comparisons, plots of the key chemical species, including NO and NO_2 (which are rarely included in tabular comparisons) are most useful. Therefore, we also provide a number of figures in each subsection to supplement the tabulated data (all figures appear at the end of the section). In these plots, symbols represent experimental data and lines represent simulation results.

For each group of simulations discussed, two types of tables are included. The first describes initial and experimental conditions; the second provides experimental data for a few specific points. As noted in Section 5, initial and chamber conditions were kept within limits felt to be reasonable for the conditions of each experiment. Unless noted in the initial condition tables, these conditions were matched for both sides of the UNC chamber for a specific day. The experimental systems for which we demonstrate CBM-IV performance include aldehydes (including formaldehyde), ethane, alkenes, toluene, xylenes, isoprene, α-pinene, and various mix-

tures of hydrocarbons. We have omitted simulations of individual alkane-/NO_x experiments because there are only a few alkane data sets (mostly butane) and simulation of these systems is highly uncertain because the constraints of the experimental facilities conflict with the relatively unreactive nature of alkanes. Most experiments were performed at extremely high hydrocarbon/NO_x ratios so that ozone formation could be measured. Unfortunately, under these conditions the chemistry is highly sensitive to heterogeneous chamber effects and the results are very uncertain. Hence, it is not clear what fraction of the reactivity is initiated by heterogenous chamber reactions. Other experiments with more realistic initial conditions formed ozone at concentrations characteristic of only background hydrocarbon levels. In either case, it is very difficult to differentiate between reactivity due to chamber effects and that due to alkane kinetics. Because we do not wish to demonstrate CBM-IV performance under highly uncertain conditions, we utilize the complex mixture experiments with high initial alkane loadings to demonstrate the performance of the alkane chemistry under more realistic conditions. We conclude this section with a discussion of the relationship between mechanism predictions and experimental measurements.

ALDEHYDES (FORM AND ALD2) AND PAN

Formaldehyde chemistry plus the ICRS form one of the simplest ozone-producing organic systems containing the characteristics of photochemical smog. In addition, formaldehyde is an extremely common product formed from the atmospheric oxidation of almost all organic species. For these reasons, we attempted to simulate formaldehyde/NO_x smog chamber experiments as an initial step in our hierarchical model development protocol. Unfortunately, as noted in Section 5, the interaction of formaldehyde with chamber walls is a known, though poorly understood, process that adds uncertainty to most smog chamber experiments (and therefore to the chemical mechanism developed from these data). These effects are all the more obvious in a smog chamber system where formaldehyde is the only organic species. Nevertheless, such simulations are very important to our understanding of the more complex systems discussed later. The simulation results discussed next demonstrate both the uncertainty associated with formaldedyde smog chamber simulation and formaldehyde oxidation chemistry.

Table 6-1 lists the initial conditions for seven formaldehyde experiments performed in the UNC chamber that represent a range of satisfactory data and light conditions throughout each day. Simulation results are provided in Table 6-2 and data traces are plotted in Figures 6-1 through 6-7. Except for the 9 October 1984 experiments (the only ones in which effective drying was performed), these data are all from the 1979-1980 experimental seasons. Data for the 1984 day were collected during testing of

the Unisearch Associates tunable diode laser measurement system at UNC. As shown in Table 6-2, the overall correspondence between experimental and predicted maximum ozone concentrations was good, but with a rather large error that indicates significant uncertainties in these simulations. This is to be expected, however, because of the high impact of chamber-related processes. CO production was also well predicted, but this agreement gives little indication of the accuracy of the chemical processes since CO is always an ultimate product of formaldehyde oxidation.

Because formaldehyde/NO_x experiments are relatively simple and test the chemistry of a very important organic species, they are more significant as indicators of specific formaldehyde chamber processes than as a meaningful measure of mechanism capability for accurate atmospheric predictions. For this reason we point out a few important characteristics in these simulations and in systems discussed later.

First, there appears to always be a discrepancy of about 15 to 20 minutes between the simulation results and the formaldehyde data. Whether this is due to a delay in instrument response, inadequate representation of formaldehyde wall effects, or chamber light intensity is not clear; however, the temporal shift is usually evenly applied over the entire day (see Figures 6-1 and 6-3 through 6-5). More important and possibly related, are the afternoon effects seen in formaldehyde/NO_x systems. The maximum ozone concentration produced in systems with higher hydrocarbon-to-NO_x ratios is usually simulated more accurately than that of smog chamber systems with lower initial loadings of formaldehyde. This appears to be because the midday radical flux is higher in the formaldehyde simulations with higher HC/NO_x, producing the most ozone at that time (see Figure 6-4). In the experiments with lower formaldehyde loading, ozone is produced in the smog chamber through the late afternoon (when wall-related processes can become dominant because of the depletion of all organic precursors), while the simulations often predict much lower reactivity since formaldehyde is depleted to near zero. An example of this can be seen in Figure 6-5 where the production of both ozone and CO increases through the end of the experiment, while the simulation, based only on the homogenous gas-phase chemistry of the initial formaldehyde, underpredicts reactivity for this period. If formaldehyde is forced to follow the measured values during the simulation, this extension of ozone and CO formation can be accurately simulated. This indicates the need for a better representation of formaldehyde wall processes, especially for experiments where high formaldehyde concentrations are achieved either through initial conditions or homogenous gas-phase production (as in ethylene experiments).

Because formaldehyde photolysis (producing HO_2) occurs during all daylight hours and NO (the major sink of HO_2) is depleted early in these simulations, the prominant odd-hydrogen radical species in the late afternoon is HO_2. As noted in Section 3, the kinetic data for HO_2 and RO_2 termination reactions is sparse and uncertain, leading to much uncertainty in smog

chamber simulations under these conditions. In addition, such late afternoon conditions are especially difficult to simulate for these formaldehyde experiments because wall termination of either HO_2 or peroxides could become a dominant factor when most of the formaldehyde is depleted. Therefore, these formaldehyde data sets, as well as other more complex mixtures that rapidly deplete NO, offer a test bed for conditions of high RO_2 and low NO. We suggest that future kinetic investigations utilize the afternoon-period data from these experiments to investigate chemical aspects under these conditions. Future experiments might also start with initial NO and NO_2 concentrations closer to the NO_x crossover point in order to provide longer periods for low NO_x data collection. Such data would be extremely useful for validating a chemical mechanism for conditions more akin to those of the rural environment. It would, of course, be necessary to first separate chamber influences from homogenous chemical effects. For instance, consider the effect of CO in the 9 October 1984 experiments of Figures 6-1 and 6-2. While the NO_x and ozone concentrations are well suited for the side with low CO (Figure 6-1), ozone formation is overpredicted for the high CO (50 ppm) experiment (Figure 6-2). Because the addition of CO has been shown to significantly enhance hydrogen peroxide destruction in smog chambers (Jeffries, 1987), we suggest these data may be evidence of enhanced, wall-related depletion of radicals or their sources. Analysis of other high CO days for such an impact could aid in indicating the magnitude of the effect and whether it is operative only in the HO_2 regime of odd-hydrogen, as seen here, or throughout the day. Fortunately, the types of uncertainties discussed above for formaldehyde/NO_x experiments appear to be mitigated in more complex systems. This is particularly true for

(1) Experiments with lower formaldehyde concentrations, and

(2) Experiments with some remaining organic species near the conclusion of an experiment.

These conditions tend to prevent artificial processes from dominating over homogenous gas-phase chemistry.

Acetaldehyde simulations were performed in the development of the new PAN chemistry and some results were given in Section 3 (Figures 3-2 through 3-7). Table 6-3 shows the initial conditions for those experiments as well as two additional acetaldehyde and two propionaldehyde experiments from UNC (shown in Figures 6-8 through 6-11). Simulation results and comparisons with experimental data are shown in Table 6-4. Maximum ozone concentration predictions were very good, averaging an overprediction of 4 and 5 (±8) percent for both the UNC acetaldehyde simulations and the overall set of all acetaldehyde and propionaldehyde experiments. Further-

more, these simulations occur over a wide range of temperature conditions, indicating that the good correlation is due to improved PAN chemistry.

The overall average underprediction of PAN (and PPN for propionaldehyde) was 4 ± 16 percent, or about 9 ± 32 ppb. Not only do these data indicate that the PAN chemistry is functioning accurately in terms of maximum concentration, but the PAN traces in Figures 3-2 through 3-7 and Figures 6-7 through 6-11 show a very good fit with experimental data throughout the day. In further plots we will indicate some similarly good fits, but it must be kept in mind that just as ALD2 is used as a surrogate for higher molecular weight aldehydes, so is PAN used as a surrogate for larger peroxyacyl nitrates. Thus, comparisons of overall simulation PAN(s) versus measured PAN may not be accurate. Nonetheless, because peroxyacyl nitrate species are expected to have similar temperature dependencies, the curve shapes should be similar to the measured values if the radical processes are being handled correctly throughout the day. As noted in Section 3, we feel the improvements to the C_2O_3 (and other radicals) chemistry has led to better radical concentration calculations, resulting in improvements not only to PAN but also to hydrocarbon decay predictions.

Finally, formaldehyde concentrations were calculated to be underpredicted by about 10 ppb. This is based on limited experimental data, however, and cannot be considered strong evidence for good predictive capabilities. On the other hand, since all other fits are good and the chemical kinetics of the acetaldehyde/NO_x systems appear to be simple, such a good comparison would be expected.

ETHENE (ETH) AND OLEFINS (OLE)

Because the kinetic and mechanistic information available for ethene and other olefin chemistries has changed little in recent years, we have included some demonstration simulations to show that the new changes in inorganic and minor updates to olefin chemistry have not deteriorated the quality of agreement between recent computer simulations and observed data. The following discussion also concentrates on questions remaining in the data, especially for the key aldehyde products.

Initial conditions for eleven ethene experiments are given in Table 6-5, results are summarized in Table 6-6, and the data are compared to the corresponding simulations in Figures 6-12 through 6-22. The July 1986 experiments (Figures 6-20 through 6-22) were performed during the EPA-sponsored formaldehyde intercomparison study in the UNC chambers. As noted, it has been our experience in simulating experiments of high formaldehyde concentrations, such as these ethene/NO_x experiments, that water vapor concentrations and carbon balances can provide useful information

for modeling both chemistry and chamber effects. In particular, two interesting features of the 9 July data are the carbon mass balance and the formaldehyde delay. In Figure 6-20 at 400 minutes, the data show a carbon total for CO, ethene, and formaldehyde of about 2.4 ppmC. This is very close to the initial value and leaves no room for additional carbon lost to dilution or existing as unmeasured CO_2, formic acid, and glycolaledyde products. Hence, either one or more of the three carbon-containing data traces is too high at 400 minutes or contamination from the walls and the dilution air is significant.

The delay in simulated ozone coupled with the somewhat early prediction of the NO_x crossover point shown in Figure 6-20 is consistant with formaldehyde initially being condensed to the wet chamber walls and then later (as the walls become drier and warmer) released. If formaldehyde condensed to the walls and did not photolyze there, then less radical formation and fewer reactions with hydroxyl radicals could occur in the gas phase. Fewer radicals and hydroxyl reactions would delay the crossover point when NO_2 becomes equal to NO. Because the simulation does not account for the condensation of formaldehyde to the chamber walls, the simulated crossover occurs earlier than the observed crossover point. Later, the formaldehyde condensed on the chamber walls may be released into the gas phase and photolyze, thereby accelerating the formation of ozone due to the extra photolytic radicals and hydroxyl reactions from the extra formaldehyde. Again, the simulations lack this feature and the simulated ozone appears later than the observed ozone.

A feature of the formaldehyde data, which is also seen in other formaldehyde-generating smog chamber experiments, is the lack of accumulation of formaldehyde during the early morning even though the other data (such as ethene decay) indicate that formaldehyde formation should be occurring in the gas phase. We believe these data are indicative of the above noted collection of formaldehyde by the walls. It is especially obvious in these ethene experiments and in mixtures with large initial fractions of ethene, because formaldehyde is a very high yield product of ethene oxidation.

The demonstration of the CBM-IV for propene and higher olefins, as with ethene, involves the selection of only a few simulations from the UCR and UNC chambers. Initial conditions for the 14 simulations (which include propene, 1-butene, and trans-2-butene experiments in the UNC and UCR chambers) are given in Table 6-7. Results are summarized in Table 6-8 and compared with data in Figures 6-23 through 6-36.

Most of the simulations are for propene in the UNC chamber. As shown in the initial conditions (Table 6-7), all the UNC-propene simulations assumed initial HONO and formaldehyde concentrations of zero. Although

such assumptions are not used in other simulations, they highlight two features: (1) the propene mechanism may be overly reactive due to overly high radical yields from the oxygen atom reaction and the rate constant used for hydroxyl reaction, and (2) the light flux in the early hours of UNC simulations may be overestimated. Note, for instance, that the standard initial HONO and formaldehyde concentrations were used in the UCR-EC simulations. The rapidly changing solar light flux at UNC adds a challenge to the simulation of smog chamber data not present in chambers with constant light flux. The adjustment of assumed chamber effects such as initial HONO and formaldehyde allows the simulation to at least more closely match the crossover point. Without such an adjustment the poor comparison with observed data cannot easily be assessed. For example, the mechanism may correctly simulate chemistry after, but not before, the crossover. If the mechanism is too reactive or not reactive enough before the crossover, performance after crossover is confounded by the rapid change in light flux that typically occurs during crossover.

Except for the need for fewer chamber effects to simulate the chemistry of propene to the NO_x crossover point, the simulations show quite good performance for the propene mechanism. However, the exceptionally low simulated PAN in the 13 July 1986 experiment (Figure 6-23) is difficult to explain.

Figure 6-29 shows a comparison of the propene and butene-1 chemistries for the dual chamber at UNC. Unfortunately, the CBM-IV mechanism appears to be overly reactive for both sides on this day. However, the trend between propene and 1-butene toward less reactivity in the 1-butene experiment is simulated by the CBM-IV.

In Whitten et al. (1979) simulations of trans-2-butene experiments in the UCR chamber seemed adequate when 2 times the molecular concentration of acetaldehyde was used as a surrogate for this internal olefin. However, the performance is poor for the CBM-IV using this simplification, as shown in Figure 6-31 for the blue side of the UNC chamber on 27 September 1983. One reason for this poor performance is the drastic reduction in photolysis for acetaldehyde as now used in the CBM-IV compared to earlier CBM versions. Nevertheless, the internal olefins may no longer be as important in urban smog as in previous years and the need for another olefin species in the CBM-IV may not be great enough for this to be a serious problem.

AROMATICS (TOL AND XYL)

As noted in Section 4, we have attempted to simulate all usable toluene and xylene experiments from the UNC and UCR-EC chambers. Initial condi-

tions for these experiments are given in Tables 6-9 and 6-11 in order of HC/NO_x ratio. Results are summarized in Tables 6-10 and 6-12. Ozone, NO_x, hydrocarbon, PAN and formaldehyde concentrations are presented in Figures 6-37 through 6-48, for toluene, and Figures 6-49 through 6-53 for xylenes. We also noted that a number of the hydrocarbon-reactivity mixture experiments performed at UNC were substitutions of aromatic species into otherwise identical mixtures. The results of these simulations are presented in the mixture subsection that follows.

For the toluene simulations (Table 6-10), the results for UNC data are shown in Figures 6-37 through 6-43 and UCR-EC traces are shown in Figures 6-44 through 6-48. As noted in Section 4, the UNC simulations were the basis for development efforts; in particular, JL3080R, JN2784B and OC2782R had the best sunlight profiles. All other days had some overcast periods, and all days from the complete UNC data set (not listed here) had problems with severe sunlight or missing data. The average maximum ozone concentration overprediction for all UNC days was 4 ± 8 percent. This is rather remarkable, considering that the average ozone fit for a subset of these experiments by Carter et al. (1986) was high by a factor of 2 and the earlier version of CBM-X toluene chemistry had equally poor fits. Previously, one of the most difficult experiments to simulate was that of OC2782R (Figure 6-42) perhaps because, though this was a clear October day, the spectral distribution of actinic flux may differ enough to affect the photolytically-active dicarbonyl species in a way that is not accounted for in the models. The current mechanism is a vast improvement over previous mechanisms for this data set. The original CBM-X predicted 0.45 ppm ozone for this day, and the CALL (Carter et al., 1986) yielded 0.40 ppm. The improvement, explained by the improved timing of the OH, NO_3, and HO_2 processes in the new mechanism, is due to the different product splits produced. If one compares the new UNC simulations of lower light and lower HC/NO_x ratios with mechanisms using higher dicarbonyl yields, it is obvious that the "prompt" and high yields of dicarbonyls were oversimplifications of product chemistry.

Another important result is the timing and shapes of the curves representing the various species in each experiment. The shape agreement is much improved over that for earlier versions of toluene/NO_x chemistry. Consider, for example, the results of JL3080R (Figure 6-38), which was a clear day that should be less difficult to simulate. The current model presents a good fit throughout the day, while earlier mechanisms (Figure 6-54) show typical overprediction of ozone on clear days due to excess dicarbonyl production. However, though we feel the current formulation has tightened the error bands on prediction of ozone production from toluene/NO_x systems, it is only an improved representation of a still ambiguous process. This is evident from the mechanism fits in the second half of the experiments where ozone can still be overpredicted with under-

prediction of toluene loss. Therefore, though there has been improvement (especially in terms of the timing and magnitude of all species), additional information about product distributions and their chemical reactions well into the day (when NO_x is depleted and HO_2 accumulates) would be very helpful for developing a better representation for this period.

Unfortunately, data from the EC do not help this uncertainty because most experiments were terminated prior to this period. Also, though the average EC maximum ozone comparison statistics were very good, this may be fortuitous since the uncertainty of the wall OH contribution allows alteration of ozone concentrations 20 to 30 percent in either direction. The major advantages of using data from the EC chamber were that it allowed us to test our assumptions concerning the photolysis rates of the dicarbonyl species and to verify that the process of ratioing dicarbonyl j-values to j_{HCHOr} was not blatantly wrong. Finally, although formaldehyde results are not tablulated, analysis of the results from the figures shows that the predicted values are within the rather large experimantal error bands for both chambers.

Xylene results are shown in Figures 6-49 through 6-52 (m-xylene) and Figure 6-53 (o-xylene). Only one UNC m-xylene/NO_x experiment exists, but fortunately it had good data collection and light conditions. As seen in Figure 6-49, the explicit m-xylene chemistry of XYL fits these data as well as can be expected. The UCR-EC simulations fit the general trends of toluene. They slightly overpredict ozone and would benefit from a lower OH wall source and higher O_3 dilution. A fourth EC experiment (EC-343) was not used because of solar simulator power problems. It is unfortunate that these experiments represent the only m-xylene data available for model development and that, therefore, strong uncertainty must be associated with this section of all mechansims.

Four UNC o-xylene experiments (there were no EC experiments) were modeled using the XYL chemical surrogate for o-xylene. As seen in Table 6-12 this approximation worked, on the average, but included a large variability. For instance, the JL3080B ozone trace in Figure 6-53 shows the effect of PAN decomposition later in the experiment as a second increase in ozone concentration. This is typical of PAN-producing systems. Because o-xylene produces biacetyl, which is not reactive with OH but photolyzes to produce two acetylperoxy radicals, PAN yields are underpredicted by the XYL reaction scheme as shown in the figure. This is an extreme case, however, occurring at the end of a very clear July day with the highest HC/NO_x ratio of the UNC xylene experiments. The other cases show better agreement between experimental and predicted ozone, with overprediction appearing to occur at lower HC/NO_x ratios (though the AU2782 day had terrible light). Again, the fit is acceptable considering the constraints of existing data and the surrogate approach used; however, additional data

would be very useful for the development of a more kinetically-based surrogate approach in the future.

BIOGENIC HYDROCARBONS (ISOP AND α-PINENE)

Initial conditions for the UNC experiments used to test the new condensed isoprene representation and the new α-pinene carbon bond splits are given in Table 6-13. Simulation results are given in Table 6-14 and shown in Figures 6-55 through 6-66 for isoprene and Figures 6-67 through 6-75 for α-pinene. For isoprene, the average of the percent difference between prediction and measured maximum ozone concentrations was about 6 (±23) percent overprediction for the 12 experiments simulated. We consider this very good evidence that the new condensed isoprene chemistry successfully represents the photochemical processes in these systems. This is especially gratifying since the isoprene condensation was a more complex process than that performed for carbon species such as OLE or PAR. As many of the figures indicate (including Figures 6-55 through 6-58), the characteristic second ozone peak caused by thermal decomposition of PAN or PAN-like species under high afternoon temperatures was successfully simulated for most experiments.

Because isoprene is often used to represent the photochemistry of biogenic hydrocarbons, it was also our intention to develop a condensed isoprene representation that would predict PAN and formaldehyde concentrations as accurately as possible. Both the maximum concentration comparisons in Table 6-14 and the plots in Figures 6-55 through 6-66 indicate very good fits, particularly in the timing and shape of the formaldehyde curves.

The new carbon-bond splits for α-pinene were determined to be 0.5 OLE, 1.5 ALD2, and 6.0 PAR (altered slightly from previous values of 1.0 OLE and 8.0 PAR). These resulted in a closer simulation of maximum ozone concentrations, while retaining adequate PAN predictions. Both ozone and formaldehyde were overpredicted by about 20 percent on the average, although formaldehyde data upon which to base a comparison were scarce. The average PAN overprediction in Table 6-14 is very large (almost 200 percent), but in absolute terms it is about 50 ppb. Thus, α-pinene is not a major source of PAN and its relative overprediction is insignificant in an absolute sense.

MIXTURES

To demonstrate the applicability of the CBM-IV for simulating a range of different reactive hydrocarbon mixtures, we selected sets of experimental data from the UNC dual smog chambers and the UCR EC and ITC smog cham-

bers. We present these simulation results, starting with general mixture experiments, followed by more complex substitution patterns, and ending with the simulation of actual automobile exhaust.

Hydrocarbon Surrogate Mixtures

From UNC we simulated 19 synthetic hydrocarbon-mixture experiments performed during the 1983 and 1984 run seasons. The mixtures were of automobile and urban surrogates designated "SynAuto" and "SynUrban," plus a combination known as "SynAutoUrban." The primary difference between the mixtures is that the SynAuto mixture is higher than the SynUrban in aromatic (particularly xylene) and olefin fractions; it is also much higher in ethylene than the SynUrban mixture. Initial conditions for these experiments are given in Table 6-15 and some results are compared with the experimental data in Table 6-16. Figures 6-76 through 6-81 show SynUrban results; Figures 6-82 through 6-92 are SynAuto simulations; and, SynAutoUrban results are shown in Figures 6-93 through 6-97. Analysis of these plots indicates that the NO_x curves and initial ozone buildup are usually simulated quite closely, with divergence of the ozone curve (if any) occuring in the late afternoon. Maximum ozone concentrations varied between mixtures, with a relative underprediction of 6 percent for the Synurban mixtures and 1 percent for the SynAuto mixtures.

Interestingly, the SynAutoUrban mixtures were overpredicted by an average 8 percent. Although these differences are not large, the data in Table 6-16 indicate that this may be due to the fact that the SynAutoUrban mixture experiments were all performed at a hydrocarbon-to-NO_x ratio of about 7, whereas many of the other tests were done with initial hydrocarbon-to-NO_xratios of around 3 or 4. Many of the higher ratio SynAuto and SynUrban mixture experiments were the most overpredicted, while the lower ratios runs were the most underpredicted. As noted earlier, experiments starting with lower hydrocarbon loading might be more susceptible to uncertain, chamber-related radical termination or organic offgassing processes in the late afternoon because the gas-phase organic precursors are mostly depleted. On the other hand, the differences may easily be due to uncertainties within the mechanistic representation. Certainly the SynAuto mixtures, with their higher ethylene fractions, appear to have characteristics that are seen earlier in the ethylene simulations.

The average predictions of PAN and formaldehyde exhibit similarities based on the type of mixture. However, the absolute values, especially for formaldehyde, often approach the sensitivity limits of the monitoring instrument. This suggests that the relative trends are either less formidable, on the basis of small absolute changes in low concentration

data, or dominated by individual comparisons such as the relative formaldehyde comparison for the red side experiment of 4 August 1984-Red.

The calculations performed to develop PAR oxidation stoichiometry were based on an assumed atmospheric mixture. In some cases (such as the Syn-Auto mixture and, more obviously, in the EC seven-component experiments and the ITC multi-day tests) accurate simulations of a mixture sufficiently dissimilar to urban atmospheres would be expected to cause difficulties in predicting smog chamber photochemistry. We have found that these differences can account for up to a 10 percent variation in the maximum ozone prediction for a few cases. Because the UCR-EC seven component experiments and the UCR-ITC multi-day surrogate experiments used simple alkane mixtures that were somewhat different than the previously-described atmospheric mix, we simulated those experiments with modified stoichiometric parameters and other alkyl carbon rate constants that represented those mixtures. In the EC seven-component experiment simulations, the modified alkyl carbon mechanism appears to have been slightly more reactive than the default mechanism, despite the latter's higher OH rate constant. (This is probably related to a reduced alkyl nitrate formation rate in the butane/2,3-dimethylbutane mixture.)

For some of the fractions of initial hydrocarbon species in these experiments the urban surrogate mixtures generally have a higher proportion of reactive olefins than do observed atmospheric mixes due to the use of these olefins as a reactivity replacement for lower molecular weight aldehydes (that are difficult to accurately inject). For instance, in the ITC multi-day experiments, hydrocarbon reactivity on the first day is strongly affected by the isobutene component of the mixture. Isobutene was originally added to the synthetic urban mix as a surrogate for initial formaldehyde. Subsequent experiments with isobutene show this approximation to be inappropriate in many respects (e.g., isobutene oxidation yields PAN, whereas formaldehyde does not). As simulations become more complex, the effects of the surrogate approximation in the CBM-IV that treats reactive olefins as aldehydes becomes more obvious. In the EC seven-component experiments, and to a lesser degree in the UNCmix experiments described later, some of the initial delay in the simulations is probably due to the surrogate aldehyde approximation. For the ITC multi-day simulations, we utilized a simple isobutene oxidation mechanism to eliminate the situation where the demonstration of CBM-IV performance was primarily affected by isobutene chemistry.

Initial conditions and results of the UCR-EC seven-component hydrocarbon surrogate simulation are provided in Tables 6-17 and 6-18. Plots showing the concentrations of NO_x, O_3, PAN and formaldehyde are shown in Figures 6-98 through 6-108. The overall simulation results are good and no unique deviations from the data were observed. Prediction of the maximum ozone

concentration was high on the average, by about 10 percent or 46 ppb; however, this is partially attributed to the overprediction of EC-232, an experiment that was terminated before the ozone concentration reached a maximum value. Comparison of the formaldehyde results with UNC mixture experiments (Table 6-16) indicates that whereas formaldehyde was very closely predicted in the EC (overpredicted by 8 ± 13 percent or 40 ± 70 ppb absolute in experiments that produced 500 to 700 ppb), the UNC results were usually underpredicted. Whether this is a chamber, monitor or mechanistic problem is not certain; however, Carter et al. (1986) reported similar findings. This independent verification seems to point to either a more sensitive monitor at UNC (it could, of course be responding to species other than HCHO) or a stronger loss mechanism for formaldehyde in the EC. CBM-IV PAN predictions are usually high compared to EC data and these experiments follow that trend (high by 43 percent on the average).

The UCR-ITC multi-day simulations are often used to determine if a chemical kinetics mechanism can succesfully simulate the transition between daylight and nocturnal regimes. Initial conditions for the UCR-ITC experiments are provided in Table 6-19, with concentration traces shown in Figures 6-109 through 6-113. Comparisons of daily ozone maxima and overall PAN and formaldehyde maxima are given in Table 6-20. Considering the evidence discussed in Section 5 that unanticipated chamber effects occur between the first and second days of ITC multi-day experiments, we find that the predicted and measured concentrations for the species listed in Table 6-20 agree quite well. The average absolute difference between predicted and measured maximum ozone concentrations is essentially zero, with a standard deviation of ± 32 ppb. The second through fourth day comparisons are similar for ozone maxima and for PAN and formaldehyde maxima as well. In addition, the concentration profiles follow the diurnal trends of the experimental data as closely as can be expected for smog chamber experiments of up to four days.

Substituted and Complex Mixtures

We also selected a set of UNC experiments from the 1981 and 1982 hydrocarbon reactivity tests in order to focus more closely on the chemical effects of substituting aromatics (and a few other species) in surrogate hydrocarbon mixtures. Table 6-21 provides information concerning initial concentrations and characteristics of each experiment. The two base mixtures used in these experiments, SIMmix and UNCmix, consist of approximately 70 percent paraffin and 30 percent olefin carbons. The difference between them is that SIMmix contains only butane, pentane, ethylene and propylene, while UNCmix is a mixture of eleven paraffin and olefin species. (It was later used as the paraffin and olefin basis from which the SynUrban mixture was generated.) Most experiments simulated in the

UNC study were UNCmix substitutions, using either a complex (COMARO) or simple (SIMARO) mixture of aromatics as shown in Table 6-21.

Simulation plots are presented in Figures 6-114 through 6-135 and comparison of maxima for measured and simulated ozone, PAN and formaldehyde are given in Table 6-22. Considering the chemical range of substitution species (see Table 6-21), ozone prediction results are very good, showing an average overprediction of 8 (±78) ppb or 7 (±25) percent. However, we again caution against using simple statistics in these comparisons. For example, the 7 December and 11 November 1982 experiments are extremely difficult to simulate because of the low temperature conditions present throughout the day. Removal of these datasets from our average reduces the overprediction percentage to 4 (± 17) percent. In the work of Carter et al. (1986), a similar removal of the three December and November experiments from the compilation of 25 simulations changes the average prediction from a 21 (±95) percent overprediction to a 7 (±24) percent underprediction.

We also note that the best simulations for this group of hydrocarbon reactivity experiments occurred on days when drying was performed and no condensation was observed. This subset of experiments (AU3181, SE1481, SE1682, SE1081 and AU2681 [SE0381 was eliminated due to bad light on that day]) contained substitutions of butane, toluene, xylene, ethylbenzene, and the SIMARO and COMARO mixtures. The fact that both maxima values and overall goodness-of-fit for ozone and NO_x curves were the best for these days indicates the benefit of chamber drying.

Overall, formaldehyde predictions were good for these hydrocarbon reactivity simulations, resulting in an average underprediction of only 30 (± 30) ppb or 18 (± 25) percent. PAN prediction was high, as it was in the earlier UCR-EC experiments, probably because the CBM-IV used PAN to represent all peroxyacyl nitrates. We note again that the formaldehyde plots in Figures 6-114 through 6-135 show a delayed, but then rapidly increasing formaldehyde concentration similar to that occurring in the ethylene simulations. This appears to indicate the early collection of formaldehyde or formaldehyde precursors on the chamber walls, followed by a midday release that produces in-chamber concentrations more rapidly than the values predicted for homogenous gas-phase chemistry in the simulation. The identification and simulation of such a process would probably enhance the goodness-of-fit for the midday period of these experiments.

Because there are so few individual aromatic/NO_x smog chamber data sets other than for toluene and the common xylenes, these simulations provide the only useful tests of the approximations used in the CBM-IV for higher molecular weight aromatic species. Although the complexity of these experimental mixtures precludes definate verification that the carbon bond

representations of these aromatic species is accurate, we may conclude that the CBM-IV representations are satisfactory enough to produce correct fits for a number of indicator species and a relatively good prediction of ozone and formaldehyde. One final simulation comparison can be made for the 19 September 1984 experiments, which were tests of the high molecular weight aromatic fraction (toluene, m-xylene, o-xylene, and 1,2,4-trimethylbenzene) of the SynAuto mixture. Initial conditions for these experiments are given in Table 6-21 and results are shown in Figures 6-134 and 6-135, and in Table 6-22. The interesting aspect of these experiments is that the side with higher initial hydrocarbon concentration (the NO_x concentrations were matched between sides) produced significantly less ozone, but at a faster rate. This is characteristic of rapid formation of radicals in xylene systems, followed by depletion of virtually all NO (and later, NO_2), and termination of ozone formation potential. The new aromatic reaction representation provides a better fit with these data than was previously obtained from the earlier versions of the CBM. However, uncertainties are still apparent in the mechanism. On the red side (high HC/NO_x shown in Figure 6-135) the radical flux is high for a brief period of around 200 minutes before NO_2 is depleted (the remaining NO_2 in the experimental data is a PAN response of the UNC chemiluminescent NO_x meter). This high radical flux, caused mainly by the prompt formation of radicals from xylenes, removes a large fraction of toluene to form additional reactive products. In the blue side (Figure 6-134) this prompt formation is less dramatic, and the decay of ozone is somewhat underpredicted (with the accompanying underprediction of radical reaction products), resulting in slower ozone formation. The fact that NO_x remains in the system for a longer period, however, results in a correspondingly longer period before the system is effectively "shut down" by delpetion of NO_x. This eventually produces higher ozone concentrations at the lower HC/NO_x ratio.

SUMMARY OF SIMULATION RESULTS

The overall ability of the CBM-IV to predict maximum ozone and formaldehyde concentrations in smog chamber experiments appears to be good for the evaluation tests discussed above. Figures 6-136 through 6-138 give scatter plots of simulation results compared to measured ozone maximum concentrations for the following groupings:

(1) Formaldehyde and larger aldehydes,

(2) Ethylene and olefins,

(3) Toluene and xylenes,

(4) Isoprene and α-pinene,

(5) The various mixtures from UNC and UCR, and

(6) All data from groups (1) through (5).

Figures 6-139 through 6-141 give similar diagrams for maximum formaldehyde concentrations.

The predictive bias for ozone was rather small in all cases. The largest overprediction was for the isoprene and α-pinene set (13 ± 31 percent) and primarily attributable to a few α-pinene outliers. The average overprediction for the mixtures (excluding only one outlier, the first day ozone calculation for ITC-633) was 2 percent with a ± 22 percent standard deviation. Similarly, the overall average overpredition, including every experiment, was 5 percent with a ± 23 percent standard deviation.

For formaldehyde, the uncertainties were larger. This was not unanticipated, however, since formation reactions of formaldehyde are not clearly defined, nor is the measurement as precise as that for ozone. As we noted earlier, the isoprene mechanism, which produces high formaldehyde yields, predicted the experimental data quite well. The average overprediction was 5 (± 16) percent for the isoprene and α-pinene experiments combined. For the 68 mixtures simulated, the maximum formaldehyde concentration was underpredicted by 9 (± 34) percent. These results are considered good because of the uncertainties noted.

We caution against comparison of the associated uncertainties with those presented by other researchers, since the range of tests (i.e., smog chamber data sets) performed between any two such studies undoubtedly differs. The mechanism demonstration and evaluation discussed here has been based on the simulation of smog chamber data sets selected because they were the best available and, hopefully, provided a reasonable standard against which to test. However, some uncertainty still exists in the initial and environmental conditions of the experiments that will translate into a portion of the error noted in these comparisons.

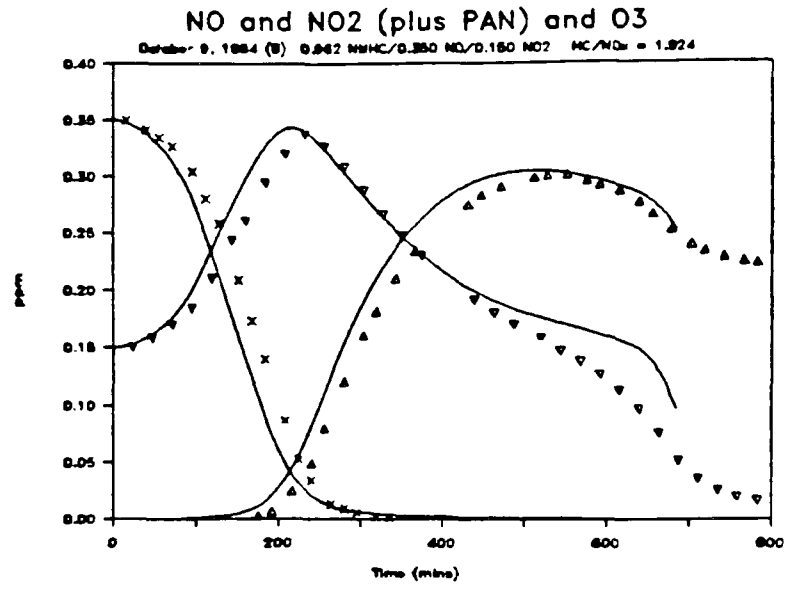

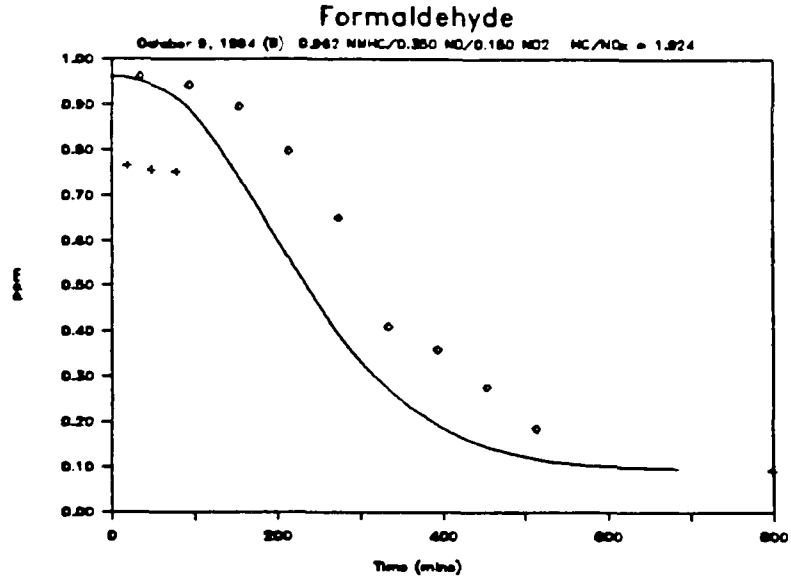

FIGURE 6-1. Simulation results for UNC experiment OC0984B (symbols are experimental measurements)

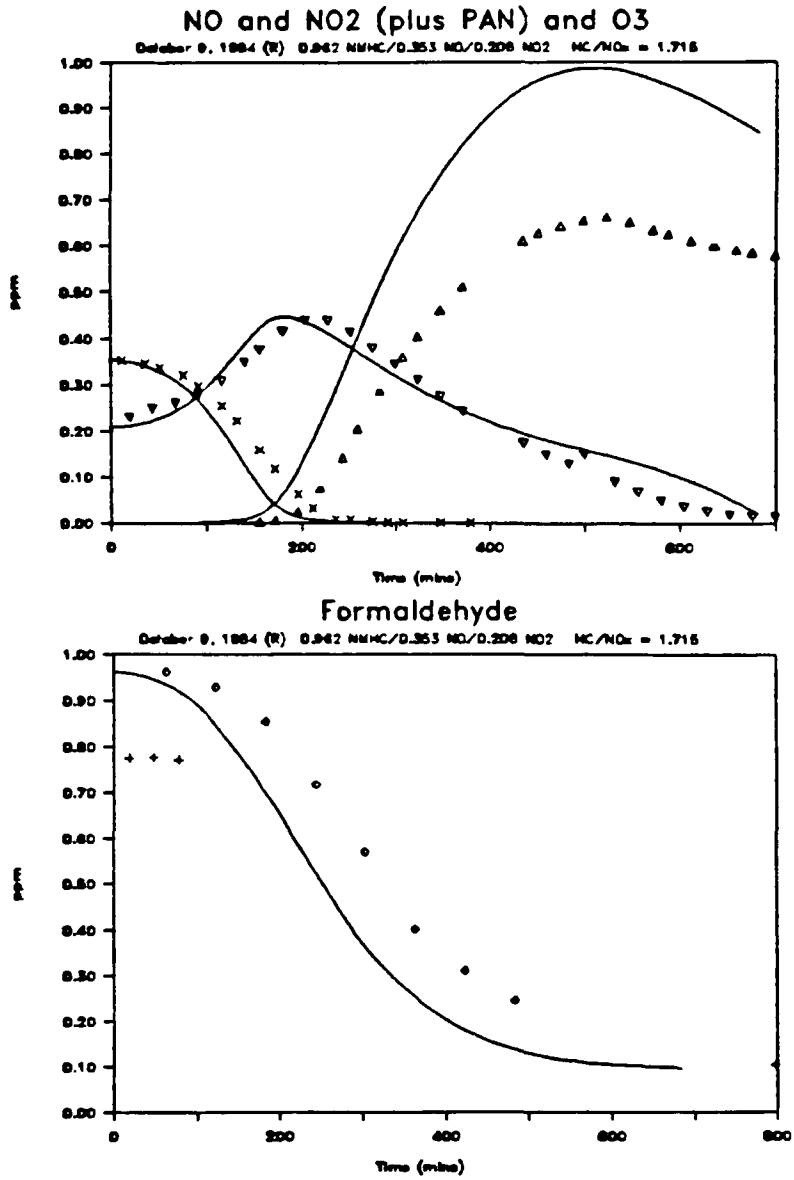

FIGURE 6-2. Simulation results for UNC experiment OC0984R (symbols are experimental measurements)

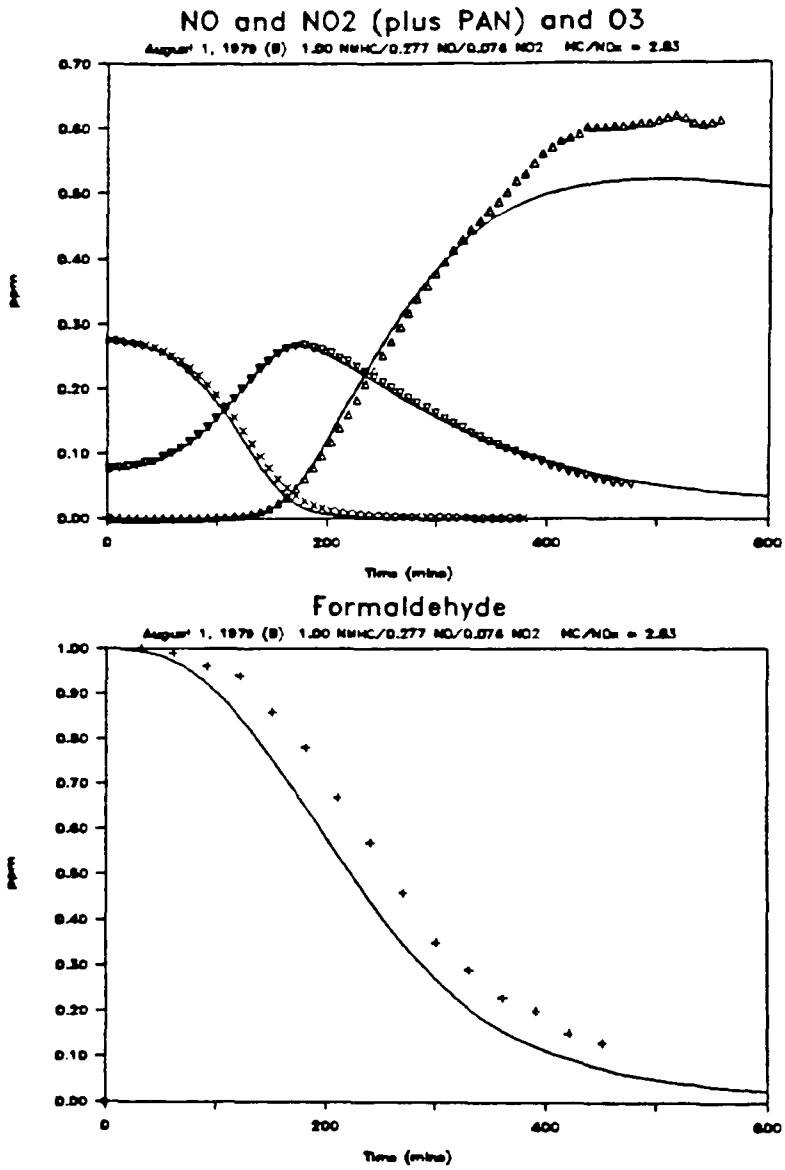

FIGURE 6-3. Simulation results for UNC experiment AU0179B (symbols are experimental measurements)

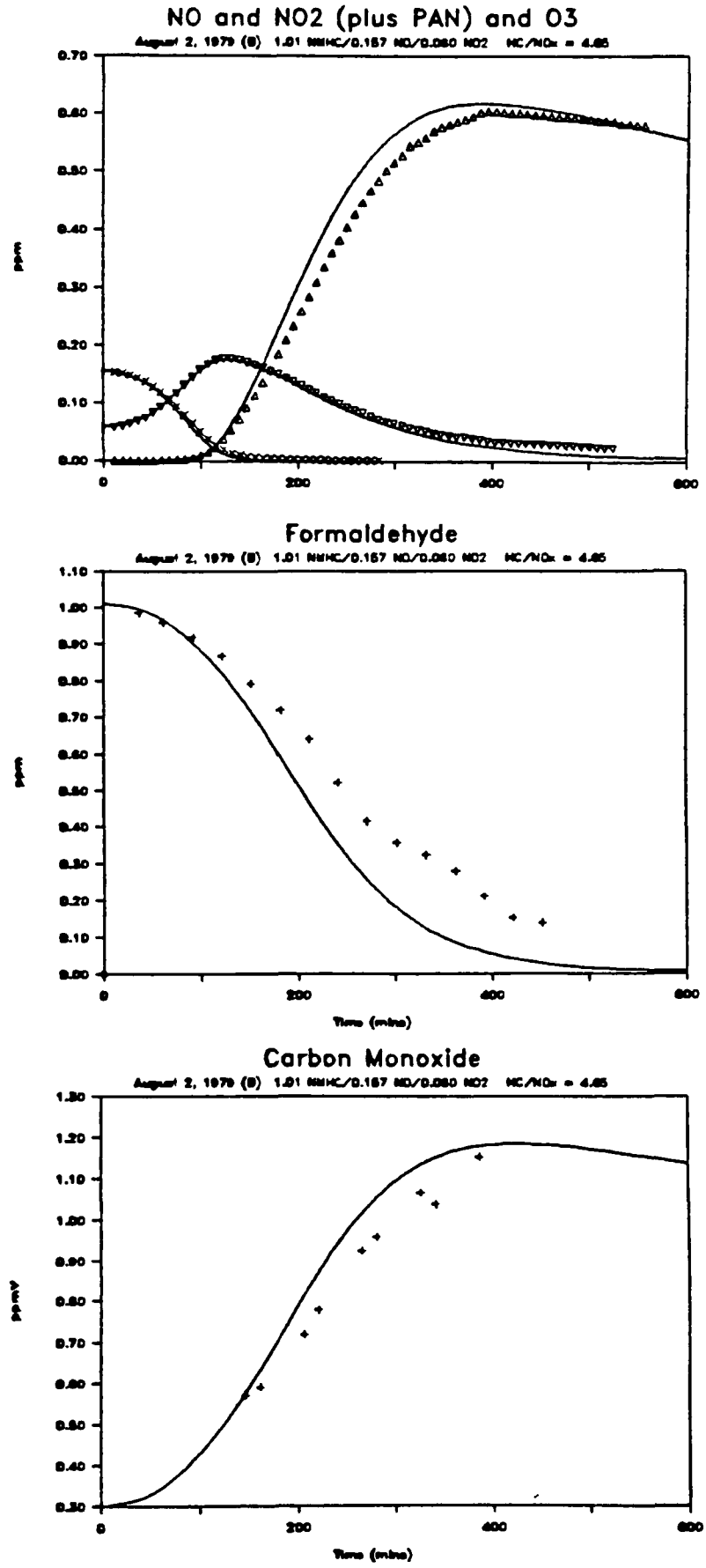

FIGURE 6-4. Simulation results for UNC experiment AU0279B (symbols are experimental measurements)

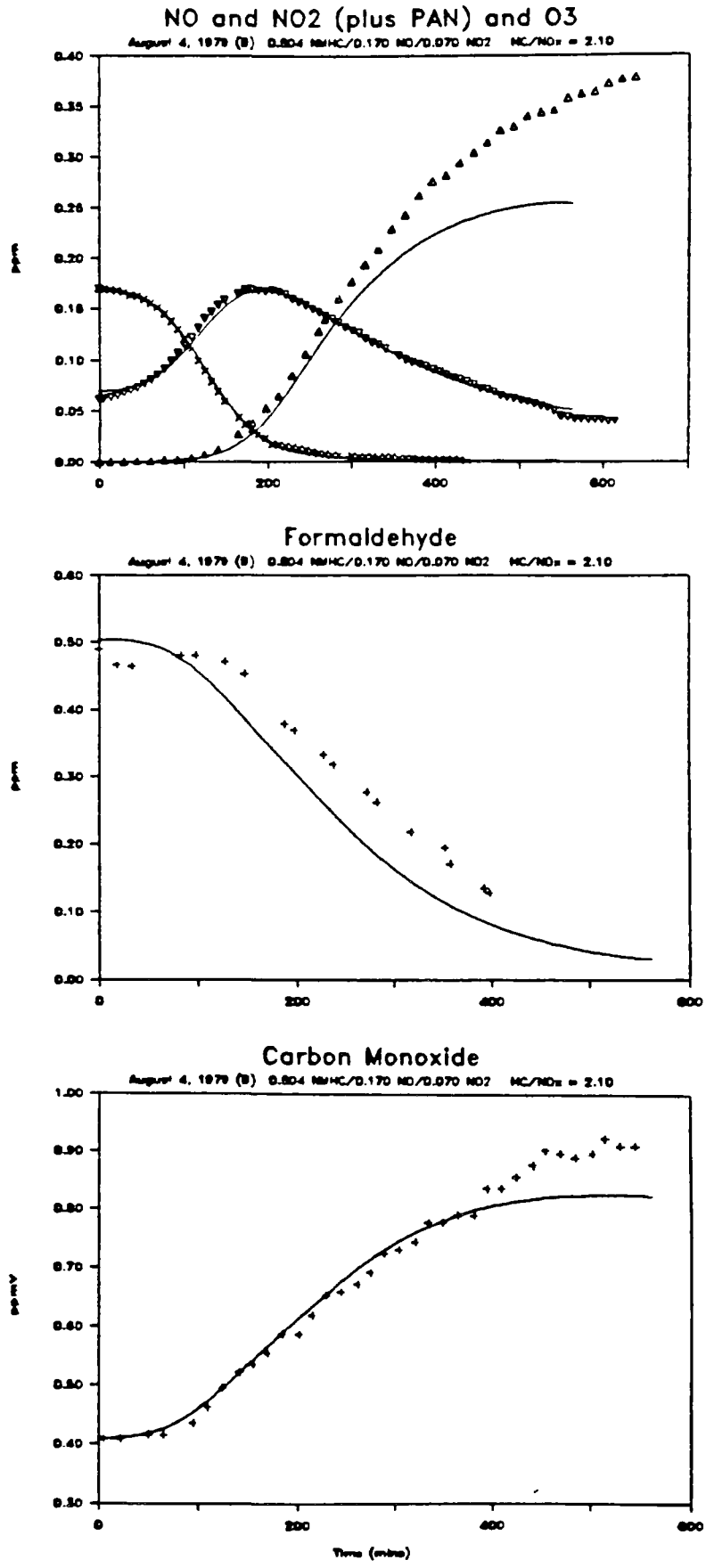

FIGURE 6-5. Simulation results for UNC experiment AU0479B (symbols are experimental measurements)

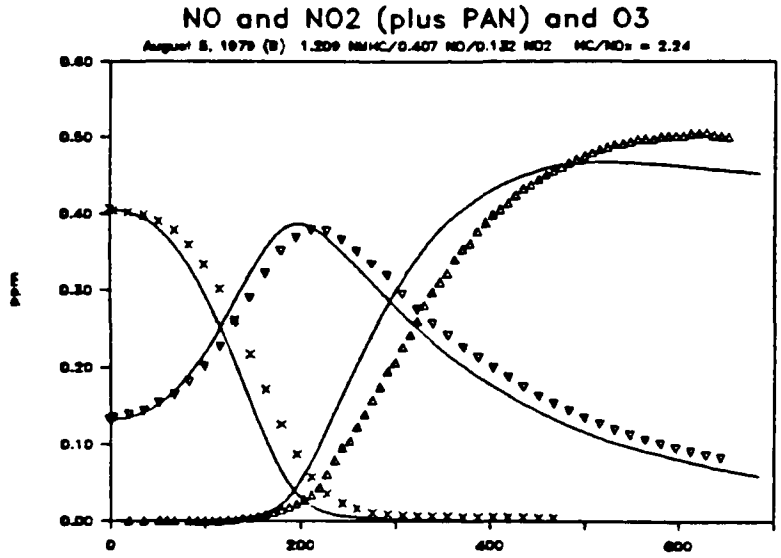

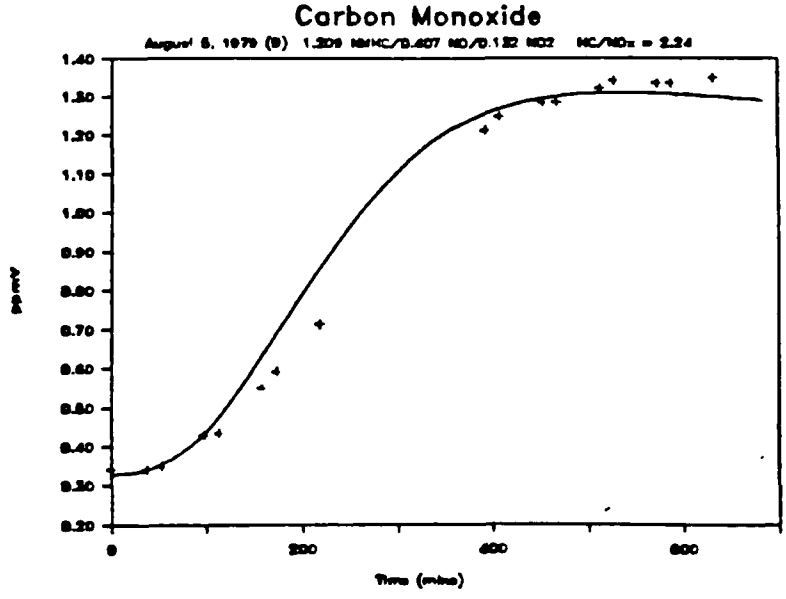

FIGURE 6-6. Simulation results for UNC experiment AU0579B (symbols are experimental measurements)

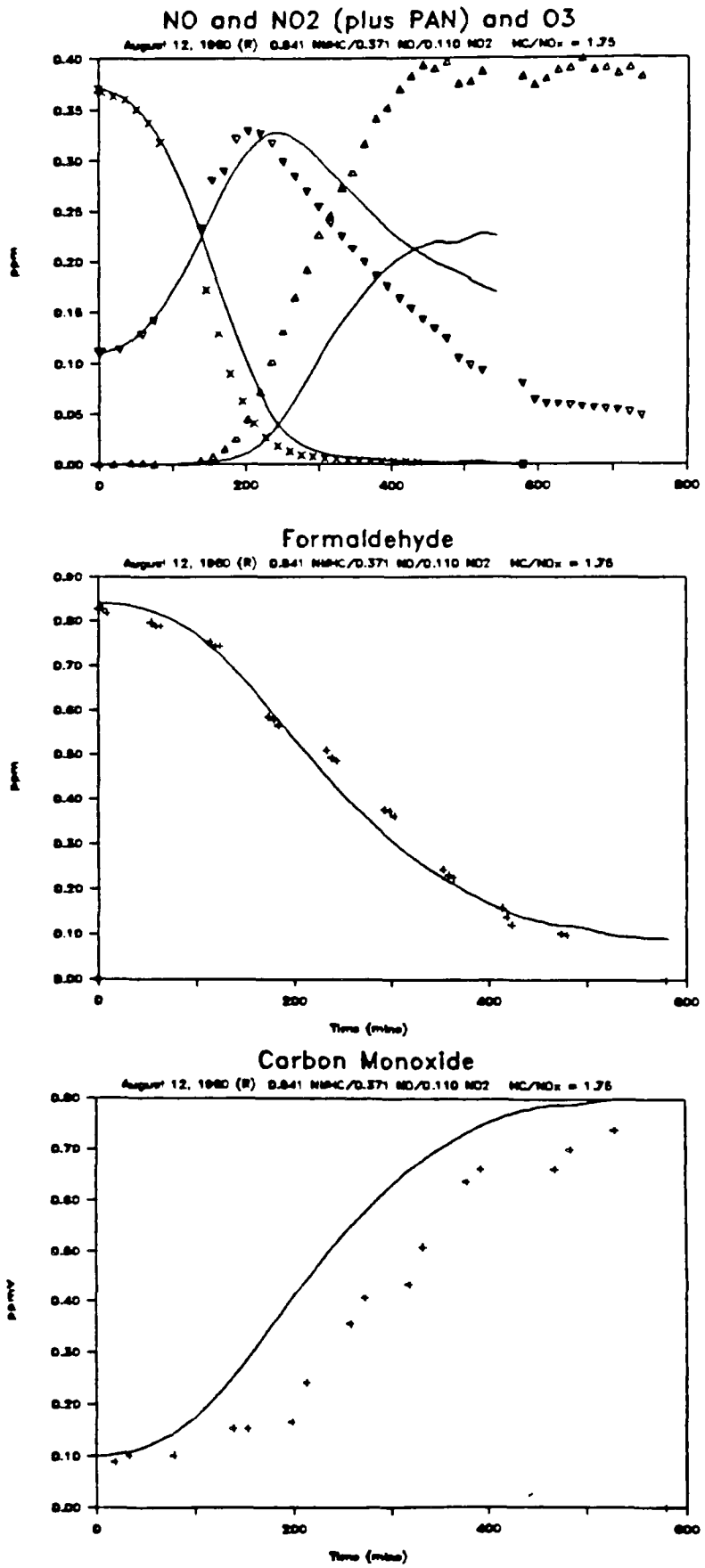

FIGURE 6-7. Simulation results for UNC experiment AU1280R (symbols are experimental measurements)

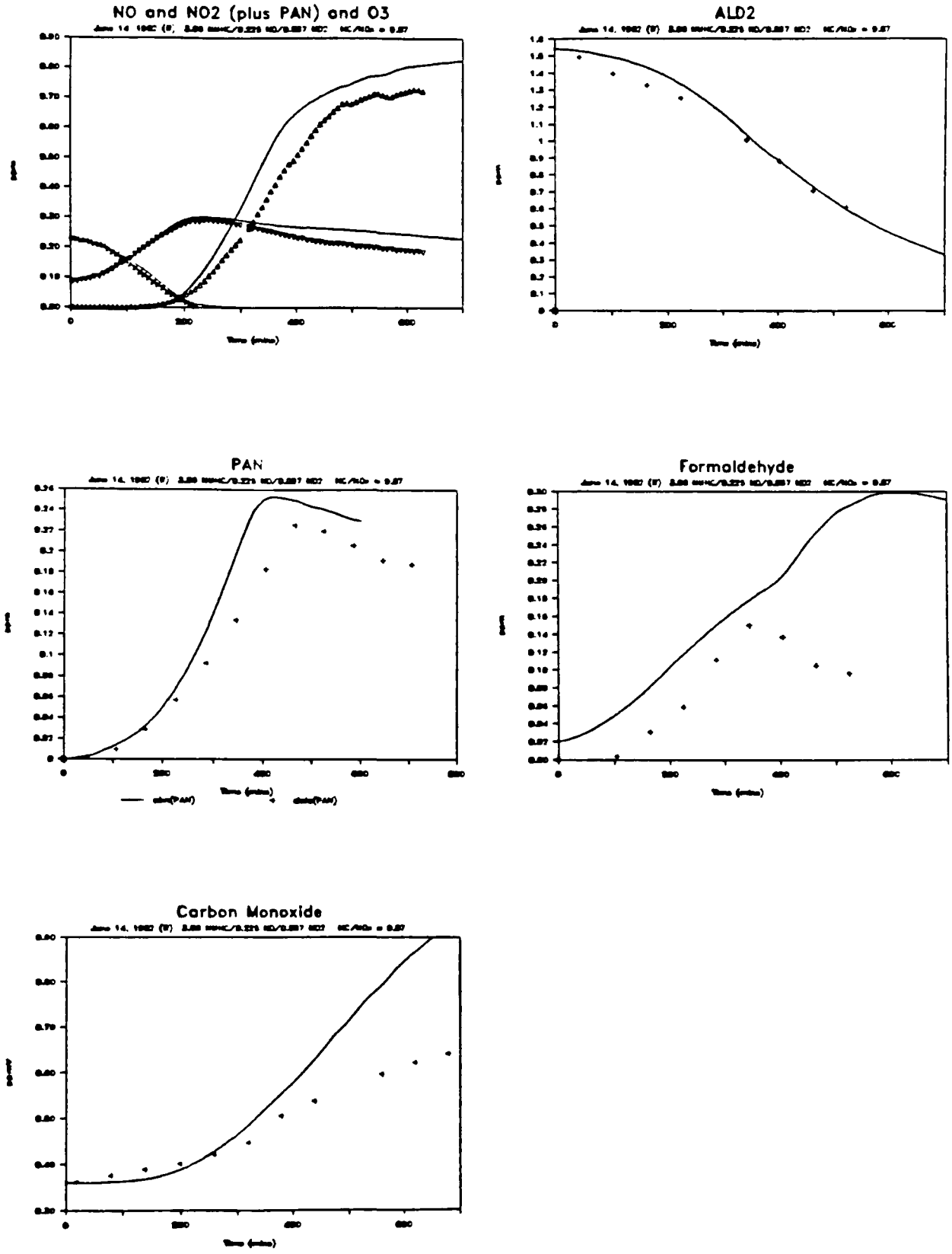

FIGURE 6-8. Simulation results for UNC experiment JN1482R (symbols are experimental measurements)

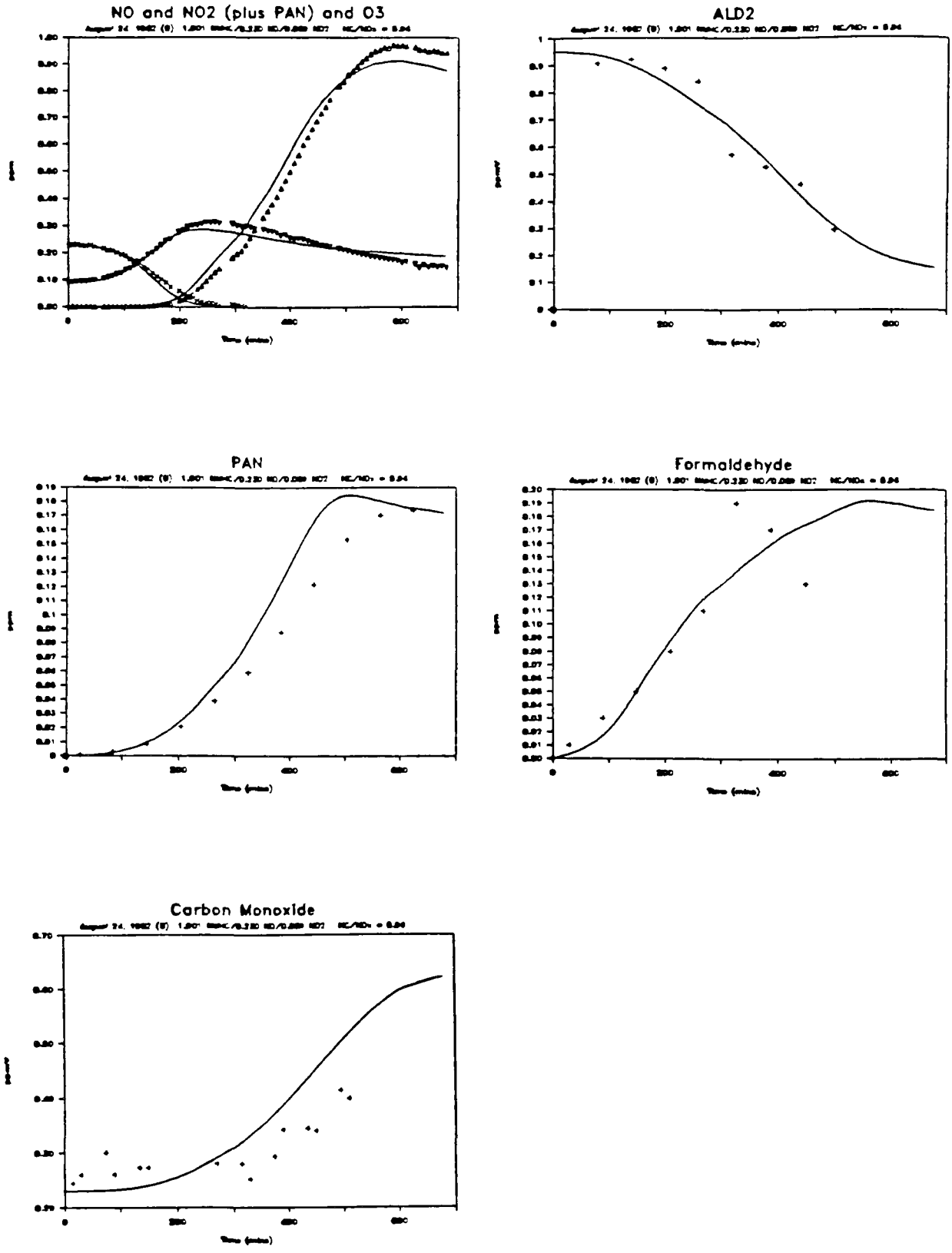

FIGURE 6-9. Simulation results for UNC experiment AU2482B (symbols are experimental measurements)

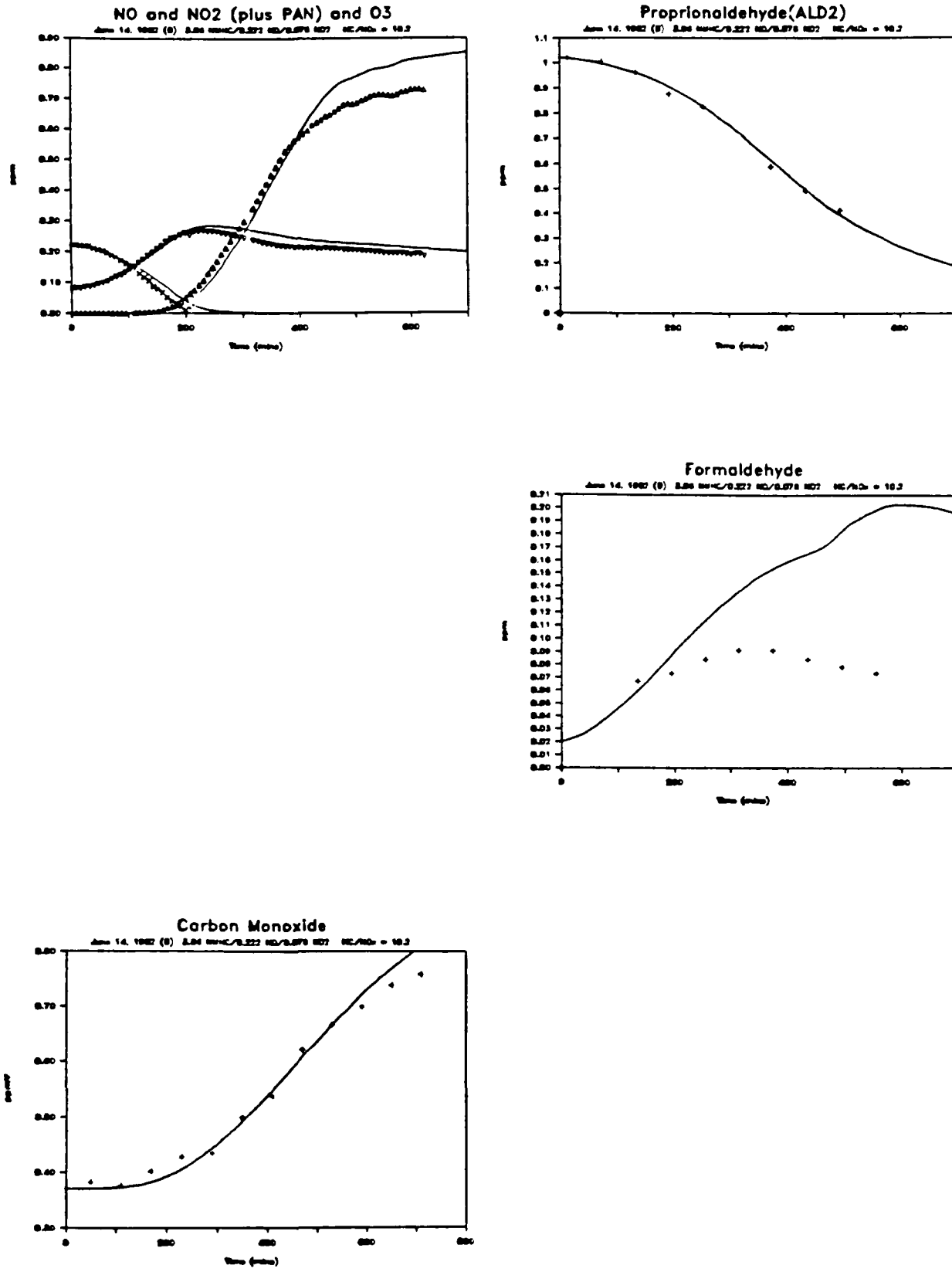

FIGURE 6-10. Simulation results for UNC experiment JN1482B (symbols are experimental measurements)

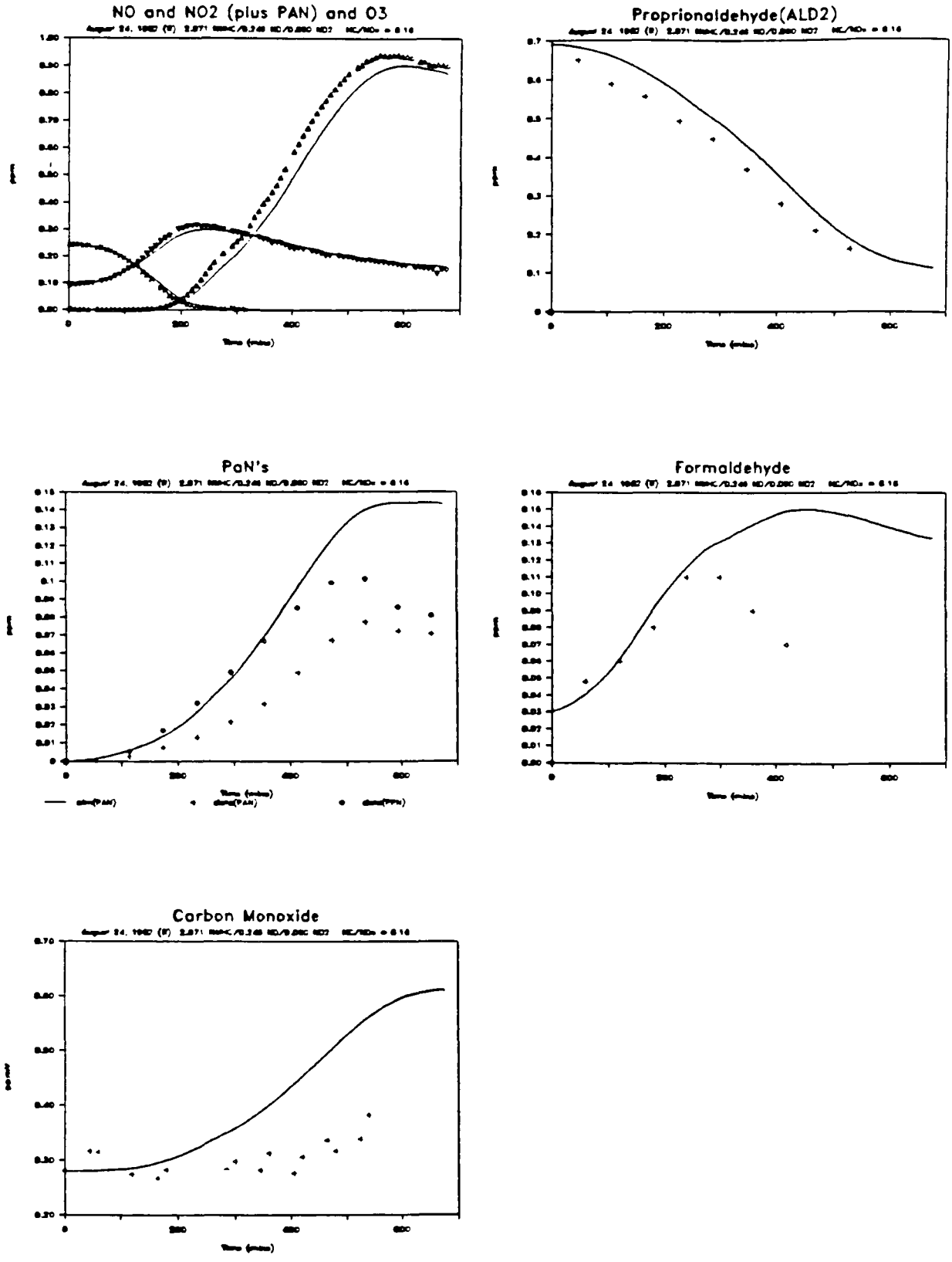

FIGURE 6-11. Simulation results for UNC experiment AU2482R (symbols are experimental measurements)

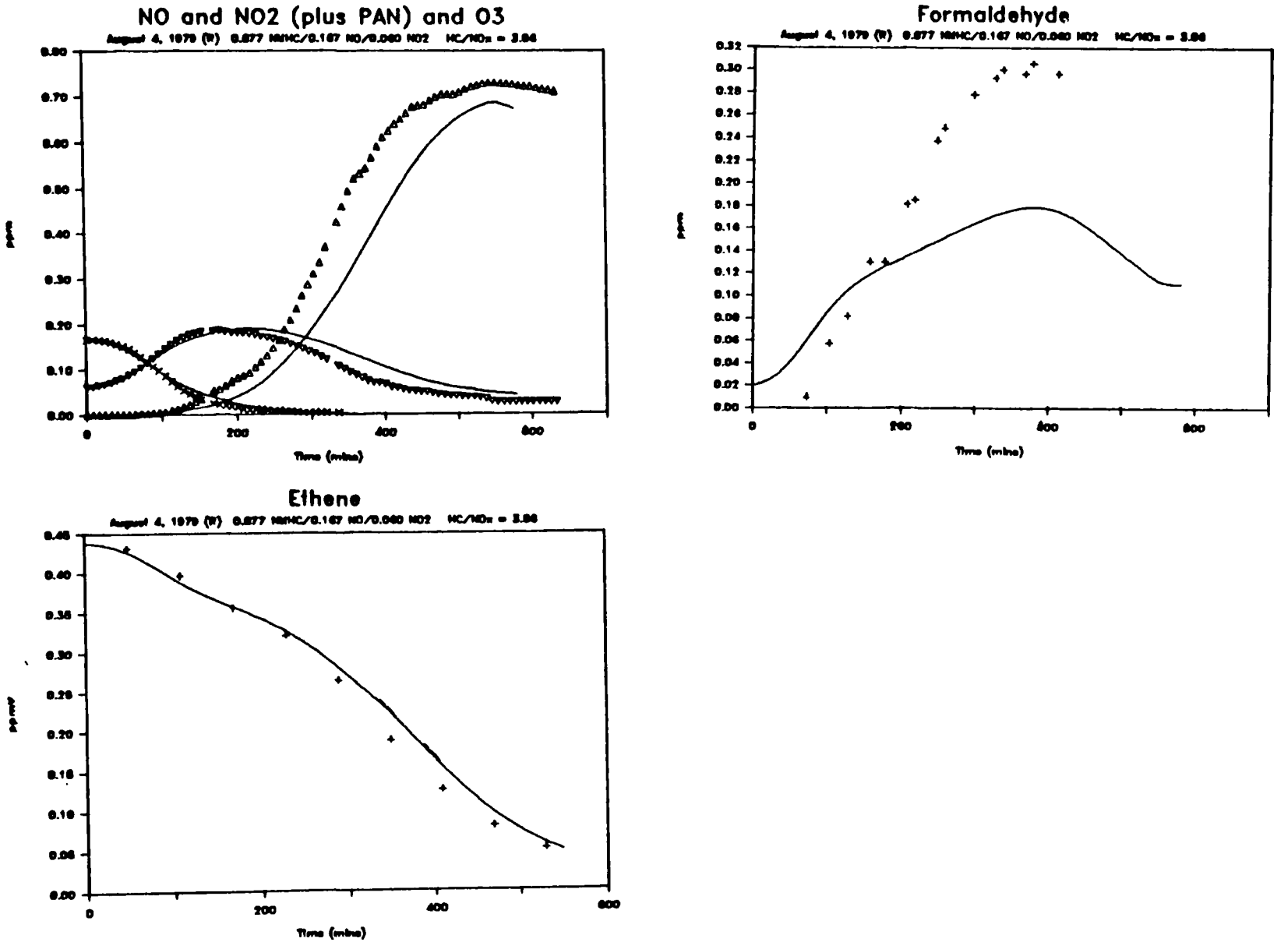

FIGURE 6-12. Simulation results for UNC experiment AU0479R (symbols are experimental measurements)

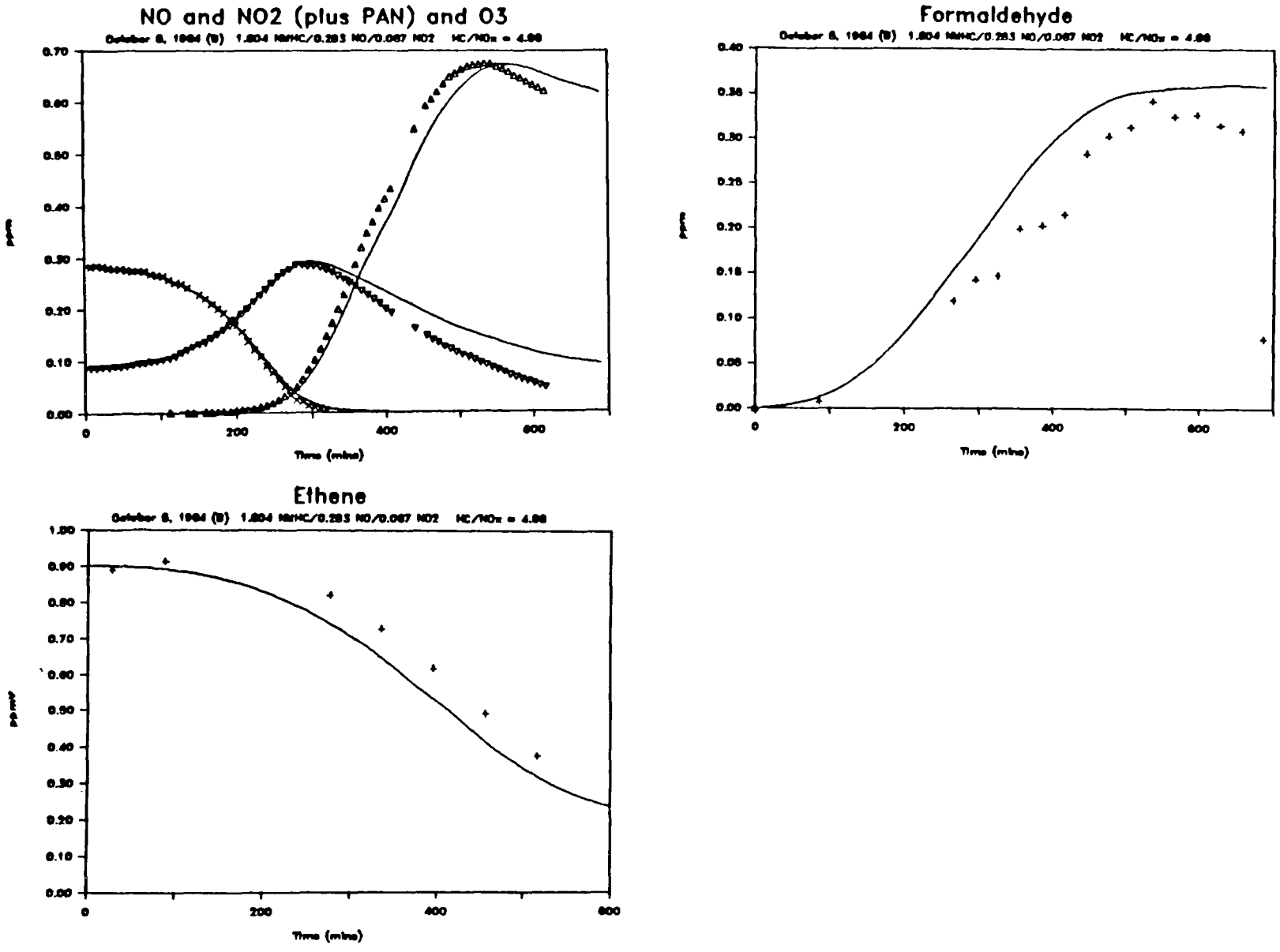

FIGURE 6-13. Simulation results for UNC experiment OC0584B
(symbols are experimental measurements)

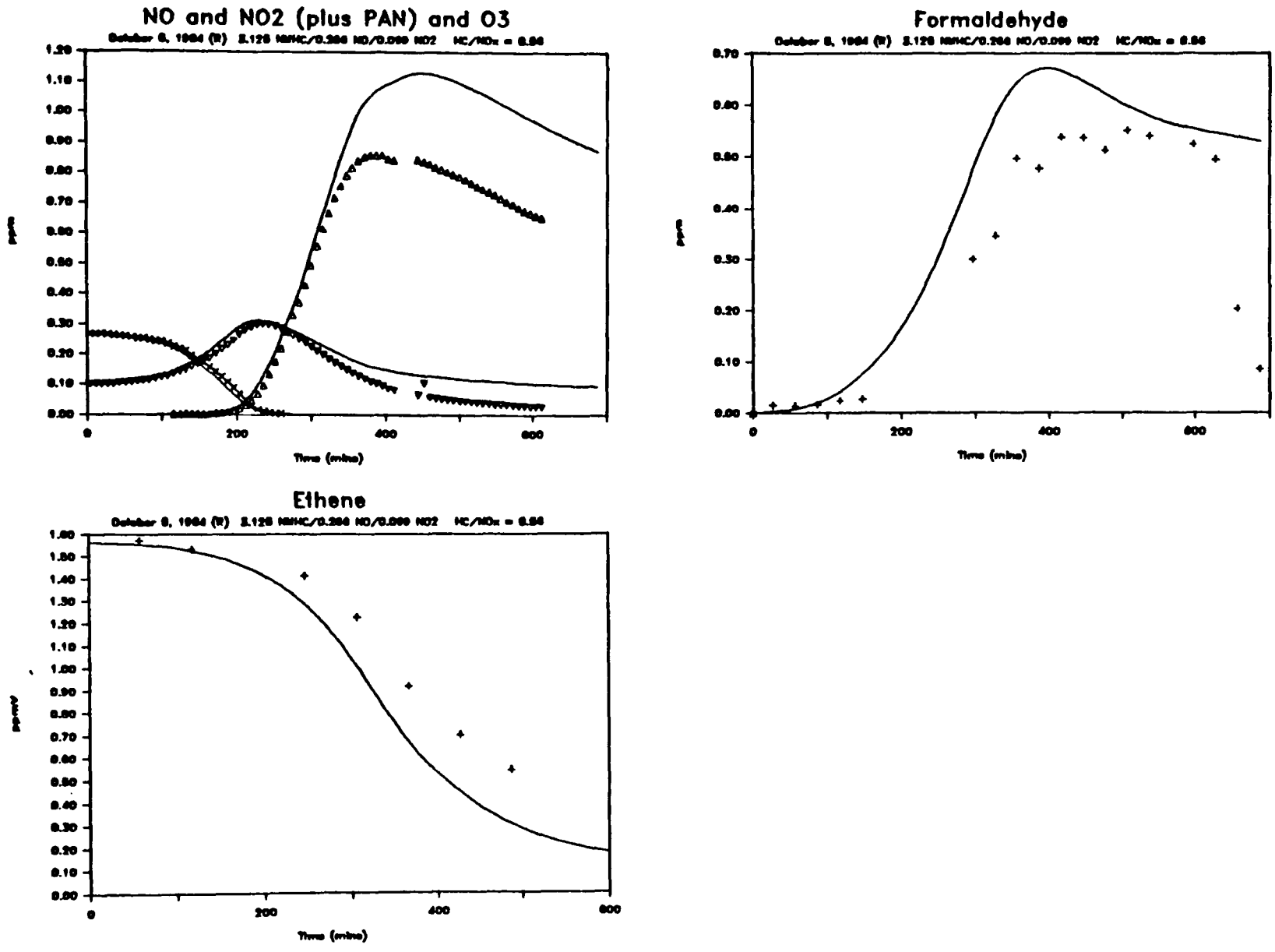

FIGURE 6-14. Simulation results for UNC experiment OC0584R (symbols are experimental measurements)

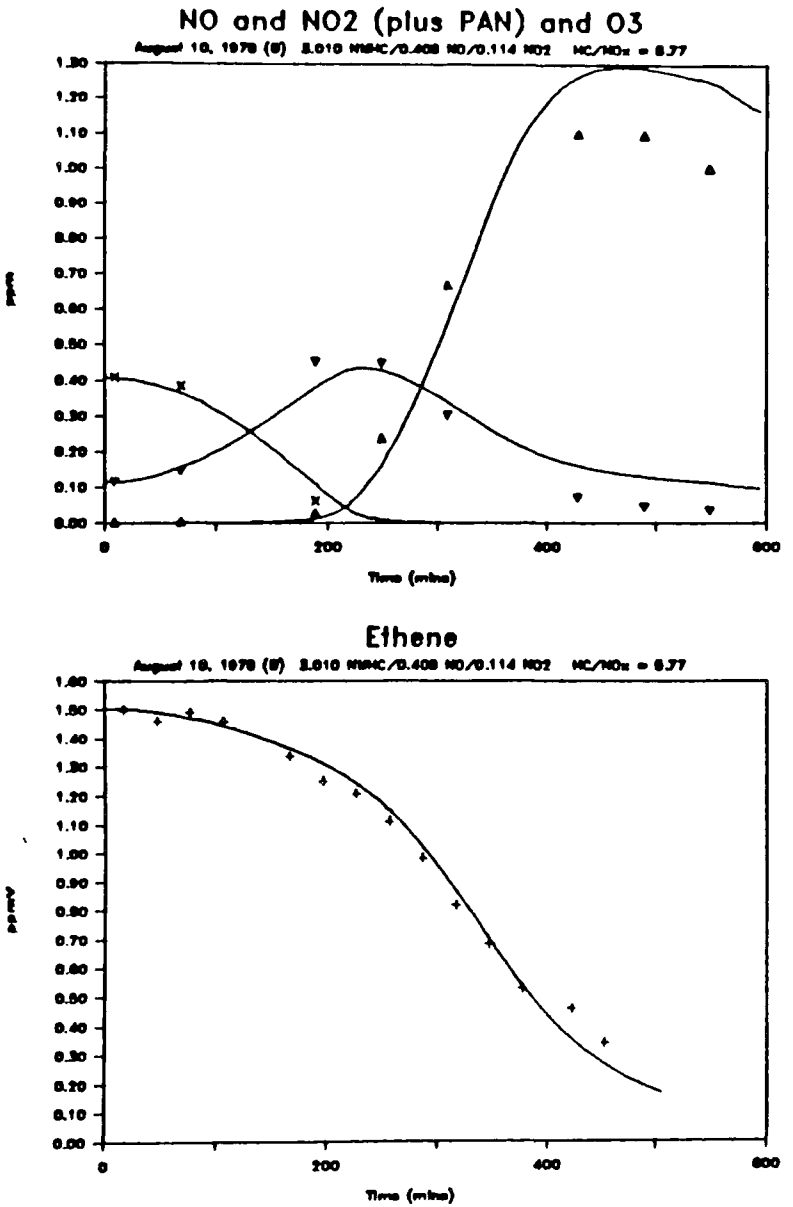

FIGURE 6-15. Simulation results for UNC experiment AU1078B
(symbols are experimental measurements)

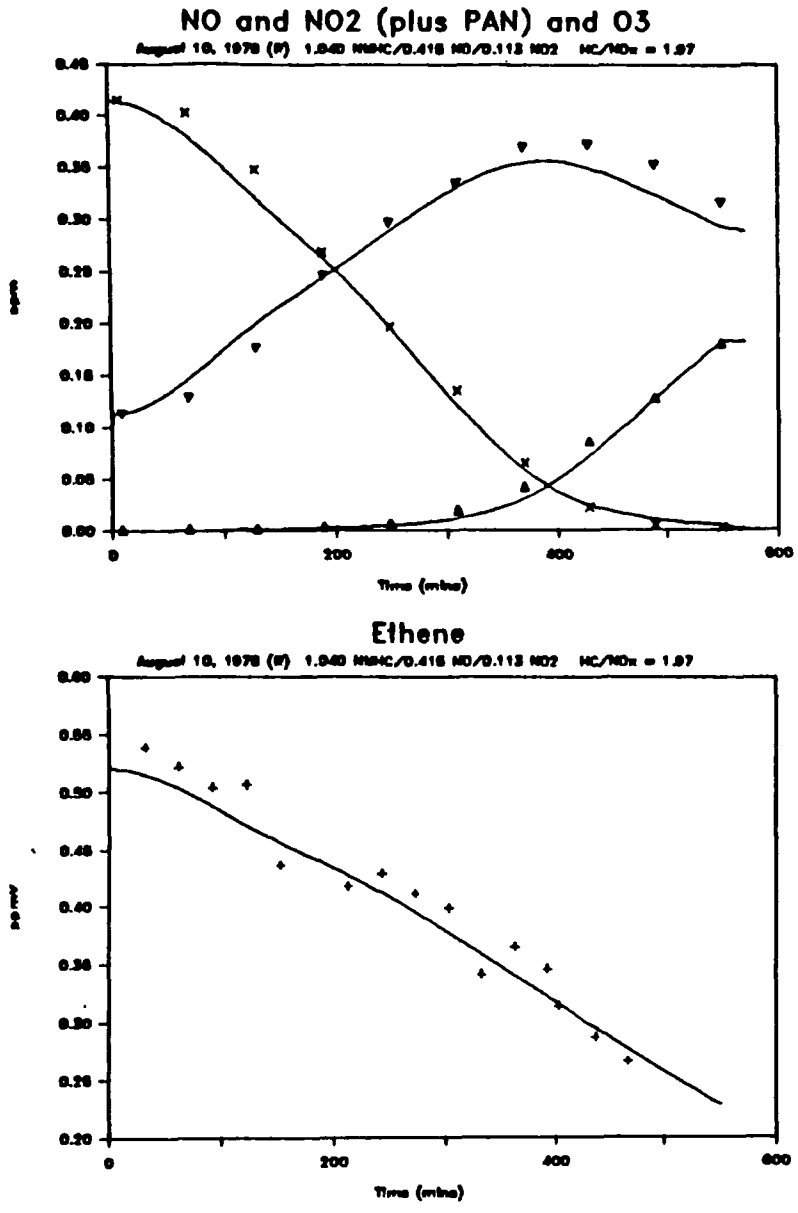

FIGURE 6-16. Simulation results for UNC experiment AU1078R
(symbols are experimental measurements)

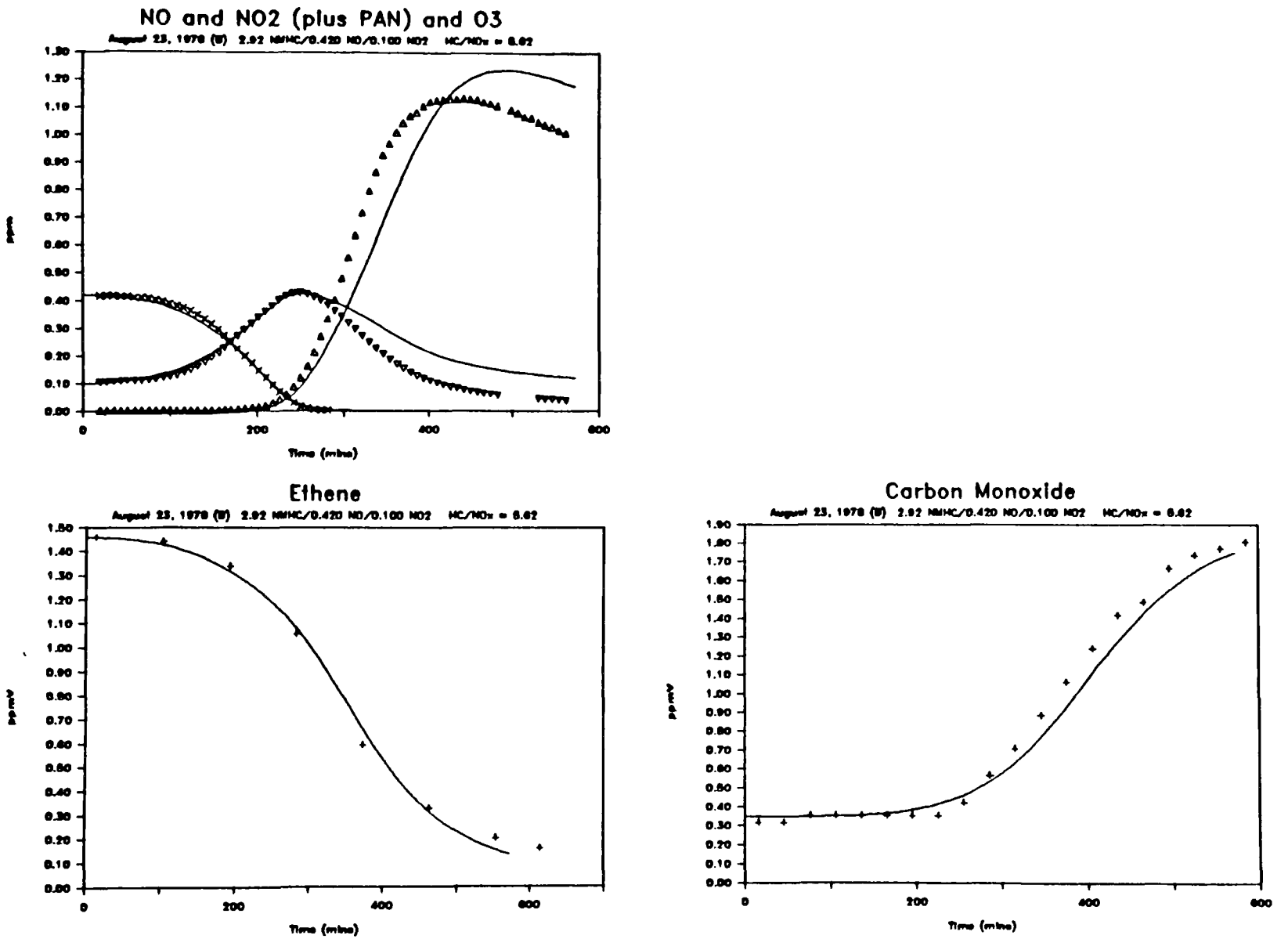

FIGURE 6-17. Simulation results for UNC experiment AU2378B
(symbols are experimental measurements)

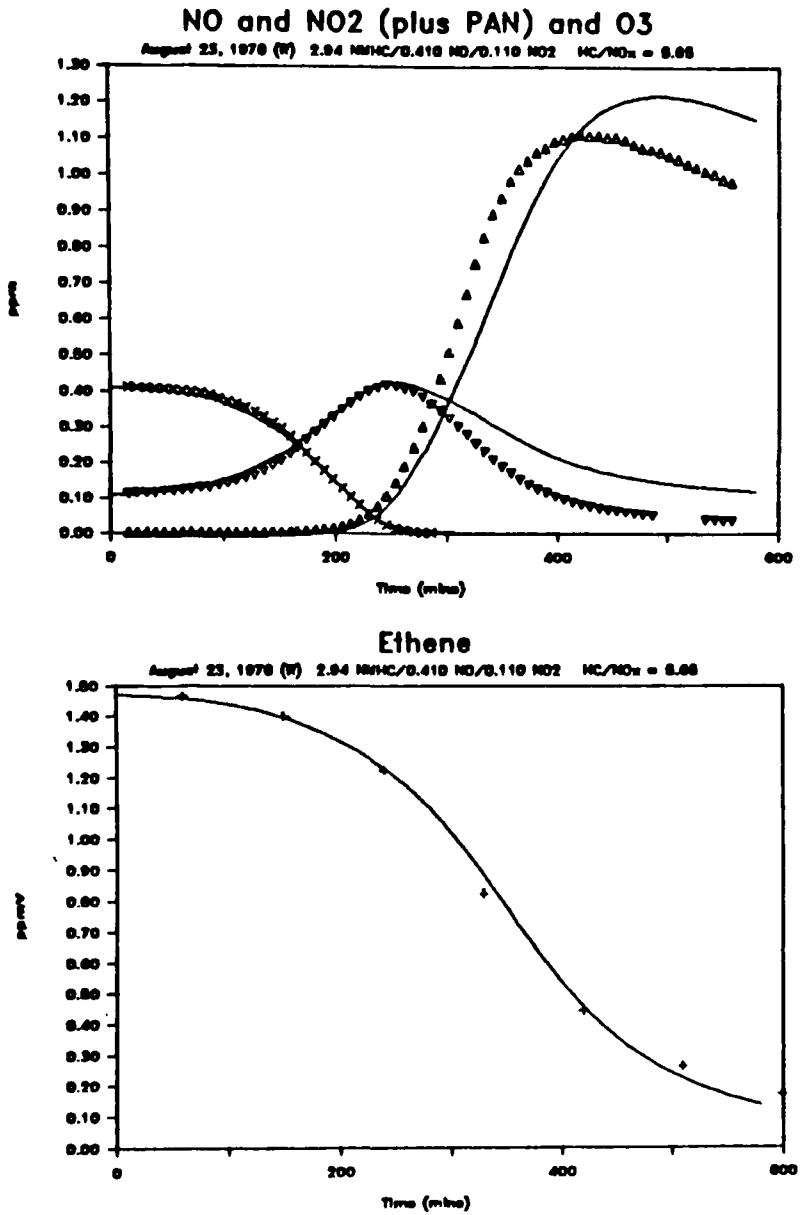

FIGURE 6-18. Simulation results for UNC experiment AU2378R (symbols are experimental measurements)

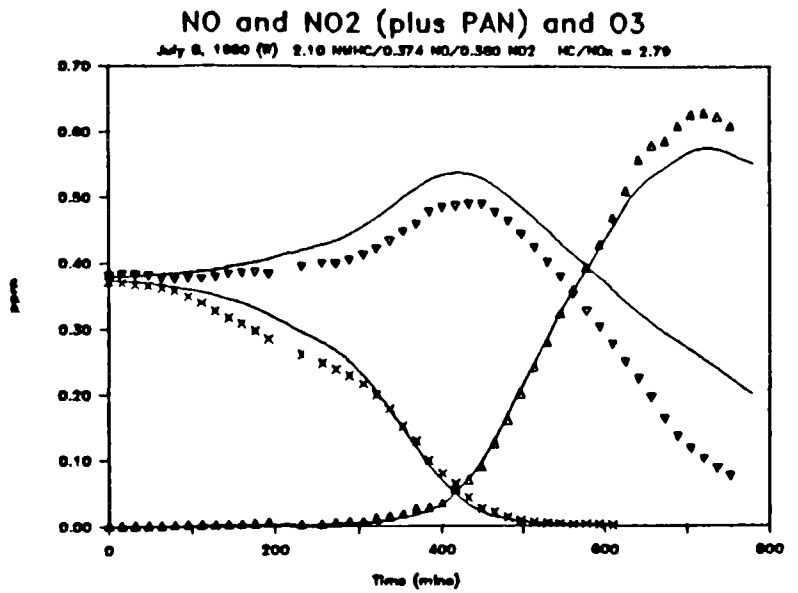

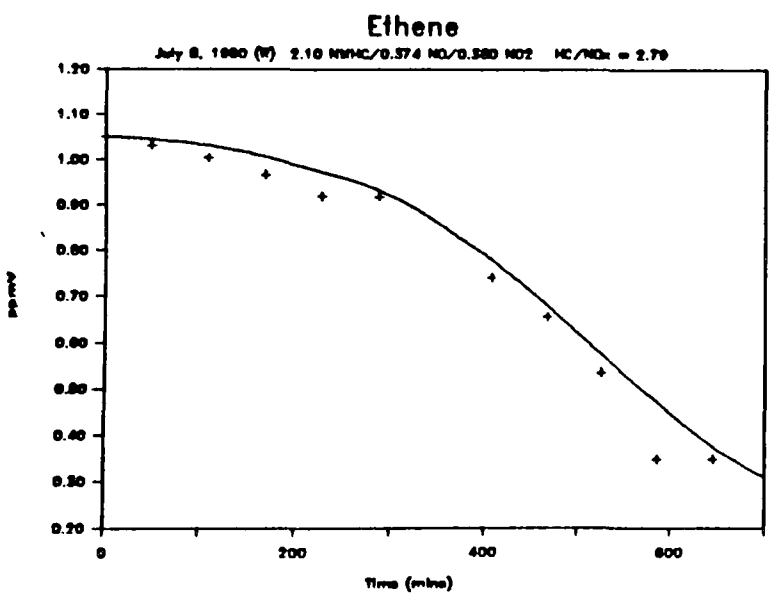

FIGURE 6-19. Simulation results for UNC experiment JL0880R (symbols are experimental measurements)

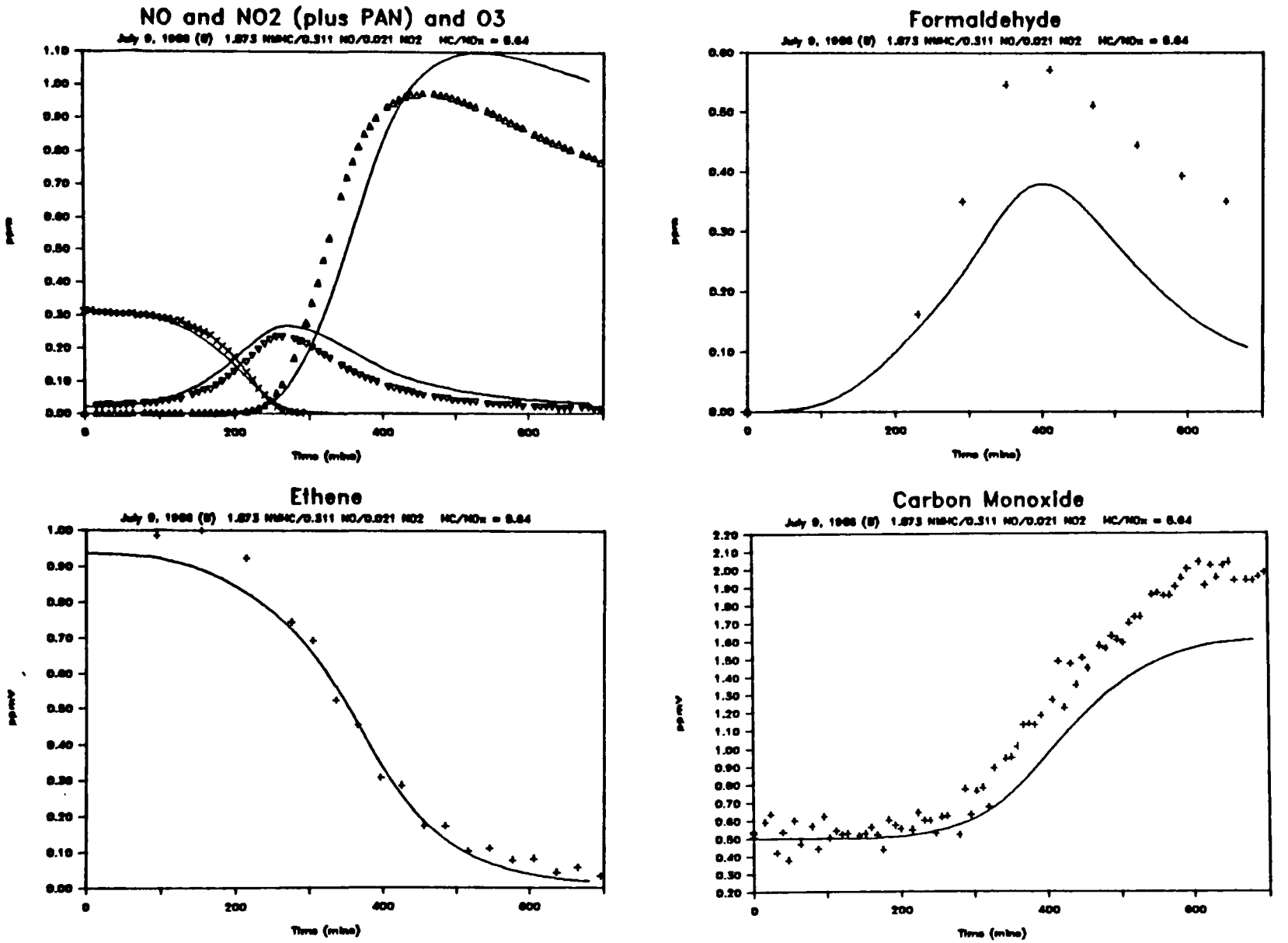

FIGURE 6-20. Simulation results for UNC experiment JL0986B (symbols are experimental measurements)

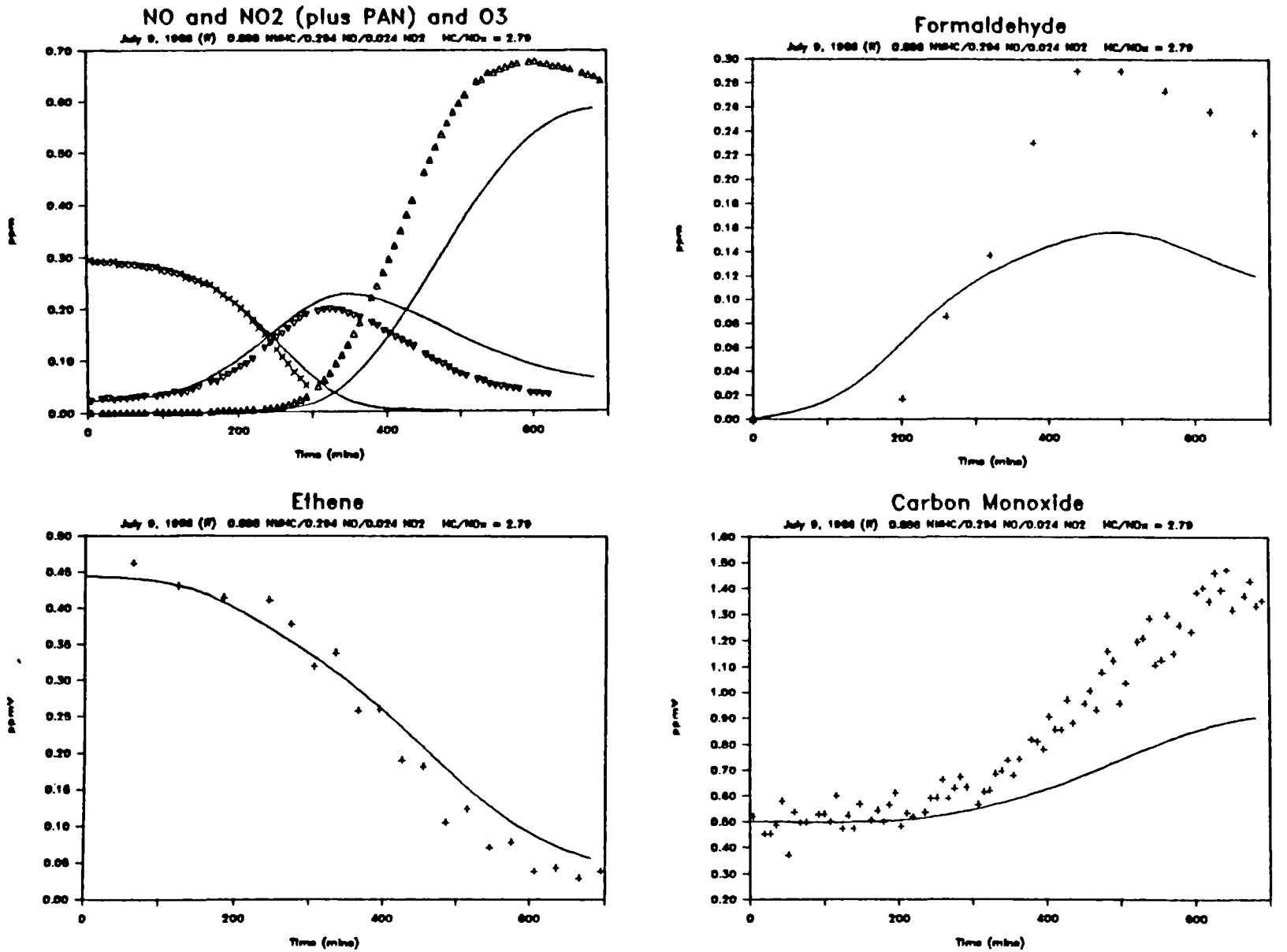

FIGURE 6-21. Simulation results for UNC experiment JL0986R
(symbols are experimental measurements)

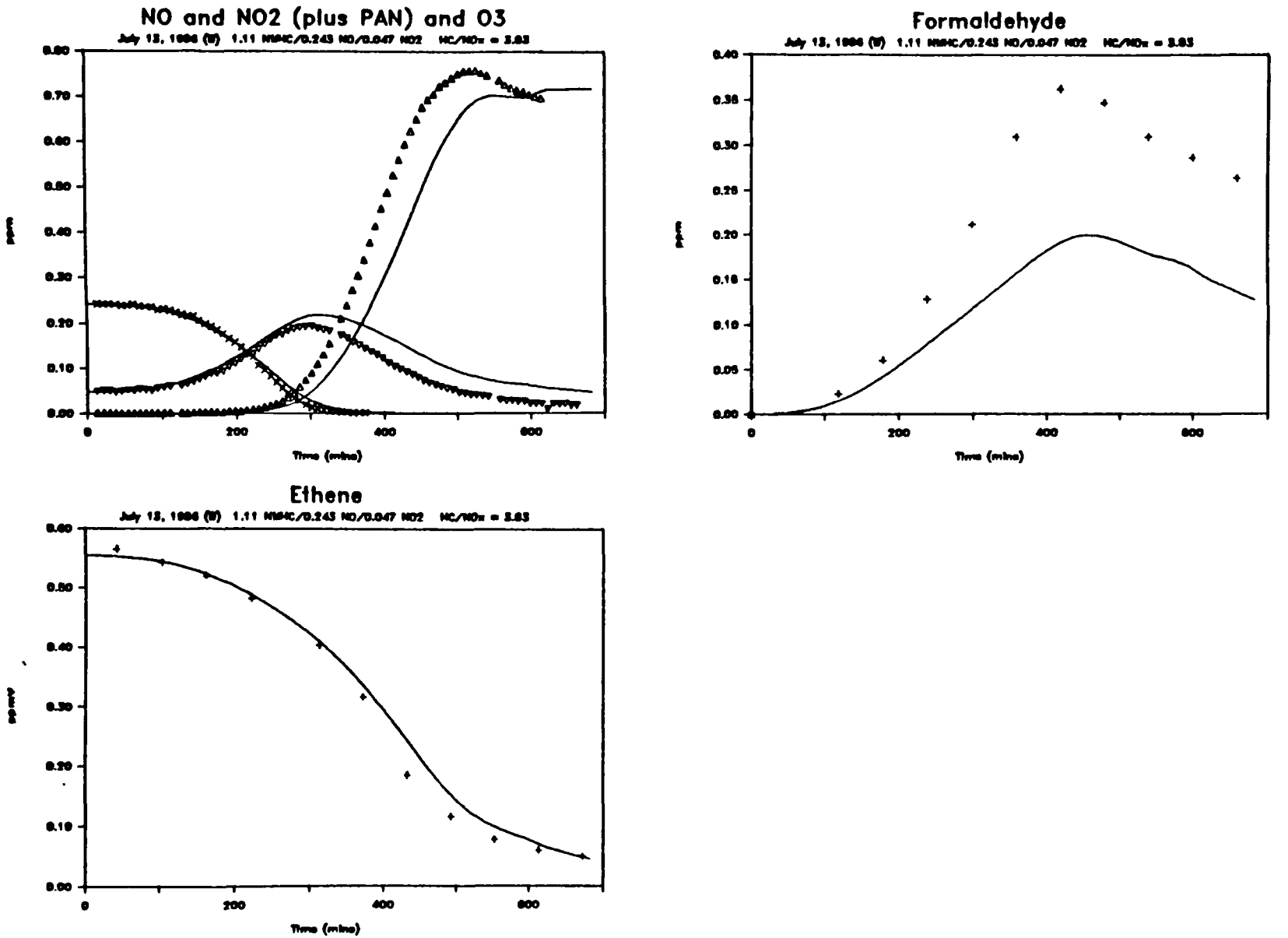

FIGURE 6-22. Simulation results for UNC experiment JL1386B
(symbols are experimental measurements)

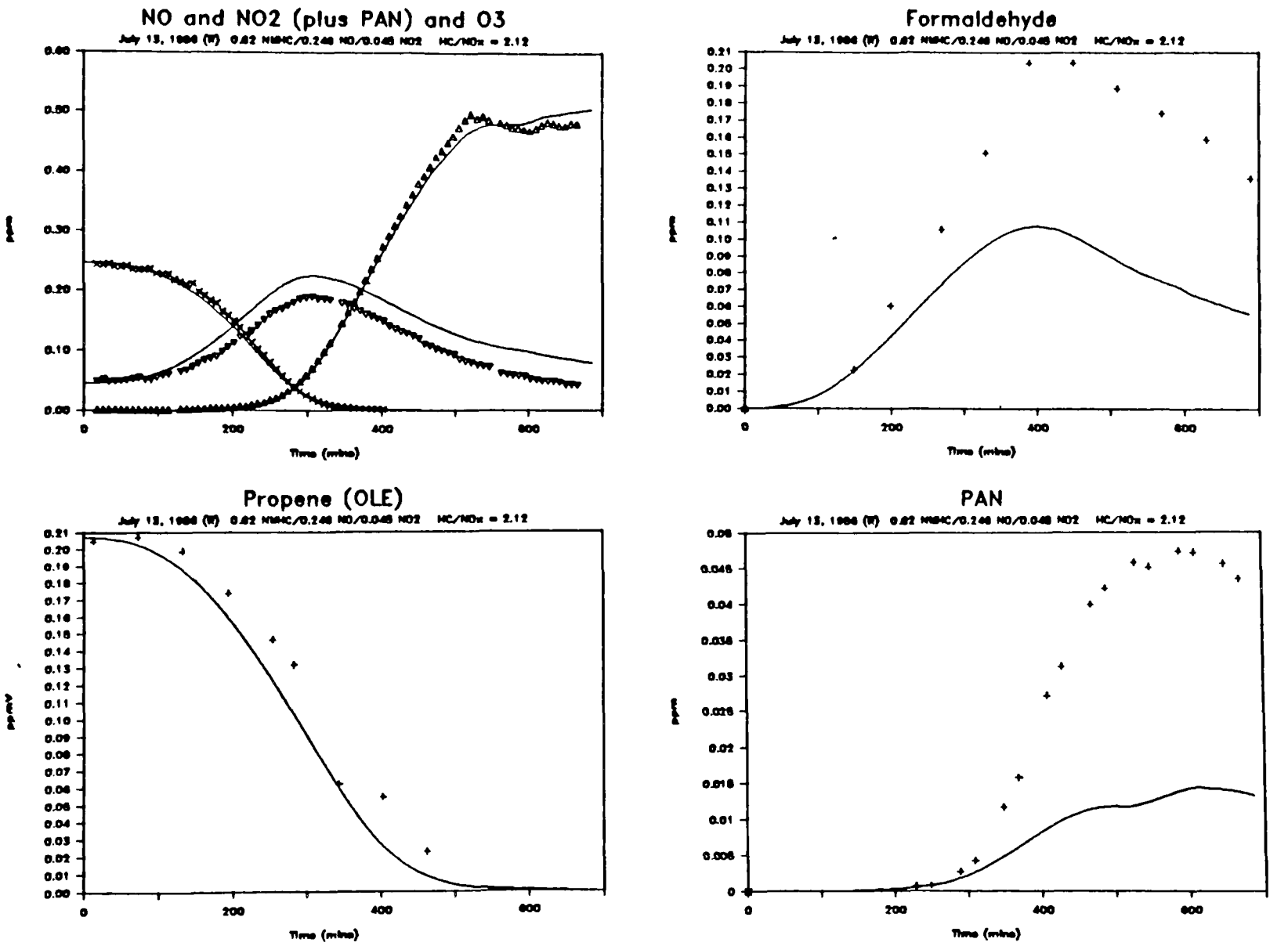

FIGURE 6-23. Simulation results for UNC experiment JL1386R
(symbols are experimental measurements)

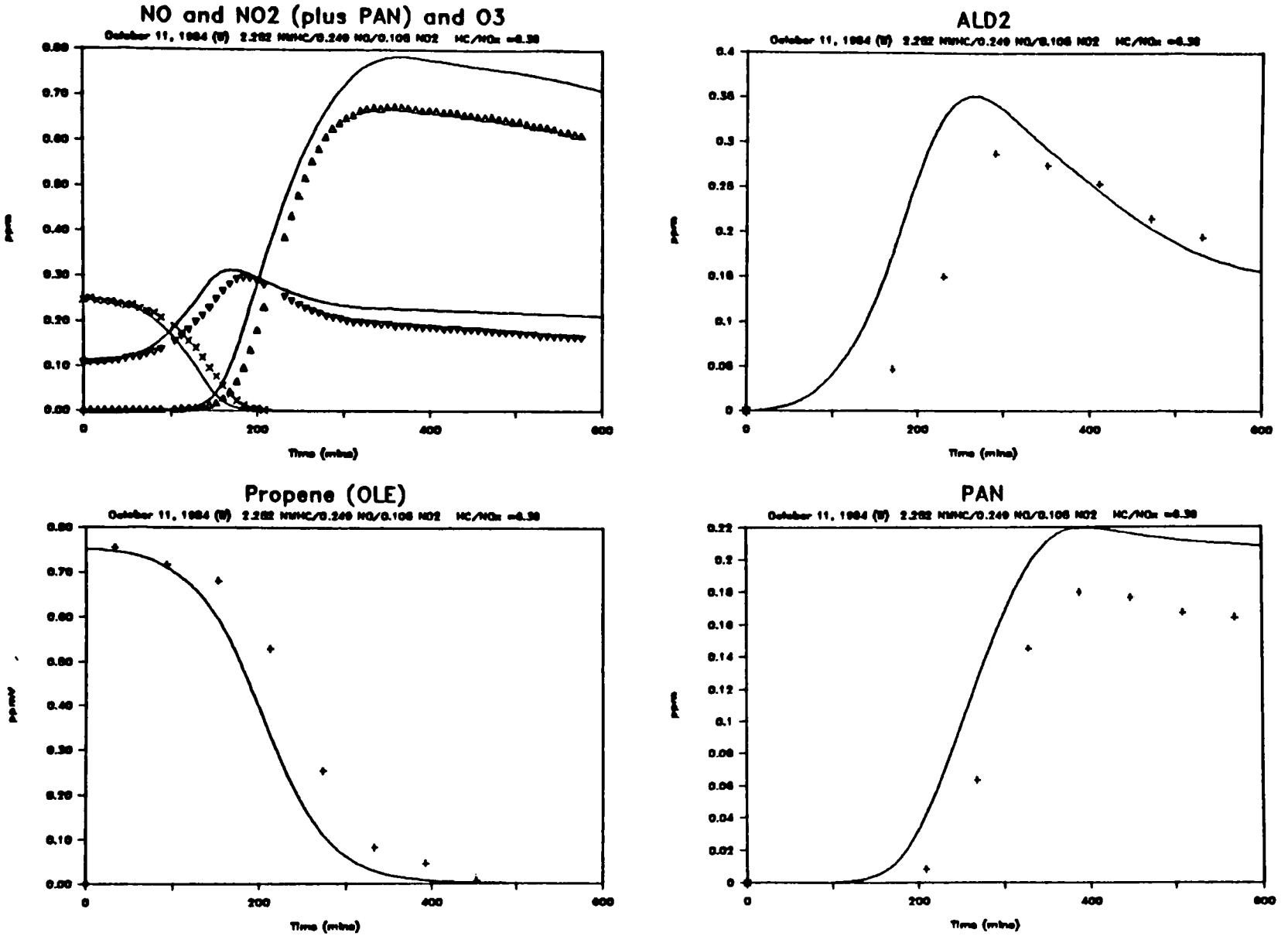

FIGURE 6-24. Simulation results for UNC experiment OC1184B
(symbols are experimental measurements)

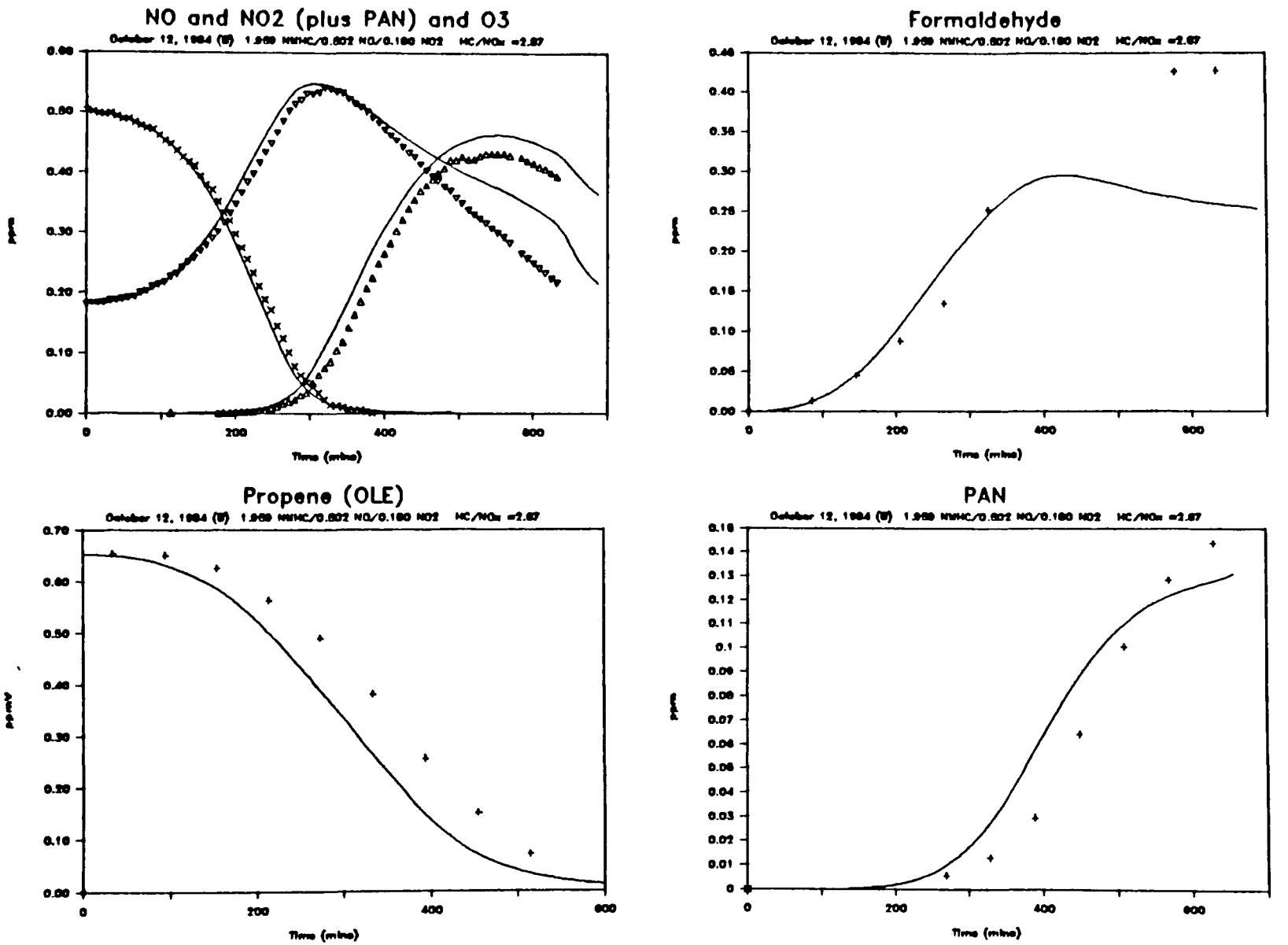

FIGURE 6-25. Simulation results for UNC experiment OC1284B
(symbols are experimental measurements)

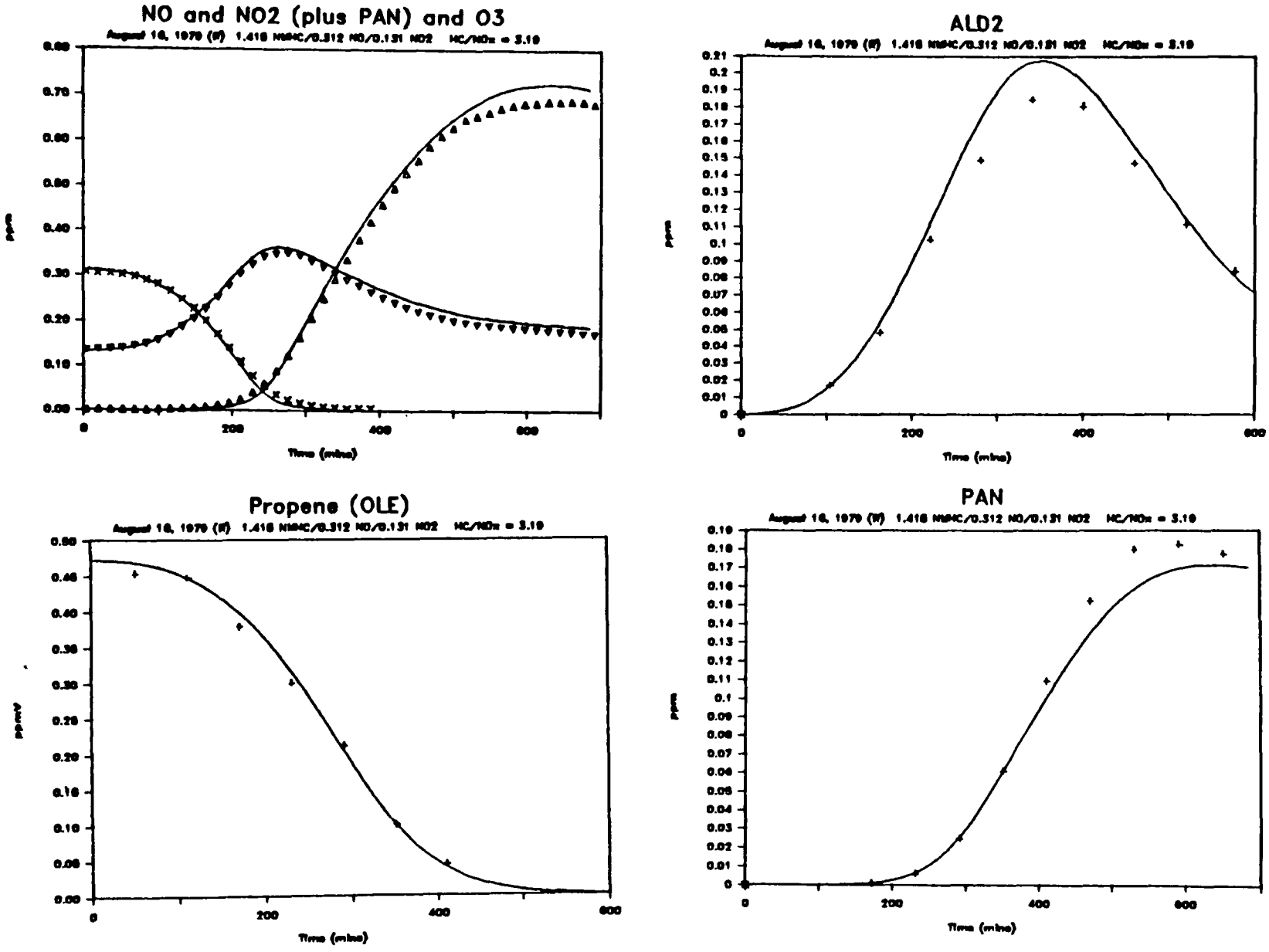

FIGURE 6-26. Simulation results for UNC experiment AU1679R (symbols are experimental measurements)

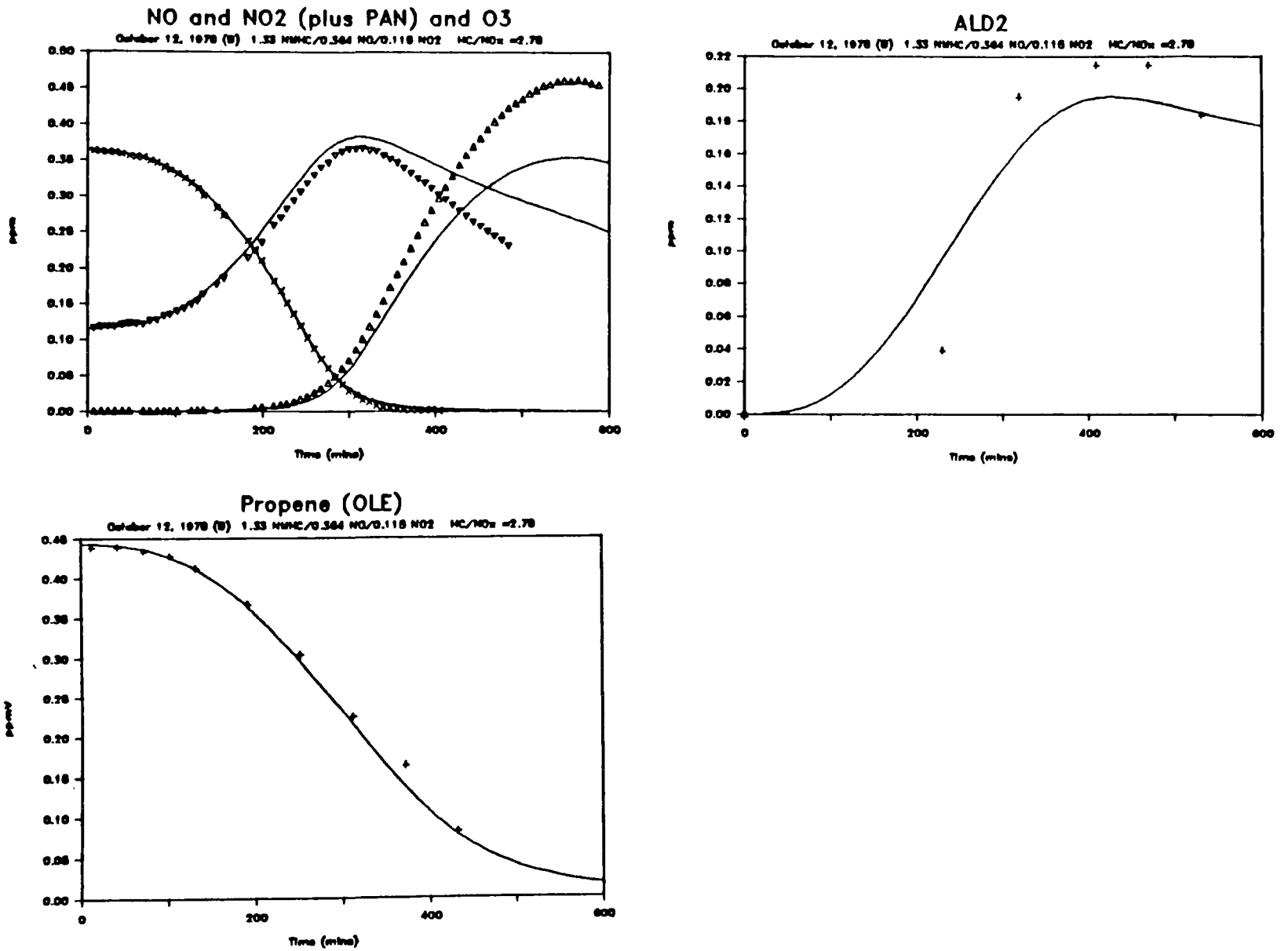

FIGURE 6-27. Simulation results for UNC experiment OC1278B (symbols are experimental measurements)

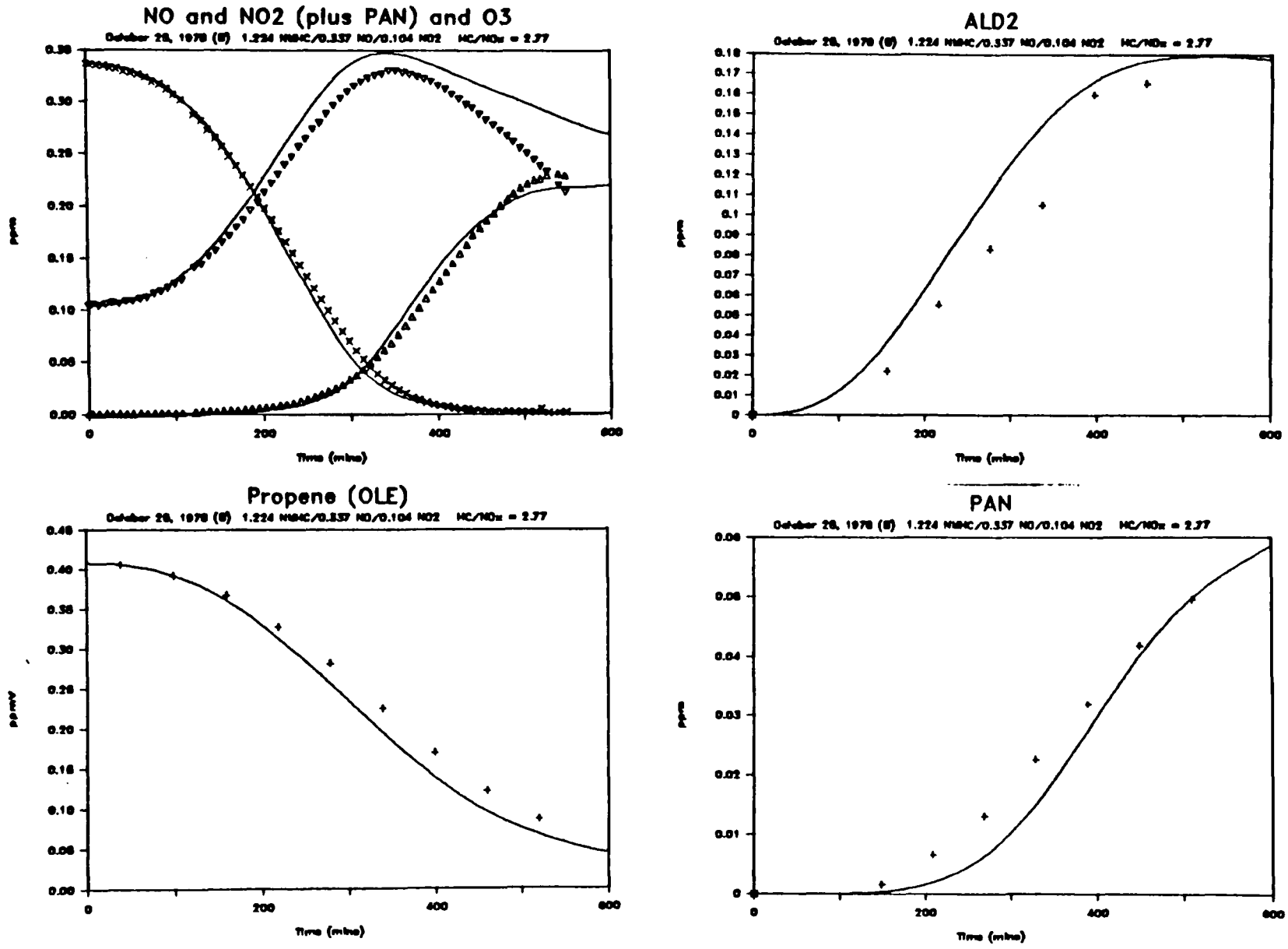

FIGURE 6-28. Simulation results for UNC experiment OC2578B (symbols are experimental measurements)

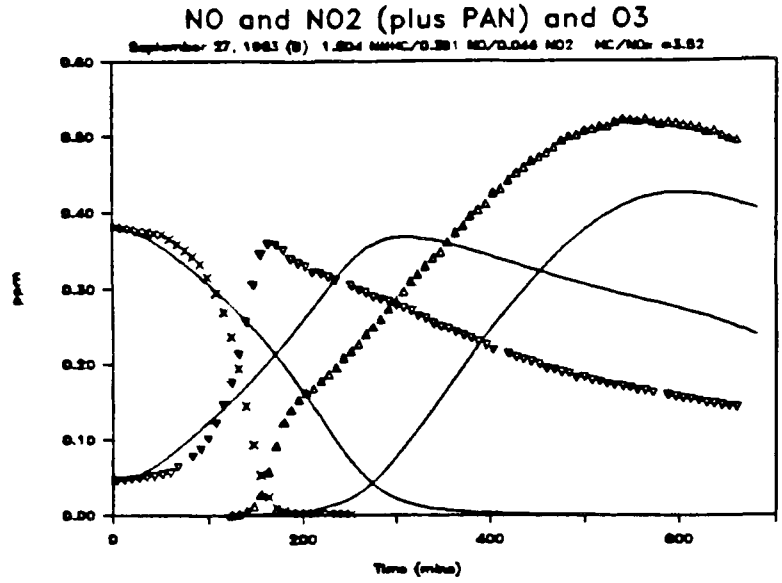

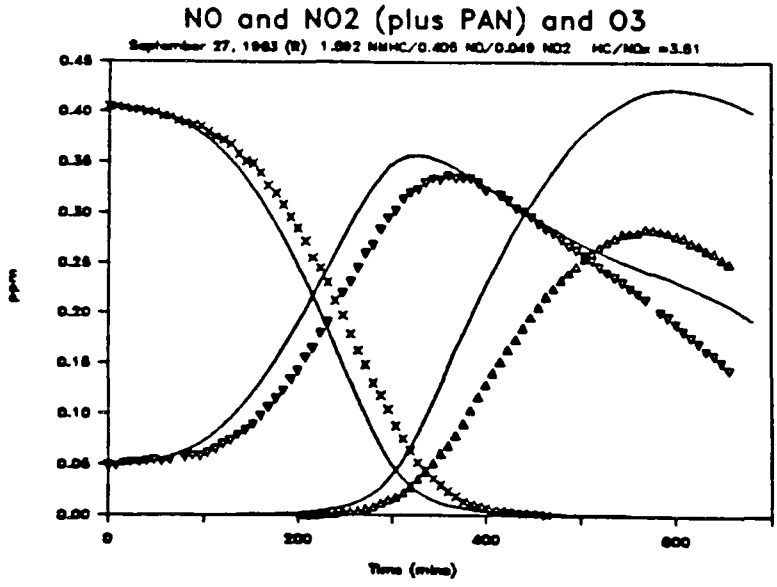

FIGURE 6-29. Simulation results for UNC experiment SE2383B, and SE2383R (symbols are experimental measurements)

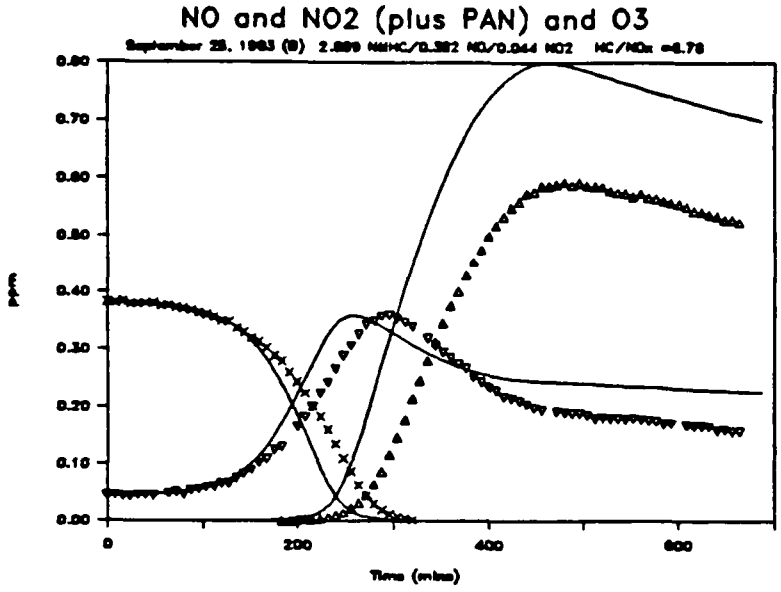

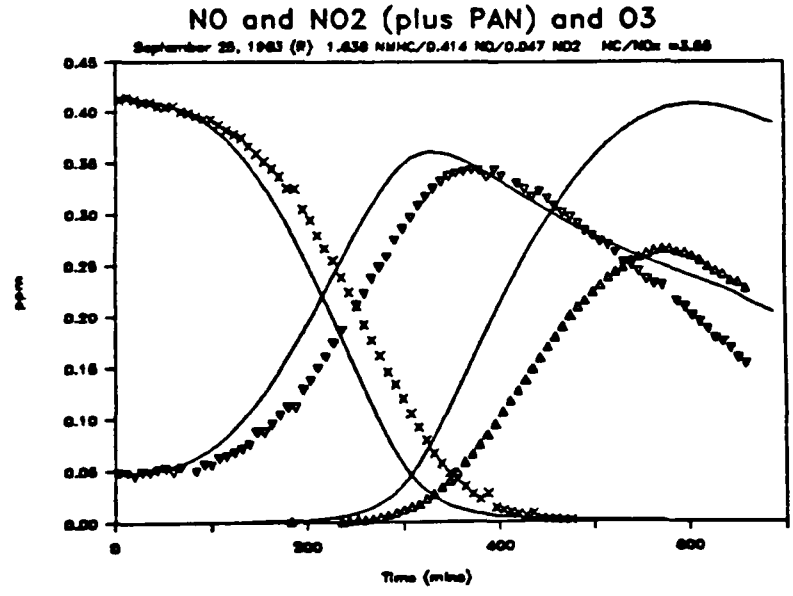

FIGURE 6-30. Simulation results for UNC experiment SE2583B, and SE2583R (symbols are experimental measurements)

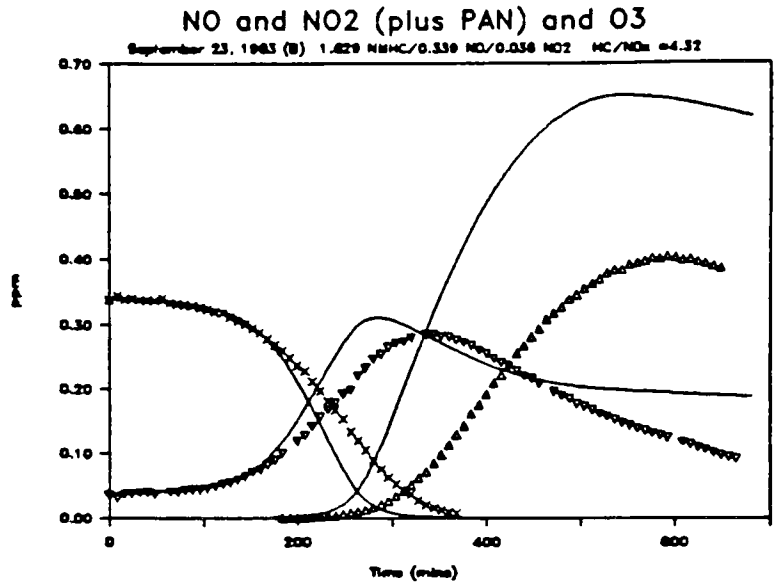

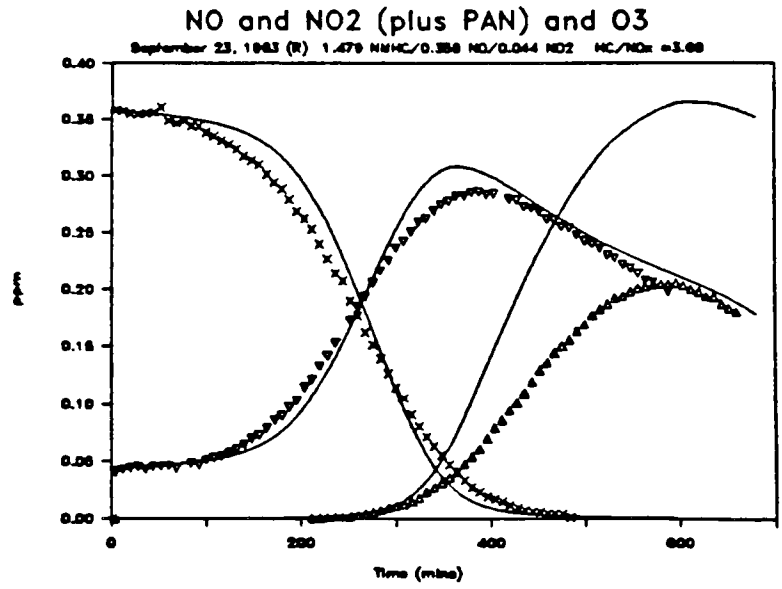

FIGURE 6-31. Simulation results for UNC experiment SE2783B, and SE2783R (symbols are experimental measurements)

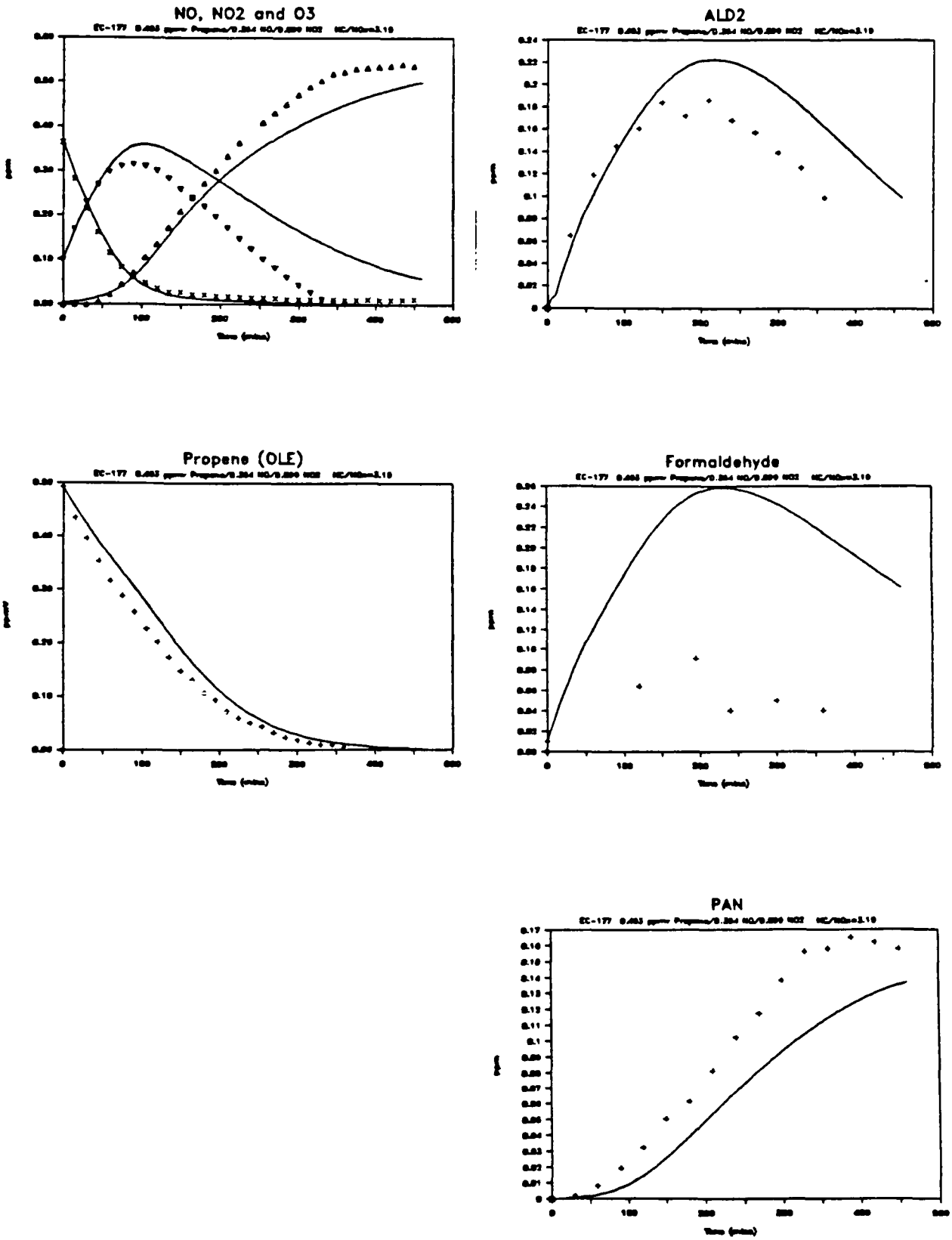

FIGURE 6-32. Simulation results for UCR experiment EC-177 (symbols are experimental measurements)

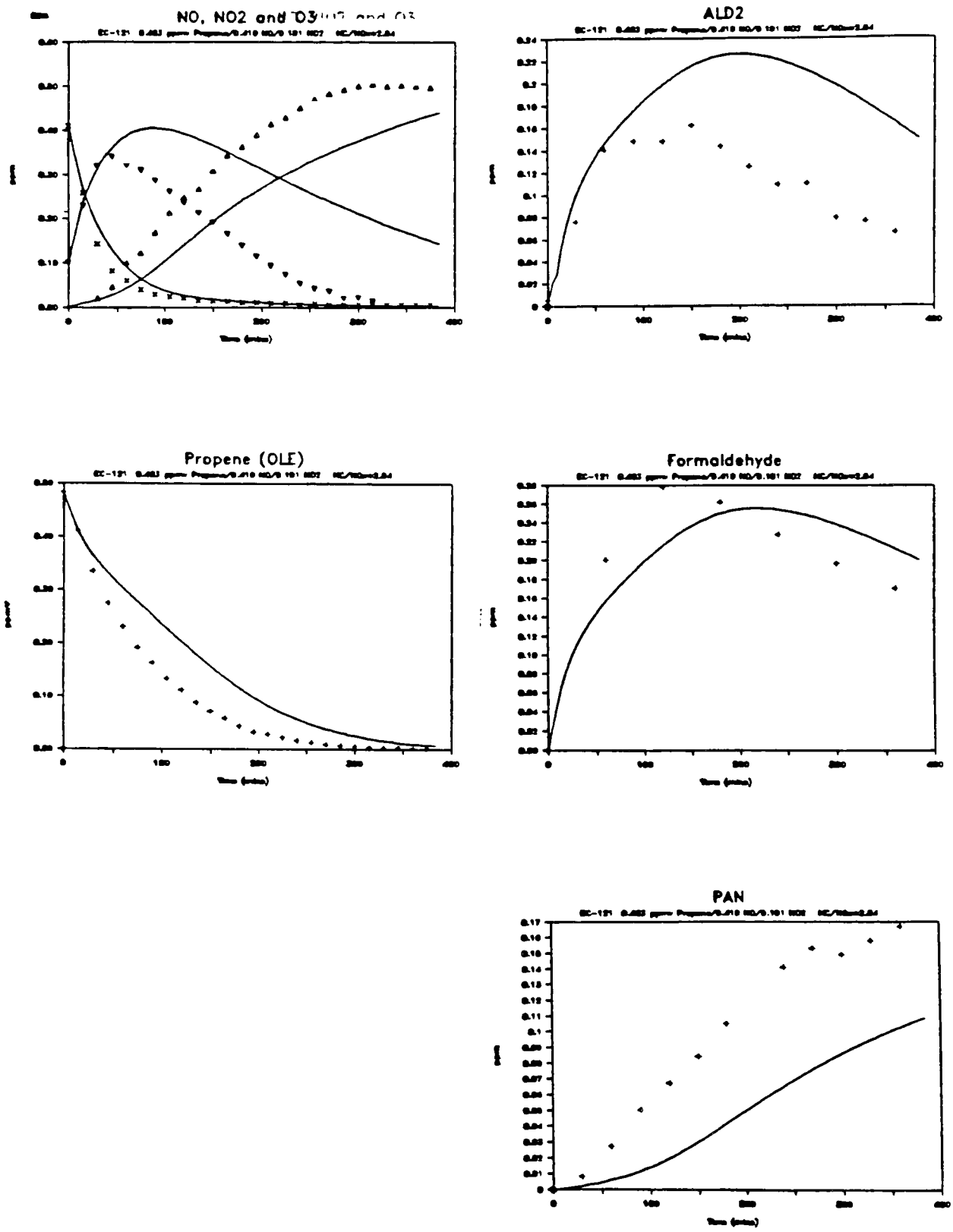

FIGURE 6-33. Simulation results for UCR experiment EC-121 (symbols are experimental measurements)

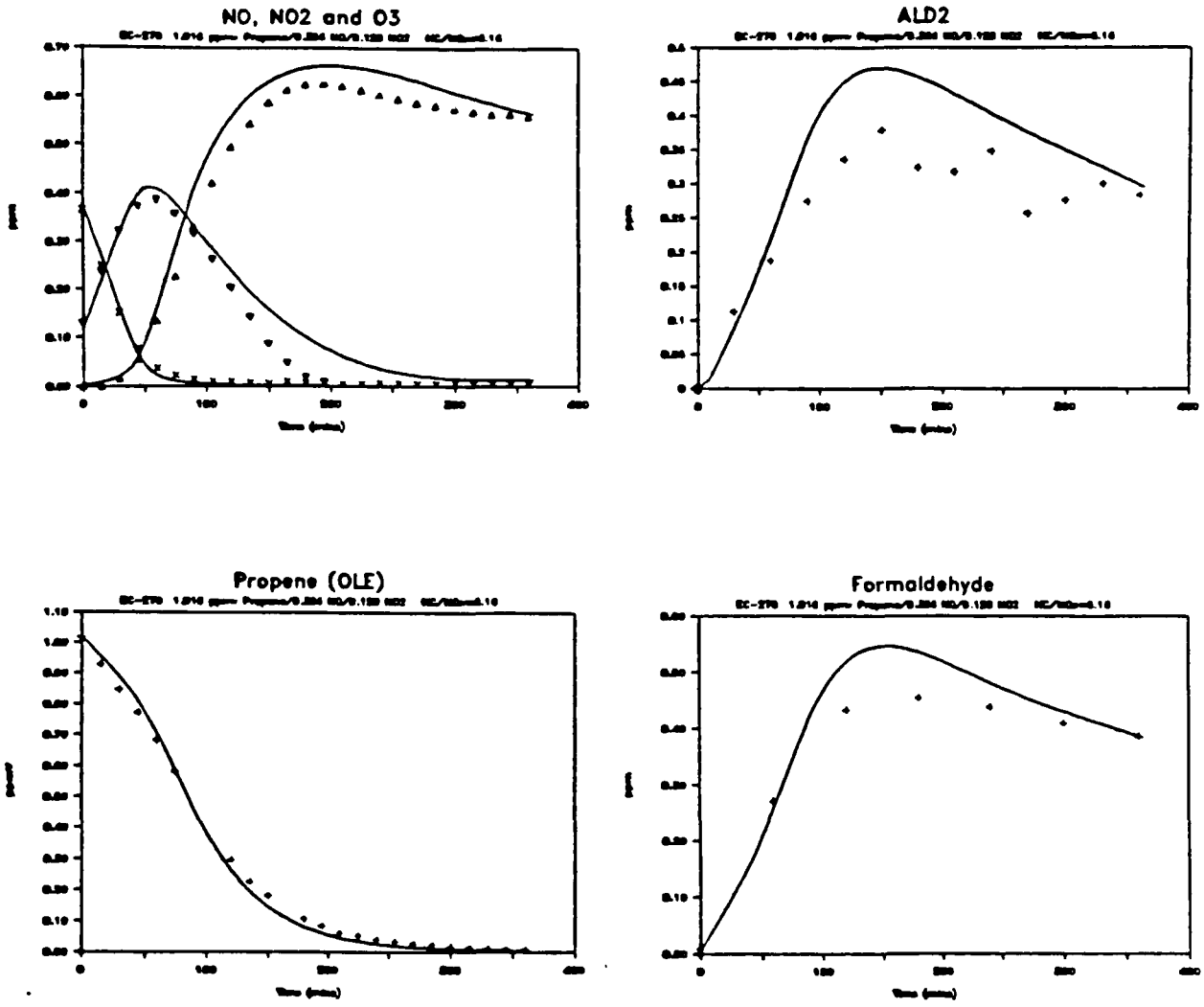

FIGURE 6-34. Simulation results for UCR experiment EC-278 (symbols are experimental measurements)

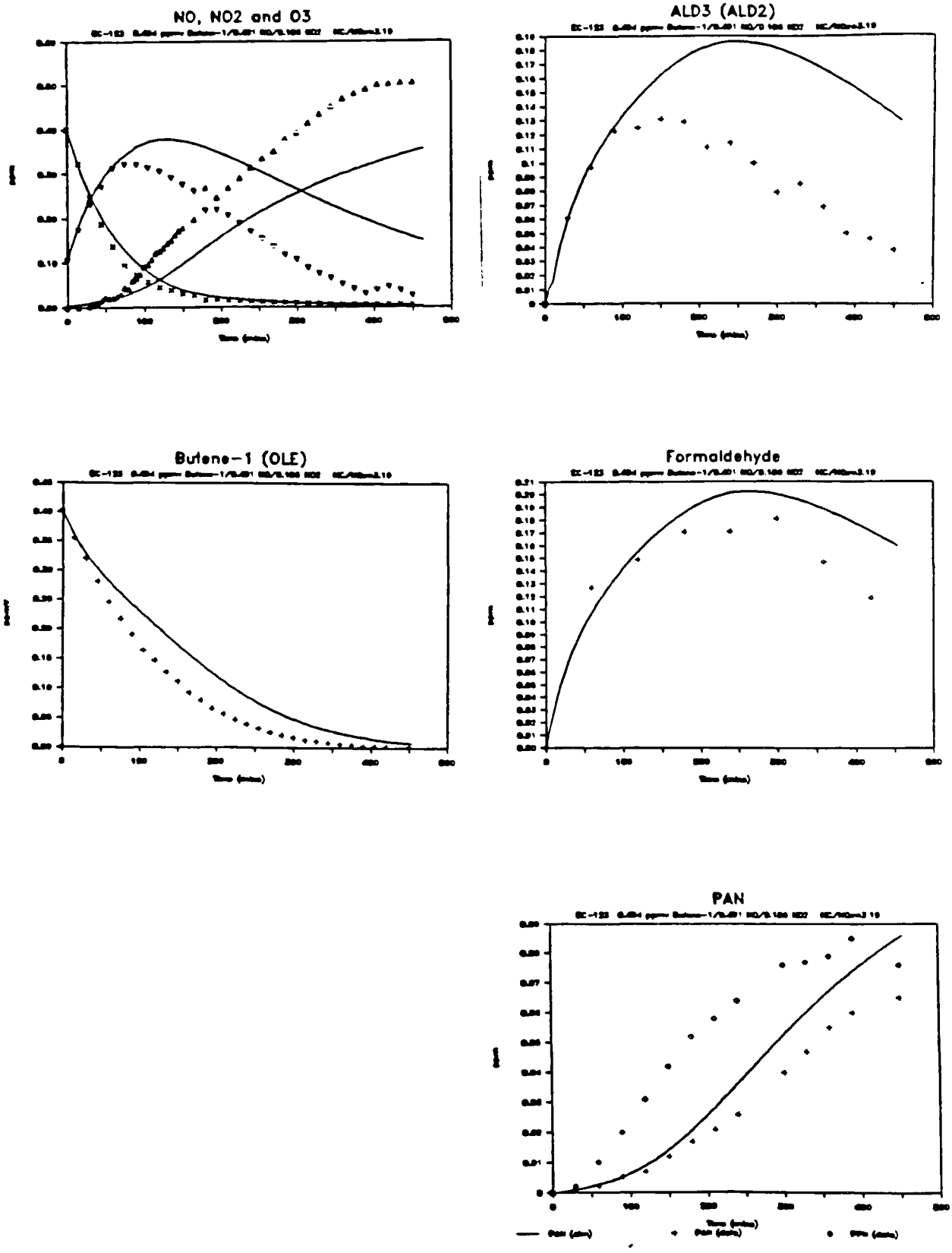

FIGURE 6-35. Simulation results for UCR experiment EC-123 (symbols are experimental measurements)

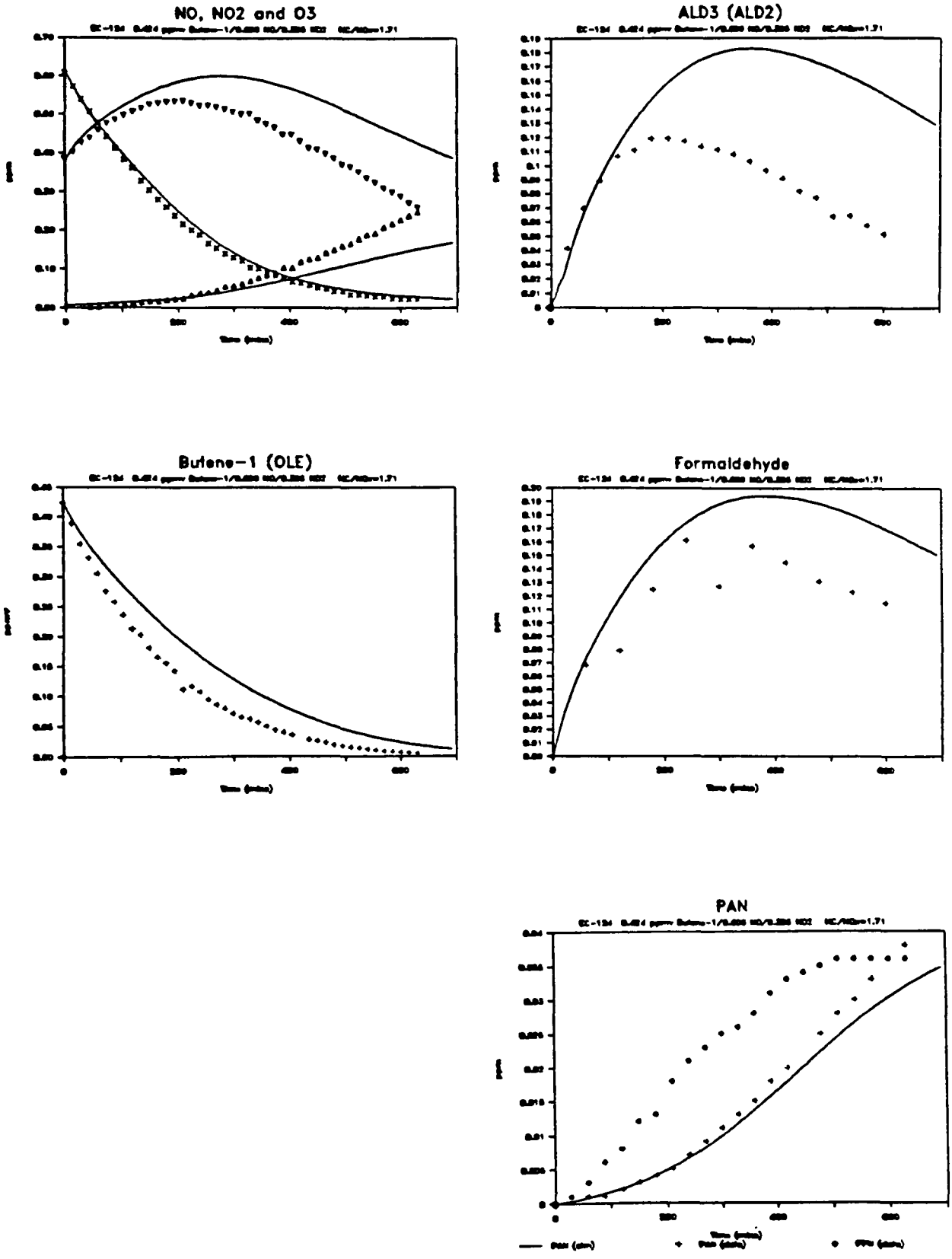

FIGURE 6-36. Simulation results for UCR experiment EC-124 (symbols are experimental measurements)

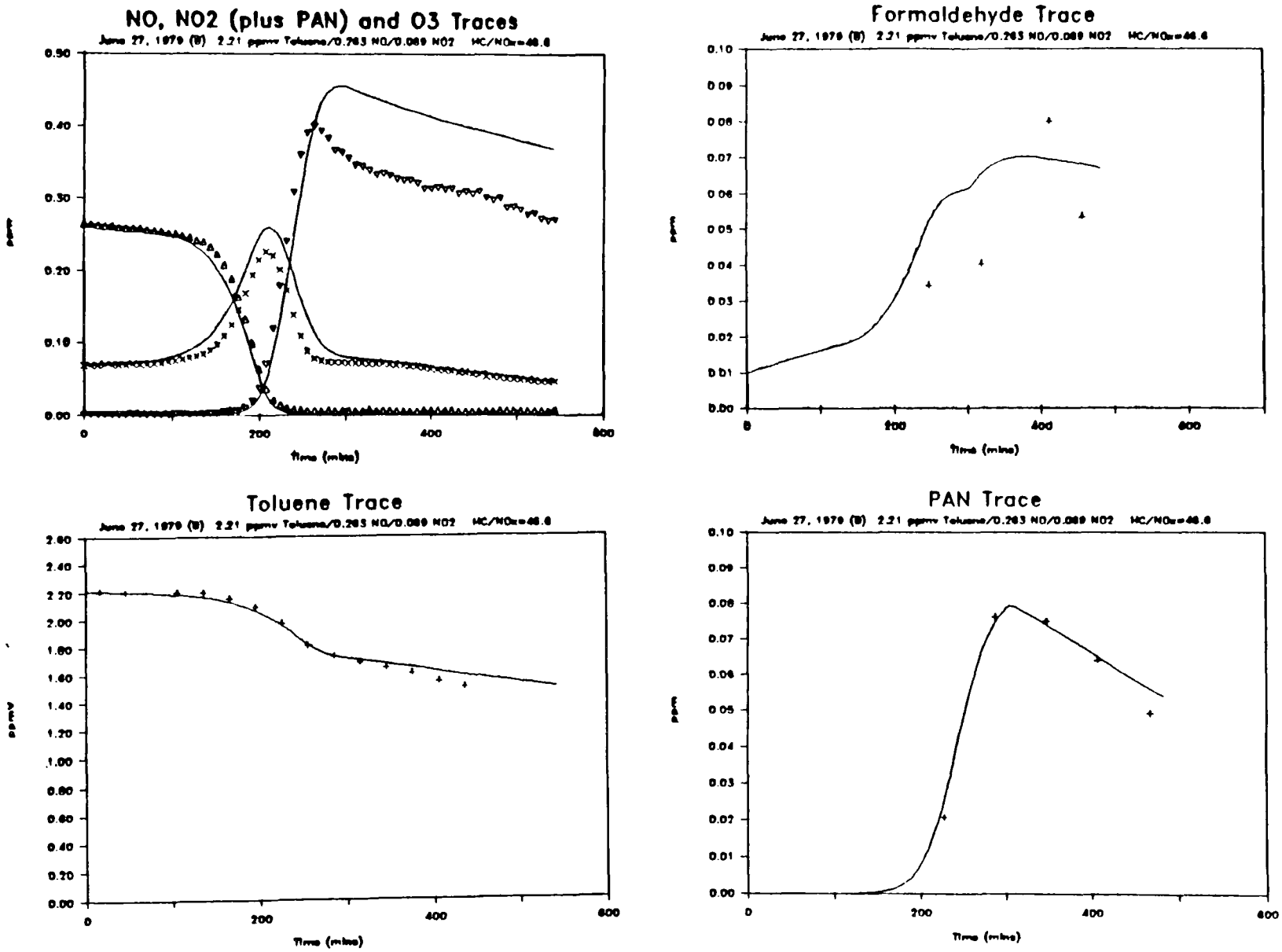

FIGURE 6-37. Simulation results for UNC experiment JN2779B
(symbols are experimental measurements)

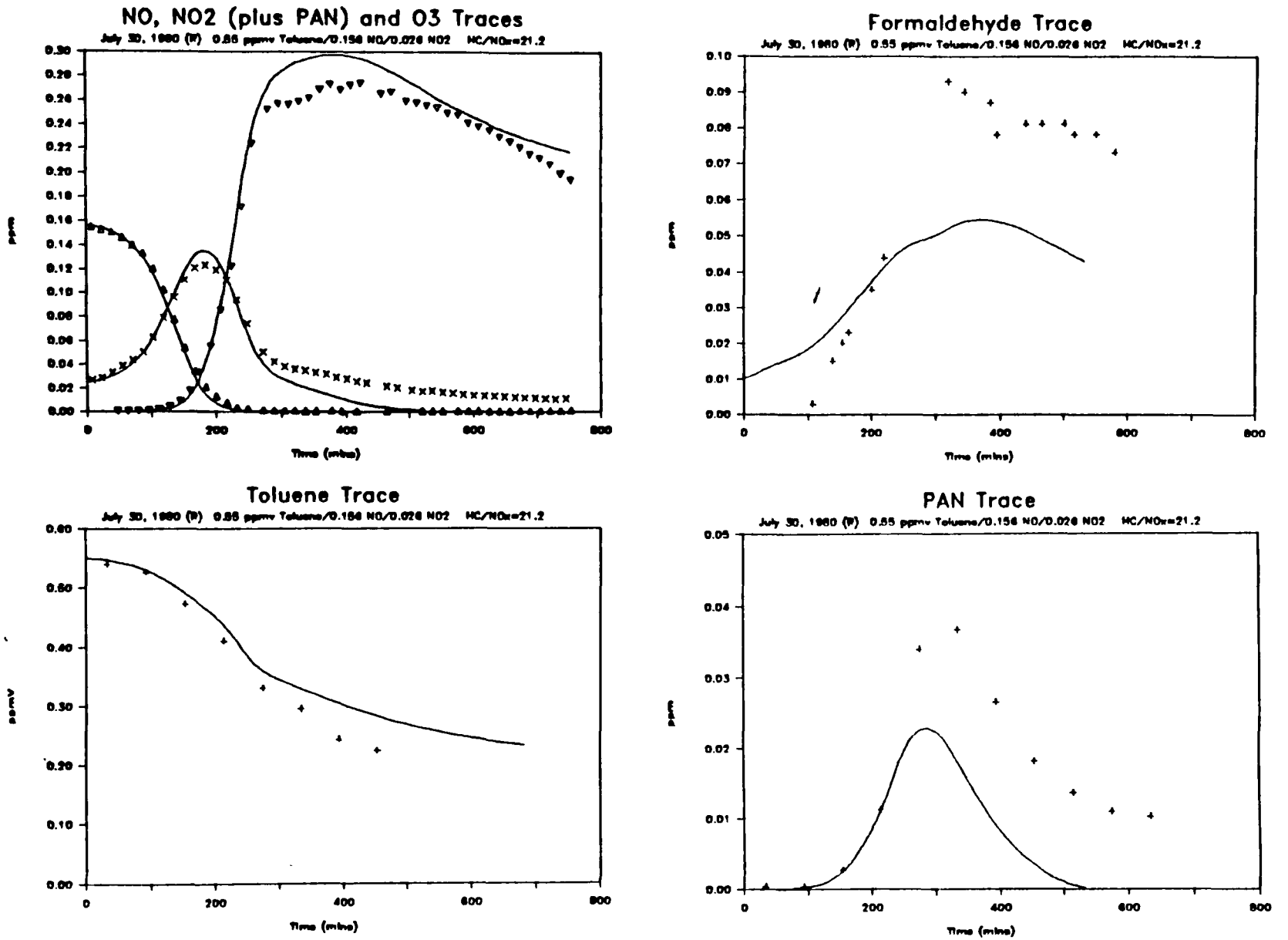

FIGURE 6-38. Simulation results for UNC experiment JL3080R (symbols are experimental measurements)

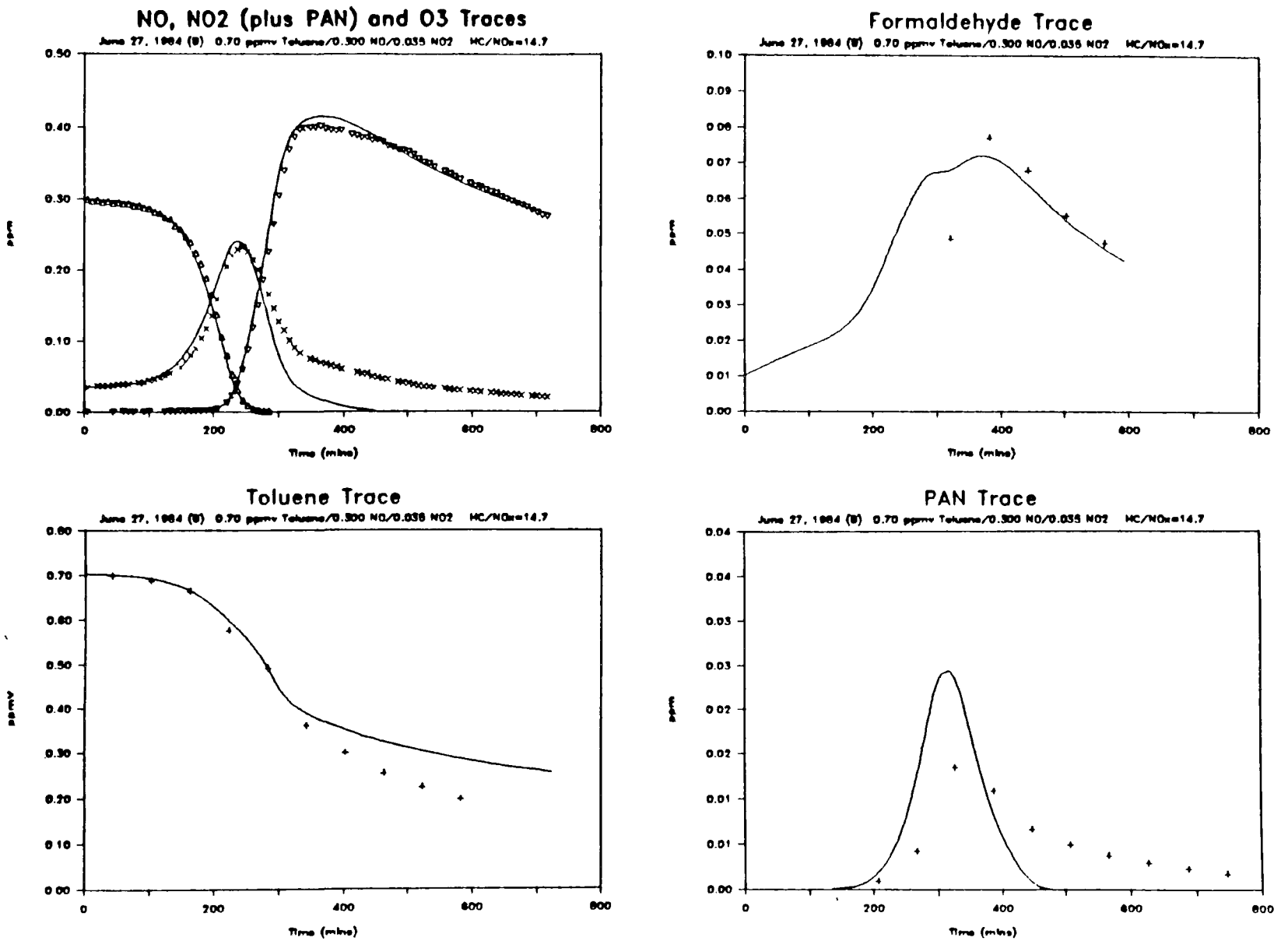

FIGURE 6-39. Simulation results for UNC experiment JN2784B
(symbols are experimental measurements)

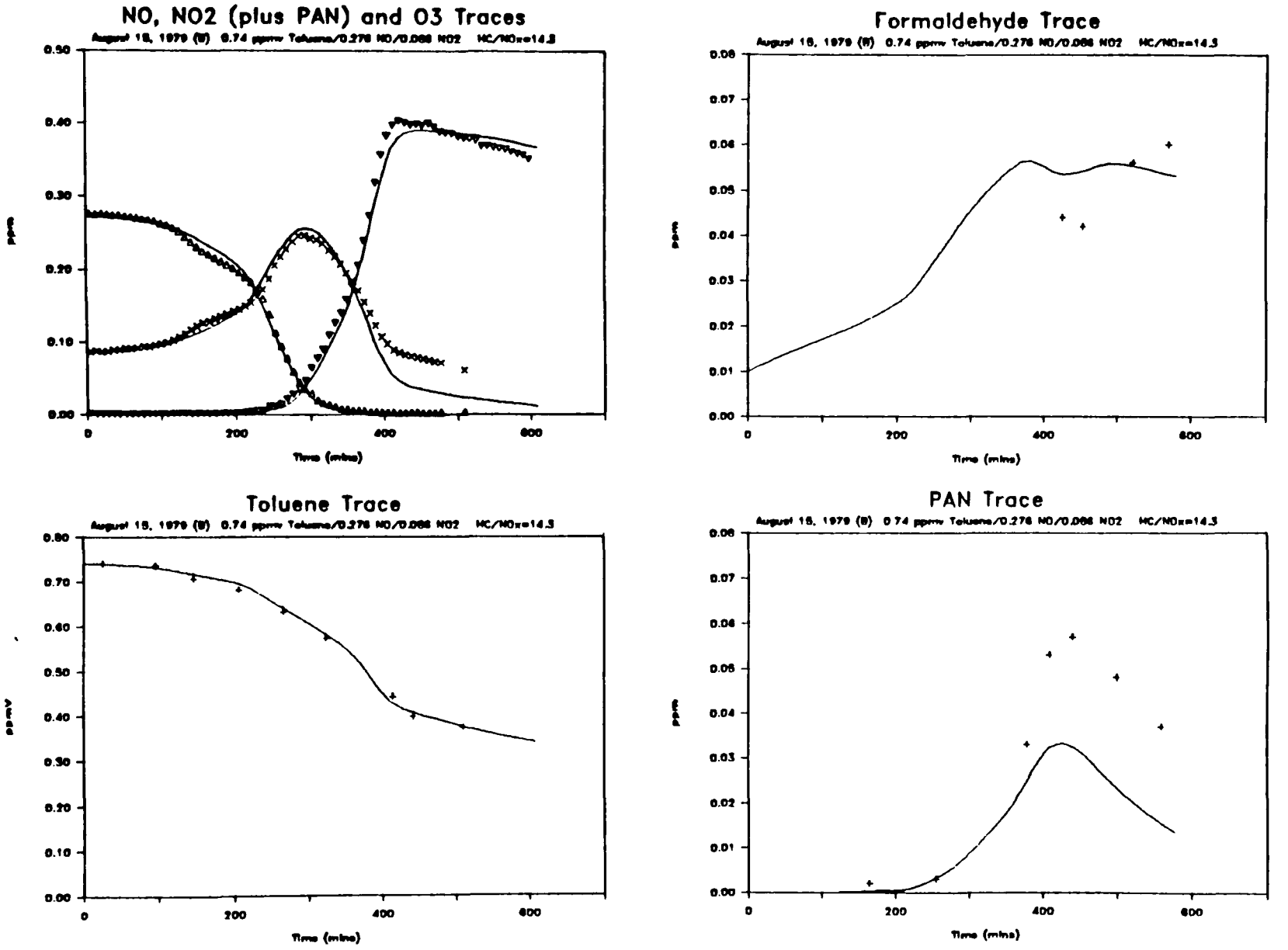

FIGURE 6-40. Simulation results for UNC experiment AU1579B (symbols are experimental measurements)

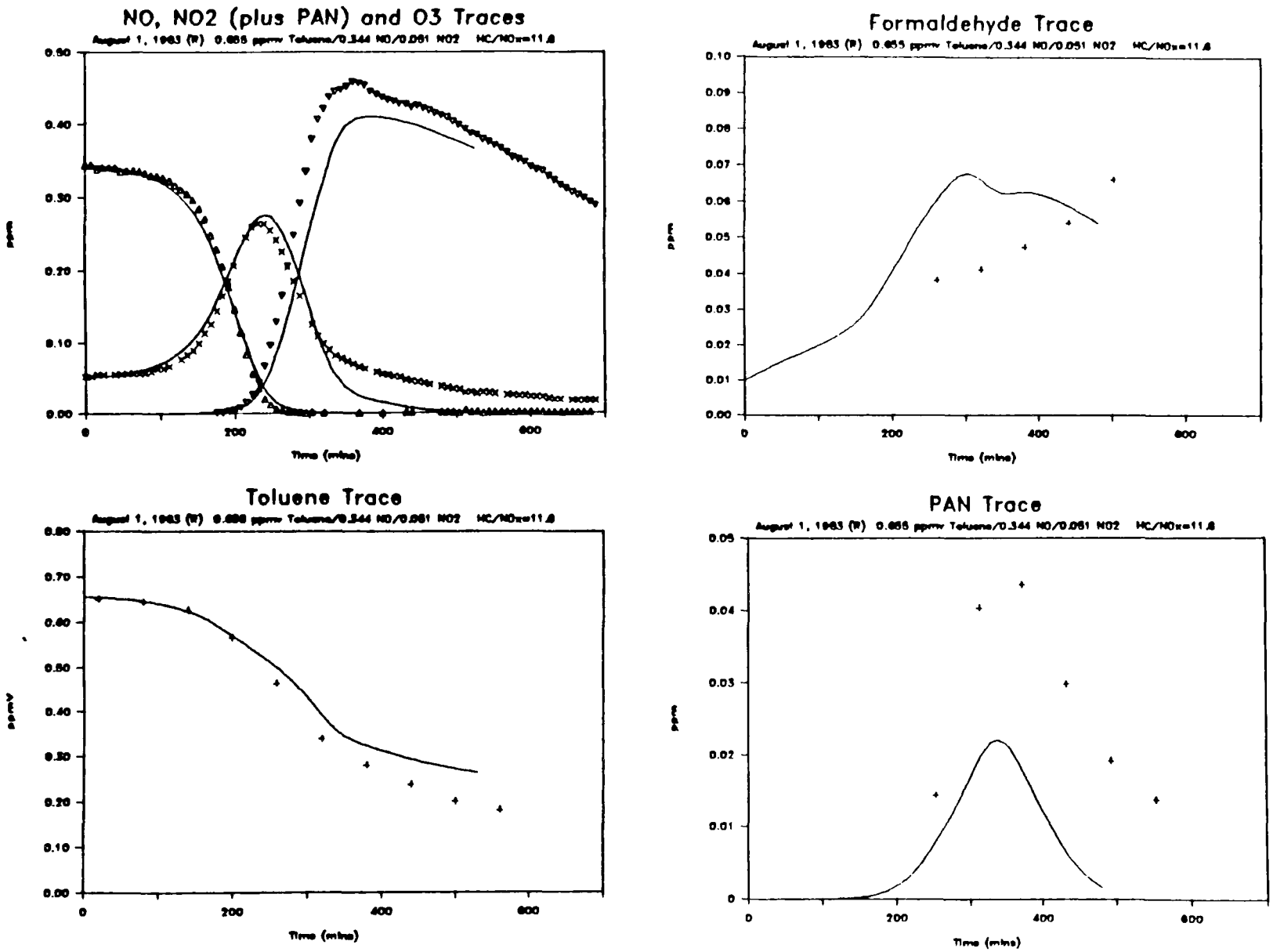

FIGURE 6-41. Simulation results for UNC experiment AU0183R (symbols are experimental measurements)

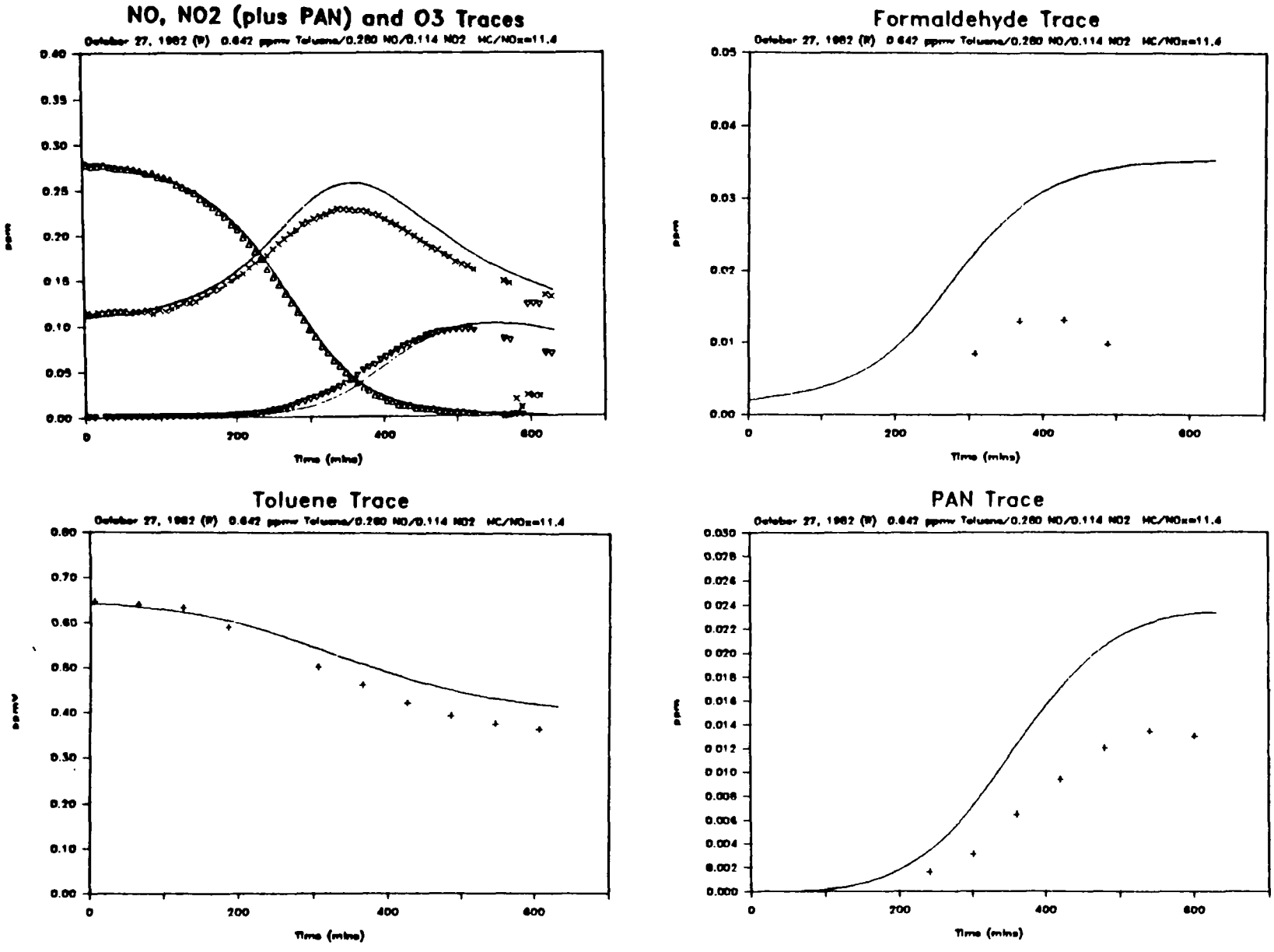

FIGURE 6-42. Simulation results for UNC experiment OC2782R (symbols are experimental measurements)

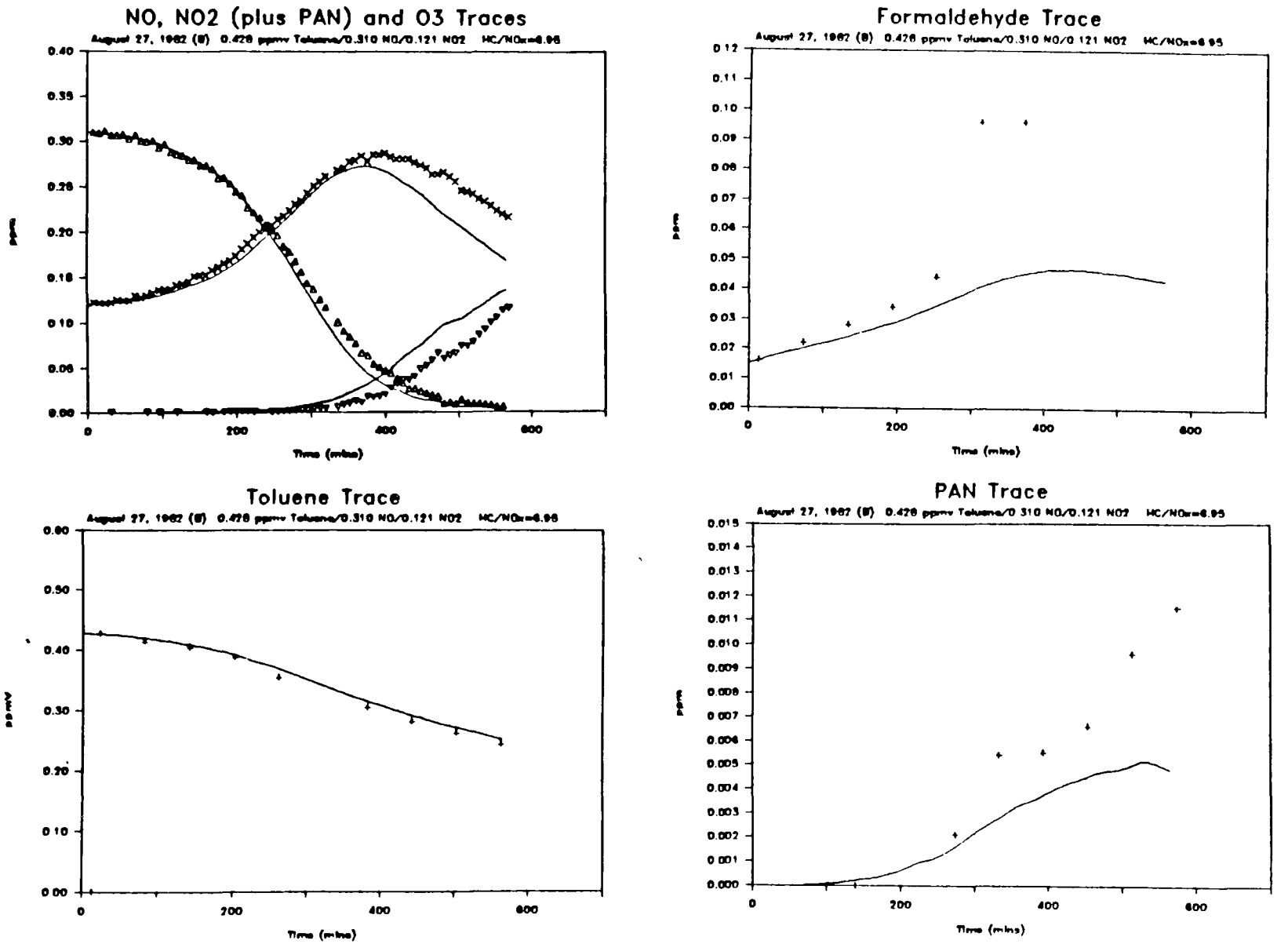

FIGURE 6-43. Simulation results for UNC experiment AU2782B (symbols are experimental measurements)

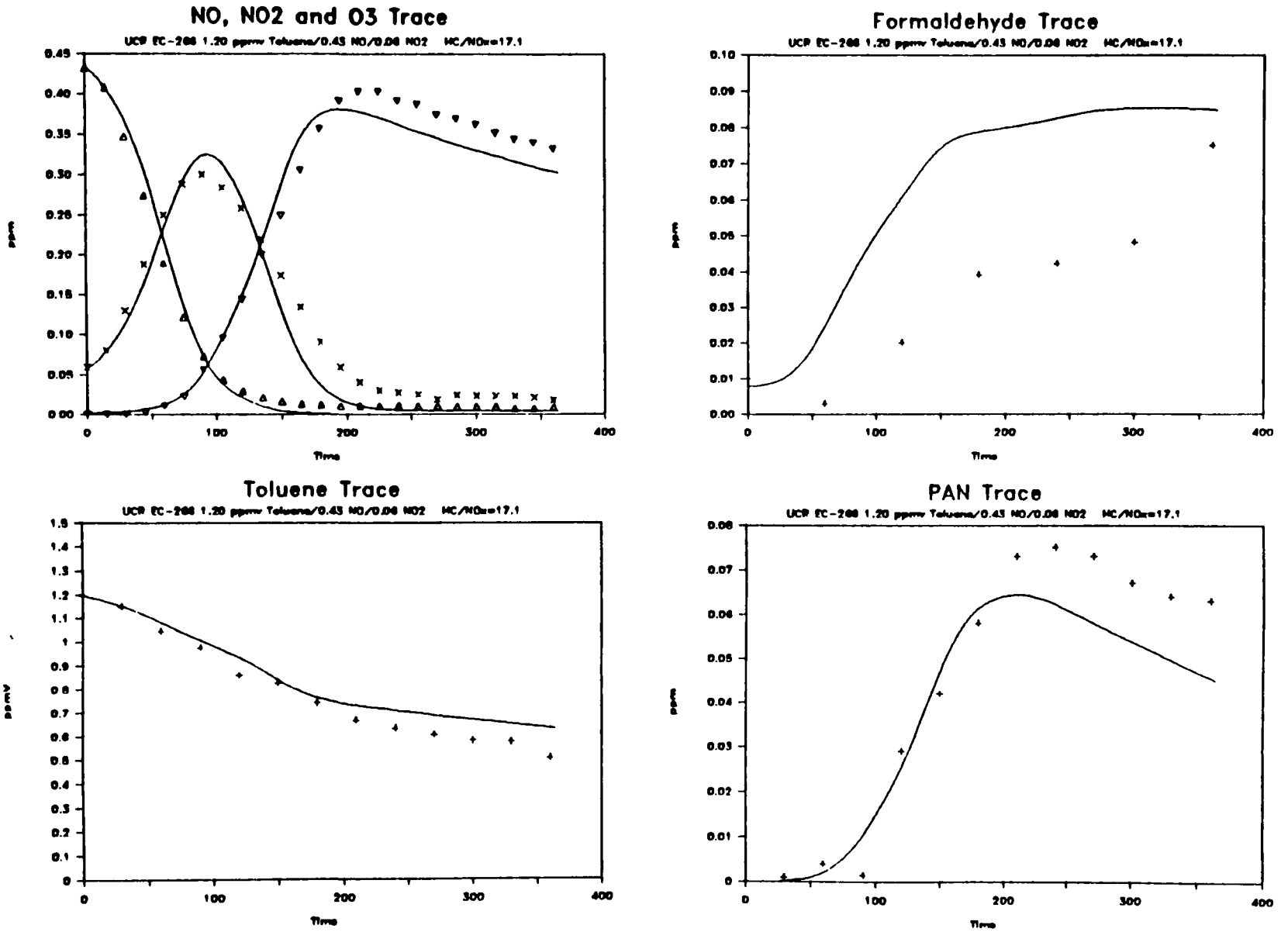

FIGURE 6-44. Simulation results for UCR experiment EC-266 (symbols are experimental measurements)

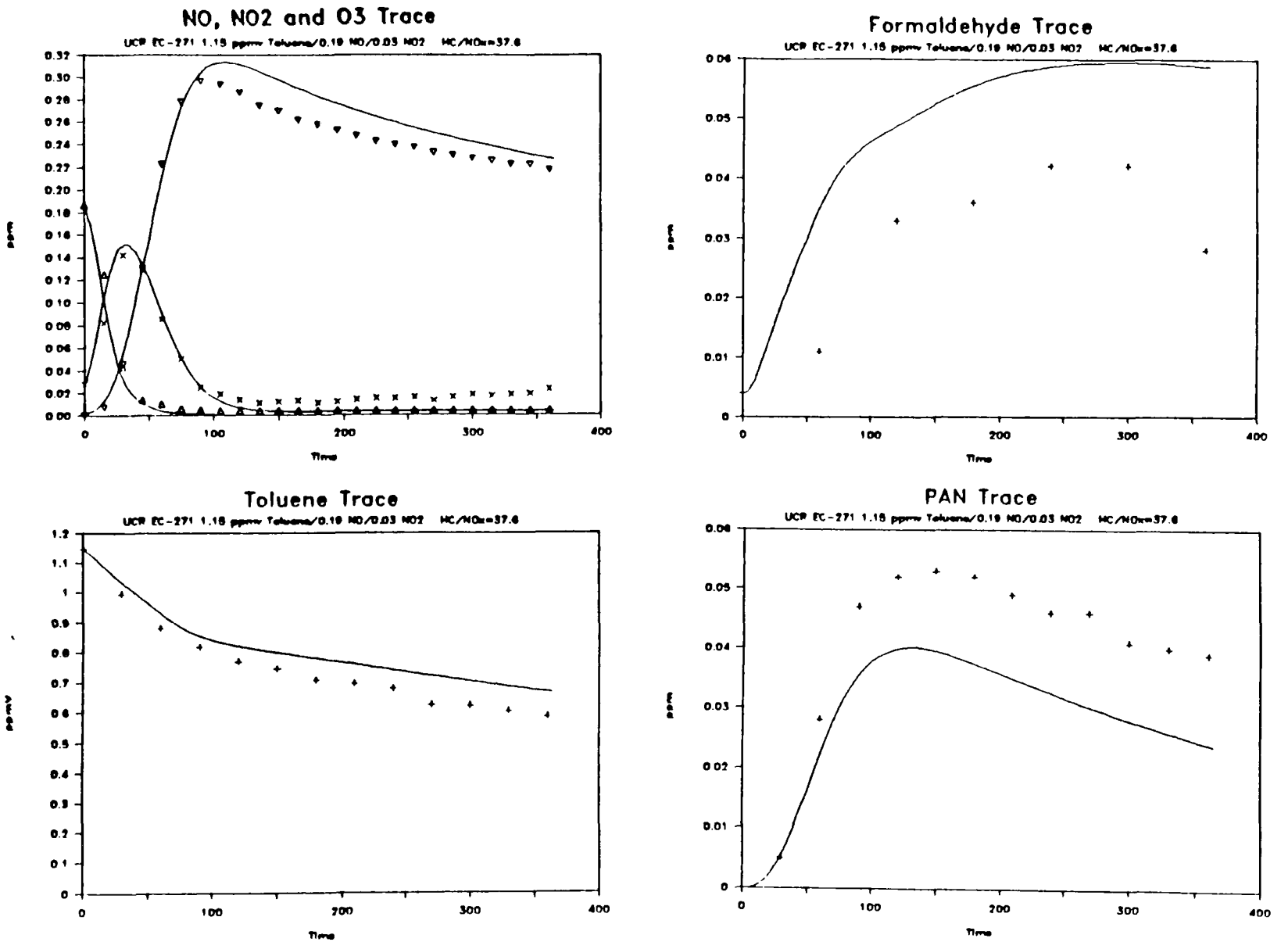

FIGURE 6-45. Simulation results for UCR experiment EC-271 (symbols are experimental measurements)

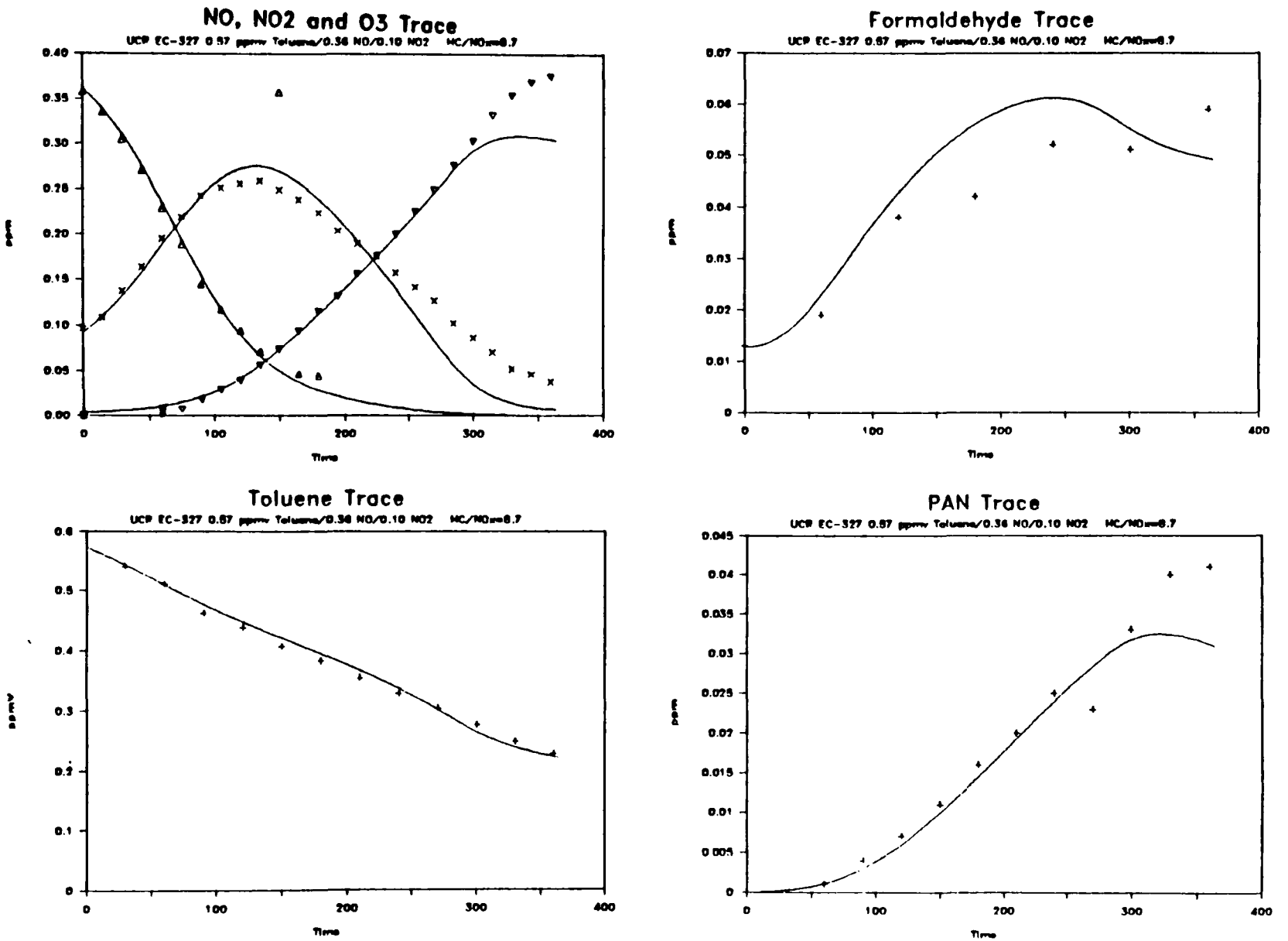

FIGURE 6-46. Simulation results for UCR experiment EC-327 (symbols are experimental measurements)

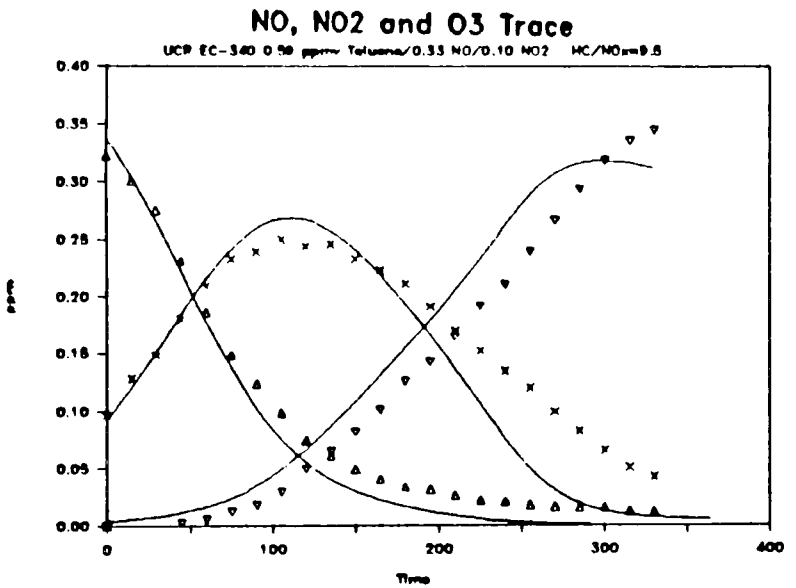

FIGURE 6-47. Simulation results for UCR experiment EC-340 (symbols are experimental measurements)

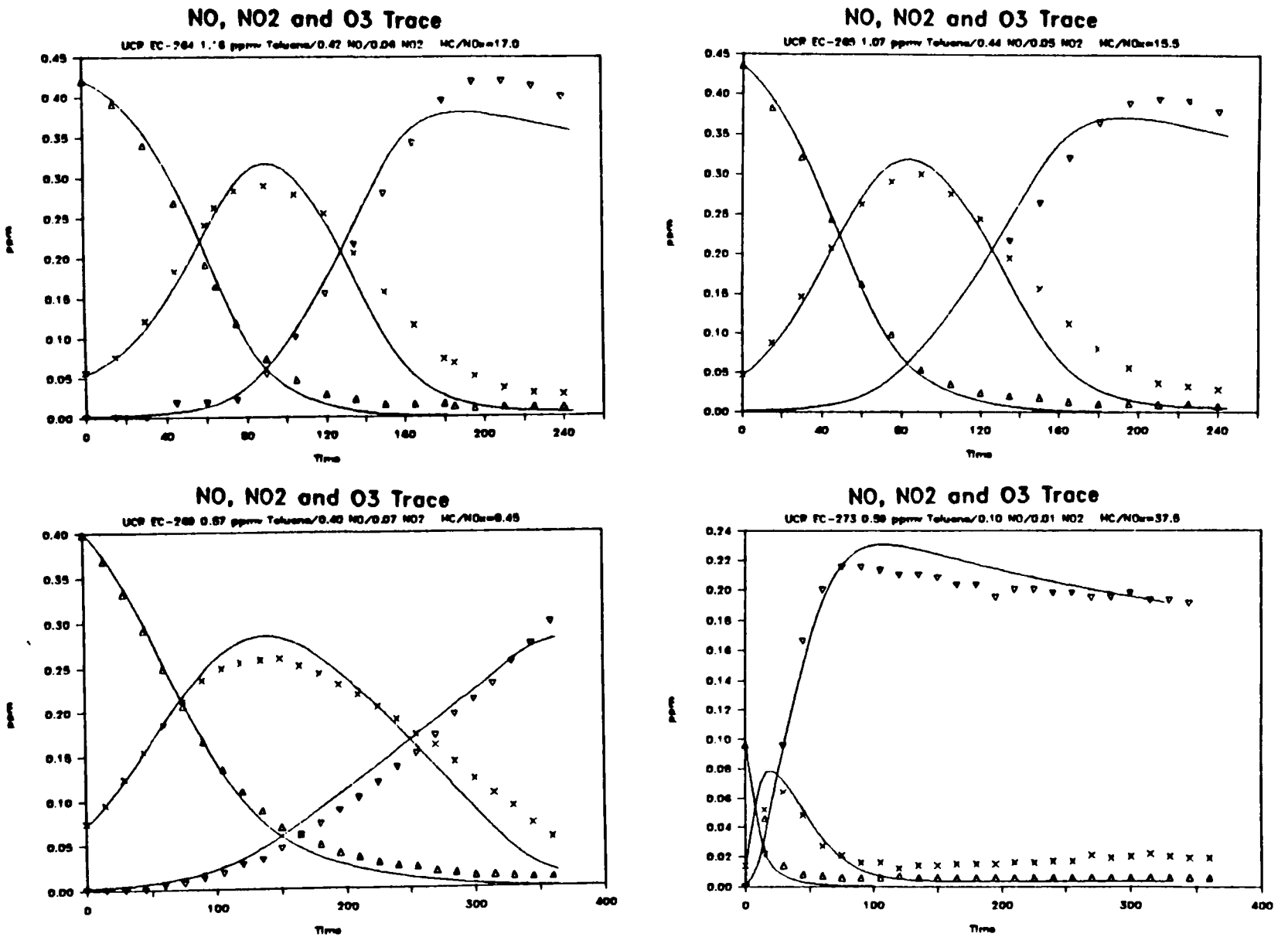

FIGURE 6-48. Simulation results for UCR experiments EC-264,EC-265, EC-269, and EC-273 (symbols are experimental measurements)

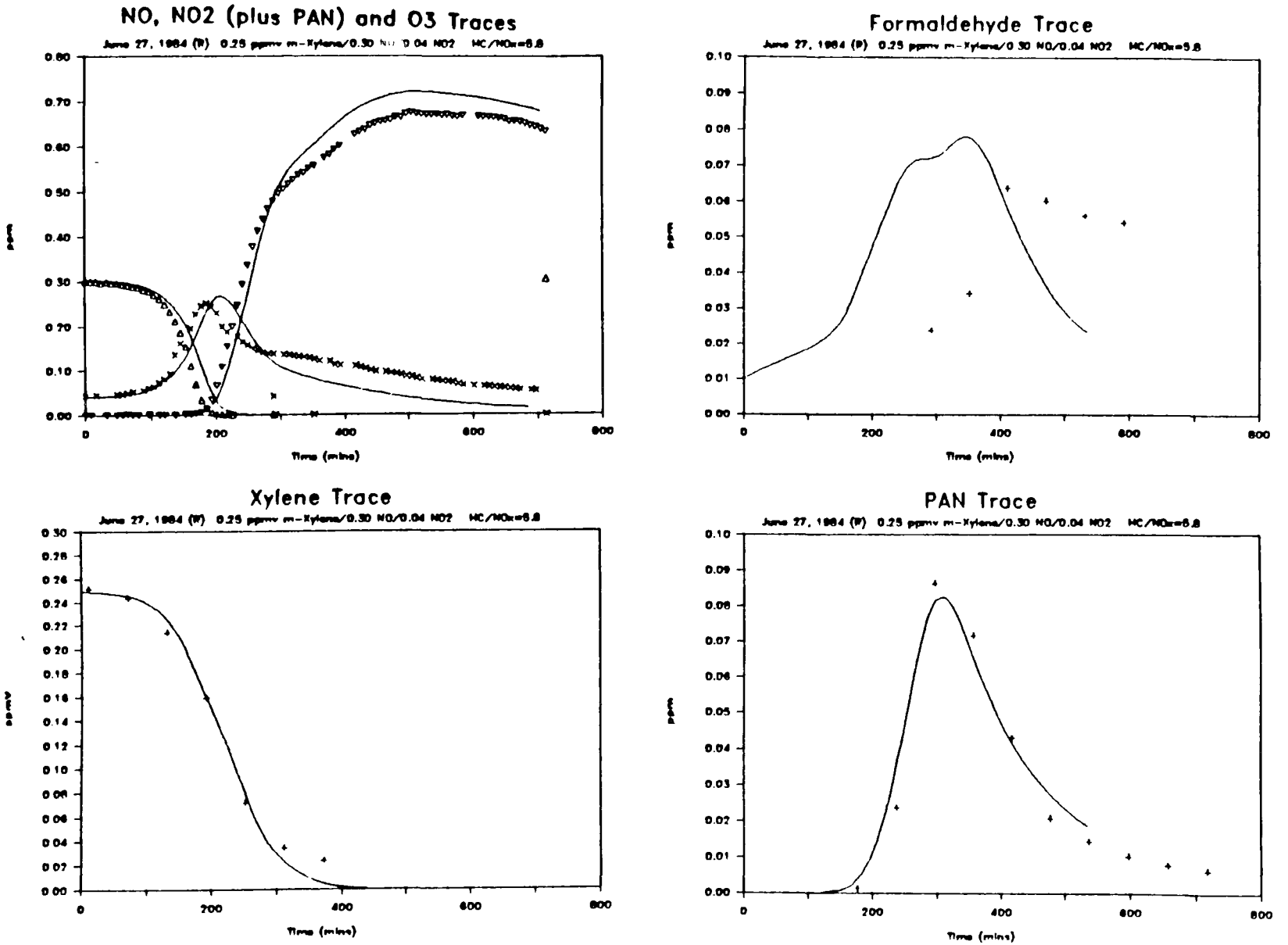

FIGURE 6-49. Simulation results for UNC experiment JN2784R (symbols are experimental measurements)

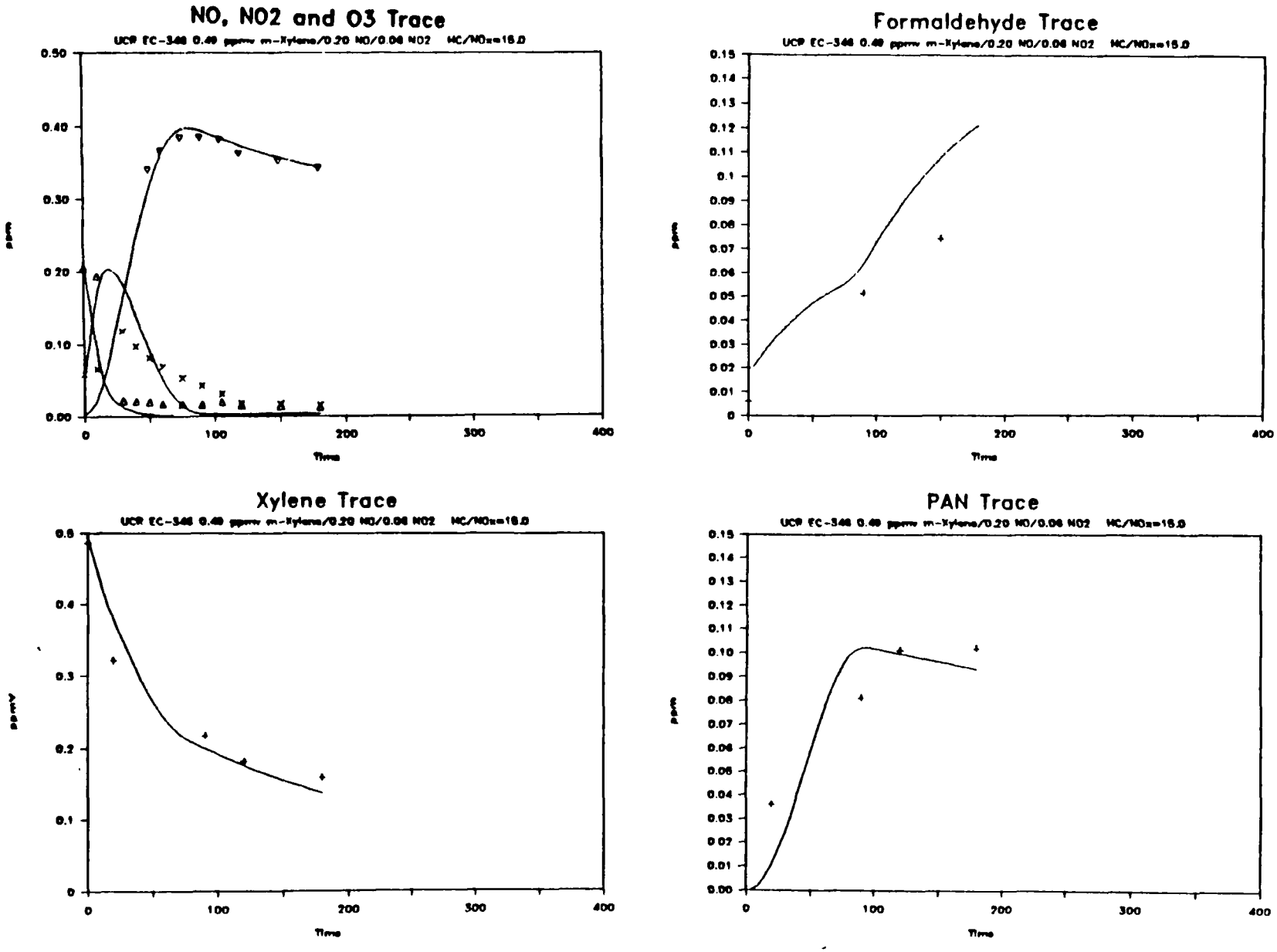

FIGURE 6-50. Simulation results for UCR experiment EC-346
(symbols are experimental measurements)

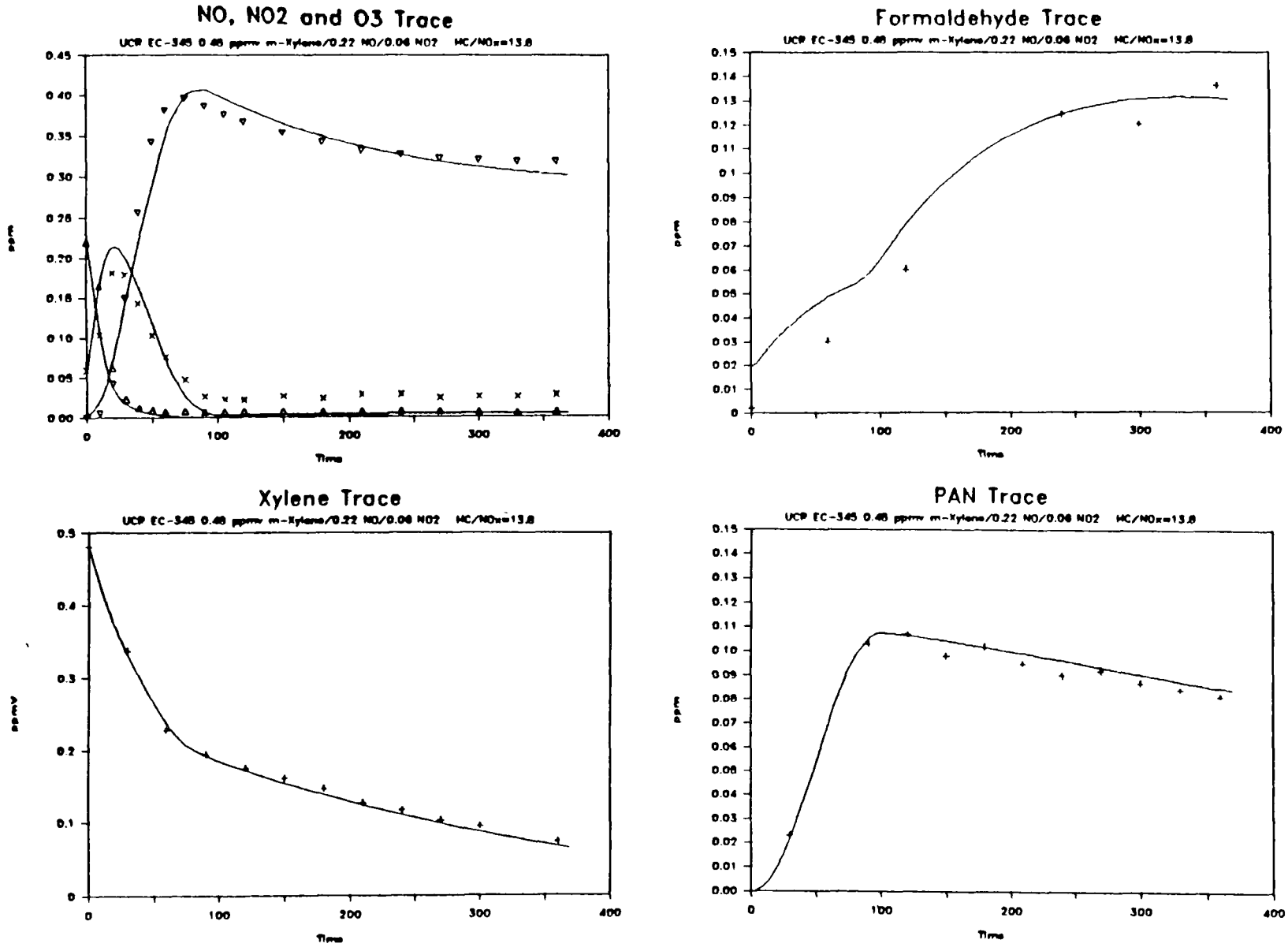

FIGURE 6-51. Simulation results for UCR experiment EC-345 (symbols are experimental measurements)

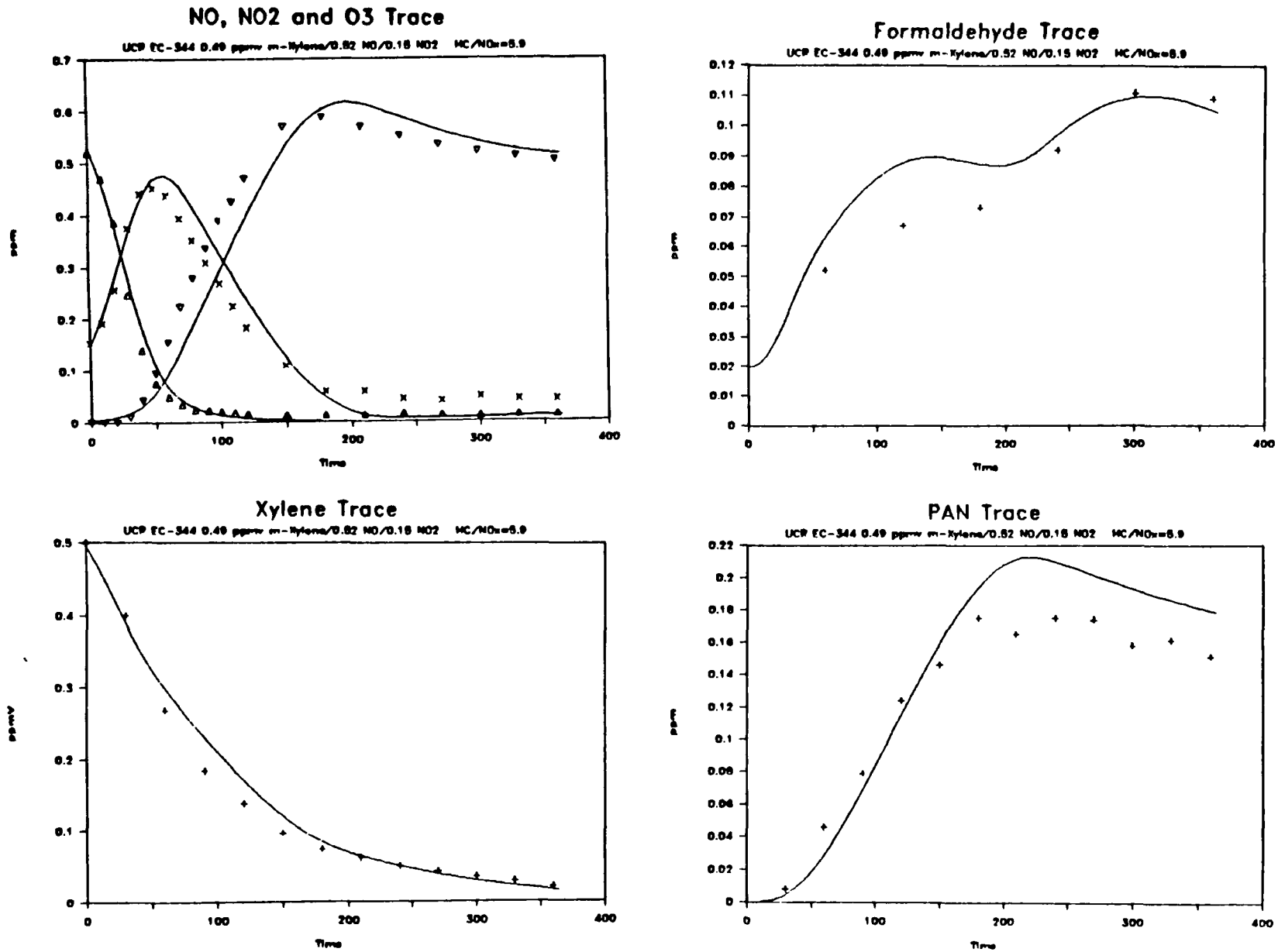

FIGURE 6-52. Simulation results for UCR experiment EC-344 (symbols are experimental measurements)

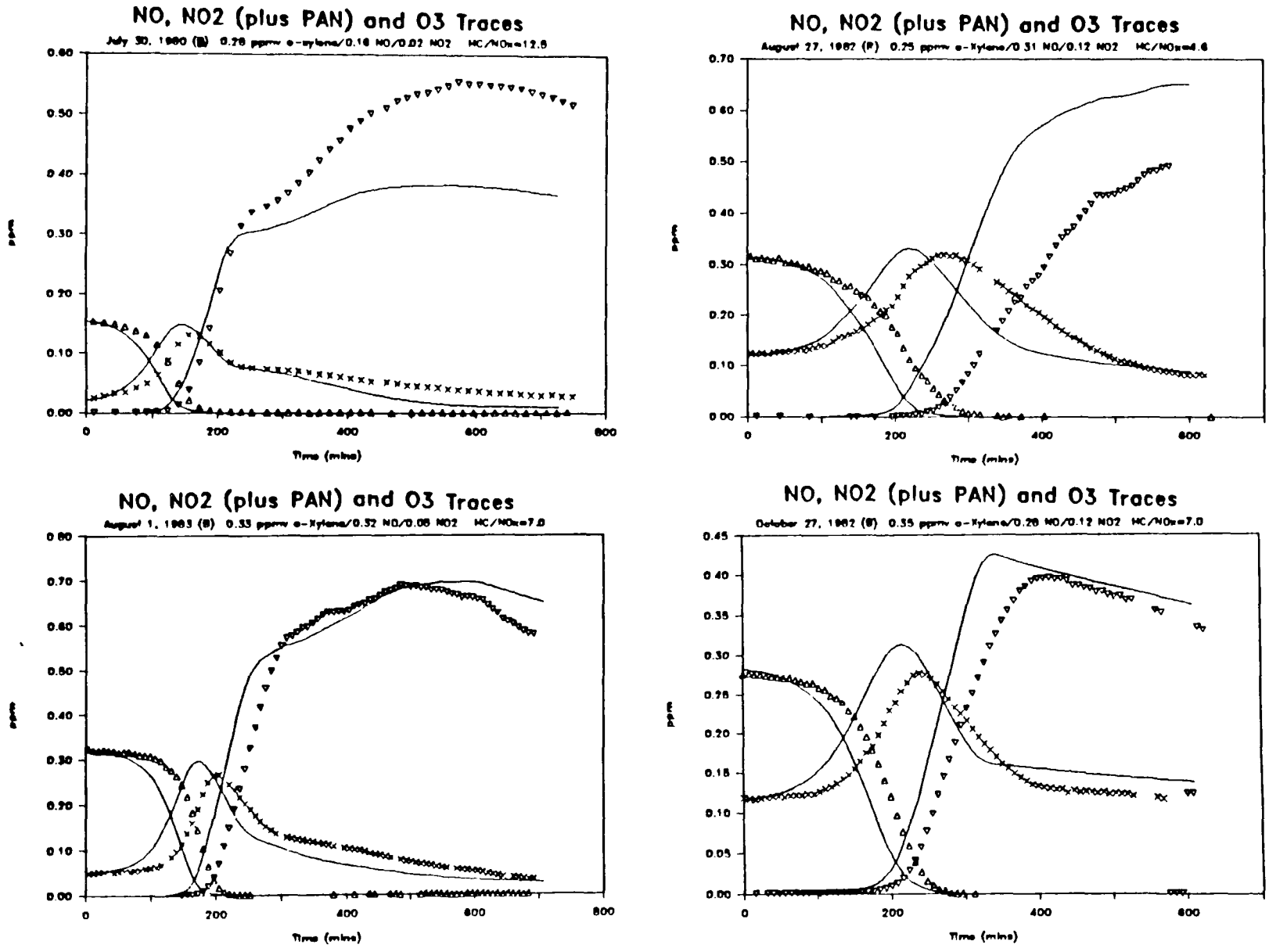

FIGURE 6-53. Simulation results for UNC experiments JL3080B, AU2782R, AU0183B, and OC2782B (symbols are experimental measurements)

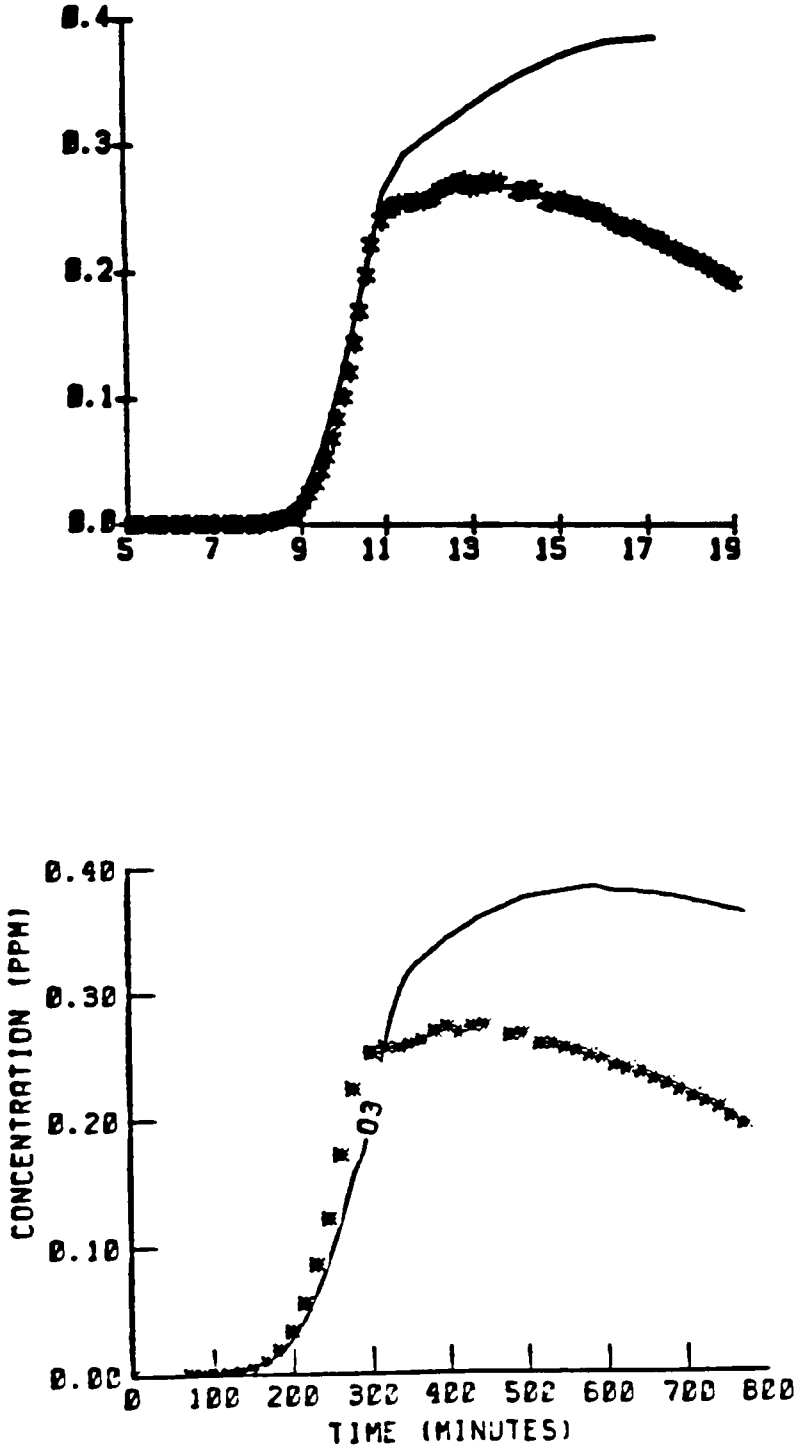

FIGURE 6-54. Simulation results from the CALL (Carter et al., 1986) and earlier CBMX (Whitten et al., 1985) mechanisms from UNC JL3U8OR.

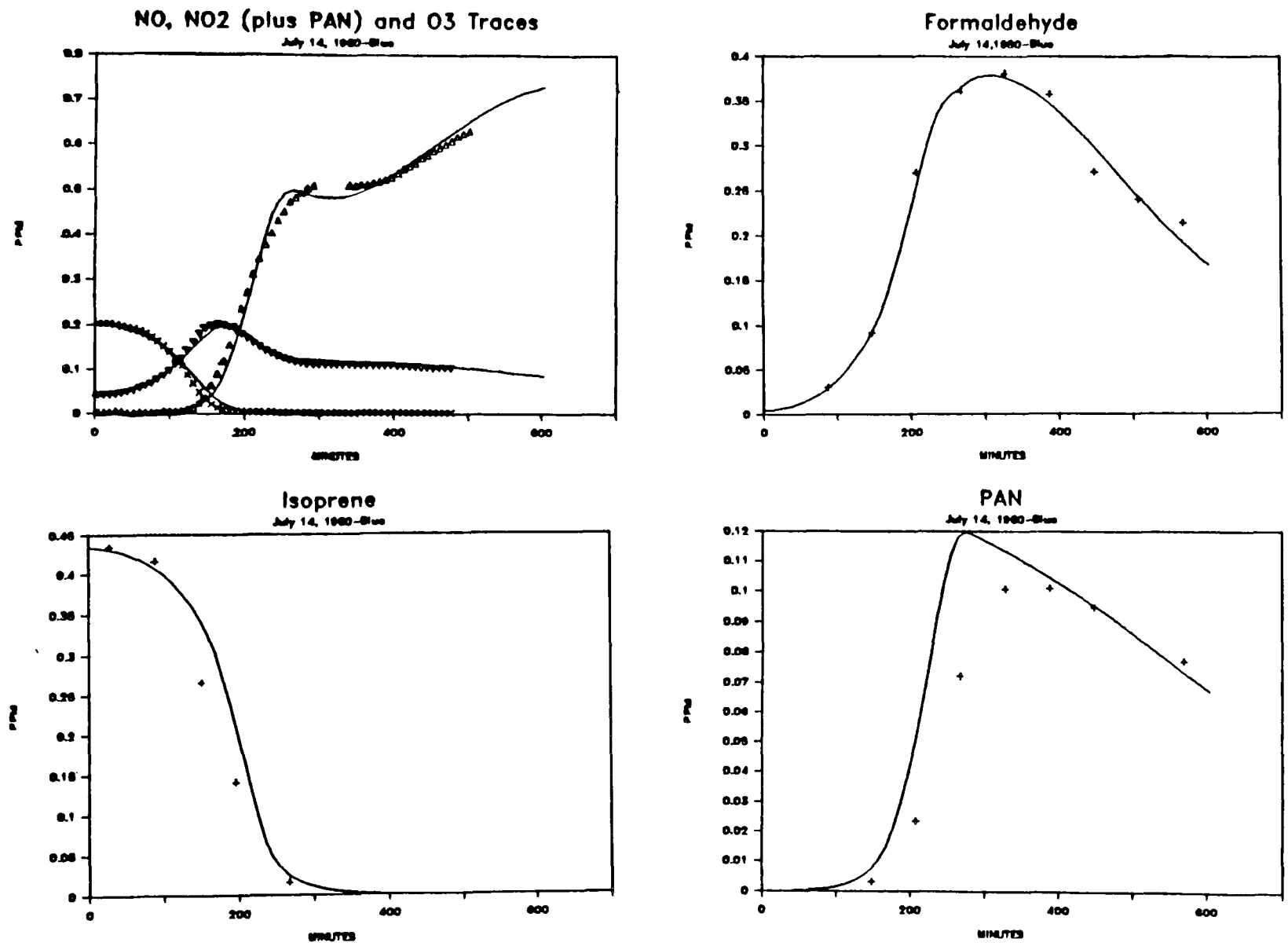

FIGURE 6-55. Simulation results for UNC experiment JL1480B
(symbols are experimental measurements)

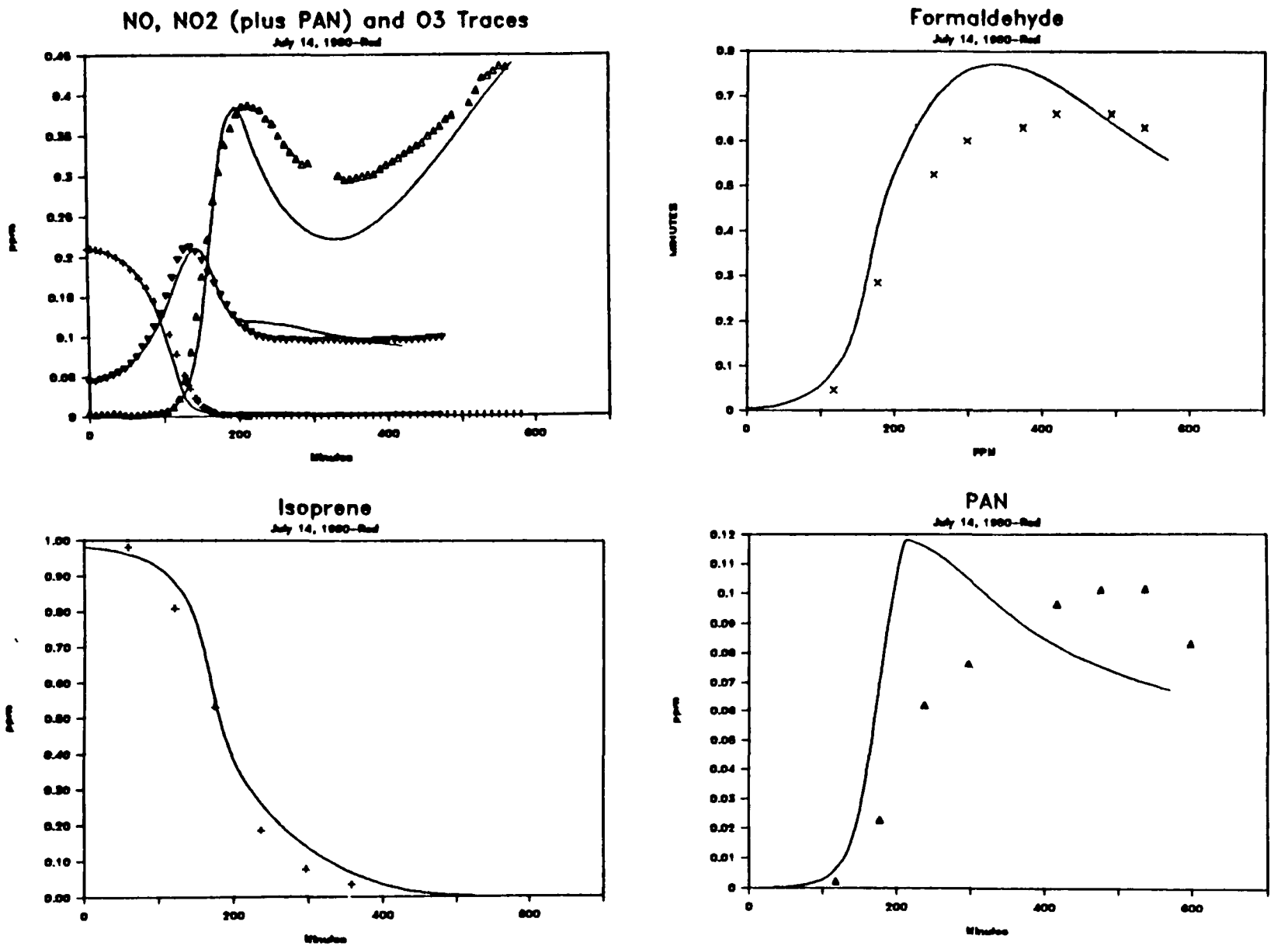

FIGURE 6-56. Simulation results for UNC experiment JL1480R
(symbols are experimental measurements)

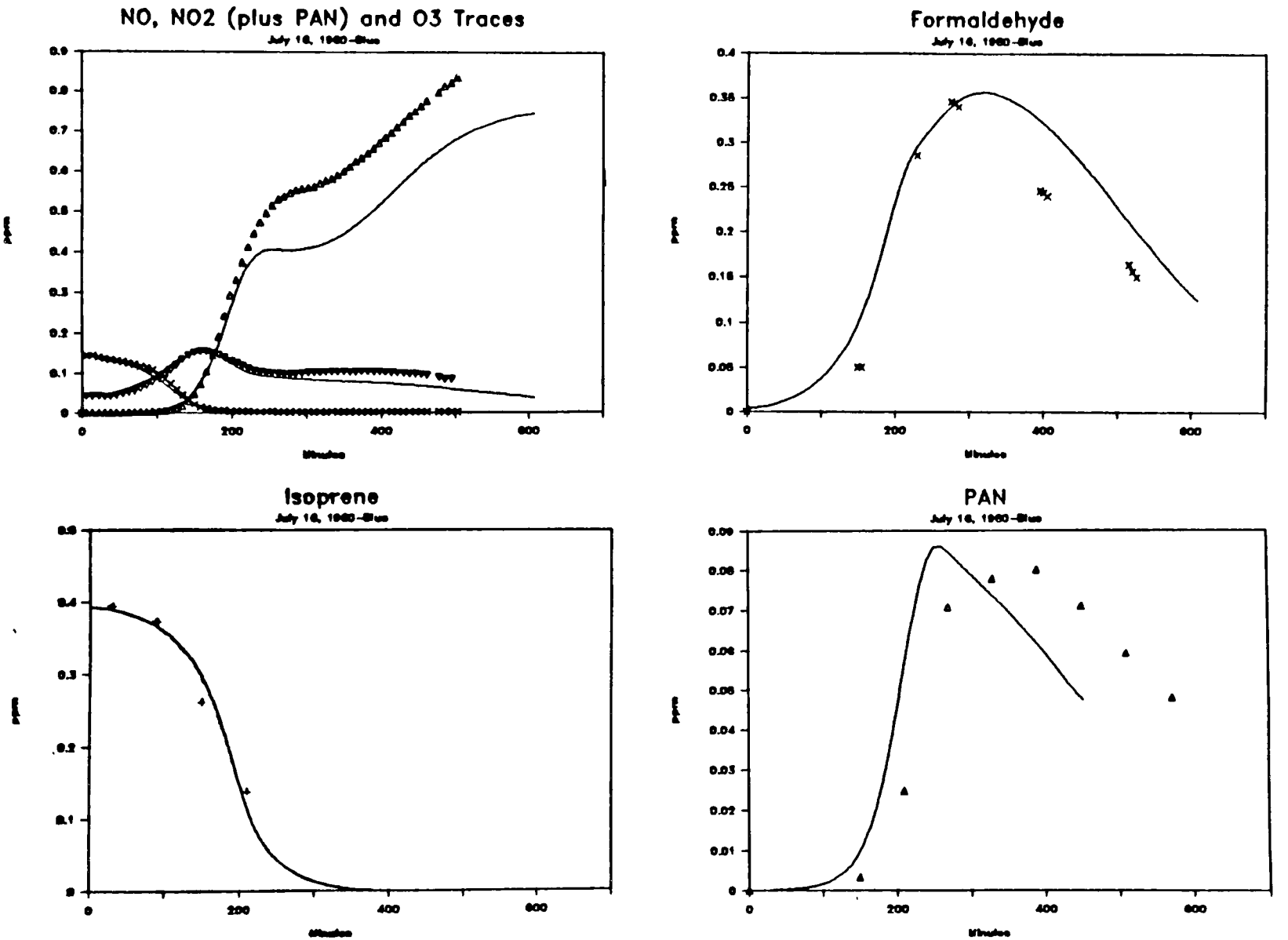

FIGURE 6-57. Simulation results for UNC experiment JL1680B
(symbols are experimental measurements)

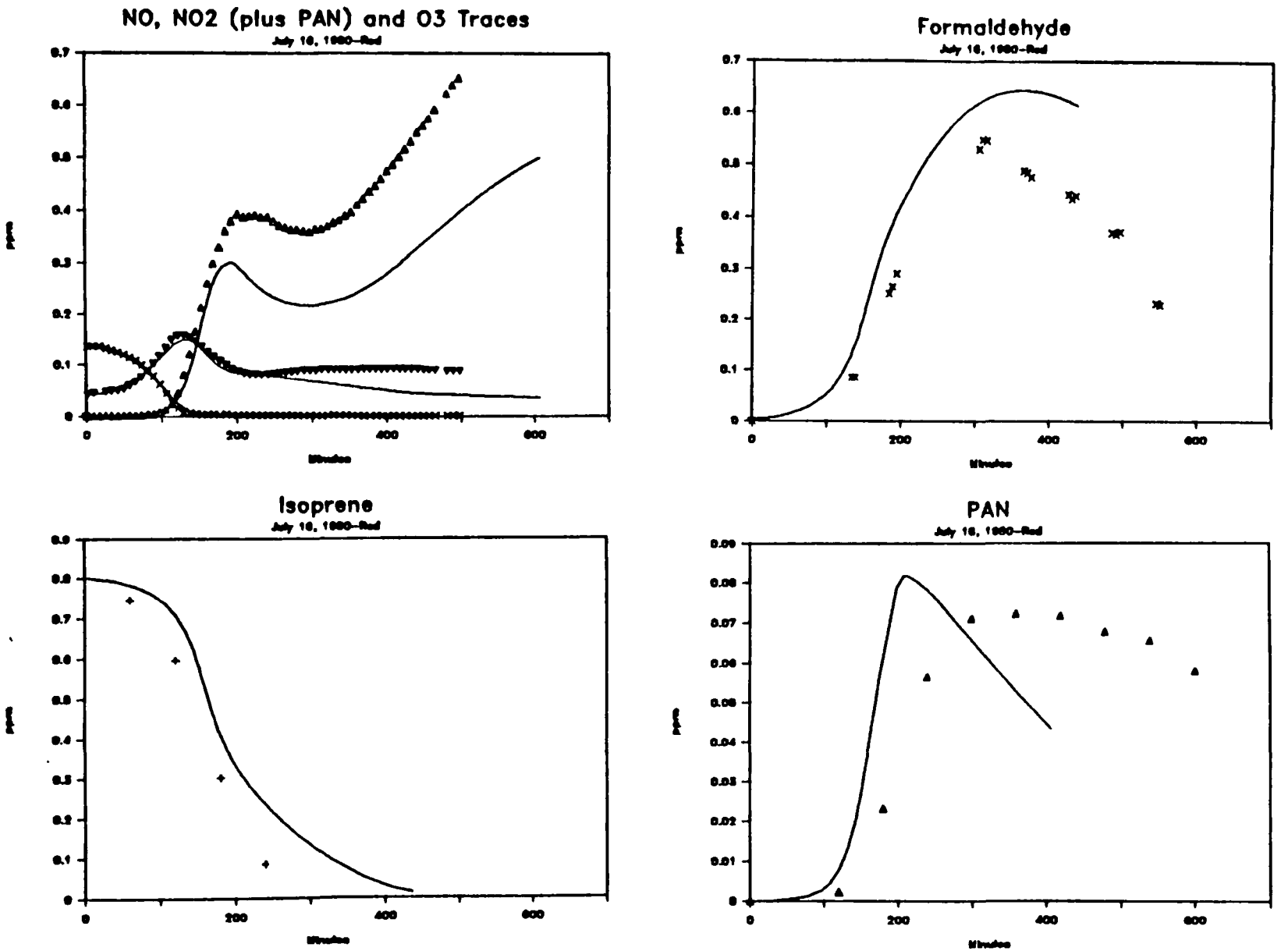

FIGURE 6-58. Simulation results for UNC experiment JL1680R (symbols are experimental measurements)

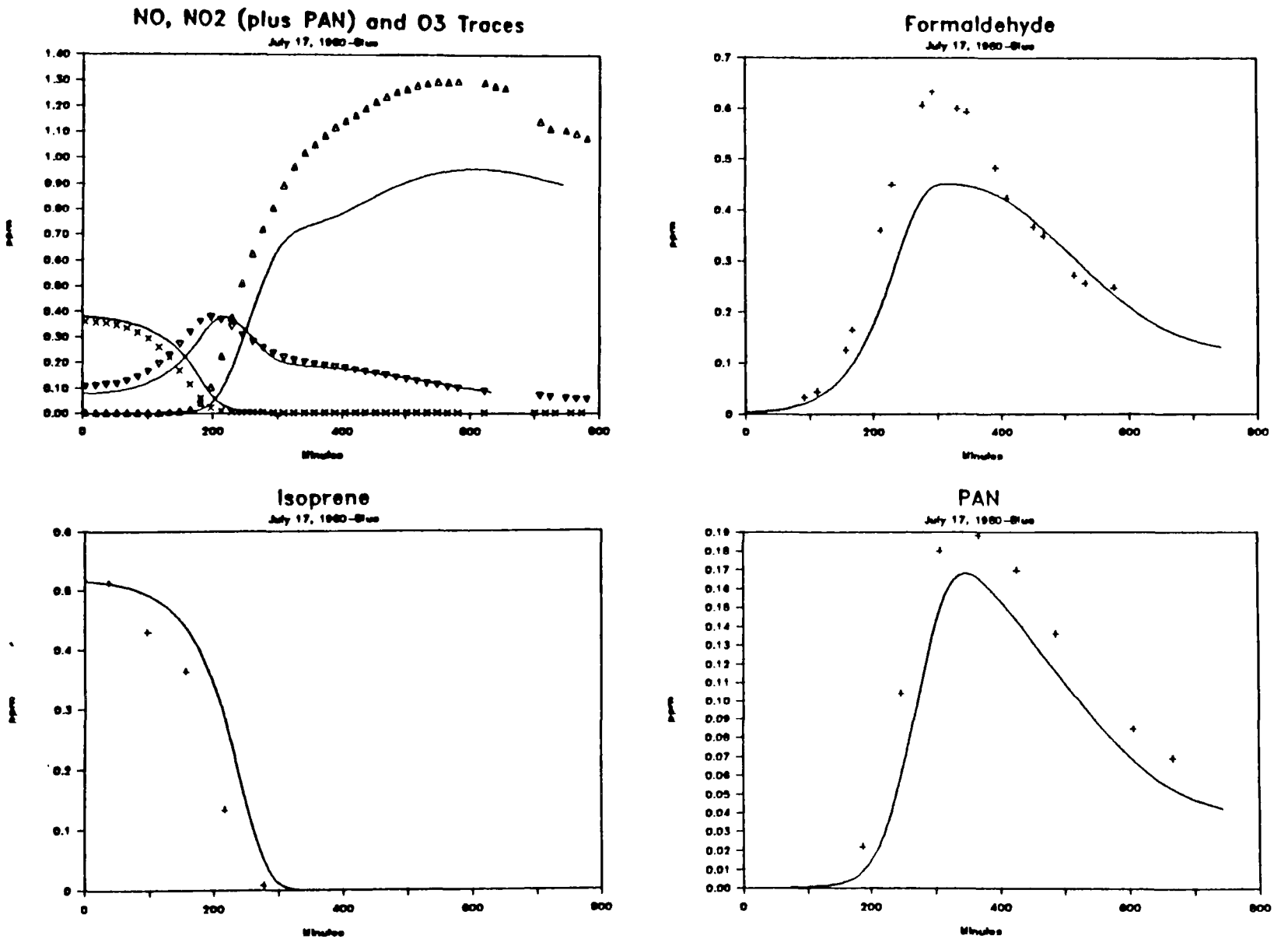

FIGURE 6-59. Simulation results for UNC experiment JL1780B (symbols are experimental measurements)

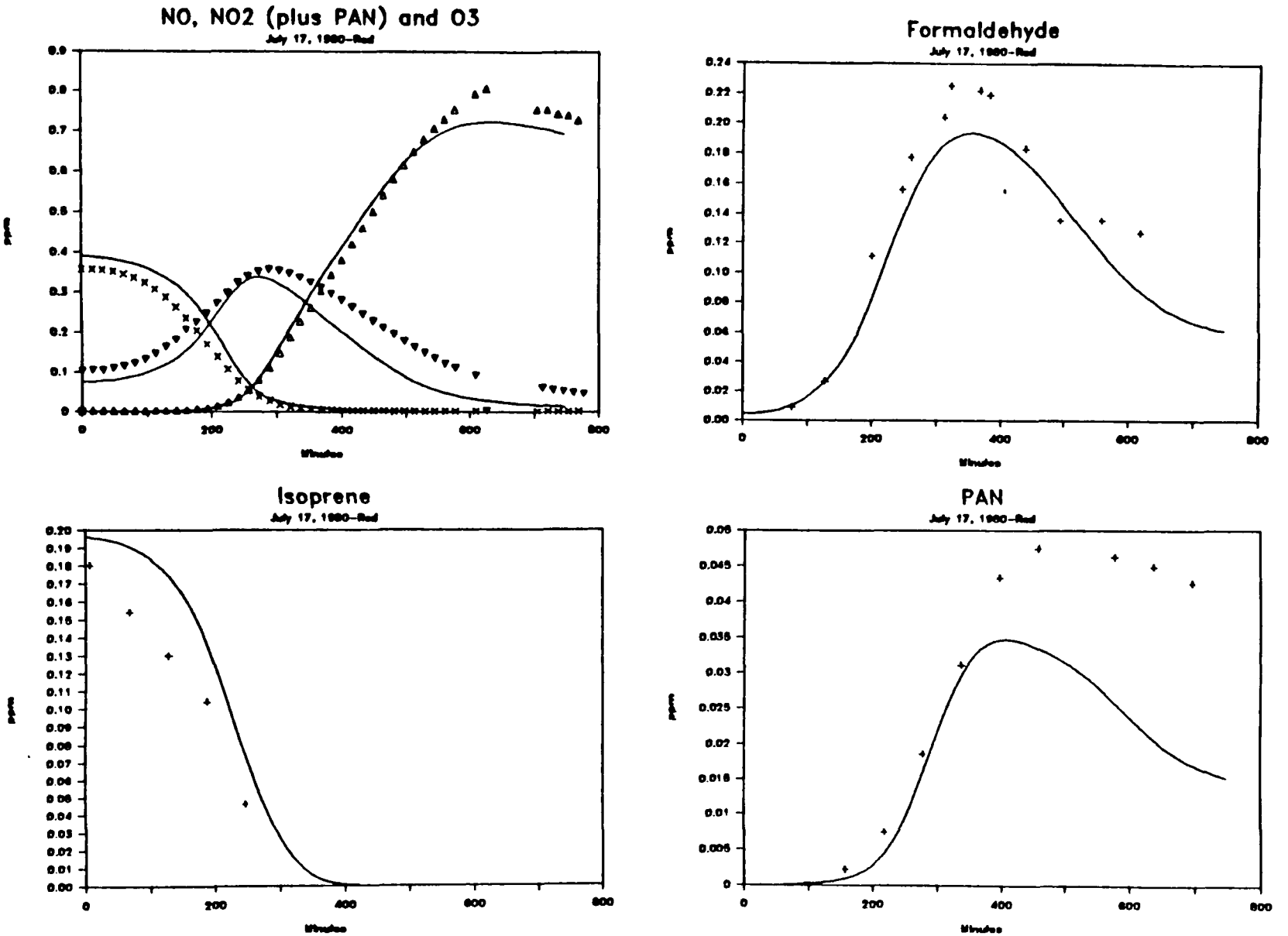

FIGURE 6-60. Simulation results for UNC experiment JL178OR (symbols are experimental measurements)

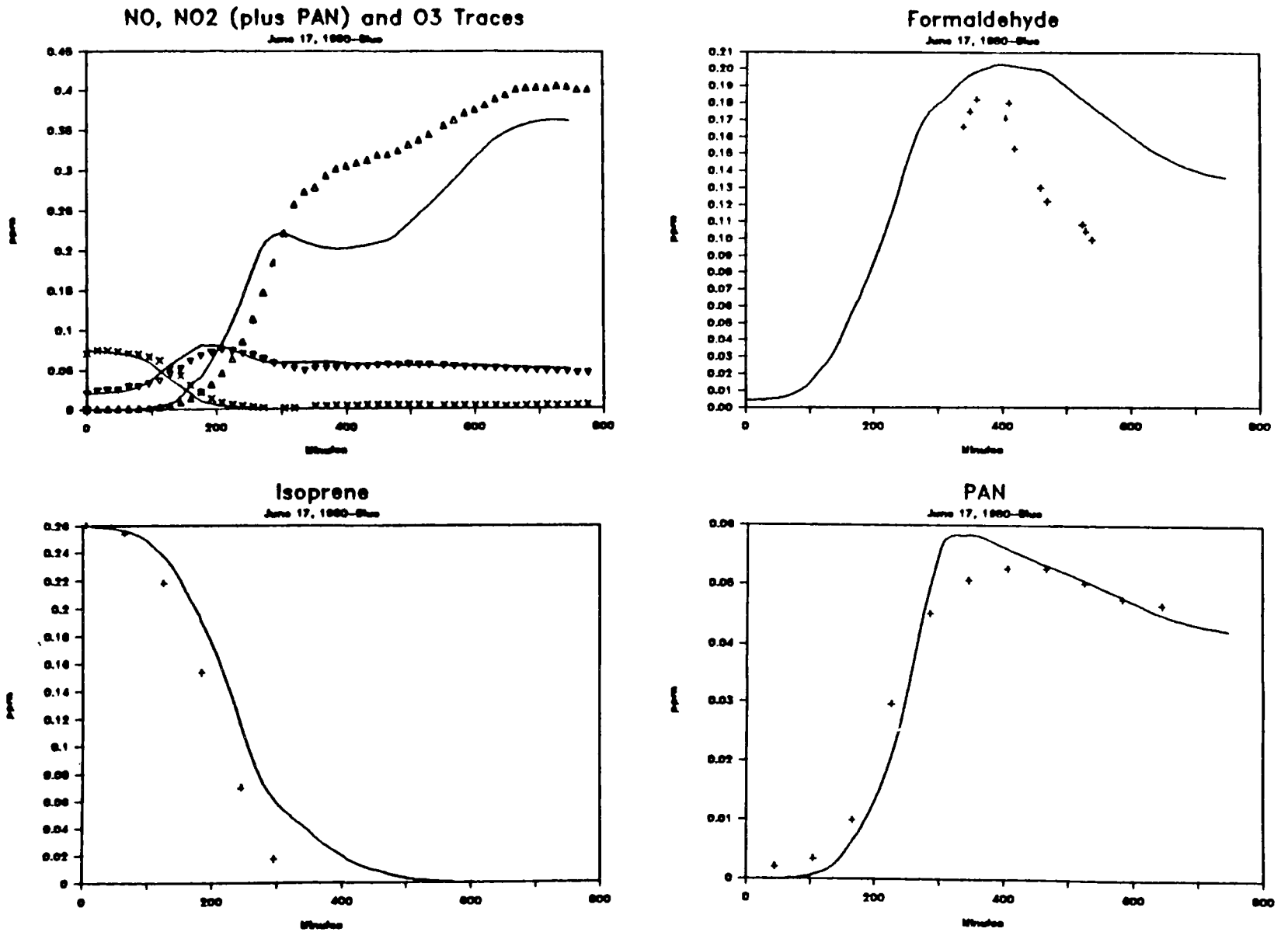

FIGURE 6-61. Simulation results for UNC experiment JN1780B
(symbols are experimental measurements)

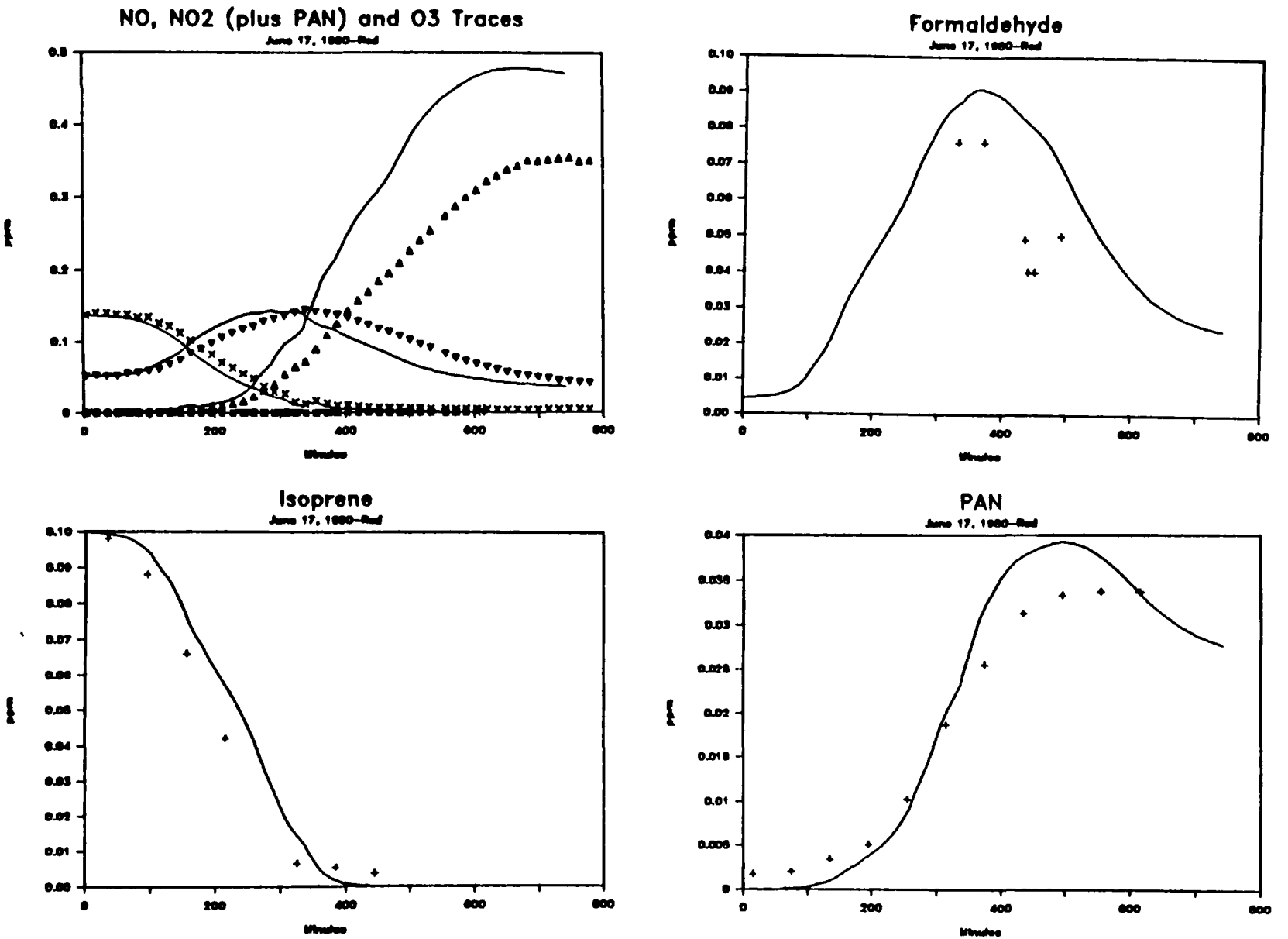

FIGURE 6-62. Simulation results for UNC experiment JN178OR
(symbols are experimental measurements)

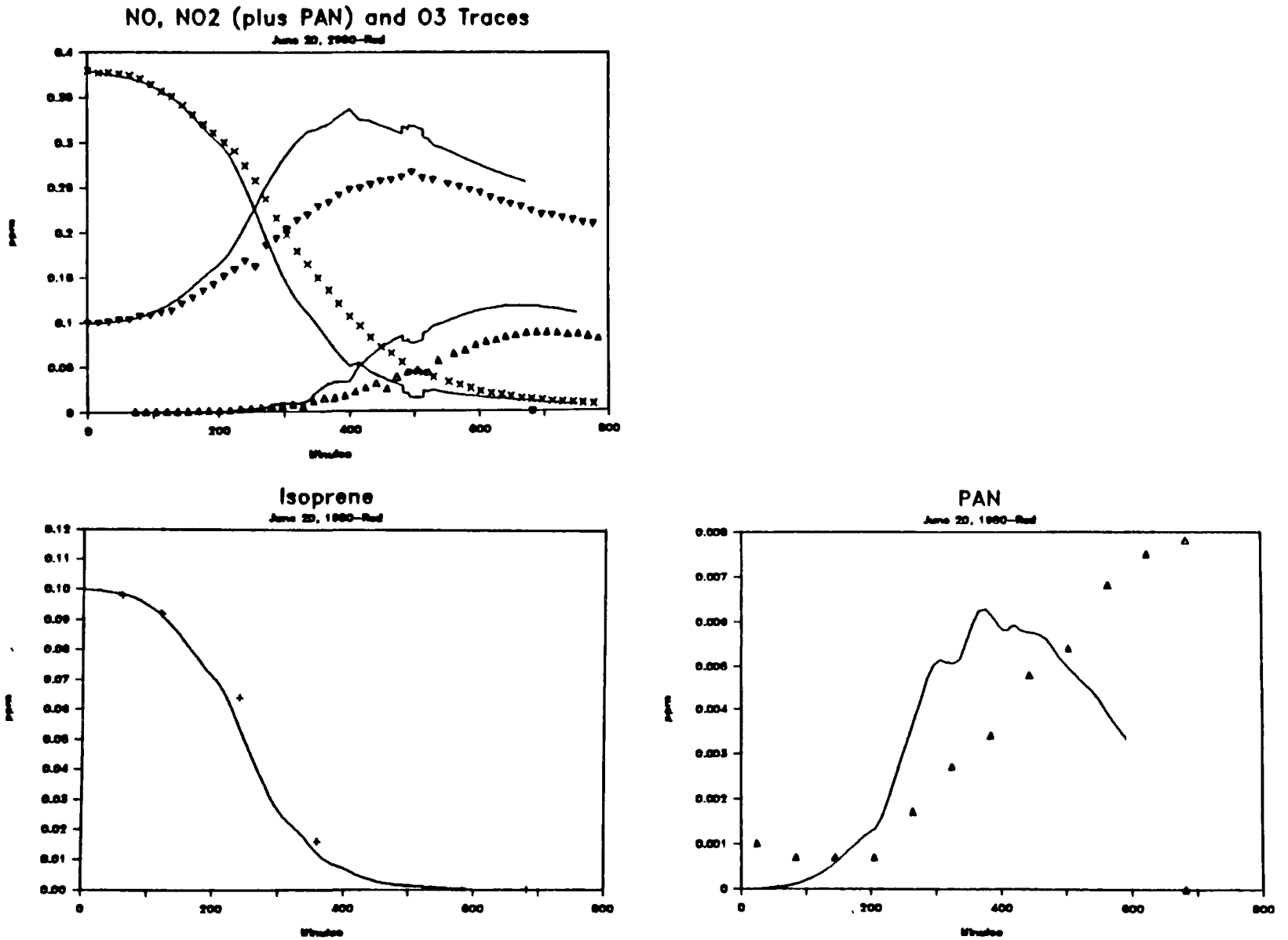

FIGURE 6-63. Simulation results for UNC experiment JN208OR
(symbols are experimental measurements)

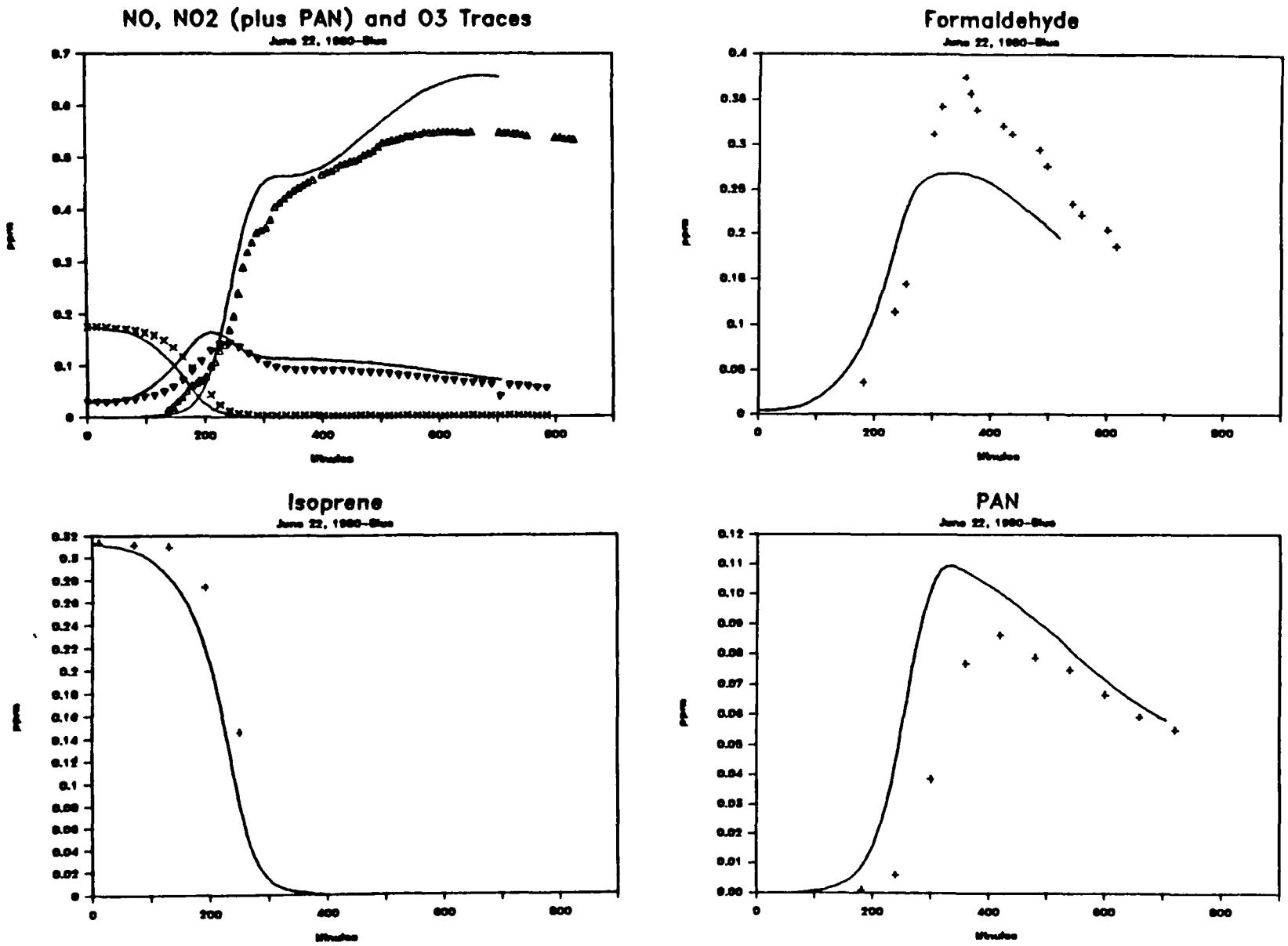

FIGURE 6-64. Simulation results for UNC experiment JN2280B
(symbols are experimental measurements)

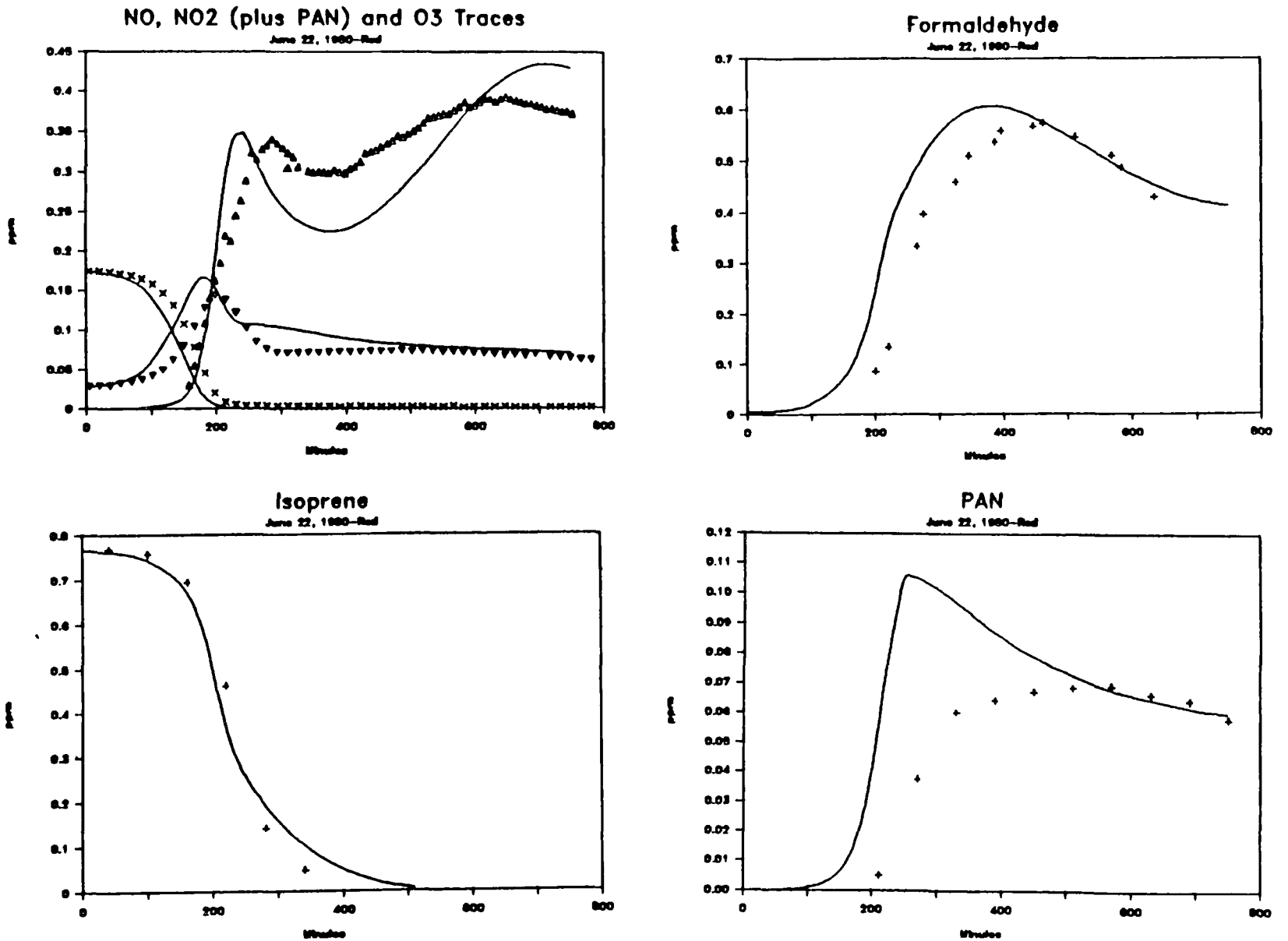

FIGURE 6-65. Simulation results for UNC experiment JN228OR
(symbols are experimental measurements)

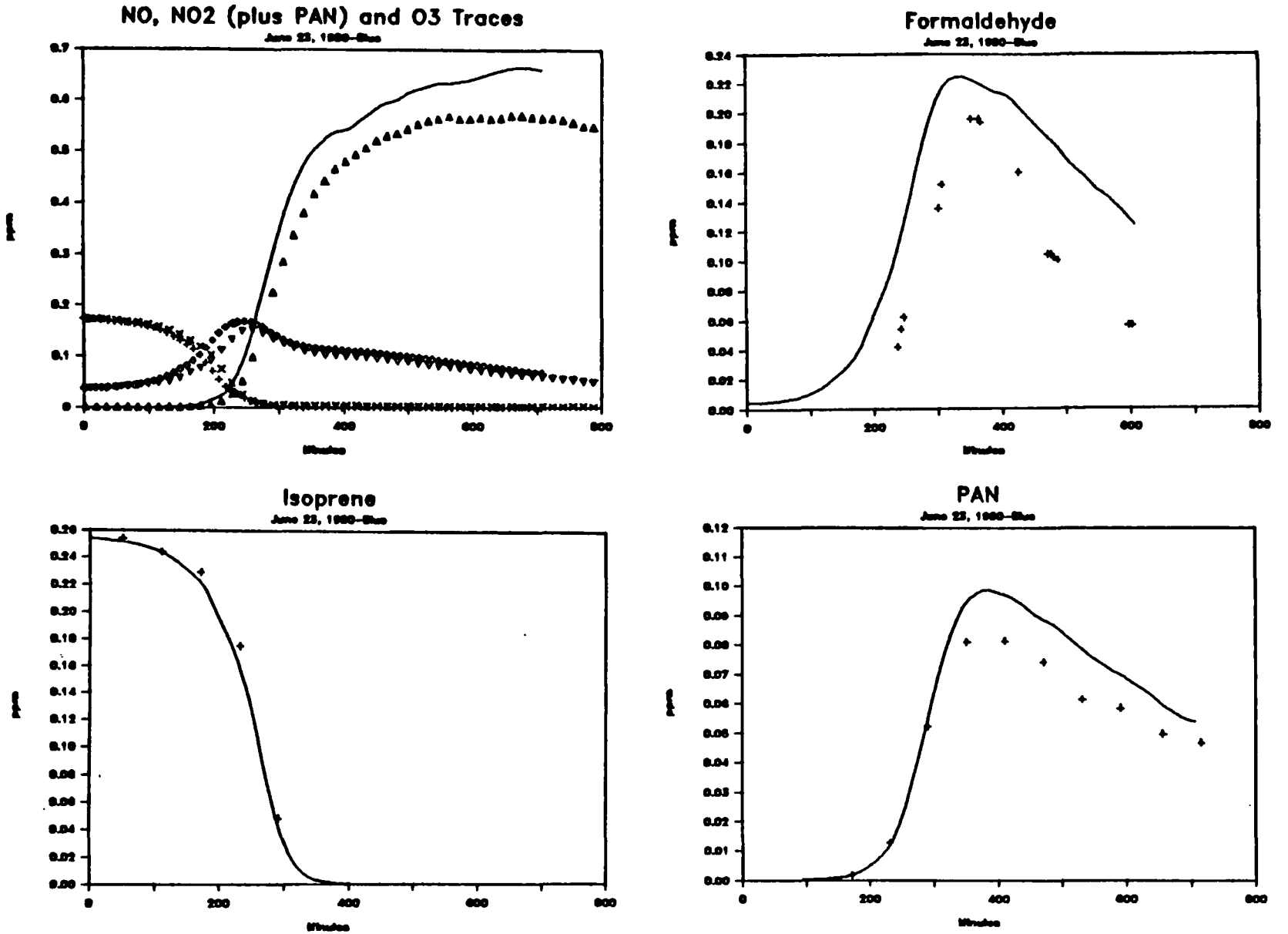

FIGURE 6-66. Simulation results for UNC experiment JN2380B
(symbols are experimental measurements)

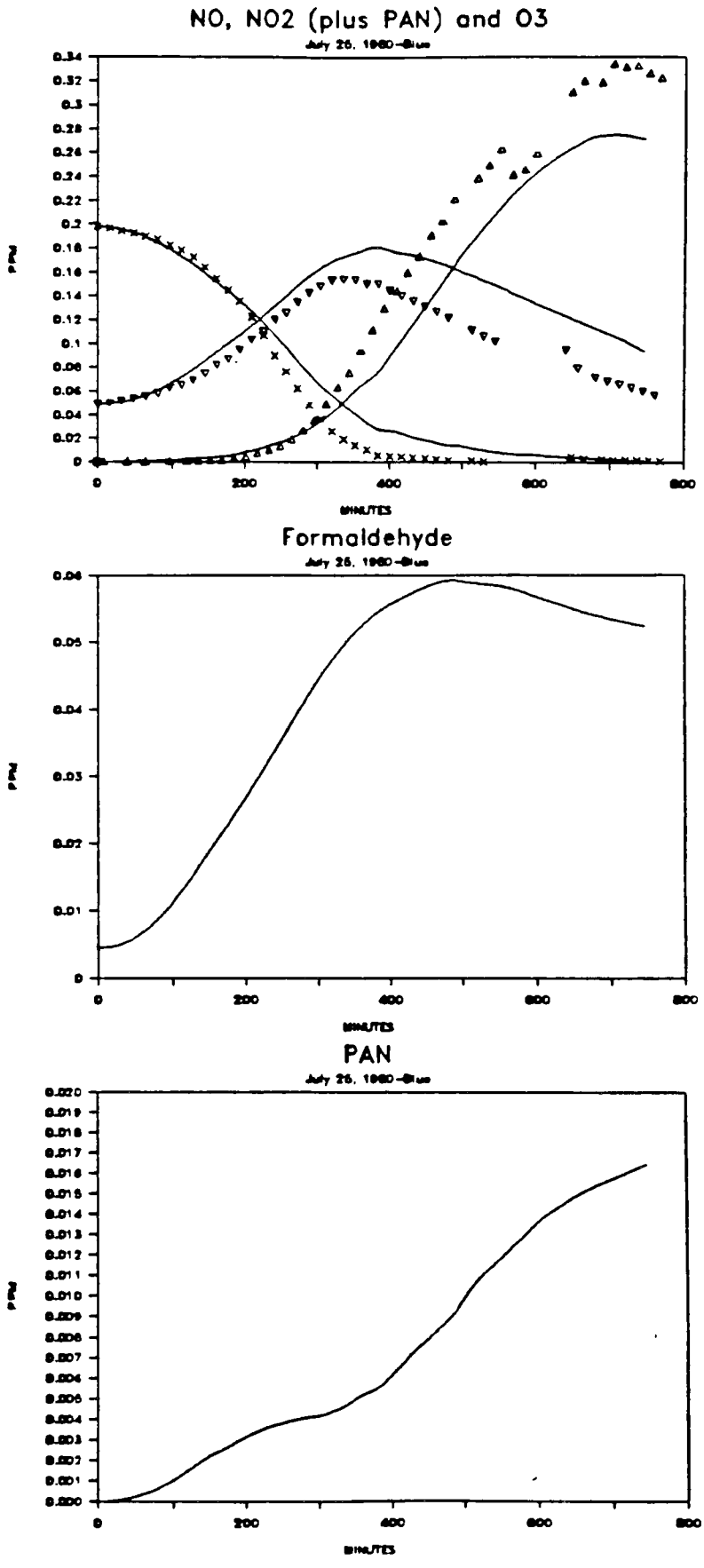

FIGURE 6-67. Simulation results for UNC experiment JL2580B (symbols are experimental measurements)

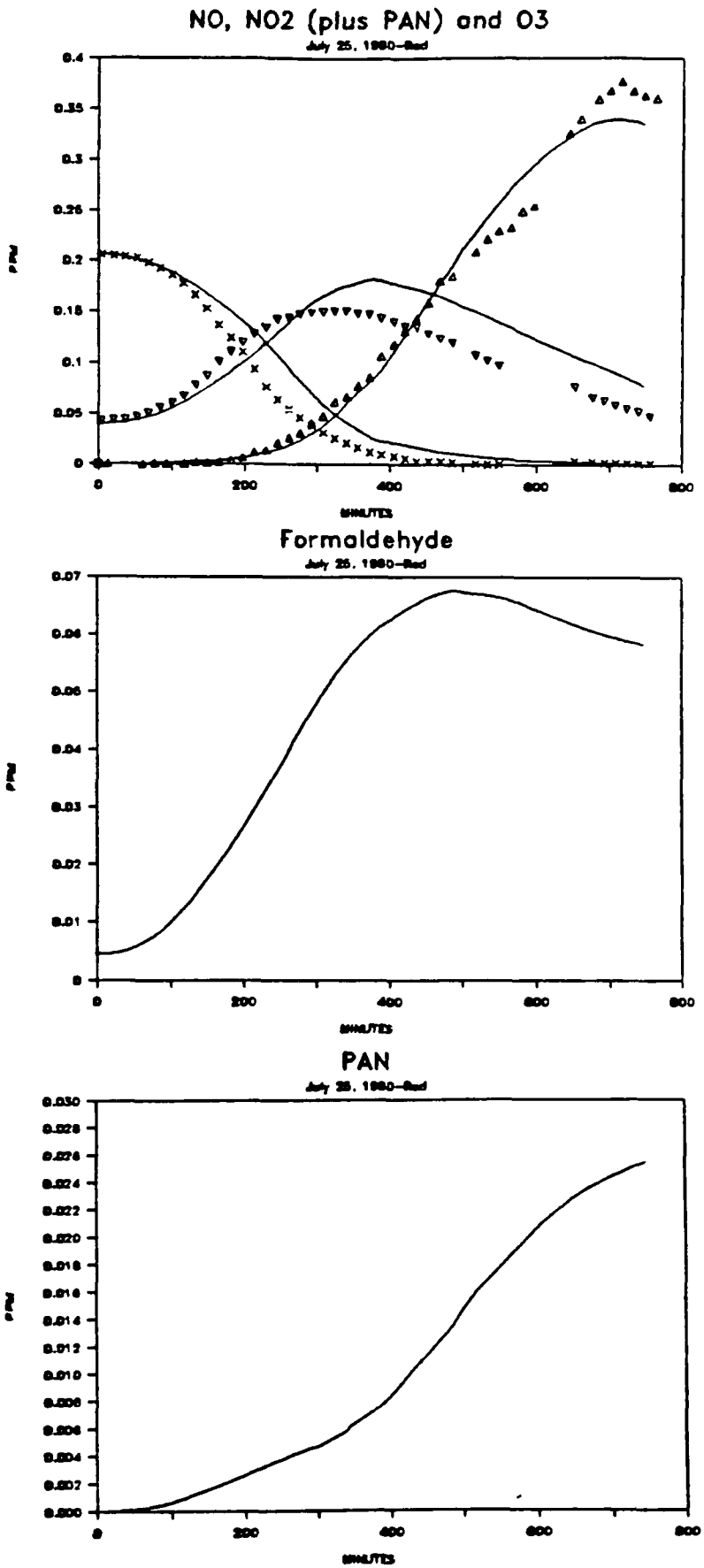

FIGURE 6-68. Simulation results for UNC experiment JL2580R (symbols are experimental measurements)

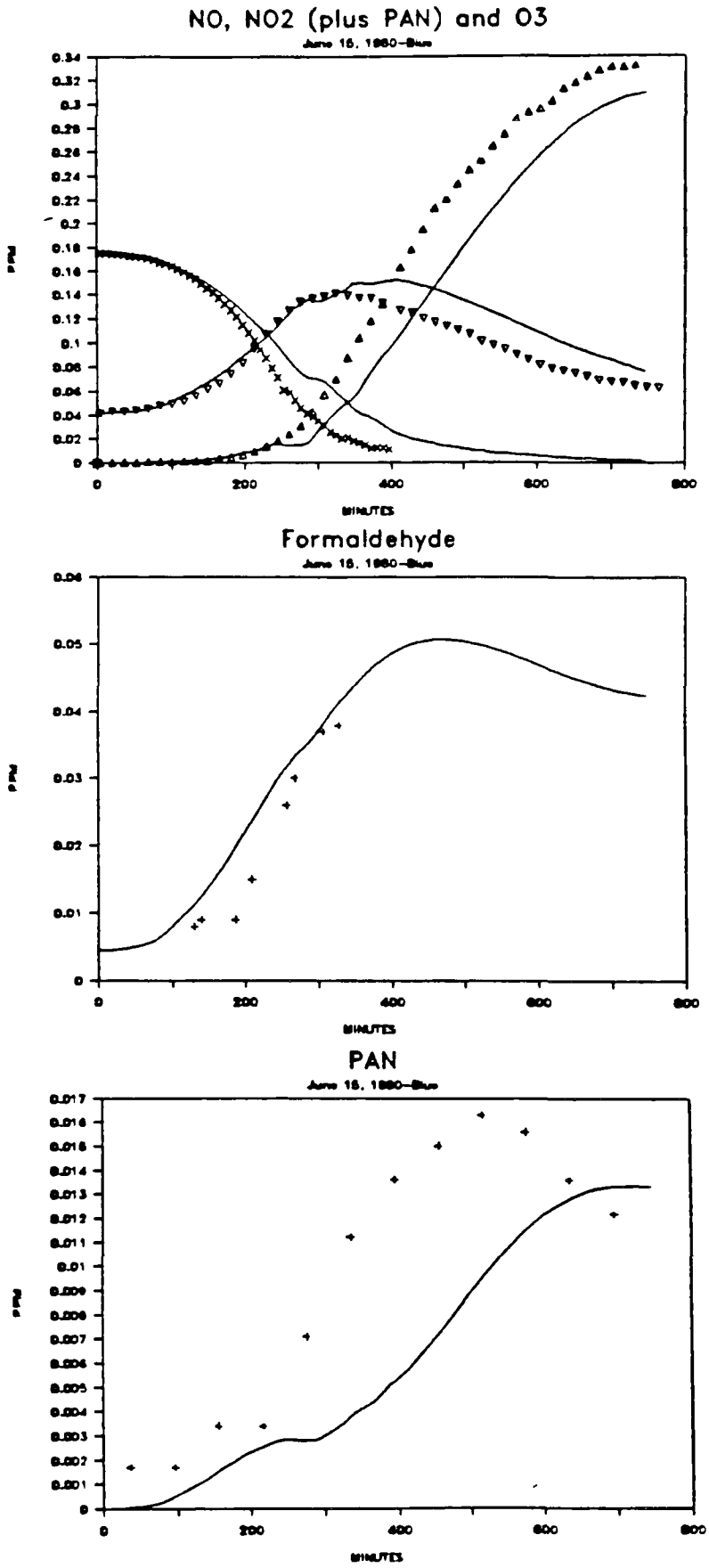

FIGURE 6-69. Simulation results for UNC experiment JN1580B (symbols are experimental measurements)

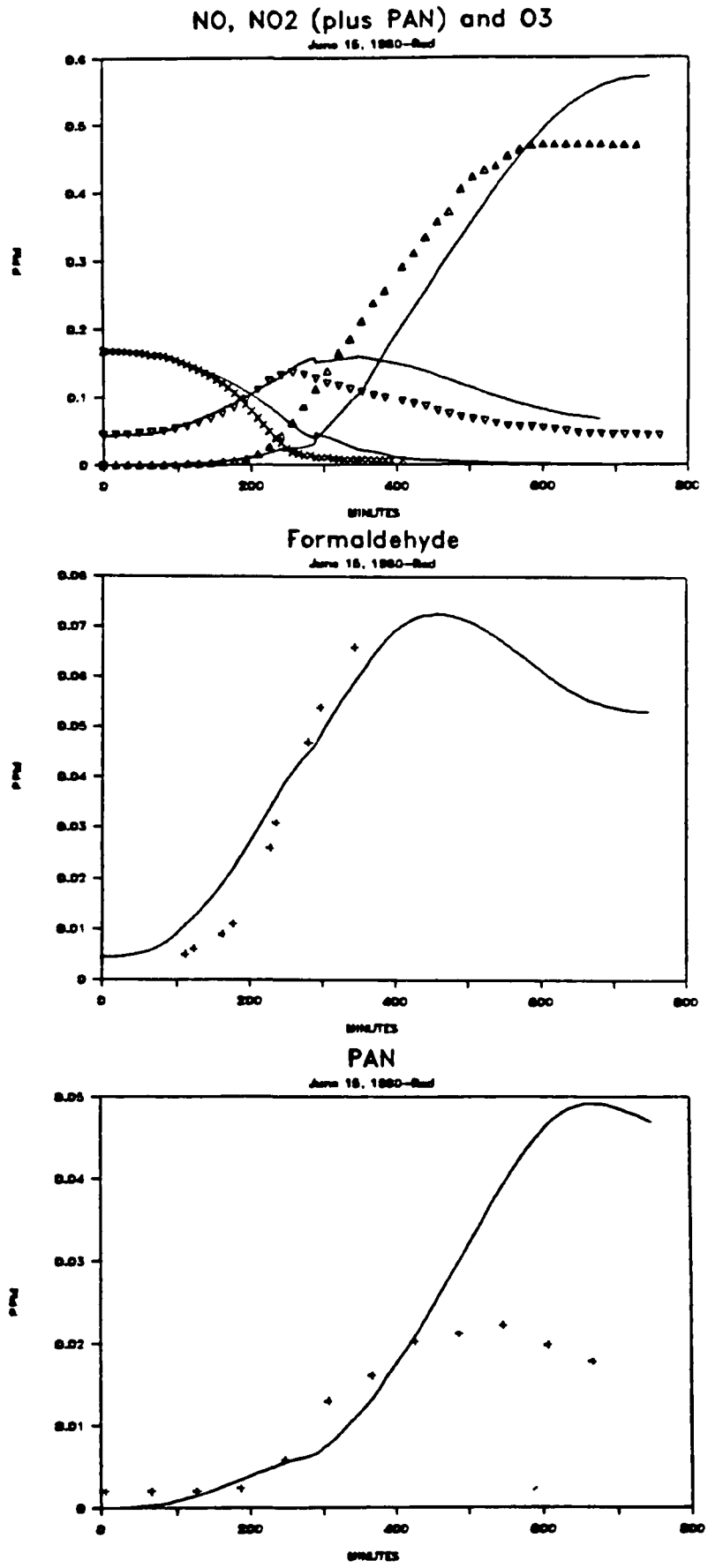

FIGURE 6-70. Simulation results for UNC experiment JN1580R (symbols are experimental measurements)

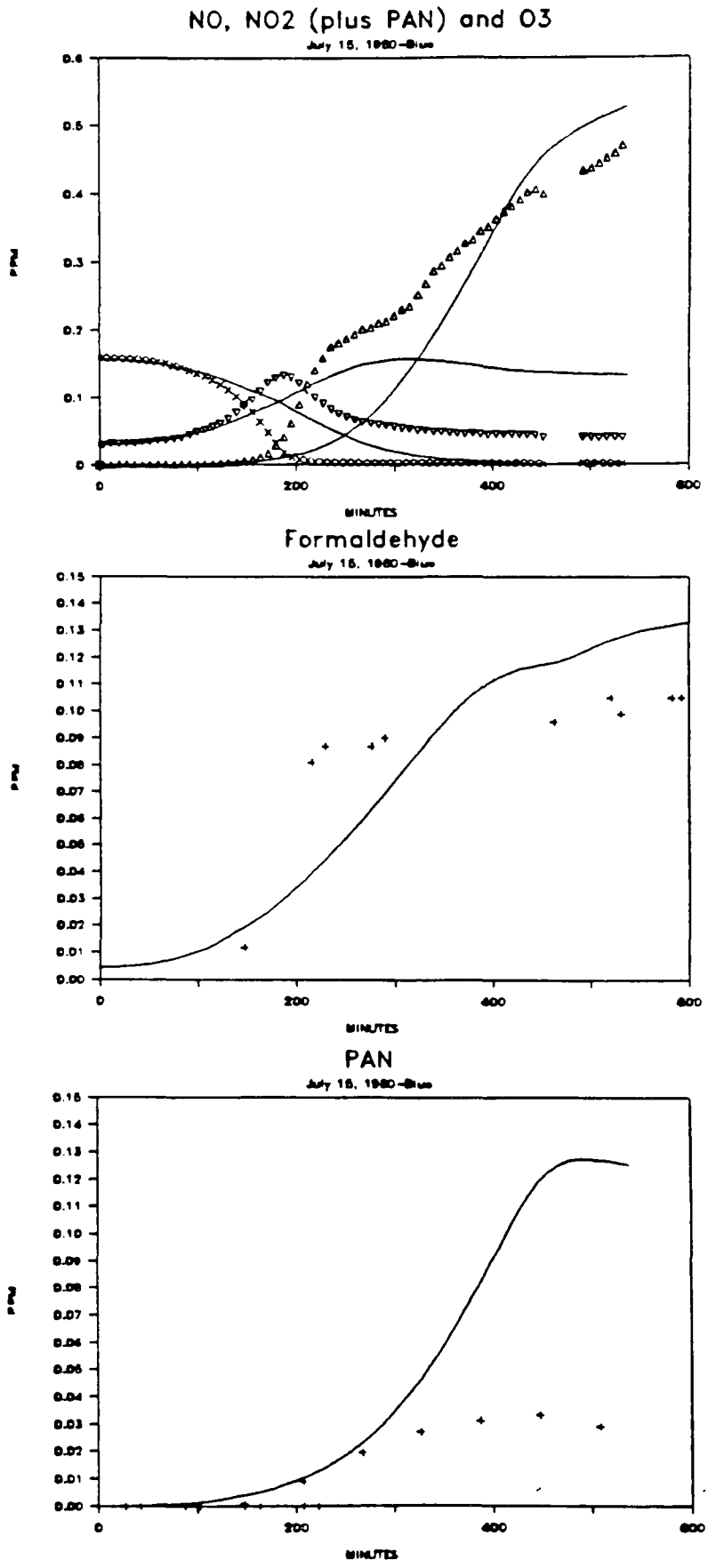

FIGURE 6-71. Simulation results for UNC experiment JL1580B (symbols are experimental measurements)

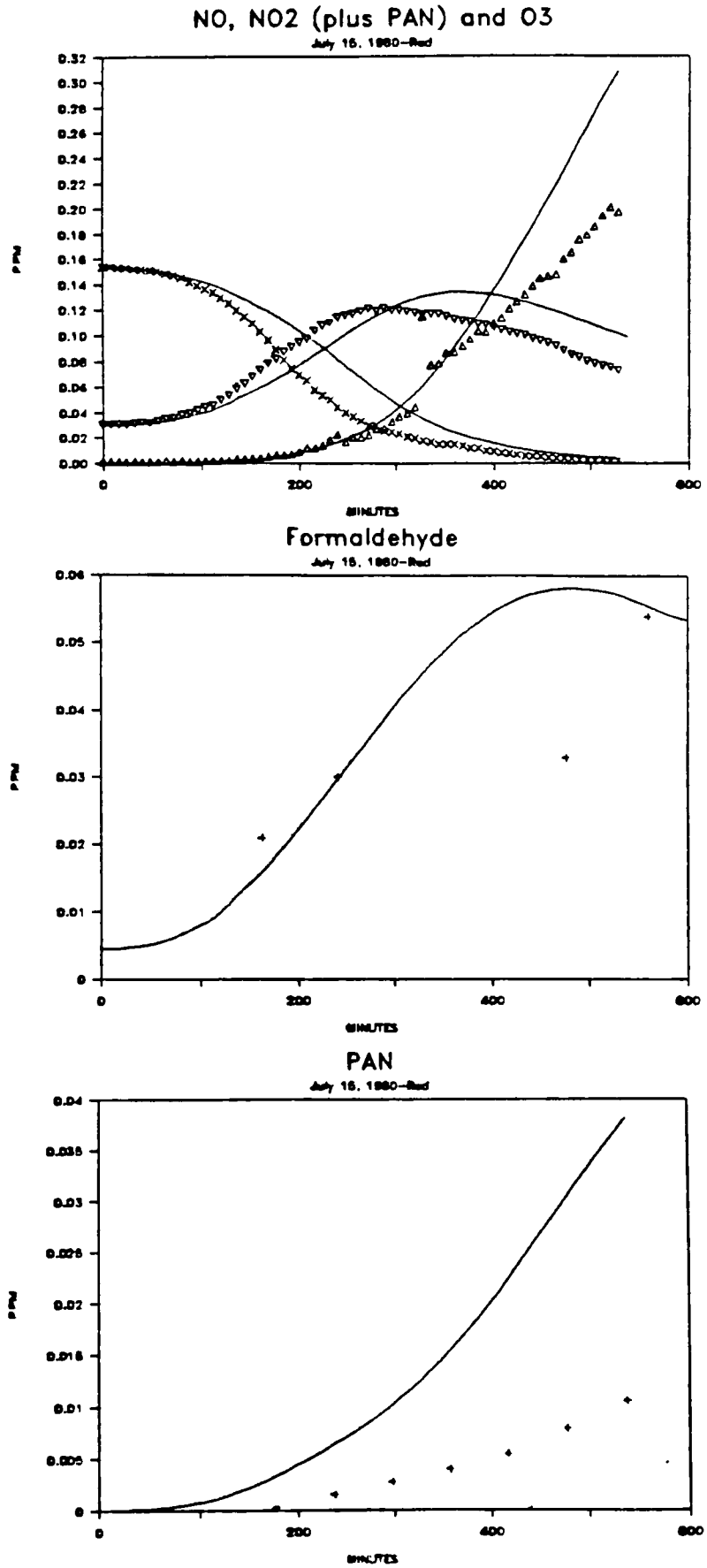

FIGURE 6-72. Simulation results for UNC experiment JL1580R (symbols are experimental measurements)

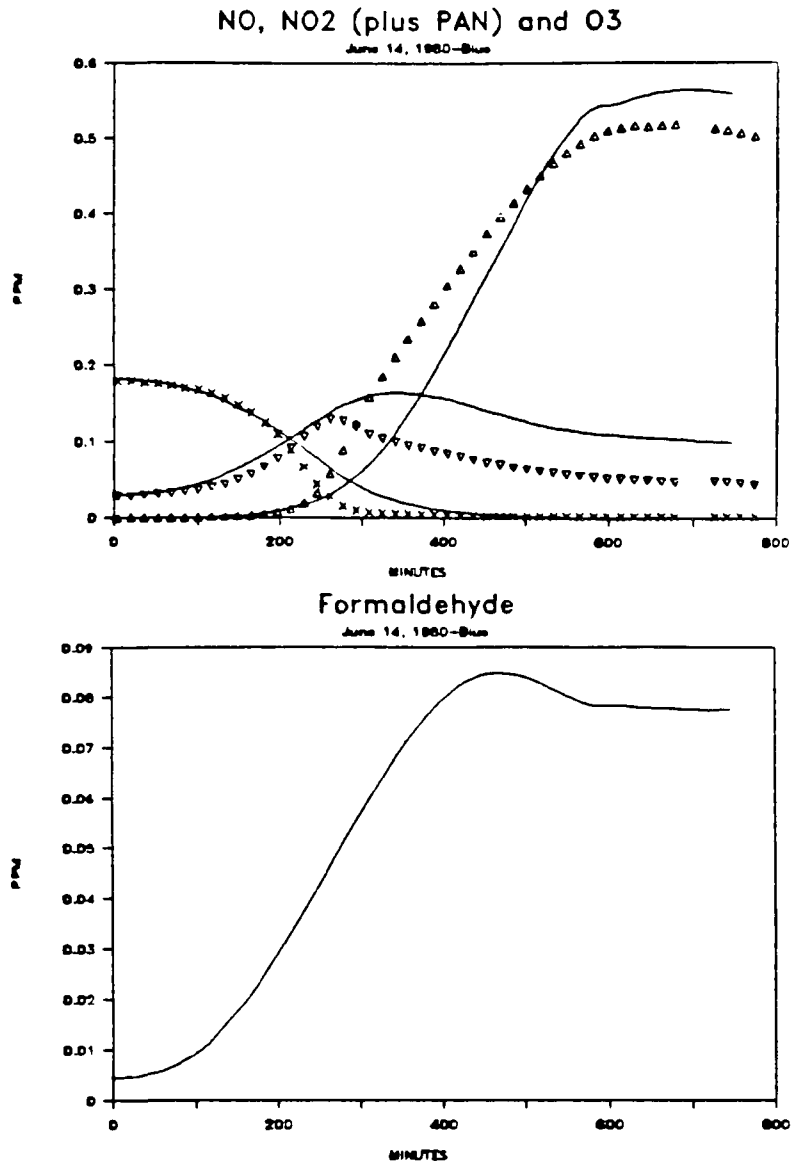

FIGURE 6-73. Simulation results for UNC experiment JN1480B (symbols are experimental measurements)

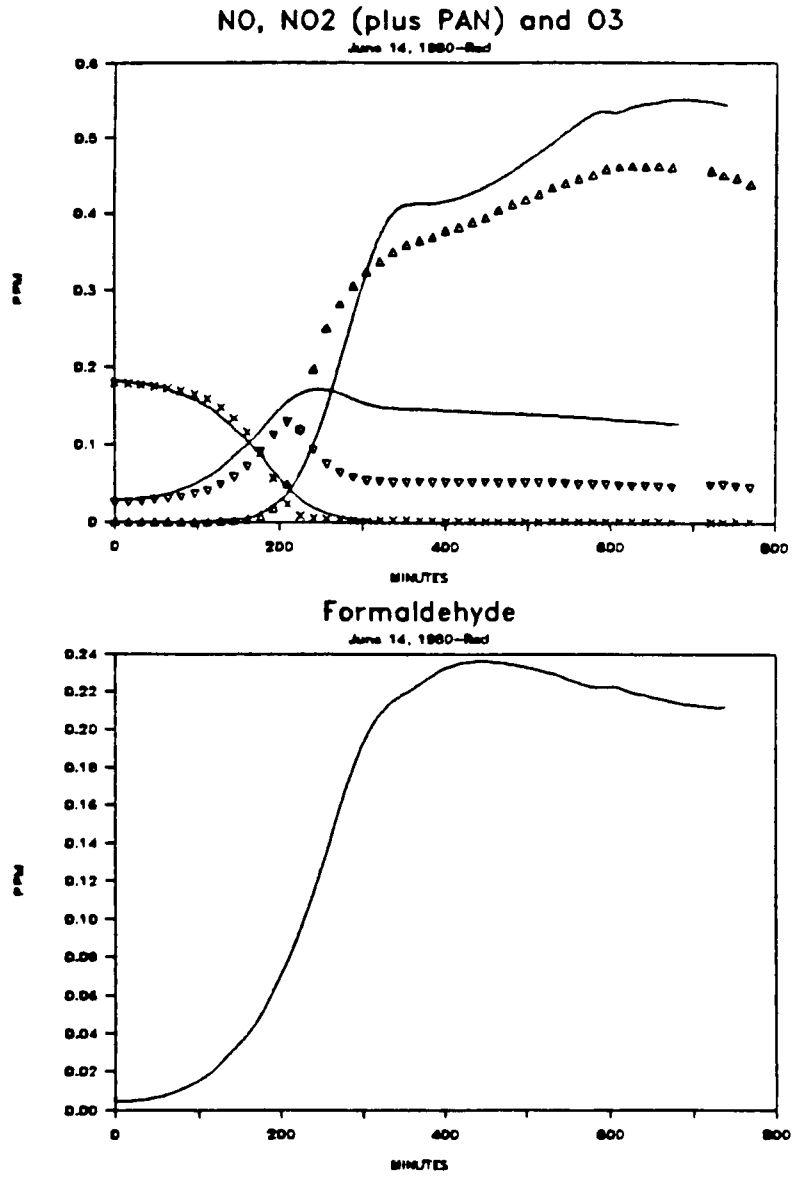

FIGURE 6-74. Simulation results for UNC experiment JN1480R (symbols are experimental measurements)

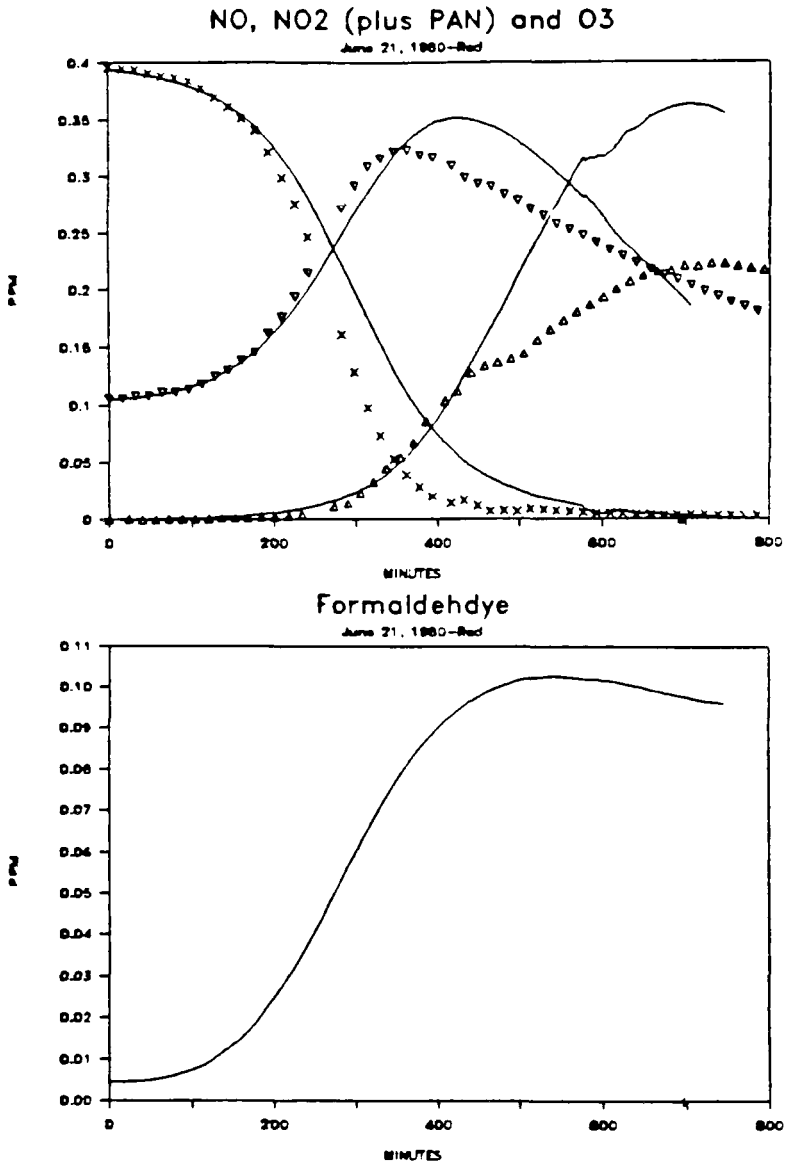

FIGURE 6-75. Simulation results for UNC experiment JN2180R (symbols are experimental measurements)

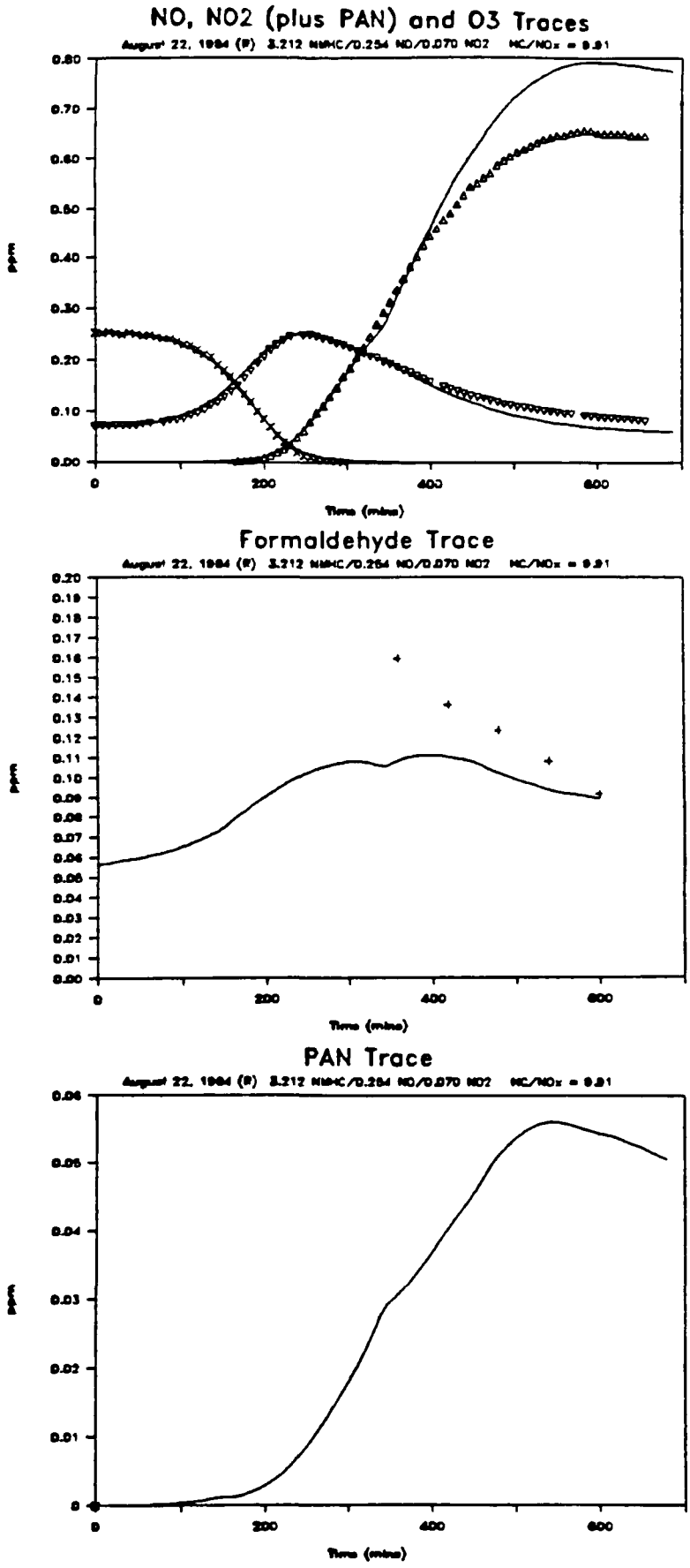

FIGURE 6-76. Simulation results for UNC experiment AU2284R (symbols are experimental measurements)

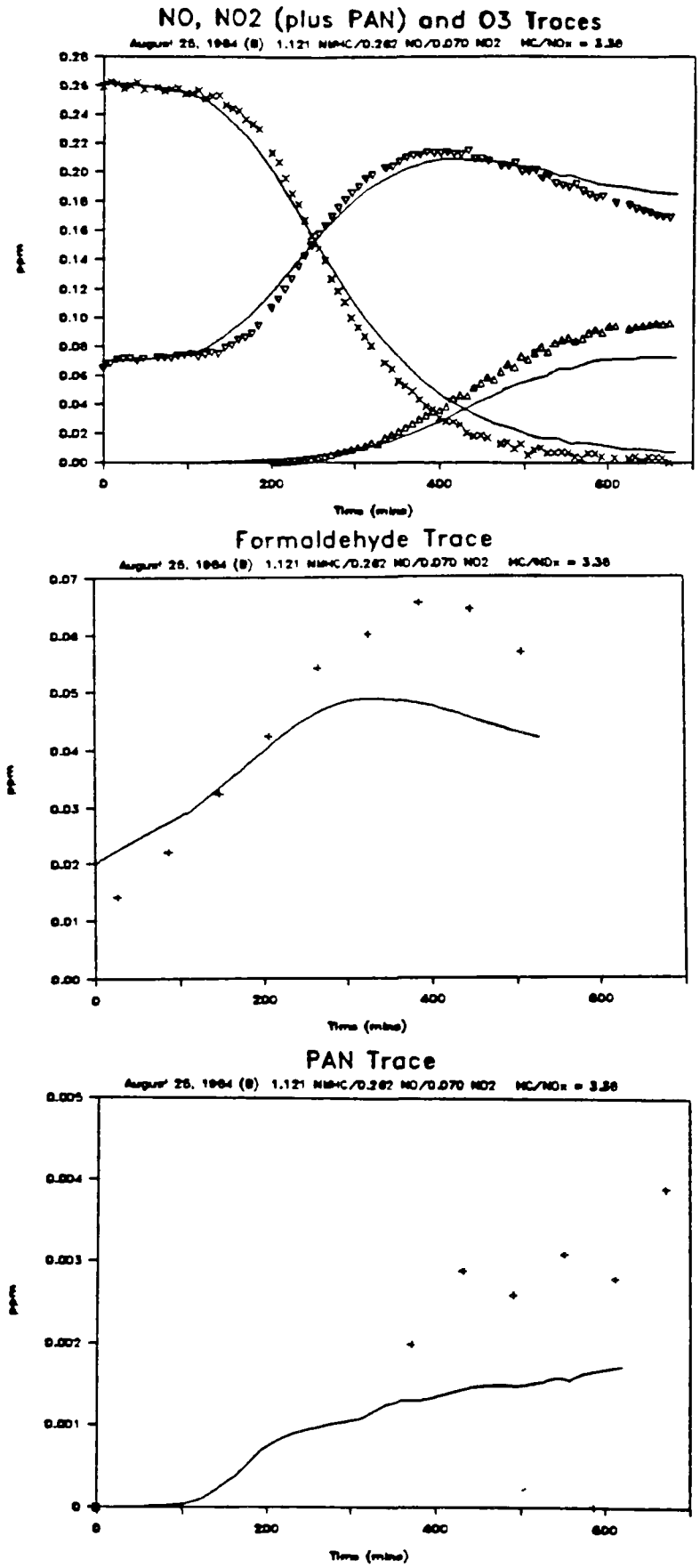

FIGURE 6-77. Simulation results for UNC experiment AU2584B (symbols are experimental measurements)

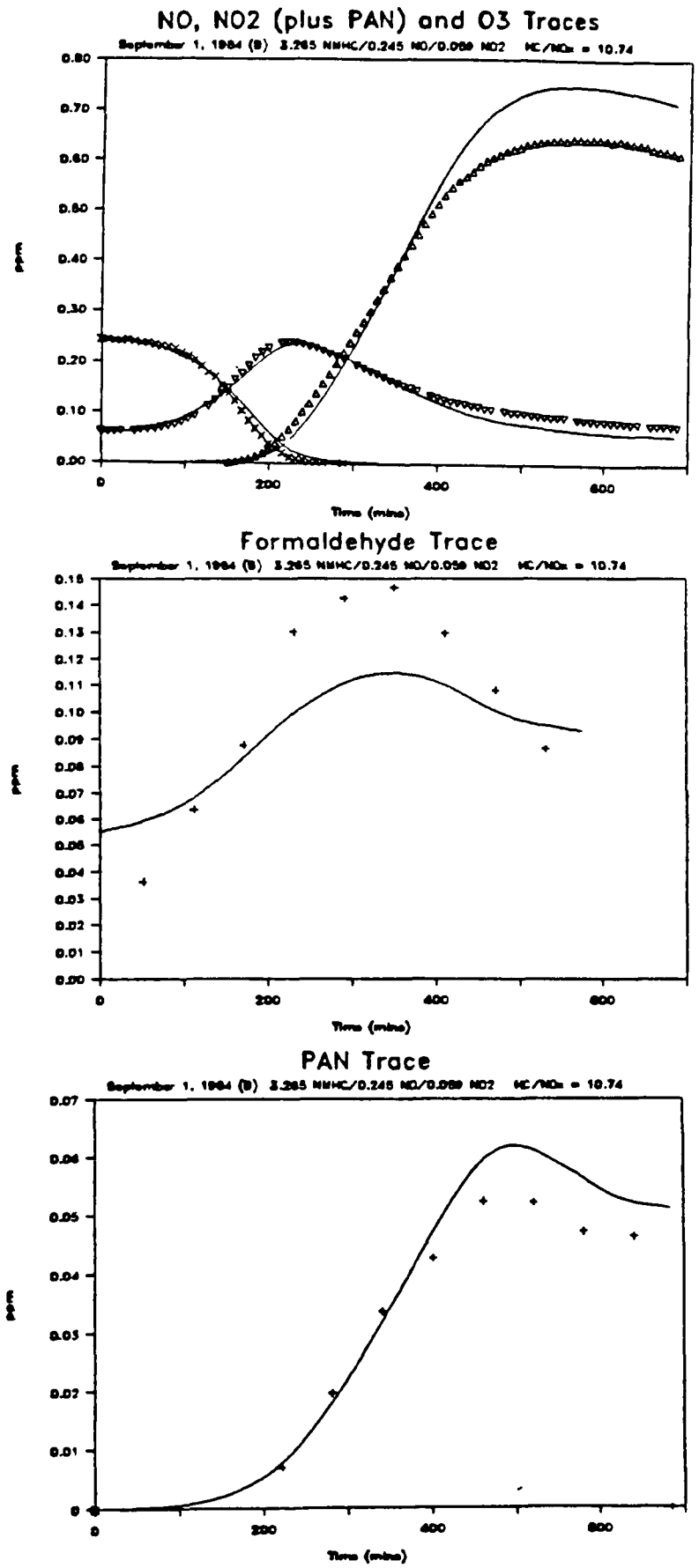

FIGURE 6-78. Simulation results for UNC experiment ST0184B (symbols are experimental measurements)

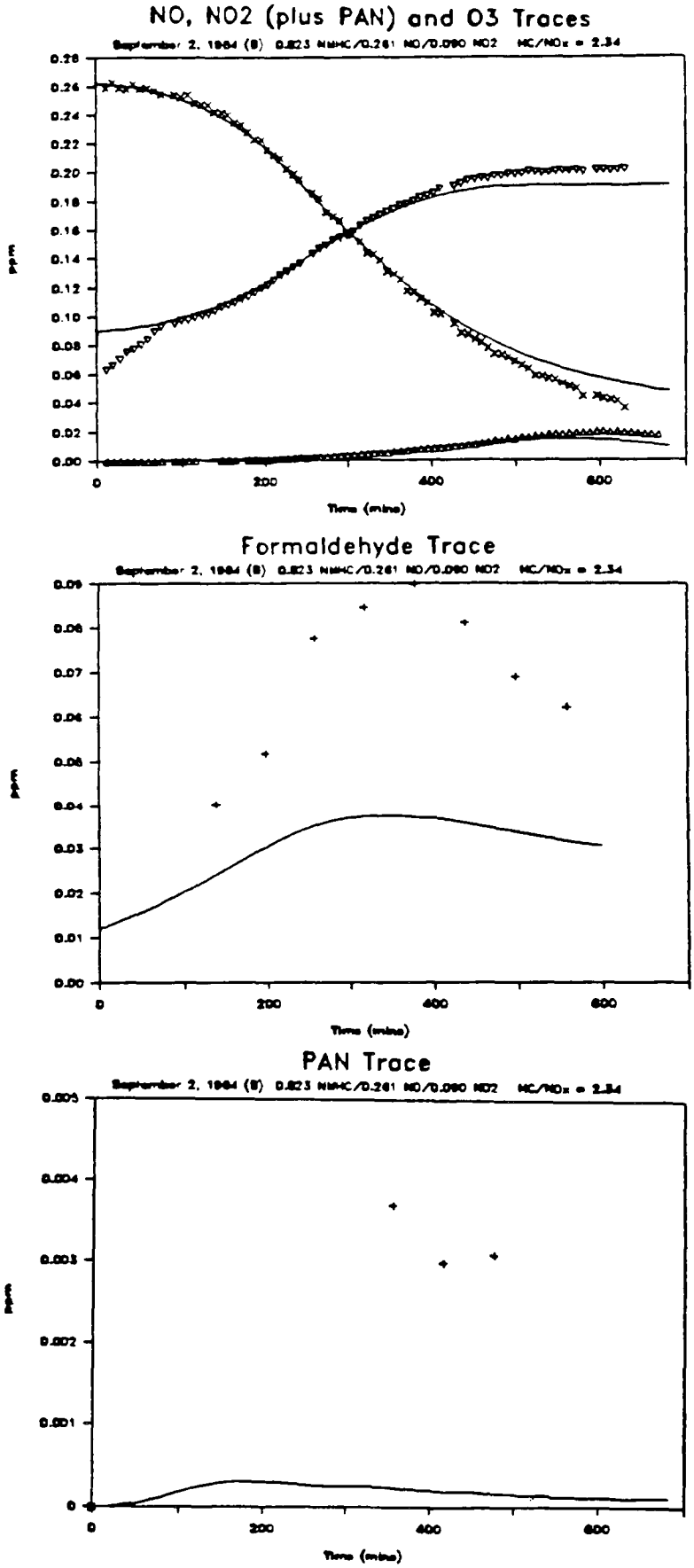

FIGURE 6-79. Simulation results for UNC experiment STO284B (symbols are experimental measurements)

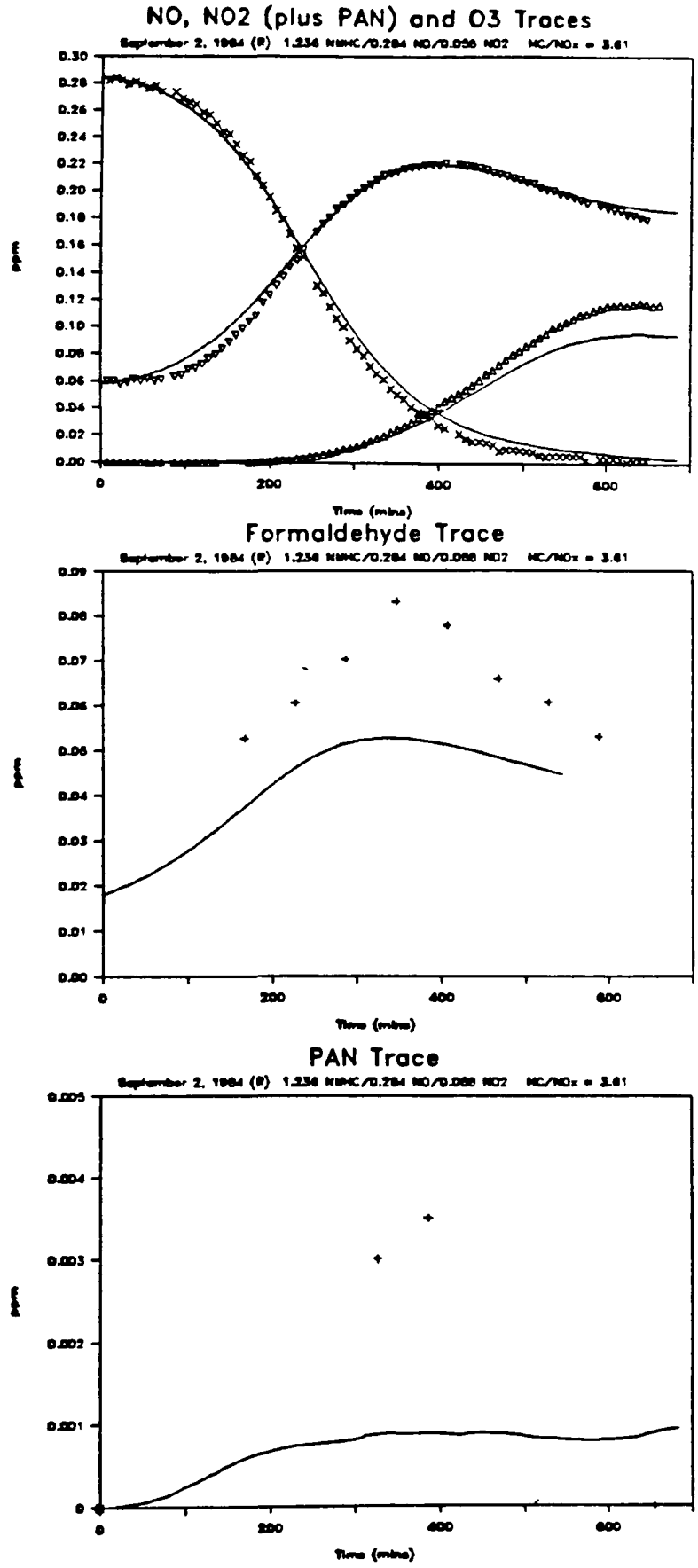

FIGURE 6-80. Simulation results for UNC experiment ST0284R (symbols are experimental measurements)

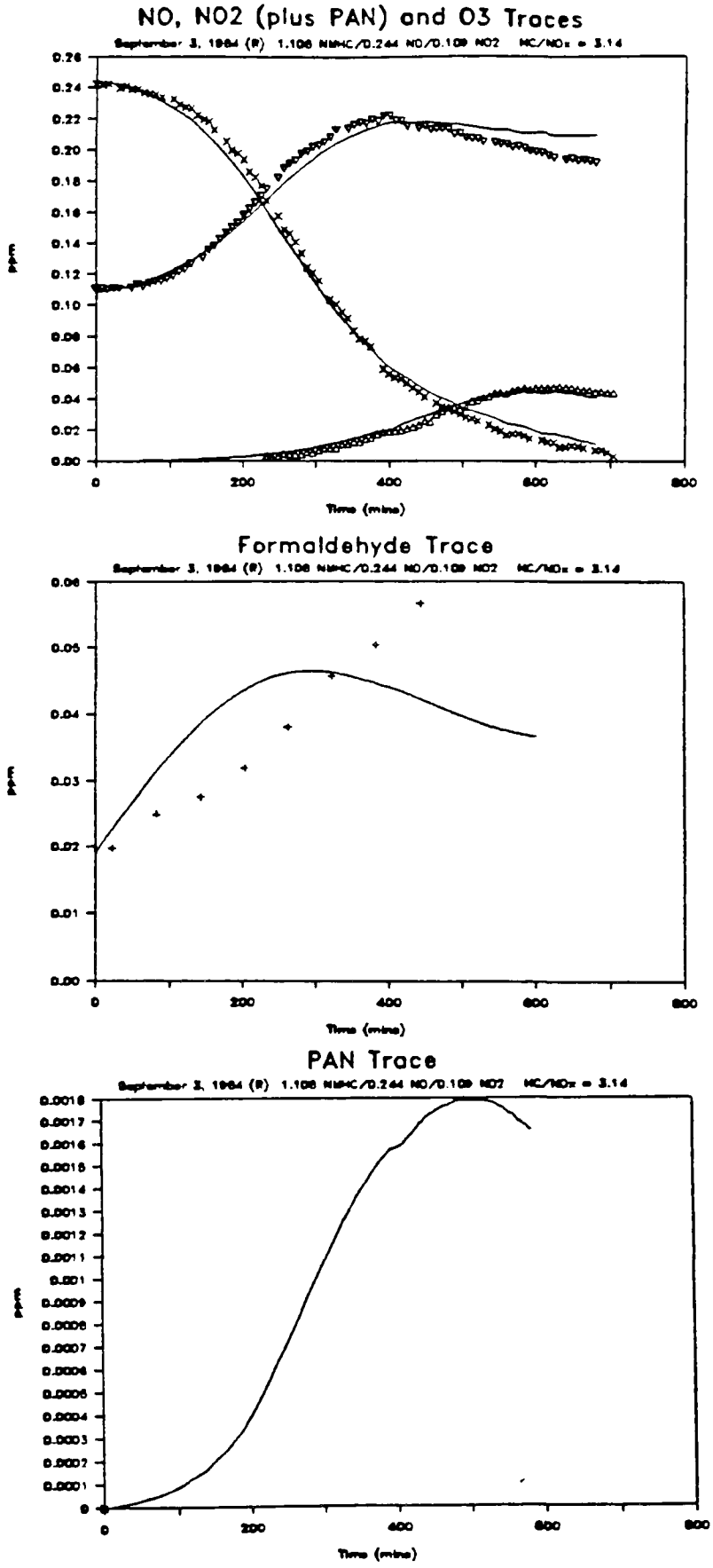

FIGURE 6-81. Simulation results for UNC experiment ST0384R (symbols are experimental measurements)

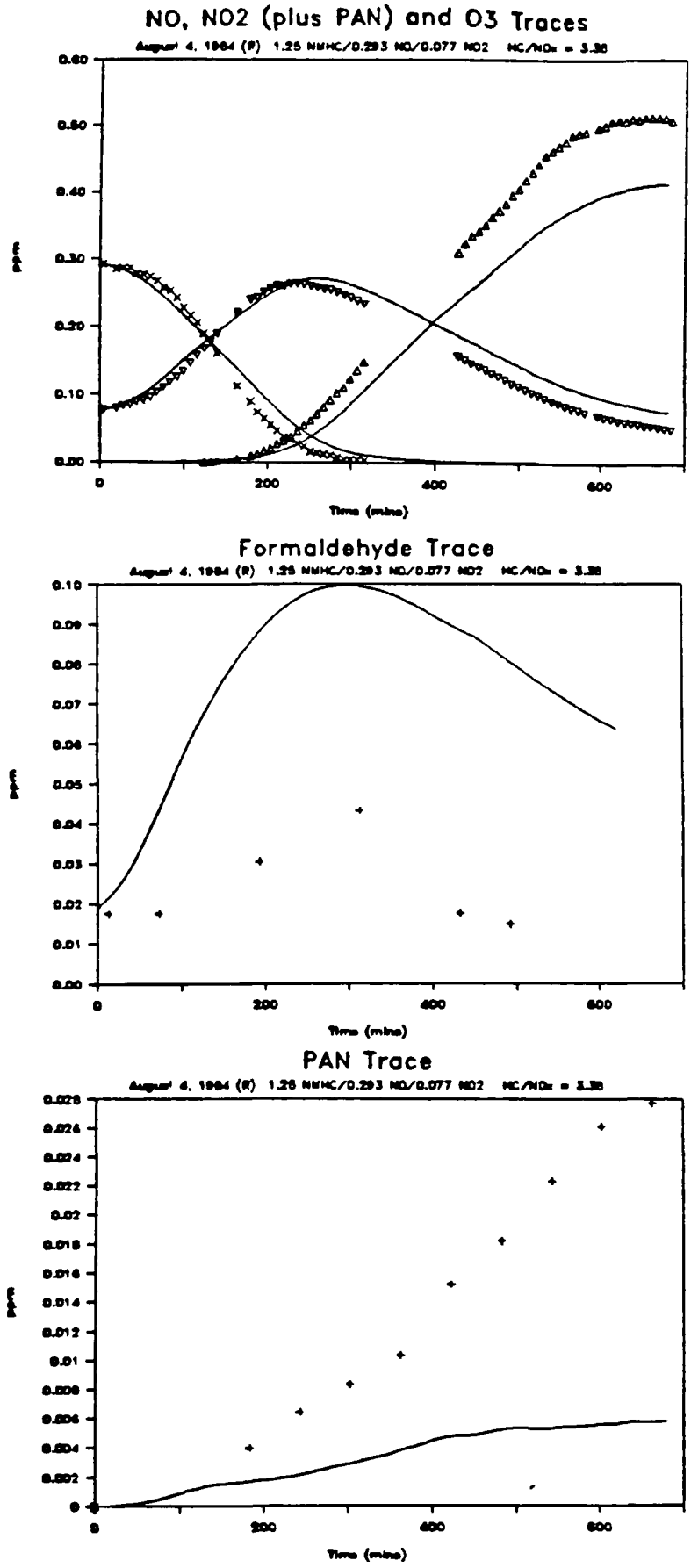

FIGURE 6-82. Simulation results for UNC experiment AU0484R (symbols are experimental measurements)

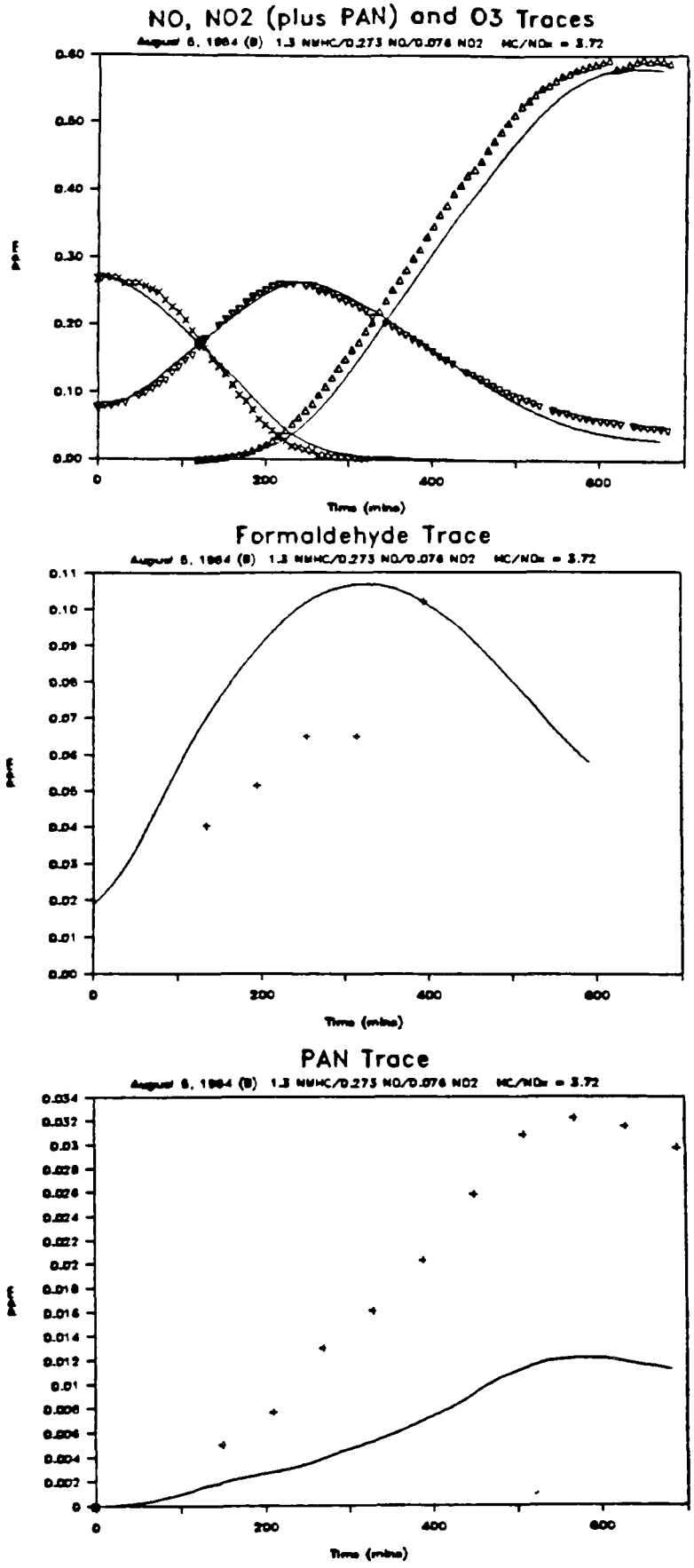

FIGURE 6-83. Simulation results for UNC experiment AU0584B (symbols are experimental measurements)

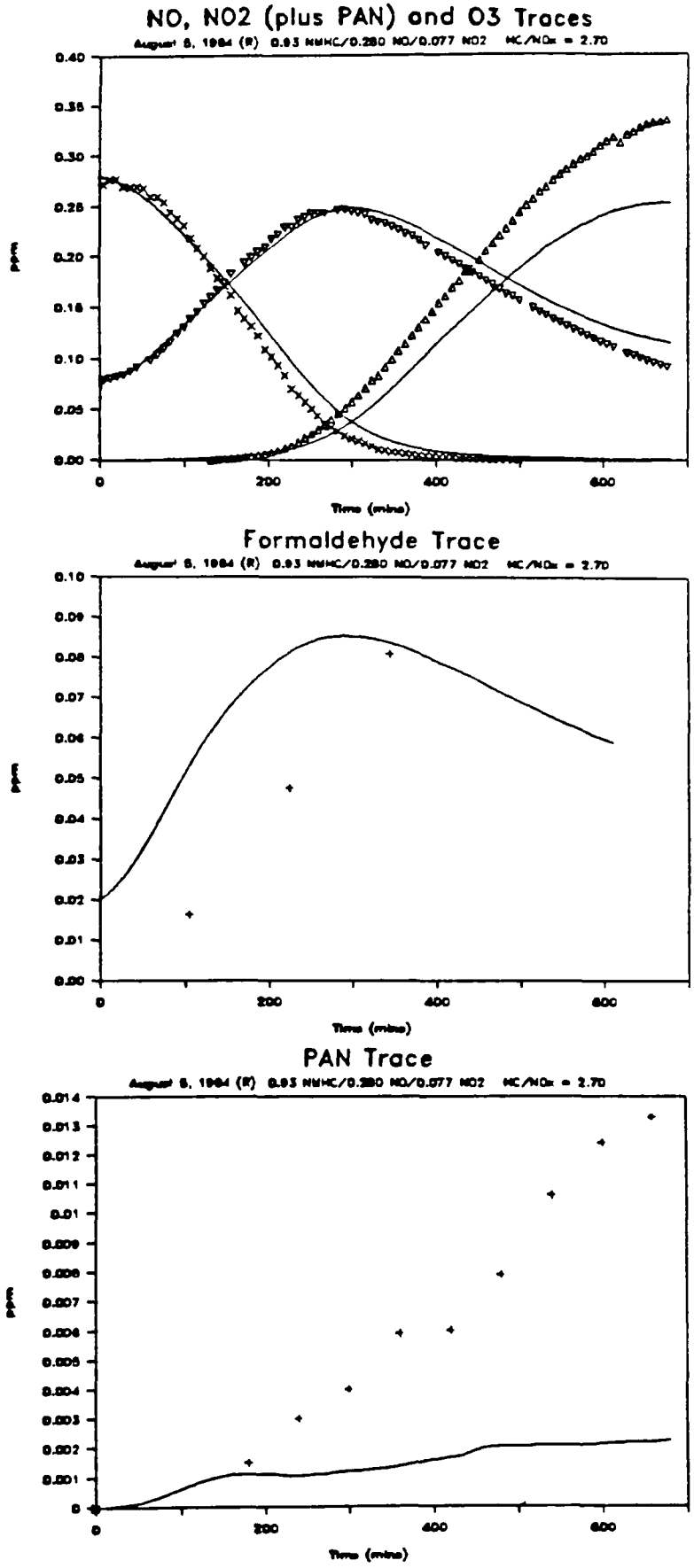

FIGURE 6-84. Simulation results for UNC experiment AU0584R (symbols are experimental measurements)

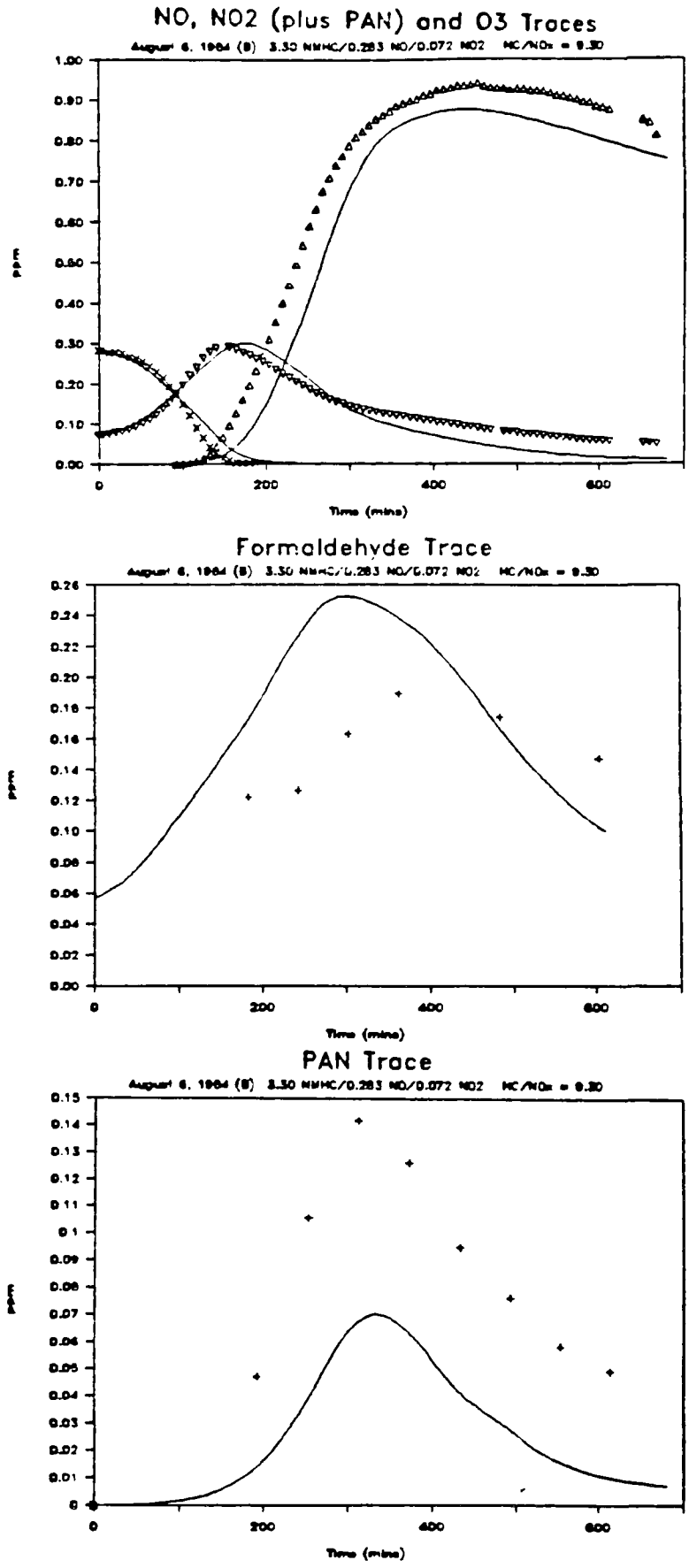

FIGURE 6-85. Simulation results for UNC experiment AU0684B (symbols are experimental measurements)

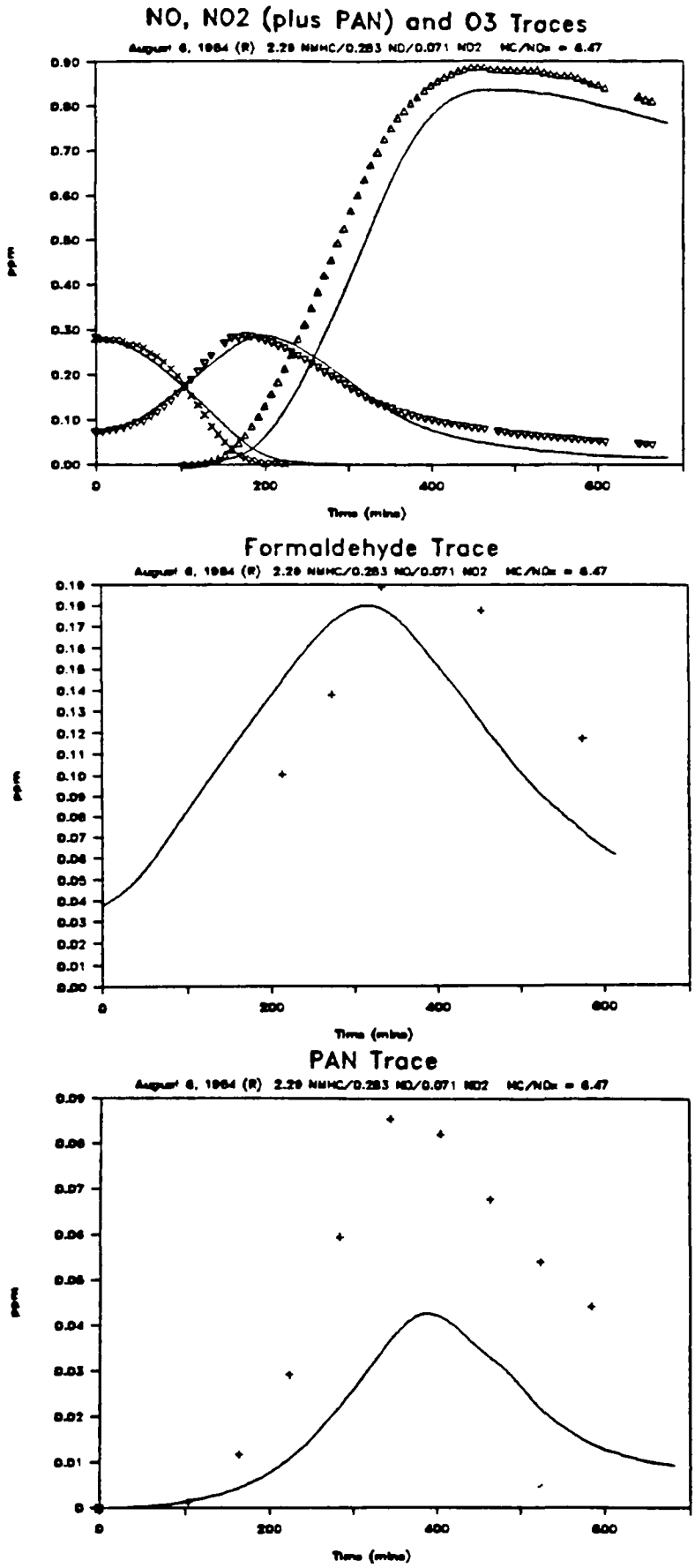

FIGURE 6-86. Simulation results for UNC experiment AU0684R (symbols are experimental measurements)

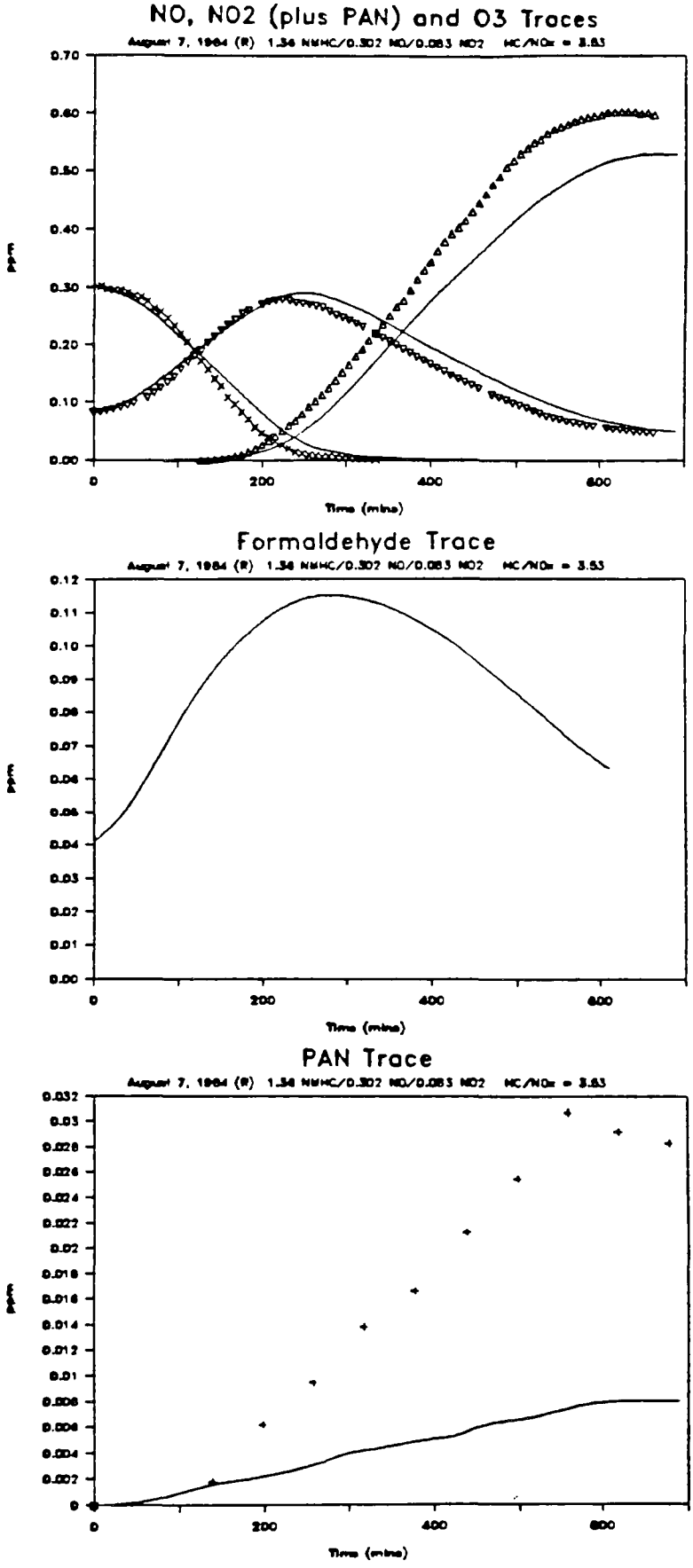

FIGURE 6-87. Simulation results for UNC experiment AU0784R (symbols are experimental measurements)

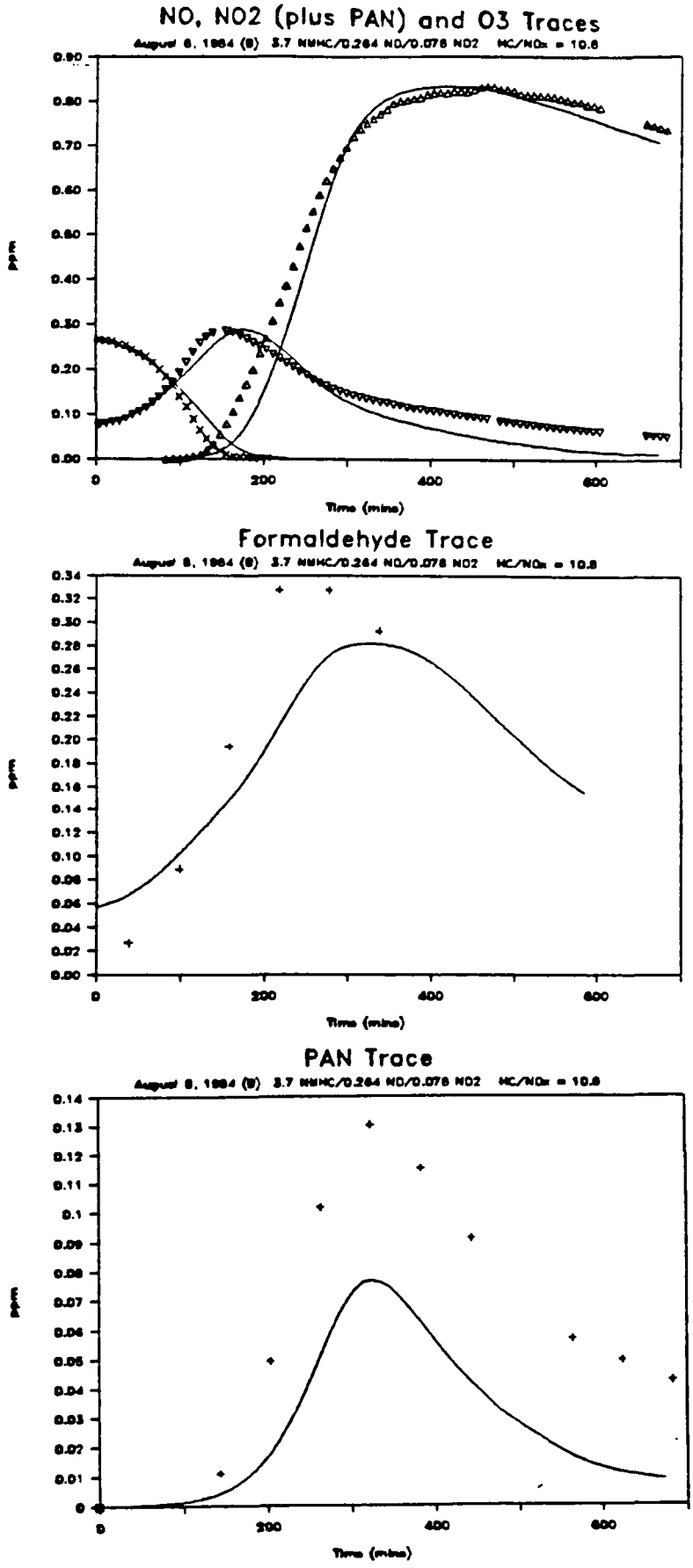

FIGURE 6-88. Simulation results for UNC experiment AU0884B (symbols are experimental measurements)

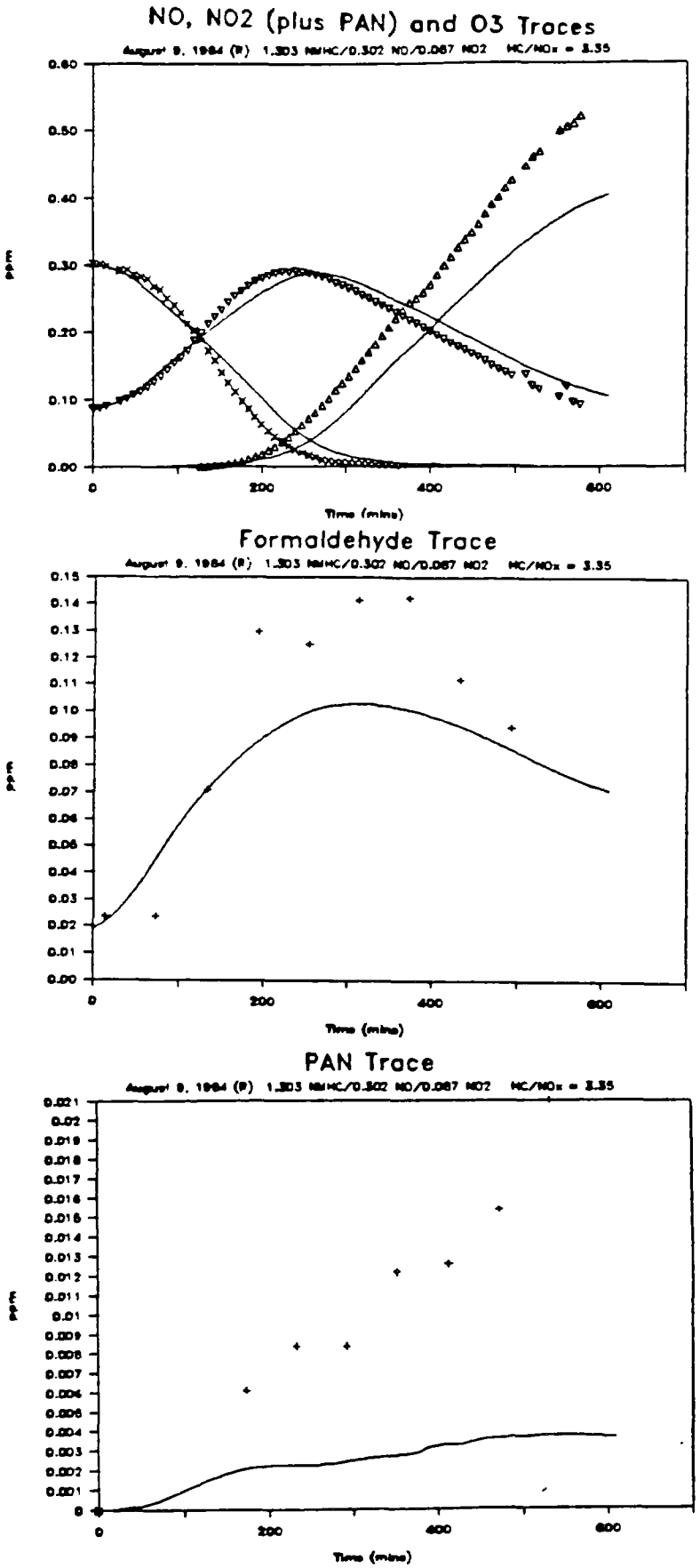

FIGURE 6-89. Simulation results for UNC experiment AU0984R (symbols are experimental measurements)

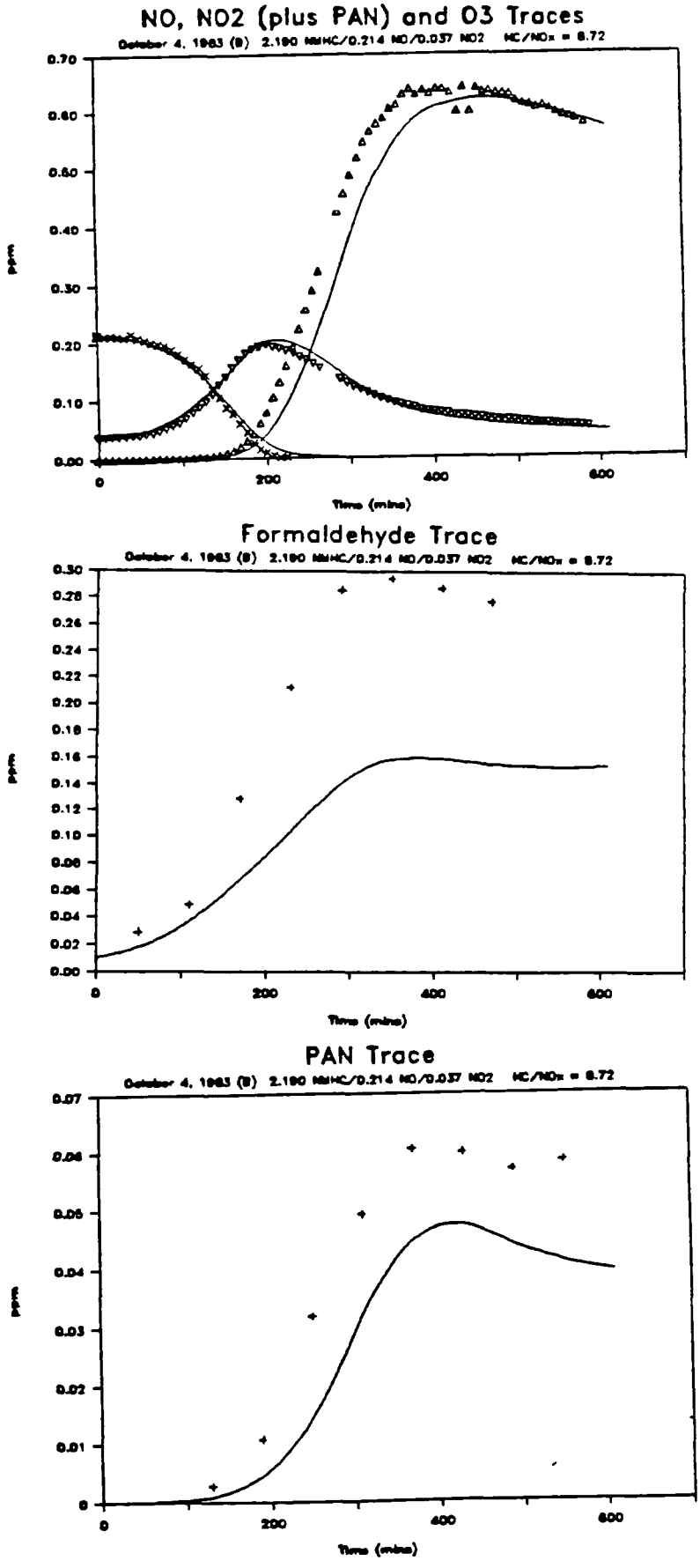

FIGURE 6-90. Simulation results for UNC experiment OC0483B (symbols are experimental measurements)

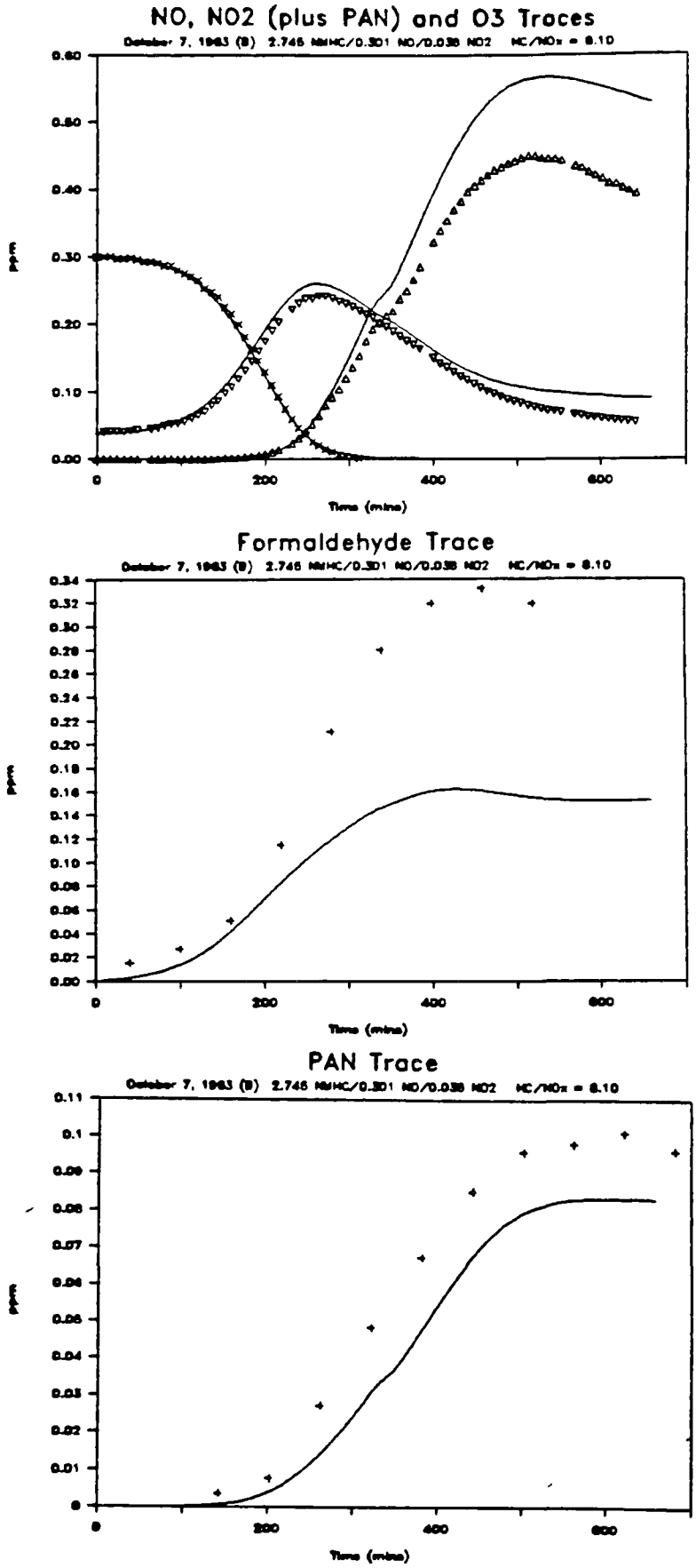

FIGURE 6-91. Simulation results for UNC experiment OC0783B (symbols are experimental measurements)

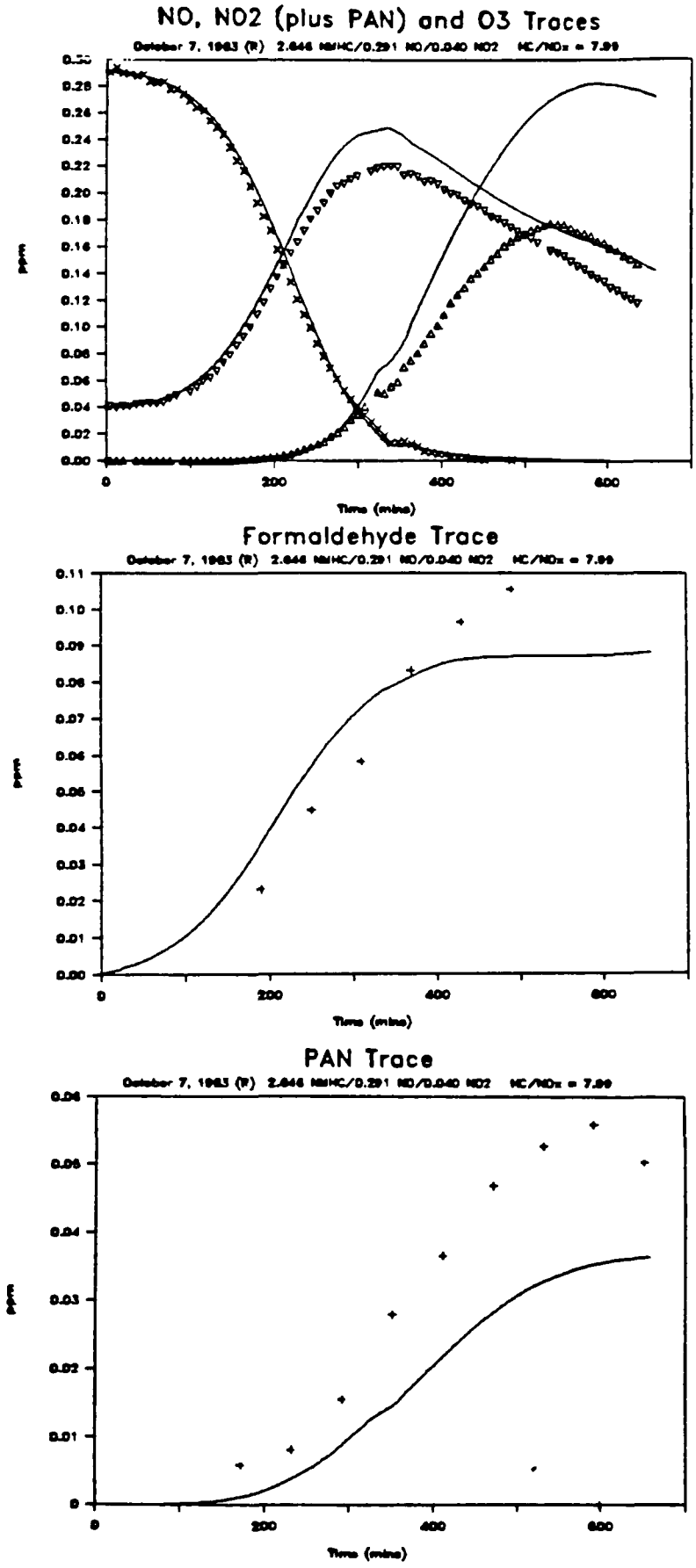

FIGURE 6-92. Simulation results for UNC experiment OC0783R (symbols are experimental measurements)

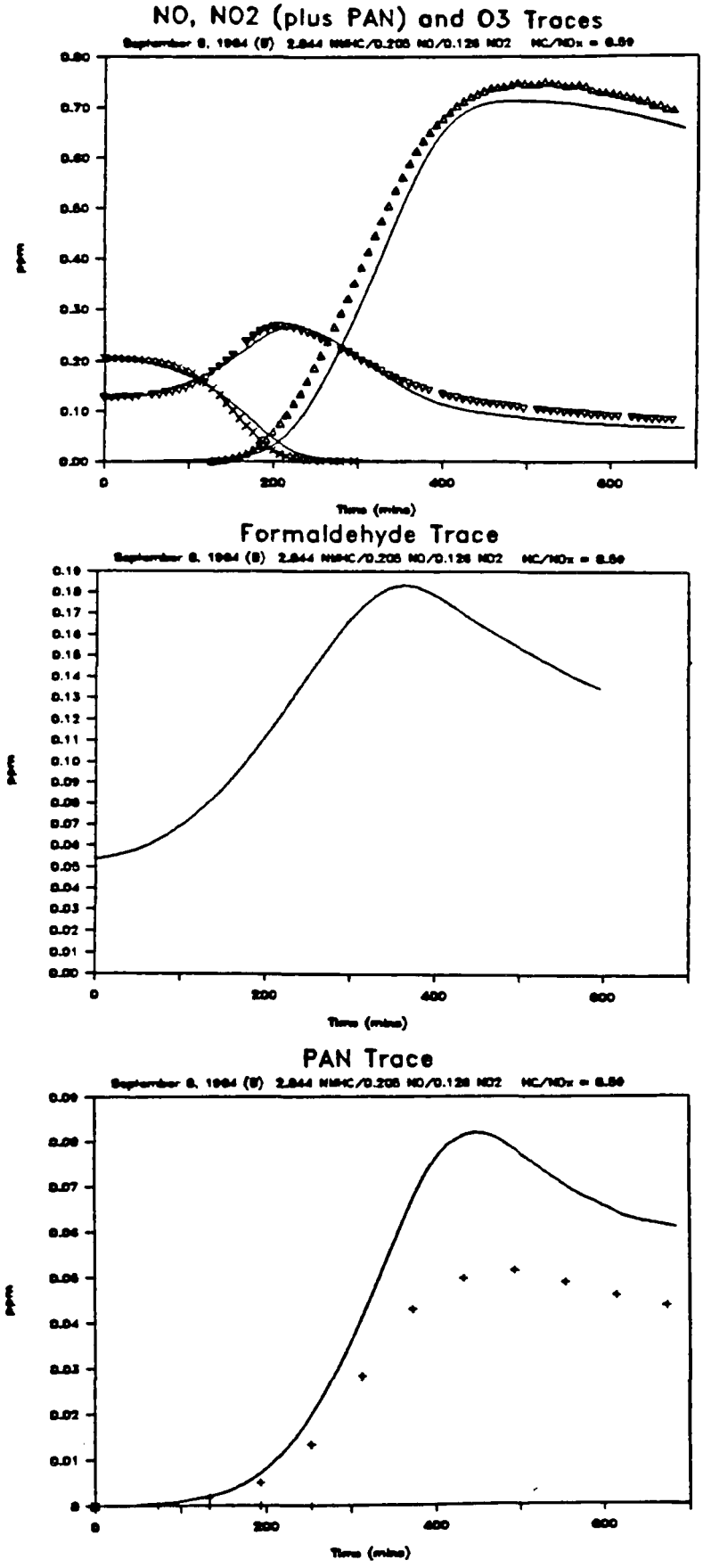

FIGURE 6-93. Simulation results for UNC experiment ST0884B (symbols are experimental measurements)

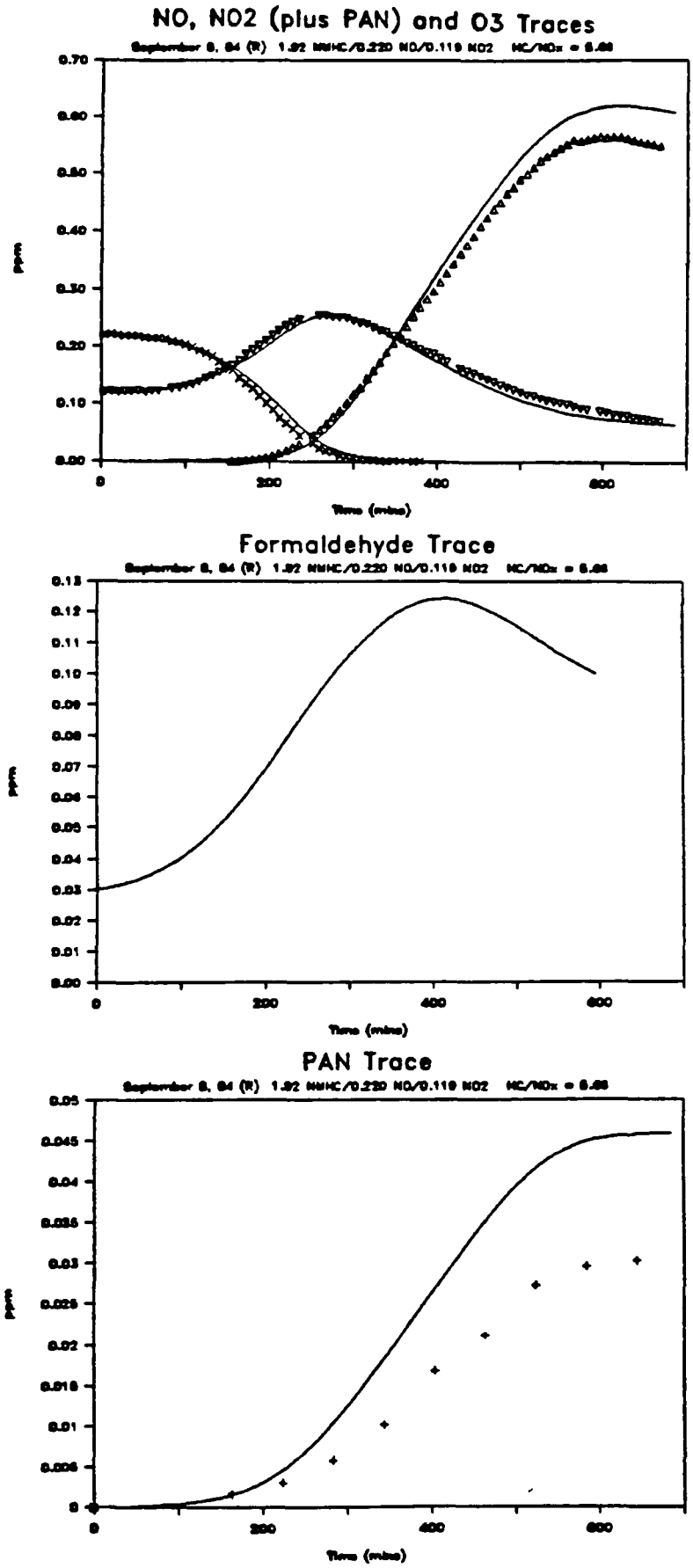

FIGURE 6-94. Simulation results for UNC experiment ST0884R (symbols are experimental measurements)

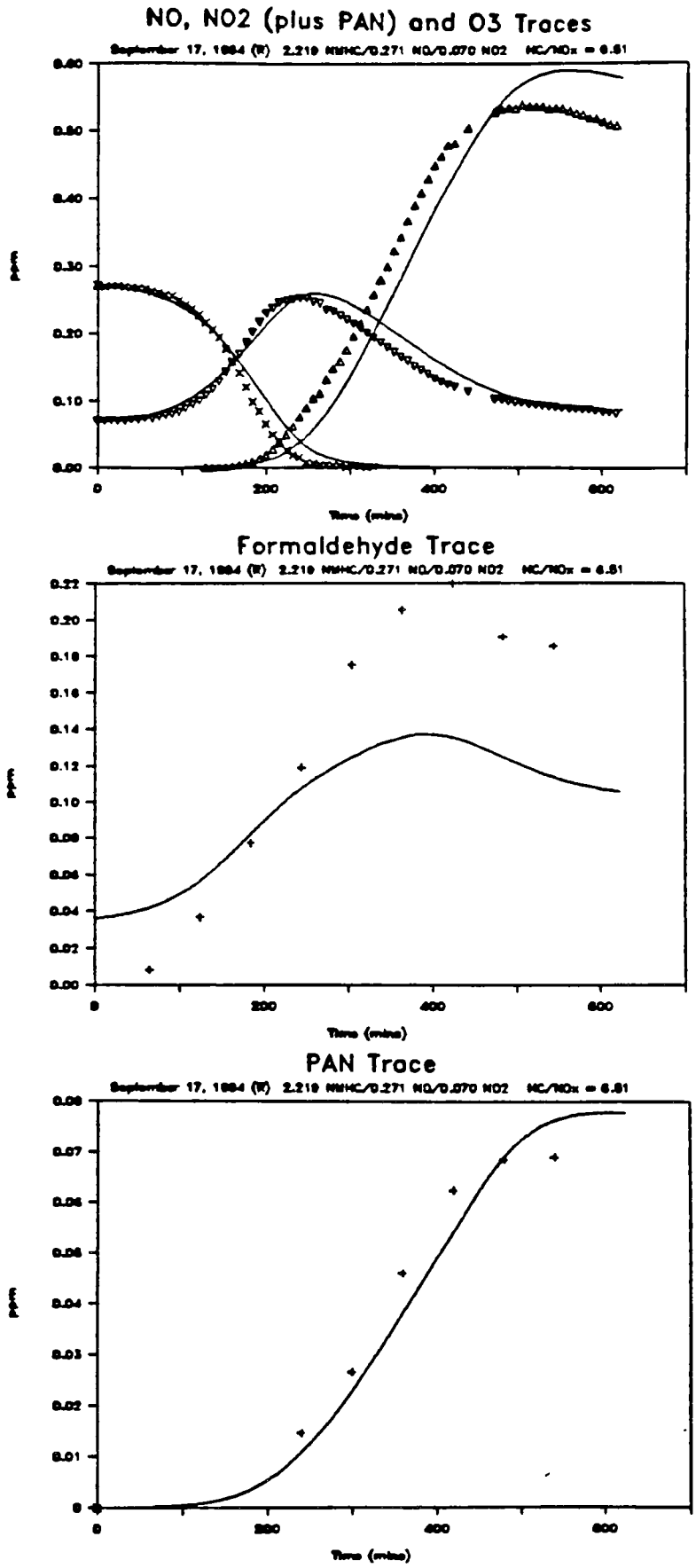

FIGURE 6-95. Simulation results for UNC experiment ST1784R (symbols are experimental measurements)

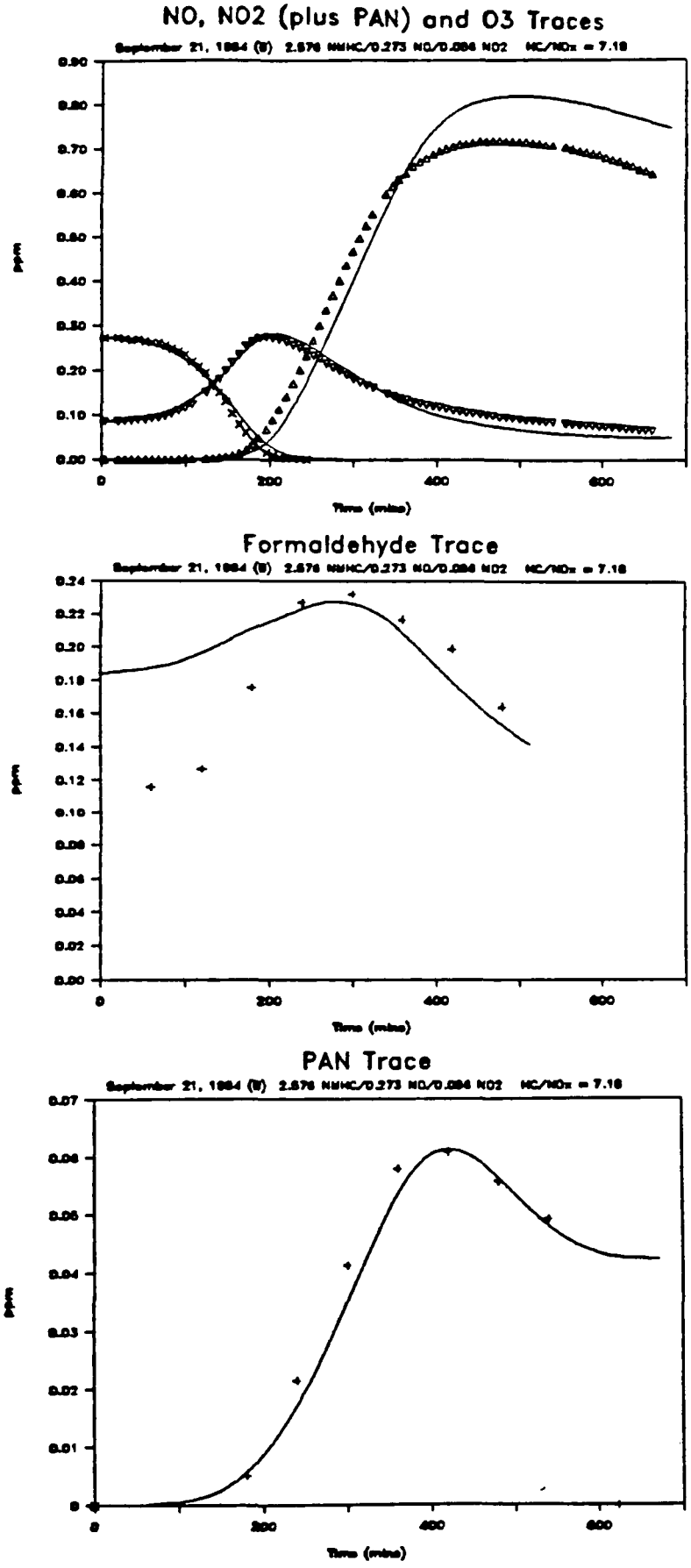

FIGURE 6-96. Simulation results for UNC experiment ST2184B (symbols are experimental measurements)

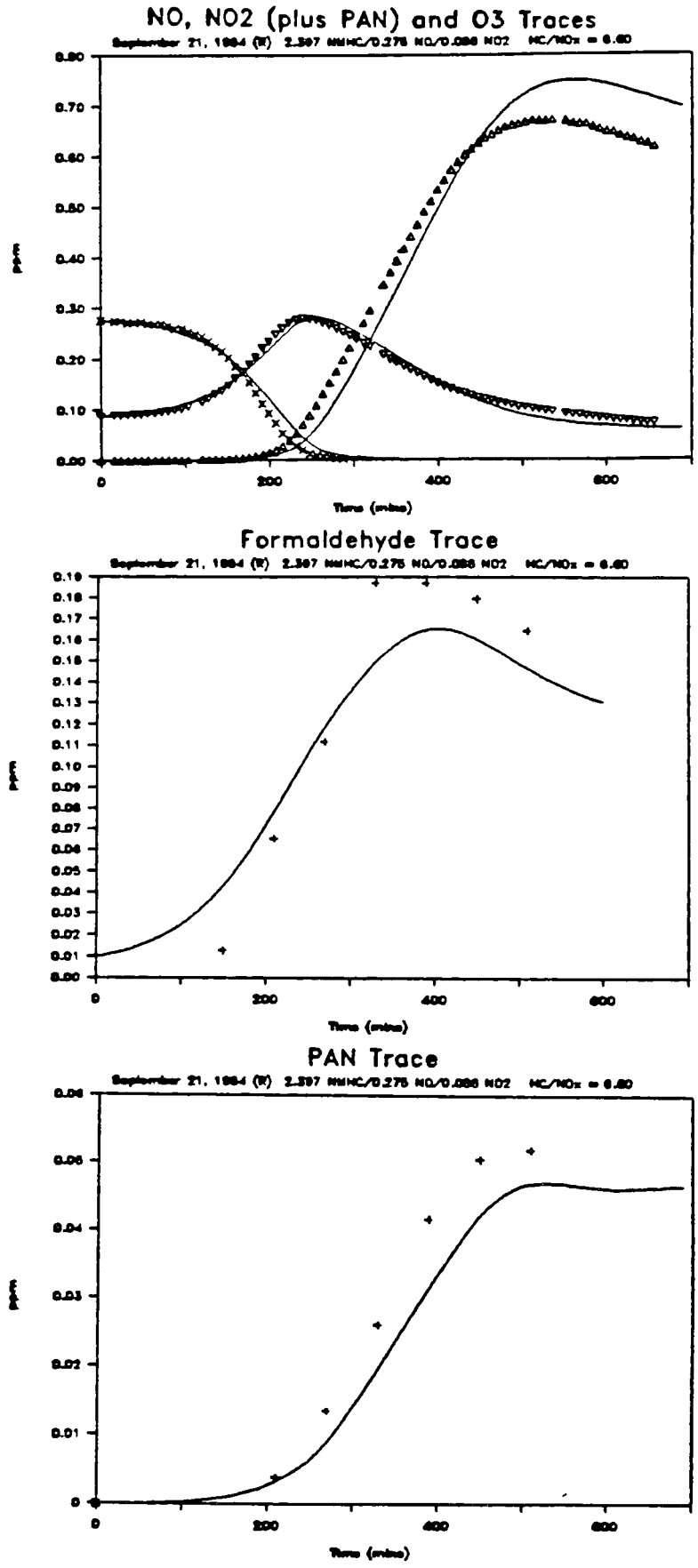

FIGURE 6-97. Simulation results for UNC experiment ST2184R (symbols are experimental measurements)

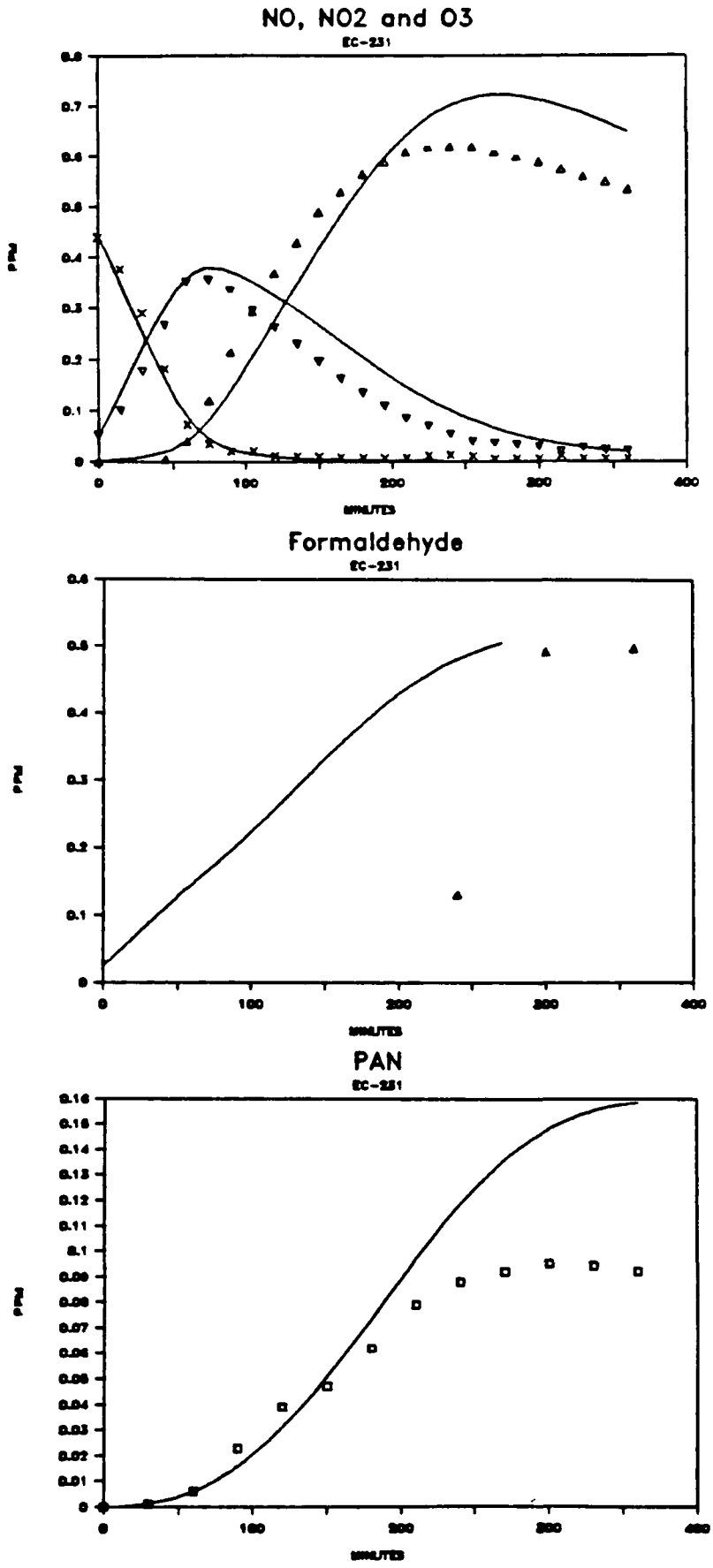

FIGURE 6-98. Simulation results for UCR experiment EC-231 (symbols are experimental measurements)

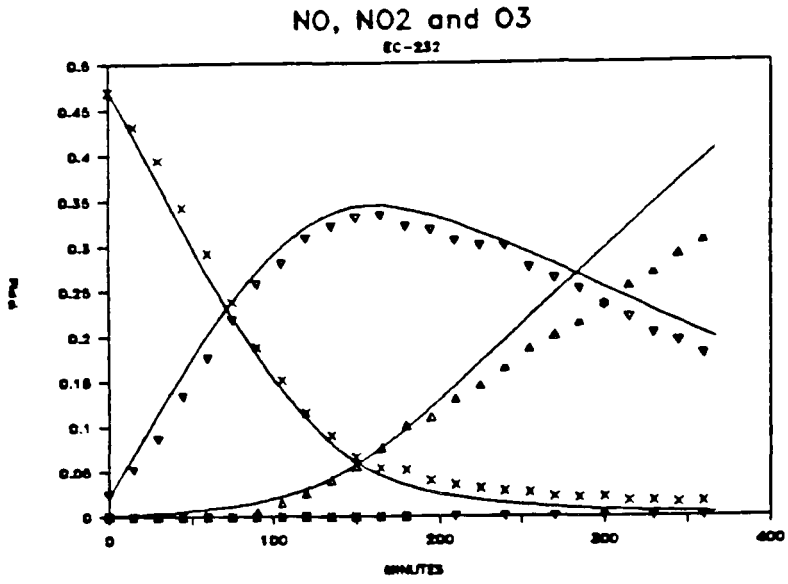

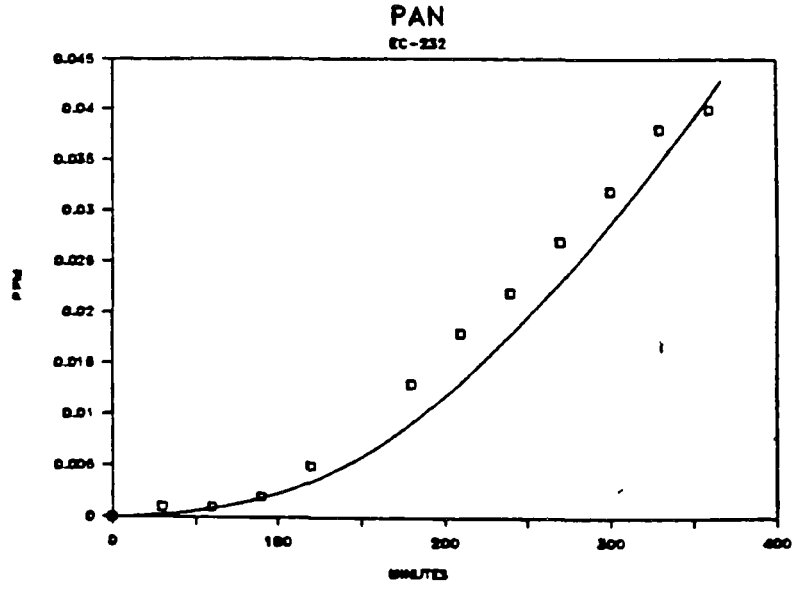

FIGURE 6-99. Simulation results for UCR experiment EC-232 (symbols are experimental measurements)

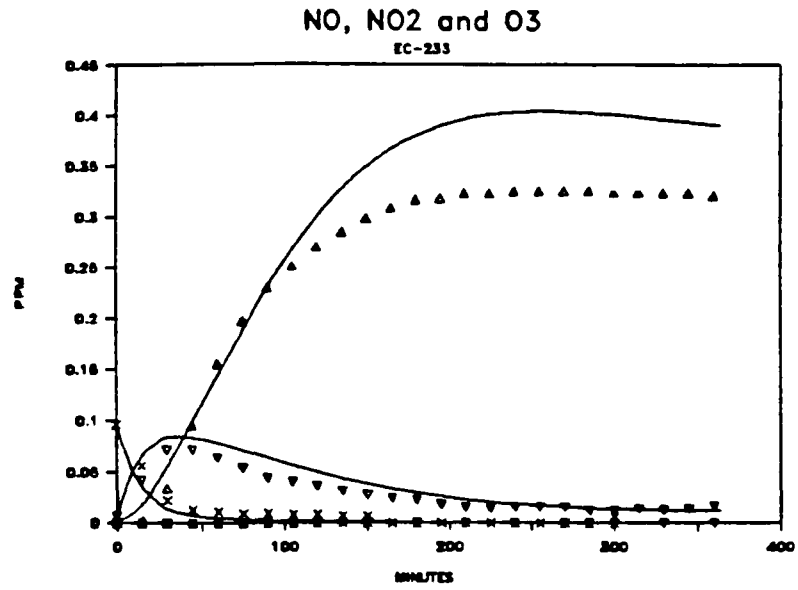

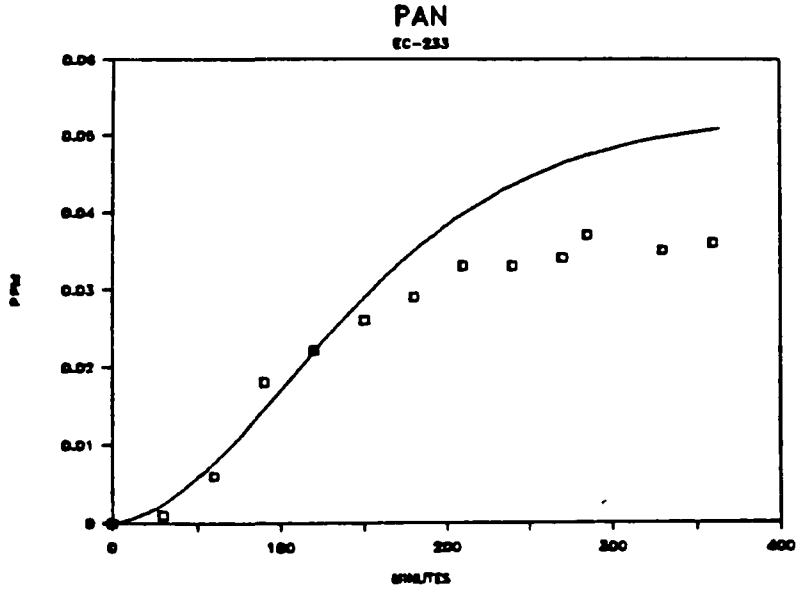

FIGURE 6-100. Simulation results for UCR experiment EC-233 (symbols are experimental measurements)

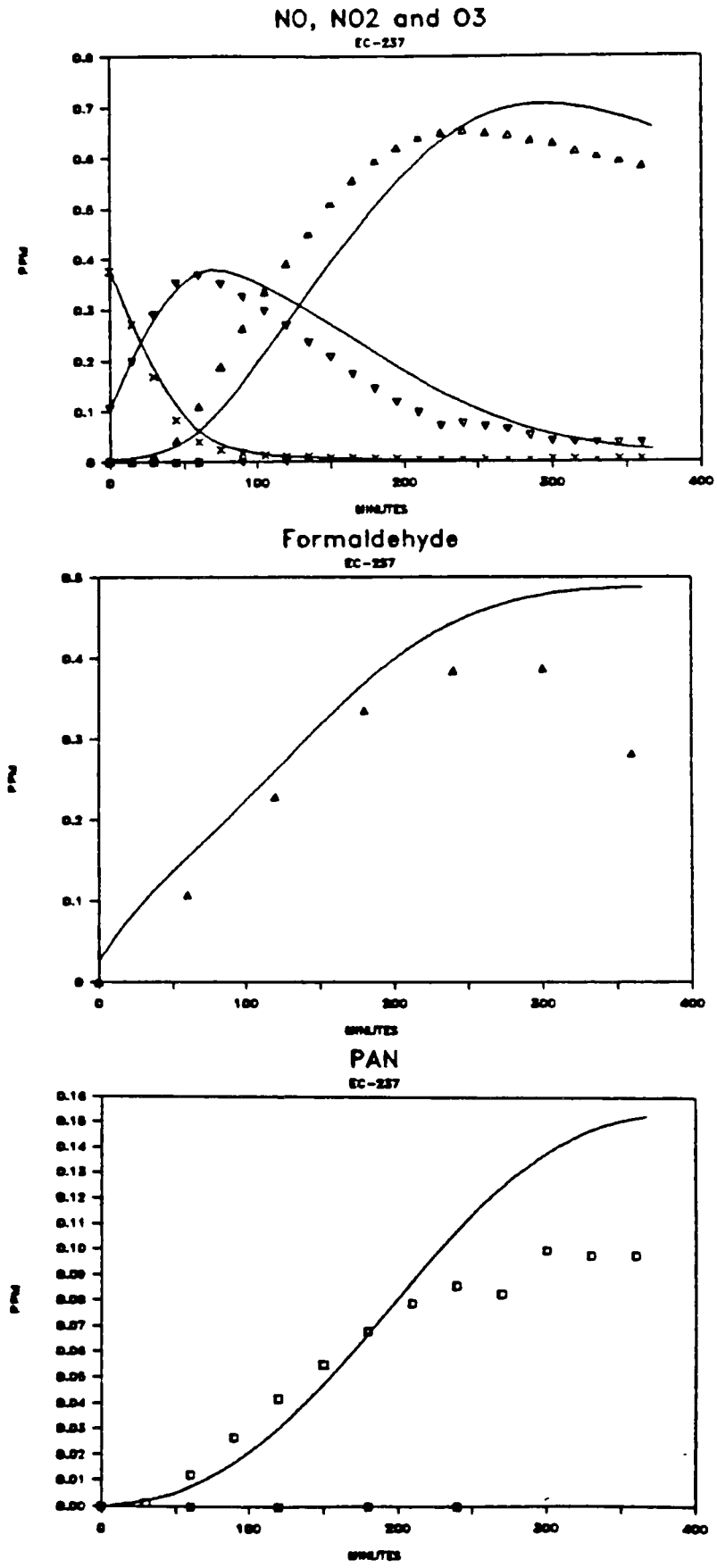

FIGURE 6-101. Simulation results for UCR experiment EC-237 (symbols are experimental measurements)

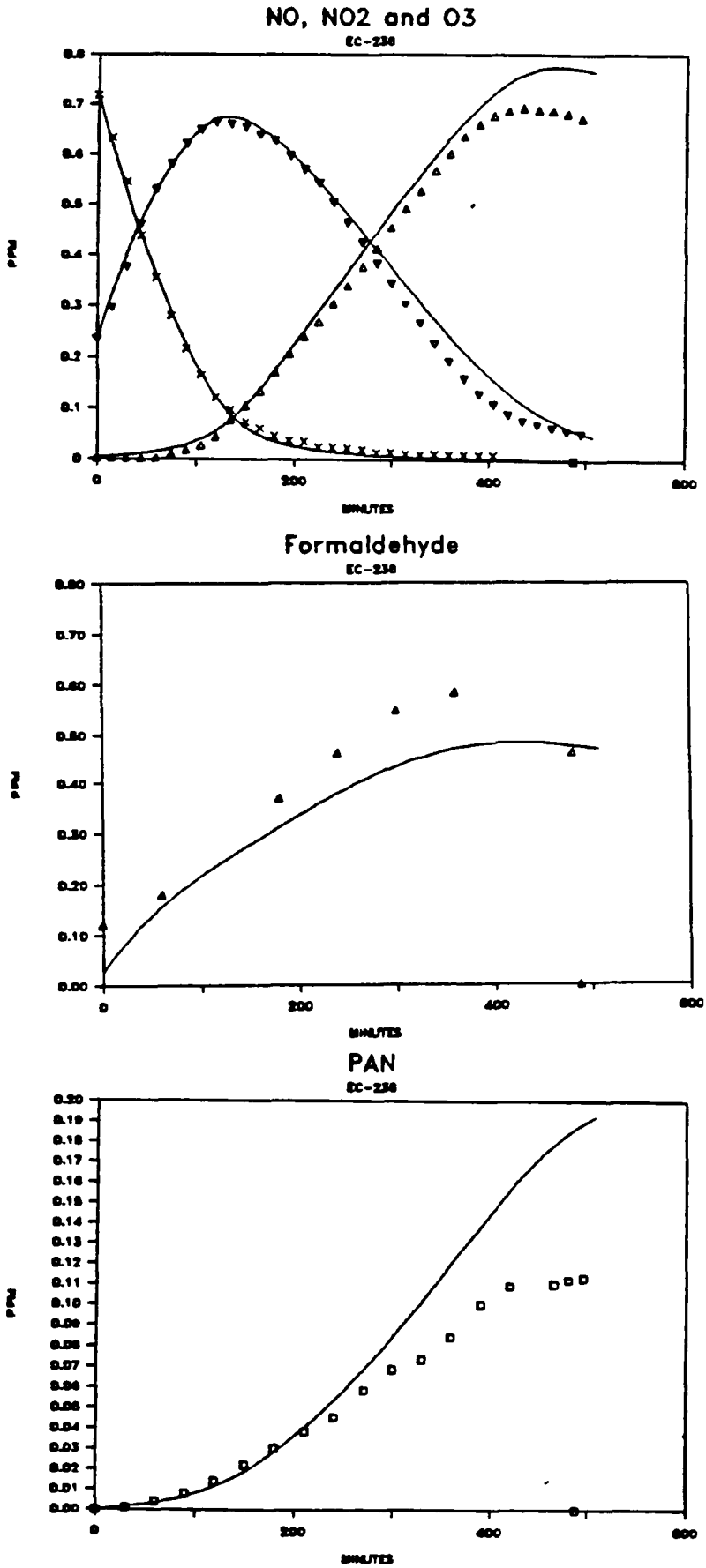

FIGURE 6-102. Simulation results for UCR experiment EC-238 (symbols are experimental measurements)

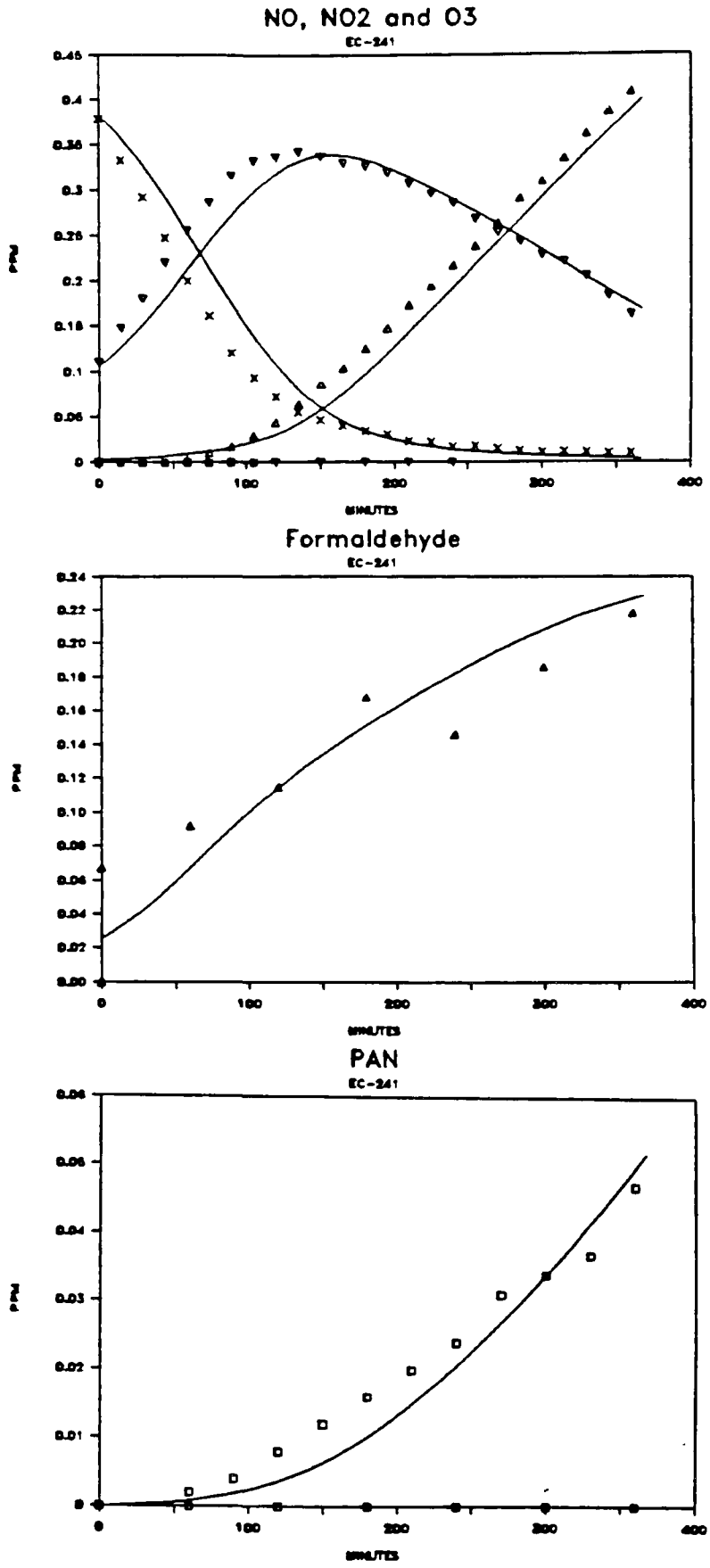

FIGURE 6-103. Simulation results for UCR experiment EC-241 (symbols are experimental measurements)

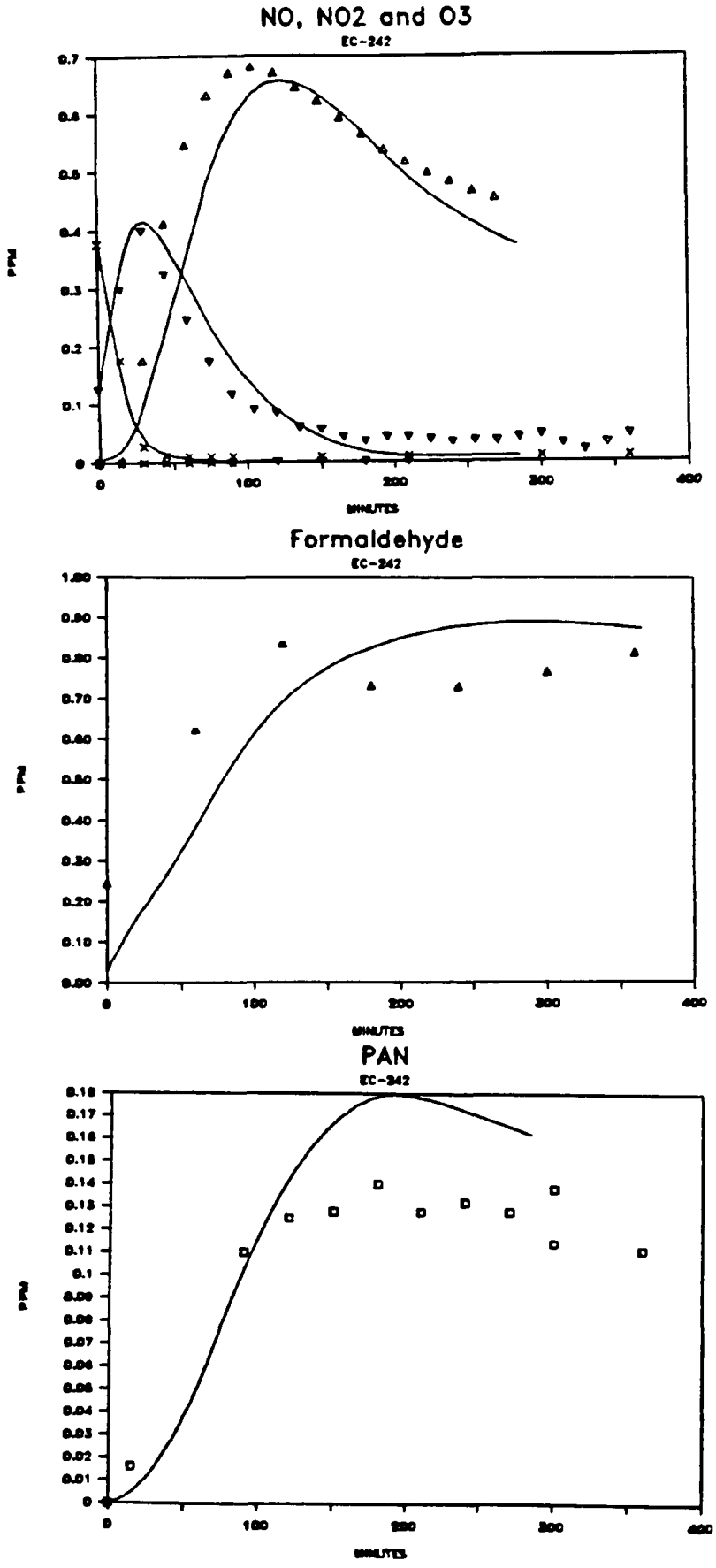

FIGURE 6-104. Simulation results for UCR experiment EC-242 (symbols are experimental measurements)

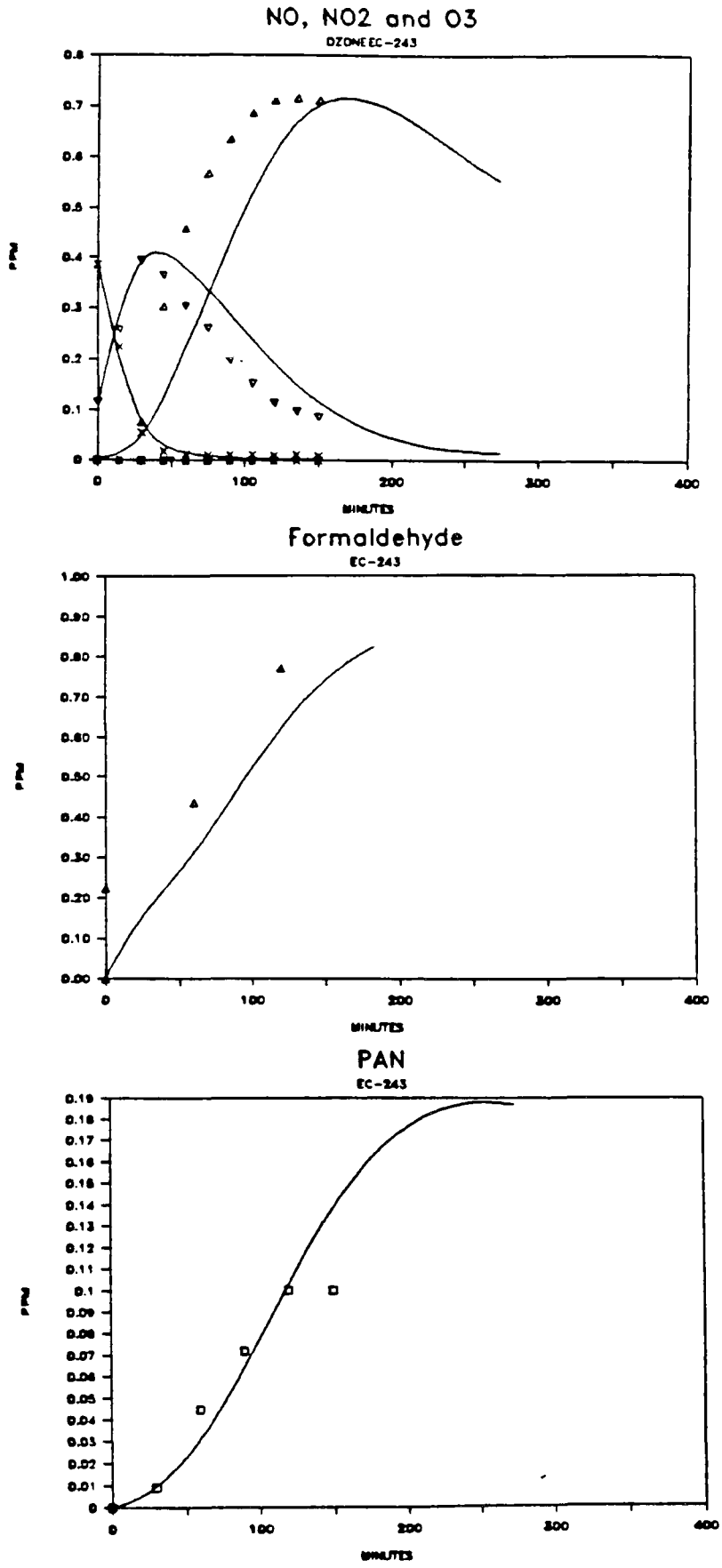

FIGURE 6-105. Simulation results for UCR experiment EC-243 (symbols are experimental measurements)

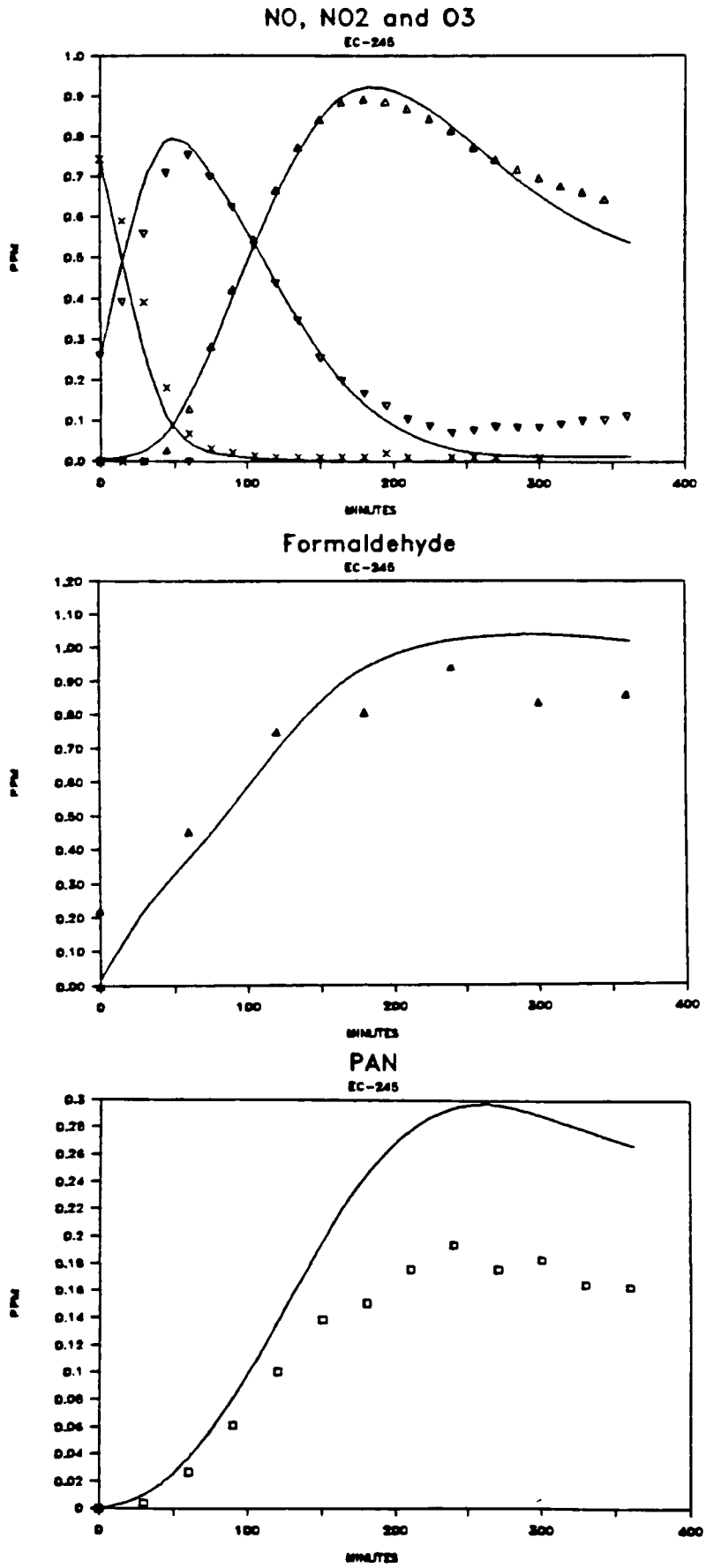

FIGURE 6-106. Simulation results for UCR experiment EC-245 (symbols are experimental measurements)

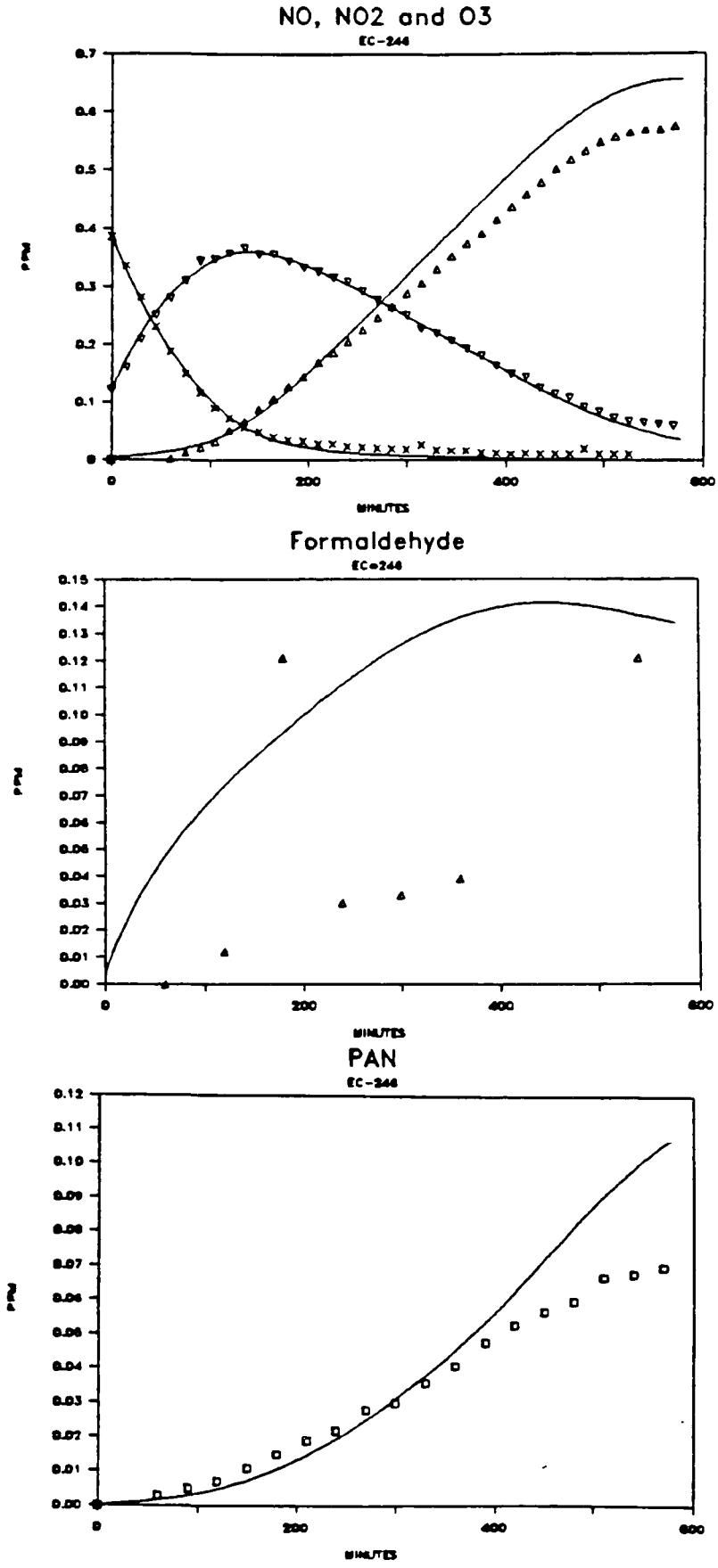

FIGURE 6-107. Simulation results for UCR experiment EC-246 (symbols are experimental measurements)

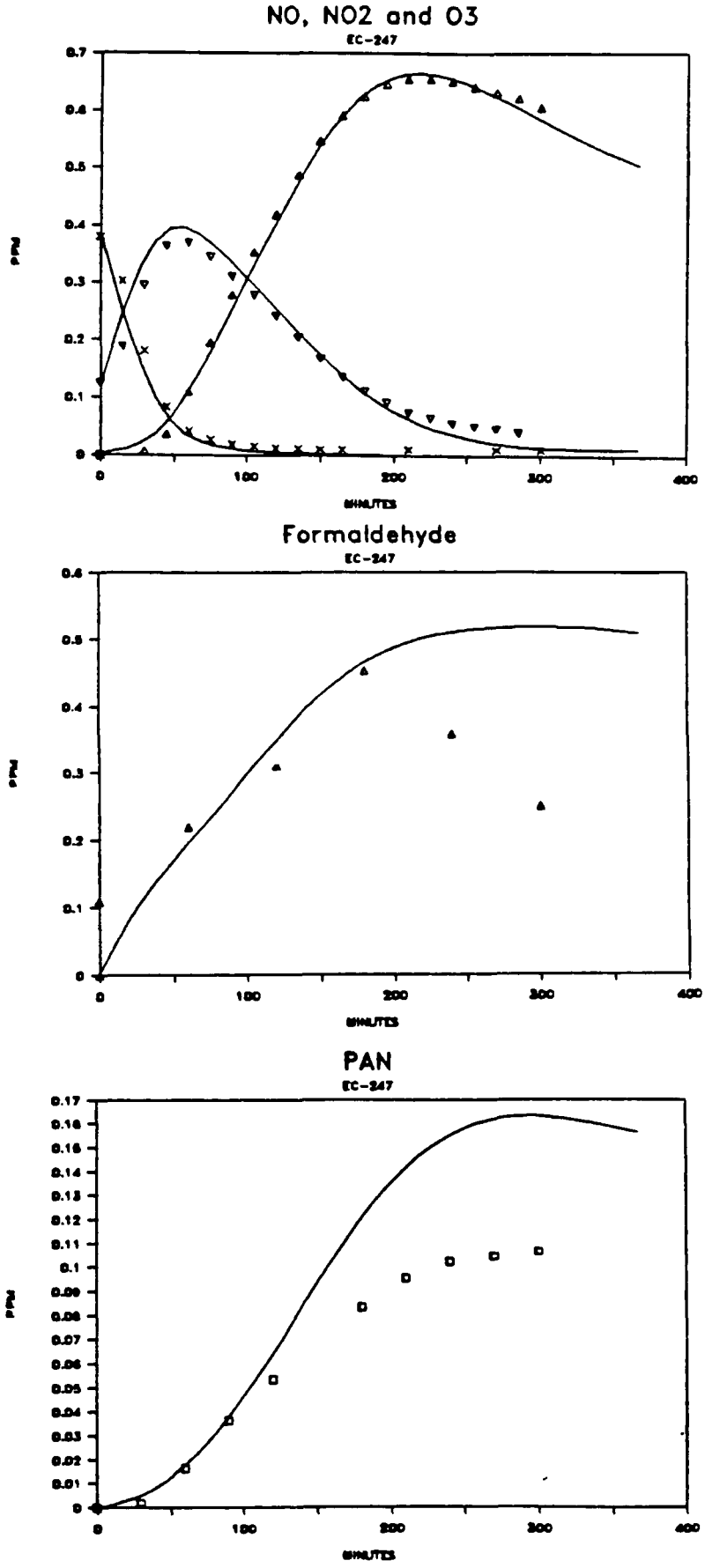

FIGURE 6-108. Simulation results for UCR experiment EC-247 (symbols are experimental measurements)

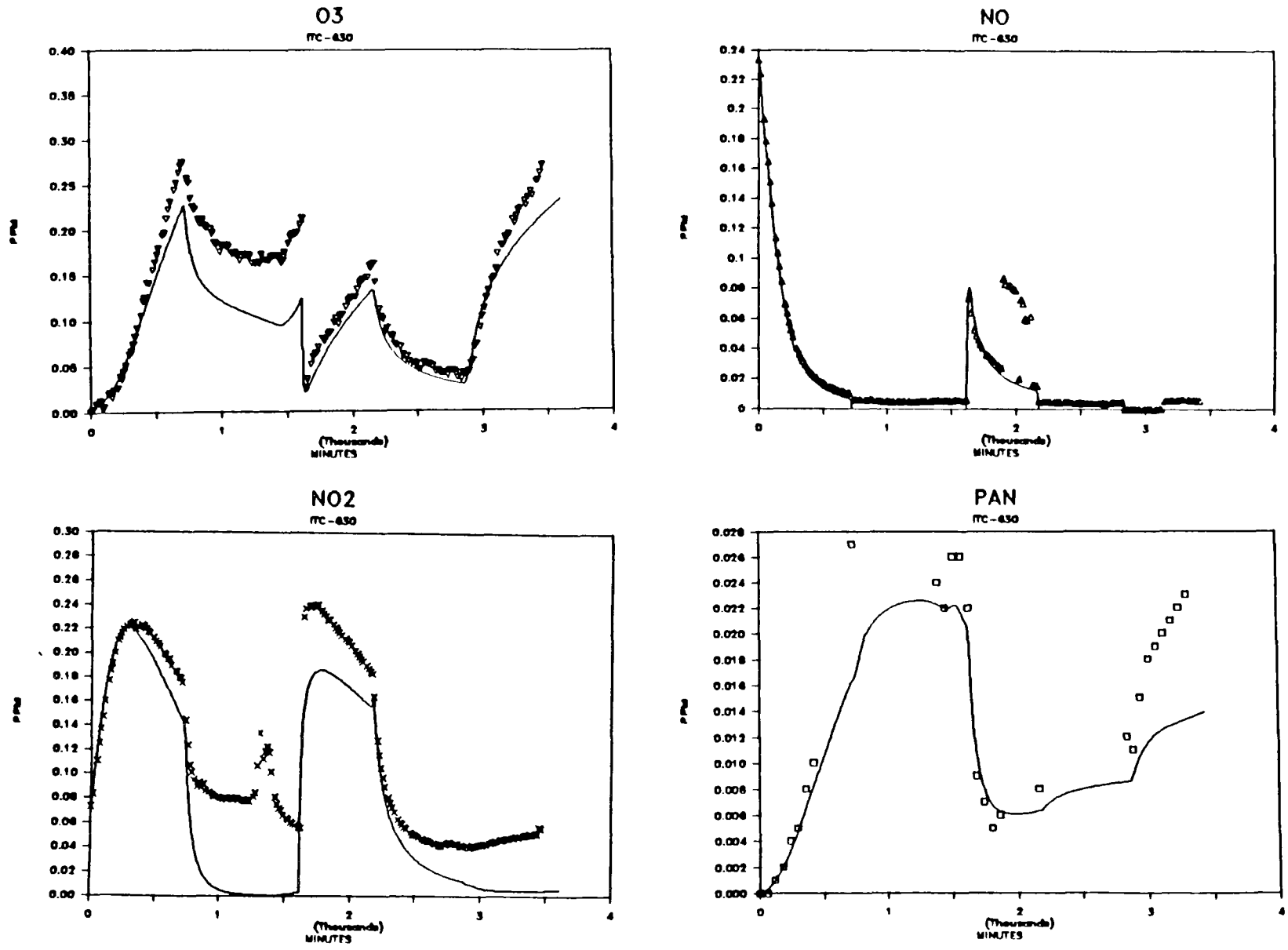

FIGURE 6-109. Simulation results for UCR experiment ITC-630
(symbols are experimental measurements)

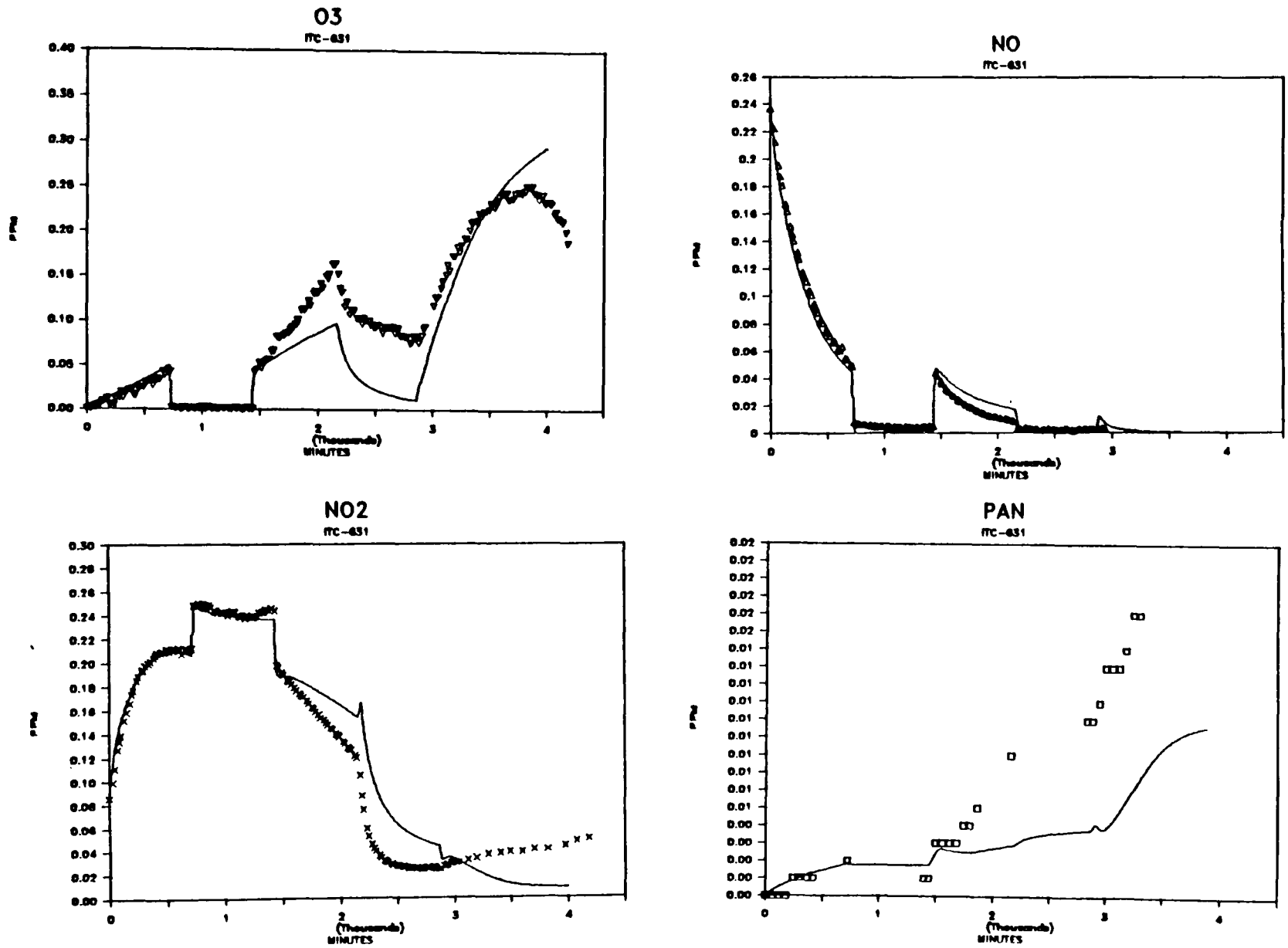

FIGURE 6-110. Simulation results for UCR experiment ITC-631
(symbols are experimental measurements)

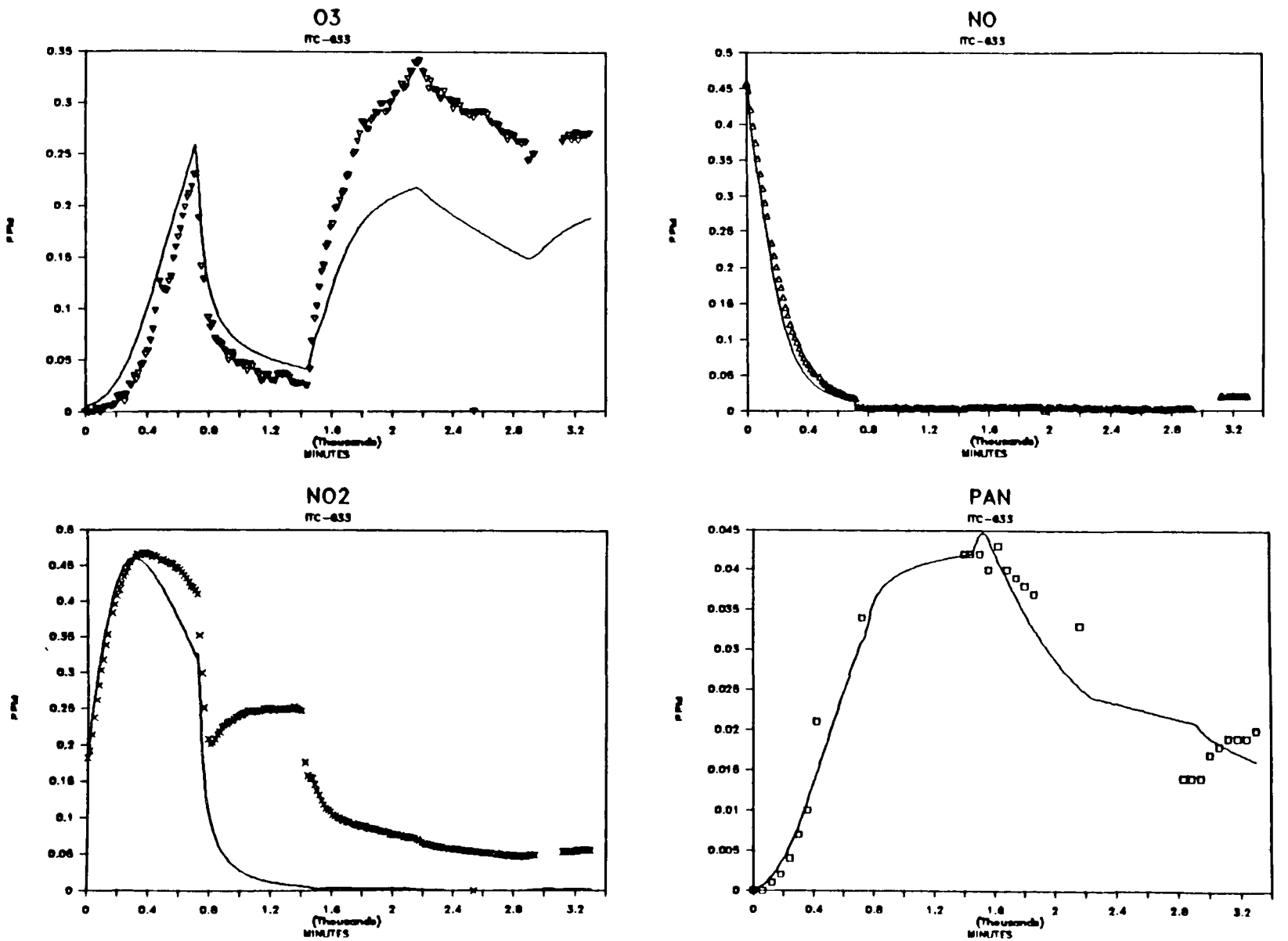

FIGURE 6-111. Simulation results for UCR experiment ITC-633
(symbols are experimental measurements)

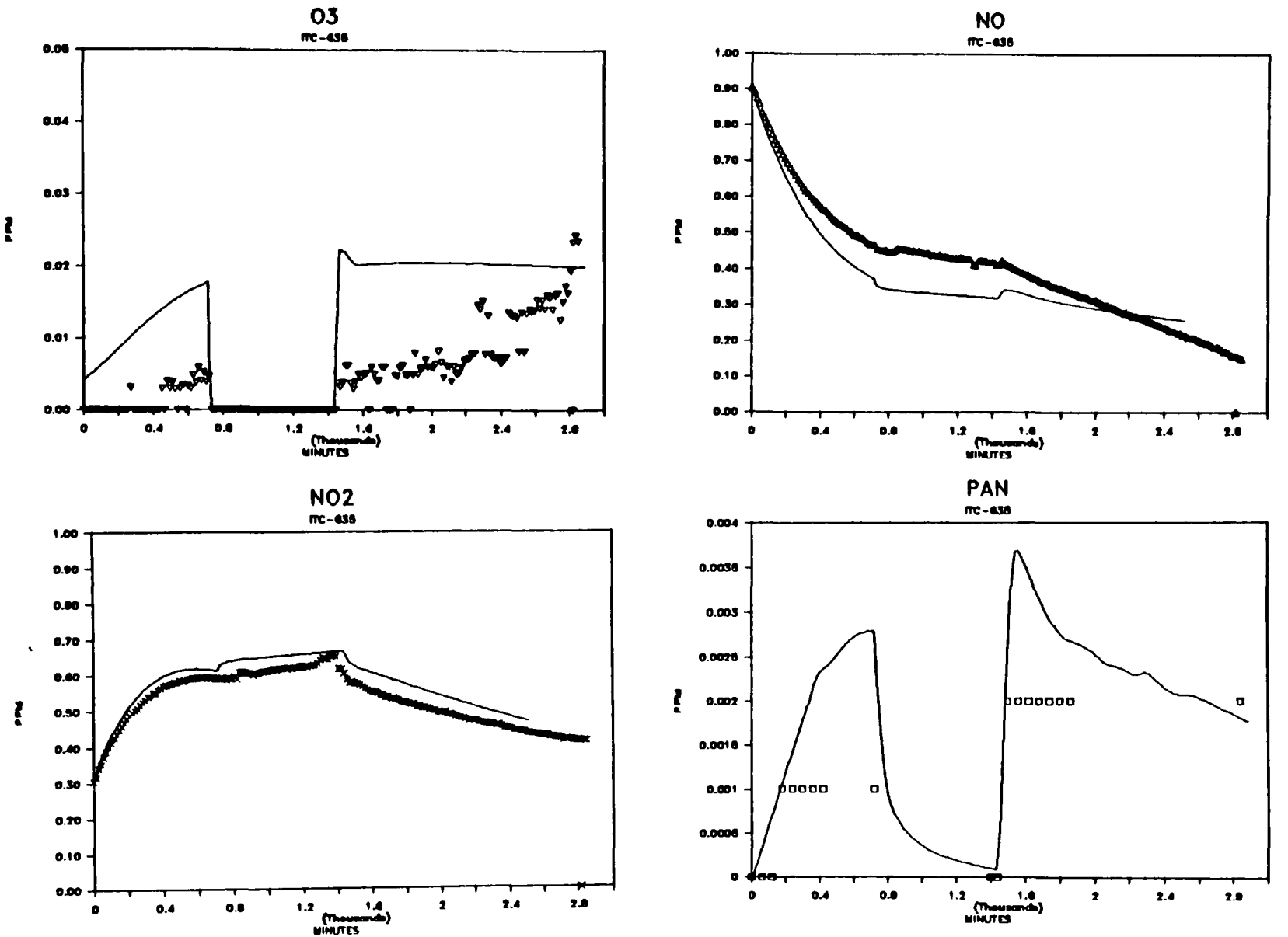

FIGURE 6-112. Simulation results for UCR experiment ITC-635
(symbols are experimental measurements)

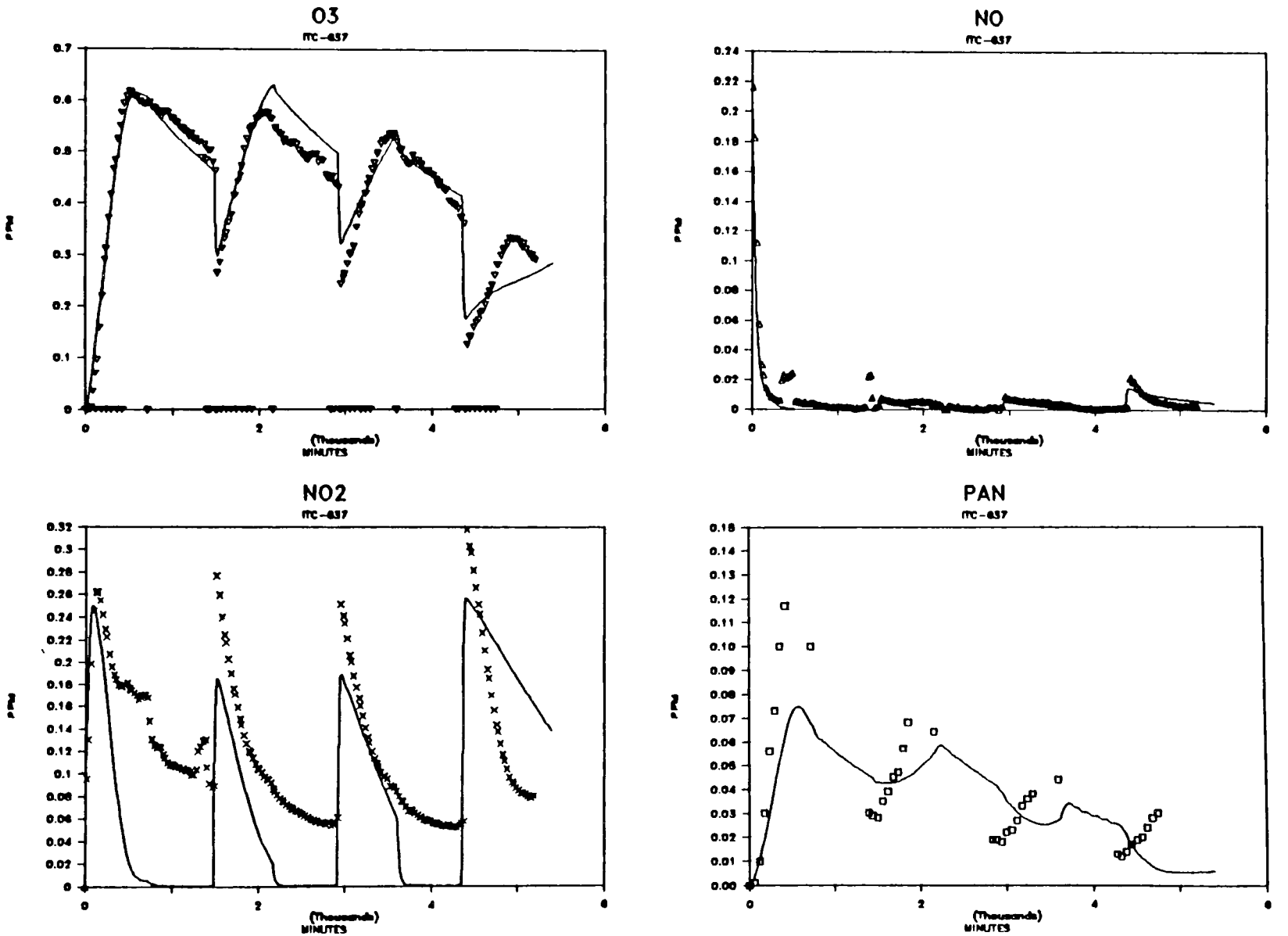

FIGURE 6-113. Simulation results for UCR experiment ITC-637
(symbols are experimental measurements)

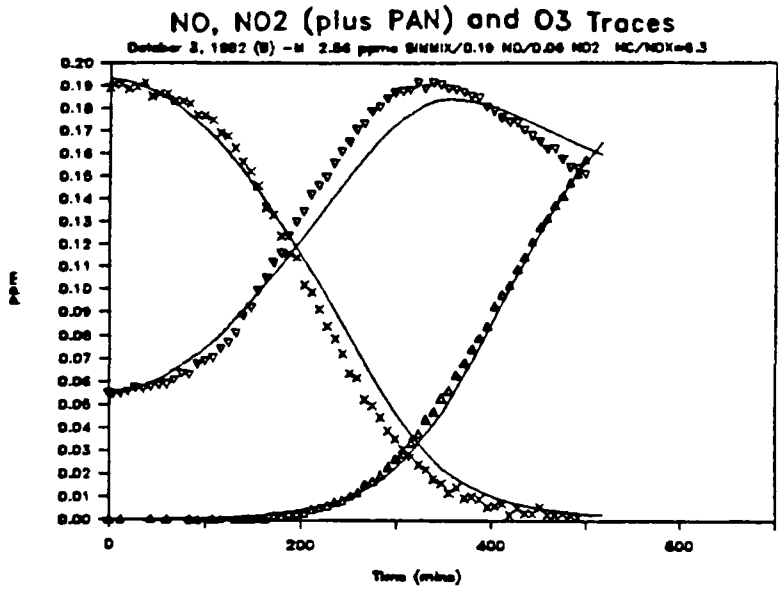

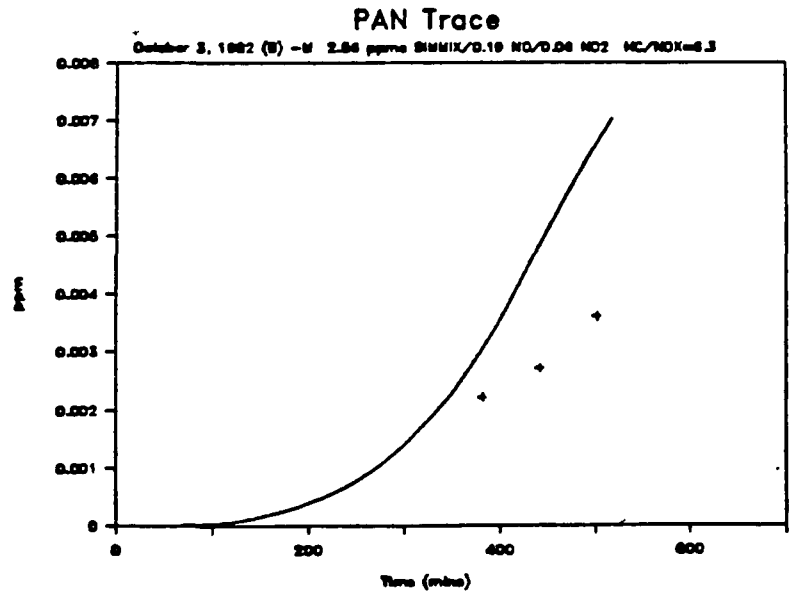

FIGURE 6-114. Simulation results for UNC experiment OC0382B (symbols are experimental measurements)

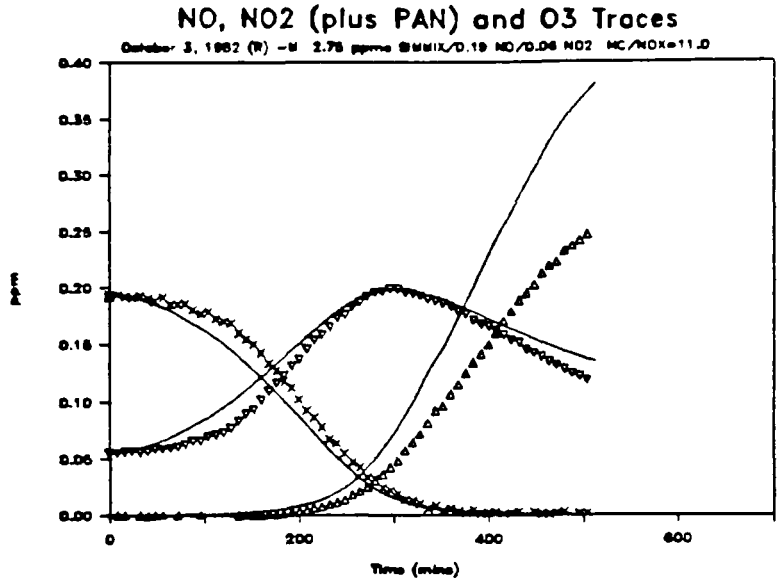

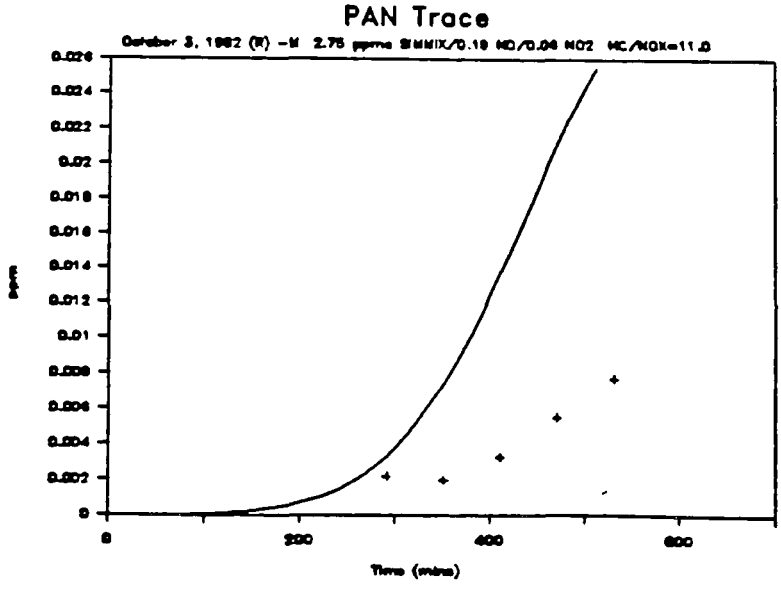

FIGURE 6-115. Simulation results for UNC experiment OC0382R (symbols are experimental measurements)

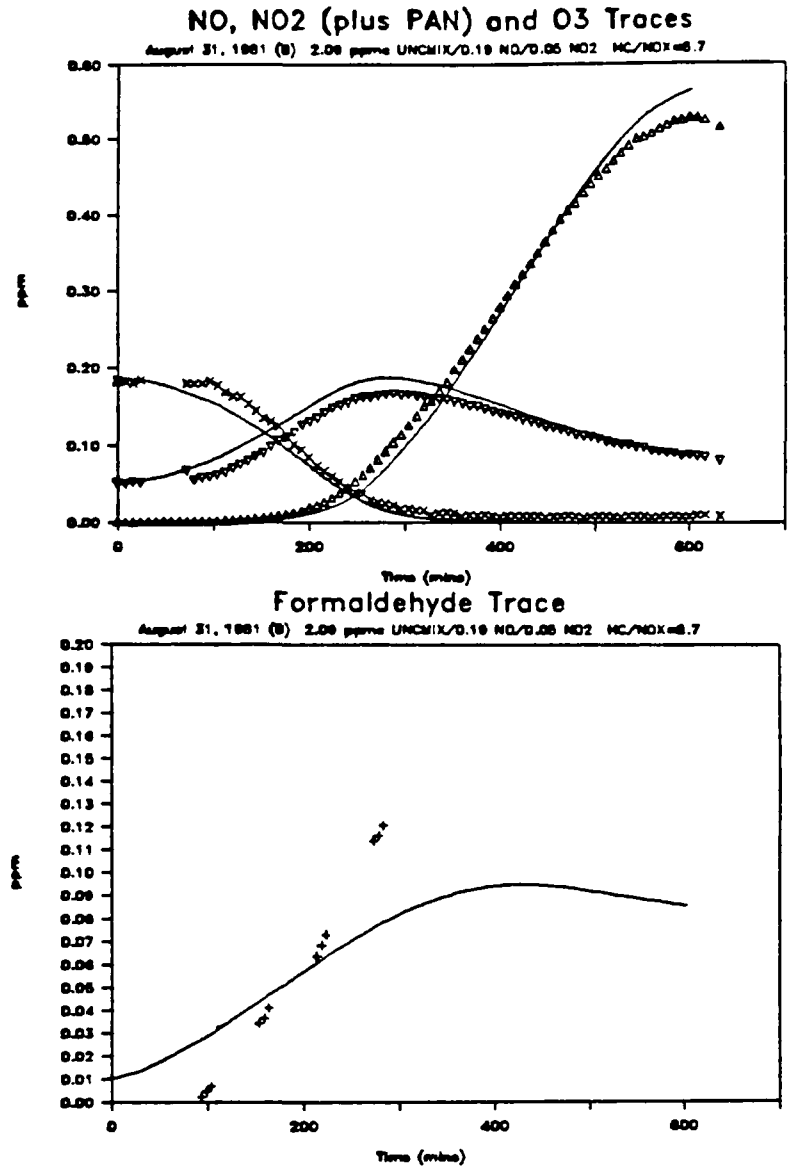

FIGURE 6-116. Simulation results for UNC experiment AU3181B (symbols are experimental measurements)

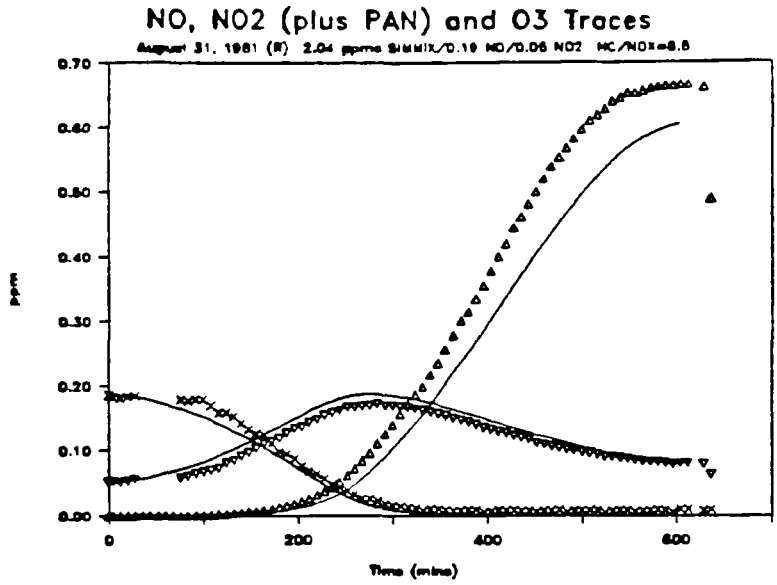

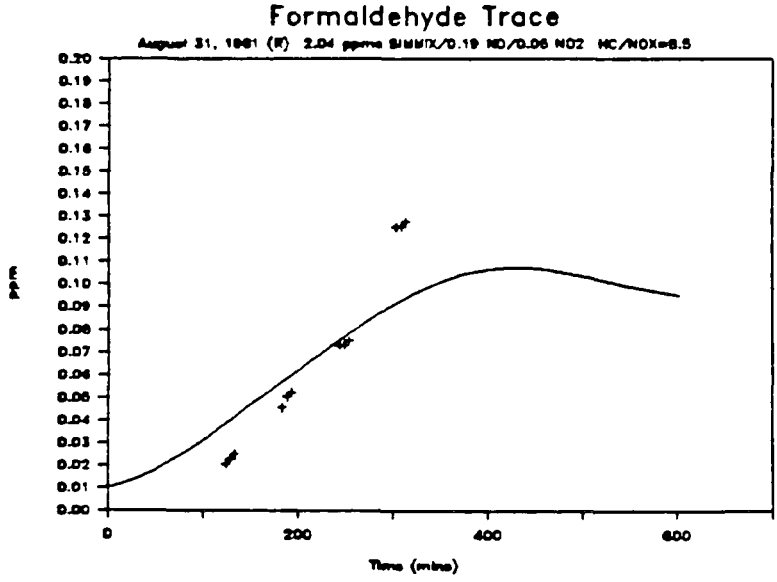

FIGURE 6-117. Simulation results for UNC experiment AU3181R (symbols are experimental measurements)

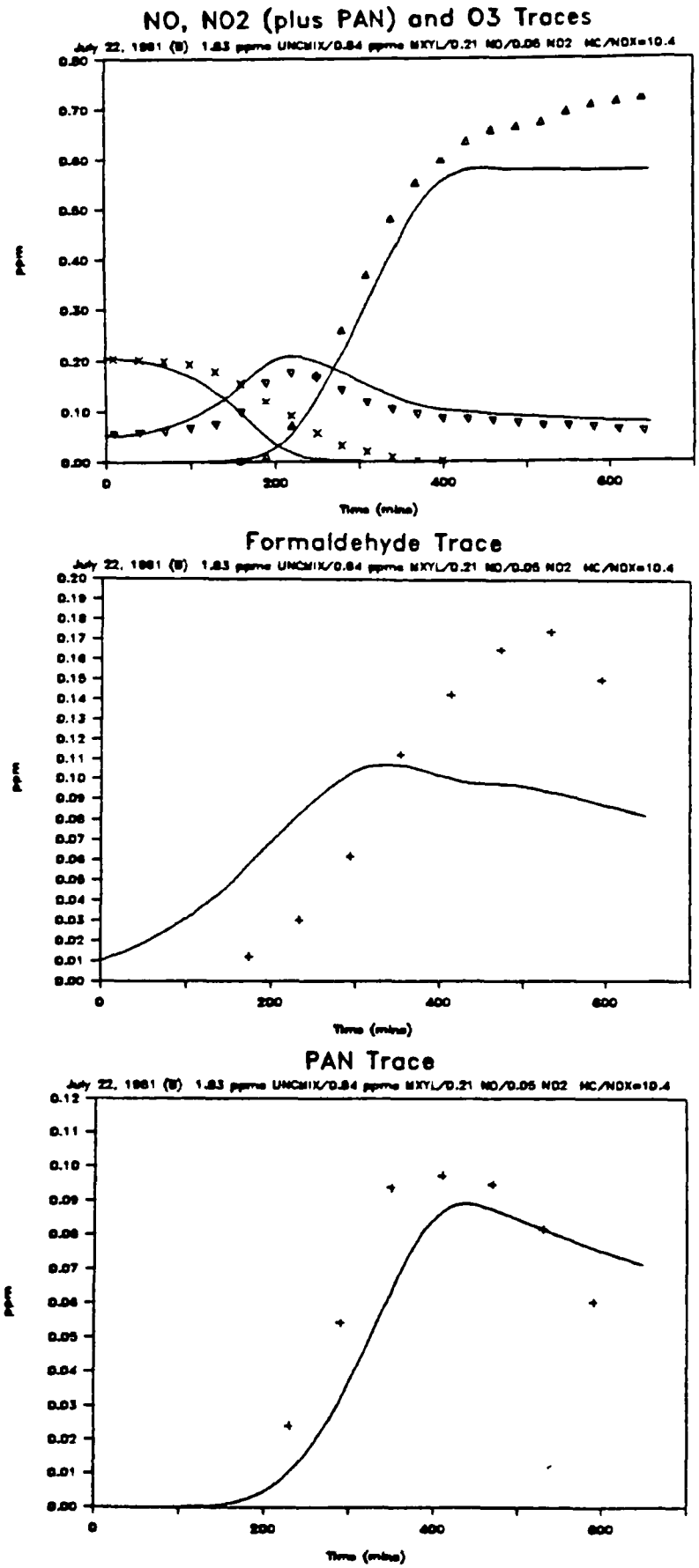

FIGURE 6-118. Simulation results for UNC experiment JL2281B (symbols are experimental measurements)

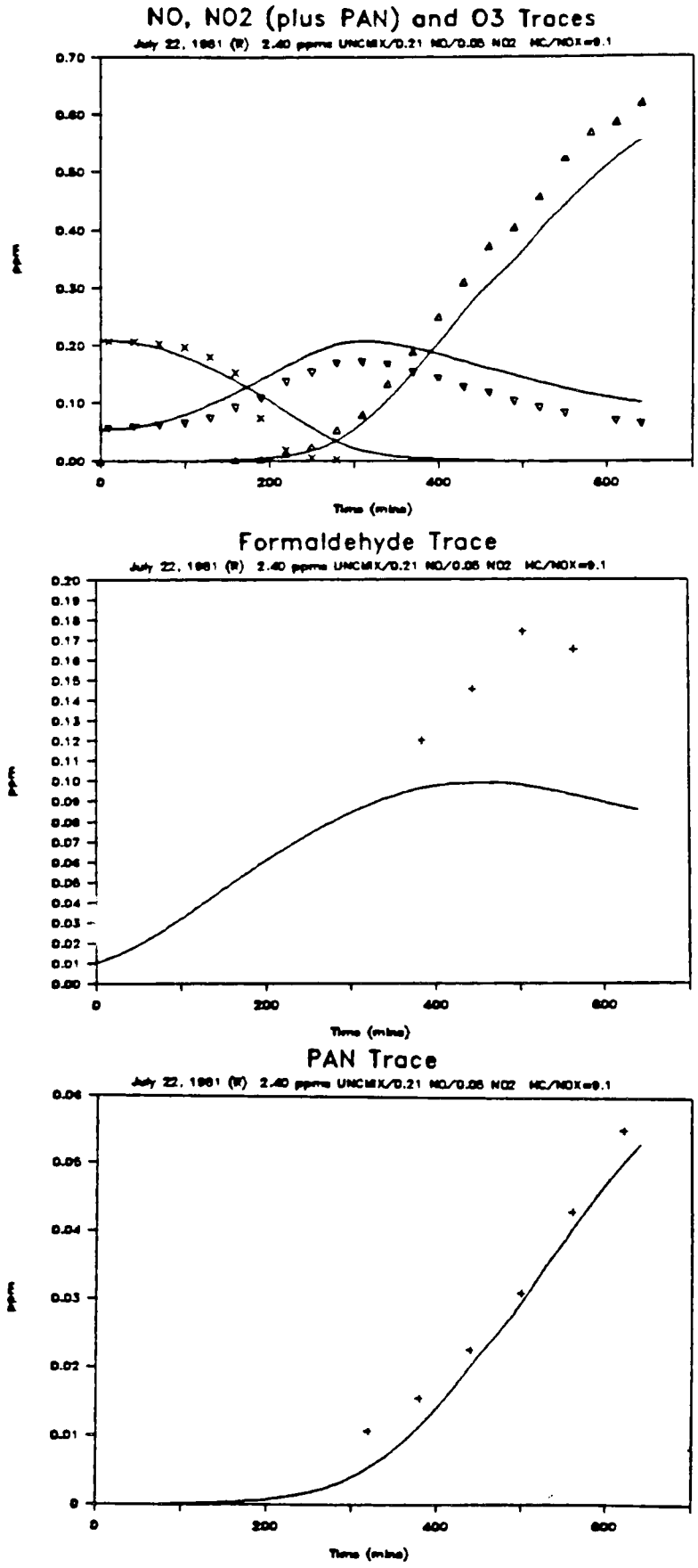

FIGURE 6-119. Simulation results for UNC experiment JL2281R (symbols are experimental measurements)

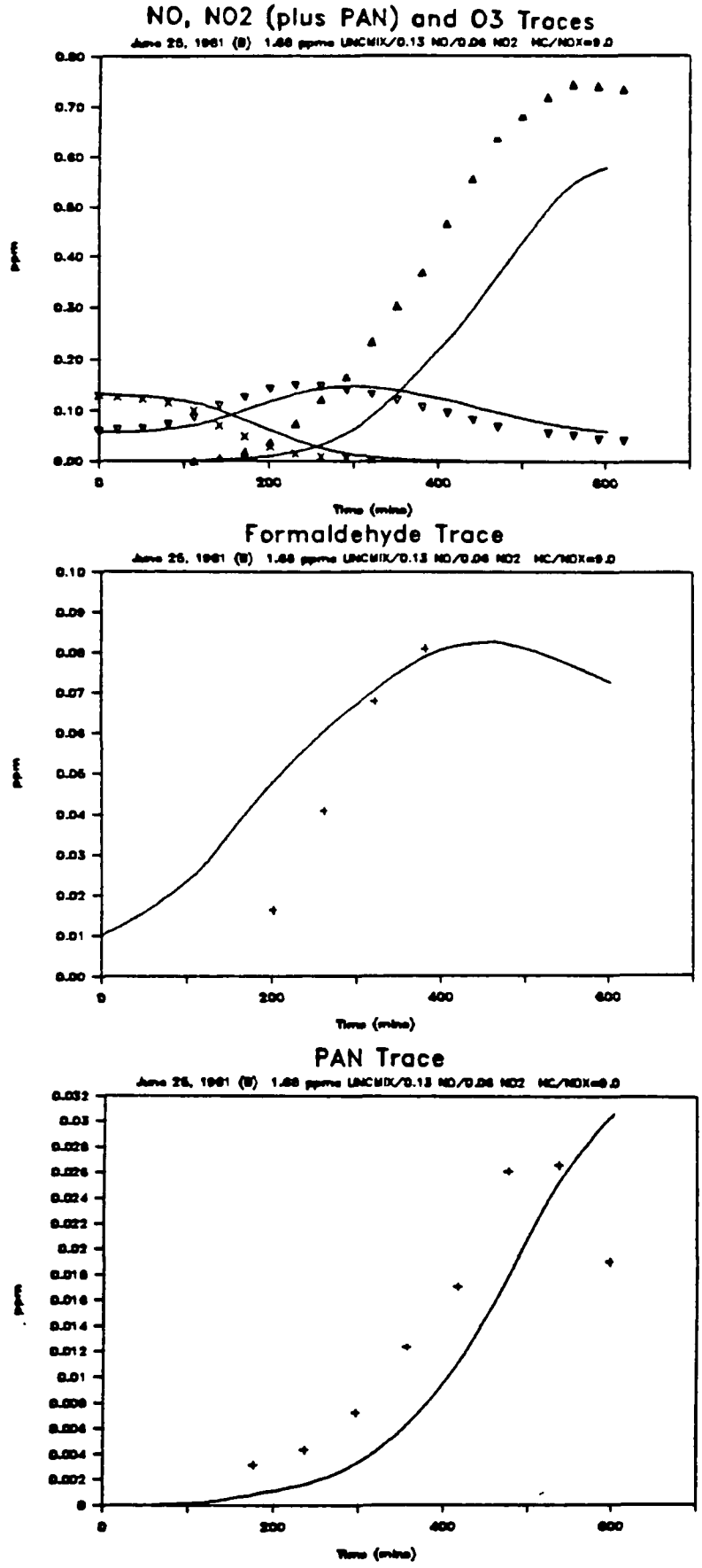

FIGURE 6-120. Simulation results for UNC experiment JN2581B (symbols are experimental measurements)

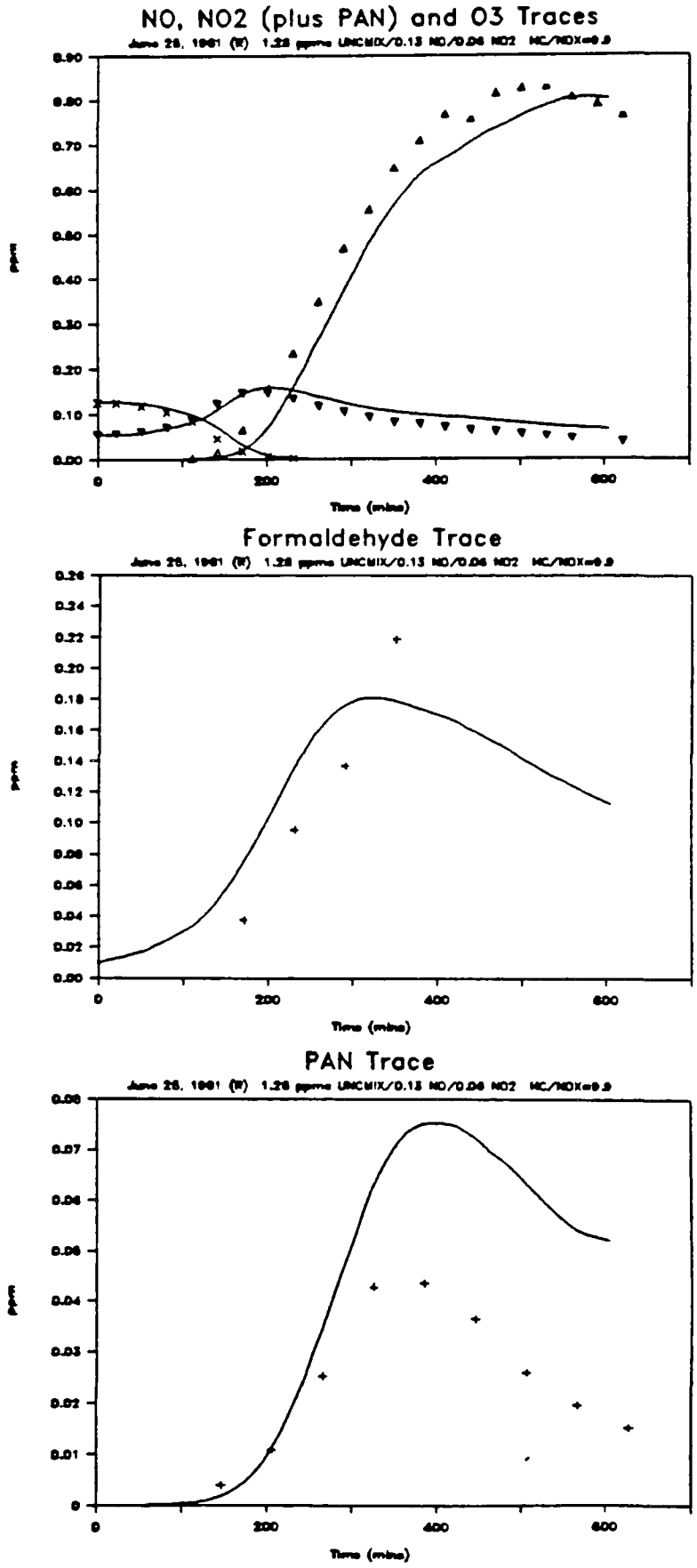

FIGURE 6-121. Simulation results for UNC experiment JN2581R (symbols are experimental measurements)

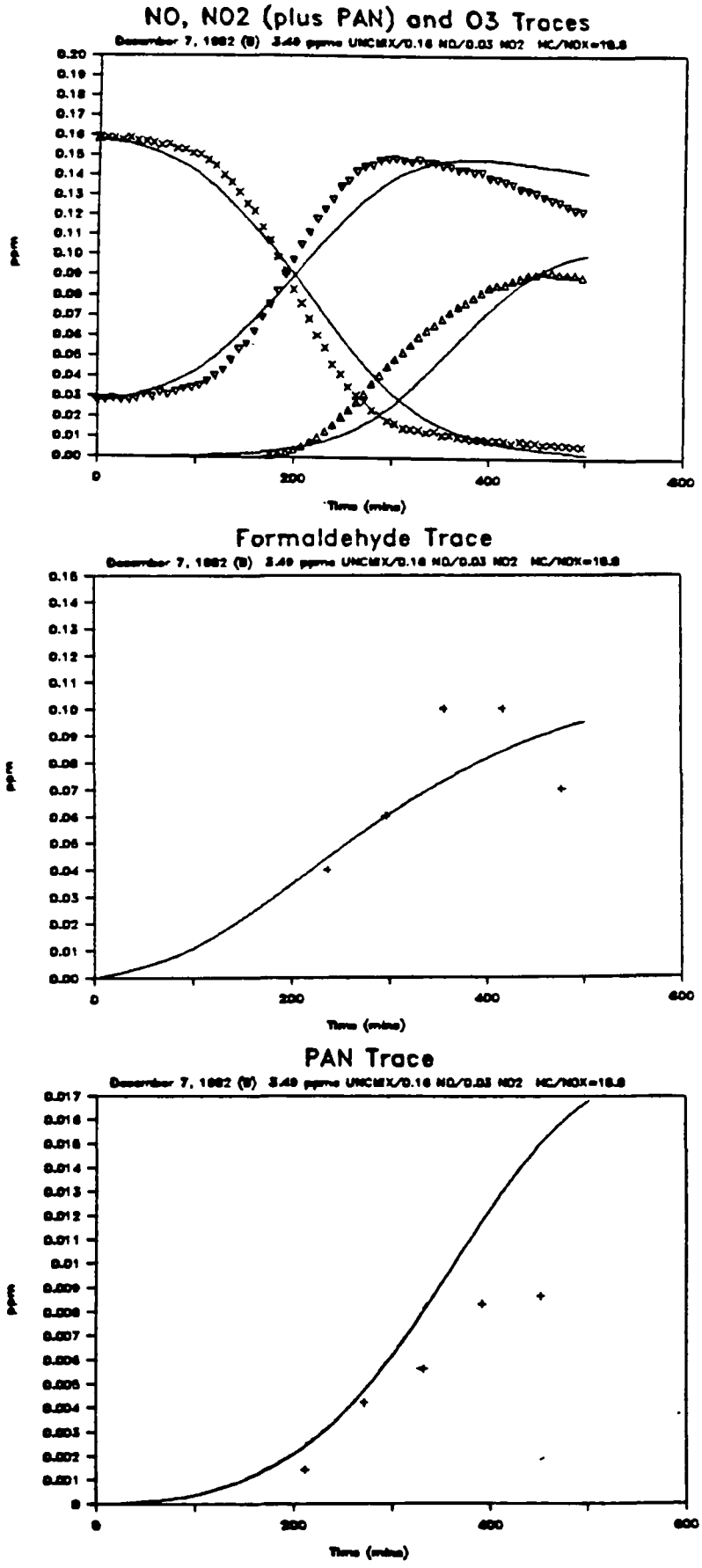

FIGURE 6-122. Simulation results for UNC experiment DE0782B (symbols are experimental measurements)

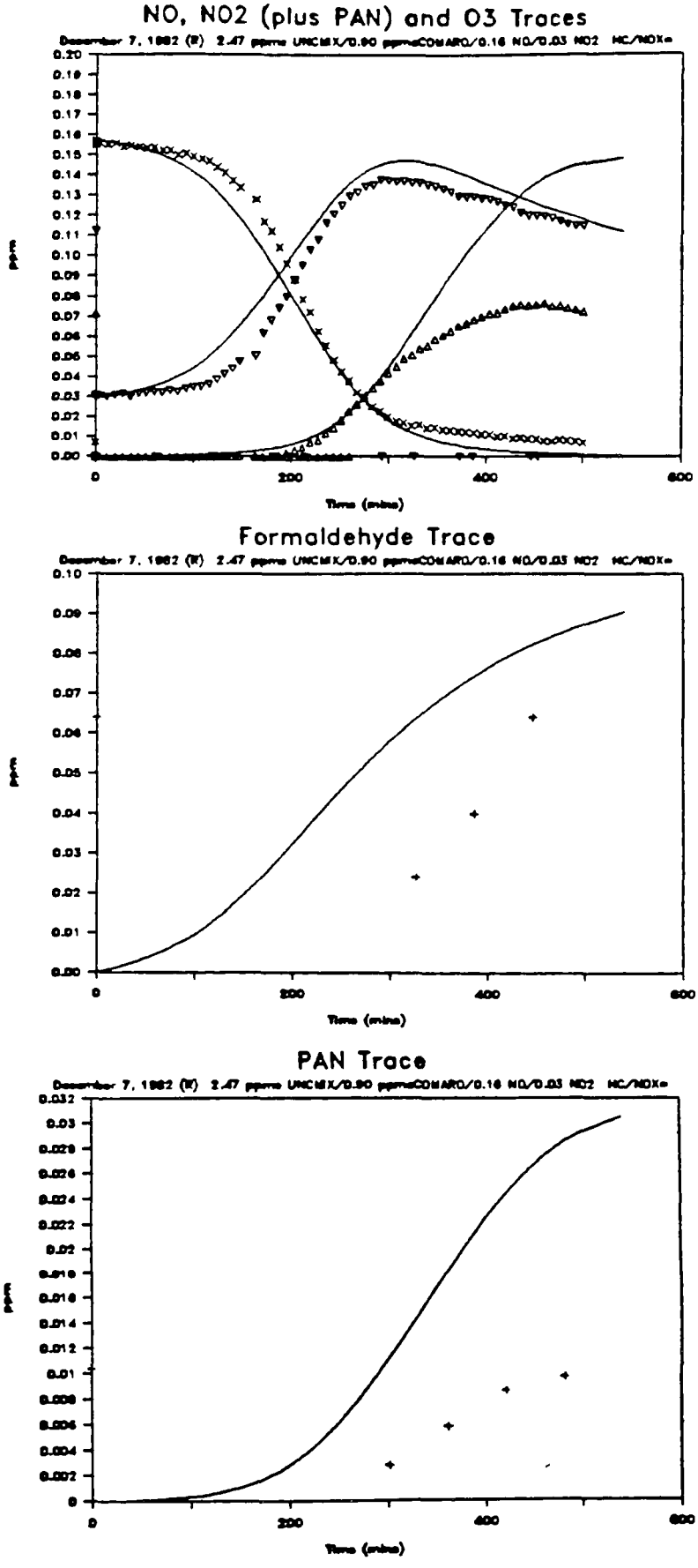

FIGURE 6-123. Simulation results for UNC experiment DE0782R (symbols are experimental measurements)

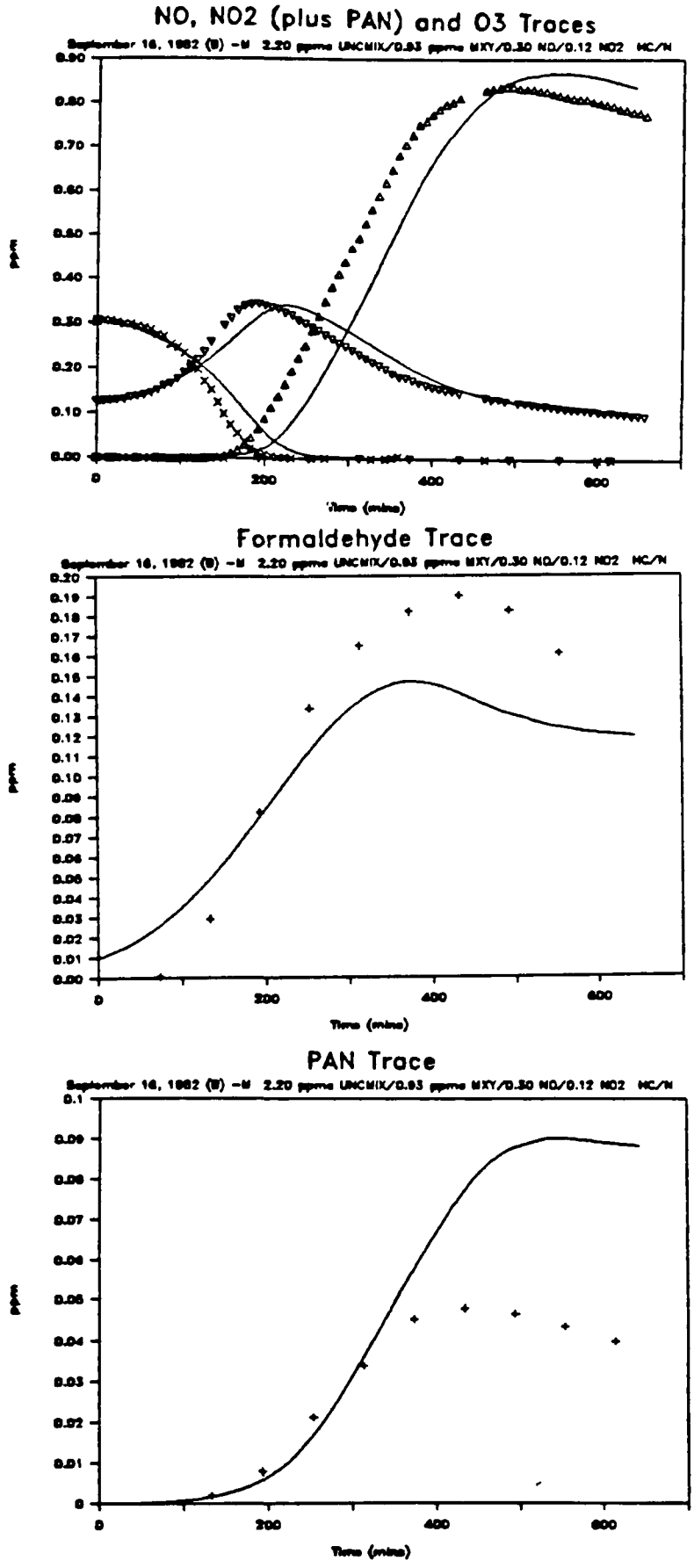

FIGURE 6-124. Simulation results for UNC experiment SE1682B (symbols are experimental measurements)

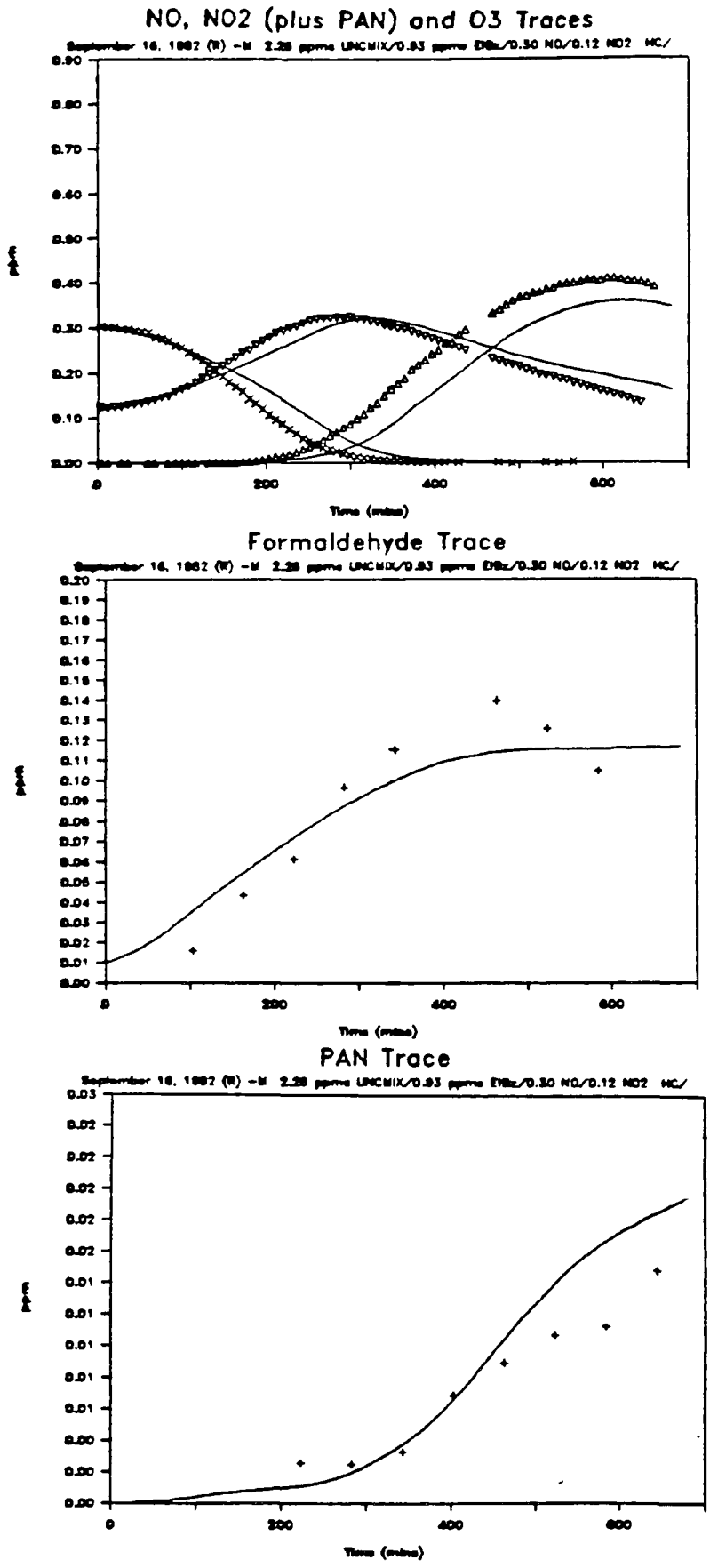

FIGURE 6-125. Simulation results for UNC experiment SE1682R (symbols are experimental measurements)

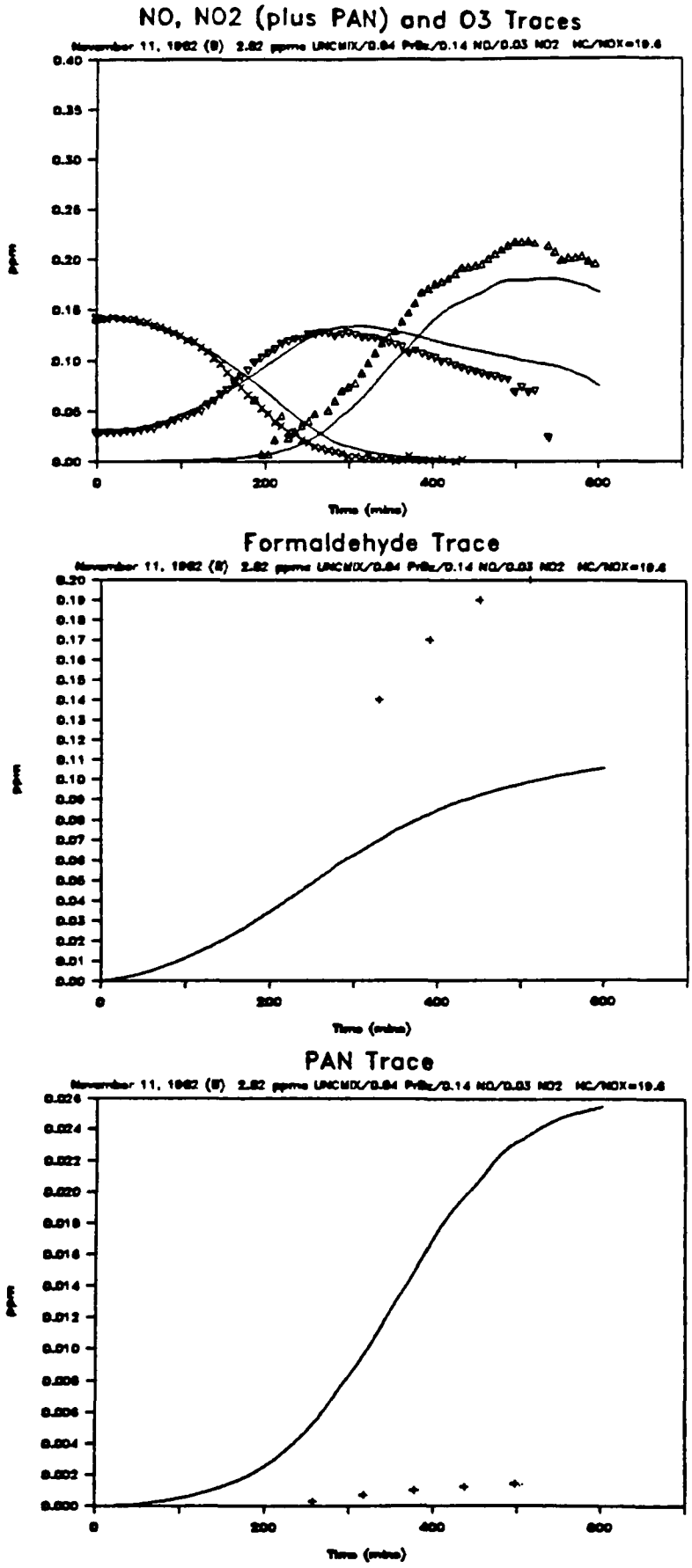

FIGURE 6-126. Simulation results for UNC experiment NV1182B (symbols are experimental measurements)

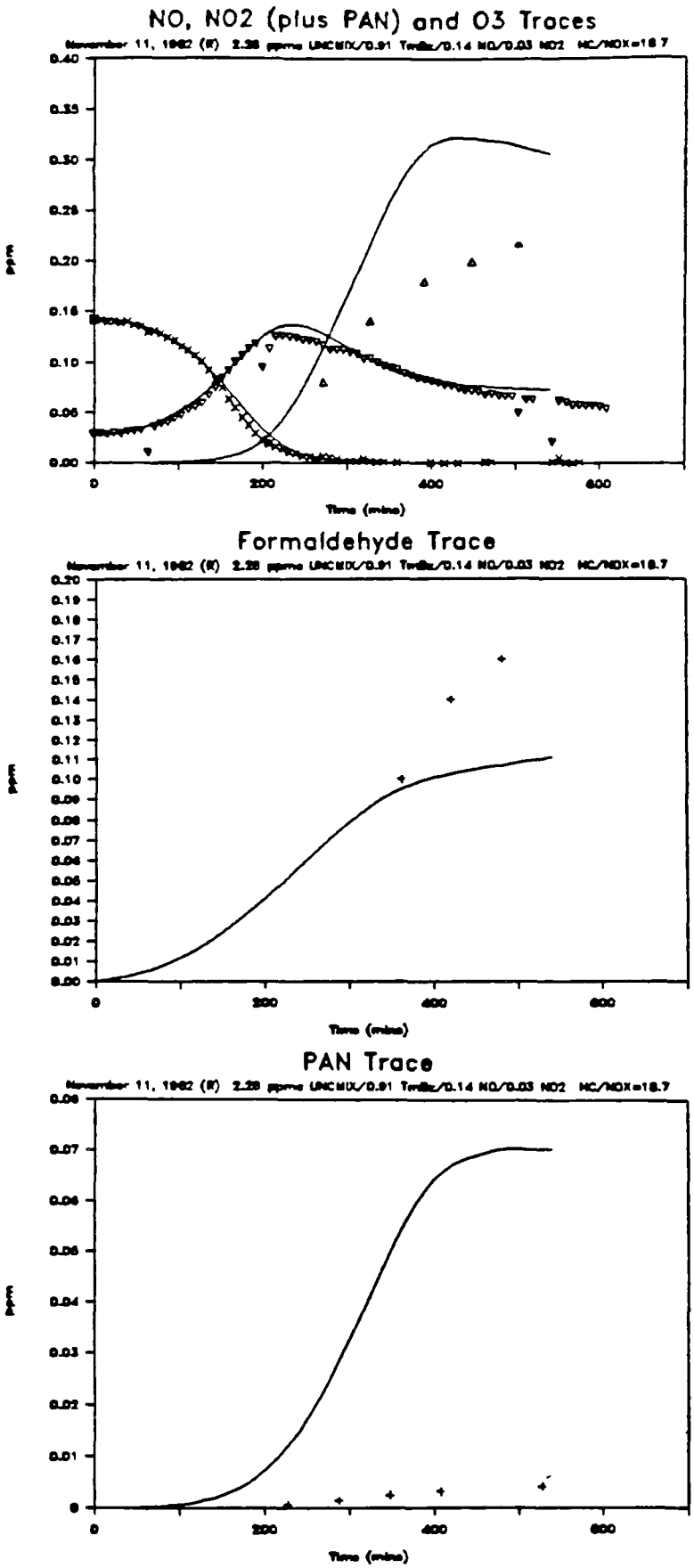

FIGURE 6-127. Simulation results for UNC experiment NV1182R (symbols are experimental measurements)

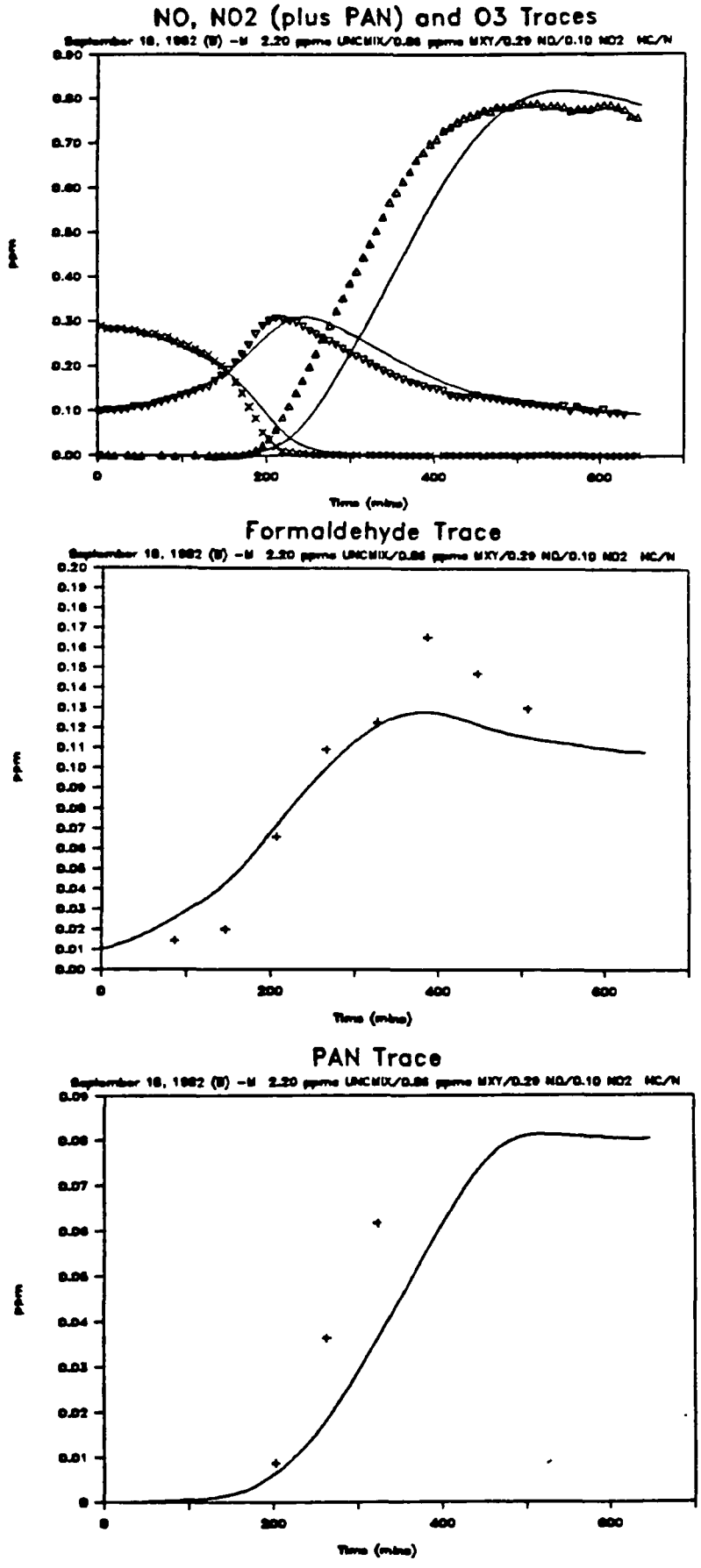

FIGURE 6-128. Simulation results for UNC experiment SE1882B (symbols are experimental measurements)

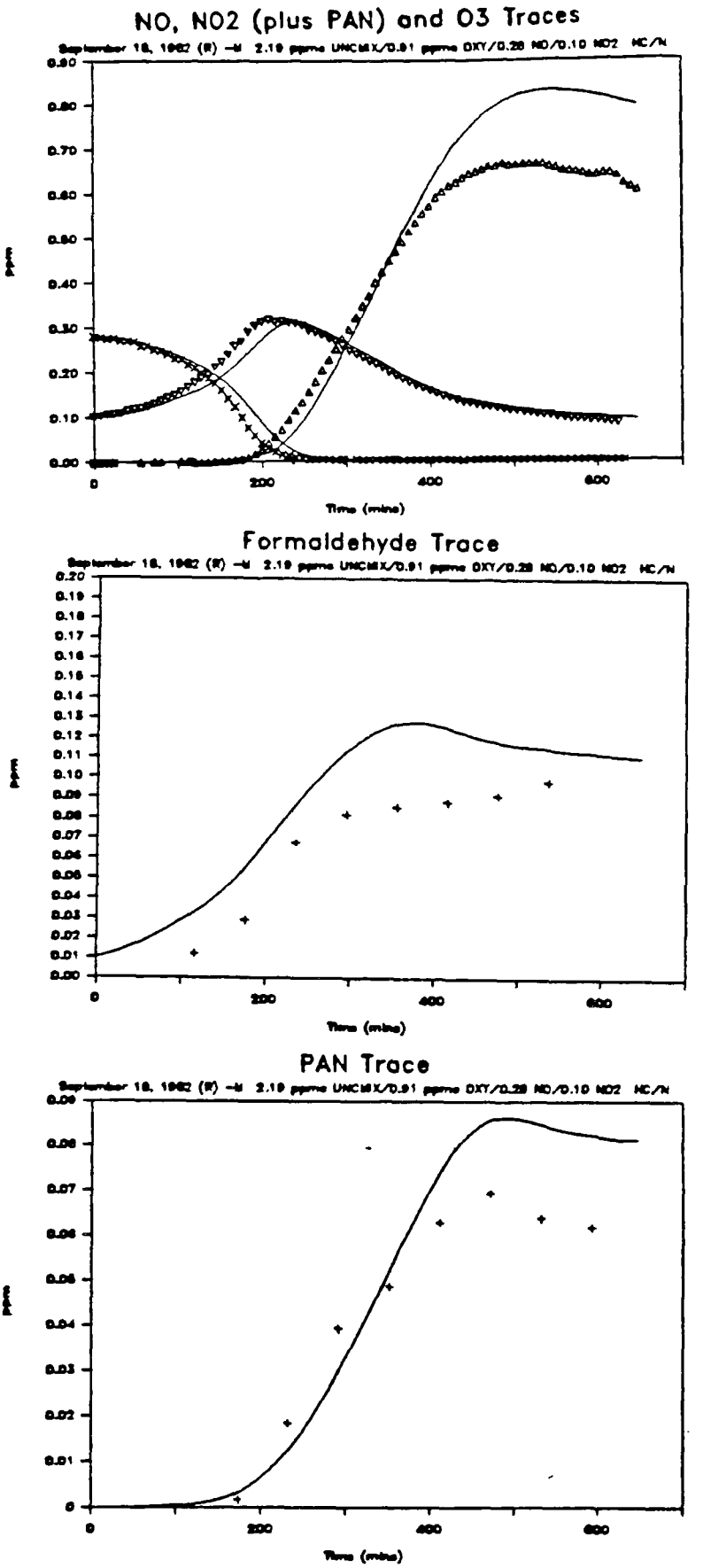

FIGURE 6-129. Simulation results for UNC experiment SE1882R (symbols are experimental measurements)

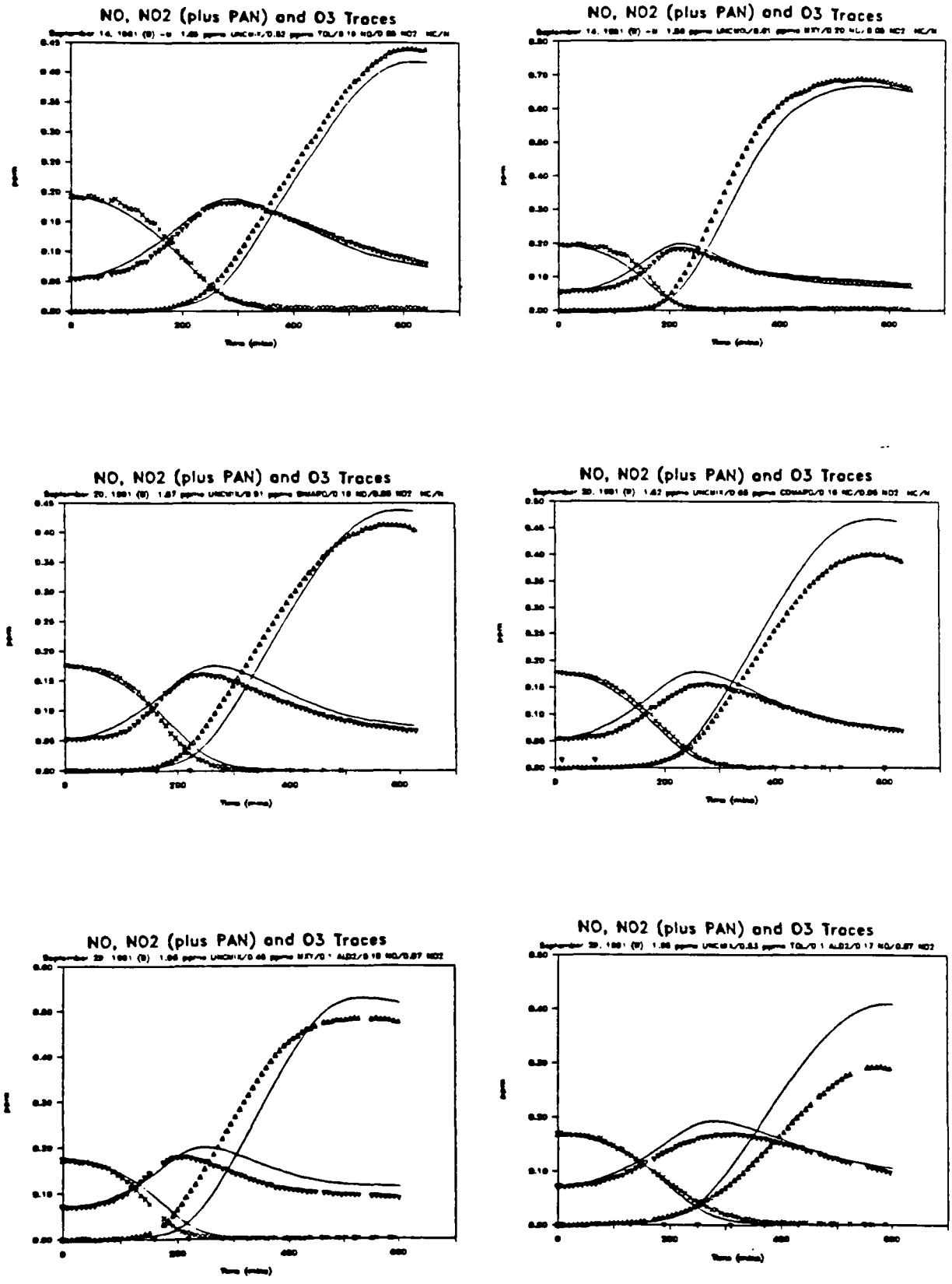

FIGURE 6-130. Simulation results for both sides of UNC experiments SE1481, SE2081, and SE2981 (symbols are experimental measurements)

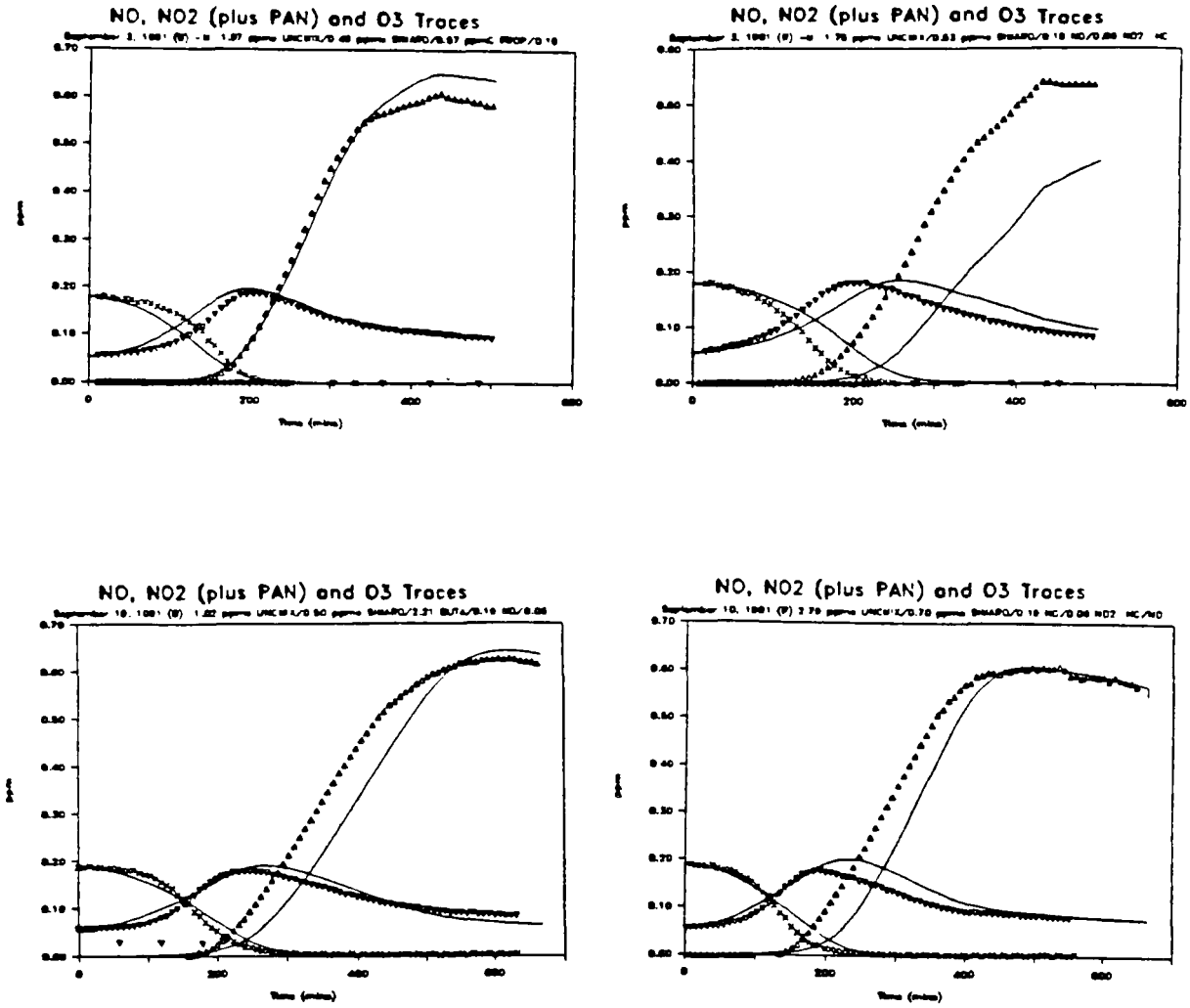

FIGURE 6-131. Simulation results for both sides of UNC experiments SE0381 and SE1081 (symbols are experimental measurements)

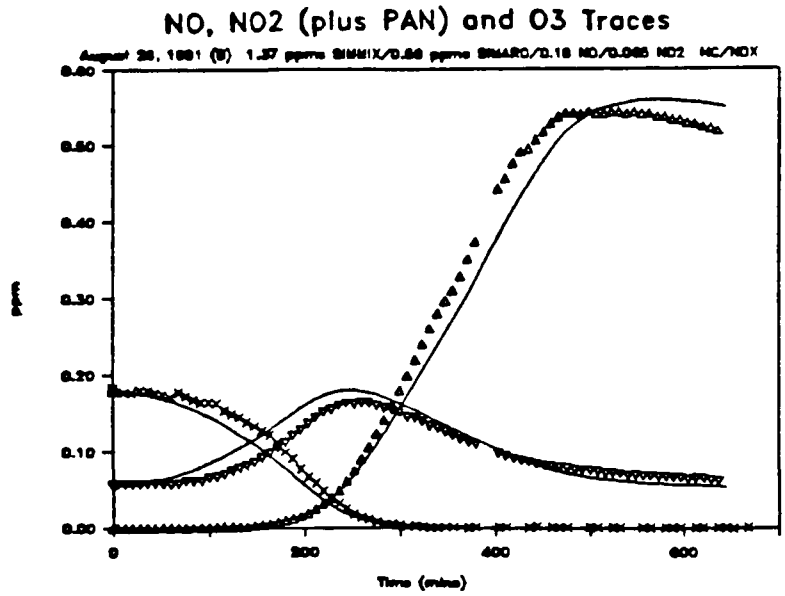

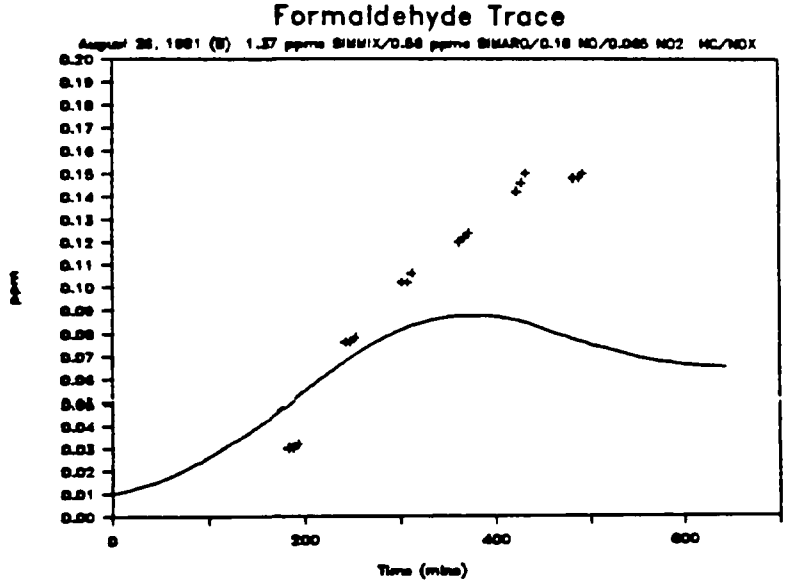

FIGURE 6-132. Simulation results for UNC experiment AU2681B (symbols are experimental measurements)

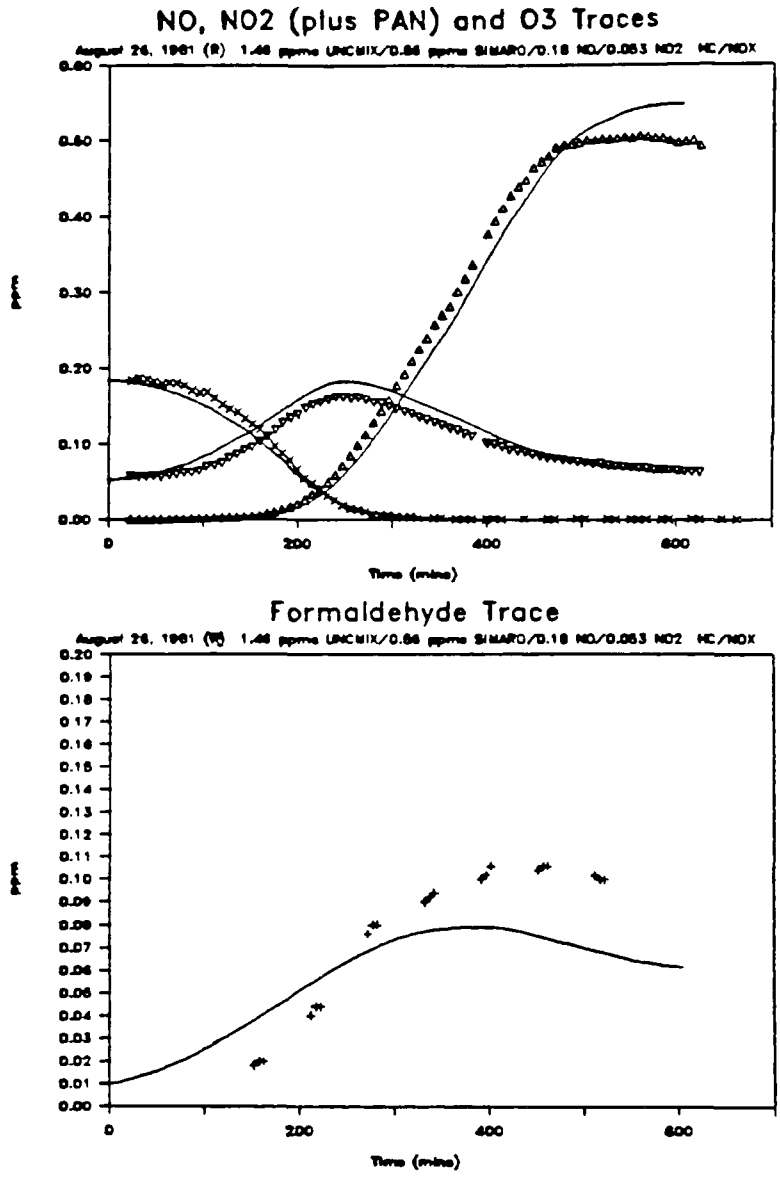

FIGURE 6-133. Simulation results for UNC experiment AU2681R (symbols are experimental measurements)

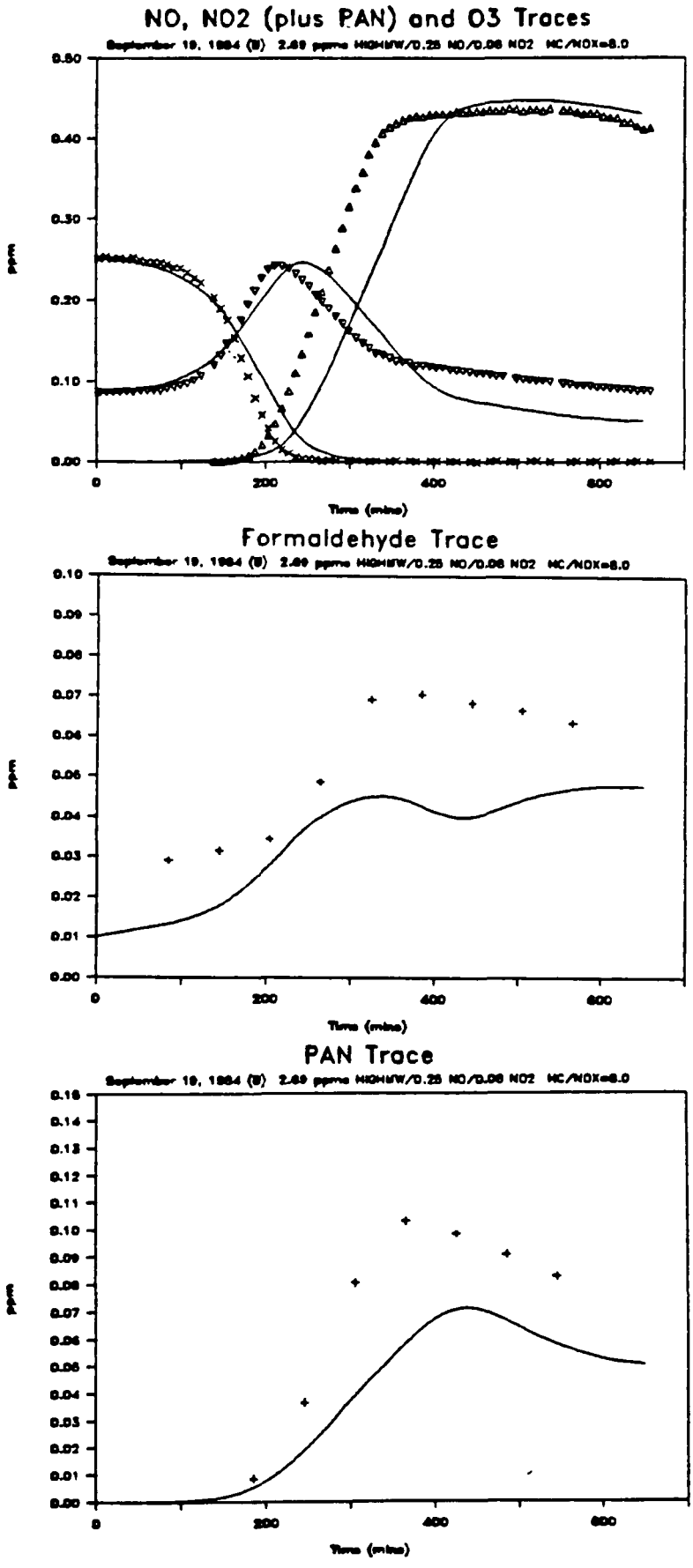

FIGURE 6-134. Simulation results for UNC experiment SE1984B (symbols are experimental measurements)

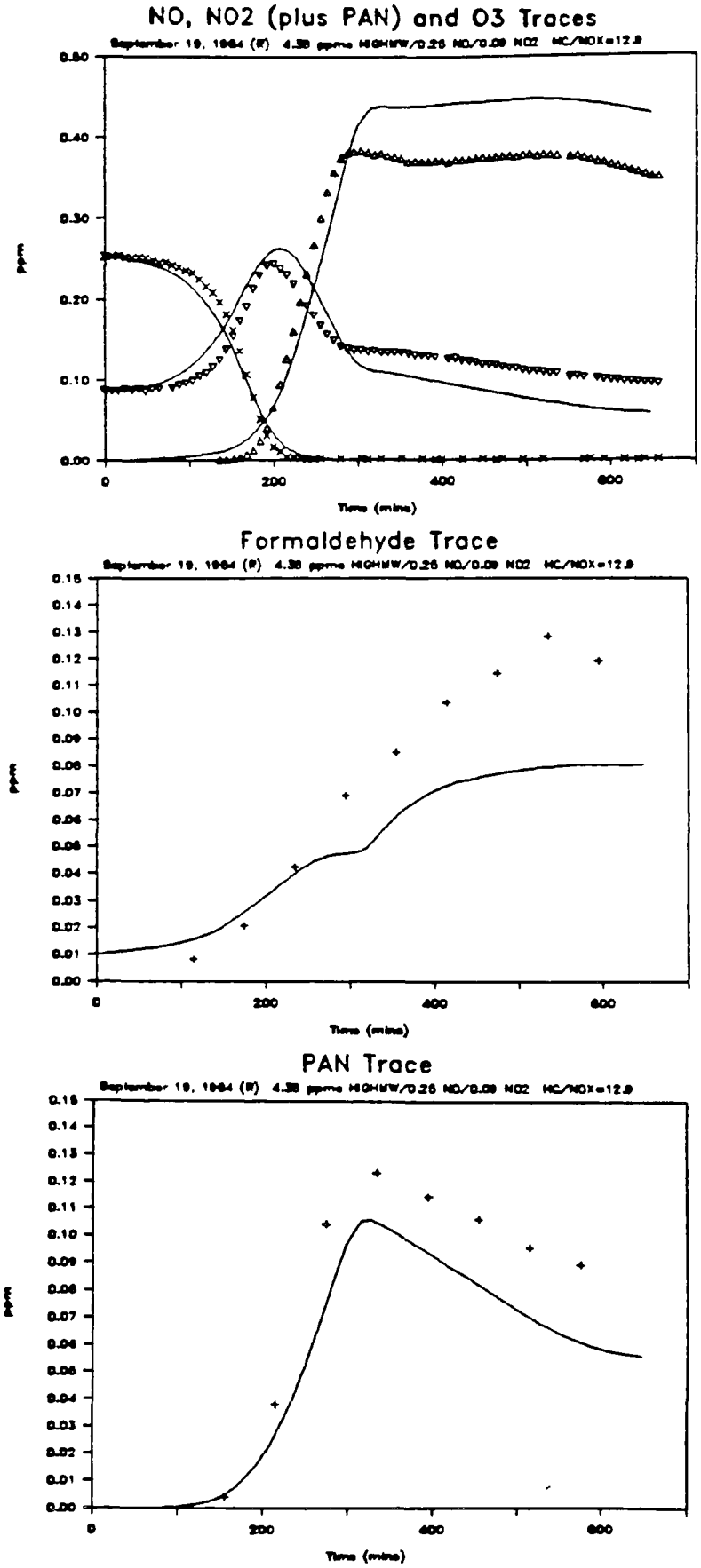

FIGURE 6-135. Simulation results for UNC experiment SE1984R (symbols are experimental measurements)

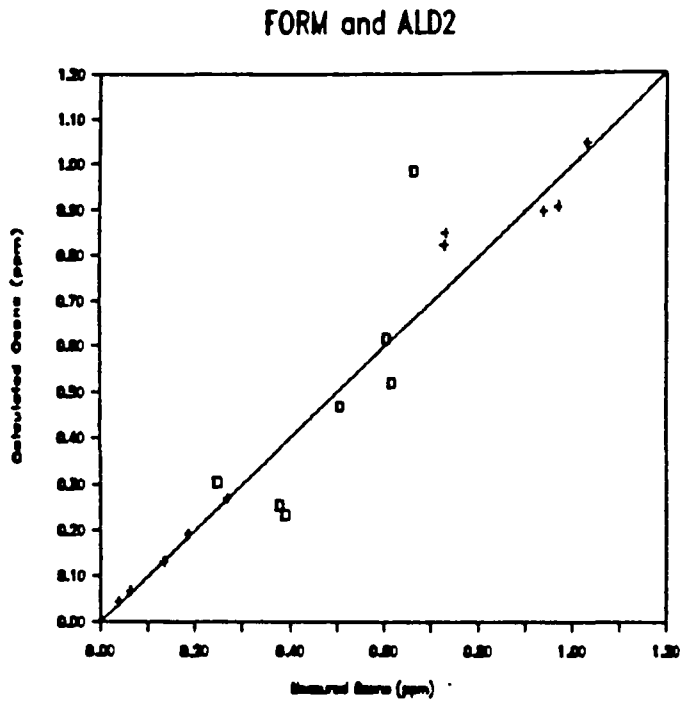

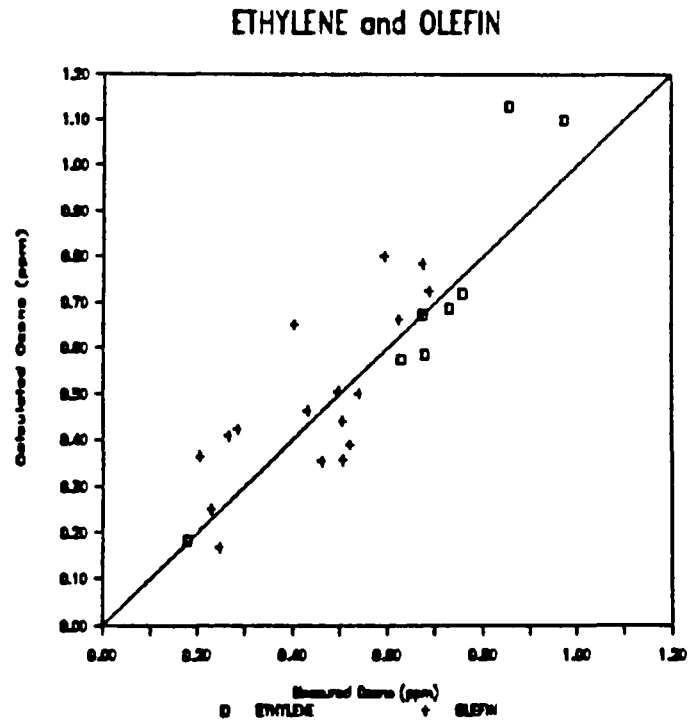

FIGURE 6-136. Scatter diagrams comparing predicted maximum ozone concentration versus measured values for aldehyde (top) and alkene (bottom) smog chamber experiments.

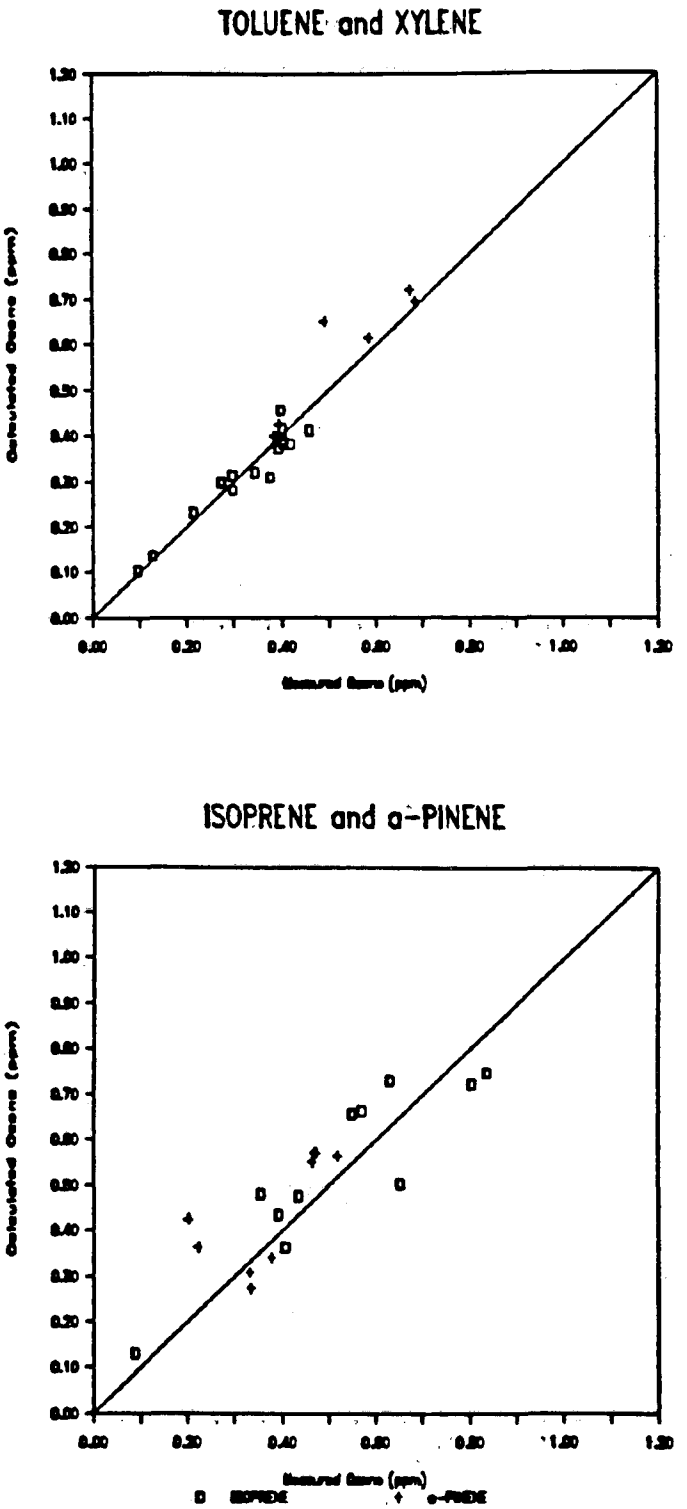

FIGURE 6-137. Scatter diagrams comparing predicted maximum ozone concentration versus measured values for aromatic (top) and biogenic hydrocarbon (bottom) smog chamber experiments.

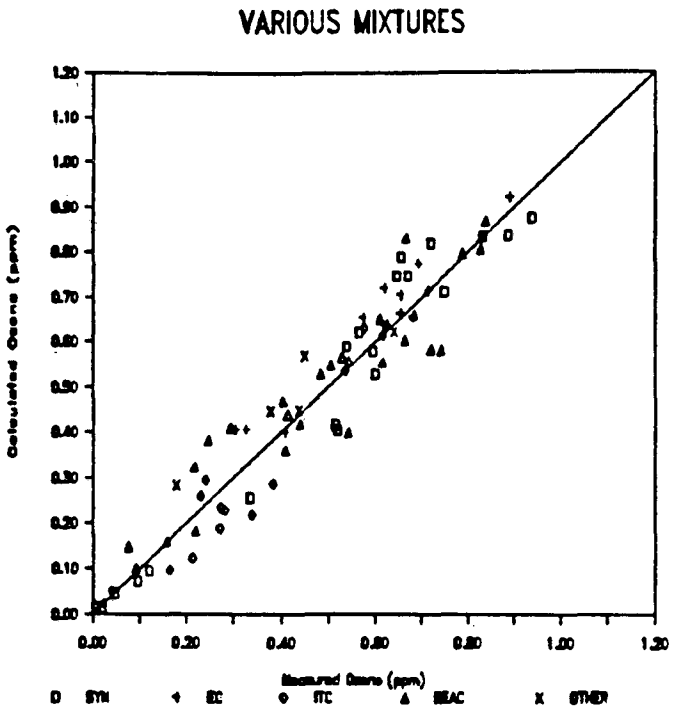

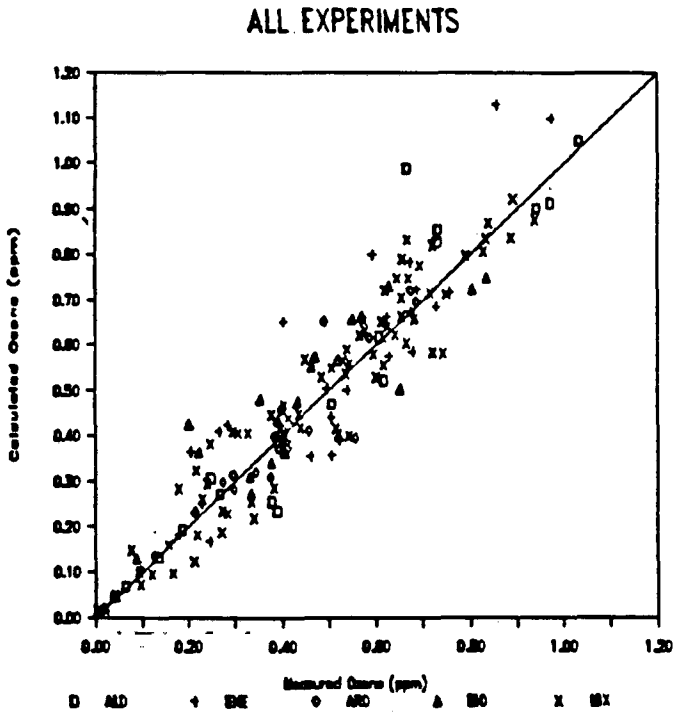

FIGURE 6-138. Scatter diagrams comparing predicted maximum ozone concentration versus measured values for reactive hydrocarbon mixture experiments (top) and all simulated experiments (bottom).

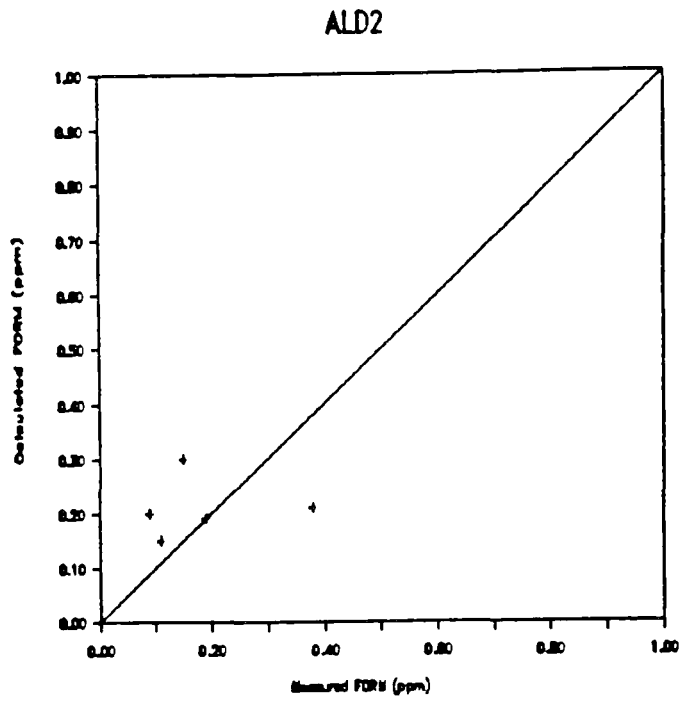

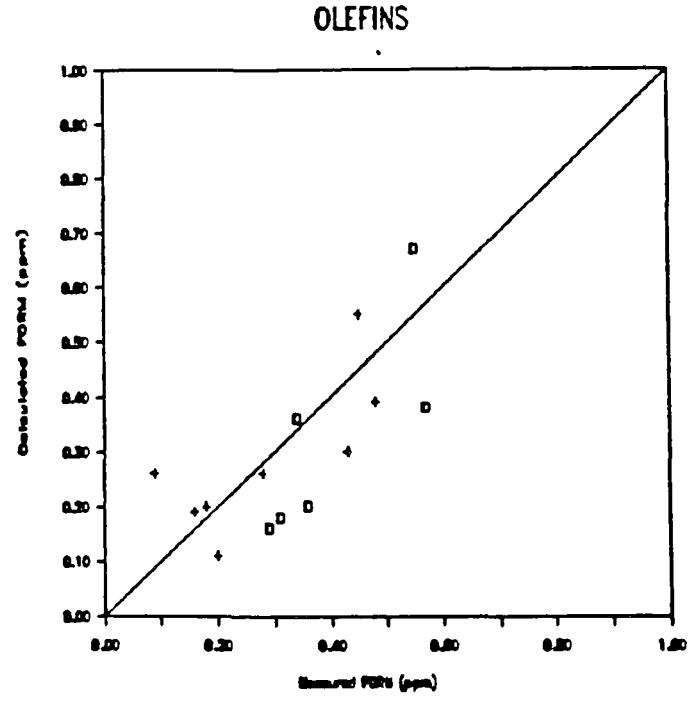

FIGURE 6-139. Scatter diagrams comparing predicted maximum formaldehyde concentration versus measured values for aldehyde (top) and alkene (bottom) smog chamber experiments.

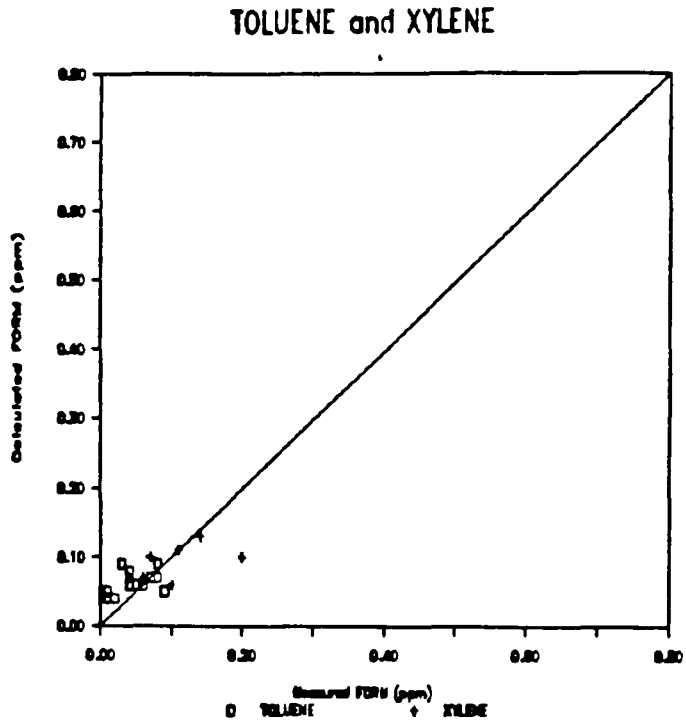

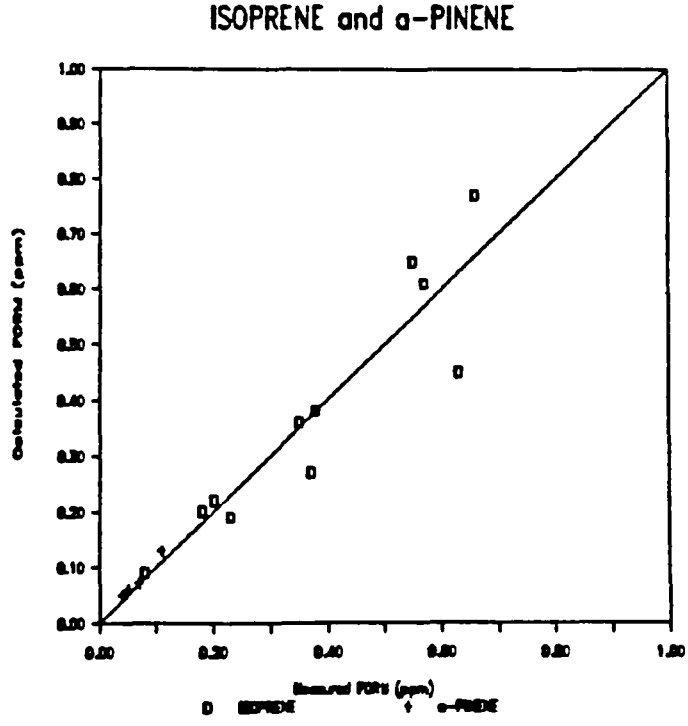

FIGURE 6-140. Scatter diagrams comparing predicted maximum formaldehyde concentration versus measured values for aromatic (top) and biogenic hydrocarbon (bottom) smog chamber experiments.

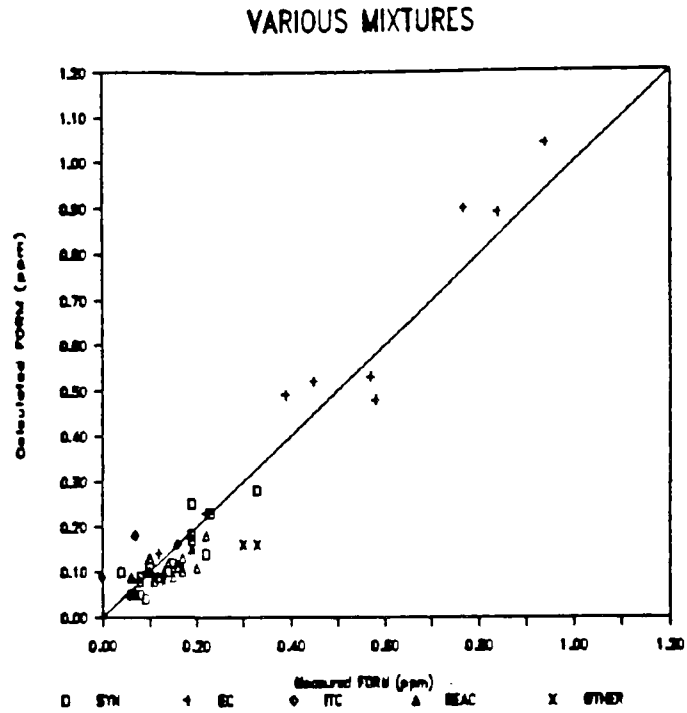

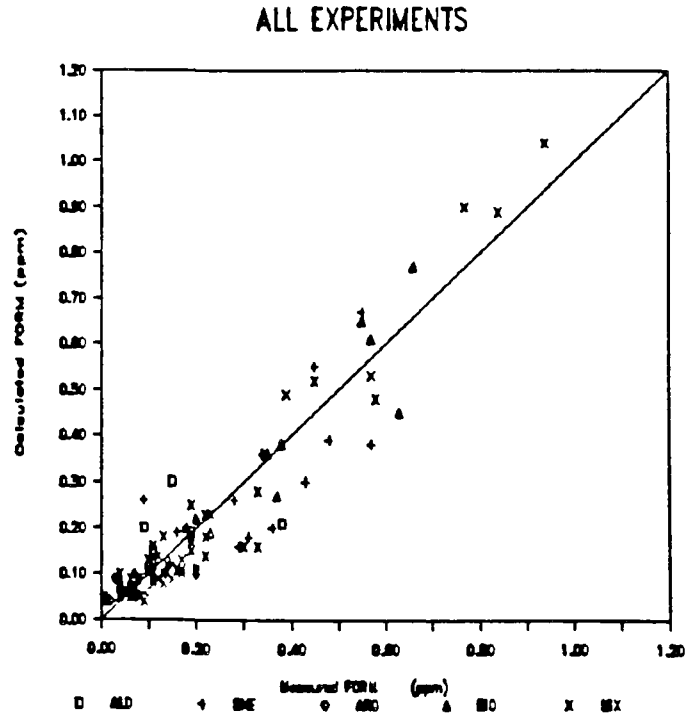

FIGURE 6-141. Scatter diagrams comparing predicted maximum formaldehyde concentration versus measured values for reactive hydrocarbon mixture experiments (top) and all simulated experiments (bottom).

TABLE 6-1. Initial conditions for UNC formaldehyde smog chamber simulations.

Experiment Number	Initial Concentrations (ppm)							Other Conditions				
	Gas Phase					Walls		Water Vapor (ppm)		Temperature (K)		Light Conditions
	NO	NO_2	HONO	HCHO	CO	HCHO	k_{HONO}	Initial	Final	Initial	Final	
OC0984B	0.352	0.148	0.000	0.962	0.30	0.000	0.00E-0	8000	10500	285.8	297.0	Good
OC0984R	0.353	0.210	0.000	0.962	50.00	0.000	0.00E-0	8000	10500	285.8	297.0	Good
AU0179B	0.277	0.076	0.000	1.000	0.30	0.040	2.50E-5	20000	20000	296.0	311.7	Good
AU0279B	0.157	0.060	0.002	1.010	0.30	0.040	2.50E-5	21000	21000	296.0	311.7	Good
AU0479B	0.170	0.070	0.003	0.504	0.41	0.040	2.50E-5	20500	21000	294.3	307.9	Good
AU0579B	0.407	0.132	0.000	1.209	0.33	0.000	2.50E-5	29000	40000	295.1	310.8	Good
AU1280R	0.371	0.110	0.015	0.841	0.10	0.040	2.50E-5	29000	38000	294.6	302.6	OK

TABLE 6-2. Results of UNC formaldehyde simulations.

Experiment Number	Initial Conditions			Maximum Ozone (ppm)			
	NO_x	NO_2/NO_x	HC/NO_x	Calc. (ppm)	Meas. (ppm)	Abs. Diff.	Pct. Diff.
OC0984B	0.500	0.298	1.9	0.305	0.248	0.057	23.0%
OC0984R	0.563	0.373	1.7	0.988	0.666	0.322	48.3%
AU0179B	0.353	0.215	2.8	0.521	0.618	-0.097	-15.7%
AU0279B	0.217	0.276	4.7	0.619	0.606	0.013	2.1%
AU0479B	0.240	0.292	2.1	0.255	0.378	-0.123	-32.5%
AU0579B	0.539	0.245	2.2	0.470	0.507	-0.037	- 7.3%
AU1280R	0.481	0.229	1.8	0.233	0.390	-0.157	-40.3%
			UNC Average			-0.003	- 3.2%
			Std. Deviation			±0.162	±31.0%

Experiment Number	Maximum PAN (ppm)				Maximum CO (ppm)			
	Calc. (ppm)	Meas. (ppm)	Abs. Diff.	Pct. Diff.	Calc. (ppm)	Meas. (ppm)	Abs. Diff.	Pct. Diff.
OC0984B	-	0.004	-	-	1.04	-	-	-
OC0984R	-	0.005	-	-	50.00	50.00	-	-
AU0179B	-	0.008	-	-	1.16	1.17	-0.01	- 1%
AU0279B	-	0.009	-	-	1.18	1.15	0.03	3%
AU0479B	-	-	-	-	0.83	0.92	-0.09	- 10%
AU0579B	-	-	-	-	1.31	1.35	-0.04	- 3%
AU1280R	-	0.016	-	-	0.80	0.74	0.06	8%
			UNC Average				-0.01	- 1%
			Std. Deviation				±0.06	± 7%

TABLE 6-3. Initial conditions for acetldehyde and propionaldehyde smog chamber simulations.

Experiment Number	Initial Concentrations (ppm)								Other Conditions				
	Gas Phase						Walls		Water Vapor (ppm)		Temperature (K)		Light Conditions
	NO	NO_2	RCHO	HONO	HCHO	CO	HCHO	k_{HONO}	Initial	Final	Initial	Final	
UNC (acetladehyde):													
JN1482R	0.225	0.087	1.540	0.015	0.020	0.36	0.040	2.50E-5	19500	23500	298.2	306.5	OK
AU2482B	0.230	0.089	0.950	0.000	0.000	0.23	0.040	2.50E-5	13000	21000	293.1	307.9	OK
AU0880R	0.317	0.104	0.950	0.020	0.014	0.00	0.000	2.50E-5	26000	26000	294.4	310.4	Good
DE2677B	0.290	0.117	1.908	0.005	0.010	0.25	0.000	2.50E-5	5000	5000	269.5	274.7	Good
NV1977B	0.393	0.119	1.940	0.000	0.020	0.25	0.000	2.E0E-5	4400	4400	271.0	289.1	Good
NV2077B	0.775	0.170	1.930	0.000	0.020	0.25	0.000	2.50E-5	5800	5800	271.0	289.8	Good
UCR-EC (acetaldehyde):													
EC-253	0.000	0.000	0.546	0.005	0.001	2.11	0.000	1.17E-4	21180	21180	302.6	304.4	Constant
EC-254	0.085	0.027	0.508	0.005	0.012	2.70	0.000	1.17E-4	21180	21180	303.4	303.4	Constant
UNC (propionaldehyde):													
JN1482B	0.222	0.078	1.020	0.015	0.020	0.37	0.040	2.50E-5	18000	20500	298.2	306.5	OK
AU2482R	0.246	0.090	0.690	0.005	0.030	0.28	0.040	2.50E-5	13000	21000	293.1	307.9	OK

TABLE 6-4. Results of acetaldehyde and propionaldehyde simulations.

Experiment Number	Initial Conditions			Maximum Ozone (ppm)			
	NO_x	NO_2/NO_x	HC/NO_x	Calc. (ppm)	Meas. (ppm)	Abs. Diff.	Pct. Diff.
UNC (acetaldehyde):							
JN1482R	0.312	0.279	9.9	0.828	0.731	0.097	13.3%
AU2482B	0.319	0.279	6.0	0.912	0.972	-0.060	- 6.2%
AU0880R	0.421	0.247	2.2	1.050	1.033	0.017	1.6%
DE2677B	0.407	0.287	4.7	0.044	0.039	0.005	12.8%
NV1977B	0.512	0.232	3.8	0.193	0.187	0.006	3.2%
NV2077B	0.945	0.180	2.0	0.068	0.063	0.005	7.9%
			UNC Average			0.012	5.4%
			Std. Deviation			±0.050	±7.4%
UCR-EC (acetaldehyde):							
EC-253	0.000	-	-	0.132	0.135	-0.003	- 2.2%
EC-254	0.112	0.241	4.5	0.270	0.268	0.002	0.7%
UNC (propionaldehyde):							
JN1482B			10.2	0.854	0.733	0.121	16.5%
AU2482R			6.2	0.902	0.941	-0.039	- 4.1%
			ALD2 Average			0.015	4.4%
			Std. Deviation			±0.055	± 7.9%

(continued)

TABLE 6-4. (concluded)

Experiment Number	Maximum PAN or PPN (ppm) Calc. (ppm)	Meas. (ppm)	Abs. Diff.	Pct. Diff.	Maximum HCHO (ppm) Calc. (ppm)	Meas. (ppm)	Abs. Diff.	Pct. Diff.
UNC (acetaldehyde):								
JN1482R	0.253	0.226	0.027	12%	0.30	0.15	0.15	100%
AU2482B	0.184	0.174	0.010	6%	0.19	0.19	0.00	0%
AU0880R	0.163	0.240	-0.077	- 32%	0.21	0.38	-0.17	- 45%
DE2677B	0.143	0.142	0.001	1%	-	-	-	-
NV1977B	0.235	0.265	-0.030	- 11%	-	-	-	-
NV2077B	0.195	0.198	0.003	- 2%	-	-	-	-
UNC Average			-0.011	- 4%			-0.01	18%
Std. Deviation			±0.037	± 16%			±0.16	± 74%
UCR-EC (acetaldehyde):								
EC-253	0.041	0.044	-0.003	- 7%	-	-	-	-
EC-254	0.088	0.073	0.015	21%	-	-	-	-
UNC (propionaldehyde):								
JN1482B	0.215	-	-	-	0.20	0.09	0.11	122%
AU2482R	0.144	0.179	-0.035	- 20%	0.15	0.11	0.04	36%
ALD2 Average			-0.009	- 4%			0.03	43%
Std. Deviation			±0.032	± 16%			±0.12	± 69%

TABLE 6-5. Initial conditions for UNC ethene smog chamber simulations.

Experiment Number	Initial Concentrations (ppm)								Other Conditions				
	Gas Phase						Walls		Water Vapor (ppm)		Temperature (K)		Light Conditions
	NO	NO_2	ETH	HONO	HCHO	CO	HCHO	k_{HONO}	Initial	Final	Initial	Final	
AU0479R	0.167	0.060	0.438	0.025	0.020	0.300	0.040	2.50E-5	20500	21200	294.3	307.9	Good
OCU584B	0.283	0.087	0.902	0.000	0.000	0.300	0.040	2.50E-5	9000	11000	284.1	298.1	Choppy
OCU584R	0.266	0.099	1.562	0.000	0.000	0.300	0.040	2.50E-5	9000	11000	284.1	298.1	Choppy
AU1078B	0.408	0.114	1.505	0.008	0.020	0.300	0.040	2.50E-5	21000	21000	294.3	307.9	Good
AU1078R	0.415	0.113	0.520	0.025	0.020	0.300	0.040	2.50E-5	21000	21000	294.3	307.9	Good
AU2378B	0.420	0.100	1.460	0.001	0.020	0.350	0.040	2.50E-5	14000	14000	285.5	306.2	Good
AU2378R	0.410	0.110	1.470	0.001	0.020	0.350	0.040	2.50E-5	15000	15000	285.5	306.2	Good
JL0880R	0.374	0.380	1.050	0.002	0.020	0.300	0.000	2.50E-5	13000	22000	291.2	306.4	Choppy
JL0986B	0.311	0.021	0.936	0.000	0.000	0.500	0.040	2.50E-5	16800	20600	295.7	314.3	Good
JL0986R	0.294	0.024	0.444	0.000	0.000	0.500	0.000	2.50E-5	16800	20600	295.7	314.3	Good
JL1386B	0.243	0.047	0.555	0.000	0.000	0.200	0.040	2.50E-5	15000	18000	294.2	310.1	Good

TABLE 6-6. Results of UNC ethene simulations.

Experiment Number	Initial Conditions NO_x	NO_2/NO_x	HC/NO_x	Maximum Ozone (ppm) Calc. (ppm)	Meas. (ppm)	Abs. Diff.	Pct. Diff.
AU0479R	0.227	0.264	3.9	0.687	0.729	-0.042	- 5.8%
OC0584B	0.370	0.235	4.9	0.674	0.675	-0.001	- 0.1%
OC0584R	0.365	0.271	8.6	1.129	0.856	0.273	31.9%
AU1078B	0.522	0.218	5.8	1.293	1.100	0.193	17.5%
AU1078R	0.528	0.214	2.0	0.183	0.180	0.003	1.7%
AU2378B	0.520	0.192	5.6	1.237	1.133	0.104	9.2%
AU2378R	0.520	0.212	5.7	1.218	1.109	0.109	9.8%
JL0880R	0.754	0.504	2.8	0.576	0.629	-0.053	- 8.4%
JL0986B	0.332	0.063	5.6	1.098	0.975	0.123	12.6%
JL0986R	0.318	0.075	2.8	0.586	0.679	-0.093	-13.7%
JL1386B	0.290	0.162	3.8	0.719	0.758	-0.039	- 5.1%
			UNC Average			0.052	4.5%
			Std. Deviation			±0.116	±13.3%

Experiment Number	Maximum HCHO (ppm) Calc. (ppm)	Meas. (ppm)	Abs. Diff.	Pct. Diff.
AU0479R	0.18	0.31	-0.13	- 42%
OC0584B	0.36	0.34	0.02	6%
OC0584R	0.67	0.55	0.12	22%
AU1078B	0.63	-	-	-
AU1078R	0.15	-	-	-
AU2378B	0.60	-	-	-
AU2378R	0.60	-	-	-
JL0880R	0.37	-	-	-
JL0986B	0.38	0.57	-0.19	- 33%
JL0986R	0.16	0.29	-0.13	- 45%
JL1386B	0.20	0.36	-0.16	- 44%
UNC Average			-0.08	-23%
Std. Deviation			±0.12	±29%

TABLE 6-7. Initial conditions for olefin smog chamber simulations.

Experiment Number	Initial Concentrations (ppm)								Other Conditions				
	Gas Phase						Walls		Water Vapor (ppm)		Temperature (K)		Light Conditions
	NO	NO_2	OLE	HONO	HCHO	CO	HCHO	k_{HONO}	Initial	Final	Initial	Final	
UNC:													
JL1386R[1]	0.246	0.045	0.207	0.000	0.000	0.200	0.000	2.50E-5	15000	18000	294.2	310.1	Good
OC1184B[1]	0.249	0.105	0.751	0.000	0.000	0.250	0.000	2.50E-5	11500	12500	289.9	297.2	Good
OC1284B[1]	0.502	0.180	0.653	0.000	0.000	0.250	0.000	2.50E-5	10500	12000	285.0	296.7	Choppy
AU1679R[1]	0.312	0.131	0.472	0.000	0.000	0.280	0.040	2.50E-5	20000	20000	287.1	301.3	Good
OC1278B[1]	0.364	0.115	0.443	0.000	0.000	0.350	0.040	2.50E-5	8500	20500	278.6	298.2	Good
OC2578B[1]	0.337	0.104	0.408	0.000	0.000	0.550	0.040	2.50E-5	8000	17000	271.9	294.2	OK
SE2383B[1]	0.339	0.038	0.543	0.000	0.000	0.250	0.000	0.00E-0	20000	25000	278.1	297.8	Good
SE2383R[2]	0.358	0.044	0.370	0.000	0.000	0.250	0.000	0.00E-0	20000	26000	278.1	297.8	Good
SE2583B[2]	0.382	0.044	0.722	0.000	0.000	0.250	0.000	0.00E-0	10500	21000	277.6	296.2	Good
SE2583R[2]	0.414	0.047	0.410	0.000	0.000	0.250	0.000	2.50E-5	10500	19500	277.6	296.2	Good
SE2783B[3]	0.381	0.046	0.752	0.015	0.000	0.250	0.040	2.50E-5	12500	21500	281.5	298.4	OK
SE2783R[2]	0.405	0.049	0.398	0.000	0.000	0.250	0.000	2.50E-5	11500	20500	281.5	298.4	OK
UCR-EC:													
EC-121[1]	0.410	0.101	0.483	0.030	0.000	2.193	0.000	1.17E-4	25480	25480	303.7	305.4	constant
EC-177[1]	0.364	0.099	0.493	0.010	0.010	2.193	0.000	1.17E-4	33930	33930	303.7	305.4	constant
EC-278[1]	0.366	0.128	1.016	0.005	0.008	0.030	0.000	1.17E-4	19000	19000	302.5	303.2	constant
EC-123[2]	0.401	0.106	0.404	0.020	0.000	1.881	0.000	1.17E-4	26700	26700	302.5	303.2	constant
EC-124[2]	0.608	0.385	0.424	0.020	0.000	1.872	0.000	1.17E-4	24400	24400	302.5	303.2	constant

[1] propylene, [2] 1-butene, [3] trans-2-butene.

TABLE 6-8. Results of olefin simulations.

Experiment Number	Initial Conditions NO_x	NO_2/NO_x	HC/NO_x	Maximum Ozone (ppm) Calc. (ppm)	Meas. (ppm)	Abs. Diff.	Pct. Diff.
UNC:							
JL1386R[1]	0.291	0.155	2.1	0.505	0.496	0.009	1.8%
OC1184B[1]	0.354	0.297	6.4	0.784	0.674	0.110	16.3%
OC1284B[1]	0.682	0.264	2.9	0.464	0.432	0.032	7.4%
AU1679R[1]	0.443	0.296	3.2	0.724	0.688	0.036	5.2%
OC1278B[1]	0.479	0.240	2.8	0.354	0.462	-0.108	-23.4%
OC2578B[1]	0.441	0.236	2.8	0.250	0.230	0.020	8.7%
SE2383B[1]	0.377	0.101	4.3	0.651	0.405	0.246	60.7%
SE2383R[2]	0.402	0.109	3.7	0.365	0.206	0.159	77.2%
SE2583B[2]	0.426	0.103	6.8	0.800	0.594	0.206	34.7%
SE2583R[2]	0.461	0.102	3.6	0.409	0.266	0.143	53.8%
SE2783B[3]	0.427	0.108	3.5	0.389	0.523	-0.134	-25.6%
SE2783R[2]	0.454	0.108	3.5	0.423	0.285	0.138	48.4%
			UNC Average			0.071	22.1%
			Std. Deviation			±0.117	±32.8
UCR-EC:							
EC-121[1]	0.511	0.198	2.8	0.441	0.506	-0.065	-12.8%
EC-177[1]	0.463	0.214	3.2	0.500	0.540	-0.040	- 7.4%
EC-278[2]	0.494	0.259	6.2	0.662	0.625	0.037	5.9%
EC-123[2]	0.507	0.209	3.2	0.356	0.506	-0.150	-29.6%
EC-124[2]	0.993	0.388	1.7	0.168	0.247	-0.079	-32.0%
			UCR-EC Average			-0.059	-15.2%
			Std. Deviation			±0.068	±15.8%
			OLE Average			0.033	11.1%
			Std. Deviation			±0.120	±33.3%

(continued)

TABLE 6-8. (concluded)

Experiment Number	Maximum PAN (ppm) Calc. (ppm)	Meas. (ppm)	Abs. Diff.	Pct. Diff.	Maximum HCHO (ppm) Calc. (ppm)	Meas. (ppm)	Abs. Diff.	Pct. Diff.
JL1386R	0.014	0.047	-0.033	- 70%	0.11	0.20	-0.09	- 45%
OC1184B	0.20	0.180	0.040	22%	0.39	0.48	-0.09	- 18%
OC1278B	0.083	0.000	0.083	100%	0.21	-	-	-
AU1679R	0.171	0.182	-0.011	- 6%	0.22	-	-	-
OC2578B	0.075	0.050	0.025	50%	0.19	-	-	-
OC1284B	0.138	0.144	-0.006	- 4%	0.30	0.43	-0.13	- 30%
SE2383B	0.187	-	-	-	0.25	-	-	-
SE2383R	0.076	-	-	-	0.15	-	-	-
SE2583B	0.238	-	-	-	0.34	-	-	-
SE2583R	0.097	-	-	-	0.17	-	-	-
SE2783B	0.122	-	-	-	0.11	-	-	-
SE2783R	0.085	-	-	-	0.17	-	-	-
UNC Average			0.016	15%			-0.07	- 31%
Std. Deviation			±0.042	± 57%			±0.04	± 14%
UCR-EC:								
EC-121[1]	0.069	0.167	-0.098	- 59%	0.26	0.28	-0.02	- 7%
EC-177[1]	0.093	0.165	-0.072	- 44%	0.26	0.09	0.17	189%
EC-278[2]	0.276	-	-	-	0.55	0.45	0.10	22%
EC-123[2]	0.088	0.065	0.023	35%	0.20	0.18	0.02	11%
EC-124[2]	0.035	0.038	-0.003	- 8%	0.19	0.16	0.03	19%
UCR-EC Average			-0.038	- 19%			0.06	47%
Std. Deviation			±0.057	± 42%			±0.08	± 80%
OLE Average			-0.005	2%			0.00	18%
Std. Deviation			±0.053	± 52%			±0.10	± 73%

[1]propylene, [2]1-butene, [3]trans-2-butene.

TABLE 6-9. Initial conditions for toluene smog chamber simulations.

Experiment Number	Initial Concentrations (ppm)								Other Conditions				
	Gas Phase						Walls		Water Vapor (ppm)		Temperature (K)		Light Conditions
	NO	NO_2	TOL	HONO	HCHO	CO	HCHO	k_{HONO}	Initial	Final	Initial	Final	
UNC:													
JN2779B	0.263	0.069	2.210	0.001	0.010	0.323	0.040	5.00E-6	21400	38000	286.5	298.1	Good
JL3080R	0.156	0.026	0.550	0.005	0.010	0.200	0.040	2.50E-5	20600	39800	292.7	308.5	Good
JN2784B	0.300	0.035	0.702	0.001	0.010	0.213	0.040	2.50E-5	20000	38000	293.8	311.8	Good
AU1579B	0.276	0.086	0.740	0.001	0.010	0.338	0.040	2.50E-5	10000	15000	291.2	304.4	Choppy
AU0183R	0.344	0.051	0.655	0.003	0.010	0.323	0.040	2.50E-5	21100	23600	297.2	310.5	Good
OC2782R	0.280	0.110	0.642	0.004	0.002	0.320	0.020	2.00E-5	6500	23800	278.2	290.9	Good
AU2782B	0.310	0.121	0.428	0.005	0.015	0.195	0.040	2.50E-5	17900	18600	291.3	306.0	Choppy
UCR-EC:													
EC-264	0.420	0.056	1.156	0.005	0.008	0.300	0.000	1.37E-4	18390	18390	304.0	304.0	constant
EC-265	0.435	0.047	1.070	0.010	0.012	0.330	0.000	1.37E-4	22040	22040	302.6	302.6	constant
EC-266	0.432	0.059	1.196	0.005	0.008	0.330	0.000	1.37E-4	19280	19280	302.6	302.6	constant
EC-269	0.398	0.074	0.566	0.015	0.003	0.200	0.000	1.37E-4	18920	18920	302.7	302.7	constant
EC-271	0.186	0.028	1.146	0.010	0.004	0.200	0.000	1.40E-4	20070	20070	302.5	302.5	constant
EC-273	0.096	0.014	0.587	0.015	0.002	0.326	0.000	1.37E-4	20920	20920	303.5	303.5	constant
EC-327	0.357	0.096	0.573	0.010	0.013	0.200	0.000	1.56E-4	24840	24840	303.0	303.0	constant
EC-340	0.333	0.096	0.585	0.015	0.005	2.593	0.000	1.56E-4	25900	25900	303.0	303.0	constant

TABLE 6-10. Results of toluene simulations.

Experiment Number	Initial Conditions			Maximum Ozone (ppm)			
	NO_x	NO_2/NO_x	HC/NO_x	Calc. (ppm)	Meas. (ppm)	Abs. Diff.	Pct. Diff.
UNC:							
JN2779B	0.332	0.208	46.6	0.456	0.399	0.057	14.3%
JL3080R	0.182	0.143	21.2	0.297	0.274	0.023	8.4%
JN2784B	0.335	0.104	14.7	0.415	0.401	0.014	3.5%
AU1579B	0.362	0.238	14.3	0.390	0.403	-0.013	- 3.2%
AU0183R	0.395	0.129	11.6	0.411	0.458	-0.047	-10.3%
OC2782R	0.390	0.282	11.4	0.102	0.095	0.007	7.4%
AU2782B	0.431	0.281	7.0	0.136	0.128	0.008	6.3%
			UNC Average			0.007	3.8%
			Std. Deviation			±0.032	±8.1%
UCR-EC:							
EC-273	0.110	0.127	37.6	0.231	0.215	0.016	7.4%
EC-271	0.214	0.131	37.5	0.313	0.296	0.017	5.7%
EC-266	0.491	0.120	17.1	0.382	0.403	-0.021	- 5.2%
EC-264	0.476	0.118	17.0	0.381	0.419	-0.038	- 9.1%
EC-265	0.482	0.098	15.5	0.371	0.393	-0.022	- 5.6%
EC-340	0.429	0.224	9.5	0.318	0.344	-0.026	- 7.6%
EC-327	0.453	0.212	8.9	0.309	0.376	-0.067	-17.8%
EC-269	0.472	0.157	8.4	0.281	0.298	-0.017	- 5.7%
			UCR-EC Average			-0.020	-4.7%
			Std. Deviation			±0.027	±8.1%
			Toluene Average			-0.007	0.6%
			Std. Deviation			±0.032	±9.0%

(continued)

TABLE 6-10. (concluded)

Experiment Number	Maximum PAN (ppm) Calc. (ppm)	Meas. (ppm)	Abs. Diff.	Pct. Diff.	Maximum HCHO (ppm) Calc. (ppm)	Meas. (ppm)	Abs. Diff.	Pct. Diff.
UNC:								
JN2779B	0.079	0.076	0.003	4%	0.07	0.08	-0.01	- 13%
JL3080R	0.023	0.037	-0.014	- 38%	0.05	0.09	-0.04	- 44%
JN2784B	0.024	0.013	0.011	85%	0.07	0.08	-0.01	- 13%
AU1579B	0.033	0.057	-0.024	- 42%	0.06	0.06	0.00	0%
AU0183R	0.022	0.044	-0.022	- 59%	0.07	0.07	0.00	0%
OC2782R	0.023	0.013	0.010	77%	0.04	0.01	0.03	300%
AU2782B	0.005	0.012	-0.007	- 58%	0.05	0.01	0.04	400%
UNC Average			-0.006	- 4%			0.00	90%
Std. Deviation			±0.015	± 62%			±0.03	±181%
UCR-EC:								
EC-273	0.022	0.032	-0.010	- 31%	0.04	0.02	0.02	100%
EC-271	0.040	0.053	-0.013	- 25%	0.06	0.04	0.02	50%
EC-266	0.064	0.075	-0.011	- 15%	0.09	0.08	0.01	13%
EC-264	0.058	0.071	-0.013	- 18%	0.09	0.03	0.06	200%
EC-265	0.062	0.072	-0.010	- 14%	0.08	0.04	0.04	100%
EC-340	0.033	0.042	-0.009	- 21%	0.06	0.05	0.01	20%
EC-327	0.032	0.041	-0.009	- 22%	0.06	0.06	0.00	0%
EC-269	0.030	0.050	-0.020	- 40%	0.06	0.04	0.02	50%
UCR-EC Average			-0.012	- 23%			0.02	67%
Std. Deviation			±0.004	± 9%			±0.02	± 66%
Toluene Average			-0.009	- 14%			0.01	78%
Std. Deviation			±0.010	± 42%			±0.02	±128%

TABLE 6-11. Initial conditions for xylene smog chamber simulations.

Experiment Number	Initial Concentrations (ppm)								Other Conditions				
	Gas Phase						Walls		Water Vapor (ppm)		Temperature (K)		Light Conditions
	NO	NO_2	XYL	HONO	HCHO	CO	HCHO	k_{HONO}	Initial	Final	Initial	Final	
UNC (m-xylene):													
JN2784R	0.303	0.040	0.249	0.001	0.010	0.213	0.040	2.50E-5	20000	38000	293.8	311.8	Good
UNC (o-xylene):													
JL3080B	0.155	0.023	0.279	0.005	0.010	0.200	0.040	2.50E-5	20600	39800	292.7	308.5	Good
AU0183B	0.323	0.049	0.328	0.003	0.010	0.323	0.040	2.50E-5	21100	23600	297.2	310.5	Good
OC2782B	0.282	0.117	0.347	0.004	0.002	0.320	0.020	2.00E-5	6500	23800	278.2	290.9	Good
AU2782R	0.314	0.120	0.249	0.005	0.015	0.195	0.040	2.50E-5	17900	18600	291.3	306.0	Choppy
UCR-EC (m-xylene):													
EC-346	0.204	0.059	0.494	0.015	0.020	0.798	0.000	1.53E-4	26530	26530	304.2	304.2	constant
EC-345	0.220	0.059	0.480	0.015	0.020	5.206	0.000	1.53E-4	25210	25210	303.1	303.1	constant
EC-344	0.520	0.154	0.494	0.015	0.020	1.858	0.000	1.57E-4	28990	28990	303.2	303.2	constant

TABLE 6-12. Results of xylene simulations.

Experiment Number	Initial Conditions			Maximum Ozone (ppm)			
	NO_x	NO_2/NO_x	HC/NO_x	Calc. (ppm)	Meas. (ppm)	Abs. Diff.	Pct. Diff.
UNC (m-xylene):							
JN2784R	0.343	0.120	5.8	0.722	0.675	0.047	7.0%
UNC (o-xylene):							
JL3080B	0.178	0.129	12.5	0.396	0.555	-0.159	-28.6%
AU0183B	0.274	0.179	7.0	0.697	0.686	0.011	1.6%
OC2782B	0.399	0.293	7.0	0.425	0.395	0.030	7.6%
AU2782R	0.434	0.276	4.6	0.652	0.491	0.161	32.8%
			UNC Average			0.018	4.1%
			Std. Deviation			±0.115	±21.9%
UCR-EC (m-xylene):							
EC-346	0.263	0.224	15.0	0.398	0.384	0.014	3.6%
EC-345	0.279	0.211	13.8	0.406	0.396	0.010	2.5%
EC-344	0.674	0.228	5.9	0.616	0.586	0.030	5.1%
			UCR-EC Average			0.018	3.7%
			Std. Deviation			±0.011	±1.3%
			Xylene Average			0.018	4.0%
			Std. Deviation			±0.087	±16.6%

(continued)

TABLE 6-12. (concluded)

Experiment Number	Maximum PAN (ppm) Calc. (ppm)	Meas. (ppm)	Abs. Diff.	Pct. Diff.	Maximum HCHO (ppm) Calc. (ppm)	Meas. (ppm)	Abs. Diff.	Pct. Diff.
UNC (m-xylene):								
JN2784R	0.082	0.086	-0.004	- 5%	0.07	0.06	0.01	17%
UNC (o-xylene):								
JL3080B	0.073	0.091	-0.018	- 20%	0.10	0.20	-0.10	- 50%
AU0183B	0.112	0.102	0.010	10%	0.11			
OC2782B	0.158	0.112	0.046	41%	0.07	0.04	0.03	75%
AU2782R	0.107	0.093	0.014	15%	0.06	0.10	-0.04	- 40%
UNC Average			0.010	8%			-0.03	1%
Std. Deviation			±0.024	± 23%			±0.06	± 58%
UCR-EC (m-xylene):								
EC-346	0.102	0.102	0.000	0%	0.10	0.07	0.03	43%
EC-345	0.108	0.107	0.001	1%	0.13	0.14	-0.01	- 7%
EC-344	0.213	0.175	0.038	22%	0.11	0.11	0.00	0%
UCR-EC Average			0.013	8%			0.01	12%
Std. Deviation			±0.022	± 12%			±0.02	± 27%
Xylene Average			0.011	8%			-0.01	5%
Std. Deviation			±0.022	± 19%			±0.05	± 44%

TABLE 6-13. Initial conditions for UNC isoprene and α-pinene smog chamber simulations.

Experiment Number	Initial Concentrations (ppm)								Other Conditions				
	Gas Phase						Walls		Water Vapor (ppm)		Temperature (K)		Light Conditions
	NO	NO_2	HCHO	HONO	CO	NMHC	HCHO	k_{HONO}	Initial	Final	Initial	Final	
Isoprene:													
JL1480B	0.202	0.041	0.005	0.003	0.413	2.170	0.020	2.50E-5	26000	26000	292	307	Good
JL1480R	0.211	0.044	0.005	0.003	0.413	4.900	0.020	2.50E-5	26000	26000	292	307	Good
JL1680B	0.144	0.042	0.005	0.003	0.393	1.965	0.020	2.50E-5	26000	26000	293	310	Good
JL1680R	0.137	0.043	0.005	0.003	0.330	4.035	0.020	2.50E-5	26000	26000	293	310	Good
JL1780B	0.380	0.080	0.005	0.003	0.360	2.580	0.020	2.50E-5	26000	26000	294	311	Good
JL1780R	0.391	0.075	0.005	0.003	0.388	0.980	0.020	2.50E-5	26000	26000	294	311	Good
JN1780B	0.075	0.021	0.005	0.003	0.360	1.300	0.020	2.50E-5	26000	26000	291	303	Choppy
JN1780R	0.137	0.052	0.005	0.003	0.388	0.500	0.020	2.50E-5	26000	26000	291	303	Choppy
JN2080R	0.379	0.098	0.005	0.003	0.413	0.500	0.020	2.50E-5	26000	26000	287	305	Choppy
JN2280B	0.175	0.030	0.005	0.001	0.413	1.560	0.020	2.50E-5	26000	26000	284	306	Good
JN2280R	0.174	0.029	0.005	0.003	0.413	3.830	0.020	2.50E-5	26000	26000	284	306	Good
JN2380B	0.173	0.038	0.005	0.003	0.413	1.270	0.020	2.50E-5	26000	26000	286	306	Choppy
α-Pinene:													
JL2580B	0.198	0.049	0.005	0.006	0.388	0.940	0.020	2.50E-5	26000	26000	291	304	Choppy
JL2580R	0.207	0.040	0.005	0.003	0.388	1.020	0.020	2.50E-5	26000	26000	291	304	Choppy
JN1580B	0.177	0.042	0.005	0.003	0.388	0.800	0.020	2.50E-5	26000	26000	288	308	Choppy
JN1580R	0.169	0.044	0.005	0.003	0.388	1.220	0.020	2.50E-5	26000	26000	288	308	Choppy
JL1580B	0.157	0.031	0.005	0.003	0.388	2.680	0.020	2.50E-5	26000	26000	290	304	Good
JL1580R	0.157	0.030	0.005	0.003	0.388	1.040	0.020	2.50E-5	26000	26000	290	304	Good
JN1480B	0.182	0.030	0.005	0.003	0.388	1.700	0.020	2.50E-5	26000	26000	283	305	Good
JN1480R*	0.182	0.028	0.005	0.003	0.388	3.150	0.020	2.50E-5	26000	26000	283	305	Good
JN2180R	0.394	0.105	0.005	0.003	0.388	1.970	0.020	2.50E-5	26000	26000	286	302	Choppy

*2.25 ppmC α-pinene and 0.90 ppmC isoprene.

TABLE 6-14. Results of UNC isoprene and α-pinene simulations.

Experiment Number	Initial Conditions			Maximum Ozone (ppm)			
	NO_x	NO_2/NO_x	HC/NO_x	Calc. (ppm)	Meas. (ppm)	Abs. Diff.	Pct. Diff.
Isoprene:							
JL1480B	0.243	0.169	8.9	0.730	0.630	0.100	15.9%
JL1480R	0.255	0.173	19.2	0.475	0.435	0.040	9.3%
JL1680B	0.186	0.226	10.6	0.748	0.837	-0.089	-10.6%
JL1680R	0.180	0.239	22.4	0.502	0.652	-0.150	-23.0%
JL1780B	0.460	0.174	5.6	0.959	1.297	-0.338	-26.1%
JL1780R	0.466	0.161	2.1	0.725	0.806	-0.081	-10.0%
JN1780B	0.096	0.219	13.5	0.363	0.406	-0.043	-10.6%
JN1780R	0.189	0.275	2.6	0.479	0.354	0.125	35.3%
JN2080R	0.478	0.205	1.0	0.130	0.088	0.042	47.7%
JN2280B	0.205	0.146	7.6	0.658	0.550	0.108	19.6%
JN2280R	0.203	0.143	18.9	0.434	0.392	0.042	10.7%
JN2380B	0.210	0.181	6.0	0.665	0.570	0.094	16.5%
			Isoprene Average			-0.013	6.3%
			Std. Deviation			±0.136	±22.8%
α-Pinene:							
JL2580B	0.247	0.198	3.8	0.274	0.334	-0.060	-18.0%
JL2580R	0.247	0.162	4.1	0.340	0.377	-0.037	- 9.8%
JN1580B	0.219	0.192	3.7	0.309	0.332	-0.023	- 6.9%
JN1580R	0.213	0.207	5.7	0.572	0.473	0.099	20.9%
JL1580B	0.188	0.165	14.3	0.573	0.470	0.103	21.9%
JL1580R	0.184	0.163	5.7	0.425	0.202	0.223	110.4%
JN1480B	0.212	0.142	8.0	0.564	0.519	0.045	8.7%
JN1480R	0.210	0.133	15.0	0.552	0.465	0.087	18.7%
JN2180R	0.499	0.210	3.9	0.363	0.223	0.140	63.2%
			α-Pinene Average			0.064	23.2%
			Std. Deviation			±0.092	±40.5%
			Biogenic HC Average			0.020	13.5%
			Std. Deviation			±0.123	±31.9%

(continued)

TABLE 6-14. (concluded)

Experiment Number	Maximum PAN (ppm) Calc. (ppm)	Meas. (ppm)	Abs. Diff.	Pct. Diff.	Maximum HCHO (ppm) Calc. (ppm)	Meas. (ppm)	Abs. Diff.	Pct. Diff.
Isoprene:								
JL1480B	0.120	0.101	0.019	19%	0.379	0.381	-0.002	- 1%
JL1480R	0.118	0.101	0.017	17%	0.772	0.660	0.112	17%
JL1680B	0.086	0.080	0.006	8%	0.357	0.346	0.011	3%
JL1680R	0.082	0.072	0.010	14%	0.643	0.548	0.095	17%
JL1780B	0.168	0.188	-0.020	- 11%	0.452	0.633	-0.181	- 29%
JL1780R	0.035	0.047	-0.012	- 26%	0.194	0.230	-0.036	- 16%
JN1780B	0.058	0.053	0.005	9%	0.203	0.182	0.021	12%
JN1780R	0.039	0.034	0.005	15%	0.091	0.076	0.015	20%
JN2080R	0.006	0.008	-0.002	- 25%	0.099	-	-	-
JN2280B	0.109	0.086	0.023	27%	0.269	0.374	-0.105	- 28%
JN2280R	0.106	0.069	0.037	54%	0.607	0.572	0.035	6%
JN2380B	0.099	0.081	0.018	22%	0.224	0.196	0.028	14%
Isoprene Average			0.009	10%			-0.001	1%
Std. Deviation			±0.016	± 22%			±0.083	± 18%
a-Pinene:								
JL2580B	0.016	-	-	-	0.059	-	-	-
JL2580R	0.025	-	-	-	0.068	-	-	-
JN1580B	0.013	0.016	-0.003	- 19%	0.051	0.038	0.013	34%
JN1580R	0.049	0.022	0.027	123%	0.073	0.066	0.007	11%
JL1580B	0.128	0.033	0.095	288%	0.134	0.105	0.029	28%
JL1580R	0.048	0.011	0.037	336%	0.058	0.054	0.004	7%
JN1480B	0.096	0.032	0.064	200%	0.085	-	-	-
JN1480R	0.143	0.046	0.097	211%	0.236	-	-	-
JN2180R	0.054	-	-	-	0.103	-	-	-
α-Pinene Average			0.053	190%			0.013	20%
Std. Deviation			±0.040	±126%			±0.011	± 13%
Biogenic HC Average			0.024	70%			0.003	6%
Std. Deviation			±0.033	±112%			±0.071	± 18%

TABLE 6-15. Initial conditions for UNC SynUrban and SynAuto mixture simulations.

Experiment Number	Initial Concentrations (ppm)								Other Conditions				
	Gas Phase						Walls		Water Vapor (ppm)		Temperature (K)		Light Conditions
	NO	NO_2	NMOC (ppmC)	HONO	HCHO	CO	HCHO	k_{HONO}	Initial	Final	Initial	Final	
SynUrban:													
AU2284R	0.254	0.070	3.04	0.001	0.056	0.300	0.040	2.50E-5	8000	10000	288.4	306.7	Good
AU2584B	0.262	0.070	1.07	0.005	0.020	0.300	0.040	2.50E-5	21000	22000	292.2	303.9	Choppy
ST0184B	0.245	0.059	3.31	0.002	0.055	0.300	0.040	2.50E-5	14000	17000	287.0	306.7	Good
ST0284B	0.262	0.090	0.76	0.005	0.012	0.300	0.040	2.50E-5	16000	20000	288.2	310.0	Good
ST0284R	0.284	0.058	1.10	0.005	0.018	0.300	0.040	2.50E-5	16000	20000	288.2	310.0	Good
ST0384R	0.244	0.109	1.10	0.005	0.019	0.300	0.040	2.50E-5	14000	17000	303.0	303.0	Choppy
SynAuto:													
OC0483B	0.214	0.037	2.20	0.001	0.010	20.30	0.080	2.50E-5	15000	26000	285.6	301.7	OK
OC0783B	0.301	0.038	2.70	0.000	0.000	0.230	0.040	2.50E-5	20000	30000	286.4	295.0	Good
OC0783R	0.291	0.040	2.70	0.000	0.000	0.210	0.040	2.50E-5	12000	18000	286.4	295.0	Good
AU0484R	0.293	0.077	1.23	0.030	0.019	0.300	0.040	2.50E-5	33000	37000	296.1	310.9	Late Chop
AU0584B	0.273	0.076	1.32	0.025	0.019	0.300	0.040	2.50E-5	29000	46000	295.1	310.8	Good
AU0584R	0.280	0.077	0.91	0.025	0.020	0.300	0.040	2.50E-5	33000	48000	295.1	310.8	Good
AU0684B	0.283	0.072	3.24	0.015	0.057	0.300	0.040	2.50E-5	29000	42000	295.0	312.0	Good
AU0684R	0.283	0.071	2.25	0.018	0.038	0.300	0.040	2.50E-5	27000	43000	295.0	312.0	Good
AU0784R	0.302	0.083	1.32	0.030	0.041	0.300	0.040	2.50E-5	25000	37000	296.0	311.3	Good
AU0884B	0.264	0.078	3.68	0.010	0.057	0.300	0.040	2.50E-5	26000	30000	295.3	311.2	Late Chop
AU0984R	0.302	0.087	1.28	0.035	0.019	0.300	0.040	2.50E-5	29000	33000	296.2	313.7	OK
SynutoUrban:													
ST0884B	0.206	0.126	2.79	0.004	0.054	0.300	0.040	2.50E-5	7000	10000	281.6	303.7	Good
ST0884R	0.220	0.119	1.84	0.002	0.030	0.300	0.040	2.50E-5	6000	8000	281.6	303.7	Good
ST1784R	0.271	0.070	2.14	0.002	0.036	0.300	0.040	2.50E-5	20000	20000	280.0	296.2	Choppy
ST2184B	0.273	0.086	2.42	0.001	0.184	0.300	0.040	2.50E-5	9000	10000	285.5	305.6	Good
ST2184R	0.275	0.088	2.43	0.002	0.010	0.300	0.040	2.50E-5	7000	7500	285.5	305.6	Good

TABLE 6-16. Results of UNC SynUrban and SynAuto mixture simulations.

Experiment Number	Initial Conditions			Maximum Ozone (ppm)			
	NO_x	NO_2/NO_x	HC/NO_x	Calc. (ppm)	Meas. (ppm)	Abs. Diff.	Pct. Diff.
SynUrban:							
AU2284R	0.324	0.216	9.9	0.791	0.657	0.134	20.4%
AU2584B	0.332	0.211	3.4	0.073	0.096	-0.023	-24.0%
ST0184B	0.304	0.194	10.7	0.748	0.646	0.102	15.8%
ST0284B	0.352	0.256	2.3	0.015	0.020	-0.005	-25.0%
ST0284R	0.342	0.170	3.6	0.096	0.119	-0.023	-19.3%
ST0384R	0.353	0.304	3.1	0.045	0.048	-0.003	- 6.3%
			SynUrban Average			0.030	- 6.4%
			Std. Deviation			±0.069	±20.2%
SynAuto:							
OC0483B	0.251	0.147	8.7	0.623	0.642	-0.019	- 3.0%
OC0783B	0.339	0.112	8.1	0.567	0.451	0.116	25.7%
OC0783R	0.331	0.121	8.0	0.282	0.179	0.103	57.5%
AU0484R	0.370	0.208	3.4	0.415	0.515	-0.100	-19.4%
AU0584B	0.349	0.218	3.7	0.580	0.595	-0.015	- 2.5%
AU0584R	0.357	0.216	2.7	0.254	0.335	-0.081	-24.2%
AU0684B	0.355	0.203	9.3	0.876	0.940	-0.064	- 6.8%
AU0684R	0.354	0.201	6.5	0.836	0.887	-0.051	- 5.7%
AU0784R	0.385	0.216	3.5	0.528	0.602	-0.074	-12.3%
AU0884B	0.342	0.228	10.8	0.834	0.834	0.000	0.0%
AU0984R	0.389	0.224	3.4	0.404	0.521	-0.117	-22.5%
			SynAuto Average			-0.027	- 1.2%
			Std. Deviation			±0.077	±23.8%
SynAutoUrban:							
ST0884B	0.331	0 380	8.6	0.712	0.750	-0.038	- 5.1%
ST0884R	0.339	0.351	5.7	0.621	0.566	0.055	9.7%
ST1784R	0.341	0.205	6.5	0.589	0.539	0.050	9.3%
ST2184B	0.359	0.240	7.2	0.820	0.721	0.099	13.7%
ST2184R	0.363	0.242	6.6	0.748	0.671	0.077	11.5%
			SynAutoUrban Average			0.049	7.8%
			Std. Deviation			±0.052	7.4%
			Synthetic Mix Average			0.006	- 0.6%
			Std. Deviation			±0.075	±20.1%

(continued)

TABLE 6-16. (concluded)

Experiment Number	Maximum PAN (ppm) Calc. (ppm)	Meas. (ppm)	Abs. Diff.	Pct. Diff.	Maximum HCHO (ppm) Calc. (ppm)	Meas. (ppm)	Abs. Diff.	Pct. Diff.
SynUrban:								
AU2284R	0.056	-	-	-	0.11	0.16	-0.05	- 31%
AU2584B	0.002	0.004	-0.002	- 50%	0.05	0.07	-0.02	- 29%
ST0184B	0.062	0.052	0.010	16%	0.12	0.15	-0.03	- 20%
ST0284B	0.000	0.004	-0.004	-	0.04	0.09	-0.05	- 56%
ST0284R	0.001	0.004	-0.003	- 75%	0.05	0.08	-0.03	- 38%
ST0384R	0.002	-	-	-	0.05	0.06	-0.01	- 17%
SynUrban Average			0.000	- 36%			-0.03	- 32%
Std. Deviation			±0.007	± 47%			±0.02	± 14%
SynAuto:								
OC0483B	0.047	0.060	-0.017	- 28%	0.16	0.30	-0.14	- 47%
OC0783B	0.083	0.101	-0.018	- 18%	0.16	0.33	-0.17	- 52%
OC0783R	0.036	0.056	-0.020	- 36%	0.09	0.11	-0.02	- 18%
AU0484R	0.006	0.028	-0.022	- 79%	0.10	0.04	0.06	150%
AU0584B	0.012	0.032	-0.020	- 63%	0.11	0.10	0.01	10%
AU0584R	0.002	0.013	-0.011	- 85%	0.09	0.08	0.01	13%
AU0684B	0.070	0.142	-0.072	- 51%	0.25	0.19	0.06	38%
AU0684R	0.043	0.086	-0.043	- 50%	0.18	0.19	-0.01	- 5%
AU0784R	0.008	0.031	-0.023	- 74%	0.12	-	-	-
AU0884B	0.077	0.130	-0.053	- 41%	0.28	0.33	-0.05	- 15%
AU0984R	0.004	0.021	-0.017	- 81%	0.10	0.14	-0.04	- 29%
SynAuto Average			-0.029	- 55%			- 0.03	5%
Std. Deviation			±0.019	± 23%			± 0.08	± 58%
SynAutoUrban:								
ST0884B	0.082	0.052	0.030	58%	0.18	-	-	-
ST0884R	0.046	0.030	0.016	53%	0.12	-	-	-
ST1784R	0.078	0.069	0.009	13%	0.14	0.22	-0.08	- 36%
ST2184B	0.061	0.061	0.000	0%	0.23	0.23	-0.00	0%
ST2184R	0.047	0.052	-0.005	- 10%	0.17	0.19	-0.02	- 11%
SynAutoUrban Average			0.010	23%			-0.03	- 16%
Std. Deviation			±0.014	± 31%			±0.04	± 18%
Synthetic Mix Average			-0.013	- 32%			-0.03	- 10%
Std. Deviation			±0.024	± 44%			±0.06	± 45%

TABLE 6-17. Initial conditions for UCR-EC seven component hydrocarbon mixture simulations.

Experiment Number	Initial Concentrations (ppm)								Other Conditions			
	Gas Phase						Walls		Water Vapor (ppm)		Temperature (K)	
	NO	NO_2	(ppmC)	HONO	HCHO	CO	HCHO	k_{HONO}	Initial	Final	Initial	Final
EC-231	0.440	0.052	13.2	0.016	0.026	1.630	0.000	1.17E-4	17000	17000	302.6	304.4
EC-232	0.469	0.024	9.3	0.006	0.009	1.740	0.000	1.17E-4	17000	17000	302.6	304.4
EC-233	0.096	0.007	9.5	0.005	0.004	1.299	0.000	1.17E-4	17000	17000	302.6	304.4
EC-237	0.377	0.106	10.5	0.012	0.026	0.963	0.000	1.17E-4	17000	17000	302.6	304.4
EC-238	0.718	0.234	10.1	0.024	0.026	0.680	0.000	1.17E-4	17000	25500	302.6	303.4
EC-241	0.379	0.110	5.0	0.002	0.026	1.300	0.000	1.17E-4	17000	25500	302.6	303.4
EC-242	0.377	0.125	12.8	0.018	0.028	1.400	0.000	1.17E-4	17000	25500	302.6	303.4
EC-243	0.386	0.114	9.7	0.018	0.003	0.610	0.000	1.17E-4	17000	25500	302.6	303.4
EC-245	0.743	0.259	12.9	0.035	0.016	2.500	0.000	1.17E-4	17000	25500	302.6	303.4
EC-246	0.386	0.122	8.6	0.015	0.004	0.000	0.000	1.17E-4	17000	17000	302.6	304.4
EC-247	0.380	0.125	6.2	0.018	0.003	0.440	0.000	1.37E-4	17000	25500	302.6	303.4

TABLE 6-18. Results of UCR-EC seven component hydrocarbon mixture simulations.

Experiment Number	Initial Conditions			Maximum Ozone (ppm)			
	NO_x	NO_2/NO_x	HC/NO_x	Calc. (ppm)	Meas. (ppm)	Abs. Diff.	Pct. Diff.
EC-231	0.492	0.113	26.8	0.722	0.620	0.102	16.5%
EC-232	0.493	0.049	18.9	0.405	0.305	0.100	32.8%
EC-233	0.103	0.068	92.3	0.405	0.327	0.078	23.8%
EC-237	0.483	0.219	21.7	0.706	0.655	0.051	7.8%
EC-238	0.952	0.244	10.6	0.776	0.694	0.082	11.8%
EC-241	0.489	0.225	10.1	0.400	0.408	-0.008	- 2.0%
EC-242	0.502	0.249	25.6	0.658	0.682	-0.024	- 3.5%
EC-243	0.500	0.772	19.4	0.715	0.716	-0.001	0.1%
EC-245	1.002	0.742	12.8	0.922	0.892	0.030	3.4%
EC-246	0.508	0.240	16.9	0.655	0.574	0.081	14.1%
EC-247	0.505	0.752	12.2	0.665	0.655	0.010	1.5%
			UCR-EC Average			0.046	9.7%
			Std. Deviation			±0.046	±11.5%

Experiment Number	Maximum PAN (ppm)				Maximum HCHO (ppm)			
	Calc. (ppm)	Meas. (ppm)	Abs. Diff.	Pct. Diff.	Calc. (ppm)	Meas. (ppm)	Abs. Diff.	Pct. Diff.
EC-231	0.158	0.095	0.063	66%	0.53	0.57	-0.04	- 7%
EC-232	0.043	0.040	0.003	8%	0.14	-	-	-
EC-233	0.051	0.037	0.014	38%	0.18	-	-	-
EC-237	0.153	0.100	0.053	53%	0.49	0.39	0.10	26%
EC-238	0.192	0.113	0.079	70%	0.48	0.58	-0.10	- 17%
EC-241	0.052	0.047	0.005	11%	0.23	0.22	0.01	5%
EC-242	0.180	0.140	0.040	29%	0.89	0.84	0.05	6%
EC-243	0.140	0.100	0.040	40%	0.90	0.77	0.13	17%
EC-245	0.297	0.194	0.103	53%	1.04	0.94	0.10	11%
EC-246	0.107	0.070	0.037	53%	0.14	0.12	0.02	17%
EC-247	0.163	0.106	0.057	54%	0.52	0.45	0.07	16%
UCR-EC Average			0.045	43%			0.04	8%
Std. Deviation			±0.031	± 20%			±0.07	± 13%

TABLE 6-19. Initial conditions for UCR-ITC multi-day simulations.

Experiment Number	Initial Concentrations (ppm)								Other Conditions			
	Gas Phase						Walls		Water Vapor (ppm)		Temperature (K)	
	NO	NO_2	NMOC (ppmC)	HONO	HCHO	CO	k_{HCHO}	k_{HONO}	Initial	Final	Initial	Final
ITC630	0.233	0.073	1.9	0.005	0.007	0.963	1.0E-4	3.50E-5	17000	17000	293.6	300.0
ITC631	0.237	0.092	1.0	0.010	0.020	0.963	1.0E-4	3.50E-5	17000	17000	293.6	303.0
ITC633	0.457	0.182	4.0	0.010	0.013	0.963	1.0E-4	3.50E-5	17000	17000	293.6	300.0
ITC635	0.902	0.304	4.0	0.015	0.013	0.963	1.0E-4	3.50E-5	17000	17000	293.6	299.0
ITC637	0.237	0.073	4.0	0.015	0.007	0.963	1.0E-4	3.50E-5	17000	17000	293.6	302.9

TABLE 6-20. Results of UCR ITC multi-day experiment simulations.

Experiment Number	Initial Conditions			Maximum PAN (ppm)				Maximum HCHO (ppm)			
	NO_x	NO_2/NO_x	HC/NO_x	Calc. (ppm)	Meas. (ppm)	Abs. Diff.	Pct. Diff.	Calc. (ppm)	Meas. (ppm)	Abs. Diff.	Pct. Diff.
ITC-630	0.306	0.239	6.3	0.023	0.027	-0.004	- 15%	0.09	0.12	-0.03	- 25%
ITC-631	0.329	0.280	3.2	0.015	0.022	-0.007	- 32%	0.06	0.07	-0.01	- 14%
ITC-633	0.639	0.762	6.2	0.045	0.044	0.001	2%	0.17	-	-	-
ITC-635	1.206	0.252	3.3	0.004	-	-	-	0.16	0.11	0.05	45%
ITC-637	0.310	0.235	12.7	0.075	0.117	-0.042	- 36%	0.18	0.13	0.05	38%
	UCR-ITC Average					-0.013	- 20%			0.02	11%
	Std. Deviation					± 0.020	± 17%			±0.04	± 36%

(continued)

87048 5b

TABLE 6-20. (concluded)

Experiment Number	Maximum Ozone (ppm) Day 1 Calc. (ppm)	Day 1 Meas. (ppm)	Day 1 Abs. Diff.	Day 1 Pct. Diff.	Day 2 Calc. (ppm)	Day 2 Meas. (ppm)	Day 2 Abs. Diff.	Day 2 Pct. Diff.	Day 3 Calc. (ppm)	Day 3 Meas. (ppm)	Day 3 Abs. Diff.	Day 3 Pct. Diff.	Day 4 Calc. (ppm)	Day 4 Meas. (ppm)	Day 4 Abs. Diff.	Day 4 Pct. Diff.
ITC-630	0.228	0.284	-0.056	-19.7%	0.123	0.213	-0.090	- 42%	0.234	0.274	-0.040	- 15%	-	-	-	-
ITC-631	0.050	0.042	0.008	19.0%	0.097	0.165	-0.068	- 41%	0.294	0.242	0.052	21%	-	-	-	-
ITC-633	0.259	0.231	0.028	12.1%	0.218	0.340	-0.122	- 36%	0.188	0.272	-0.084	- 31%	-	-	-	-
ITC-635	0.018	0.006	0.012	200.0%	0.022	0.024	-0.002	- 8%	-	-	-	-	-	-	-	-
ITC-637	0.614	0.617	0.003	0.5%	0.630	0.577	0.053	9%	0.536	0.537	-0.001	0%	0.285	0.384	-0.099	- 26%
UCR-ITC Average			-0.001	42.4 (3.0)%			-0.046	- 24%			0.018	- 6%				
Std. Deviation			±0.032	±89.3 (16.9)%			±0.070	± 23%			±0.058	± 22%				

TABLE 6-21. Initial conditions for UNC hydrocarbon reactivity experiment simulations.

Experiment Number	Initial Concentrations (ppm)								Other Conditions				
	Gas Phase						Walls		Water Vapor (ppm)		Temperature (K)		Light Conditions
	NO	NO_2	NMOC (ppmC)	HONO	HCHO	CO	HCHO	k_{HONO}	Initial	Final	Initial	Final	
OC0382R	0.194	0.056	2.75	0.003	0.010	0.300	0.040	2.50E-5	17200	23200	288.6	301.6	Good
OC0382B	0.193	0.055	2.56	0.003	0.010	0.300	0.040	2.50E-5	17200	23200	288.6	301.6	Good
AU3181R	0.187	0.052	2.04	0.003	0.010	0.300	0.040	2.50E-5	15200	18000	291.5	304.8	Choppy
AU3181B	0.187	0.052	2.09	0.003	0.010	0.300	0.040	2.50E-5	15200	18000	291.5	304.8	Choppy
JL2281R	0.209	0.054	2.40	0.003	0.010	0.300	0.040	2.50E-5	15000	25000	303.0	303.0	Good
JL2281B	0.205	0.052	2.67	0.003	0.010	0.300	0.040	2.50E-5	15000	25000	303.0	303.0	Good
JN2581R	0.128	0.055	1.81	0.003	0.010	0.300	0.040	2.50E-5	15000	25000	296.4	307.7	Good
JN2581B	0.130	0.057	1.68	0.003	0.010	0.300	0.040	2.50E-5	15000	25000	296.4	307.7	Good
DC0782R	0.157	0.030	3.37	0.001	0.000	0.300	0.050	1.00E-5	9500	16300	279.7	289.5	Good
DC0782B	0.158	0.028	3.49	0.001	0.000	0.300	0.050	1.00E-5	9500	16300	279.7	289.5	Good
SE1481R	0.196	0.053	2.19	0.003	0.010	0.300	0.040	2.50E-5	12800	21000	289.0	302.8	Good
SE1481B	0.193	0.054	2.17	0.003	0.010	0.300	0.040	2.50E-5	12800	21000	289.0	302.8	Good
SE1682R	0.302	0.121	3.23	0.010	0.010	0.300	0.040	2.50E-5	20600	24200	294.6	306.2	Late Chop
SE1682B	0.302	0.121	3.13	0.010	0.010	0.300	0.040	2.50E-5	20600	24200	294.6	306.2	Late Chop
NV1182R	0.143	0.027	3.19	0.001	0.000	0.300	0.050	1.50E-5	7000	23000	276.7	295.5	Late Chop
NV1182B	0.143	0.028	3.36	0.001	0.000	0.300	0.050	1.50E-5	7000	23000	276.7	295.5	Late Chop
SE1882R	0.282	0.102	3.10	0.010	0.010	0.300	0.040	2.50E-5	22800	32400	291.5	306.0	Low Early
SE1882B	0.289	0.097	3.06	0.010	0.010	0.300	0.040	2.50E-5	22800	32400	291.5	306.0	Low Early
SE2081R	0.178	0.053	2.27	0.003	0.010	0.300	0.040	2.50E-5	12800	21000	279.5	298.3	Good
SE2081B	0.177	0.052	2.08	0.003	0.010	0.300	0.040	2.50E-5	12800	21000	279.5	298.3	Good
SE2981R	0.168	0.070	2.68	0.003	0.010	0.300	0.040	2.50E-5	7800	22000	278.8	296.2	Good
SE2981B	0.177	0.068	2.66	0.003	0.010	0.300	0.040	2.50E-5	7800	22000	278.8	296.2	Good
SE0381R	0.180	0.055	2.31	0.003	0.010	0.300	0.040	2.50E-5	22200	24200	292.1	303.5	Choppy
SE0381B	0.179	0.052	3.06	0.003	0.010	0.300	0.040	2.50E-5	22200	24200	292.1	303.5	Choppy
SE1081R	0.190	0.055	3.49	0.005	0.010	0.300	0.040	2.50E-5	10800	24800	283.9	302.6	Good
SE1081B	0.188	0.058	3.73	0.005	0.010	0.300	0.040	2.50E-5	10800	25800	283.9	302.6	Good
AU2681R	0.184	0.053	2.02	0.003	0.010	0.300	0.040	2.50E-5	17000	18000	287.1	302.1	Choppy
AU2681B	0.179	0.056	2.95	0.003	0.010	0.300	0.040	2.50E-5	17000	18000	287.1	302.1	Choppy
SE1984B	0.252	0.086	2.69	0.003	0.010	0.300	0.040	2.50E-5	12000	17600	280.2	299.7	Good
SE1984R	0.253	0.086	4.38	0.003	0.010	0.300	0.040	2.50E-5	12000	17600	280.2	299.7	Good

(continued)

TABLE 6-21. (continued)

Experiment Number	Experimental Design		Notes
OC0382R	Ratio Test:	2.8 SIMmix @ 11.0 to 1	Dried but HEAVY condensation
OC0382B		1.6 SIMmix @ 6.3 to 1	Vented 24 hours
AU3181R	Matched:	2.0 SIMmix @ 8.5 to 1	Dried and NO condensation
AU3181B		2.1 UNCmix @ 8.7 to 1	Vented 24 hours
JL2281R	Substitution:	2.4 UNCmix @ 9.1 to 1	No drying and NO condensation
JL2281B		1.8 UNCmix + 0.8 MXY @ 10.4 to 1	Vented 8 hours
JN2581R	Substitution:	1.3 UNCmix + 0.5 ISOP @ 9.9 to 1	No drying and NO condensation
JN2581B		1.7 UNCmix @ 9.0 to 1	Used 1982 light/choppy
DC0782R	Substitution:	2.5 UNCmix + 0.9 COMARO @ 18.0 to 1	No drying, OBSERVED condensation
DC0782B		3.5 UNCmix @ 18.8 to 1	Low initial temperature
SE1481R	Comparison:	1.6 UNCmix + 0.6 MXY @ 8.8 to 1	Dried and NO condensation
SE1481B		1.7 UNCmix + 0.5 TOL @ 8.8 to 1	Vented 7 hours
SE1682R	Comparison:	2.3 UNCmix + 0.9 EtBz @ 7.6 to 1	Dried and NO condensation
SE1682B		2.2 UNCmix + 0.9 MXY @ 7.4 to 1	Vented 24 hours
NV1182R	Comparison:	2.3 UNCmix + 0.9 TMBz @ 18.8 to 1	No drying, OBSERVED condensation
NV1182B		2.5 UNCmix + 0.8 PrBz @ 19.6 to 1	
SE1882R	Comparison:	2.2 UNCmix + 0.9 OXY @ 8.1 to 1	Dried but OBSERVED condensation
SE1882B		2.2 UNCmix + 0.9 MXY @ 7.9 to 1	Vented 6 hours, early light is low
SE2081R	Comparison:	1.6 UNCmix + 0.7 COMARO @ 9.8 to 1	Dried but SOME condensation
SE2081B		1.6 UNCmix + 0.5 SIMARO @ 9.1 to 1	Vented 7 hours

(continued)

TABLE 6-21. (concluded)

Experiment Number	Experimental Design		Notes
SE2981R	Comparison:	2.0 UNCmix + 0.5 TOL + 0.1 ALD2 @ 11.3 to 1	No drying, OBSERVED condensation
SE2981B		2.0 UNCmix + 0.5 MXY + 0.1 ALD2 @ 10.9 to 1	ALD2 not observed after injection
SE0381R	Addition:	1.8 UNCmix + 0.5 SIMARO @ 9.8 to 1	Dried and NO condensation, Vented 7 hours
SE0381B		1.9 UNCmix + 0.5 SIMARO + 0.6 PROPENE @ 13.2 to 1	High ETH on BLUE side, choppy light
SE1081R	Substitution:	2.8 UNCmix + 0.7 SIMARO @ 14.2 to 1	Dried and NO condensation
SE1081B		1.0 UNCmix + 0.5 SIMARO + 2.2 BUTANE @ 15.2 to 1	
AU2681R	Comparison:	1.5 UNCmix + 0.6 SIMARO @ 8.5 to 1	Dried and NO condensation
AU2681B		1.4 SIMmix + 0.6 SIMARO @ 8.3 to 1	Vented 7 hours
SE1984R	Ratio Test:	4.4 High MW Aromatic Fraction @ 17.2 to 1	Dried and NO condensation
SE1984B		2.7 High MW Aromatic Fraction @ 10.6 to 1	Vented 7 hours

TABLE 6-22. Results of UNC hydrocarbon reactivity experiment simulations.

Experiment Number	Initial Conditions			Maximum Ozone (ppm)			
	NO_x	NO_2/NO_x	HC/NO_x	Calc. (ppm)	Meas. (ppm)	Abs. Diff.	Pct. Diff.
OC0382B	0.248	0.222	10.3	0.159	0.158	0.001	0.6%
OC0382R	0.250	0.224	11.0	0.380	0.247	0.133	53.8%
AU3181B	0.239	0.218	8.7	0.565	0.530	0.035	6.6%
AU3181R	0.239	0.218	8.5	0.604	0.665	-0.061	- 9.2%
JL2281B	0.257	0.202	10.4	0.583	0.722	-0.139	-19.3%
JL2281R	0.263	0.205	9.1	0.555	0.618	-0.063	-10.2%
JN2581B	0.187	0.305	9.0	0.581	0.744	-0.163	-21.9%
JN2581R	0.183	0.301	9.9	0.806	0.830	-0.024	- 2.9%
DE0782B	0.186	0.151	18.8	0.100	0.093	0.007	7.5%
DE0782R	0.187	0.160	18.0	0.148	0.076	0.072	94.7%
SE1481B	0.247	0.219	8.8	0.418	0.441	-0.023	- 5.2%
SE1481R	0.249	0.215	8.8	0.663	0.685	-0.022	- 3.2%
SE1682B	0.423	0.286	7.4	0.869	0.840	0.029	3.5%
SE1682R	0.423	0.286	7.6	0.359	0.410	-0.051	-12.4%
NV1182B	0.171	0.164	19.6	0.182	0.220	-0.038	-17.3%
NV1182R	0.170	0.159	18.7	0.322	0.218	0.104	47.7%
SE1882B	0.386	0.251	7.9	0.798	0.791	0.007	0.9%
SE1882R	0.384	0.266	8.1	0.833	0.669	0.164	18.5%
SE2081B	0.229	0.227	9.1	0.438	0.414	0.024	5.8%
SE2081R	0.231	0.229	9.4	0.467	0.404	0.063	15.6%
SE2981B	0.245	0.273	10.4	0.528	0.485	0.043	8.9%
SE2981R	0.238	0.294	10.8	0.409	0.294	0.115	39.1%
SE0381B	0.231	0.225	10.5	0.650	0.611	0.039	6.4%
SE0381R	0.235	0.238	9.8	0.400	0.542	-0.142	-26.2%
SE1081B	0.246	0.236	15.1	0.642	0.626	0.016	2.6%
SE1081R	0.245	0.224	14.8	0.653	0.611	0.042	6.9%
AU2681B	0.235	0.238	8.3	0.559	0.544	0.015	3.8%
AU2681R	0.237	0.224	8.5	0.548	0.506	0.042	8.3%
SE1984B	0.338	0.254	10.6	0.448	0.438	0.010	2.3%
SE1984R	0.339	0.254	17.2	0.446	0.378	0.068	18.0%
			Average			0.010	7.5%
			Std. Deviation			±0.076	±25.6%

(continued)

TABLE 6-22. (concluded)

Experiment Number	Maximum PAN (ppm) Calc. (ppm)	Meas. (ppm)	Abs. Diff.	Pct. Diff.	Maximum HCHO (ppm) Calc. (ppm)	Meas. (ppm)	Abs. Diff.	Pct. Diff.
OC0382B	0.007	0.004	0.003	75%	0.09	-	-	-
OC0382R	0.025	0.008	0.017	213%	0.14	-	-	-
AU3181B		-	-	-	0.09	0.12	-0.03	- 25%
AU3181R		-	-	-	0.10	0.13	-0.03	- 23%
JL2281B	0.089	0.097	-0.008	- 8%	0.11	0.17	-0.06	- 35%
JL2281R	0.053	0.055	-0.002	- 4%	0.10	0.17	-0.07	- 41%
JN2581B	0.031	0.027	0.004	15%	0.08	0.08	0.00	0%
JN2581R	0.075	0.044	0.031	70%	0.18	0.22	-0.04	- 18%
DE0782B	0.017	0.009	0.008	89%	0.10	0.10	0.00	0%
DE0782R	0.031	0.010	0.021	210%	0.09	0.06	0.03	50%
SE1481B	0.025	-	-	-	0.08	-	-	-
SE1481R	0.066	-	-	-	0.10	-	-	-
SE1682B	0.090	0.047	0.043	91%	0.15	0.19	-0.04	- 21%
SE1682R	0.020	0.015	0.005	33%	0.12	0.14	-0.02	- 14%
NV1182B	0.025	-	-	-	0.11	0.20	-0.09	- 45%
NV1182R	0.070	-	-	-	0.11	0.16	-0.05	- 31%
SE1882B	0.079	0.087	-0.008	- 9%	0.13	0.17	-0.04	- 24%
SE1882R	0.086	0.070	0.016	23%	0.13	0.10	0.03	30%
SE2081B	0.054	-	-	-	0.08	-	-	-
SE2081R	0.061	-	-	-	0.08	-	-	-
SE2981B	0.109	-	-	-	0.10	-	-	-
SE2981R	0.066	-	-	-	0.09	-	-	-
SE0381B	0.089	-	-	-	0.18	-	-	-
SE0381R	0.034	-	-	-	0.09	-	-	-
SE1081B	0.055	-	-	-	0.06	-	-	-
SE1081R	0.085	-	-	-	0.13	-	-	-
AU2681B	0.051	-	-	-	0.09	0.15	-0.06	- 40%
AU2681R	0.053	-	-	-	0.08	0.11	-0.03	- 27%
SE1984B	0.070	0.103	-0.033	- 32%	0.05	0.07	-0.02	- 29%
SE1984R	0.106	0.124	-0.018	- 15%	0.08	0.13	-0.05	- 38%
Average			0.006	54%			-0.03	- 18%
Std. Deviation			±0.020	± 78%			±0.03	± 25%

7 SUMMARY AND CONCLUSIONS

This report documents the development and evaluation of the Carbon-Bond Mechanism-IV (CBM-IV), a gas-phase photochemical kinetics mechanism suitable for inclusion in both urban and regional air quality simulation models. It also summarizes the mechanism development philosophy that has led to the carbon-bond approach over the past fifteen years of continuous EPA support. We describe the relevant decisions on the inclusion of fundamental kinetic and stochiometric data, the approaches used to condense these data into a carbon-bond mechanistic structure, and the eventual choices made to reduce the extended CBM-X to the condensed CBM-IV. The most concise summary of this work is the CBM-IV listing provided in Table 1-3. All fundamental decisions ultimately appear in the mechanism listing.

The development of the CBM-IV initially proceeded through a gathering of recent chemical kinetic and mechanistic data-pertinent tropospheric gas-phase chemistry. The reaction rates and product yields were then updated and tested. In particular, large portions of the inorganic section were altered to reflect current thought. We also undertook the task of improving a few specific portions of the organic chemistry section where there was ample data available to test our assumptions. Specifically, we investigated

(1) The reactions of peroxyacetyl radical with NO_x species and other radicals,

(2) The kinetics and product yields of radical-radical self-reactions,

(3) New representations for toluene and xylene oxidation reactions, and

(4) The condensation of the isoprene oxidation mechanism and development of α-pinene carbon-bond fractions.

Finally, we altered all sections of the organic reaction mechanism that previously utilized formaldehyde as a surrogate for other species so that the concentration of the species FORM in the CBM-IV is now explicitly that of formaldehyde.

The improvements to the temperature-dependent kinetics of the peroxyacetyl radical reactions with NO and NO_2 were shown to lead to much better simulation of PAN formation and decay in simple acetaldehyde and biacetyl systems. These changes, combined with the improvements to the organic radical self-reaction rate constants and product yields, have led to what appears to be a more accurate simulation of radical concentrations throughout a simulation day. The basis for this assertion is the better prediction of hydrocarbon, especially aromatic hydrocarbon, decay rates (indicators of OH concentration) and the performance of the CBM-IV in simulating the shape of PAN formation and decay throughout the day.

The chemistry of aromatic hydrocarbons, particularly toluene and other mono-substituted benzenes, was updated to reflect the chemical characteristics apparent from smog chamber data for those species. Particularly important was the fact that toluene (and to a lesser extent, xylene) smog chamber systems tend to rapidly deplete NO until ozone formation is curtailed, but toluene decay continues. These data trends suggested an alternate pathway for the reaction of the initial OH-O_2-aromatic adduct when NO is sufficiently low that such a reaction could be competitive. This assumption removed the exclusive reaction of the adduct with NO (found in all other mechanisms) and led to a far better prediction of chemical dynamics in these systems.

The isoprene reaction mechanism was also reanalyzed and a new condensed formulation was performed. This resulted in a far better predictive capability for maximum ozone concentration, actually simulating the double ozone peaks characteristic of isoprene systems (due to late afternoon PAN decomposition on hot days). In addition, since the CBM-IV is now explicitly predicting the concentration of formaldehyde, the reformulation of the condensed isoprene mechanism was directed toward accurate formaldehyde product formation. Comparisons of simulation results with experimental data were very good, indicating that the use of isoprene in the CBM-IV simulation of rural systems should not be hampered by poor representations. Continuing with biogenic hydrocarbon species, we also used the available University of North Carolina smog chamber data to improve our carbon-bond fractionation scheme for α-pinene. Although the simulation results were not as astounding as those for isoprene, they were quite accurate considering the complexity of the molecule and the less-than-average light conditions for many of the simulation days.

Besides specific kinetic and mechanistic improvements to the chemical mechanism, we also provide a detailed description of some important topics not directly addressed in earlier CBM development documents. These include

(1) The basic philosophy of the carbon-bond approach and the specific implementation of that philosphy in the alkane section of the CBM-IV,

(2) The rationale used for condensation of specific sections of the CBM-X in the CBM-IV,

(3) A description of the photolysis rate data and application of photolysis reactions in specific chambers and in the atmosphere, and

(4) A discussion of the chamber artifact reactions used to simulate different smog chambers and the basis for the development of specific reaction-rate constants.

The last of these topics is fundamental to the accurate simulation of smog chamber experiments. There is, however, a great deal of uncertainty in these approximations, which we attempt to note throughout the discussion. Nevertheless, the comparison of mechanism predictions with smog chamber data must be performed to improve, and later to evaluate, the mechanism performance against a controlled but complex mixture of hydrocarbons and NO_x.

Mechanism evaluation and demonstration of the chemical dynamic characteristics of the CBM-IV were performed using approximately 170 smog chamber experiments from the different smog chambers at the University of North Carolina and the University of California at Riverside facilities. We compared maximum experimental ozone, PAN, and formaldehyde concentrations with predicted values and also provided plots of these concentration comparisons for each experiment so that we could discuss the dynamic processes and compare the goodness-of-fit over the entire experimental period.

As noted, we were particularly pleased that the improvements to the isoprene condensation and the representation of toluene (and other aromatics) oxidation processes provided much better predictions of ozone and formaldehyde than had occurred in previous mechanisms. For the isoprene tests, the mechanism overpredicted maximum ozone concentrations by 6 (±22) percent and for the aromatic experiments the overprediction was 1 (±12) percent. These results indicate that the new mechanistic representations significantly diminish the uncertainty associated with these calculations.

Less obvious in the overall results were the improvements to predictive capabilities provided by the enhanced organic radical, and peroxyacetyl reaction chemistry. These changes appear to have increased the accuracy

of the radical concentration predictions during the midday period, resulting in better agreement between PAN formation-and-decay rates and hydrocarbon decay rates over a large range of temperatures. These improvements and others described above led to a slight overprediction (2 ±22 percent) of maximum ozone concentration averaged for simulations of 68 different experimental mixtures in three different smog chambers. Maximum formaldehyde concentrations were underpredicted by 9 (±34) percent for these mixture experiments. Given the larger uncertainties in this calculation due to both ambiguous organic oxidation processes and less precise measurement methods (than for ozone), we consider these results very good.

Remaining uncertainties in the mechanism result primarily from two areas: (1) The fundamental information from which we develop mechanistic representations is sparse in certain key areas, and (2) The smog chamber data with which we test these mechanisms is itself uncertain in some respects. With regard to specific chemistry, we are most concerned with uncertainties that may exist in the alkene and aromatic representations. As we have noted, the successful predictions of the aromatic mechanism were gratifying, but since the fundamental information concerning the aromatic oxidation kinetics and mechanisms is still poorly understood, we cannot be sure the predictions are founded on the actual chemistry. Therefore, the mechanism could display anomalies outside the range of conditions in the smog chamber test environment. Conversely, though many of the basic oxidation reaction kinetics for the alkene (ethene and olefin) mechanisms have supposedly been identified, these mechanisms often perform poorly in the simulation of smog chamber measurements. Whether this is due to inconsistencies in the mechanism or uncertainties in the description of the smog chamber environment should be investigated.

Uncertainties in smog chamber information, particularly the effects of chamber surfaces and spectral distribution of in-chamber light, are currently being reviewed by a number of groups. It is imperative now that researchers and simulators merge their opinions and knowledge of these systems so that we may minimize uncertainties related to wall radical sources, surface collection and emission of key reactive species, and daily changes in both light and surface conditions. This process would not only enable us to define key experiments for mechanism testing, but should provide information for the clarification of many marginal experimental data sets, thus allowing the already existing data to be utilized in a more effective manner.

In conclusion, we find the CBM-IV an improved and well-performing mechanism, suitable for use in regional and urban air quality simulation models. Certain uncertainties remain in the mechanism due to lack of fundamental kinetic data in a few key areas, most notably in aromatic and organic radical chemistry. In addition, smog chamber information data

could be improved and utilized to better advantage if significant chamber environmental aspects (radiation and surface effects) could be better defined. We recommend a focus on these uncertainties so that more useful test cases can be employed in future mechanism development and evaluation efforts.

REFERENCES

Addison, M. C., J. P. Burrows, R. A. Cox, and R. Patrick. 1980. Absorption spectrum and kinetics of the acetylperoxy radical. Chem. Phys. Lett., 73:283-287.

Akimoto, H., M. Hoshino, G. Inoue, F. Kakamaki, N. Washida, and M. Okuda. 1979. Design and characterization of the evaluable and bakable photochemical smog chamber. Environ. Sci. Technol., 13(4):471-475.

Atkinson, R., W.P.L. Carter, K. R. Darnall, A. M. Winer, and J. N. Pitts, Jr. 1980. A smog chamber and modeling study of the gas phase NO_x-air photooxidation of toluene and the cresols. Int. J. Chem. Kinet., 12:779-836.

Atkinson, R. 1986. Kinetics and mechanisms of the gas-phase reactions of the hydroxyl radical with organic compounds under atmospheric conditions. Chem. Rev., 86:69-201.

Atkinson, R., A. C. Lloyd, and L. Winges. 1982a. An updated chemical mechanism for hydrocarbon/NO_x/SO_2 photooxidations suitable for inclusion in atmospheric simulation models. Atmos. Environ., 16(6):1341-1355.

Atkinson, R., S. M. Aschman, W.P.L. Carter, A. M. Winer, and J. N. Pitts, Jr. 1982b. Alkyl nitrate formation from the NO_x--air photooxidations of C_2-C_8 n-alkanes. J. Phys. Chem., 86:4563-4569.

Atkinson, R., S. M. Aschman, and A. M. Winer. 1987. Alkyl nitrate formation from the reaction of a series of branched RO_2 radicals with NO as a function of temperature and pressure. J. Atmos. Chem., 5:91-102.

Atkinson, R., W.P.L. Carter, and A. M. Winer. 1983. Effects of temperature and pressure on alkyl nitrate yields in the NO_x photooxidations of n-pentane and n-heptane. J. Phys. Chem., 87:2012-2018

Atkinson, R., and W.P.L. Carter. 1987. Atmospheric Chemistry of Alkanes. J. Atmos. Chem., 3:377-405.

Atkinson, R., and A. C. Lloyd. 1984. Evaluation of kinetic and mechanistic data for modeling of photochemical smog. J. Phys. Chem. Ref. Data, 13:315-444.

Atkinson, R., and W.P.L. Carter. 1984. Kinetics and mechanisms of the gas-phase reactions of ozone with organic compounds under atmospheric conditions. Chem. Rev., 84:437-470.

Atkinson, R., and S. M. Aschmann. 1984. "Rate constants for the reaction of OH radicals with a series of alkenes and dialkenes at 295 ± 1 K. Int. J. Chem. Kinet., 16:1175-1186.

Atkinson, R., S. M. Aschmann, A. M. Winer, and J. N. Pitts, Jr. 1984. Kinetics of the gas-phase reactions of NO_3 radicals with a series of dialkenes, cycloalkenes, and monoterpenes at 295 ± 1 K. Environ. Sci. Technol., 18(5):375.

Atkinson, R., and J. N. Pitts, Jr. 1977. Absolute rate constants for the reaction of $O(^3P)$ atoms with a series of olefins over the temperature range 298-439° K. J. Chem. Phys., 67:38.

Bandow, H., N. Washida, and H. Akimoto. 1985. Ring-cleavage reactions of aromatic hydrocarbons studied by FT-IR spectroscopy. I. Photooxidation of toluene and benzene in the NO_x-air system. Bull. Chem. Soc. Jpn., 58:2531-2540.

Bandow, H., and N. Washida. 1985. Ring-cleavage reactions of aromatic hydrocarbons studied by FT-IR spectroscopy. II. Photooxidation of o-, m-, and p-xylenes in the NO_x-air system. Bull. Chem. Soc. Jpn., 58:2541-2548.

Bass, A. 1985. Personal communication with Arnold M. Bass, National Bureau of Standards, Gaithersburg, Maryland.

Bass, A. M., L. C. Glasgow, C. Miller, J. P. Jesson, and D. L. Filken. 1980. Planet Space Sci., 28:675.

Barnes, I., V. Bastian, K. H. Becker, E. H. Fink, and F. Zabel. 1985. Pressure dependence of the reaction of OH with HO_2NO_2. Chem. Phys. Lets., 123:28-32.

Basco, N., and S. Parmar. 1987. The reaction of acetylperoxy radicals with NO_2. IJCR, 19:115-128.

Baulch, D. L., R. A. Cox, R. F. Hampson, Jr., J. A. Kerr, J. Troe, and R. T. Watson. 1984. Evaluated kinetic and photochemical data for atmospheric chemistry: Supplement II. CODATA Task Group on gas phase chemical kinetics. J. Phys. Chem. Ref. Data, 13(4):1259-1380.

Basemer, A. C., and H. Nieboer. 1985. The wall as a source of hydroxyl radicals in smog chambers. Atmos. Environ., 19(3):507-513.

Becker, U., M. Y. Ben-Sira, S. Fritz, F. Möller, W. Schöepp, G. Yamamoto, and N. Robinson. 1966. Solar Radiation. N. Robinson, ed. (Elsevier Publishing Company, New York).

Benson, S. W. 1976. Thermochemical Kinetics. 2nd ed., John Wiley & Sons, New York.

Benson, S. W., and J. H. Buss. 1958. J. Chem. Phys., 29:546.

Bessmer, A. C., and H. Nieboer. 1985. The wall as a source of hydroxyl radicals in smog chambers. Atmos. Environ., 19(3):507-513.

Betterton, E. A., and M. R. Hoffmann. 1987. Kinetics, mechanism, and thermodynamics of the reversible reaction of methylglyoxal (CH_3COCHO) with S(IV). J. Phys. Chem., 91:3011-3020.

Calvert, J. G. 1980. "The Homogeneous Chemistry of Formaldehyde Generation and Destruction Within the Atmosphere." Proceedings of the NATO Advanced Study Institute on Atmospheric Ozone, U.S. Department of Transportation, F.A.A., Office of Environment and Energy, High Altitude Program, Washington, D.C.

Calvert, J. G., and J. N. Pitts. 1966. Photochemistry, John Wiley, New York.

Cantrell, C. A., W. R. Stockwell, L. G. Anderson, K. L. Busarow, D. Perner, A. Schmeltekopf, J. G. Calvert, and H. S. Johnston. 1985. Kinetic study of the NO_3-CH_2O reaction and its possible role in nighttime tropospheric chemistry. J. Phys. Chem., 89:139-146.

Carter, W.P.L. 1987. Personal communication with William Carter, Statewide Air Pollution Research Center, University of California, Riverside, California.

Carter, W.P.L., A. C. Lloyd, J. L. Sprung, and J. N. Pitts, Jr. 1979. Computer modeling of smog chamber data: Progress in validation of a detailed mechanism for the photooxidation of propene and n-butane in photochemical smog. Int. J. Chem. Kinet., 11:45-103.

Carter, W.P.L., F. W. Lurmann, R. Atkinson, and A. Lloyd. 1986. "Development and Testing of a Surrogate Species Chemical Reaction Mechanism." U.S. Environmental Protection Agency, Research Triangle Park, North Carolina (EPA/600/3-86/031).

Carter, W.P.L., M. C. Dodd, W. D. Long, and R. Atkinson. 1985. "Outdoor Chamber Study to Test Multi-Day Effects--Volume I: Results and Discussion." Final Report, U.S. Environmental Protection Agency (EPA/600/3-84/115).

Carter, W.P.L., R. Atkinson, A. M. Winer, and J. N. Pitts, Jr. 1982. An experimental investigation of chamber-dependent radical sources. Int. J. Chem. Kinet., in press.

Cattell, F. C., J. Cavanagh, R. A. Cox, and M. E. Jenkin. 1986. A kinetics study of reactions of HO_2 and $C_2H_5O_2$ using diode laser absorption spectroscopy. J. Chem. Soc., 82:1999-2018.

Cox, R. A., K. F. Patrick, and S. A. Chant. 1981. Mechanisms of atmospheric photooxidation of organic compounds. Reactions of alkoxy radicals in oxidation of n-butane and simple ketones. Environ. Sci. Technol., 15:587.

Cox, R. A., and G. S. Tyndall. 1980. J. Chem. Soc., Faraday Trans II, 76:153.

Cox, R. A., and M. J. Roffey. 1977. Thermal decomposition of peroxyacetylnitrate in the presence of nitric oxide. Environ. Sci. Technol., 900-906.

Cox, R. A., and R. G. Derwent. 1975. Photolysis of Nitrous Acid in the Presence of Acetaldehyde. J. Chem. Soc., Faraday Trans. I, 72:2061-2075.

Darnall, K. R., W.P.L. Carter, A. C. Lloyd, A. M. Winer, and J. N. Pitts, Jr. 1976. Importance of RO_2 + NO in alkyl nitrate formation from C_4-C_6 alkane photooxidation under simulated atmospheric conditions. J. Phys. Chem., 80:1948-1950.

Demerjian, K. L., J. A. Kerr, and J. G. Calvert. 1974. The mechanism of photochemical smog formation. Adv. in Environ. Sci. and Tech., 4, John Wiley and Sons.

Demerjian, K. L., K. L. Schere, and J. T. Peterson. 1980. Theoretical estimates of actinic (spherically integrated) flux and photolytic rate constants of atmospheric species in the lower troposphere. Adv. Environ. Sci. Technol., 10:369-460.

DeMore, W. B., J. J. Margitan, M. J. Molina, R. T. Watson, D. M. Golden, R. F. Hampson, M. J. Kurylo, C. J. Howard, and A. R. Ravishankara. 1985. "Chemical Kinetics and Photochemical Data for Use in Stratospheric Modeling." Evaluation Number 7. Jet Propulsion Laboratory, Pasadena, California (85-37).

DeMore, W. B., M. J. Molina, R. T. Watson, D. M. Golden, R. F. Hampson, M. J. Kurylo, C. J. Howard, and A. R. Ravishankara. 1983. "Chemical Kinetics and Photochemical Data for Use in Stratospheric Modeling." Evaluation Number 6. Jet Propulsion Laboratory, Pasadena, California (83-62).

Dodge, M. C., and R. R. Arnts. 1979. A new mechanism for the reaction of ozone with olefins. Int. J. Chem. Kinet., 11:399-410.

Dumdei, B. E., and R. J. O'Brien. 1984. Toluene degradation products in simulated atmospheric conditions. Nature, 311:248-250.

Gery, M. W. 1987. "Review of Chemical Mechanism Development and Evaluation." In "Workshop on Evaluation/Documentation of Chemical Mechanisms," (EPA/600/9-87/024).

Gery, M. W., D. L. Fox, H. E. Jeffries, L. Stockburger, and W. S. Weathers. 1985. A continuous stirred tank reactor investigation of the gas-phase reaction of hydroxyl and toluene. Int. J. Chem. Kinet., 17:931-955.

Gery, M. W., D. L. Fox, R. M. Kamens, and L. Stockburger. 1987. Investigation of hydroxyl radical reactions with o-xylene and m-xylene in a continuous stirred tank reactor. Environ. Sci. Technol.. 21:339.

Graham, R. A., and H. S. Johnston. 1978. The photochemistry of NO_3 and the kinetics of the N_2O_5-O_3 system. J. Phys. Chem., 82(3):254-268.

Grosjean, D., R. Countess, K. Fung, K. Ganesan, A. Lloyd, and F. Lurmann. 1981. "Deriving Empirical Kinetic Modeling Approach Isopleths from Experimental Data: The Los Angeles Captive-Air Study." Environmental Research and Technology. Inc., Westlake Village, California.

Hammer, P. D., E. J. Dlugokencky, and C. J. Howard. 1986. Kinetics of the gas-phase reaction $NO + NO_3 \rightarrow 2NO_2$. J. Phys. Chem., 90:2491-2496.

Hendry, D. G., and R. A. Kenley. 1979. "Atmospheric Reaction Products of Organic Compounds." U.S. Environmental Protection Agency, Office of Toxic Substances, Washington, D.C. (EPA-560/12-79-001).

Herron, J. T., and R. E. Huie. 1977. Stopped-flow studies of the mechanisms of ozone-alkene reactions in the gas phase. Ethylene. J. Amer. Chem. Soc., 99(16): 5430-5435.

Horowitz, A., and J. G. Calvert. 1978. Int. J. Chem. Kinet., 10:805.

Horowitz, A., and J. G. Calvert. 1982. Wavelength dependence of the primary processes in acetaldehyde photolysis. J. Phys. Chem., 86:3105-3114.

Jeffries, H. E., R. M. Kamens, K. G. Sexton, and A. A. Gerhardt. 1982. "Outdoor Smog Chamber Experiments to Test Photochemical Models." U.S. Environmental Protection Agency, Office of Research and Development, Research Triangle Park, North Carolina (EPA-600/3-82-016).

Jeffries, H. E., and J. A. Arnold. 1987. "The Science of Photochemical Reaction Mechanism Development and Evaluation." Proceedings of the EPA Workshop on Evaluation/Documentation of Chemical Mechanisms, Raleigh, North Carolina.

Jeffries, H. E., D. Fox, and R. Kamens. 1976. Outdoor smog chamber studies: light effects relative to indoor chambers. Environ. Sci. Technol., 10(10):1006-1011.

Jeffries, H. E., K. G. Sexton, T. P. Morris, M. Jackson, R. G. Goodman, R. M. Kamens and M. S. Holleman. Outdoor Smog Chamber Experiments Using Automobile Exhaust. EPA 600/3-85-032, U.S. Environmental Protection Agency. Research Triangle Park, North Carolina, 1985a.

Jeffries, H. E. 1986. "User's Guide to Photochemical Kinetics Simulation System. PC-PKSS." University of North Carolina, Chapel Hill, North Carolina.

Jeffries, H. E., and K. G. Sexton. 1987. "Technical Discussion Related to the Choice of Photolytic Rates for Carbon Bond Mechanisms in OZIPM4/EKMA. U.S. Environmental Protection Agency, Research Triangle Park, North Carolina (EPA-450/4-87-003).

Jeffries. 1987. Personal communication with Harvey E. Jeffries, University of North Carolina, Chapel Hill, North Carolina.

Kaiser, E. W., and C. H. Wu. 1977. J. Phys. Chem., 81:1701.

Kamens, R. M., H. E. Jeffries, K. G. Sexton, and A. A. Gerhardt. 1981. "Smog Chamber Experiments to Test Oxidant Related Control Strategy Issues." Department of Environmental Sciences and Engineering, School of Public Health, University of North Carolina, Chapel Hill, North Carolina.

Kan, C. S., J. C. Calvert, and J. H. Shaw. 1980. "Reactive Channels of the CH_3O_2-CH_3O_2 Reaction." Department of Chemistry and Department of Physics, Ohio State University, Columbus, Ohio.

Kan, C. S., F. Su, J. G. Calvert, and J. H. Shaw. 1981. Mechanism of the ozone--ethene reaction in dilute N_2/O_2 mixtures near 1-atm pressure. J. Phys. Chem., 85:2359-2363.

Kelly, N. A. 1982. Characterization of fluorocarbon-film bags as smog chambers. Environ. Sci. Technol., 16(11):763.

Kerr, J. A., and J. G. Calvert. 1985. Chemical Transformation Modules for Eulerian Acid Deposition Models--Volume I: The Gas-Phase Chemistry. EPA-600/3-85-015, National Center for Atmospheric Research, Boulder, Colorado.

Killus, J. P. 1982. "Background Reactivity Estimates for Atmospheric Modeling Studies." Systems Applications, Inc., San Rafael, California. XVth Informal Conference on Photochemistry, Stanford, California (27 June-1 July 1982).

Killus, J. P., and G. W. Whitten. 1982. "A New Carbon-Bond Mechanism for Air Quality Simulation Modeling." U.S. Environmental Protection Agency, Research Triangle Park, North Carolina (EPA 600/3-82-041).

Killus, J. P., and G. Z. Whitten. 1982. A mechanism describing the photochemical oxidation of toluene in smog. Atmos. Environ., 16(8):1973-1988.

Killus, J. P., and G. Z. Whitten. 1984. Isoprene: A photochemical kinetic mechanism. Environ. Sci. Technol., 18:142-148.

Kleindienst, T. E., G. W. Harris, and J. N. Pitts, Jr. 1982. Rates and temperature dependences of the reaction of OH with isoprene, its oxidation products, and selected terpenes. Environ. Sci. Technol., 16(12):844-846.

Ledbury, W., and E. W. Blair. 1925. The partial formaldehyde vapour pressure of aqueous solutions of formaldehyde. Part II. J. Chem. Soc., 127:2832-2839.

Lee, Y. N., and S. E. Schwartz. 1981. J. Phys. Chem., 85:840.

Leone, J. A., R. C. Flagan, D. Grosjean, and J. H. Seinfeld. 1985. An outdoor smog chamber and modeling study of toluene--NO_x photooxidation. International J. Chemical Kinetics, 17:177-216.

Leone, J. A., and J. H. Seinfeld. 1984. Updated chemical mechanism for atmospheric photooxidation of toluene. Int. J. Chem. Kinet., 16:159-193.

Lurmann, F. W., W.P.L. Carter, and L. A. Coyner. 1987. "A Surrogate Species Chemical Reaction Mechanism for Urban-Scale Air Quality Simulation Models. Volume II. Guidelines for Using the Mechanism" (EPA/600/3-87/014b).

Malko, M. W., and J. Troe. 1982. Analysis of the unimolecular reaction $N_2O_5 + M \rightleftharpoons NO_2 + NO_3 + M$. Int. J. Chem. Kinet., 14:399-416.

McAdam, K., B. Veyret, and R. Lesclaux. 1987. UV absorption spectra of HO_2 and CH_3O_2 radicals and the kinetics of their mutual reactions at 298 K. Chem. Phys. Lets., 133:39-44.

Moortgat, G. K. 1986. Personal communication with Geert Moortgat, Max-Planck-Institute, Mainz, W. Germany.

Moortgat, G. K., F. Slemr, W. Seiler, and P. Warneck. 1978. Photolysis of formaldehyde: Relative quantum yields of H_2 and CO in the wavelength range 270-360 nm. Chem. Phys. Lett., 54(3):444.

Moortgat, G. K., and P. Warneck. 1979. CO and H_2 quantum yields in the photodecomposition of formaldehyde in air. J. Chem. Phys., 70(8):3639.

NCAR. 1987. "Development and Implementation of Chemical Mechanisms for the Regional Acid Deposition Model (RADM)." National Center for Atmospheric Research, U.S. Environmental Protection Agency, Research Triangle Park, North Carolina.

Niki, H., P. D. Maker, C. M. Savage, and L. P. Breitenbach. 1977. Fourier transform ir spectroscopic observation of prophylene ozonide in the gas phase reaction of ozone-cis-2-butane-formaldehyde. Chem. Phys. Lets., 46:327-330

Niki, H., P. D. Maker, C. M. Savage, and L. P. Breitenbach. 1978. Mechanism for hydroxyl radical initiated oxidation of olefin-nitric oxide mixtures in parts per million concentrations. J. Phys. Chem., 82(2):135-137.

Niki, H., P. D. Maker, C. M. Savage, and L. P. Breitenbach. 1981. A FT IR study of a transitory product in the gas-phase ozone-ethylene reaction. J. Phys. Chem., 85:1024-1027.

Niki, H., P. D. Maker, C. M. Savage, and L. P. Brietenbach. 1982. Fourier transform infrared studies of the self-reaction of CH_3O_2 radicals. J. Phys. Chem., 85:877-881.

Ohta, T., and T. Ohyama. 1985. A set of rate constants for the reactions of OH radicals with aromatic hydrocarbons. Bull. Chem. Soc. Jpn., 58:3029-3030.

Perner, D., A. Schmeltekopf, R. H. Winkler, H. S. Johnston, J. G. Calvert, C.A. Cantrell, and W. R. Stockwell. 1985. A laboratory and field study of the equilibrium $N_2O_5 \rightleftharpoons NO_3 + NO_2$. J. Geophys. Res., 90(D2):3807-3812.

Peterson, J. T. 1976. "Calculated Actinic Fluxes for Air Pollution Photochemistry Applications." U.S. Environmental Protection Agency, Research Triangle Park, North Carolina (EPA-600/4-76-002).

Peterson, J. T., E. C. Flowers, G. J. Berri, C. L. Reynolds, and J. H. Rudsill. 1981. Atmospheric turbidity over Centrol North Carolina. J. Appl. Meteorol., 20:229-241.

Pitts, J. N., Jr., K. R. Darnell, W.P.L. Carter, A. M. Winer, and R. Atkinson. 1979. "Mechanisms of Photochemical Reactions in Urban Air." U.S. Environmental Protection Agency, Research Triangle Park, North Carolina (EPA-600/3-79-110).

Pitts, J. N., Jr., A. M. Winer, and W.P.L. Carter. 1981. "Chemical Consequences of Air Quality Standards and of Control Implementation Programs." California Air Resources Board (Contract No. A8-145-31).

Pitts, J. N., Jr., E. Sanhueza, R. Atkinson, W.P.L. Carter, A. M. Winer, G. W. Harris, and C. N. Plum. 1984. An investigation of the dark formation of nitrous acid in environmental chambers. Int. J. Chem. Kinet., 16:919-939.

Pitts, J. N. 1983. "Chemical Consequences of Air Quality Standards and Control Implementation Programs." California Air Resources Board (ARB-R83-209).

Plum, C. N., E. Sanhueza, R. Atkinson, W.P.L. Carter, and J. N. Pitts, Jr. 1983. OH radical rate constants and photolysis rates of α-dicarbonyls. Environ. Sci. Technol., 17(8):479-484.

Saeger, M. 1977. "Experimental Measurements of Photolysis Rate of Nitrogen Dioxide." M. S. Technical Report, University of North Carolina.

Sakamaki, F., S. Hatakeyama, and H. Akimoto. 1983. Formation of nitrous acid and nitric oxide in the heterogeneous dark reaction of nitrogen dioxide and water vapor in a smog chamber. Int. J. Chem. Kinet., 15:1013.

Sander, S. P., and C. C. Kircher. 1986. Temperature dependence of the reaction $NO + NO_3 \rightarrow 2NO_2$. Chem. Phys. Letters, 126(2):149-152.

Sander, S. P., and M. Peterson. 1982. Temperature dependence of the $HO_2 + NO_2$ reaction and its relevance to tropospheric chemistry. 2nd Symposium: Composition of the Nonurban Troposphere. American Meteorological Society, Boston, Massachusetts.

Schwartz, S. E. 1984. "Gas-Aqueous Reactions of Sulfur and Nitrogen Oxides in Liquid-Water Clouds." In SO_2, NO, and NO_2 Oxidation Mechanisms: Atmospheric Considerations, J. G. Calvert, ed., Butterworth, Boston (pp. 173-208).

Shepson, P. B., E. O. Edney, and E. W. Corse. 1984. Ring fragmentation reactions on the photoxidations of toluene and o-xylene. J. Phys. Chem., 4122-4126.

Smalley, J. F., F. L. Nesbitt, and R. B. Klemm. 1985. Branching ratio for the hydrogen atom product channel in the reaction of ground-state atomic oxygen with ethylene. J. Phys. Chem., 90:491-497.

Stedman, D. H., R. B. Harvey, and R. R. Dickerson. 1977. "Measurement of Photons Involved in Photochemical Oxidant Formation." Int. Conf. on Photochem. Oxidant Pollution and Its Control, Proceedings, 2:753-762 (EPA-600/3-77-0016).

Su, F., J. G. Calvert, J. H. Shaw, H. Niki, P. D. Maker, C. M. Savage, and L. D. Breitenbach. 1979a. Spectroscopic and kinetic studies of a new metastable species in the photooxidation of gaseous formaldehyde. Chem. Phys. Lets., 65:221-225.

Su, F., J. G. Calvert, and J. H. Shaw. 1979b. Mechanism of the photooxidation of gaseous formaldehyde. J. Phys. Chem., 83(25):3185-3191.

Su, F., J. G. Calvert, and J. H. Shaw. 1980. A FTIR spectorscopic study of the ozone-ethene reaction mechanism in O_2-rich mixtures. J. Phys. Chem., 84:239-246.

Tuazon, E. C., H. MacLeod, R. Atkinson, and W.P.L. Carter. 1986. α-Dicarbonyl yields frm the NO_x-air photooxidations of a series of aromatic hydrocarbons in air. Environ. Sci. Technol., 20(4):383.

Veyret, B., J. Rayez, and R. Lesclaux. 1982. Mechanism of the photooxidation of formaldehyde studied by flash photolysis of CH_2-O-O_2-NO Mixtures. J. Phys. Chem., 86:3424-3430.

Whitten, G. Z., J. P. Killus, and R. G. Johnson. 1983. "Modeling of Simulated Photochemical Smog With Kinetic Mechanisms" (EPA-600/3-83/043).

Whitten, G. Z., D. R. Souten, M. W. Gery, and R. D. Edmond. 1986. "Potential Impact of Ethanol Emissions on Urban Smog: A Preliminary Modeling and Smog Chamber Study." Systems Applications, Inc., San Rafael, California (SYSAPP-86/090).

Whitten, G. Z., J. P. Killus, and R. G. Johnson. 1985a. "Modeling of Auto Exhaust Smog Chamber Data for EKMA Development." Systems Applications, Inc., San Rafael, California (EPA-600-3/85-025).

Whitten, G. Z., J. P. Killus, and R. G. Johnson. 1985b. "Development of a Chemical Kinetic Mechanism for the U.S. EPA Regional Oxidant Model." U.S. Environmental Protection Agency, Research Triangle Park, North Carolina (EPA-600/3-85-026).

Whitten, G. Z., and M. W. Gery. 1986. "Development of CBM-X Mechanisms for Urban and Regional AQSMs." U.S. Environmental Protection Agency, Research Triangle Park, North Carolina (EPA-600/3-86-012).

Whitten, G. Z., and H. Hogo. Mathematical Modeling of Simulated Photochemical Smog. EPA-600/3-77-011, U.S. Environmental Protection Agency, Research Triangle Park, North Carolina, 1977.

Whitten, G. Z., H. Hogo, and J. P. Killus. The Carbon-Bond Mechanism: A Condensed Kinetic Mechanism for Photochemical Smog. Environ. Sci. Technol., 14:699, 1980a.

Whitten, G. Z., J. P. Killus, and H. Hogo. Modeling of Simulated Photochemical Smog with Kinetic Mechanisms. EPA-600/3-80-028a, U.S. Environmental Protection Agency, Research Triangle Park, North Carolina, 1980b.

Whitten, G. Z. The Chemistry of Smog Formation: A Review of Current Knowledge. Environ. Int., 9:447-463, 1983.

Whitten, G. Z., H. Hogo, M. J. Meldgin, J. P. Killus, and P. J. Bekowies. 1979. "Modeling of Simulated Photochemical Smog With Kinetic Mechanisms" (EPA-600/3-79-001a).

Winer, A. M., K. R. Darnall, R. Atkinson, and J. N. Pitts, Jr. 1978. J. Phys. Chem. Ref. Data, 13(2):1984.

Zafonte, L., P. L. Rieger, and J. R. Holmes. 1976. "Nitrogen Dioxide Photolysis in the Los Angeles Atmosphere." Californa Air Resources Board, El Monte, California (Publication No. DTS-76-18).